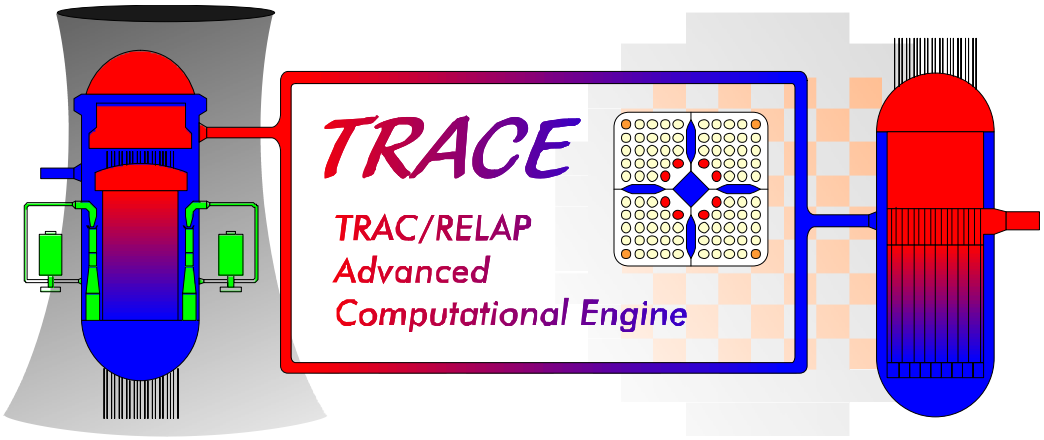

TRACE V5.0
THEORY MANUAL

Field Equations, Solution Methods, and Physical Models

Division of Risk Assessment and Special Projects
Office of Nuclear Regulatory Research
U. S. Nuclear Regulatory Commission
Washington, DC 20555-0001

This page intentionally left blank

Acknowledgements

Many individuals have contributed to the NRC code consolidation effort and to this manual, in particular. In a project of this magnitude and complexity, and given the long histories of the NRC predecessor codes and their associated manuals (from which this manual has evolved), it is rather difficult to sort out and keep track of each and every individual contribution of authorship. Rather than attempt to cite individual contributors to this particular manual (and run the risk of excluding somebody, either past or present), we simply acknowledge all known contributors to the TRACE code development and assessment project, in general.

Nuclear Regulatory Commission (NRC): Stephen Bajorek, Mirela Gavrilas, Chester Gingrich, James Han, Kevin Hogan, Joseph Kelly, William Krotiuk, Norman Lauben, Shanlai Lu, Christopher Murray, Frank Odar, Gene Rhee, Michael Rubin, Simon Smith, Joseph Staudenmeier, Jennifer Uhle, Weidong Wang, Kent Welter, James Han, Veronica Klein, William Burton, James Danna, John Jolicoeur, Sudhamay Basu, Imtiaz Madni, Shawn Marshall, Alex Velazquez, Prasad Kadambi, Dave Bessette, Margaret Bennet, Michael Salay, Andrew Ireland, William Macon, Farouk Eltawila

Advanced Systems Technology and Management (AdSTM): Yue Guan, David Ebert, Duke Du, Tong Fang, Weidong He, Millan Straka, Don Palmrose

Applied Programming Technologies (APT): Ken Jones

Applied Research Laboratory/Penn State (ARL/PSU): John Mahaffy, Mario Trujillo, Michal Jelinek, Matt Lazor, Brian Hansell, Justin Watson, Michael Meholic

Information System Laboratories (ISL): Birol Aktas, Colleen Amoruso, Doug Barber, Mark Bolander, Dave Caraher, Claudio Delfino, Don Fletcher, Dave Larson, Scott Lucas, Glen Mortensen, Vesselin Palazov, Daniel Prelewicz, Rex Shumway, Randy Tompot, Dean Wang, Jay Spore

Los Alamos National Laboratory (LANL): Brent Boyack, Skip Dearing, Joseph Durkee, Jay Elson, Paul Giguere, Russell Johns, James Lime, Ju-Chuan Lin, David Pimentel

Purdue University: Tom Downar, Matt Miller, Jun Gan, Han Joo, Yunlin Xu, Tomasz Kozlowski, Doek Jung Lee

Universidad Politecnica de Madrid: Roberto Herrero

Korean Nuclear Fuel Co: Jae Hoon Jeong

Korean Institute of Nuclear Safety: Chang Wook Huh, Ahn Dong Shin

Preface

Advanced computing plays a critical role in the design, licensing and operation of nuclear power plants. The modern nuclear reactor system operates at a level of sophistication whereby human reasoning and simple theoretical models are simply not capable of bringing to light full understanding of a system's response to some proposed perturbation, and yet, there is an inherent need to acquire such understanding. Over the last 30 years or so, there has been a concerted effort on the part of the power utilities, the U. S. Nuclear Regulatory Commission (USNRC), and foreign organizations to develop advanced computational tools for simulating reactor system behavior during real and hypothetical transient scenarios. The lessons learned from simulations carried out with these tools help form the basis for decisions made concerning plant design, operation, and safety.

The TRAC/RELAP Advanced Computational Engine (TRACE - formerly called TRAC-M) is the latest in a series of advanced, best-estimate reactor systems codes developed by the U.S. Nuclear Regulatory Commission for analyzing transient and steady-state neutronic-thermal-hydraulic behavior in light water reactors. It is the product of a long term effort to combine the capabilities of the NRC's four main systems codes (TRAC-P, TRAC-B, RELAP5 and RAMONA) into one modernized computational tool..

This manual is one of three manuals that comprise the basic TRACE documentation set. The other two are the Users' Manual and Developmental Assessment Manual.

Overview of TRACE

TRACE has been designed to perform best-estimate analyses of loss-of-coolant accidents (LOCAs), operational transients, and other accident scenarios in pressurized light-water reactors (PWRs) and boiling light-water reactors (BWRs). It can also model phenomena occuring in experimental facilities designed to simulate transients in reactor systems. Models used include multidimensional two-phase flow, nonequilibrium thermo-dynamics, generalized heat transfer, reflood, level tracking, and reactor kinetics. Automatic steady-state and dump/restart capabilities are also provided.

The partial differential equations that describe two-phase flow and heat transfer are solved using finite volume numerical methods. The heat-transfer equations are evaluated using a semi-implicit

time-differencing technique. The fluid-dynamics equations in the spatial one-dimensional (1D), and three-dimensional (3D) components use, by default, a multi-step time-differencing procedure that allows the material Courant-limit condition to be exceeded. A more straightforward semi-implicit time-differencing method is also available, should the user demand it. The finite-difference equations for hydrodynamic phenomena form a system of coupled, nonlinear equations that are solved by the Newton-Raphson iteration method. The resulting linearized equations are solved by direct matrix inversion. For the 1D network matrix, this is done by a direct full-matrix solver; for the multiple-vessel matrix, this is done by the capacitance-matrix method using a direct banded-matrix solver.

TRACE takes a component-based approach to modeling a reactor system. Each physical piece of equipment in a flow loop can be represented as some type of component, and each component can be further nodalized into some number of physical volumes (also called cells) over which the fluid, conduction, and kinetics equations are averaged. The number of reactor components in the problem and the manner in which they are coupled is arbitrary. There is no built-in limit for the number of components or volumes that can be modeled; the size of a problem is theoretically only limited by the available computer memory. Reactor hydraulic components in TRACE include PIPEs, PLENUMs, PRIZERs (pressurizers), CHANs (BWR fuel channels), PUMPs, JETPs (jet pumps), SEPDs (separators), TEEs, TURBs (turbines), HEATRs (feedwater heaters), CONTANs (containment), VALVEs, and VESSELs (with associated internals). HTSTR (heat structure) and REPEAT-HTSTR components modeling fuel elements or heated walls in the reactor system are available to compute two-dimensional conduction and surface-convection heat transfer in Cartesian or cylindrical geometries. POWER components are available as a means for delivering energy to the fluid via the HTSTR or hydraulic component walls. FLPOWER (fluid power) components are capable of delivering energy directly to the fluid (such as might happen in waste transmutation facilities). RADENC (radiation enclosures) components may be used to simulate radiation heat transfer between multiple arbitrary surfaces. FILL and BREAK components are used to apply the desired coolant-flow and pressure boundary conditions, respectively, in the reactor system to perform steady-state and transient calculations. EXTERIOR components are available to facilitate the development of input models designed to exploit TRACE's parallel execution features.

The code's computer execution time is highly problem dependent and is a function of the total number of mesh cells, the maximum allowable timestep size, and the rate of change of the neutronic and thermal-hydraulic phenomena being evaluated. The stability-enhancing two-step (SETS) numerics in hydraulic components allows the material Courant limit to be exceeded. This allows very large time steps to be used in slow transients. This, in turn, can lead to significant speedups in simulations (one or two orders of magnitude) of slow-developing accidents and operational transients.

While we do not wish to overstate the performance of the numerical techniques incorporated in TRACE, we believe that the current schemes demonstrate exceptional stability and robustness that will serve adequately in codes like TRACE for years to come. However, the models and correlations in the code can have a significant impact on the speed of a calculation; they can (and frequently do) affect adversely the time-step size and the number of iterations used. Because of the impact on the speed of the calculation and because the models and correlations greatly affect

the accuracy of the results, the area of model/correlation development may result in significant improvements in overall code performance.

TRACE Characteristics

Some distinguishing characteristics of the code are summarized below.

Multi-Dimensional Fluid Dynamics

A 3D (x, y, z) Cartesian- and/or (r, θ, z) cylindrical-geometry flow calculation can be simulated within the reactor vessel or other other reactor components where 3D phenomena take place. All 3D components, such as Reactor Water Storage Tank, where 3D phenomena are modeled, are named VESSEL although they may not have any relationship with the reactor vessel. Flows within a coolant loop are usually modeled in one dimension using PIPE and TEE components. The combination of 1D and 3D components allows an accurate modeling of complex flow networks as well as local multidimensional flows. This is important in determining emergency core coolant (ECC) downcomer penetration during blowdown, refill, and reflood periods of a LOCA. The mathematical framework exists to directly treat multidimensional plenum- and core-flow effects, and upper-plenum pool formation and core penetration during reflood.

Non-homogeneous, Non-equilibrium Modeling

A full two-fluid (six-equation) hydrodynamic model evaluates gas-liquid flow, thereby allowing important phenomena such as countercurrent flow to be simulated explicitly. A stratified-flow regime has been added to the 1D hydrodynamics; a seventh field equation (mass balance) describes a noncondensable gas field; and an eigh1th field equation tracks dissolved solute in the liquid field that can plated out on surfaces when solubility in the liquid is exceeded.

Flow-Regime-Dependent Constitutive Equation Package

The thermal-hydraulic equations describe the transfer of mass, energy, and momentum between the steam-liquid phases and the interaction of these phases with heat flow from the modeled structures. Because these interactions are dependent on the flow topology, a flow-regime-dependent constitutive-equation package has been incorporated into the code. Assessment calculations performed to date indicate that many flow conditions can be calculated accurately with this package.

Comprehensive Heat Transfer Capability

TRACE can perform detailed heat-transfer analyses of the vessel and the loop components. Included is a 2D (r,z) treatment of conduction heat transfer within metal structures. Heat conduction with dynamic fine-mesh rezoning during reflood simulates the heat transfer characteristics of quench fronts. Heat transfer from the fuel rods and other structures is calculated using flow-regime-dependent heat transfer coefficients (HTC) obtained from a generalized boiling curve based on a combination of local conditions and history effects. Inner- and/or outer-surface convection heat-transfer and a tabular or point-reactor kinetics with reactivity feedback volumetric power source can be modeled. One-dimensional or three-dimensional reactor kinetics capabilities are possible through coupling with the Purdue Advanced Reactor Core Simulator (PARCS) program.

Component and Functional Modularity

The TRACE code is completely modular by component. The components in a calculation are specified through input data; available components allow the user to model virtually any PWR or BWR design or experimental configuration. Thus, TRACE has great versatility in its range of applications. This feature also allows component modules to be improved, modified, or added without disturbing the remainder of the code. TRACE component modules currently include BREAKs, FILLs, CHANs, CONTANs, EXTERIORs, FLPOWERs, HEATRs, HTSTRs, JETPs, POWERs, PIPEs, PLENUMs, PRIZERs, PUMPs, RADENCs, REPEAT-HTSTRs, SEPDs, TEEs, TURBs, VALVEs, and VESSELs with associated internals (downcomer, lower plenum, reactor core, and upper plenum).

The TRACE program is also modular by function; that is, the major aspects of the calculations are performed in separate modules. For example, the basic 1D hydrodynamics solution algorithm, the wall-temperature field solution algorithm, heat transfer coefficient (HTC) selection, and other functions are performed in separate sets of routines that can be accessed by all component modules. This modularity allows the code to be upgraded readily with minimal effort and minimal potential for error as improved correlations and test information become available.

Physical Phenomena Considered

As part of the detailed modeling in TRACE, the code can simulate physical phenomena that are important in large-break and small-break LOCA analyses, such as:

1) ECC downcomer penetration and bypass, including the effects of countercurrent flow and hot walls;
2) lower-plenum refill with entrainment and phase-separation effects;
3) bottom-reflood and falling-film quench fronts;

4) multidimensional flow patterns in the reactor-core and plenum regions;
5) pool formation and countercurrent flow at the upper-core support-plate (UCSP) region;
6) pool formation in the upper plenum;
7) steam binding;
8) water level tracking,
9) average-rod and hot-rod cladding-temperature histories;
10) alternate ECC injection systems, including hot-leg and upper-head injection;
11) direct injection of subcooled ECC water, without artificial mixing zones;
12) critical flow (choking);
13) liquid carryover during reflood;
14) metal-water reaction;
15) water-hammer pack and stretch effects;
16) wall friction losses;
17) horizontally stratified flow, including reflux cooling,
18) gas or liquid separator modeling;
19) noncondensable-gas effects on evaporation and condensation;
20) dissolved-solute tracking in liquid flow;
21) reactivity-feedback effects on reactor-core power kinetics;
22) two-phase bottom, side, and top offtake flow of a tee side channel; and reversible and irreversible form-loss flow effects on the pressure distribution

Limitations on Use

As a general rule, computational codes like TRACE are really only applicable within their assessment range. TRACE has been qualified to analyze the ESBWR design as well as conventional PWR and BWR large and small break LOCAs (excluding B&W designs). At this point, assessment has not been officially performed for BWR stability analysis, or other operational transients.

The TRACE code is not appropriate for modeling situations in which transfer of momentum plays an important role at a localized level. For example, TRACE makes no attempt to capture, in detail, the fluid dynamics in a pipe branch or plenum, or flows in which the radial velocity profile across the pipe is not flat.

The TRACE code is not appropriate for transients in which there are large changing asymmetries in the reactor-core power such as would occur in a control-rod-ejection transient unless it is used in conjunction with the PARCS spatial kinetics module. In TRACE, neutronics are evaluated on a core-wide basis by a point-reactor kinetics model with reactivity feedback, and the spatially local neutronic response associated with the ejection of a single control rod cannot be modeled.

The typical system model cannot be applied directly to those transients in which one expects to observe thermal stratification of the liquid phase in the 1D components. The VESSEL component can resolve the thermal stratification of liquid only within the modeling of its multidimensional noding when horizontal stratification is not perfect.

The TRACE field equations have been derived assuming that viscous shear stresses are negligible (to a first-order approximation) and explicit turbulence modeling is not coupled to the conservation equations (although turbulence effects can be accounted for with specialized engineering models for specific situations). Thus, TRACE should not be employed to model those scenarios where the viscous stresses are comparable to, or larger than, the wall (and/or interfacial, if applicable) shear stresses. For example, TRACE is incapable of modeling circulation patterns within a large open region, regardless of the choice of mesh size.

TRACE does not evaluate the stress/strain effect of temperature gradients in structures. The effect of fuel-rod gas-gap closure due to thermal expansion or material swelling is not modeled explicitly. TRACE can be useful as a support to other, more detailed, analysis tools in resolving questions such as pressurized thermal shock.

The TRACE field equations are derived such that viscous heating terms within the fluid is generally ignored. A special model is, however, available within the PUMP component to account for direct heating of fluid by the pump rotor.

Approximations in the wall and interface heat flux terms prevent accurate calculations of such phenomena as collapse of a steam bubble blocking natural circulation through a B&W candy-cane, or of the details of steam condensation at the water surface in an AP1000 core makeup tank.

Intended Audience

This document is not intended to serve as a textbook on thermal-hydraulic phenomena or modeling. We do assume that the reader has been educated in the area of two-phase flow. Instead, it is intended to describe the underlying theory at such a level that scientists and engineers not closely involved in the development of TRACE can review the documentation and gain sufficient confidence that TRACE is adequate for its intended purpose. Along these lines, this document provides a baseline against which to measure the adequacy of the current models and correlations and a tool to help prioritize future experiment and development activities. We have done our best to ensure that discussions are kept at a level that precludes the need to introduce code-specific implementation details like subroutine or variable names.

We have also written this document for the TRACE code user who desires to understand the reasons behind the qualitative and quantitative nature of the comparisons between calculated results and data; to determine the applicability of the code to particular facilities and/or transients; or to determine the appropriateness of calculated results, with or without data to support the calculations. The definition of code user includes anyone who is involved in running the code or in analyzing its calculated results. Some chapters, particulary those that discuss the component and flow-process models, do presume some knowledge of the general TRACE modeling approach and its nomenclature (i.e. component names, global input variables that control overall code behavior, etc), such as might be gained from a quick read of the User's Manual.

Individuals involved in the development of TRACE (or similar codes) should find the information contained in this document useful because it provides insight into the many problems associated with closure and demonstrates methodologies for obtaining continuity at the boundaries among correlation sets that, because of their mathematical forms and different databases, are inherently discontinuous. This document provides one example of how one could select correlations and models and define logic to link them into a coherent system to describe, in conjunction with the field equations, a large variety of thermal-hydraulic conditions and transients. Even within the field of reactor safety in the United States other, similar calculational tools exist (e.g. RELAP5, COBRA/TRAC, TRAC-BWR, TRAC-PWR, CATHARE, RETRAN) in which different objectives, constraints, and histories have led to different choices for solution strategies, models, and correlations.

Organization of This Manual

This document is designed to serve as the resource for understanding the mathematical models that the code uses, how they are solved, and their limitations. In particular, it discusses the two-phase flow equations, their transformation into finite volume methods, the overall solution process, the heat conduction equations, the core power and fuel rod models, and the various constitutive models and closure relationships employed (without necessarily delving into the low-level details of how they were developed).

Reporting Code Errors

It is vitally important that the USNRC receive feedback from the TRACE user community. To that end, we have established a support website at *http://www.nrccodes.com*. It contains the TRACEZilla bug tracking system, latest documentation, a list of the updates currently waiting to be integrated into the main development trunk (called the HoldingBin), and the recent build history showing what changes have been made, when, and by whom. Access to the TRACE-specific areas of the site are password-protected. Details for obtaining access are provided on the public portion of the site.

Conventions Used in This Manual

In general. items appearing in this manual use the Times New Roman font. Sometimes, text is given a special appearance to set it apart from the regular text. Here's how they look (colored text will, of course, not appear colored when printed in black and white)

ALL CAPS

Used for TRACE component names and input variable names

BOLD RED, ALL CAPS

Used for TRACE variable identifiers in the component card tables (column 2)

Bold Italic

Used for chapter and section headings

Bold Blue

Used for TRACE card titles, note headings, table headings, cross references

Plain Red

Used for XTV graphics variable names

Bold

Used for filenames, pathnames, table titles, headings for some tables, and AcGrace dialog box names

Italic

Used for references to a website URL and AcGrace menu items

`Fixed Width Courier`

Used to indicate user input, command lines, file listings, or otherwise, any text that you would see or type on the screen

Note – This icon represents a Note. It is used to emphasize various informational messages that might be of interest to the reader.

Warning – This icon represents a Warning. It is used to emphazize important information that you need to be aware of while you are working with TRACE.

Tip – This icon represents a Tip. It is used to dispense bits of wisdom that might be of particular interest to the reader.

For brevity, when we refer to filenames that TRACE either takes as input or outputs, we will generally refer to it using its default internal hardwired name (as opposed to the prefix naming convention to which you will be introduced in the following chapters). So for example, references to the TRACE input file name would use **tracin**; references to the output file would use **trcout**, etc.

1

Field Equations

This chapter describes the fluid field equations used by TRACE to model two-phase flow, and the numerical approximations made to solve these equations. Derivation of the equation set used in TRACE starts with single phase Navier-Stokes equations in each phase, and jump conditions between the phases. Time averaging is applied to this combination of equations, to obtain a useful set of two-fluid, two-phase conservation equations. TRACE uses this flow model in both one and three dimensions. Kocamustafaogullari (Ref. 1-1), Ishii (Ref. 1-2), and Bergles et al. (Ref. 1-3) have provided detailed derivations of the equations similar to those used in TRACE, and a more concise derivation related to the TRACE equations is available in a report by Addessio (Ref. 1-4). That this model is formally ill-posed was the subject of considerable debate many years ago and is discussed by Stewart and Wendroff (Ref. 1-5). Our experience, however, has always been that this is a moot point, since the numerical solution procedures effectively introduce minor modifications to the field equations, making them well-posed. A paper by Stewart (Ref. 1-6) confirms these observations and demonstrates clearly that with normal models for interfacial drag and reasonable finite-difference nodalizations, the problem solved numerically is well-posed.

The basic two-fluid, two-phase field equation set consists of separate mass, energy, and momentum conservations for the liquid and gas fields. This gives a starting point of six partial differential equations (PDEs) to model steam/water flows. For a wide range of reactor safety analysis, noncondensable gas may enter the system and mix with the steam. At any given location TRACE assumes that all components of the gas mixture are moving at the same velocity and are at the same temperature. As a result a single momentum equation and a single energy equation are used for the gas mixture. Relative concentrations of steam and noncondensable are determined by using separate mass equations for each component of the gas field. In a typical LOCA nitrogen will eventually enter the primary loops from the accumulators, and air from the containment. Because the properties of nitrogen and air are so similar, users normally treat both noncondensable sources as air, adding one mass equation to the set of PDEs that must be solved. However, TRACE permits users to treat nitrogen and air as two separate components of the gas field (two additional mass equations), and allows requests for more noncondensable mass equations if needed (e.g. for hydrogen).

The set of field equations can be further extended if a user chooses to follow the boron concentration in the system. An additional mass conservation equation can be activated to follow the concentration of boric acid, moving with the liquid. Total content of boric acid is assumed to be small enough that its mass is not used in the liquid momentum equation and it does not

contribute to the thermodynamic or other physical properties of the liquid. Boron tracking capabilities are extended through the use of a model for solubility of boric acid, and a simple inventory of boric acid plated out in each cell in the system. Another solute could be modeled through a user option to replace the default solubility curve.

The TRACE code, as well as most other codes like it, invokes a quasi-steady approach to the heat-transfer coupling between the wall and the fluid as well as the closure relations for interfacial and wall-to-fluid heat transfer and drag. This approach assumes detailed knowledge of the local fluid parameters and ignores time dependencies so that the time rate of change in the closure relationships becomes infinite and the time constants are zero. It has the advantages of being reasonably simple (and, therefore, generally applicable to a wide range of problems) and not requiring previous knowledge of a given transient. Where appropriate, we integrate the effects of the quasi-steady approach; however, in the interests of brevity, the description of the quasi-steady methodology presented in this chapter is somewhat limited. **Appendix A** contains a much more detailed discussion of the quasi-steady assumption and the averaging operators used in the code.

Nomenclature

Before presenting the fluid field equations, we need to define certain terminology. In our nomenclature, the term "gas" implies a general mixture of water vapor and the noncondensable gas. The subscript g will denote a property or parameter applying to the gas mixture; the subscript v indicates a quantity applying specifically to water vapor (referred to as simply "vapor"); and the subscript a (for "air") signifies a quantity associated with mixture of one or more noncondensable gases. The term "liquid" implies pure liquid water, and the subscript l denotes a quantity applying specifically to liquid water. For convenience, we define the following terms that will be used in the subsequent equations and list them alphabetically, with the Greek symbols and subscripts to follow. The following notation applies to the discussion of numerical methods. A caret ($\hat{}$) above a variable denotes an explicit predictor value. A tilde ($\tilde{}$) above a variable denotes an intermediate result, and a line ($\bar{}$) above denotes an average operation. Details of the specific average are provided in discussion of the equations in which it occurs. A horizontal arrow (or half-arrow) above a variable denotes a vector quantity (in the physical sense such that it has both a magnitude and direction).

A = flow area between mesh cells

A_i = interfacial area per unit volume between the liquid and gas phases

c = speed of sound

C = shear coefficient

E_i = rate of energy transfer per unit volume across phase interfaces

e = internal energy

f = force per unit volume

$\vec{g}$ or $\vec{g}$ = gravity vector

g = magnitude of the gravity vector

h = heat-transfer coefficient (HTC)

h_{sg} = gas saturation enthalpy

$h_{wg} = (1 - f_l)\, h'_{wg}$, the effective wall HTC to gas

$h_{wl} = f_l\, h'_{wl}$, the effective wall HTC to liquid

h_l' = liquid enthalpy of the bulk liquid if the liquid is vaporizing or the liquid saturation enthalpy if vapor is condensing

h_v' = vapor enthalpy of the bulk vapor if the vapor is condensing or the vapor saturation enthalpy if liquid is vaporizing

K = form-loss coefficient or wall friction coefficient

m = solute concentration in the liquid (mass of solute per unit mass of liquid)

M_i = rate of momentum transfer per unit volume across phase interfaces

P = fluid pressure or total pressure

q = heat-transfer rate per unit volume

q_d = power deposited directly to the gas or liquid (without heat-conduction process)

q_{gl} = liquid-to-gas sensible heat transfer

q' = heat flux

r = radius

R = ideal gas constant (including effects of molecular weight)

R = Reynolds/viscous stress tensor

S = factor applied to the 1D component so that its positive flow direction becomes the positive flow direction of the vessel

S_c = plated-out solute density (mass of plated solute divided by cell volume)

SC = product of an orifice factor

S_m = source term in the solute-mass differential equation

t = time

T = temperature

T = stress tensor

T_{sv} = saturation temperature corresponding to the vapor partial pressure

$\vec{V}$ or $\vec{V}$ = velocity vector

V = magnitude of the velocity

vol = hydrodynamic-cell volume

w = weighting factor

x = distance

X = mass fraction of an additional noncondensable gas species

Y = dummy variable

z = axial coordinate

Greek

α = gas volume fraction

β = momentum-convection temporal expansion flags

γ = weighting factor

Γ = interfacial mass-transfer rate (positive from liquid to gas)

Γ^+ = maximum of Γ and 0

Γ^- = minimum of Γ and 0

ρ = density

ΔP = pressure difference

Δr = radial ring increment for 3D components

Δt = time-step size

ΔV = velocity change

Δx = cell length for 1D components

Δz = axial level increment for 3D components

$\Delta\theta$ = azimuthal segment increment for 3D components

δP = linear Taylor series expansion term for pressure

δT = linear Taylor series expansion term for temperature

$\delta\alpha$ = linear Taylor series expansion term for void fraction

θ = inclination angle from vertical or the azimuthal coordinate

ϕ = angle between the main and side tubes in a TEE component

Subscripts

$1D$ = one dimensional

$3D$ = three dimensional

$donor$ = donor cell

T = the first cell in the side leg of the TEE or the interface between the j^{th} cell of the primary and the first cell in the side leg

a = noncondensable gas

d = 1) generic index for r, θ, or z or i, j, or k ; 2) denotes direct heating when used with energy source (q)

g = gas mixture

i = interfacial

j = cell-center index

$j+1$ = downstream cell-center index

$j+1/2$ = downstream cell-edge index

$j-1$ = upstream cell-center index

$j-1/2$ = upstream cell-edge index

k = index on additional noncondensable gas species

l = liquid

max = maximum

min = minimum

r = radial

sat = saturation

v = water vapor

w = wall

z = axial

θ = azimuthal

Superscripts

n = current-time quantity

$n+1$ = new-time quantity

′ = last estimate

In the discussion of the finite-difference equations, all quantities except for the velocities are centered in the hydrodynamic cell (cell-centered), and the velocities are cell-edge quantities.

Fluid Field Equations

Time averaging of the single phase gas and single phase liquid conservation equations combined with interface jump conditions results in a starting point summarized in Eqs. (1-1) through (1-6). In these equations an overbar represents a time average, α is the probability that a point in space is occupied by gas, and Γ, E_i, and M_i represent the contribution of time averaged interface jump conditions to transfer of mass, energy and momentum respectively. In addition *q'* is conductive heat flux, q_d is direct heating (e.g. radioactive decay) and T is the full stress tensor. Subscripts of "g" and "l" distinguish between gas specific and liquid specific terms respectively.

Time Averaged Mass Equations

$$\frac{\partial[(1-\alpha)\overline{\rho}_l]}{\partial t} + \nabla \cdot \left[(1-\alpha)\overline{\rho}_l \overline{\vec{V}_l}\right] = -\overline{\Gamma} \tag{1-1}$$

$$\frac{\partial(\alpha\overline{\rho}_g)}{\partial t} + \nabla \cdot \left[\alpha\overline{\rho}_g \overline{\vec{V}_g}\right] = \overline{\Gamma} \tag{1-2}$$

Time Averaged Energy Equations

$$\frac{\partial\left[(1-\alpha)\overline{\rho}_l\left(\overline{e_l + V_l^2/2}\right)\right]}{\partial t} + \nabla \cdot \left[(1-\alpha)\overline{\rho}_l \overline{(e_l + V_l^2/2)\vec{V}_l}\right] \tag{1-3}$$

$$= -\nabla \cdot \left[(1-\alpha)\overline{\vec{q}'_l}\right] + \nabla \cdot \left[(1-\alpha)\left(\overline{\mathsf{T}_l \cdot \vec{V}_l}\right)\right] + (1-\alpha)\overline{\rho}_l \overline{\vec{g} \cdot \vec{V}_l} - \overline{E}_i + \overline{q_{dl}}$$

$$\frac{\partial\left[\alpha\overline{\rho}_g\left(\overline{e_g+V_g^2/2}\right)\right]}{\partial t}+\nabla\cdot\left[\alpha\overline{\rho}_g\overline{(e_g+V_g^2/2)\vec{V}_g}\right] \tag{1-4}$$
$$=-\nabla\cdot\left[\alpha\overline{\vec{q}'_g}\right]+\nabla\cdot\left[\alpha\left(\overline{\mathbf{T}_g\cdot\vec{V}_g}\right)\right]+\alpha\overline{\rho}_g\vec{g}\cdot\overline{\vec{V}_g}+\overline{E}_i+\overline{q_{dg}}$$

Time Averaged Momentum Equations

$$\frac{\partial\left[(1-\alpha)\overline{\rho}_l\overline{\vec{V}_l}\right]}{\partial t}+\nabla\cdot(1-\alpha)\overline{\rho}_l\overline{\vec{V}_l\vec{V}_l}\;=\;\nabla\cdot[(1-\alpha)\overline{\mathbf{T}}_l]+(1-\alpha)\overline{\rho}_l\vec{g}-\overline{M}_i \tag{1-5}$$

$$\frac{\partial\left[\alpha\overline{\rho}_g\overline{\vec{V}_g}\right]}{\partial t}+\nabla\cdot\alpha\overline{\rho}_g\overline{\vec{V}_g\vec{V}_g}\;=\;\nabla\cdot[\alpha\overline{\mathbf{T}}_g]+\alpha\overline{\rho}_g\vec{g}+\overline{M}_i \tag{1-6}$$

The equations are consistent with Reynolds averaging and splitting the velocities into mean and fluctuating contributions will yield expressions familiar to those who work with turbulence. However, contributions from the Reynolds stress, as well as most of the terms on the right hand side of the energy and momentum equations will be modeled with engineering correlations, so the following forms of the energy and momentum equations do not include full notation from classic turbulence formulation. In the energy equation the term *q'* is redefined to include energy flux due to turbulent diffusion. Energy carried with mass transfer at the interface is represented by the products of mass transfer rate and appropriate stagnation enthalpy at the interface ($\Gamma h'_v$ and $\Gamma h'_l$). Work done on the fluid is split into that due to the pressure terms in the stress tensor, and a term simply labeled "*W*", containing work done by shear stress and by interfacial force terms.

Revised Time Average Energy Equations

$$\frac{\partial\left[(1-\alpha)\overline{\rho}_l\left(\overline{e_l+V_l^2/2}\right)\right]}{\partial t}+\nabla\cdot\left[(1-\alpha)\overline{\rho}_l\left(\overline{\left(e_l+\frac{P}{\rho_l}+V_l^2/2\right)\vec{V}_l}\right)\right] \tag{1-7}$$
$$=-\nabla\cdot\left[(1-\alpha)\overline{\vec{q}'_l}\right]+(1-\alpha)\overline{\rho}_l\vec{g}\cdot\overline{\vec{V}_l}-\Gamma h'_l+W_l+q_{dl}$$

$$\frac{\partial\left[\alpha\overline{\rho}_g\left(\overline{e_g+V_g^2/2}\right)\right]}{\partial t}+\nabla\cdot\left[\alpha\overline{\rho}_g\left(\overline{\left(e_g+\frac{P}{\rho_g}+V_g^2/2\right)\vec{V}_g}\right)\right] \tag{1-8}$$
$$=-\nabla\cdot\left[\alpha\overline{\vec{q}'_g}\right]+\alpha\overline{\rho}_g\vec{g}\cdot\overline{\vec{V}}_g+\Gamma h'_v+W_g+q_{dg}$$

In the momentum equations pressure is also isolated from the stress tensor, and for purposes of this derivation the viscous shear stress terms are combined with the Reynolds stress into a single tensor R.

Revised Time Average Momentum Equations

$$\frac{\partial\left[(1-\alpha)\overline{\rho}_l\overline{\vec{V}}_l\right]}{\partial t}+\nabla\cdot(1-\alpha)\overline{\rho}_l\overline{\vec{V}}_l\overline{\vec{V}}_l=\nabla\cdot[(1-\alpha)\overline{R}_l]+(1-\alpha)\overline{\rho}_l\vec{g}-\overline{M}_i \tag{1-9}$$

$$\frac{\partial\left[\alpha\overline{\rho}_g\overline{\vec{V}}_g\right]}{\partial t}+\nabla\cdot\alpha\overline{\rho}_g\overline{\vec{V}}_g\overline{\vec{V}}_g=\nabla\cdot[\alpha\overline{R}_g]+\alpha\overline{\rho}_g\vec{g}+\overline{M}_i \tag{1-10}$$

At this point it is possible to move on to the finite volume conservation equations. However, the next round of approximations made in the TRACE flow model can also be illustrated by considering a volume averaged form of the above field equations. First the overbar is dropped and all variables are treated as time averages. Next the overbar is returned to the notation as a volume average of terms in the conservation equations.

Volume Averaged Mass Equations

$$\frac{\partial[\overline{(1-\alpha)}\overline{\rho}_l]}{\partial t}+\overline{\nabla\cdot[(1-\alpha)\rho_l\vec{V}_l]}=-\overline{\Gamma} \tag{1-11}$$

$$\frac{\partial(\overline{\alpha\rho}_g)}{\partial t}+\nabla\cdot\left[\overline{\alpha\rho_g\vec{V}_g}\right]=\overline{\Gamma} \tag{1-12}$$

Volume Averaged Energy Equations

$$\frac{\partial\left[\overline{(1-\alpha)\rho_l(e_l+V_l^2/2)}\right]}{\partial t}+\overline{\nabla\cdot\left[(1-\alpha)\rho_l\left(e_l+\frac{P}{\rho_l}+V_l^2/2\right)\vec{V}_l\right]} \tag{1-13}$$

$$=-\overline{\nabla\cdot[(1-\alpha)\vec{q}'_l]}+\overline{(1-\alpha)\rho_l\vec{g}\cdot\vec{V}_l-\Gamma h'_i+W_l}+\overline{q_{dl}}$$

$$\frac{\partial\left[\overline{\alpha\rho_g(e_g+V_g^2/2)}\right]}{\partial t}+\overline{\nabla\cdot\left[\alpha\rho_g\left(\left(e_g+\frac{P}{\rho_g}+V_g^2/2\right)\vec{V}_g\right)\right]} \tag{1-14}$$

$$=\overline{-\nabla\cdot[\alpha\vec{q}'_g]}+\overline{\alpha\rho_g\vec{g}\cdot\vec{V}_g}+\overline{\Gamma h'_v+W_g}+\overline{q_{dg}}$$

Volume Averaged Momentum Equations

$$\frac{\partial\overline{[(1-\alpha)\rho_l\vec{V}_l]}}{\partial t}+\overline{\nabla\cdot(1-\alpha)\rho_l\vec{V}_l\vec{V}_l}=\overline{\nabla\cdot[(1-\alpha)\boldsymbol{R}_l]}+\overline{(1-\alpha)\rho_l\vec{g}-M_i} \tag{1-15}$$

$$\frac{\partial\overline{[\alpha\rho_g\vec{V}_g]}}{\partial t}+\overline{\nabla\cdot\alpha\rho_g\vec{V}_g\vec{V}_g}=\overline{\nabla\cdot[\alpha\boldsymbol{R}_g]}+\overline{\alpha\rho_g\vec{g}}+\overline{M_i} \tag{1-16}$$

Now a series of approximations are made.

1) The volume average of a product is assumed to be equal to the product of volume averages. This is reasonable if the averaging volume is small enough, but eventually when applied within the finite volume context to reactor systems, the averaging volume will span flow channels. In this case, the approximation is good for most turbulent flows due to the flat profile across most of the flow cross-section. However, for laminar single phase flow in a circular channel cross-section, when the average of the product of two parabolic profiles is replaced by the product of the average velocities, momentum flux terms will be low by 25%. Flows with rising droplets and falling wall film or certain vertical slug flows will also present problems.

2) Only contributions from wall heat fluxes and heat fluxes at phase interfaces within the averaging volume are normally included in the volume average of the divergence of heat flux. An option exists to include the conduction heat flux within the fluid (perhaps useful for liquid metal flow), but no provision has been made for turbulent heat flux between averaging volumes. In effect, heat flux is a subgrid model. This approximation prevents accurate calculations of such phenomena as collapse of a steam bubble blocking natural circulation through a B&W candy-cane, or of the details of steam condensation at the water surface in an AP1000 core makeup tank. From a practical standpoint, lack of the volume to volume heat diffusion terms will not make a major difference in a simulation. For any normal spatial discretization the numerical diffusion (see (Ref. 1-7)) will significantly exceed the physical thermal diffusion.

3) Only contributions from the stress tensor due to shear at metal surfaces or phase interfaces within the averaging volume are considered. No contributions due to shear between flows in adjacent averaging volumes is included. Again from a practical standpoint, numerical diffusion terms exceed any physical terms dropped by this approximation. However, code users need to understand that field equations with this approximation are not capable of modeling circulation patterns within a large open region regardless of the choice of mesh size.

4) Only those portions of the work terms W_l and W_g that contribute to change in bulk kinetic energy of motion are retained. Viscous heating is ignored, except as a special model within pump components, accounting for heating of the fluid by a pump rotor. through the direct heating source term q_{dl}.

As a result of the first approximation, overbars are eliminated from the following equations, and a combination of time and volume average is implied for all state variables. At this point a switch is made in the definition of α from a probability that a point is space is gas, to the fraction of the averaging volume occupied by gas (void fraction). Heat transferred from the interface to gas and to liquid (W/m^3) is represented by the terms q_{ig} and q_{il} respectively. Similar expressions (q_{wg}, q_{wl}) are used for heat transferred from surfaces of structures to the fluid. Expressions for all of these will come from correlations developed from steady state data, and they replace the heat transport terms in Equations (1-13) and (1-14) as shown in the following expressions

$$-\overline{\nabla \cdot [(1-\alpha)\vec{q}'_l]} \Rightarrow q_{il} + q_{wl} \tag{1-17}$$

$$-\overline{\nabla \cdot [\alpha \vec{q}'_g]} \Rightarrow q_{ig} + q_{wg} \tag{1-18}$$

Under the third approximation the right hand sides of the momentum equations are changed to a simpler form:

$$\frac{\partial[(1-\alpha)\rho_l \vec{V}_l]}{\partial t} + \nabla \cdot (1-\alpha)\rho_l \vec{V}_l \vec{V}_l + (1-\alpha)\nabla P = \vec{f}_i + \overrightarrow{f_{wl}} + (1-\alpha)\rho_l \vec{g} - \Gamma \vec{V}_i \quad (1\text{-}19)$$

$$\frac{\partial[\alpha\rho_g \vec{V}_g]}{\partial t} + \nabla \cdot \alpha\rho_g \vec{V}_g \vec{V}_g + \alpha\nabla P = \overrightarrow{-f_i} + \overrightarrow{f_{wg}} + \alpha\rho_g \vec{g} + \Gamma \vec{V}_i \quad (1\text{-}20)$$

where f_i is the force per unit volume due to shear at the phase interface, f_{wl} is the wall shear force per unit volume acting on the liquid, f_{wg} is the wall shear force per unit volume acting on the gas, and V_i is the flow velocity at the phase interface.

Given the above notation for force terms, and the fourth assumption, the energy equations can be written in the form:

$$\frac{\partial\left[(1-\alpha)\rho_l(e_l + V_l^2/2)\right]}{\partial t} + \nabla \cdot \left[(1-\alpha)\rho_l\left(e_l + \frac{P}{\rho_l} + V_l^2/2\right)\vec{V}_l\right] \quad (1\text{-}21)$$

$$= q_{il} + q_{wl} + q_{dl} + (1-\alpha)\rho_l \vec{g} \cdot \vec{V}_l - \Gamma h'_l + (\vec{f}_i + \overrightarrow{f_{wl}}) \cdot \vec{V}_l$$

$$\frac{\partial\left[\alpha\rho_g(e_g + V_g^2/2)\right]}{\partial t} + \nabla \cdot \left[\alpha\rho_g\left(e_g + \frac{P}{\rho_g} + V_g^2/2\right)\vec{V}_g\right] \quad (1\text{-}22)$$

$$= q_{ig} + q_{wg} + q_{dg} + \alpha\rho_g \vec{g} \cdot \vec{V}_g + \Gamma h'_v + (-\vec{f}_i + \overrightarrow{f_{wg}}) \cdot \vec{V}_g$$

Under the notation used in Equations (1-19) through (1-22), the mass equations for the two fluid model, become:

$$\frac{\partial[(1-\alpha)\rho_l]}{\partial t} + \nabla \cdot [(1-\alpha)\rho_l \vec{V}_l] = -\Gamma \quad (1\text{-}23)$$

$$\frac{\partial(\alpha\rho_g)}{\partial t} + \nabla \cdot [\alpha\rho_g \overrightarrow{V}_g] = \Gamma \tag{1-24}$$

Closure is obtained for these equations using normal thermodynamic relations and correlations for phase change, heat source and force terms. These equations do not directly require the quasi-steady assumption for the closure terms as long as the correct closure relations for the given transient exist. A real difficulty arises because, depending on how the closure relations were developed, a different set of closure relations may be required for each transient, and each set must comply with the assumptions associated with the definition of the time- and volume-averaging used in the field equations. If a steady- or quasi-steady-state database or a relationship derived from such a database is used to represent a closure relation, the code necessarily applies the quasi-steady assumption, as detailed in **Appendix A**. This latter case applies for the closure relations within TRACE.

The phase-change rate required by the equation set is evaluated from a simple thermal-energy-jump relation, often called a heat conduction limited model.

$$\Gamma = \frac{-(q_{ig} + q_{il})}{(h_v' - h_l')} \tag{1-25}$$

where the interfacial heat transfer per unit volume on the gas and liquid sides are

$$q_{ig} = \frac{P_v}{P} h_{ig} a_i (T_{sv} - T_v) \tag{1-26}$$

and

$$q_{il} = h_{il} a_i (T_{sv} - T_l) \ . \tag{1-27}$$

Here a_i is the interfacial area per unit volume, h_{ig} and h_{il} are HTCs at the liquid/gas interface, and T_{sv} is the saturation temperature corresponding to the partial steam pressure (P_v). **Chapter 5** discusses the closure relationships used to define a_i, h_{ig}, and h_{il}. The quantities h_v' and h_l' are the appropriate enthalpies of the vapor and liquid, respectively. These enthalpies are the bulk fluid enthalpy for the phase moving to the interface and the saturation enthalpy for the product of the phase change. This choice of enthalpies was inherited from both the RELAP and TRAC code series. Use of bulk enthalpy for the phase moving to the interface was necessary to prevent unphysical thermal runaways.

One example of such runaway behavior can occur when subcooled liquid is driving the condensation of a superheated vapor and the interfacial heat transfer on the gas side is very low. In this situation the bulk gas temperature increases if steam is removed at the interface at the saturation temperature, but no significant interfacial heat transfer (diffusion) from bulk gas to

interface is present to provide a balancing cooling effect for the bulk gas. Removal of steam at a temperature less than the bulk temperature, leaves the remaining gas hotter. The root of this problem is in the use of the heat conduction limited model. It is meant for a diffusion dominated process and the heat transfer coefficients selected to represent the boundary conditions at the interface assume diffusion dominates the energy transfer. In fact when the full advection/diffusion problem is considered the diffusive heat flux at the boundary is strongly enhanced as the advection becomes important (see, for example, the temperature profiles in the advection/ diffusion example presented by Roach (Ref. 1-8)). In this limit of negligible interfacial heat transfer on the gas side, use of the bulk gas temperature to evaluate the steam enthalpy in Eqs. (1-22) and (1-25) is rigorously correct. In any case, except for very unusual circumstances, temperatures are close enough to saturation that use of a bulk enthalpy rather than a saturation enthalpy in Eqs. (1-22) and (1-25) will make much less difference in results than the inherent range of uncertainty associated with interfacial heat transfer equations.

Using Newton's law of cooling extended to a thermal nonequilibrium situation, the wall heat-transfer terms assume the form

$$q_{wg} = h_{wg} a_w (T_w - T_g) = q'_{wg} a_w \tag{1-28}$$

and

$$q_{wl} = h_{wl} a_w (T_w - T_l) = q'_{wl}\ a_w \tag{1-29}$$

where a_w is the heated surface area per volume of fluid (only meaningful in a volume averaged or finite volume context). The heat transfer coefficients h_{wg} and h_{wl} include the information regarding the portion of the wall having gas and liquid contact. **Chapter 6** discusses the closure relationships used to define h_{wg} and h_{wl}.

Force terms f_i, f_{wg}, and f_{wl} are cast in the following forms, relying on correlations for friction coefficients C_i, C_{wg}. and C_{wl}.

$$f_i = C_i (\vec{V}_g - \vec{V}_l) \left| \vec{V}_g - \vec{V}_l \right| \tag{1-30}$$

$$f_{wg} = -C_{wg} \vec{V}_g \left| \vec{V}_g \right| \tag{1-31}$$

$$f_l = -C_{wl} \vec{V}_l \left| \vec{V}_l \right| \tag{1-32}$$

By representing interfacial force with Eq. (1-30), two contributions to interfacial force have been neglected. Terms proportional to acceleration (virtual mass terms) have been ignored because of no evidence of significance in reactor safety problems, combined with significant increase in

complexity of the solution procedure when they are present with semi-implicit or SETS solution procedures. Virtual mass terms will be reconsidered if higher order numerical methods are introduced into a future version of TRACE and a well-posed set of PDEs becomes important. Lift forces perpendicular to the flow direction have also been dropped. However, some representation of this term will be necessary in future TRACE versions containing the ability to do sub-channel analysis in a reactor core.

Rearrangement of Equations for Numerical Solution

TRACE does not solve the field equations in the form presented above. To cut complexity and computer time of the numerical solution, the fully conservative forms of the energy and momentum equations are rearranged to provide internal energy and motion equations. The steps to the next form of the field equations are rigorous mathematically, and involve no formal approximations. However, in finite volume form, the internal energy equations have problems with very large changes in pressure between two cells that are not present when the fully conservative forms of the energy equations are implemented directly into a finite volume approach. In such cases the prediction of temperature change between two volumes deteriorates significantly when the pressure change between the volumes is very large. This problem was inherited from RELAP and TRAC, and from a practical standpoint has only been apparent when the code has been used to model both the reactor primary and the containment during a LOCA. Fortunately, one portion of the TRACE development effort was a task to provide direct time step by time step linkage between parallel executions of TRACE and CONTAIN. CONTAIN was developed for the USNRC at Sandia National Laboratory to simulate a reactor containment's transient behavior during a LOCA. In a coupled calculation TRACE only simulates the reactor coolant system (vessel, primary loops, and steam generator secondary system) while CONTAIN simulates the containment side of the problem. Development of the linkage between TRACE and CONTAIN included adjustments to the energy flux terms between the codes to preserve the correct temperature change in fluid as it moves from a high pressure volume in TRACE to a low pressure volume in CONTAIN.

Use of motion equations, rather than fully conservative momentum equations, generally works very well. However, exaggerated momentum transfer can occur in TRACE V5.0 (or earlier) when a steam/droplet mixture flows down towards the surface of a liquid pool (often in a downcomer during reflood). When practical, the solution to this problem is to engage the TRACE interface tracking model.

An internal energy conservation equation (gas or liquid) is obtained by taking the dot product of the corresponding momentum equation with its velocity and subtracting the results from the fully conservative energy equation. For gas the result is:

$$\frac{\partial(\alpha\rho_g e_g)}{\partial t} + \nabla\cdot(\alpha\rho_g e_g \overrightarrow{V}_g) = -P\frac{\partial\alpha}{\partial t} - P\nabla\cdot(\alpha\overrightarrow{V}_g) + q_{wg} + q_{dg} + q_{ig} + \Gamma h_v' \qquad (1\text{-}33)$$

A similar operation is performed on the liquid energy equation, but rather than using it in that form, the result is added to the gas energy equation to produce a mixture energy conservation equation.

$$\frac{\partial\left[(1-\alpha)\rho_l e_l + \alpha\rho_g e_g\right]}{\partial t} + \nabla\cdot\left[(1-\alpha)\rho_l e_l \vec{V}_l + \alpha\rho_g e_g \vec{V}_g\right] \tag{1-34}$$
$$= -P\nabla\cdot\left[(1-\alpha)\vec{V}_l + \alpha\vec{V}_g\right] + q_{wl} + q_{wg} + q_{dl} + q_{dg}$$

When included in the finite volume equation solution, the mixture energy equation makes it easier to deal with transitions from two-phase to single-phase flow during a step in the time integration. To fully achieve this advantage during a transition, a similar pair of gas and mixture mass equations must be used in the actual solution.

$$\frac{\partial(\alpha\rho_g)}{\partial t} + \nabla\cdot[\alpha\rho_g\vec{V}_g] = \Gamma \tag{1-35}$$

$$\frac{\partial\left[(1-\alpha)\rho_l + \alpha\rho_g\right]}{\partial t} + \nabla\cdot\left[(1-\alpha)\rho_l\vec{V}_l + \alpha\rho_g\vec{V}_g\right] = 0 \tag{1-36}$$

Motion equations are obtained by the standard means of multiplying the mass conservation equation for a phase (Eq. (1-23) or Eq. (1-24)) by that phase's velocity, subtracting it from the corresponding momentum conservation equation (Eq. (1-19) or Eq. (1-20)), and dividing the result by the appropriate macroscopic density.

$$\frac{\partial\vec{V}_l}{\partial t} + \vec{V}_l\cdot\nabla\vec{V}_l = -\frac{1}{\rho_l}\nabla P + \frac{\left[f_i - \Gamma(\vec{V}_i - \vec{V}_l) + f_{wl}\right]}{(1-\alpha)\rho_l} + \vec{g} \tag{1-37}$$

$$\frac{\partial\vec{V}_g}{\partial t} + \vec{V}_g\cdot\nabla\vec{V}_g = -\frac{1}{\rho_g}\nabla P + \frac{\left[f_{wg} - f_i - \Gamma(\vec{V}_g - \vec{V}_i)\right]}{\alpha\rho_g} + \vec{g} \tag{1-38}$$

Eq. (1-37) and Eq. (1-38) are generally referred to as the nonconservative form of the momentum equations, because it is not possible to write a finite volume method that guarantees some numerical integral of momentum over a system does not change from one time step to the next in

the absence of force terms. Use of this form permits simpler numerical solution strategies particularly for a semi-implicit method, and can generally be justified because the presence of wall friction makes the fully conservative form of the momentum equation far less useful. When sharp flow-area changes exist, however, numerical solution of the nonconservative motion equations can produce significant errors. For these situations, the motion equations have been modified to force Bernoulli flow (see **Conserving Convected Momentum** later in this chapter).

Terms in the momentum equation associated with phase change at the interface can produce non-physical velocity runaways that are analogous to the thermal runaways discussed above. Consider the case of moving steam condensing onto a stratified relatively stagnant liquid. The interfacial drag term will not be significant, and the negative value of Γ combined with an interface velocity with any significant relation to the liquid velocity will result in a positive acceleration to the gas. To avoid such velocity runaways the interface velocity appearing in Equations (1-37) and (1-38) is set to V_l when Γ is positive (boiling) and to V_g when Γ is negative.

Noncondensable Gas

Normally only one noncondensable gas field is modeled with TRACE, but it supports multiple gas species if the user is willing to increase run time by using extra field equations. The noncondensable gas mixture is assumed to be in thermal equilibrium with any steam that is present and to move with the same velocity as the steam (mechanical equilibrium). Hence, only a single gas momentum (Eq. (1-38)) and a single gas energy equation (Eq. (1-33)) are needed. Mass conservation is provided with a total noncondensable mixture mass equation:

Noncondensable Mixture Mass Equation

$$\frac{\partial(\alpha\rho_a)}{\partial t} + \nabla \cdot \left[\alpha\rho_a \overrightarrow{V_g}\right] = 0\,, \tag{1-39}$$

and equations for each additional species in the mixture beyond the first.

Additional Non-Condensable Mass Equations (k^{th} species)

$$\frac{\partial\left(\alpha X_k \rho_a\right)}{\partial t} + \nabla \cdot \left[\alpha X_k \rho_a \overrightarrow{V_g}\right] = 0 \tag{1-40}$$

We could have skipped use of the mixture gas conservation Eq. (1-39) in favor of individual species equation (1-40) for all species present. However, in analogy to justification for use of a

full mixture mass equation (1-36), inclusion of the full mixture mass equation aids in enforcement of mass conservation when individual gas species disappear from a computational volume.

For pure non-condensable gases, air, and mixtures of these gases, an ideal gas equation of state is normally assumed. The only exception occurs when helium is the only noncondensable gas present in a flow simulation. In that case, you are permitted to select a non-ideal helium equation (see **Chapter 11**). In terms of the ideal gas model, the mixture density is obtained from:

$$\rho_a = \frac{P}{R_{mix} T} \tag{1-41}$$

With this field present, the total gas density and energy are sums of the vapor and the noncondensable components,

$$\rho_g = \rho_v + \rho_a \tag{1-42}$$

and

$$e_g \rho_g = e_v \rho_v + e_a \rho_a \tag{1-43}$$

where specific internal energy of the noncondensable mixture is the sum of mass weighted contributions from all noncondensable gas species.

$$e_a = X_{NC,1} e_{NC,1} + X_{NC,2} e_{NC,2} + \ldots \tag{1-44}$$

We assume Dalton's law applies; therefore,

$$P = P_v + P_a . \tag{1-45}$$

TRACE, by default, applies the thermodynamic properties for air to a single noncondensable gas. The code user may, however, select hydrogen, helium, nitrogen, argon, krypton, or xenon as the single gas, or use any of these in a mixture.

Liquid Solute

TRACE includes an optional mass-continuity equation for a solute (default is orthoboric acid) moving with the liquid field.

Liquid-Solute Concentration Equation

$$\frac{\partial[(1-\alpha)m\rho_l]}{\partial t} + \nabla \cdot \left[(1-\alpha)m\rho_l \vec{V}_l\right] = S_m \tag{1-46}$$

where *m* is the solute concentration (mass of solute/unit mass of liquid water) in the liquid phase.

The solute does not affect the hydrodynamics directly. However, the amount of the dissolved and the plated-out orthoboric acid in a reactor core may affect the hydrodynamics indirectly through neutronic-reactivity feedback corresponding to user-specified input values obtained from a boron-mass reactivity-coefficient table (see **Chapter 9,** *Reactivity Feedback*). If the solute concentration exceeds the orthoboric-acid solubility at the liquid temperature in a specific hydrodynamic cell, TRACE assumes that the excess solute in that cell plates out. Plating on structures can occur if the cell liquid boils and thus increases the concentration beyond the solubility limit. TRACE also assumes that any plated-out solute instantaneously redissolves to the maximum allowable concentration if more liquid enters the cell. Because the solute does not affect the hydrodynamics directly, the solute variable may also be used as a tag to track the movement of liquid from a specific source through the system.

Application Specific Usage of these Equations

TRACE utilizes the time and volume averaged equations presented in the previous section in two contexts. The first is in a 1-D form in which fluid behavior in the other two dimensions is hidden by an average of the flow over the cross-section of the flow channel. As will be seen below, this procedure permits modeling of flow channels with variable cross-sectional area, but loses the ability to capture the effects of flow structures (e.g. recirculation zones) associated with changes in cross-sectional area. The second context is 3-D modeling, where a porous media approach is followed in the actual implementation. When the field equations are averaged over a 3-D region, provisions are made for metal structures filling portions of the geometric volumes and bounding flow areas, reducing the actual space available for flow. Changes of available flow area within this context, combined with sizes of the averaging volumes will also mask details of flow patterns. In both cases empirical modeling is required to capture the average effects of flows not resolved. The primary contribution to this modeling seen by the user is the need to specify empirical loss coefficients for the momentum equations.

1-D Equations

The use of the term "one-dimensional" in association with the equations used by TRACE to model piping in reactors or experiments can be an immediate source of confusion. The tendency is to think in terms of three-dimensional Cartesian geometry, and a pipe running straight in a single direction. However, piping runs in these systems have a number of bends, and a true one-

dimensional equation has only one "momentum" equation. What is done in TRACE, and was done in its predecessors TRAC and RELAP, is to think in terms of a coordinate system in which the one dimension follows the centerline of the entire piping run. Within this view, the flows in all piping segments shown in Figure 1-1 are all one-dimensional, and the vectors at the entrance and exit of each example are in the same coordinate direction.

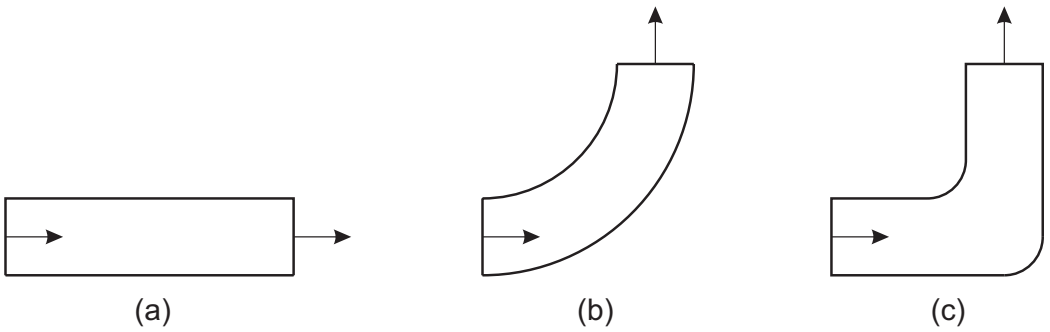

Figure. 1-1. Sample 1-D Piping Segments

The first pipe segment in Figure 1-1 represents the standard view of 1-D flow and a single coordinate momentum equation will work well as long as the flow is turbulent, giving a flat velocity profile over most of the flow cross-section. For the second pipe segment, the dimension along the pipe could be the theta direction in a cylindrical coordinate system. Although this change in coordinate system simplifies the construction of an area averaged momentum equation, the turn can't always be ignored. For single phase flow centrifugal force terms alter velocity profiles and can have a small impact of the wall friction term. For two phase flow, the centrifugal force term in the un-modeled radial momentum equation can have a significant effect on flow regime, and through that, the relative velocity between the phases and the wall heat transfer (e.g. helical heat exchanger tube). In sharper bends separation should be expected for flow coming past the inside of the bend, and irrecoverable pressure losses will occur up to the limit predicted by a simple two-dimensional right angle turn analysis. All of these details are lost in averaging over the flow cross-section, and if important must be captured with special sub-grid models.

Similar loss of information occurs for flow through a straight run of variable area pipe (see Figure 1-2). Recirculation zones downstream of an expansion, vena contracta downstream of a contraction, and pressure distributions associated with these phenomena will not be captured. That is a job for CFD. The approach in TRACE and its predecessors has been to structure the discrete implementation to introduce the minimum irrecoverable loss at an abrupt area change and to rely on user input of loss coefficients to model physical processes lost in the coarse nodalization. For the flow illustrated in Figure 1-2 the goal is to have a discrete form of the momentum equation that, absent wall friction terms, produces a pressure change between inlet and outlet that is as consistent as possible with Bernoulli flow. Irrecoverable pressure losses associated with unresolved details of the flow are again covered by user input loss coefficients.

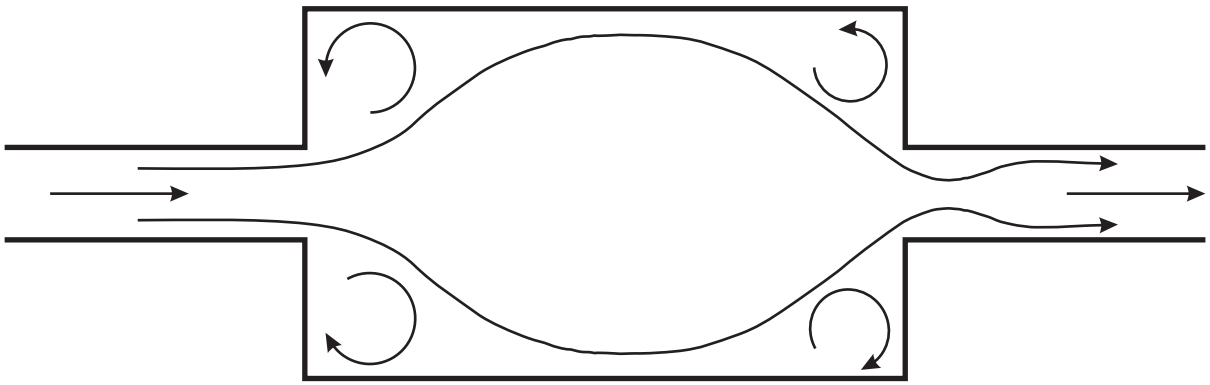

Figure. 1-2. Abrupt Expansion and Contraction

Pseudo 2-D Flow

One-dimensional modeling is complicated by the fact that pipes modeled by one dimensional cross-section averaged equations can have connections through their walls from other pipes. Within reactor systems these connections are necessary to model Emergency Core Cooling Systems (ECCS) and jet pumps. Topologically, connections can range from a right angle "T", through angled connections to the wall, to injection pipes that are interior and parallel to a larger pipe at the point of injection (see Figure 1-3).

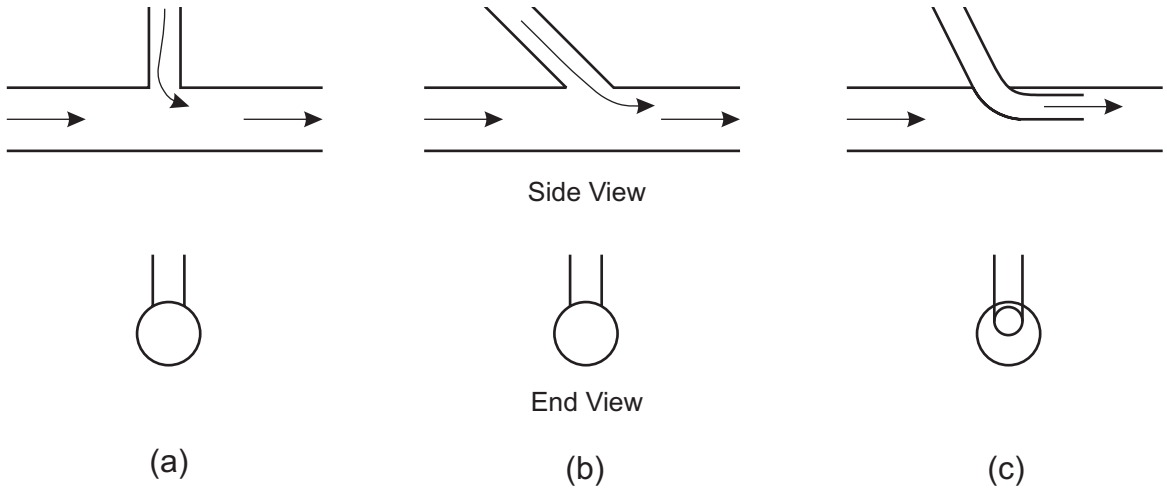

Figure. 1-3. Tee connections

Derivations of the finite volume equations in the next section include provisions for such side junctions to a 1-D flow path. However, there are certain limitations within the current TRACE

implementation that should be noted now. For reactor system transients the injection flow patterns illustrated in Figure 1-3 are the situations where the momentum transport terms are the most significant. In particular it is very important to transfer momentum correctly within a jet pump model, and in situations where ECCS liquid is being injected into a steam flow through a reactor coolant pipe. A rigorous formulation for momentum transfer terms has not been developed for the case were flow is out through the side connection. When this happens in normal reactor scenarios, the split in mass flows between the main and side legs of the connection is driven by pressure rather than momentum terms. In addition TRACE currently expects the main channel to have a constant cross-sectional area over the volume with the side flow connection. Abrupt area changes across a volume containing a side junction can lead to distortions in momentum transfer terms. If the impact of momentum transfer in such a location is not clearly understood to be minimal, user guidelines on nodalization at a side junction should be followed.

One aspect of outflow from a side junction has been given special treatment. When the main channel has stratified two-phase flow and a large enough pressure drop occurs through the side connection, the volume fraction of fluid pulled through the side junction is not equal to the mean volume fraction in the main flow channel. TRACE uses a special offtake model, documented in **Chapter 10**, to determine the void fraction of the fluid convected out of the side junction.

3-D Equations

The 3-D implementation of the field equations suffer from two primary limitations. The first has already been mentioned. There is no model for turbulent diffusion and shear between fluid cells, making TRACE unsuitable for modeling circulation patterns in large open regions. The second is related to the large computational volumes used in models of reactor vessels. Flow turns from the cold leg into the downcomer and normally from the downcomer to the lower plenum within a single volume. This yields an irrecoverable pressure loss within the calculation that is the same as can be obtained from a simple back of the envelop calculation for a sharp right angle turn. In fact the streamlines curve, and the pressure distribution is such that the actual pressure loss will be less than the right angle limit.

Basic Finite-Volume Approximations to the Flow Equations

To avoid confusion a few words are necessary about notation used in this section. We use a fairly standard notation to represent a volume integral. For example mass in a volume would be written as

$$mass = \int_V \rho \, dV \tag{1-47}$$

Unfortunately, an upper case "V" is also used when writing velocities. However, there will be no integration over velocities in this documentation, so that the combination of a "V" below an integral sign and a "dV" should always be interpreted as a volume integral. To avoid confusion when integrals are not present in notation, we define

$$Vol = \int_V dV \tag{1-48}$$

Integrals are further abreviated through use of overbar averaging notation. For example the mean density in a volume is expressed as

$$\bar{\rho} = \frac{\left(\int_V \rho dV \right)}{Vol} \tag{1-49}$$

The field equations introduced in the previous section have gone through a volume averaging process to generate the wall terms in the energy and momentum equations, and fit well with a finite volume solution approach. Consider the region in a flow channel illustrated in Figure 1-4. In this example the surface bounding the volume of fluid is divided into the channel wall area, and three areas (A_1, A_2, A_3) through which flow can occur. The integral form of the gas mass conservation equation for this volume is:

$$\frac{\partial}{\partial t}\int_V \alpha\rho_g dV + \int_V \nabla \cdot (\alpha\rho_g \vec{V}_g) dV = \int_V \Gamma dV \tag{1-50}$$

or applying Gauss' Theorem:

$$\frac{\partial}{\partial t}\int_V \alpha\rho_g dV + \oint_S \alpha\rho_g \vec{V}_g \cdot d\vec{S} = \int_V \Gamma dV. \tag{1-51}$$

Hence the time derivative of the total gas mass in the region can be written as:

$$\frac{\partial(\overline{\alpha\rho_g})}{\partial t} Vol + \left(\overline{\alpha\rho_g \vec{V}_g}\right)_1 \cdot \vec{A}_1 + \left(\overline{\alpha\rho_g \vec{V}_g}\right)_2 \cdot \vec{A}_2 + \left(\overline{\alpha\rho_g \vec{V}_g}\right)_3 \cdot \vec{A}_3 = \bar{\Gamma} \cdot Vol \tag{1-52}$$

where the positive sense of an area vector is directed out from the volume.

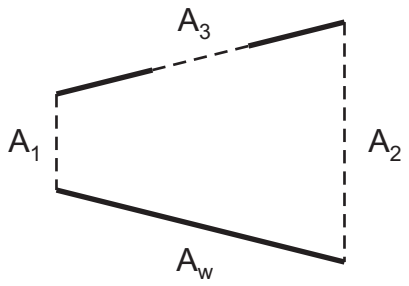

Figure. 1-4. Volume in a Flow Channel

Four approximations must be made to convert Eq. (1-52) to a useful discrete approximation to the gas mass conservation equation. First the volume average of vapor macroscopic density must be related to the volume centered values. In TRACE, the simple first order assumption is made that state quantities are constant throughout a volume, so the volume average is taken to be equal to the volume center value. The next approximation converts the partial derivative with respect to time to a simple algebraic expression, given as

$$\frac{\partial(\overline{\alpha\rho}_g)}{\partial t} = \frac{\overline{\alpha\rho}_g^{\,n+1} - \overline{\alpha\rho}_g^{\,n}}{\Delta t}, \tag{1-53}$$

where:

1) a superscript "n" denotes known values at the current level in time;

2) a superscript "$n+1$" denotes a value at the next level in time that must be determined from solution of the equations; and

3) Δt is the increment in time between levels n and $n+1$.

The third approximation is that for all expressions, the average of a product is equal to the product of individual average state variables. In this case, Eq. (1-52) becomes

$$\frac{\partial \bar{\alpha}\bar{\rho}_g}{\partial t} Vol + \left(\bar{\alpha}\bar{\rho}_g\overrightarrow{\overline{V}_g}\right)_1 \cdot \vec{A}_1 + \left(\bar{\alpha}\bar{\rho}_g\overrightarrow{\overline{V}_g}\right)_2 \cdot \vec{A}_2 + \left(\bar{\alpha}\bar{\rho}_g\overrightarrow{\overline{V}_g}\right)_3 \cdot \vec{A}_3 = \bar{\Gamma} \cdot Vol \ . \tag{1-54}$$

The fourth approximation relates values of state variables at volume edge flow faces to volume centered quantities. In the case of Eq. (1-54), when void fraction and gas density are needed to

calculate a mass flux at a flow surface (A_1, A_2, or A_3), the values are obtained from the nearest volume center upstream (as determined by gas velocity) from the flow surface. This is a first order upwind method. Momentum equations are evaluated at the edges of the volumes used for mass and energy conservation, so no upwind approximation is needed to obtain the velocity used in mass flux terms. One important piece of information missing from Eq. (1-54) is the time level of state variables in the mass flux terms. Options for this choice within TRACE are discussed later in this chapter.

Similar derivations can be followed to obtain discrete forms for other mass and energy conservation equations. For liquid mass or energy equations, the upwind cell center is determined from the liquid velocity.

Generation of a discrete approximation to the momentum equation is more complex due to the fact that velocities and associated momentum equations are not evaluated at the same locations as thermodynamic state variables. Momentum equations and the primary associated velocities are evaluated at the surfaces separating the volumes used for conservation of mass and energy. Figure 1-5 illustrates the edge (labeled $j+1/2$) between two adjacent mass/energy conservation volumes (j and $j+1$). It illustrates the fact that a given computational volume can have a non-

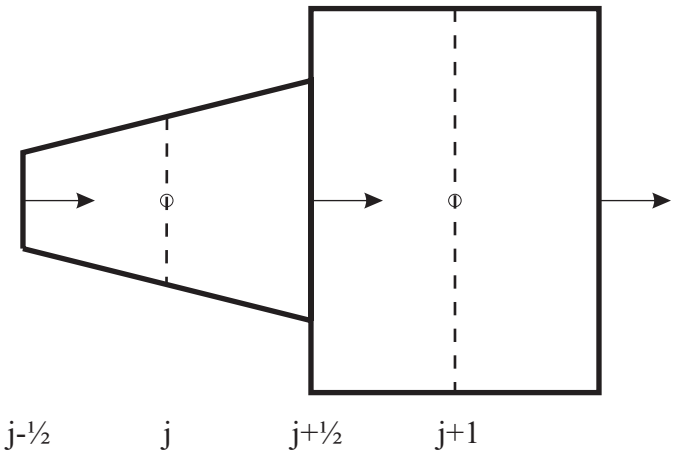

Figure. 1-5. Two mass/energy conservation volumes

uniform cross-sectional area, and that discontinuous changes in flow area can be modeled at the junction between volumes. The center of a mass conservation volume is taken to be halfway between the bounding flow surfaces along the center of the flow channel. Dotted lines through these center points represent surfaces that will bound a volume to be used in the derivation of the finite volume form of the momentum equation. Since the fundamental evaluation of velocities is not at these dotted surfaces through points j and $j+1$, a special averaging procedure is needed to obtain velocities at these surfaces for use in momentum transport terms. This needs to be consistent with the upwind procedure discussed for the mass conservation equation. However,

because rapid area changes are permitted from volume to volume, the upwind approach is applied to volumetric flow rather than velocity and for the flow direction chosen in Figure 1-5 we get

$$V_{j+1} = \frac{A_{j+1/2} V_{j+1/2}}{A_{j+1}}$$

and

$$V_j = \frac{A_{j-1/2} V_{j-1/2}}{A_j}.$$

A detailed derivation of the discrete momentum equation and an alternative derivation based upon kinetic energy are provided in **Appendix B**. However, key steps in the process are provided here. Figure 1-6 focuses on the momentum volume consisting of the right half of mass volume j and left half of mass volume $j+1$. To cut the length of subscript notation, the surfaces at locations j and $j+1$ in Figure 1-5 are now designated by subscripts 1 and 2 respectively and assigned areas A_1 and A_2. The central surface between the two mass volumes is given a subscript c, and to cover side junctions in the derivation, side flow through an area A_3 is permitted. Users need to know that more than one such side junction may exist. Because of the upstream approximations used for spatial averages, only those side junctions upstream from the center of the momentum cell can contribute to momentum fluxes. In the final implementation of the finite volume momentum equation, this upstream requirement can result in a shift in association of a side junction from one momentum volume to its immediate neighbor as flow velocities switch sign.

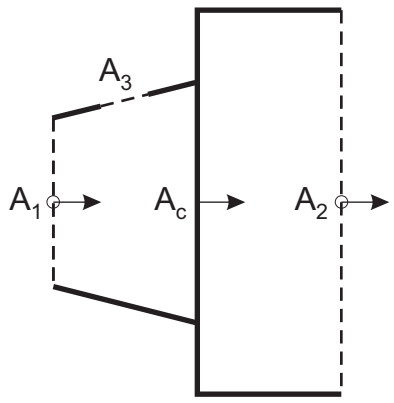

Figure. 1-6. Momentum Volume

Basic approximations used in generation of the final discrete equations are modified slightly. Thermodynamic state variables such as density, pressure, and volume fraction are still constant

over mass conservation volumes, so within the momentum volume, density (for example) has one uniform value upstream of the central flow area (A_c), and a second uniform value downstream of the central area. However, it is the product of velocity and channel flow area (volumetric flow) that is treated as constant on either side of the central flow area.

As a simple example of generation of a discrete momentum equation, integrate the gas momentum equation over the momentum volume associated with flow surface A_c located between two mass/energy conservation volumes.

$$\int_V \frac{\partial}{\partial t}(\alpha\rho_g \vec{V}_g)\,dV + \int_S (\alpha\rho_g \vec{V}_g \vec{V}_g)\cdot d\vec{S} + \int_V \alpha\nabla P\,dV = \int_V (\Gamma \vec{V}_i + \vec{f}_i + \vec{f}_w + \alpha\rho\vec{g})\,dV \qquad (1\text{-}55)$$

or

$$\int_V \frac{\partial}{\partial t}(\alpha\rho_g \vec{V}_g)\,dV + \sum_{k=1,3} \overline{(\alpha\rho_g \vec{V}_g \vec{V}_g)}_k \cdot \vec{A}_k + \int_V \alpha\nabla P\,dV = \int_V (\Gamma \vec{V}_i + \vec{f}_i + \vec{f}_w + \alpha\rho\vec{g})\,dV. \qquad (1\text{-}56)$$

Next integrate the mass conservation equations over the portions of the volume to the left and right of A_c. Area vectors for areas 1 through 3 are chosen to have a positive sense out of the momentum volume. The area vector associated with an area splitting the momentum volume in the middle has a sign convention that is positive towards end area 2.

$$\int_{V_r} \frac{\partial}{\partial t}(\alpha\rho_g)\,dV - \overline{(\alpha\rho_g \vec{V}_g)}_c \cdot \vec{A}_c + \overline{(\alpha\rho_g \vec{V}_g)}_2 \cdot \vec{A}_2 = \int_{V_r} \Gamma\,dV \qquad (1\text{-}57)$$

and

$$\int_{V_l} \frac{\partial}{\partial t}(\alpha\rho_g)\,dV + \overline{(\alpha\rho_g \vec{V}_g)}_1 \cdot \vec{A}_1 + \overline{(\alpha\rho_g \vec{V}_g)}_c \cdot \vec{A}_c + \overline{(\alpha\rho_g \vec{V}_g)}_3 \cdot \vec{A}_3 = \int_{V_l} \Gamma\,dV \qquad (1\text{-}58)$$

Changing notation to use of the volume and area averages seen in the derivation of the finite volume mass equation, the integrated momentum equation can be written as:

$$\frac{\partial}{\partial t}\overline{(\alpha\rho_g\vec{V}_g)}\,Vol_{j+1/2} + \sum_{k=1,3}\overline{(\alpha\rho_g\vec{V}_g\vec{V}_g)_k}\cdot\vec{A}_k \tag{1-59}$$

$$+\,\overline{\alpha\nabla P}\,Vol_{j+1/2} = \left(\overline{\Gamma\vec{V}_i} + \overline{\vec{f}_i} + \overline{\vec{f}_w} + \overline{\alpha\rho\vec{g}}\right)Vol_{j+1/2}$$

The mass equations for the left (subscript l) and right (subscript r) halves of the momentum volume are:

$$\frac{\partial}{\partial t}(\overline{\alpha\rho_g})\,Vol_l + \overline{(\alpha\rho_g\vec{V}_g)_1}\cdot\vec{A}_1 + \overline{(\alpha\rho_g\vec{V}_g)_c}\cdot\vec{A}_c + \overline{(\alpha\rho_g\vec{V}_g)_3}\cdot\vec{A}_3 = \overline{\Gamma}_l Vol_l \tag{1-60}$$

and

$$\frac{\partial}{\partial t}(\overline{\alpha\rho_g})_r\,Vol_r - \overline{(\alpha\rho_g\vec{V}_g)_c}\cdot\vec{A}_c + \overline{(\alpha\rho_g\vec{V}_g)_2}\cdot\vec{A}_2 = \overline{\Gamma}_r Vol_r \tag{1-61}$$

Next rearrange these mass equations to get end fluxes along the primary direction of flow.

$$\overline{(\alpha\rho_g\vec{V}_g)_1}\cdot\vec{A}_1 = \overline{\Gamma}_l Vol_l - \frac{\partial}{\partial t}(\overline{\alpha\rho_g})_l\,Vol_l - \overline{(\alpha\rho_g\vec{V}_g)_c}\cdot\vec{A}_c - \overline{(\alpha\rho_g\vec{V}_g)_3}\cdot\vec{A}_3 \tag{1-62}$$

and

$$\overline{(\alpha\rho_g\vec{V}_g)_2}\cdot\vec{A}_2 = \overline{\Gamma}_r Vol_r - \frac{\partial}{\partial t}(\overline{\alpha\rho_g})_r\,Vol_r + \overline{(\alpha\rho_g\vec{V}_g)_c}\cdot\vec{A}_c \tag{1-63}$$

At this point we use the assumption that the volume average of the products is equal to the product of the volume averages. By this point all velocities are time averaged, and turbulence effects have been included in wall and interfacial force terms, so no further loss of turbulence effects is implied. As mentioned in the previous section, this assumption works well in most cases, but some cases exist where this will introduce difficulties. To simplify notation beyond this point we will drop the bar over flow variables. Eq. (1-59) becomes:

$$\frac{\partial}{\partial t}(\alpha\rho_g\vec{V}_g)\,Vol_{j+1/2} + \sum_{k=1,3}(\alpha\rho_g\vec{V}_g\vec{V}_g)_k\cdot\vec{A}_k \tag{1-64}$$

$$+\,(\alpha\nabla P)\,Vol_{j+1/2} = \left(\Gamma\vec{V}_i + \vec{f}_i + \vec{f}_w + \alpha\rho\vec{g}\right)Vol_{j+1/2}$$

Flux terms in Eq. (1-64) are expanded by multiplying Eq. (1-62) by $V_{g,1}$ and Eq. (1-63) by $V_{g,2}$, giving us

$$(\alpha\rho_g \overrightarrow{V_g}\overrightarrow{V_g})_l \cdot \overrightarrow{A_l} = \Gamma_l V_{g,1} Vol_l - V_{g,1}\frac{\partial}{\partial t}(\alpha\rho_g)_l Vol_l - V_{g,1}(\alpha\rho_g \vec{V}_g)_c \cdot \vec{A}_c - V_{g,1}(\alpha\rho_g \vec{V}_g)_3 \cdot \vec{A}_3 \quad (1\text{-}65)$$

$$(\alpha\rho_g \overrightarrow{V_g}\overrightarrow{V_g})_2 \cdot \overrightarrow{A_2} = \Gamma_r V_{g,2}\ Vol_r - V_{g,2}\frac{\partial}{\partial t}(\alpha\rho_g)_r Vol_r + V_{g,2}\ (\alpha\rho_g \vec{V}_g)_c \cdot \vec{A}_c\ . \quad (1\text{-}66)$$

Eq. (1-65) and Eq. (1-66) provide expressions for the first two terms in the momentum flux summation from Eq. (1-64), giving:

$$\sum_{k=1,3}(\alpha\rho_g \overrightarrow{V_g}\overrightarrow{V_g})_k \cdot \overrightarrow{A_k} = \vec{V}_{g,2}\ (\alpha\rho_g \vec{V}_g)_c \cdot \vec{A}_c - \vec{V}_{g,1}\ (\alpha\rho_g \vec{V}_g)_c \cdot \vec{A}_c \quad (1\text{-}67)$$

$$+ (\vec{V}_{g,3} - \vec{V}_{g,1})(\alpha\rho_g \vec{V}_g)_3 \cdot \vec{A}_3 + \Gamma_r \vec{V}_{g,2}\ Vol_r + \Gamma_l \vec{V}_{g,1}\ Vol_l$$

$$- \vec{V}_{g,2}\frac{\partial}{\partial t}(\alpha\rho_g)_r Vol_r - \vec{V}_{g,1}\frac{\partial}{\partial t}(\alpha\rho_g)_l Vol_l$$

or

$$\sum_{k=1,3}(\alpha\rho_g \overrightarrow{V_g}\overrightarrow{V_g})_k \cdot \overrightarrow{A_k} = (\alpha\rho_g \vec{V}_g)_c \cdot \vec{A}_c\left(\vec{V}_{g,2} - \vec{V}_{g,1}\right) \quad (1\text{-}68)$$

$$+ (\vec{V}_{g,3} - \vec{V}_{g,1})(\alpha\rho_g \vec{V}_g)_3 \cdot \vec{A}_3 + \Gamma_r \vec{V}_{g,2}\ Vol_r + \Gamma_l \vec{V}_{g,1}\ Vol_l$$

$$- \vec{V}_{g,2}\frac{\partial}{\partial t}(\alpha\rho_g)_r Vol_r - \vec{V}_{g,1}\frac{\partial}{\partial t}(\alpha\rho_g)_l Vol_l$$

Given that the only permitted location for area discontinuity is at the center of the momentum volume, and that the final numerical method is restricted to first order accuracy, we can write:

$$\frac{\partial}{\partial t}(\alpha\rho_g \overrightarrow{V_g})\, Vol_{j+1/2} - \vec{V}_{g,2}\frac{\partial}{\partial t}(\alpha\rho_g)_r\, Vol_r \qquad (1\text{-}69)$$
$$- \vec{V}_{g,1}\frac{\partial}{\partial t}(\alpha\rho_g)_l\, Vol_l = \alpha\rho_g \frac{\partial}{\partial t}(\vec{V}_g)\, Vol_{j+1/2}$$

and

$$\Gamma\vec{V}_i\, Vol_{j+1/2} - \Gamma_r\vec{V}_{g,2}\, Vol_r - \Gamma_l\vec{V}_{g,1}\, Vol_l = \Gamma(\vec{V}_i - \vec{V}_g)\, Vol_{j+1/2} \qquad (1\text{-}70)$$

Eqs. (1-69) and (1-70) can be substituted into Eq. (1-68), and the result substituted into Eq. (1-64), to give a simpler form of the finite volume momentum equation.

$$\alpha\rho_g \frac{\partial}{\partial t}(\vec{V}_g)\, Vol_{j+1/2} + (\alpha\rho_g\vec{V}_g)_c \cdot \vec{A}_c\left(\vec{V}_{g,2} - \vec{V}_{g,1}\right) \qquad (1\text{-}71)$$
$$+\left(\vec{V}_{g,3} - \vec{V}_{g,1}\right)(\alpha\rho_g\vec{V}_g)_3 \cdot \vec{A}_3 + \alpha\nabla P\, Vol_{j+1/2}$$
$$= \left[\Gamma(\overrightarrow{V_i} - \overrightarrow{V_g}) + \vec{f}_i + \vec{f}_w + \alpha\rho\vec{g}\right] Vol_{j+1/2}$$

At this point, to obtain results useful for a computer solution, we need to employ the previously mentioned assumptions about the spatial dependence of state variables within the volumes of interest. Here void fraction, densities, and pressure are taken as constant within the left portion of the momentum volume and a separate set of constant values over the right portion of the momentum volume. The basis functions for velocities are slightly modified to deal with the possibility of discontinuous change in area at the center of the momentum volume. Rather than taking the velocity to be constant, the product of area averaged velocity and area is taken as constant.

Expressions for volume averages need to be reexamined under the first order assumptions to provide useful forms for these terms. One additional quantity that will be useful in this context will be the distance "dx" along the primary flow path between bounding areas A_1 and A_2. Three of the averages in Eq. (1-71) are:

$$\alpha\rho_g \frac{\partial}{\partial t}(\vec{V}_g)\, Vol_{j+1/2} = \int_V \alpha\rho_g \frac{\partial}{\partial t}(\vec{V}_g)\, dV = \int_{dx}\int_A \alpha\rho_g \frac{\partial}{\partial t}(\vec{V}_g)\, dA\, dx \tag{1-72}$$

$$= \int_{dx} \alpha\rho_g \int_A \frac{\partial}{\partial t}(\vec{V}_g)\, dA\, dx = \left[(\alpha\rho_g dx)_l + (\alpha\rho_g dx)_r\right] \frac{\partial}{\partial t}(\vec{V}_{g,c})\, A_c$$

$$= \overline{\alpha\rho_g}\, \frac{\partial}{\partial t}(\vec{V}_{g,c})\, A_c dx$$

$$\Gamma(\vec{V}_i - \vec{V}_g)\, Vol_{j+1/2} = \int_V \Gamma(\vec{V}_i - \vec{V}_g)\, dV = \int_{dx}\int_A \Gamma(\vec{V}_i - \vec{V}_g)\, dA\, dx \tag{1-73}$$

$$= \int_{dx} \Gamma \int_A (\vec{V}_i - \vec{V}_g)\, dA\, dx = [(\Gamma\, dx)_l + (\Gamma\, dx)_r](\vec{V}_i - \vec{V}_g)_c A_c$$

$$= \bar{\Gamma}\,(\vec{V}_i - \vec{V}_g)_c\, A_c dx$$

and

$$\alpha\rho_g \vec{g}\, Vol_{j+1/2} = \int_V \alpha\rho_g\, \vec{g} dV = (\alpha\rho_g)_l Vol_l\, \vec{g_l} + (\alpha\rho_g)_r Vol_r\, \vec{g_r} = \overline{\alpha\rho_g \vec{g}}\; Vol_{j+1/2} \tag{1-74}$$

Evaluation of the total contribution of pressure forces is greatly simplified by the first order assumption that state variables are constant over sub-regions of the integration volume. For this particular case with pressure and void constant to the left and right of A_c, we divide the integral of the pressure force term into integration over three sub-volumes. One is centered on A_c with an infinitesimal thickness perpendicular to A_c. The other two sub-volumes cover the remainder of the momentum volume to the left and right of A_c. The integral over these two large volumes will be zero because the pressure gradient is zero throughout both. However, the integral over the central volume is non-zero due to the discontinuity in pressure. The result is obtained through use of Heaviside step functions to represent the functional forms of pressure and void fraction.

$$\int_V \alpha \nabla P dV = A_c \int_{-\delta}^{\delta} \alpha \nabla P dx = A_c \frac{(\alpha_l + \alpha_r)}{2}(P_r - P_l) \tag{1-75}$$

For those accustomed to the derivation of loss coefficients for an abrupt expansion, this approximation will look wrong. In the classic abrupt expansion case, the pressure P_1 is assumed to also be appropriate in the right sub-volume over the wall area aligned with the center surface of the momentum volume. Unfortunately, the finite volume calculation must be able to deal with a wide variety of channel shapes. Rather than doing subgrid calculations to obtain better values of surface pressure distributions, we have elected to account for the discrepancy by using loss coefficients. The approach taken in Eq. (1-75) produces the lowest irrecoverable pressure loss of all possible assumptions about wall pressure distribution. It is up to the user to provide loss coefficients in the model's input specification that result in the correct irrecoverable pressure loss.

The force terms for interfacial and wall shear have proportionality to velocity, so the volume multiplying those terms ($Vol_{j+1/2}$) can be converted to the product $A_c \cdot \mathrm{dx}$. Substituting all of the approximations to the volume integrals into the last form of the momentum equation and dividing everything by $\alpha\rho_g A_c \mathrm{dx}$ gives

$$\frac{\partial}{\partial t}(\overrightarrow{V_g}) + \frac{(\alpha\rho_g \vec{V}_g)_c}{\overline{\alpha\rho_g} A_c dx} \cdot \overrightarrow{A_c}\left(\vec{V}_{g,2} - \vec{V}_{g,1}\right) + \frac{\left(\vec{V}_{g,3} - \vec{V}_{g,1}\right)}{\overline{\alpha\rho_g} A_c dx}(\alpha\rho_g \vec{V}_g)_3 \cdot \overrightarrow{A_3} \tag{1-76}$$

$$+ \frac{\overline{\alpha}(p_r - p_l)}{\overline{\alpha\rho_g}\, dx}\hat{i} = \frac{1}{\overline{\alpha\rho_g}}\left[\Gamma(\vec{V}_{i,c} - \vec{V}_{g,c}) + \overrightarrow{f_{i,c}} + \overrightarrow{f_{w,c}} + \overline{\alpha\rho_g}\vec{g}\ \frac{Vol_{j+1/2}}{A_c dx}\right]$$

The actual momentum equations in TRACE were derived from a finite difference approach, and ratios with the product of volume fraction and density in numerator and denominator are set to one.

$$\frac{\partial}{\partial t}(\overrightarrow{V_g}) + \frac{(\vec{V}_g)_c}{A_c dx} \cdot \overrightarrow{A_c}\left(\vec{V}_{g,2} - \vec{V}_{g,1}\right) + \frac{\left(\vec{V}_{g,3} - \vec{V}_{g,1}\right)}{\overline{\alpha\rho_g} A_c dx}(\alpha\rho_g \vec{V}_g)_3 \cdot \overrightarrow{A_3} \tag{1-77}$$

$$+ \frac{\overline{\alpha}(p_r - p_l)}{\overline{\alpha\rho_g}\, dx}\hat{i} = \frac{1}{\overline{\alpha\rho_g}}\left[\Gamma(\vec{V}_{i,c} - \vec{V}_{g,c}) + \overrightarrow{f_{i,c}} + \overrightarrow{f_{w,c}}\right] + \vec{g}$$

To this point the time and volume averaged momentum equation is still 3-D. Three steps are necessary to make it useful for a 1-D model. First the equation is recast into a coordinate system in which one dimension follows the flow channel. From the standpoint of this coordinate system, there are no bends in the piping. The piping's centerline can be treated as the axis of the primary dimension. Second, take the dot product of Eq. (1-77) with a unit vector along the primary dimension to isolate the component of the velocity along the piping. Finally introduce a term to account for irrecoverable losses lost in the volume averaging and collapse to one dimension. This

accounts for wall pressure distributions and effects of recirculation zones not resolved due the scale of volume averaging.

$$\frac{\partial V_g}{\partial t} + \frac{(V_g)_c}{dx}\left(V_{g,2} - V_{g,1}\right) + \frac{V_{g,3}\cos\phi - V_{g,1}}{\overline{\alpha\rho_g} A_c dx}(\alpha\rho_g V_g)_3 A_3 \tag{1-78}$$

$$+ \frac{\overline{\alpha}(p_r - p_l)}{\overline{\alpha\rho_g}\, dx} = \frac{1}{\overline{\alpha\rho_g}}\left[\Gamma\left(V_{i,c} - V_{g,c}\right) + f_{i,c} + f_{w,c}\right] + \vec{g}\cos\theta$$

In the above equation ϕ is the angle between the pipe centerline and the primary flow direction through face A_3, and θ is the angle between a vector along the centerline in a positive direction and a vector pointing vertically upward (against gravity).

During the evolution of the TRACE momentum equation implementation several deviations have occurred from the formal definition of terms in this derivation.

- The mean volume fraction of gas used in the pressure gradient term is currently a cell length weighted rather than simple average.
- The value of $\alpha\rho_g$ in the denominator of the flux term for side connection momentum is currently donor cell averaged rather than cell length weighted.
- The final coefficient for the gravitational source term must be consistent with static gravitational pressure head in a two phase column of liquid
- V_1 and V_2 are obtained from area scaling of upwind edge velocities, and in the momentum flux term $V_{g,c}$ is a simple area weighted average of V_1 and V_2, chosen this way to give Bernoulli equation results in the limit of steady state and constant density.

Time Level Selection

TRACE contains the option to select one of two related numerical methods for solution of the two-phase-flow equations. The default Stability Enhancing Two-Step (SETS) method has the advantage of avoiding Courant stability limits on time-step size but the disadvantage of relatively high numerical diffusion. A namelist input option permits selection of a semi-implicit method that can have substantially less numerical diffusion but has time-step sizes restricted by a material Courant limit. This should be the method of choice for BWR stability analysis. Currently, a single method must be used for the entire system. It is not possible, for example to use a semi-implicit vessel and SETS for the 1-D loops.

Both basic finite-volume models are descendents of the Implicit Continuous Eulerian technique (ICE) (Ref. 1-9). The key improvement introduced by Liles and Reed (Ref. 1-10) in their semi-implicit method was a tighter coupling of the energy equation to the mass and momentum equations than that used in ICE. This coupling is crucial to stable modeling of two-phase flows

with substantial boiling or condensation. The SETS method (Refs. 1-11 and 1-12) includes the semi-implicit method at its core and increases stability with an additional evaluation of each field equation during each time step.

In the following subsections, the semi-implicit and SETS methods will be described at three levels of detail. The basic aspects of each method are illustrated for simple 1D single-phase-flow equations as follows:

$$\frac{\partial \rho}{\partial t} + \frac{\partial}{\partial x}(\rho V) = 0\,, \tag{1-79}$$

$$\frac{\partial (\rho e)}{\partial t} + \frac{\partial}{\partial x}(\rho e V) = -P\frac{\partial V}{\partial x} + h_w \frac{A_w}{vol}(T_w - T)\,, \tag{1-80}$$

and

$$\frac{\partial V}{\partial t} + V\frac{\partial V}{\partial x} = -\frac{1}{\rho}\frac{\partial P}{\partial x} - KV|V| \quad , \tag{1-81}$$

where K is a wall friction coefficient that may be a function of velocity and fluid properties and T_w is a pipe wall temperature. More detail is then provided through explanation of special adaptations to improve robust simulation of single- and/or two-phase flow. Finally, the full two-phase-flow equations are presented.

Fairly standard notation is used in presenting the finite-volume equations. A superscript "n" indicates known values at the beginning of a step in the time integration (old-time value). A superscript "$n+1$" labels a variable value at the end of the current time step (new-time value), which must be obtained as part of the solution of the equations. Subscripts provide information on spatial location as illustrated in **Figure 1-5**. Integer subscripts such as "j" or "$j+1$" label volume center information (e.g., P_j^{n+1} is the new-time pressure in volume "j"). A half-integer subscript indicates a value obtained at the surface separating two volumes (e.g., $V_{j+1/2}^{n}$ is the old-time velocity at the surface separating volume "j" from volume "$j+1$").

When values of cell-centered variables are needed at cell edges, an average of some form is required. The methods discussed here use values only from the volumes immediately adjacent to the given edge, so the averages are always in the following form:

$$\langle Y \rangle_{j+1/2} = w_{j+1/2} Y_j + (1 - w_{j+1/2}) Y_{j+1}\,. \tag{1-82}$$

For simple 1D flow, terms expressing mass and energy flow for the j^{th} finite volume then have the following form:

$$\frac{\partial}{\partial x_j}(YV) = \frac{\langle Y\rangle_{j+1/2} V_{j+1/2} - \langle Y\rangle_{j-1/2} V_{j-1/2}}{\Delta x}$$
$$= \frac{\left[w_{j+1/2} Y_j + \left(1 - w_{j+1/2}\right) Y_{j+1}\right] V_{j+1/2} - \left[w_{j-1/2} Y_{j-1} + \left(1 - w_{j-1/2}\right) Y_j\right] V_{j-1/2}}{\Delta x} . \quad (1\text{-}83)$$

The form is more complex for 1D flow with a spatially varying cross-sectional flow area. In this case the mass flux term is abbreviated as

$$\nabla_j \cdot (YV) = \frac{\left[w_{j+1/2} Y_j + \left(1 - w_{j+1/2}\right) Y_{j+1}\right]\left(A_{j+1/2} V_{j+1/2}\right) - \left[w_{j-1/2} Y_{j-1} + \left(1 - w_{j-1/2}\right) Y_j\right]\left(A_{j-1/2} V_{j-1/2}\right)}{vol_j} , \quad (1\text{-}84)$$

where $A_{j+1/2}$ is the flow area between cells j and $j+1$ and vol_j is the volume of the *j*th cell.

The related derivative used in the finite-difference momentum flux involves the use of a more complicated averaging method. This is driven by a need to model Bernoulli flows when appropriate and to conserve momentum properly when a side-junction flow is present. Details of this methodology are presented in **Conserving Convected Momentum**. To aid in understanding the basic numerical methods, it is worth noting that with no area changes or side junctions, the numerical form of the velocity gradient is

$$\left.\frac{\partial V}{\partial x}\right|_{j+1/2} = \frac{(1 - w_{j+1/2}) V_{j+3/2} + (2w_{j+1/2} - 1) V_{j+1/2} - w_{j+1/2} V_{j-1/2}}{\Delta x} . \quad (1\text{-}85)$$

For flows in 1D channels with variable cross-sectional area, the momentum-transfer term is abbreviated as $V_{j+1/2} \nabla_{j+1/2} V$.

Although the basics of the finite volume spatial discretization have already been covered, further details are provided in later sections of this document. **3D Finite-Difference Methods** presents a generalization of the methods to 3D geometry. Special treatment of transition to single-phase flow and conditions beyond the critical point is described in **Modifications to the Basic Equation Set**. The section **Conserving Convected Momentum** describes details of special treatment used for momentum-flux terms. The actual solution of these equations is described in **Chapter 2**.

Basics of the Semi-Implicit Method

When fluid flow is modeled with a fully explicit method, time-step sizes are restricted by the Courant limit as

$$\Delta t \leq k \cdot \frac{\Delta x}{|V| + c}, \tag{1-86}$$

where Δx is a characteristic mesh length, V is the flow velocity, c is the speed of sound, and parameter k varies in value depending on the details of the method, but here can be taken to be 1.0. This simple class of methods is appropriate when it is important to track the details of pressure wave propagation (e.g., shock waves). However, in most reactor transients, this level of detail is not important. At most, continuity waves (moving liquid levels or froth fronts) must be followed. Frequently the transient is simply an evolution between quasi-steady states.

Both the ICE and semi-implicit methods relax the explicit restrictions on time-step size by evaluating terms involved in pressure wave propagation at the new $(n+1)$ time level. For a simple form of the momentum equation, this requires new-time values in the pressure gradient term as given by

$$\frac{\left(V^{n+1}_{j+1/2} - V^{n}_{j+1/2}\right)}{\Delta t} + V^{n}_{j+1/2} \left.\frac{\partial V^{n}}{\partial x}\right|_{j+1/2} \quad . \tag{1-87}$$

$$+ \frac{1}{\langle \rho \rangle^{n}_{j+1/2}} \frac{(P^{n+1}_{j+1} - P^{n+1}_{j})}{\Delta x} + K^{n}_{j+1/2} V^{n+1}_{j+1/2} \left| V^{n}_{j+1/2} \right| = 0$$

Similarly, relaxation of the restrictions on time-step size also requires that velocities involved in flux of mass and energy be evaluated at the new-time level. The equations then become

$$\frac{(\rho^{n+1}_{j} - \rho^{n}_{j})}{\Delta t} + \frac{\partial}{\partial x_j}(\rho^{n} V^{n+1}) = 0 \tag{1-88}$$

and

$$\frac{(\rho^{n+1}_{j} e^{n+1}_{j} - \rho^{n}_{j} e^{n}_{j})}{\Delta t} + \frac{\partial}{\partial x_j}(\rho^{n} e^{n} V^{n+1}) + P^{n+1}_{j} \frac{\left(V^{n+1}_{j+1/2} - V^{n+1}_{j-1/2}\right)}{\Delta x} \quad . \tag{1-89}$$

$$= \text{heat sources } (\text{W/m}^3)$$

By using the above equation structure, information on a pressure disturbance in any cell is available to any other cell during the same time step. This eliminates the sound speed from the Courant stability limit, leaving what is commonly referred to as the "material Courant" stability limit ($\Delta t < (\Delta x)/|V|$). The absolute value of flow velocity remains in the denominator of the expression because information relevant to continuity waves is still propagated only one cell per time step by the semi-implicit method. It is worth noting here that the numerical diffusion associated with a semi-implicit method is at a minimum when the time step is equal to the material Courant stability limit (see Reference 1-7). Numerical diffusion increases as the time step decreases approaching that of a fully implicit or SETS method in the limit of very small time steps.

Completion of the problem definition requires a choice of two independent variables from the four thermodynamic variables: pressure, temperature, density, and specific internal energy. Density is not a good choice because of the need to model liquid solid regions. Given the low compressibility of liquid, a small error in a solution for density can translate to a significant error in pressure. When pressure is designated as an independent variable, a small error in the solution for pressure results in an even smaller fractional error in density. The choice of the second independent variable is driven by considerations beyond the simple equations presented above. Multi-phase and multi-component systems tend toward an equilibrium in which the phases and/or components are all at the same temperature. This behavior is reflected in constitutive relations for interphase (or wall-to-fluid) heat transfer that depend on differences of temperatures and that must be evaluated implicitly with respect to these temperature differences in the numerical equations. When the gas phase contains a mixture of species, all species are assumed to be at the same temperature. Selecting temperature as an independent variable in these situations can significantly simplify final solution of the equations.

Equations of state provide density and internal energy as functions of pressure and temperature. The relationships are generally nonlinear; therefore, the combination of discretized flow equations and state equations yields a coupled set of nonlinear equations. A key feature of TRACE is the use of an iterative method (see **Chapter 2**) to obtain a solution to the nonlinear equations. The nonlinear equations are not simply replaced by a linearized approximation, as is done in RELAP5 (Ref. 1-16).

A stability analysis of these semi-implicit equations introduces limitations on weighting factors used for cell-edge averages. The equations are unconditionally unstable unless

$$\begin{aligned} w_{j+1/2} &\geq (1/2)\left(1+\frac{\Delta t\left|V_{j+1/2}\right|}{\Delta x_{j+1/2}}\right) \quad \text{for} \quad V_{j+1/2} \geq 0 \quad \text{and} \\ w_{j+1/2} &\leq (1/2)\left(1-\frac{\Delta t\left|V_{j+1/2}\right|}{\Delta x_{j+1/2}}\right) \quad \text{for} \quad V_{j+1/2} < 0. \end{aligned} \qquad (1\text{-}90)$$

When the inequalities are replaced with equalities in the above expression, a difference scheme with the minimal permitted numerical diffusion results. However, experience with a range of two-phase-flow problems has resulted in the final adoption of the following more robust choice of weighting factors:

$$w_{j+1/2} = \begin{cases} 1 & \text{for} \quad V_{j+1/2} \geq 0 \\ 0 & \text{for} \quad V_{j+1/2} < 0 \end{cases} . \tag{1-91}$$

This is the standard donor-cell or first order upwind difference method.

Enhancements to the Semi-Implicit Method

The finite-volume equations given above reflect the semi-implicit method as implemented in early versions of TRAC-PF1 (Ref. 1-16). However, the discovery of instabilities in bubbly flow (Ref. 1-13) resulted in improvements to the wall friction term in Eq. (1-87) and, more importantly, to the interfacial friction term in the two-phase momentum equations. Optimal stability would be obtained by evaluating the friction terms fully implicitly. Unfortunately, this would result in serious complications for the solution procedure outlined in **Chapter 2**. The existing solution procedure relies on the finite-difference motion equations containing no more than the first power of the new-time velocity. This permits a direct solution for V^{n+1} as a linear function of adjacent new-time pressures.

More stable force terms can be obtained from linearization of a fully implicit force term. First, assume that the new-time velocity is not very different from the old-time velocity, or

$$V^{n+1}_{j+1/2} = V^{n}_{j+1/2} + \delta V_{j+1/2} . \tag{1-92}$$

Now, substitute this expression into the fully implicit wall friction term as follows:

$$K^{n}_{j+1/2} V^{n+1}_{j+1/2} \left| V^{n+1}_{j+1/2} \right| = K^{n}_{j+1/2} \left(V^{n}_{j+1/2} + \delta V_{j+1/2} \right) \left| V^{n}_{j+1/2} + \delta V_{j+1/2} \right| \tag{1-93}$$

$$= 2 K^{n}_{j+1/2} \left| V^{n}_{j+1/2} \right| \delta V_{j+1/2} + K^{n}_{j+1/2} V^{n}_{j+1/2} \left| V^{n}_{j+1/2} \right| + O(\delta V^2)$$

Finally, drop terms containing δV^2 and replace δV with the difference between the new- and old-time velocity to give

$$K^{n}_{j+1/2} V^{n+1}_{j+1/2} \left| V^{n+1}_{j+1/2} \right| \approx 2 K^{n}_{j+1/2} V^{n+1}_{j+1/2} \left| V^{n}_{j+1/2} \right| - K^{n}_{j+1/2} V^{n}_{j+1/2} \left| V^{n}_{j+1/2} \right| . \qquad (1\text{-}94)$$

In the two-phase-flow equations, the same linearized implicit approximation is applied to the interfacial drag term.

The history of use of the semi-implicit equations within TRACE has resulted in a related approximation in the momentum flux terms for the semi-implicit method. When using the semi-implicit equations as part of the SETS method, it was found that a linearization of the implicit momentum-flux term can improve the stability of the motion equation. Details of this linearization are presented in the next subsection. Within the context of a pure semi-implicit equation the consistent development has been that the momentum flux term originally written in Eq. (1-87) is changed to:

$$V^{n+1}_{j+1/2} \frac{\partial V}{\partial x}\bigg|^{n}_{j+1/2} \qquad (1\text{-}95)$$

when the velocity derivative is positive. When the velocity derivative is negative, the form in Eq. (1-87) must be maintained to avoid an instability. The momentum flux term can be written in a single expression as:

$$V_{j+1/2} \frac{\partial V}{\partial x}\bigg|^{n}_{j+1/2} = [\beta V^{n+1}_{j+1/2} + (1-\beta) V^{n}_{j+1/2}] \frac{\partial V^{n}}{\partial x}\bigg|_{j+1/2} , \qquad (1\text{-}96)$$

where

$$\beta = \begin{bmatrix} 1 & for \ \dfrac{\partial V^{n}}{\partial x}\bigg|_{j+1/2} \geq 0 \\ 0 & for \ \dfrac{\partial V^{n}}{\partial x}\bigg|_{j+1/2} < 0 \end{bmatrix} . \qquad (1\text{-}97)$$

With the special modifications to momentum flux and friction terms, the finite-difference form of the motion equation becomes

$$\frac{(V^{n+1}_{j+1/2} - V^{n}_{j+1/2})}{\Delta t} + \left[\beta V^{n+1}_{j+1/2} + (1-\beta) V^{n}_{j+1/2}\right]\left(\frac{\partial V^{n}}{\partial x}\right)\Bigg|_{j+1/2} \quad . \tag{1-98}$$

$$+ \frac{1}{\langle \rho \rangle^{n}_{j+1/2}} \frac{(P^{n+1}_{j+1} - P^{n+1}_{j})}{\Delta x} + 2K^{n}_{j+1/2} V^{n+1}_{j+1/2} \left| V^{n}_{j+1/2} \right|$$

$$- K^{n}_{j+1/2} V^{n}_{j+1/2} \left| V^{n}_{j+1/2} \right| = 0$$

Semi-Implicit Method Adapted to Two-Phase Flow

Extension of the numerical method to the two-phase, two-fluid model is relatively straightforward. Special modifications to the method are necessary to treat changes from two-phase to single-phase flow and are described below. Source terms are present to model phase change and heat transfer. These are generally implicit in any driving temperature difference and explicit in any coefficient. The importance of gravitationally driven liquid flow requires an accurate model of gravitational force along the direction of motion. This uses an input angle (θ) between a vector from the center of cell j to the center of cell $j+1$ and a vector directed against gravity. In the application of the code, θ is more generally the inverse cosine ($\cos^{-1}$) of the change in elevation between cell centers divided by the flow length between cell centers.

To shorten notation in the following difference equations, some subscripts associated with location have been eliminated. For velocities not contained in spatial differences, the subscript denoting spatial location is assumed to be $j+1/2$. For cell-centered variables, the assumed subscript is j. The phrase "combined gas" refers to the mixture of noncondensable gas and steam, which is assumed to move with no interspecies diffusion.

Semi-Implicit Equations of Motion

Combined Gas

$$\frac{(V^{n+1}_{g} - V^{n}_{g})}{\Delta t} + [\beta_g V^{n+1}_{g} + (1-\beta_g) V^{n}_{g}] \nabla_{j+1/2} V^{n}_{g}$$

$$+ \frac{C^{n}_{i} \left| V^{n}_{g} - V^{n}_{l} \right|}{\langle \alpha \rho_g \rangle^{n}_{j+1/2}} [2(V^{n+1}_{g} - V^{n+1}_{l}) - (V^{n}_{g} - V^{n}_{l})]$$

$$+\frac{1}{\langle\rho_g\rangle^n_{j+1/2}}\frac{(P^{n+1}_{j+1}-P^{n+1}_j)}{\Delta x_{j+1/2}}+\frac{\Gamma^{+^n}_{j+1/2}}{\langle\alpha\rho_g\rangle^n_{j+1/2}}(V^{n+1}_g-V^{n+1}_l)$$

$$+\frac{C_{wg}}{\langle\alpha\rho_g\rangle^n_{j+1/2}}(2V^{n+1}_g-V^n_g)\left|V^n_g\right|+g\cos\theta=0. \quad (1\text{-}99)$$

Liquid

$$\frac{V^{n+1}_l-V^n_l}{\Delta t}+[\beta_l V^{n+1}_l+(1-\beta_l)V^n_l]\nabla_{j+1/2}V^n_l$$

$$+\frac{C^n_i\left|V^n_l-V^n_g\right|}{\langle(1-\alpha)\rho_l\rangle^n_{j+1/2}}[2(V^{n+1}_l-V^{n+1}_g)-(V^n_l-V^n_g)]$$

$$+\frac{1}{\langle\rho_l\rangle^n_{j+1/2}}\frac{(P^{n+1}_{j+1}-P^{n+1}_j)}{\Delta x_{j+1/2}}-\frac{\Gamma^{-^n}_{j+1/2}}{\langle(1-\alpha)\rho_l\rangle^n_{j+1/2}}(V^{n+1}_l-V^{n+1}_g)$$

$$+\frac{C_{wl}}{\langle(1-\alpha)\rho_l\rangle^n_{j+1/2}}(2V^{n+1}_l-V^n_l)\left|V^n_l\right|+g\cos\theta=0. \quad (1\text{-}100)$$

Semi-Implicit Mass Equations

Combined Gas

$$\frac{\alpha^{n+1}_j\rho^{n+1}_{gj}-\alpha^n_j\rho^n_{gj}}{\Delta t}+\nabla_j\cdot[\alpha^n\rho^n_g V^{n+1}_g]=\Gamma^{n+1}. \quad (1\text{-}101)$$

Noncondensable Gas

$$\frac{[\alpha^{n+1}_j\rho^{n+1}_{aj}-\alpha^n_j\rho^n_{aj}]}{\Delta t}+\nabla_j\cdot[\alpha^n\rho^n_a V^{n+1}_g]=0. \quad (1\text{-}102)$$

Additional Noncondensable Mass Equations (k^{th} species)

$$\frac{[\alpha X_k\rho_a]^{n+1}_j-[\alpha X_k\rho_a]^n_j}{\Delta t}+\nabla_j\cdot[(\alpha X_k\rho_a)^n\vec{V}^{n+1}_g]=0 \quad (1\text{-}103)$$

Liquid

$$\frac{[(1-\alpha_j^{n+1})\rho_{lj}^{n+1}-(1-\alpha_j^{n})\rho_{lj}^{n}]}{\Delta t}+\nabla_j\cdot[(1-\alpha^{n})\rho_l^{n}V_l^{n+1}]=-\Gamma^{n+1}. \quad (1\text{-}104)$$

Semi-Implicit Energy Equations

Combined Gas

$$\frac{[\alpha_j^{n+1}\rho_{gj}^{n+1}e_{gj}^{n+1}-\alpha_j^{n}\rho_{gj}^{n}e_{gj}^{n}]}{\Delta t}+\nabla_j\cdot[\alpha^{n}\rho_g^{n}e_g^{n}\vec{V}_g^{n+1}]$$

$$+P^{n+1}\left[\frac{(\alpha^{n+1}-\alpha^{n})}{\Delta t}+\nabla_j\cdot(\alpha^{n}\vec{V}_g^{n+1})\right]$$

$$=q_{wg}^{n+1}+q_{dg}^{n}+q_{ig}^{n+1}+\Gamma^{n+1}h_{sg}^{n+1}. \quad (1\text{-}105)$$

Total Fluid (gas and liquid)

$$\frac{[\alpha_j^{n+1}\rho_{gj}^{n+1}e_{gj}^{n+1}+(1-\alpha_j^{n+1})\rho_{lj}^{n+1}e_{lj}^{n+1}]-\alpha_j^{n}\rho_{gj}^{n}e_{gj}^{n}+(1-\alpha_j^{n})(\rho_{lj}^{n}e_{lj}^{n})}{\Delta t}$$

$$+\nabla_j\cdot[\alpha^{n}\rho_g^{n}e_g^{n}V_g^{n+1}+(1-\alpha^{n})\rho_l^{n}e_l^{n}V_l^{n+1}]$$

$$+P^{n+1}\nabla_j\cdot[(1-\alpha)^{n}V_l^{n+1}+\alpha^{n}V_g^{n+1}]$$

$$=q_{wg}^{n+1}+q_{wl}^{n+1}+q_{dl}^{n}+q_{dg}^{n}. \quad (1\text{-}106)$$

The wall heat transfer to the gas and liquid, q_{wg} and q_{wl}, and the interfacial mass-transfer rate, Γ, also require further definition. Note the mixture of old- and new-time values in these terms. The choice of old-time heat-transfer coefficients was driven by the desire to simplify the implementation of the method, but can result in bounded instabilities during calculations. These terms are given by

$$q_{wl}^{n+1}=h_{wl}^{n}a_w(T_w^{n+1}-T_l^{n+1}), \quad (1\text{-}107)$$

$$q_{wg}^{n+1}=h_{wg}^{n}a_w(T_w^{n+1}-T_g^{n+1}), \quad (1\text{-}108)$$

and

$$\Gamma^{n+1} = \frac{-(q_{ig}^{n+1} + q_{il}^{n+1})}{(h_v')^{n+1} - (h_l')^{n+1}}, \tag{1-109}$$

where

$$q_{ig}^{n+1} = h_{ig}^{n} a_i^{n} (T_{\mathrm{sat}}^{n+1} - T_g^{n+1}) \tag{1-110}$$

and

$$q_{il}^{n+1} = h_{il}^{n} a_i^{n} (T_{\mathrm{sat}}^{n+1} - T_l^{n+1}) \ . \tag{1-111}$$

The interfacial heat transfer coefficients ($h_{il},\ h_{ig}$), wall heat transfer coefficients ($h_{wl},\ h_{wg}$), interfacial drag coefficient (C_i) and wall friction coefficients ($C_{wg},\ C_{wl}$) all are the result of nonlinear functions associated obtained from correlations. Old time (explicit) evaluation of these coefficients can result in bounded instabilities.

Further definition is also needed for a special set of density averages used in the momentum equations. Cell-edge densities used in the denominator of Eq. (1-99) and Eq. (1-100) are defined to produce a good prediction of hydrostatic pressure heads. For example, the edge-average gas macroscopic density is defined as

$$\langle \alpha\rho \rangle_{j+1/2}^{n} = \frac{\Delta x_j (\alpha\rho)_j^n + \Delta x_{j+1} (\alpha\rho)_{j+1}^n}{\Delta x_j + \Delta x_{j+1}} \ . \tag{1-112}$$

A similar definition holds for the cell-edge liquid macroscopic density. The edge-average microscopic densities are somewhat more complex. For example,

$$\langle \rho_g \rangle_{j+1/2}^{n} = \langle \alpha\rho_g \rangle_{j+1/2}^{n} \left[\frac{\Delta x_j \alpha_j^n + \Delta x_{j+1} \alpha_{j+1}^n}{\Delta x_j + \Delta x_{j+1}} \right]^{-1} \ . \tag{1-113}$$

This particular average is necessary for consistency within the SETS equations (see **The SETS Method Adapted to Two-Phase Flow**), where macroscopic densities have a more fundamental importance within the solution.

The above finite-volume-flow equations hold only when a two-phase mixture is present at both the old- and new-time levels. Modifications are necessary when the old- or new-time-level fluid state is single phase; these are described in **Modifications to the Basic Equation Set**

Liquid Solute

Treatment of the liquid solute field (defaults to boric acid) requires a bit more discussion than the basic equations above. The primary variable used for following the solute is its mass fraction (*m*). Because the rate of transition between the dissolved and plated components of the solute field is taken to be instantaneous when the solubility limit is reached, the time evolution of solute mass fraction (concentration) is modeled in a two step process. First the change in solute mass fraction over a time step is predicted based upon a standard mass conservation equation accounting for fluid flow alone.

$$\frac{[(1-\alpha)^{n+1}\tilde{m}^{n+1}\rho_l^{n+1}-(1-\alpha)^n m^n \rho_l^n]_j}{\Delta t}+\nabla_j\cdot[(1-\alpha)^n m^n \rho_l^n V_l^{n+1}]=0, \tag{1-114}$$

Next a correlation is checked for the maximum mass fraction m_{max} of solute that can be dissolved in the liquid at the current temperature. This is either a correlation for boric acid or a replacement provided by a TRACE user as optional input. The highest possible dissolved mass fraction at the end of a time step is the sum of the result from Eq. (1-114) and available mass of plated solute per mass of liquid in the volume. The final end of time step mass fraction must be the smaller of this limit and m_{max}.

$$m^{n+1}=Min\left[\tilde{m}^{n+1}+\frac{S_c^n}{(1-\alpha)^{n+1}\rho_l^{n+1}}\,,\,m_{max}\right], \tag{1-115}$$

In the above equation S_c is the plated solute mass divided by the volume of the computational cell in which it is plated. Whatever plated solute was not taken into solution by Eq. (1-115) remains in the inventory of plated solute at the end of the step. This can be expressed mathematically as:

$$S_c^{n+1}=(\tilde{m}^{n+1}-m^{n+1})(1-\alpha)^{n+1}\rho_l^{n+1}+S_c^n. \tag{1-116}$$

Basics of the SETS Method

The goal of the SETS method was to eliminate the material Courant stability limit with minimal alterations to the existing semi-implicit method. Given the success of the semi-implicit method in propagating information about sound waves, a correction step was devised to perform a similar propagation of information on continuity waves. As a very simple example, consider the single-phase mass equation. For each time step, the semi-implicit method is used to establish the new-time velocity field. Next, the following correction (or "stabilizer") step is used to obtain a final value of the new-time density:

$$\frac{(\rho_j^{n+1}-\rho_j^n)}{\Delta t}+\frac{\partial}{\partial x_j}(\rho^{n+1}V^{n+1})=0\,. \tag{1-117}$$

On the surface, this appears to be a fully implicit finite-difference equation. It is not, however, because the new-time velocities (V^{n+1}) are all known numbers, obtained from the semi-implicit step. New-time densities are the only unknowns in this system of equations. Information about a density change in any given computational cell is propagated to all other cells within the same time step. Formal stability analysis and direct testing confirm expectations based on information propagation. The material Courant stability limit actually is eliminated. This does not imply unconditional stability for the method. The only modifications to the semi-implicit method involve flux terms. The continued practice of evaluating heat-transfer and friction coefficients at the old time results in other poorly defined problems with bounded instabilities.

One unusual aspect of SETS as implemented in the code is that the pattern of evaluation of semi-implicit and stabilizer equations is not the same for the motion equations as it is for the mass and energy equations. All mass and energy equations follow the above pattern of a semi-implicit step followed by a stabilizer step. However, the analogous momentum-stabilizer equation is evaluated before the evaluation of the semi-implicit equations. This pattern was established during the original development of SETS through tests of the various combinations of equation ordering. In these tests, two-phase-flow problems ran smoothly at significantly higher time steps with the current equation ordering than with others. The physical explanation for this behavior is the importance of the pressure gradient term in problems of interest. A solution is better behaved when the velocity used for transport of mass and energy is a direct result of a pressure-balanced solution.

For our special example of 1D single-phase flow, the SETS difference equations are

Stabilizer Motion Equation

$$\frac{\left(\tilde{V}_{j+1/2}^{n+1}-V_{j+1/2}^{n}\right)}{\Delta t}+V_{j+1/2}^{n}\left.\frac{\partial \tilde{V}^{n+1}}{\partial x}\right|_{j+1/2}$$

$$+\frac{1}{\langle\rho\rangle_{j+1/2}^{n}}\frac{P_{j+1}^{n}-P_j^{n}}{\Delta x}+K_{j+1/2}^{n}\left(2\tilde{V}_{j+1/2}^{n+1}-V_{j+1/2}^{n}\right)\left|V_{j+1/2}^{n}\right|=0\,. \tag{1-118}$$

Semi-Implicit Equation Step

$$\left.\frac{\left(V^{n+1}_{j+1/2} - V^{n}_{j+1/2}\right)}{\Delta t} + V^{n}_{j+1/2}\frac{\partial \tilde{V}^{n+1}}{\partial x}\right|_{j+1/2}$$

$$+ \frac{1}{\langle\rho\rangle^{n}_{j+1/2}}\frac{(\tilde{P}^{n+1}_{j+1} - \tilde{P}^{n+1}_{j})}{\Delta x} + K^{n}_{j+1/2}\left(2\,V^{n+1}_{j+1/2} - V^{n}_{j+1/2}\right)\left|V^{n}_{j+1/2}\right| = 0\,, \tag{1-119}$$

$$\frac{(\tilde{\rho}^{n+1}_{j} - \rho^{n}_{j})}{\Delta t} + \frac{\partial}{\partial x_j}\rho^{n} V^{n+1} = 0\,, \text{ and} \tag{1-120}$$

$$\frac{(\tilde{\rho}^{n+1}_{j}\tilde{e}^{n+1}_{j} - (\rho e)^{n}_{j})}{\Delta t} + \frac{\partial}{\partial x_j}\rho^{n} e^{n} V^{n+1} + \tilde{P}^{n+1}_{j}\frac{V^{n+1}_{j+1/2} - V^{n+1}_{j-1/2}}{\Delta x} = 0\,. \tag{1-121}$$

Stabilizer Mass and Energy Equations

$$\frac{(\rho^{n+1}_{j} - \rho^{n}_{j})}{\Delta t} + \frac{\partial}{\partial x_j}(\rho^{n+1} V^{n+1}) = 0\,, \text{ and} \tag{1-122}$$

$$\frac{(\rho e)^{n+1}_{j} - (\rho e)^{n}_{j}}{\Delta t} + \frac{\partial}{\partial x_j}[(\rho e)^{n+1} V^{n+1}] + \tilde{P}^{n+1}_{j}\frac{V^{n+1}_{j+1/2} - V^{n+1}_{j-1/2}}{\Delta x} = 0\,. \tag{1-123}$$

A tilde above a variable indicates that it is a first estimate of the new-time value. Actual new-time variables have a superscript "$n+1$" and no tilde. Note that the only result of the above semi-implicit step appears to be just a new-time velocity field. In practice the situation is more complex. To save computational time, temperatures and pressures that are fully consistent with the densities and energies obtained from solving the stabilizer mass and energy equations are never calculated. If the correlation used to obtain an old-time wall friction coefficient requires temperature or pressure, the values used would be those obtained during the solution of the semi-implicit equation step.

As will be clear in the discussion of the solution of the SETS equations, each of the above equations is solved once per time step. During development of the method, attempts were made to make repeated evaluations of a form of the SETS equations during each time step to produce an iterative solution to the fully implicit method. This approach was found to converge poorly or not at all, particularly at time steps in excess of the material Courant limit.

Enhancements to the SETS Method

As with the semi-implicit method, linearized implicit terms are introduced in the motion equation to improve the behavior of friction and momentum transfer. The improved friction terms are identical to those derived in **Enhancements to the Semi-Implicit Method**. The momentum-transfer terms are somewhat more complex. First, the new-time velocity and velocity gradient are linearized in the following forms:

$$\tilde{V}^{n+1}_{j+1/2} = V^{n}_{j+1/2} + \delta V_{j+1/2} \text{ and} \tag{1-124}$$

$$\nabla \tilde{V}^{n+1}_{j+1/2} = \nabla \tilde{V}^{n}_{j+1/2} + \delta(\nabla V_{j+1/2}). \tag{1-125}$$

Substitution of these relationships into the implicit form of the momentum-transfer term gives

$$\begin{aligned} V^{n+1}_{j+1/2} \nabla \tilde{V}^{n+1}_{j+1/2} &= \left(V^{n}_{j+1/2} + \delta V_{j+1/2} \right)\left(\nabla \tilde{V}^{n}_{j+1/2} + \delta\left(\nabla V_{j+1/2} \right) \right) \\ &= V^{n}_{j+1/2} \nabla \tilde{V}^{n}_{j+1/2} + \delta V^{n}_{j+1/2} \nabla \tilde{V}^{n}_{j+1/2} \\ &+ V^{n}_{j+1/2} \delta(\nabla V_{j+1/2}) + \delta V^{n}_{j+1/2} \delta(\nabla V_{j+1/2}) \end{aligned} \tag{1-126}$$

Keeping only terms with no more than the first power of a variation and back-substituting the variations in terms of differences between old- and new-time variables gives

$$\tilde{V}^{n+1}_{j+1/2} \nabla \tilde{V}^{n+1}_{j+1/2} \approx V^{n}_{j+1/2} \nabla \tilde{V}^{n+1}_{j+1/2} + \left(\tilde{V}^{n}_{j+1/2} - V^{n}_{j+1/2} \right) \nabla \tilde{V}^{n}_{j+1/2}. \tag{1-127}$$

The difference in base points for the linearizations of Eqs. (1-124) and (1-125) is not an error in the equations. It is the result of numerical experimentation with the three possible alternatives. The situation is further complicated by instabilities resulting from negative values of the gradient or sign discrepancies between final and intermediate (tilde) velocities. Numerical experimentation resulted in the following robust form of the linearized implicit momentum-transfer term:

$$\begin{aligned} \tilde{V}^{n+1}_{j+1/2} \nabla \tilde{V}^{n+1}_{j+1/2} &\approx V^{n}_{j+1/2} \nabla_{j+1/2} \tilde{V}^{n+1}_{j+1/2} \\ &+ \beta\left(\tilde{V}^{n+1}_{j+1/2} - V^{n}_{j+1/2} \right) \nabla_{j+1/2} \tilde{V}^{n}_{j+1/2} \end{aligned} \quad , \tag{1-128}$$

where

$$\beta = \begin{bmatrix} 1 \quad for \quad \left.\frac{\partial V^n}{\partial x}\right|_{j+1/2} \geq 0 \ and \ V^n_{j+1/2}\tilde{V}^n_{j+1/2} > 0 \\ \\ 0 \quad for \quad \left.\frac{\partial V^n}{\partial x}\right|_{j+1/2} < 0 \ or \ V^n_{j+1/2}\tilde{V}^n_{j+1/2} \leq 0 \end{bmatrix}. \tag{1-129}$$

With these modifications, the final form of the stabilizer motion equation is

$$\frac{\left(\tilde{V}^{n+1}_{j+1/2} - V^n_{j+1/2}\right)}{\Delta t} + V^n_{j+1/2}\nabla_{j+1/2}\tilde{V}^{n+1}_{j+1/2} + \beta\left(\tilde{V}^{n+1}_{j+1/2} - V^n_{j+1/2}\right)\nabla_{j+1/2}\tilde{V}^n_{j+1/2}$$

$$+ \frac{1}{\langle\rho\rangle^n_{j+1/2}}\frac{(P^n_{j+1} - P^n_j)}{\Delta x} + K^n_{j+1/2}(2\tilde{V}^{n+1}_{j+1/2} - V^n_{j+1/2})\left|V^n_{j+1/2}\right| = 0. \tag{1-130}$$

The following revised form of the motion equation in the semi-implicit step contains the revised flux term to increase the robustness of the method:

$$\frac{\left(V^{n+1}_{j+1/2} - V^n_{j+1/2}\right)}{\Delta t} + V^n_{j+1/2}\nabla_{j+1/2}\tilde{V}^{n+1}_{j+1/2} + \beta\left(V^{n+1}_{j+1/2} - V^n_{j+1/2}\right)\nabla_{j+1/2}\tilde{V}^n_{j+1/2}$$

$$+ \frac{1}{\langle\rho\rangle^n_{j+1/2}}\frac{(P^{n+1}_{j+1} - P^{n+1}_j)}{\Delta x} + K^n_{j+1/2}(2V^{n+1}_{j+1/2} - V^n_{j+1/2})\left|V^n_{j+1/2}\right| = 0. \tag{1-131}$$

One significant modification is introduced in the stabilizer mass and energy equations. To save computational effort and overhead associated with the communication of more variables, the stabilizer equations listed in the previous section are not directly solved. Instead, the actual equations solved are the result of subtracting the semi-implicit equations from the corresponding stabilizer equations.

Stabilizer Mass and Energy Equations as Solved

$$\frac{(\rho^{n+1}_j - \tilde{\rho}^{n+1}_j)}{\Delta t} + \frac{\partial}{\partial x_j}(\rho^{n+1}V^{n+1}) = \frac{\partial}{\partial x_j}(\rho^n V^{n+1}), \text{ and} \tag{1-132}$$

$$\frac{(\rho e)_j^{n+1} - \tilde{\rho}_j^{n+1}\tilde{e}_j^{n+1}}{\Delta t} + \frac{\partial}{\partial x_j}((\rho e)^{n+1} V^{n+1}) = \frac{\partial}{\partial x_j}((\rho e)^n V^{n+1}). \quad (1\text{-}133)$$

Note that these appear to be conservation equations, but on close examination what appears to be a time derivative is in fact a difference between two time derivatives. The advantage of this approach is more apparent in the application of the method to the full two-phase-flow equations. In that case, all source terms (mass and energy transfer) are canceled out of the equations to be solved. The disadvantage of this approach is that the rigorous mass conservation of Eq. (1-122) is lost. Mass conservation associated with Eq. (1-132) depends on the level of convergence of the iterative solution for the semi-implicit equations.

The SETS Method Adapted to Two-Phase Flow

The two-phase forms of the SETS equations contain some significant modifications. The first, which improves code robustness, is an initial evaluation of the equations of motion that is used solely to provide an improved prediction of the interfacial force terms needed in the standard stabilizer motion equations.

Equations for Prediction of Interfacial Drag Force

Combined Gas

$$\begin{aligned}
&\frac{(\hat{V}_g^{n+1} - V_g^n)}{\Delta t} + V_g^n \nabla_{j+1/2} \tilde{V}_g^n + \beta(\hat{V}_g^{n+1} - V_g^n)\nabla_{j+1/2}\tilde{V}_g^n \\
&+ \frac{C_i^n \left| V_g^n - V_l^n \right|}{\langle \alpha\rho_g \rangle_{j+1/2}^n}[2(\hat{V}_g^{n+1} - \hat{V}_l^{n+1}) - (V_g^n - V_l^n)] \\
&+ \frac{1}{\langle \rho_g \rangle_{j+1/2}^n} \frac{(P_{j+1}^n - P_j^n)}{\Delta x_{j+1/2}} + \frac{\Gamma^{+n}_{j+1/2}}{\langle \alpha\rho_g \rangle_{j+1/2}^n}(\hat{V}_g^{n+1} - \hat{V}_l^{n+1}) \\
&+ \frac{C_{wg}}{\langle \alpha\rho_g \rangle_{j+1/2}^n}(2\hat{V}_g^{n+1} - V_g^n)\left| V_g^n \right| + g\cos\theta = 0,
\end{aligned} \quad (1\text{-}134)$$

where

$$\beta = \begin{bmatrix} 0 & \text{if} \quad \nabla_{j+1/2} V^n < 0 \quad \text{and} \quad V^n \tilde{V}^n < 0 \\ 1 & \text{if} \quad \nabla_{j+1/2} V^n \geq 0 \quad \text{and} \quad V^n \tilde{V}^n \geq 0 \end{bmatrix} \tag{1-135}$$

Liquid

$$\begin{aligned} &\frac{(\hat{V}_l^{n+1} - V_l^n)}{\Delta t} + V_l^n \nabla_{j+1/2} \tilde{V}_l^n + \beta(\hat{V}_l^{n+1} - V_l^n) \nabla_{j+1/2} \tilde{V}_l^n \\ &+ \frac{C_i^n \left| V_g^n + V_l^n \right|}{\langle (1-\alpha)\rho_l \rangle_{j+1/2}^n} [2(\hat{V}_l^{n+1} - \hat{V}_g^{n+1}) - (V_l^n - V_g^n)] \\ &+ \frac{1}{\langle \rho_l \rangle_{j+1/2}^n} \frac{(P_{j+1}^n - P_j^n)}{\Delta x_{j+1/2}} - \frac{\Gamma_{j+1/2}^n}{\langle (1-\alpha)\rho_l \rangle_{j+1/2}^n} (\hat{V}_l^{n+1} - \hat{V}_g^{n+1}) \\ &+ \frac{C_{wl}}{\langle (1-\alpha)\rho_l \rangle_{j+1/2}^n} (2\hat{V}_l^{n+1} - V_l^n) \left| V_l^n \right| + g\cos\theta = 0 . \end{aligned} \tag{1-136}$$

Edge-average densities follow the definitions provided in the discussion of the semi-implicit method [Eqs. (1-112) and (1-113)].

The velocities obtained from the above equations are used to decouple the vapor and liquid stabilizer motion equations. The prediction of the interfacial force term is good enough that the interfacial force term in the following stabilizer equations does not need to depend on the new-time stabilizer velocities. As a result, the liquid stabilizer motion equation contains only liquid stabilizer (tilde) velocities as unknowns. The liquid and gas equations are two completely independent systems of equations, which are solved separately.

Stabilizer Equations of Motion

Combined Gas

$$\frac{(\tilde{V}_g^{n+1} - V_g^n)}{\Delta t} + V_g^n \nabla_{j+1/2} \tilde{V}_g^{n+1} + \beta(\tilde{V}_g^{n+1} - V_g^n) \nabla_{j+1/2} \tilde{V}_g^n$$

$$+\frac{C_i^n\left|V_g^n-V_l^n\right|}{\langle\alpha\rho_g\rangle_{j+1/2}^n}[2(\hat{V}_g^{n+1}-\hat{V}_l^{n+1})-(V_g^n-V_l^n)]$$

$$+\frac{1}{\langle\rho_g\rangle_{j+1/2}^n}\frac{(P_{j+1}^n-P_j^n)}{\Delta x_{j+1/2}}+\frac{\Gamma^{+^n}{}_{j+1/2}}{\langle\alpha\rho_g\rangle_{j+1/2}^n}(\hat{V}_g^{n+1}-\hat{V}_l^{n+1})$$

$$+\frac{C_{wg}}{\langle\alpha\rho_g\rangle_{j+1/2}^n}(2\tilde{V}_g^{n+1}-V_g^n)\left|V_g^n\right|+g\cos\theta=0. \quad (1\text{-}137)$$

Liquid

$$\frac{(\tilde{V}_l^{n+1}-V_l^n)}{\Delta t}+V_l^n\nabla_{j+1/2}\tilde{V}_l^{n+1}+\beta(\tilde{V}_l^{n+1}-V_l^n)\nabla_{j+1/2}\tilde{V}_l^n$$

$$+\frac{C_i^n\left|V_g^n-V_l^n\right|}{\langle(1-\alpha)\rho_l\rangle_{j+1/2}^n}[2(\hat{V}_l^{n+1}-\hat{V}_g^{n+1})-(V_l^n-V_g^n)]$$

$$+\frac{1}{\langle\rho_l\rangle_{j+1/2}^n}\frac{(P_{j+1}^n-P_j^n)}{\Delta x_{j+1/2}}-\frac{\Gamma^{-^n}{}_{j+1/2}}{\langle(1-\alpha)\rho_l\rangle_{j+1/2}^n}(\hat{V}_l^{n+1}-\hat{V}_g^{n+1})$$

$$+\frac{C_{wl}}{\langle(1-\alpha)\rho_l\rangle_{j+1/2}^n}(2\tilde{V}_l^{n+1}-V_l^n)\left|V_l^n\right|+g\cos\theta=0. \quad (1\text{-}138)$$

Equations of Motion for the SETS Semi-Implicit Step

The equations solved during the semi-implicit step are almost identical to those presented in **Semi-Implicit Method Adapted to Two-Phase Flow** but are reproduced here in their entirety to avoid ambiguity in details of the implementation. The primary difference between the motion equation in a pure semi-implicit method and its corresponding form in the semi-implicit step of SETS is the use of stabilizer velocities for momentum transport.

Combined Gas

$$\frac{(V_g^{n+1}-V_g^n)}{\Delta t}+V_g^n\nabla_{j+1/2}\tilde{V}_g^{n+1}+\beta(V_g^{n+1}-V_g^n)\nabla_{j+1/2}\tilde{V}_g^n$$

$$+\frac{C_i^n\left|V_g^n-V_l^n\right|}{\langle\alpha\rho_g\rangle_{j+1/2}^n}[2(V_g^{n+1}-V_l^{n+1})-(V_g^n-V_l^n)]$$

$$+\frac{1}{\langle\rho_g\rangle_{j+1/2}^n}\frac{(\tilde{P}_{j+1}^{n+1}-\tilde{P}_j^{n+1})}{\Delta x_{j+1/2}}+\frac{\tilde{\Gamma}^{+^n}_{j+1/2}}{\langle\alpha\rho_g\rangle_{j+1/2}^n}(V_g^{n+1}-V_l^{n+1})$$

$$+\frac{C_{wg}}{\langle\alpha\rho_g\rangle_{j+1/2}^n}(2V_g^{n+1}-V_g^n)\left|V_g^n\right|+g\cos\theta=0. \quad (1\text{-}139)$$

Liquid

$$\frac{(V_l^{n+1}-V_l^n)}{\Delta t}+V_l^n\nabla_{j+1/2}\tilde{V}_l^{n+1}+\beta(V_l^{n+1}-V_l^n)\nabla_{j+1/2}\tilde{V}_l^n$$

$$+\frac{C_i^n\left|V_l^n-V_g^n\right|}{\langle(1-\alpha)\rho_l\rangle_{j+1/2}^n}[2(V_l^{n+1}-V_g^{n+1})-(V_l^n-V_g^n)]$$

$$+\frac{1}{\langle\rho_l\rangle_{j+1/2}^n}\frac{(\tilde{P}_{j+1}^{n+1}-\tilde{P}_j^{n+1})}{\Delta x_{j+1/2}}-\frac{\tilde{\Gamma}^{-^n}_{j+1/2}}{\langle(1-\alpha)\rho_l\rangle_{j+1/2}^n}(V_l^{n+1}-V_g^{n+1})$$

$$+\frac{C_{wl}}{\langle(1-\alpha)\rho_l\rangle_{j+1/2}^n}(2V_l^{n+1}-V_l^n)\left|V_l^n\right|+g\cos\theta=0. \quad (1\text{-}140)$$

Basic Semi-Implicit Mass Equations

These equations differ from those in a pure semi-implicit method; the resulting void fraction and new-time thermodynamic variables are intermediate results. Final new-time values for these variables are formally set by the stabilizer mass and energy equations. Individual thermodynamic variables also are carefully distinguished from products that comprise macroscopic densities and energies. These macroscopic quantities [e.g., $(\alpha\rho_g)$] are a direct result of the solution of the stabilizer mass and energy equations at the end of the previous time step. Another key difference is found in the modified form of the divergence operator, which can involve an unusual mixture of new- and old-time values [see Eq. (1-147)].

Combined Gas

$$\frac{\left[\tilde{\alpha}_j^{n+1}\tilde{\rho}_{gj}^{n+1} - (\alpha\rho_g)_j^n\right]}{\Delta t} + \nabla_j \cdot [(\alpha\rho_g)^n V_g^{n+1}] = \tilde{\Gamma}^{n+1}. \quad (1\text{-}141)$$

Noncondensable Mixture

$$\frac{[\tilde{\alpha}\tilde{\rho}_a]_j^{n+1} - [\alpha\rho_a]_j^n}{\Delta t} + \nabla_j \cdot [(\alpha\rho_a)^n \vec{V}_g^{n+1}] = 0 \quad (1\text{-}142)$$

Additional Noncondensable Mass Equations (k^{th} species)

$$\frac{[\tilde{\alpha}\tilde{X}_k\tilde{\rho}_a]_j^{n+1} - [\alpha X_k\rho_a]_j^n}{\Delta t} + \nabla_j \cdot [(\alpha X_k\rho_a)^n \vec{V}_g^{n+1}] = 0 \quad (1\text{-}143)$$

Liquid

$$\frac{\left|(1-\tilde{\alpha}_j^{n+1})\tilde{\rho}_{lj}^{n+1} - [(1-\alpha)\rho_l]_j^n\right|}{\Delta t} + \nabla_j \cdot [(1-\alpha)\rho_l]^n V_l^{n+1} = -\tilde{\Gamma}^{n+1}. \quad (1\text{-}144)$$

Basic Energy Equations

Combined Gas

$$\frac{[\tilde{\alpha}_j^{n+1}\tilde{\rho}_{gj}^{n+1}\tilde{e}_{gj}^{n+1} - (\alpha\rho_g e_g)_j^n]}{\Delta t} + \nabla_j \cdot [(\alpha\rho_g e_g)^n V_g^{n+1}]$$

$$+ \tilde{P}^{n+1}\left[\frac{(\tilde{\alpha}^{n+1} - \alpha^n)}{\Delta t} + \nabla_j \cdot (\alpha^n V_g^{n+1})\right]$$

$$= \tilde{q}_{wg}^{n+1} + q_{dg}^n + \tilde{q}_{ig}^{n+1} + \tilde{\Gamma}^{n+1}\tilde{h}_{sg}^{n+1}. \quad (1\text{-}145)$$

Total Fluid (gas and liquid)

$$\frac{\left\{\tilde{\alpha}_j^{n+1}\tilde{\rho}_{gj}^{n+1}\tilde{e}_{gj}^{n+1} + (1-\tilde{\alpha}_{gj}^{n+1})\tilde{\rho}_{gj}^{n+1}\tilde{e}_j^{n+1} - [(\alpha\rho_g e_g)_j^n + (1-\alpha)\rho_l e_l]_j^n\right\}}{\Delta t}$$

$$+ \nabla_j \cdot \{(\alpha\rho_g e_g)^n V_g^{n+1} + [(1-\alpha)\rho_l e_l]^n V_l^{n+1}\}$$

$$+ \tilde{P}^{n+1} \nabla_j \cdot [(1-\alpha)^n V_l^{n+1} + \alpha^n V_g^{n+1}]$$

$$= \tilde{q}_{wg}^{n+1} + \tilde{q}_{wl}^{n+1} + q_{dl}^n + q_{dg}^n. \quad (1\text{-}146)$$

The divergence operator is revised during the semi-implicit step to improve modeling accuracy of situations in which flux can be predominately attributed to phase change in the cell for which the continuity equation is being evaluated. The idea is to use new-time information for that portion of the flux associated with the same cell as the equation (cell j). This makes the local solution more sensitive to variation in phase-change rates. In terms of the notation used for the basic definition of the divergence operator, the revised form is

$$\tilde{\nabla}_j \cdot (Y^n V_g^{n+1}) = \frac{\left[w_{j+1/2} Y'_j + \left(1 - w_{j+1/2}\right) Y_{j+1}^n\right] A_{j+1/2} V_{j+1/2} - \langle w_{j-1/2} Y_{j-1}^n + \left(1 - w_{j-1/2}\right) Y'_j \rangle A_{j-1/2} V_{j-1/2}}{vol_j} \quad (1\text{-}147)$$

The special feature of this operator is that all occurrences of Y'_i in the normal finite volume divergence operator are replaced by a mixed time average defined as

$$Y'_j = \gamma Y_j^{n+1} + (1-\gamma) Y_j^n. \quad (1\text{-}148)$$

The weighting factor γ is determined by several considerations. For flow that is single phase over the entire time step, γ is set to zero. When the net predicted flow out of a cell of either phase exceeds the current mass in that cell, the weight is set to one (new-time cell-centered quantities are fluxed). For less dramatic situations, three ratios are computed. The first ratio has as a numerator the sum of the change in cell vapor mass for the time step due to all mass fluxes plus twice the change due to boiling. The ratio's denominator is the cell's mass decrease due only to outwardly directed vapor mass flows (positive number). The second ratio is the analog of the first as applied to the liquid phase. For the third ratio, the numerator adds half the old-time cell liquid mass to the predicted change in cell liquid mass for the time step. The denominator is half of the mass change due to outwardly directed flows at the cell's edges (negative number). When other considerations are not in control, the maximum of the three ratios is limited to the range of zero through one and is used for γ.

The ratios used to compute the weighting factor were obtained after a long period of experimentation with two-phase-flow problems. The first two ratios force the use of a cell-centered implicit value when outflow of a phase is almost exclusively the result of phase-change terms. The factor will also force this implicit evaluation when phase change is not significant and inflow significantly exceeds the outflow. The third ratio becomes important when some liquid outflow is present and a prediction is made that over half of the existing liquid mass will flow or boil away during the time step.

The mixture of old- and new-time values of the quantity being fluxed results in a difference scheme for this step that is not rigorously conservative. However, the standard finite-volume divergence operator is applied in the stabilizer mass and energy equations, restoring conservation to the final fluxes of mass and energy.

To understand the stabilizer mass and energy equations, it is important to remember what is unknown and what quantities have fixed values. In this respect, the superscript "$n+1$" can be deceptive. New-time velocity values are fixed by the semi-implicit step, as are all new-time terms marked with a tilde. In the stabilizer combined-gas mass equation, the only unknown new-time variables are the macroscopic gas densities $(\alpha\rho_g)^{n+1}$. For the noncondensable mass equation, the only unknowns are the terms $(\alpha\rho_a)^{n+1}$, and for the liquid mass equation, the only unknowns are the terms $[(1-\alpha)\rho_l]^{n+1}$. In the stabilizer combined-gas energy equation, the only unknown new-time variables are the macroscopic gas energy densities $(\alpha\rho_g e_g)^{n+1}$. For the liquid energy equation, the only unknowns are the terms $[(1-\alpha)\rho_l e_l]^{n+1}$.

Stabilizer Mass Equations

Combined Gas

$$\frac{[(\alpha\rho_g)_j^{n+1}-(\alpha\rho_g)_j^n]}{\Delta t}+\nabla_j\cdot[(\alpha\rho_g)^{n+1}V_g^{n+1}]=\tilde{\Gamma}_j^{n+1}. \tag{1-149}$$

Noncondensable Gas

$$\frac{[(\alpha\rho_a)_j^{n+1}-(\alpha\rho_a)_j^n]}{\Delta t}+\nabla_j\cdot[(\alpha\rho_a)^{n+1}V_g^{n+1}]=0. \tag{1-150}$$

Additional Noncondensable Mass Equations (k^{th} species)

$$\frac{[\alpha X_k\rho_a]_j^{n+1}-[\alpha X_k\rho_a]_j^n}{\Delta t}+\nabla_j\cdot[(\alpha X_k\rho_a)^{n+1}\vec{V}_g^{n+1}]=0 \tag{1-151}$$

Liquid

$$\frac{[(1-\alpha)\rho_l]_j^{n+1}-[(1-\alpha)\rho_l]_j^n}{\Delta t}+\nabla_j\cdot\{[(1-\alpha)\rho_l]^{n+1}\cdot V_l^{n+1}\}=-\tilde{\Gamma}_j^{n+1}. \tag{1-152}$$

Liquid Solute (see the semi-implicit section for a description)

$$\frac{[(1-\alpha)_j^{n+1}\tilde{m}_j^{n+1}\rho_{lj}^{n+1} - (1-\alpha)_j^n m_j^n \rho_{lj}^n]}{\Delta t} + \nabla_j \cdot \left[(1-\alpha)^{n+1}\tilde{m}^{n+1}\rho_l^{n+1} V_l^{n+1}\right] = 0 \quad (1\text{-}153)$$

$$m_j^{n+1} = \min\left[\tilde{m}_j^{n+1} + \frac{S_{cj}^n}{(1-\alpha)_j^{n+1}\rho_{lj}^{n+1}},\ m_{\max}\right], \quad (1\text{-}154)$$

and

$$S_{cj}^{n+1} = (\tilde{m}_j^{n+1} - m_j^{n+1})(1-\alpha)_j^{n+1}\rho_{lj}^{n+1} + S_{cj}^n . \quad (1\text{-}155)$$

Stabilizer Energy Equations

Combined Gas

$$\frac{[(\alpha\rho_g e_g)_j^{n+1} - (\alpha\rho_g e_g)_j^n]}{\Delta t} + \nabla_j \cdot [(\alpha\rho_g e_g)^{n+1} V_g^{n+1}]$$

$$+ \tilde{P}_j^{n+1}\left[\frac{(\tilde{\alpha}_j^{n+1} - \alpha_j^n)}{\Delta t} + \nabla_j \cdot (\alpha^n V_g^{n+1})\right]$$

$$= \tilde{q}_{wg}^{n+1} + q_{dg}^n + \tilde{q}_{ig}^{n+1} + \tilde{\Gamma}_j^{n+1}\tilde{h}_{sg}^{n+1} . \quad (1\text{-}156)$$

Liquid

$$\frac{[(1-\alpha)\rho_l e_l]_j^{n+1} - [(1-\alpha)\rho_l e_l]_j^n}{\Delta t} + \nabla_j \cdot \{[(1-\alpha)\rho_l e_l]^{n+1} V_l^{n+1}\}$$

$$+ \tilde{P}_j^{n+1}\left\{\frac{(\alpha_j^n - \tilde{\alpha}_j^{n+1})}{\Delta t} + \nabla_j \cdot [(1-\alpha)^n V_l^{n+1}]\right\}$$

$$= \tilde{q}_{wl}^{n+1} + q_{dl}^n - \tilde{q}_{ig}^{n+1} - \tilde{\Gamma}_j^{n+1}\tilde{h}_{sg}^{n+1} . \quad (1\text{-}157)$$

As indicated in **Enhancements to the SETS Method**, the code does not directly solve all of the above stabilizer equations. The actual equations solved are differences between these equations and their corresponding equations from the semi-implicit step. For the case of solute transport, no corresponding equation exists in the semi-implicit step. As a result, the stabilizer solute-transport equation, Eq. (1-154), is solved exactly as listed above. The final forms of the other equations as set in TRACE follow:

Stabilizer Mass Equations

Combined Gas

$$\frac{[(\alpha\rho_g)_j^{n+1} - \tilde{\alpha}_j^{n+1}\tilde{\rho}_{gj}^{n+1}]}{\Delta t} + \nabla_j \cdot [(\alpha\rho_g)^{n+1} V_g^{n+1}] = \nabla_j \cdot [(\alpha\rho_g)^n V_g^{n+1}]. \quad (1\text{-}158)$$

Noncondensable Gas

$$\frac{[(\alpha\rho_a)_j^{n+1} - \tilde{\alpha}_j^{n+1}\tilde{\rho}_{gj}^{n+1}]}{\Delta t} + \nabla_j \cdot [(\alpha\rho_a)^{n+1} V_g^{n+1}] = \nabla_j \cdot [(\alpha\rho_a)^n V_g^{n+1}]. \quad (1\text{-}159)$$

Additional Noncondensable Mass Equations (k^{th} species)

$$\frac{[\alpha X_k \rho_a]_j^{n+1} - [\tilde{\alpha}\tilde{X}_k\tilde{\rho}_a]_j^{n+1}}{\Delta t} + \nabla_j \cdot [(\alpha X_k \rho_a)^{n+1} \vec{V}_g^{n+1}] = \nabla_j \cdot [(\alpha X_k \rho_a)^n \vec{V}_g^{n+1}] \quad (1\text{-}160)$$

Liquid

$$\frac{[(1-\alpha)\rho_l]_j^{n+1} - (1-\tilde{\alpha}_j^{n+1})\tilde{\rho}_{lj}^{n+1}}{\Delta t}.$$

$$+ \nabla_j \cdot \{[(1-\alpha)\rho_l]^{n+1} V_l^{n+1}\} = \nabla_j \cdot \{[(1-\alpha)\rho_l]^n V_l^{n+1}\} \quad (1\text{-}161)$$

Stabilizer Energy Equations

Combined Gas

$$\frac{[(\alpha\rho_g e_g)_j^{n+1} - \tilde{\alpha}_j^{n+1}\tilde{\rho}_{gj}^{n+1}\tilde{e}_{gj}^{n+1}]}{\Delta t}$$

$$+ \nabla_j \cdot [(\alpha\rho_g e_g)^{n+1} V_g^{n+1}] = \nabla_j \cdot [(\alpha\rho_g e_g)^n V_g^{n+1}]. \quad (1\text{-}162)$$

Liquid

$$\frac{\left\{[(1-\alpha)\rho_l e_l]_j^{n+1} - (1-\tilde{\alpha}_j^{n+1})\tilde{\rho}_{lj}^{n+1}\tilde{e}_{lj}^{n+1}\right\}}{\Delta t} + \nabla_j \cdot \{[(1-\alpha)\rho_l e_l]^{n+1} V_l^{n+1}\}$$

$$= \nabla_j \cdot \{[(1-\alpha)\rho_l e_l]^n V_l^{n+1}\}. \quad (1\text{-}163)$$

Source terms in the SETS equations follow the definitions provided during the discussion of the semi-implicit methods. They are redefined below to clarify the use of intermediate variables.

$$\tilde{q}_{wl}^{n+1} = h_{wl}^n a_w (T_w^n - \tilde{T}_l^{n+1}) \quad , \quad (1\text{-}164)$$

$$\tilde{q}_{wg}^{n+1} = h_{wg}^n a_w (T_w^n - \tilde{T}_g^{n+1}) \quad , \quad (1\text{-}165)$$

and

$$\tilde{\Gamma}^{n+1} = \frac{-\left(\tilde{q}_{ig}^{n+1} + \tilde{\tilde{q}}_{il}^{n+1}\right)}{(h_v')^{n+1} - (h_l')^{n+1}}, \quad (1\text{-}166)$$

where

$$\tilde{q}_{ig}^{n+1} = h_{ig}^n a_i^n (\tilde{T}_{\mathrm{sat}}^{n+1} - \tilde{T}_g^{n+1}) \quad (1\text{-}167)$$

and

$$\tilde{q}_{il}^{n+1} = h_{il}^n a_i^n (\tilde{T}_{\mathrm{sat}}^{n+1} - \tilde{T}_l^{n+1}). \quad (1\text{-}168)$$

As mentioned in **Enhancements to the SETS Method**, an important subtlety in the SETS application is the use of thermodynamic variables in the evaluation of specific terms. The current form of the SETS solution provides only final new-time values for void fraction (α), macroscopic densities $[\alpha\rho_g, \alpha\rho_a, (1-\alpha)\rho_l]$, and macroscopic energies $[\alpha\rho_g e_g, (1-\alpha)\rho_l e_l]$. A final call to the thermodynamics equation-of-state does not occur after the solution of the stabilizer mass and energy equations. As a result, when basic thermodynamic variables are needed for evaluation of properties such as viscosity or heat-transfer coefficients, values obtained from the previous semi-implicit step are used.

Eq. (1-134) and Eq. (1-136) do not involve any implicit coupling between cells and can be solved directly for the gas and liquid (caret) velocities at each mesh-cell interface. Eq. (1-137) and Eq. (1-138) are not coupled to each other. Each of these systems is implicitly coupled in space through the momentum-convection term, and each requires the solution of a tridiagonal linear system. Equations (1-139) through (1-146), combined with the necessary thermodynamic and constitutive equations, form a coupled system of nonlinear equations. Eq. (1-139) and Eq. (1-140) are solved directly to obtain V_g^{n+1} and V_l^{n+1} as linear functions of $\tilde{P}^{n+1}$. After substituting these equations for velocity into Eqs. (1-141) through (1-146), the resulting system is solved with

a standard Newton iteration for the independent variables $\tilde{P}^{n+1}$, $\tilde{P}_a^{n+1}$, $\tilde{T}_g^{n+1}$, $\tilde{T}_l^{n+1}$, $\tilde{\alpha}^{n+1}$ and any $\tilde{X}_k^{n+1}$ with $k>1$, including all coupling between cells. In practice, the linearized equations solved during this Newton iteration are reduced easily to a system is tridiagonal or dominately tridiagonal involving only total pressures. The final stabilizer mass and energy equations [Eq. (1-149) through Eq. (1-157)] also are simple tridiagonal linear systems because V_g^{n+1} and V_l^{n+1} are known after solving Eq. (1-139) through Eq. (1-146).

3D Finite-Difference Methods

All basic equations and stabilizer equations for the 3D VESSEL component are solved in the same form as the 1D components. The vector form of the motion equation separates into three orthogonal-coordinate velocity-component motion equations. We present only the combined-gas equations with the understanding that the liquid equations are treated analogously. The 3D VESSEL component can be modeled by the TRACE user in either cylindrical or Cartesian geometry. The following equations in cylindrical geometry convert to Cartesian geometry by replacing the r divisor by unity and deleting the V^2/r term in the divergence operator that models momentum convection. The r and θ dependence is replaced by *x*- and *y*-dependence. For an orthogonal, right-handed, cylindrical coordinate system, the three velocity-component forms of the combined-gas motion differential equation are as follows:

Axial Velocity (*z*) Component

$$\frac{\partial V_{gz}}{\partial t}+\left(V_{gr}\frac{\partial V_{gz}}{\partial r}+\frac{V_{g\theta}}{r}\frac{\partial V_{gz}}{\partial \theta}+V_{gz}\frac{\partial V_{gz}}{\partial z}\right)=-\frac{1}{\rho_g}\frac{\partial P}{\partial z}-\frac{\Gamma^+}{\alpha\rho_g}(V_{gz}-V_{lz})$$

$$-\frac{C_{iz}}{\alpha\rho_g}(V_{gz}-V_{lz})\left|\vec{V}_g-\vec{V}_l\right|-\frac{C_{wgz}}{\alpha\rho_g}V_{gz}\left|\vec{V}_g\right|-gg_z \qquad (1\text{-}169)$$

Radial Velocity (*r*) Component

$$\frac{\partial V_{gr}}{\partial t}+\left(V_{gr}\frac{\partial V_{gr}}{\partial r}+\frac{V_{g\theta}}{r}\frac{\partial V_{gr}}{\partial \theta}-\frac{V_{g\theta}^2}{r}+V_{gz}\frac{\partial V_{gr}}{\partial z}\right)=-\frac{1}{\rho_g}\frac{\partial P}{\partial r}-\frac{\Gamma^+}{\alpha\rho_g}(V_{gr}-V_{lr})$$

$$-\frac{C_{ir}}{\alpha\rho_g}(V_{gr}-V_{lr})\left|\vec{V}_g-\vec{V}_l\right|-\frac{C_{wgr}}{\alpha\rho_g}V_{gr}\left|\vec{V}_g\right|-gg_r. \qquad (1\text{-}170)$$

Azimuthal Velocity (θ) Component

$$\frac{\partial V_{g\theta}}{\partial t}+\left(V_{gr}\frac{\partial V_{g\theta}}{\partial r}+\frac{V_{g\theta}}{r}\frac{\partial V_{g\theta}}{\partial \theta}+\frac{V_{gr}V_{g\theta}}{r}+V_{gz}\frac{\partial V_{g\theta}}{\partial z}\right)=-\frac{1}{r\rho_g}\frac{\partial P}{\partial \theta}-\frac{\Gamma^{+}}{\alpha\rho_g}(V_{g\theta}-V_{l\theta})$$

$$-\frac{C_{i\theta}}{\alpha\rho_g}(V_{g\theta}-V_{l\theta})\left|\vec{V}_g-\vec{V}_l\right|-\frac{C_{wg\theta}}{\alpha\rho_g}V_{g\theta}\left|\vec{V}_g\right|-gg_\theta \qquad (1\text{-}171)$$

In the last term of each equation, g is the gravitational acceleration constant and g_z, g_r, and g_θ are the directional components of the gravity vector based on the orientation of the 3D VESSEL component. By default, TRACE internally defines $g_z=1$, $g_r=0$, and $g_\theta=0$, where the *z*-axis is oriented vertically upward for all VESSEL components in the system model. The user may, however, redefine through input the orientation of each VESSEL component to something more general.

TRACE uses a staggered-mesh scheme (Ref. 1-14) similar to that used for the 1D components in which the velocities (V) are defined at the mesh-cell interfaces and the pressure (P), gas volume fraction (α), temperature (T), internal energy (e), and density (ρ) are defined at the mesh-cell centers. The scalar field equations (mass and energy) apply to a mesh cell, whereas the velocity-component motion equations apply to an interface between mesh cells in the three velocity-component directions. The wall heat transfer and the interfacial mass transfer required by the field equations are defined with a form similar to Eqs. (1-164) through (1-168).

The difference scheme for each motion equation is lengthy because of the cross-derivative terms. Therefore, to illustrate the procedure, we will describe only the combined-gas velocity-component, *z*-direction, finite-difference basic equation of motion for a typical mesh cell interface, together with the gas basic mass and energy equations, for a typical mesh cell. The gas velocity-component basic equations of motion in the θ and r directions along with all of the liquid basic equations are similar in form. The stabilizer motion, mass, and energy equations will not be illustrated; the reader is referred to the 1D component equations - Eq. (1-134) to Eq. (1-146) and Eq. (1-149) to Eq. (1-163) - where time-level parameters with ˜, ˆ, n, and $n+1$ superscripts are changed in going from the basic equations to the stabilizer equations. The superscript n indicates a current-time quantity; the superscript $n+1$ indicates a new-time quantity. The functional dependence (r,θ,z) points to the cell center. By incrementing r or θ or z by ±1, one moves to the adjacent cell in the direction based on which coordinate is incremented and on the sign of the increment. The functional dependencies $(r-1/2,\theta,z)$ and $(r+1/2,\theta,z)$ point to the inside and outside radial faces of the cell, respectively; $(r,\theta-1/2,z)$ and $(r,\theta+1/2,z)$, the right and left azimuthal faces of the cell (based on a perspective of looking radially out of the cell), respectively; and $(r,\theta,z-1/2)$ and

$(r, \theta, z+1/2)$, the bottom and top axial faces of the cell, respectively. The subscript g (for gas) is dropped unless it is needed for clarity.

The finite-difference combined-gas basic equation of motion in the *z*-direction has the following form:

Combined-Gas Basic Equation of Motion in the z-Direction

$$
\begin{aligned}
V_z^{n+1}(r,\theta,z+1/2) = {} & V_z^n(r,\theta,z+1/2) \\
& -\Delta t\Bigg[\frac{(V_r\Delta_r V_z^{n+1})}{\Delta r}+\frac{V_\theta\Delta_\theta V_z^{n+1}}{r\Delta\theta}+\frac{1}{2}\left(\frac{A_{z+1/2}}{A_{z+1}}+\frac{A_{z+1/2}}{A_z}\right)\frac{V_z^{n+1}(r,\theta,z+1/2)}{\Delta z} \\
& \left[\frac{A_{Z+1/2}}{A_{Z+1}}\tilde{V}_z^{n+1}(r,\theta,Z+1/2)-\frac{A_{Z-1/2}}{A_Z}\tilde{V}_z^{n+1}(r,\theta,Z-1/2)\right] \\
& -\frac{[P(r,\theta,z+1)-P(r,\theta,z)]^{n+1}}{\rho^n(r,\theta,z+1/2)\Delta z}-\frac{C_{iz}^n(r,\theta,z+1/2)}{(\alpha,\rho)^n(r,\theta,z+1/2)} \\
& \times\Bigg\{\left[\left|\vec{V}_g-\vec{V}_l\right|^n+\frac{((V_{gz}-V_{lz})^n(r,\theta,z+1/2))^2}{\left|\vec{V}_g-\vec{V}_l\right|^n}\right](V_{gz}-V_{lz})^{n+1}(r,\theta,z+1/2) \\
& -\frac{((V_{gz}-V_{lz})^n(r,\theta,z+1/2))^3}{\left|\vec{V}_g-\vec{V}_l\right|^n}\Bigg\} \\
& -\frac{\Gamma^{+n}(r,\theta,z+1/2)(V_{gz}-V_{lz})^{n+1}(r,\theta,z+1/2)}{(\alpha,\rho)^n(r,\theta,z+1/2)}-gg_z \\
& -\frac{C_{wz}^n(r,\theta,z+1/2)\left\{\left[\left|\vec{V}_g\right|^n+\frac{(V_z^n(r,\theta,z+1/2))^2}{\left|\vec{V}_g\right|^n}\right]V_z^{n+1}(r,\theta,z+1/2)-\frac{(V_z^n(r,\theta,z+1/2))^3}{\left|\vec{V}_g\right|^n}\right\}}{(\alpha,\rho)^n(r,\theta,z+1/2)}\Bigg], \quad (1\text{-}172)
\end{aligned}
$$

where $Z = z$ if $V_z^n(r, \theta, z+1/2) \geq 0$ and $Z = z+1$ if $V_z^n(r, \theta, z+1/2) < 0$

Any finite-difference scheme requires certain quantities at locations where they are not defined formally; therefore, additional relations are needed. TRACE obtains the volume-averaged properties $\alpha\rho$ and ρ at the cell axial interface from a cell-length weighted average,

$$(\alpha\rho)(r, \theta, z+1/2) = \tag{1-173}$$

$$\frac{\Delta z(z)\alpha(r, \theta, z)\rho(r, \theta, z) + \Delta z(z+1)\alpha(r, \theta, z+1)\rho(r, \theta, z+1)}{\Delta z(z) + \Delta z(z+1)}$$

and

$$\rho(r, \theta, z+1/2) = \frac{(\alpha\rho)(r, \theta, z+1/2)}{\alpha(r, \theta, z+1/2)} = \tag{1-174}$$

$$\frac{\Delta z(z)\alpha(r, \theta, z)\rho(r, \theta, z) + \Delta z(z+1)\alpha(r, \theta, z+1)\rho(r, \theta, z+1)}{\Delta z(z)\alpha(r, \theta, z) + \Delta z(z+1)\alpha(r, \theta, z+1)}$$

This averaging is necessary to compute pressure heads accurately. The code obtains Γ at the cell interface from its phasic velocity donor cell as follows:

The cross-derivative term $V_r\Delta_r V_z^{n+1}$ reflects a donor-cell average:

$$V_r\Delta_r V_z^{n+1} = \tilde{V}_r(r+1/2, \theta, z+1/2)[\tilde{V}_z(r+1, \theta, z+1/2) - \tilde{V}_z(r, \theta, z+1/2)]$$

$$+ \tilde{V}_r(r-1/2, \theta, z+1/2)[\tilde{V}_z(r, \theta, z+1/2) - \tilde{V}_z(r-1, \theta, z+1/2)], \tag{1-175}$$

where

$$\tilde{V}_r(r+1/2, \theta, z+1/2) = \tag{1-176}$$

$$min\left[\frac{SC_r(r+1/2, \theta, z+1)\tilde{V}_r(r+1/2, \theta, z+1)\Delta z(z) + SC_r(r+1/2, \theta, z)\tilde{V}_r(r+1/2, \theta, z)\Delta z(z+1)}{\Delta z(z) + \Delta z(z+1)}, 0\right].$$

and

$$\tilde{V}_r(r-1/2, \theta, z+1/2) = \tag{1-177}$$

$$max\left[\frac{SC_r(r-1/2\,,\theta\,,z+1)\,\tilde{V}_r(r-1/2\,,\theta\,,z+1)\Delta z(z)+SC_r(r-1/2\,,\theta\,,z)\,\tilde{V}_r(r-1/2\,,\theta\,,z)\Delta z(z+1)}{\Delta z(z)+\Delta z(z+1)}\,,0\right].$$

In the above equations, "min" and "max" are the mathematical functions of minimum and maximum values of the terms inside the brackets. $SC_r(r+1/2\,,\theta\,,z)$ is the product of an orifice factor that is 0 (when an orifice plate is present at the *r*+1/2 interface) or 1 and the ratio of the flow area through the $r+1/2$ interface to the $(r\,,\theta\,,z)$ cell flow area in the radial direction, $\mathrm{vol}(r\,,\theta\,,z)/\Delta r_{cell}$. The oriface factor is simply a statement that transverse momentum is not transported across an oriface. This assumption is particularly valid at the upper and lower core support plates. The area ratio contained in SC is consistent with the discussion later in this chapter of use of area ratios in momentum flux terms. An analogous expression holds for the $V_\theta \Delta_\theta V_z^{n+1}$ term.

Note that the V_z differences in the *r* and θ directions do not contain the *z*-direction flow-area weighting form. The SC_r and SC_θ factors make this correction for *z*-direction momentum convection in the r and θ directions, respectively.

In the interfacial drag terms, the magnitude of the relative velocity is defined as follows:

$$\begin{aligned}\left|\vec{V}_g-\vec{V}_l\right| = \Big\{ & [\,V_{zg}(r\,,\theta\,,z+1/2)-V_{zl}(r\,,\theta\,,z+1/2)\,]^2 \\ & +0.25[\,(\,V_{rg}(r+1/2\,,\theta\,,z)+V_{rg}(r-1/2\,,\theta\,,z) \\ & -\;V_{rl}(r+1/2\,,\theta\,,z)-V_{rl}(r-1/2\,,\theta\,,z)\,]^2 \\ & +0.25[\,V_{\theta g}(r\,,\theta+1/2\,,z)+V_{\theta g}(r\,,\theta-1/2\,,z) \\ & -\;V_{\theta l}(r\,,\theta+1/2\,,z)-V_{\theta l}(r\,,\theta-1/2\,,z)\,]^2\Big\}^{1/2}. \end{aligned} \qquad \text{(1-178)}$$

The convective terms in the finite volume relations for the scalar field equations are in conservative form. The finite-difference form of the combined-gas basic mass equation is

Combined-Gas Basic Mass Equation

$$(\tilde{\alpha}\tilde{\rho})^{n+1} = (\alpha\rho)^n - \left[\frac{\Delta t}{vol}\right]\Big\{ A_{z+1/2}\langle(\alpha\rho)^n V_z^{n+1}\rangle_{z+1/2} - A_{z-1/2}\langle(\alpha\rho)^n V_z^{n+1}\rangle_{z-1/2}$$

$$+ A_{r+1/2}\langle(\alpha\rho)^n V_r^{n+1}\rangle_{r+1/2} - A_{r-1/2}\langle(\alpha\rho)^n V_r^{n+1}\rangle_{r-1/2}$$

$$+ A_{\theta+1/2}\langle(\alpha\rho)^n V_\theta^{n+1}\rangle_{\theta+1/2} - A_{\theta-1/2}\langle(\alpha\rho)^n V_\theta^{n+1}\rangle_{\theta-1/2}\Big\} + \Delta t\,\tilde{\Gamma}^{n+1} \qquad (1\text{-}179)$$

The combined-gas basic energy equation is

Combined-Gas Basic Energy Equation

$$(\tilde{\alpha}\tilde{\rho}\tilde{e})^{n+1} = (\alpha\rho e)^n - \left[\frac{\Delta t}{vol}\right]\Big\{ A_{z+1/2}\langle(\alpha\rho e)^n V_z^{n+1}\rangle_{z+1/2} - A_{z-1/2}\langle(\alpha\rho e)^n V_z^{n+1}\rangle_{z-1/2}$$

$$+ A_{r+1/2}\langle(\alpha\rho e)^n V_r^{n+1}\rangle_{r+1/2} - A_{r-1/2}\langle(\alpha\rho e)^n V_r^{n+1}\rangle_{r-1/2}$$

$$+ A_{\theta+1/2}\langle(\alpha\rho e)^n V_\theta^{n+1}\rangle_{\theta+1/2} - A_{\theta-1/2}\langle(\alpha\rho e)^n V_\theta^{n+1}\rangle_{\theta-1/2}\Big\}$$

$$- \tilde{P}^{n+1}(\tilde{\alpha}^{n+1} - \alpha^n)$$

$$- \left[\frac{\tilde{P}^{n+1}\Delta t}{vol}\right]\Big[\langle A\alpha^n V_z^{n+1}\rangle_{z+1/2} - \langle A\alpha^n V_z^{n+1}\rangle_{z-1/2}$$

$$+ \langle A\alpha^n V_r^{n+1}\rangle_{r+1/2} - \langle A\alpha^n V_r^{n+1}\rangle_{r-1/2}$$

$$+ \langle A\alpha^n V_\theta^{n+1}\rangle_{\theta+1/2} + \langle A\alpha^n V_\theta^{n+1}\rangle_{\theta-1/2}\Big]$$

$$+ \Delta t(\tilde{q}_{wg}^{n+1} + q_{dg}^n + \tilde{q}_{ig}^{n+1} + \tilde{\Gamma}^{n+1}\tilde{h}_{sg}^{n+1}) \qquad (1\text{-}180)$$

The discrete forms for the other scalar equations (the total mass and energy equations, the noncondensable-gas mass equation, and the liquid-solute mass equation) are similar. The time level of the convected mass $\alpha\rho$ and convected energy $\alpha\rho e$ is $n+1$ in the stabilizer equations. If the stabilizer mass and energy equations are not evaluated (pure semi-implicit method), the tilde parameters in Eq. (1-179) and Eq. (1-180) are defined without tildes.

All the field equations in the 3D VESSEL component can have additional source terms to allow one or more 1D component junctions to be connected to a mesh-cell interface anywhere in the 3D VESSEL component. The source terms in the mass and energy equations follow below. The subscripts 1D and 3D indicate that quantities are obtained from the 1D component-junction interface or junction cell and the 3D VESSEL-component mesh cell, respectively. The $\langle\ \rangle$ indicates the convected quantity has either the subscript 1D or 3D of the upstream donor cell based on the direction of the phase velocity at the source-connection 1D component-junction interface, illustrated by Eqs. (1-82) and (1-91). Each of these source terms is added to the downstream mesh cell's mass or energy equation and an equivalent sink term is subtracted from the upstream mesh cell's equation.

Total Basic Mass-Equation Source Term

$$\left[\frac{\Delta t}{vol}\right]\{\langle(\alpha\rho_g)^n V_g^{n+1}\rangle_{1D}A_{1D} + \langle[(1-\alpha)\rho_\ell]^n V_\ell^{n+1}\rangle_{1D}A_{1D}\}. \tag{1-181}$$

Combined-Gas Basic Mass-Equation Source Term

$$\left[\frac{\Delta t}{vol}\right]\langle(\alpha\rho_g)^n V_g^{n+1}\rangle_{1D}A_{1D}. \tag{1-182}$$

Total Basic Energy Equation Source Term

$$\left[\frac{\Delta t}{vol}\right]\{\langle[(1-\alpha)\rho_l e_l]^n V_l^{n+1}\rangle_{1D}A_{1D} + \langle[\alpha\rho_g e_g]^n V_g^{n+1}\rangle_{1D}A_{1D} + P_{3D}[\langle\alpha^n V_g^{n+1}\rangle_{1D}A_{1D} + \langle(1-\alpha)^n V_l^{n+1}\rangle_{1D}A_{1D}]\} \tag{1-183}$$

Combined-Gas Basic Energy Equation Source Term

$$\left[\frac{\Delta t}{vol}\right]\{\langle(\alpha\rho_g e_g)^n V_g^{n+1}\rangle_{1D}A_{1D} + P_{3D}\langle\alpha^n V_g^{n+1}\rangle_{1D}A_{1D}\} \tag{1-184}$$

Mixture Noncondensable-Gas Basic Mass-Equation Source Term

$$\left[\frac{\Delta t}{vol}\right]\langle(\alpha\rho_a)^n V_g^{n+1}\rangle_{1D}A_{1D} \tag{1-185}$$

Additional Noncondensable Mass Equation Source Terms (kth species)

$$\left[\frac{\Delta t}{vol}\right]\langle(\alpha X_k \rho_a)^n V_g^{n+1}\rangle_{1D} A_{1D} \tag{1-186}$$

Liquid-Solute Basic Mass-Equation Source Term

$$\left[\frac{\Delta t}{vol}\right]\langle[(1-\alpha)X_k\, m\rho_l]^n V_l^{n+1}\rangle_{1D} A_{1D} \tag{1-187}$$

The momentum source term is complicated by the staggered differencing and by the fact that the actual 1D component may enter at an arbitrary angle. For TRACE, we assume that the 1D component attaches normal (perpendicular) to the vessel mesh-cell interface. The interface flow area A_{3D} and velocity V_{3D} are defined on the opposite side of the 3D mesh cell from the interface where the 1D component-junction source convection is made. It is that opposite mesh-cell interface from the source-convection interface that has in its motion equation the following momentum-convection source term for the combined-gas or liquid basic equation of motion when $V_{3D} \pm 1/2$ flows away from the 1D component source-convection interface into the $3D+1$ mesh cell. An S factor is applied to the 1D component so that its positive flow direction becomes the positive flow direction of the vessel.

Basic Equation-of-Motion Source Term

$$\frac{\Delta t}{2}\left(\frac{A_{3D}}{vol_{3D\pm1}/\Delta x_{3D\pm1}} + \frac{A_{3D}}{vol_{3D}/\Delta x_{3D}}\right)\frac{V_{3D}^{n+1}}{\Delta x_{3D}}\left[\frac{A_{1D} S \tilde{V}_{1D}^{n+1}}{vol_{3D}/\Delta x_{3D}}\right] \tag{1-188}$$

As with the 1-D semi-implicit equations, independent variables $\tilde{P}^{n+1}$, $\tilde{P}_a^{n+1}$, $\tilde{T}_g^{n+1}$, $\tilde{T}_l^{n+1}$, $\tilde{\alpha}^{n+1}$ and any $\tilde{X}_k^{n+1}$ with $k>1$ are used during the iterative solution of the non-linear set of flow equations. Motion equations are solved for new time liquid and gas velocities as linear functions of new time pressures, making these velocities dependent variables in the solution process. Densities and internal energies are also treated as dependent variables by using the thermal equations of state,

$$\rho_l = \rho_l(P,T_l)\ , \qquad \rho_v = \rho_v(P_v,T_g)\ , \text{ and} \qquad \rho_a = \rho_a(P_a,T_g)\ ; \tag{1-189}$$

the caloric equations of state,

$$e_l = e_l(P,T_l)\ , \qquad e_v = e_v(P_v,T_g)\ , \text{ and} \qquad e_a = e_a(P_a,T_g)\ ; \tag{1-190}$$

and the definitions for ρ_g, e_g, and *P* (Eqs. , (1-42) through (1-45)).

If one or more hardware structures exist in the 3D mesh cells, the interface flow area (A) for fluid flow and the mesh-cell fluid volume (vol) are reduced from their geometric mesh-cell values by the user through inputting fractions of their geometric area and volume. These fractions can be input with values greater than unity, but it is recommended that the user not do so for the model to be physically valid. Thus, A should be less than or equal to the geometric mesh-cell side area and "vol" should be less than or equal to the geometric mesh-cell volume. Mesh-cell fluid volumes are constrained to be $\geq 1\times10^{-12}\ \mathrm{m}^3$ by TRACE. When the flow area is defined to be zero, fluid flow across the mesh-cell interface is zero. This procedure allows large obstacles, such as the downcomer walls and flow channels, to be modeled within the VESSEL component.

Modifications to the Basic Equation Set

Because of the choice of independent variables in the solution of the 1D or 3D basic equations (total pressure, air partial pressure, void fraction, combined-gas and liquid temperatures, and mass fractions of any noncondensable species beyond the first), the basic equation set becomes singular at void fractions of zero and one. To avoid this solution difficulty the combined gas mass equation (1-141). is replaced with a simple equation setting $\alpha = 0$ or $\alpha = 1$. The combined-gas energy equation is replaced with an equation setting the temperature of the missing phase to the saturation temperature based on the total pressure.

When the transition from single-phase gas or liquid to a two-phase fluid first occurs, the combined-gas and liquid mass equations are evaluated but the replacement equation for the gas energy equation is used for one more time step. This forces the second phase to initially appear at saturation conditions, which is generally a very good approximation. It drastically reduces sporadic numerical problems associated with the use of two energy equations in which the first appearance of a phase can be associated with an exceptionally bad predicted value of its temperature. Special considerations are also made during the linearization for the Newton solution of the semi-implicit equations. When an explicit mass test suggests the first appearance of a second phase, flux of the second phase is used to estimate the new-time void fraction. If air is just appearing in a cell, an initial estimate is also made of the air partial pressure. Both of these estimates are used to specify the base state for the linearization associated with the current Newton iteration.

When the pressure exceeds the critical-point pressure, the basic equations can become singular. However, care has been taken to place a minimum value on the difference between liquid and vapor density wherever it appears in a constitutive equation. This results in a two-phase equation set that drives itself rapidly to single phase when pressure is above the critical point.

Conserving Convected Momentum

The backward difference approach given in Eq. (1-85) to determine the $V \cdot \nabla V$ term in a momentum equation is known to be stable numerically. For smooth area changes, however, this backward or upwind difference scheme is not accurate and does not conserve momentum. For abrupt area changes, it can be shown that the upwind difference scheme combining Eq. (1-85) and Eq. (1-91) for $V \cdot \nabla V$ will result in pressure changes that include both reversible and irreversible effects. Upwind differencing is accurate for abrupt expansions and overestimates the pressure change for an abrupt contraction. (see **Chapter 7,** *Form Loss Models* for details.)

It has been shown that the accuracy of a central difference representation of $V \cdot \nabla V$ is quite good for smooth area changes and for the reversible portion of an abrupt area change. It can be shown, however, through linear stability analysis, that central differencing is, in general, unconditionally unstable. An approach was developed (originally for TRAC-PF1/MOD2 and carried over into TRACE) to improve momentum conservation by determining factors based on geometry that change the upwind differencing of the $V \cdot \nabla V$ so that its accuracy is consistent with central differencing. The assumption used in developing these factors is constant volumetric flow from the cell center to the cell edge.

A central difference $V \cdot \nabla V$ for 1D flow yields

$$V \cdot \nabla V = \frac{V dV}{dx} = \frac{0.5\, d\,(V^2)}{dx} \equiv \frac{0.5(V_{j+1}^2 - V_j^2)}{\Delta x_{j+1/2}} \quad . \tag{1-191}$$

Equation (1-191) can be rewritten as

$$V \cdot \nabla V = \frac{0.5(V_{j+1} + V_j)(V_{j+1} - V_j)}{\Delta x_{j+1/2}} \tag{1-192}$$

In TRACE, velocities are calculated at cell edges, therefore cell-center velocities must be estimated from cell-edge velocities. Equation (1-192) can be written in terms of the cell-edge velocities by applying the following equations based on constant volumetric flow from cell center to the cell edge:

$$A_{j+1} V_{j+1} = A_{j+1/2} V_{j+1/2}, \tag{1-193}$$

$$A_j V_j = A_{j+1/2} V_{j+1/2}, \tag{1-194}$$

and

$$A_j V_j = A_{j-1/2} V_{j-1/2}. \tag{1-195}$$

If Eqs. (1-193) and (1-194) are substituted into the summed portion of Eq. (1-192), and Eqs. (1-193) and (1-195) are substituted into the difference portion of Eq. (1-192), an upwind difference form that is as accurate as central differencing is obtained for $V \cdot \nabla V$.

$$V \cdot \nabla V_{j+1/2} = \frac{0.5\left(\frac{A_{j+1/2}}{A_{j+1}} + \frac{A_{j+1/2}}{A_j}\right) V_{j+1/2}\left(\frac{A_{j+1/2} V_{j+1/2}}{A_{j+1}} - \frac{A_{j-1/2} V_{j-1/2}}{A_j}\right)}{\Delta x_{j+1/2}} \tag{1-196}$$

These equations assume that $V_{j+1/2} \geq 0$ but similar sets of equations can be derived for $V_{j+1/2} < 0$. In TRACE, Eq. (1-196) is the approximation used in both the 1D and 3D momentum-convection terms to improve the conservation of momentum.

In general, TRACE, even with the corrected $V \cdot \nabla V$ term, is still solving a nonconserving momentum equation. What follows is a simplified version of the derivation leading to Eq. (1-78). A conserving form of the momentum equation for single-phase flow with no momentum sources or sinks can be written as

$$\frac{d(\rho V)}{dt} = \frac{d(\rho V A V)}{A\,dx} = 0 \tag{1-197}$$

Expanding the derivatives of Eq. (1-197) yields

$$V\left\{\frac{d(\rho)}{dt} + \frac{d(\rho V A)}{A\,dx}\right\} + \rho\left\{\frac{d(V)}{dt} + V\frac{d(V)}{dx}\right\} = 0. \tag{1-198}$$

The continuity equation for single-phase flow with no sources or sinks can be written as

$$\frac{d(\rho)}{dt} + \frac{d(\rho V A)}{A\,dx} = 0 \tag{1-199}$$

Therefore, Eq. (1-198) can be written as

$$\frac{d(V)}{dt} + V\frac{d(V)}{dx} = 0\,. \tag{1-200}$$

Equation (1-200) represents the type of nonconserving form of the momentum equation solved by the TRACE code. This derivation indicates that TRACE will conserve momentum with the nonconserving form of the momentum equation if mass is conserved on a point-by-point basis. TRACE conserves mass within each hydraulic cell and assumes that within that cell, the density and void fractions are constant. This assumption may lead to errors in conserving momentum, since the nonconserving momentum equation is solved from cell center to cell center and the geometry area ratio factors developed for Eq. (1-196) assume constant density and void fraction from cell center to cell edge.

If we assume constant volumetric flow from cell edge j–1/2 to cell edge j+1/2, Eq. (1-196) in the form of the Bernoulli equation is equivalent to

$$P_{j+1} - P_j + \frac{\rho}{2}\left[\left(\frac{A_{j+1/2}}{A_{j+1}}V_{j+1/2}\right)^2 - \left(\frac{A_{j-1/2}}{A_j}V_{j-1/2}\right)^2\right] + \rho g \Delta x_{j+1/2}\cos\theta = 0\,. \tag{1-201}$$

Substitute the constant volumetric-flow relations $A_{j+1/2}V_{j+1/2} = A_{j+1}V_{j+1}$ and $A_{j-1/2}V_{j-1/2} = A_jV_j$ into the momentum-convection term of Eq. (1-201) to obtain the Bernoulli equation

$$P_{j+1} - P_j + \frac{1}{2}\rho[\,V_{j+1}^2 - V_j^2] + \rho g \Delta x_{j+1/2}\cos\theta = 0\,. \tag{1-202}$$

We see from the above derivation of the momentum-convection term and the assumptions made that the equation of motion for single-phase liquid (a near-incompressible fluid) to a very good approximation satisfies the Bernoulli equation. Convected momentum flux between momentum cells should be nearly conserved. Reversible form losses caused by flow-area and elevation changes should be evaluated correctly. This has been demonstrated (Ref. 1-15) for single-phase liquid with a variable flow-area and elevation flow-channel test problem having a total of seven 1D PIPE and VESSEL components connected in series with a FILL-component velocity and BREAK-component pressure boundary condition at each end of the flow channel, respectively. Each 1D VESSEL component was evaluated in each of three Cartesian-coordinate directions in separate calculations. Wall losses in the flow channel with flow area varying from 0.1 to 0.6 m^2 were minimized by increasing the flow-channel hydraulic diameter by a factor of 100.

A plot of the Bernoulli expression $P_j/\rho_j + V_j^2/2 + gh_j$ (as calculated using TRAC-PF1/MOD2) versus flow-channel cell number j for four different PIPE- and VESSEL-component models is

shown in Figure 1-7, with and without flow-area ratios applied in the momentum-convection term of the liquid equation of motion. Each of the four models comprised a different combination of PIPE and/or 1D VESSEL components, yet each gave the same results. The momentum equation currently used in TRACE provided an accurate evaluation of the Bernoulli equation as demonstrated by the constant value of the Bernoulli expression when flow-area ratios are applied in the momentum-convection term. Similar calculations were performed for single-phase vapor wherein TRAC-PF1/MOD2 was temporarily modified to evaluate a constant vapor microscopic density (making vapor an incompressible fluid). The results determined were similar to those of liquid, which served as a check that the combined-gas equation of motion as well as the liquid equation of motion are programmed correctly for both 1D and 3D components.

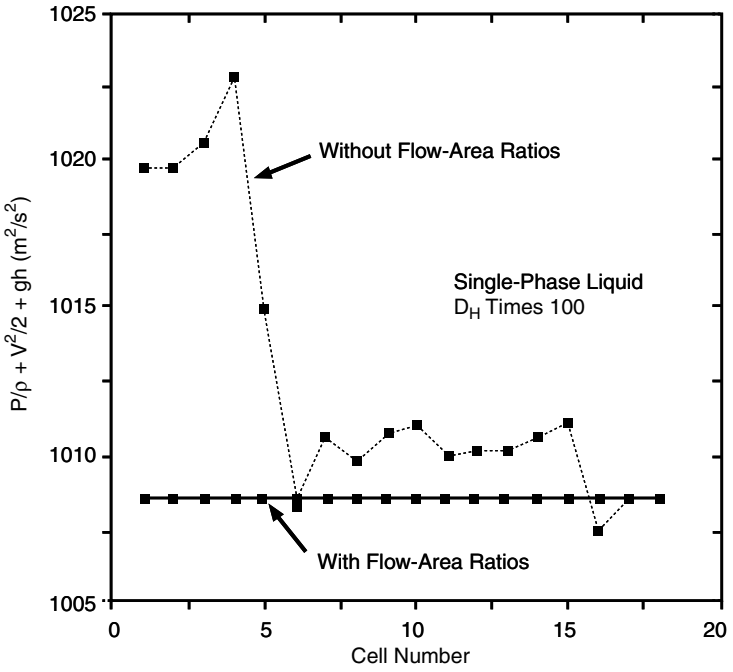

Figure. 1-7. The Bernoulli expression $P_j / \rho_j + V_j^2 / 2 + gh_j$ vs. flow-channel cell number j from a 1D flow-channel test problem having variable flow area and elevation. This calculation was performed with TRAC-PF1/MOD2.

For a compressible single-phase vapor, the change in its microscopic density because of fluid pressure and temperature variation over a mesh-cell distance generally is small. Approximating constant density within a fluid cell should cause only a small error in conserving convected vapor momentum flux between momentum cells. However, a significant spatial variation in the fluid void fraction across a mesh cell can result in a momentum-flux conservation error, in part because of the constant volumetric-flow assumption. However, for rapidly changing void fractions the larger problem in momentum conservation can be traced to the assumption equating two different averages of macroscopic density, leading to the difference between Eq. (1-76) and Eq. (1-77).

Reversible and Irreversible Form Losses.

With flow-area ratios in the momentum-convection term, TRACE approximately conserves convected momentum and evaluates only the reversible form losses of the Bernoulli equation. The TRACE user is therefore responsible for supplying input that specifies all irreversible form losses due to abrupt or semi-abrupt flow-area expansions and contractions, thin-plate-orifice-type flow restrictions, and flow redirection (turning) at an elbow or tee, as discussed in **Chapter 7,** *Form Loss Models*.

TRACE users who are adapting old TRAC-PF1/MOD1 input files need to be aware of a conflict in the way form losses are applied between TRACE and that older code. The TRAC-PF1/MOD1 momentum-convection term does not include the flow-area ratios illustrated in Eq. (1-196). That results in a numerically produced irreversible form loss that is about right for an abrupt expansion and approximately twice the irreversible form loss of an abrupt contraction. Code users who have prepared TRAC-PF1/MOD1 input-data plant models have compensated for this numerically generated irreversible form-loss error by not including other irreversible form losses at flow restrictions or at elbows and tees in order to evaluate the correct overall pressure drop through a portion or all of a flow loop. TRACE users who inherit and convert such TRAC-PF1/MOD1 input-data files into TRACE input-data files need to be aware that their plant model may have built-in compensating-error features for TRAC-PF1/MOD1 that, when evaluated by TRACE, give pressure losses along flow paths that are significantly low. The user's response to this situation should be to never use converted TRAC-PF1/MOD1 input-data files blindly. All mesh-cell interface flow areas and mesh-cell volumes and lengths (whose ratio defines mesh-cell flow area) need to be checked against plant specifications, and all input-specified FRICs or K-factors (and those that have not been specified) need to be defined to account for their actual irreversible form losses at abrupt or semi-abrupt flow-area changes, flow restrictions, and flow turns (redirections).

TRACE assists code users by not requiring them to determine values loss coefficients at abrupt expansion or contraction 1D component mesh-cell interfaces for input specification. At all such interfaces, TRACE internally evaluates the standard K-factor formulas in **Chapter 7,** *Form Loss Models*, for abrupt-expansion [$K = (1-A_{min}/A_{max})^2$] and abrupt-contraction [$K = 0.5 - 0.7(A_{min}/A_{max}) + 0.2\,(A_{min}/A_{max})^2$] form losses based on mesh-cell flow areas and adds them to the any input-specified loss coefficients. This feature is extended in TRACE to 3D VESSEL components as well.

Special Cases

The definition of flow-area ratios and irreversible form losses when evaluating momentum convection in BREAK, PLENUM, TEE (and, more generally, side junctions), and VESSEL components needs further consideration.

BREAK Component

TRACE models a BREAK component as a volume in which state conditions are prescribed by the user rather than generated through the solution of flow equations. The user specifies the volume of the cell and a characteristic length perpendicular to it's connection area. A momentum equation is evaluated at the BREAK junction area, and when an area is required from the BREAK side for use in the momentum transfer terms, it is obtained by dividing the BREAK volume by the BREAK characteristic length. TRACE user's need to think carefully about the physical configuration within which the BREAK is being used a a boundary condition to isolate a subsystem. If in the real system piping continues beyond BREAK junction, the pipe geometry must be considered in setting the BREAK geometry. If piping ends at the BREAK junction and flow enters a very large volume (e.g. containment), the ratio of volume to length in the break should give an area much larger than the flow area at the BREAK junction. The characteristic length input for the BREAK should not, however, be a characteristic length for the large physical volume. It is used in the pressure gradient term in the junction momentum equation, and should be small to reflect the fact that pressure changes rapidly as it enters the large volume. The standard guideline for TRACE is to set the length for the BREAK equal to the length of the computational volume immediately adjacent to the BREAK.

As with other points of abrupt area change, when the flow area changes between the BREAK mesh cell and the adjacent-component mesh cell, we recommend user specification of an appropriate irrecoverable loss coefficient. This can be done either as a specific coefficient, or a request that TRACE calculate an appropriate coefficient. It is important to provide a dissipative term in the equation of motion to determine the correct and numerically stable solution. A BREAK component is a pressure boundary condition that locally removes a degree of freedom from the hydrodynamic solution. The equation set becomes locally stiffer and more sensitive to error growth when there is not a dissipative term.

PLENUM Component

In general, we no longer recommend use of the PLENUM component when developing new TRACE input models. We document it here for completeness in case you find yourself maintaining or using a legacy model that includes such a component type.

The PLENUM component is a single mesh cell with a user selected number of junction interfaces connected to 1D components. Momentum can be transferred into a plenum but not across a plenum from one connecting face to another. The input for a plenum requests a characteristic length associated with each connection. This can be considered as twice the distance from the connecting face to the center of the plenum. When a plenum area is needed as part of the momentum transfer term, it is calculated as the ratio of plenum volume divided by the characteristic length associated with the junction at which the momentum equation is evaluated. When a velocity is needed from the plenum side for use in the momentum transfer term it is taken to be zero. For example if face j+1/2 in Eq. (1-196) is a plenum junction, and volume j is the plenum, the equation becomes:

$$V\Delta V_{j+1/2} = \frac{0.5\left(\frac{A_{j+1/2}}{A_{j+1}} + \frac{A_{j+1/2}}{A_j}\right) V_{j+1/2}\left(\frac{A_{j+1/2}\, V_{j+1/2}}{A_{j+1}} - 0\right)}{\Delta x_{j+1/2}} \tag{1-203}$$

where A_j is the previously mentioned ratio of plenum volume to characteristic length.

1D Side Junctions (including the TEE Component)

The TEE component has been maintained in TRACE for legacy TRAC input models, and its functionality has been captured with the side junction capability in other 1-D components. The key aspect of a TEE component or the more modern side junction is the introduction of source terms to the 1-D motion equations to properly capture the influence of momentum from the side leg flow on the momentum in the primary 1-D flow path. Less complicated capabilities are also provided to transfer momentum from the primary to secondary flow path via the boundary conditions at the side junction.

The momentum source model used for any TRACE side junction (including the TEE and other TEE-based components like the JETP or SEPD) was directly inherited from TRAC-PF1/MOD2. The basic momentum source term can be seen in Eq. (1-78) as:

$$\frac{V_{g,3}\cos\phi - V_{g,1}}{\overline{\alpha\rho_g} A_c dx} (\alpha\rho_g V_g)_3 A_3 \tag{1-204}$$

Within the final difference equation form we evaluate this source term in a linearized implicit manner analogous to the treatment of the other momentum flux terms. In the standard SETS notation, the source term is:

$$\frac{A_3 \alpha_3^n \rho_{g,3}^n}{\overline{\alpha^n \rho_g^n} A_c dx}\left[\tilde{V}_{g,3}^{n+1}\left(2\tilde{V}_{g,3}^{n}\cos\theta + \tilde{V}_{g,1}^{n}\right)\right. \tag{1-205}$$

$$\left. + \tilde{V}_{g,3}^{n}\tilde{V}_{g,1}^{n+1} - \tilde{V}_{g,3}^{n}\left(\tilde{V}_{g,3}^{n}\cos\theta + \tilde{V}_{g,1}^{n}\right)\right]$$

A similar term appears in the liquid momentum equation.

One limitation of the current implementation is that it was inherited directly from TRAC-PF1/MOD2 where a straight pipe assumption was enforced in proximity to the side connection. Best results are obtained if there are no flow area changes at any edges of the volume to which the side leg connects. In addition the cell averaged flow area in the first volume of the 1-D flow

component connected to the side junction should be the same as the side junction's area. These restrictions will be lifted with TRACE v6.0.

Differences in implementation of the momentum transport terms also affect irrecoverable loss coefficients. The option for automatic internal calculation of these coefficients is disabled at the edges of a volume containing a side junction. If area changes are present the code user needs to carefully check that pressure drops through the primary flow path are acceptable. If more pressure loss is needed, then specific values of loss coefficients should be supplied via the input. If too much pressure loss is obtained adjacent to a junction volume, then renodalization may be required.

A discussion of the side junction (TEE) model inherited from TRAC-PF1/MOD2 is given in Reference 1-17.

VESSEL Component.

Using flow-area ratios to correctly donor-cell the approximate momentum flux at a mesh-cell center (based on its interface-defined velocity a half mesh-cell distance away) is done only for momentum that is convected by its own component-direction velocity. This is not done in the cross-derivative terms of the divergence operator for momentum convection as shown in Eqs. (1-176) and (1-177).

Flow-area ratios are evaluated using the mesh-cell average flow area, $vol_{i,j,k}/\Delta_d$, where $d = i$, j, or k defines the component direction of the equation of motion. When the structure volume fraction within a 3D mesh cell is nonuniform in the d direction, the average flow area for the mesh cell can be incorrectly defined by $vol_{i,j,k}/\Delta_d$. Nonphysical mesh-cell flow areas affect the pressure solution through the Bernoulli equation by not approximating the donor-cell-approximated velocity components at the mesh-cell centers correctly. Locating 3D mesh-cell interfaces on planes of structure volume-fraction discontinuity can minimize this modeling difficulty. A modeling example that is difficult to handle correctly is representing the internal structure curved surface of a pressure vessel that bisects mesh cells in the vessel lower plenum.

A source connection to a 3D VESSEL component by a 1D component uses the $vol_{i,j,k}$ and Δ_d geometry parameters of the (i, j, k) mesh cell (where d refers to the edge direction to which the 1-D flow is connected), to define the 3D mesh-cell flow area for evaluating the source-connection junction momentum-convection term flow-area ratios. The actual d-direction flow area in the VESSEL component that the 1D component flow is expanding or contracting into may be significantly different from $vol_{i,j,k}/\Delta_d$. The sides of the mesh-cell volume $vol_{i,j,k}$ that the source-connection flow expands or contracts into may not be physical-structure surfaces that limit the flow area as in a 1D component pipe. Again the user needs to be aware of this when defining

mesh-cell interface planes and source connections to 3D mesh cells. The effect that the resulting incorrect flow-area ratios has on evaluating a Bernoulli-equation solution needs to be recognized. These area ratios also affect the irreversible flow loss coefficients that can by user request be evaluated by TRACE at the 1D to 3D junction.

References

1-1 Gunol Kocamustafaogullari, “Thermo-Fluid Dynamics of Separated Two-Phase Flow,” Ph.D. thesis, Georgia Institute of Technology (December 1971).

1-2 M. Ishii, *Thermo-Fluid Dynamic Theory of Two-Phase Flow* (Collection de la Direction des Etudes et Recherches D’Electricite de France, Eyrolles, Paris, 1975).

1-3 A. E. Bergles, J. S. Collier, J. M. Delhaye, G. F. Hewitt, and F. Mayinger, *Two-Phase Flow and Heat Transfer in the Power and Process Industries,* pp 40-122, (Hemisphere Publishing Corp., New York; McGraw-Hill Book Co., New York, 1981).

1-4 F. L. Addessio, “A Review of the Development of Two-Fluid Models,” Los Alamos National Laboratory report LA-8852 (NUREG/CR-2164) (August 1981).

1-5 H. Bruce Stewart and Burton Wendroff, “Two-Phase Flow: Models and Methods,” *Journal of Computational Physics* 56, 363-409 (1984).

1-6 H. Bruce Stewart, “Stability of Two-Phase Flow Calculation Using Two-Fluid Models,” *Journal of Computational Physics* 33, 259-270 (1979).

1-7 C. W. Hirt, "Heuristic stability theory for finite-difference, J. Comp. Phys., Vol 2. No. 2 (1967) 339-355.

1-8 P. J. Roache, "Fundamentals of Computational Fluid Dynamics," p. 179 (Hermosa Publishers, 1998

1-9 F. H. Harlow and A. A. Amsden, “A numerical fluid dynamics calculation method for all flow speeds,” J. Comput. Phys. 8 (1971) 197-213.

1-10 D. R. Liles and W. H. Reed, “A semi-implicit method for two-phase fluid dynamics,” J. Comput. Phys. 26 (1978) 390-407.

1-11 J. H. Mahaffy, “A stability enhancing two-step method for one-dimensional two-phase flow,” Los Alamos Scientific Laboratory Report LA-7951-MS, US Nuclear Regulatory Commission Report NUREG/CR-0971 (1979).

1-12 J. H. Mahaffy, “A stability-enhancing two-step method for fluid flow calculations,” J. Comput. Phys. 46 (1982) 329-341.

1-13 J. H. Mahaffy, “Numerics of Codes: Stability, Diffusion, Convergence,” Nuclear Engineering and Design, Vol. 145, pp. 131-145 (1993)

1-14 Francis H. Harlow and Anthony A. Amsden, “A Numerical Fluid Dynamics Calculation Method for All Flow Speeds,” *Journal of Computational Physics* 8, 197-213 (1971).

1-15 R. G. Steinke and J. W. Spore, “Conserving Convected Momentum in the TRAC Motion Equation,” The 18th Biennial CUBE Symposium (Albuquerque, New Mexico, November 1988), p. 116.

1-16 K. E. Carlson, R. A. Riemke, S. Z. Rouhani, R. W. Shumway, and W. L. Weaver, “RELAP5/MOD3 Code Manual, Volume 1: Code Structure, System Models, and Solution Methods (Draft),” Idaho National Engineering Laboratory report EGG-2596 (NUREG/CR-5535) (June 1990).

1-17 R. G. Steinke, “TRAC-P and Bernoulli-Equation Momentum-Convection Terms for the TEE-Component Internal-Junction Cell Interfaces,” Los Alamos National Laboratory report, LA-UR-96-3111 (August 1996).

2

Solution Methods

This chapter describes the solution methods employed by TRACE for evaluatiing the fluid equations. First, the overall solution strategy and general solution steps are outlined for the two numerical methods approximating the flow equations (semi-implicit and SETS). Next, we describe the basic solution strategy, as illustrated by a simple 1D problem, and extensions to the solution strategy required for 3D flows, respectively. A summary is provided of the Newton iteration used to solve the system of non-linear equations required by both numerical methods, as well as the solution of the sparse system of linear equations produced during each iteration of the nonlinear solution and all stabilizer steps of the SETS method. One section, in particular, is devoted to a description of the special capacitance matrix solution applied to any 3D blocks of a system matrix. Finally, we describe the treatment of a special numerical situation called water packing.

Nomenclature

Before presenting the solution methods, we need to define certain terminology. In our nomenclature, the term "gas" implies a general mixture of water vapor and the noncondensable gas. The subscript g will denote a property or parameter applying to the gas mixture; the subscript v indicates a quantity applying specifically to water vapor (referred to as simply "vapor"); and the subscript a (for "air") signifies a noncondensable-gas quantity. The term "liquid" implies pure liquid water, and the subscript l denotes a quantity applying specifically to liquid water. For convenience, we define the following terms that will be used in the subsequent equations and list them alphabetically, with the Greek symbols and subscripts to follow. The reader may note in various places that dummy variables are used. Although the dummy variables are not listed in the following nomenclature, their significance becomes obvious to the reader by reading the text. A caret (ˆ) above a variable denotes an explicit predictor value. A tilde (˜) above a variable denotes an intermediate result. A double line underneath a symbol refers to a matrix, whereas a single line underneath means a vector (1D array).

a, b, c = non-zero matrix/vector elements

$\underline{\underline{A}}$ = a known matrix

$\underline{\underline{B}}$ = banded portion of matrix $\underline{\underline{A}}$ in capacitance matrix method

$\underline{b}$ = a known vector

e = internal energy

$\underline{\underline{E}}$ = element of matrix product in capacitance matrix method

$\underline{\underline{I}}$ = intermediate result in capacitance matrix method

K = form-loss coefficient or wall friction coefficient

M = number of rows in matrix $\underline{\underline{A}}$ having non-zero elements outside the tridiagonal bandwidth

N = total number of rows and columns in matrix $\underline{\underline{A}}$

P = fluid pressure or total pressure

$\underline{\underline{R}}$ = element of matrix product in capacitance matrix method

$r,\ s.\ t.\ x$ = non-zero elements of the $\underline{\underline{A}}$ matrix in capacitance matrix method

t = time

T = temperature

V = magnitude of the velocity

x = distance

$\underline{x}$ = unknown vector to be solved (density, velocity, energy, pressure) in capacitance matrix method

Greek

α = gas volume fraction

β = momentum-convection temporal expansion flags

ρ = density

ΔP = pressure difference

Δt = time-step size

ΔV = velocity change

Δx = cell length for 1D components

δP = linear Taylor series expansion term for pressure

δT = linear Taylor series expansion term for temperature

$\delta\alpha$ = linear Taylor series expansion term for void fraction

Subscripts

a = noncondensable gas

g = gas mixture

$j+1$ = downstream cell-center index

$j+1/2$ = downstream cell-edge index

$j-1$ = upstream cell-center index

$j-1/2$ = upstream cell-edge index

l = liquid

r = radial

Superscripts

i, $i+1$ = denotes an iteration level

n = current-time quantity

$n+1$ = new-time quantity

$'$ = last estimate

Overall Solution Strategy

Solving the equations should be viewed from two perspectives. In the broadest view, we are solving an approximation to the partial differential equations modeling two-phase flow. In this context, time and spatial location are independent variables, and physical properties (pressure, temperature, etc.) are dependent variables of the system. Initial and boundary conditions are available, and the solution is integrated forward in time over the spatial domain of the problem. The size of the next step forward in time is selected based on a complex time step selection algorithm.

The second perspective on the solution ignores the original partial differential equations. Within a given time step, one or more systems of algebraic equations must be solved to obtain the state of the system at the end of the time step. In this context, time and spatial location are not independent variables. They are just contributions to constants within the algebraic equations. The independent variables for the algebraic equations are end-of-time-step state variables (e.g., velocity, temperature, pressure, and void fraction). This chapter has been written from this perspective, dealing with the solution of the algebraic equations defined in **Chapter 1,** *Basic Finite-Volume Approximations to the Flow Equations*.

Details of the solution within a given step in time are broken into three stages - a pre-pass, outer iteration (also sometimes called the semi-implicit step), and post-pass. The complexity of each stage is a function of the specific solution methodology being employed (i.e. semi-implicit or

SETS). When using the semi-implicit approximation to the flow equations, each stage represents a rather straightforward set of steps in the solution of the difference equations. First, all quantities dependent only on the state at the beginning of the time step are evaluated. This includes heat-transfer and friction coefficients and physical properties such as viscosity and conductivity. Next, the algebraic difference equations are solved. Finally, the end-of-step values are generated for various other variables needed for edits or to start the next time step.

For the SETS method, the situation is somewhat more complicated. The outer iteration step involves equations basically identical to those of the semi-implicit method and is accomplished by the same coding. However, this semi-implicit step is preceded by a solution of motion equations for "stabilizer" velocities (calculated during the pre-pass). In addition, stabilizer mass and energy equations are solved after the semi-implicit step, during the post-pass. As a result, SETS involves the solution of flow equations at all three stages of a time step.

Each equation solution follows a similar flow within the program. First, a loop is made over all system components to evaluate terms in the equation and store these terms in a system-wide database. Next, the full system of equations is solved. Finally, another loop over all components copies the values of the independent variables from the system-wide database into the component data structure and, when necessary, evaluates dependent variables.

Basic Solution Methodology

Almost all aspects of the equation solution procedure can be illustrated using the 1D single-phase-flow model introduced in **Chapter 1,** *Basic Finite-Volume Approximations to the Flow Equations*. For added clarity, examples will be presented based on some specific flow-path configurations. The solution of equations in the pure semi-implicit method is identical to the solution of the semi-implicit (or "basic") step in SETS. As a result, no specific discussion is provided for solution when the semi-implicit method is selected (namelist variable NOSETS=1).

To illustrate the 1D portion of the solution, we will describe a specific example for flow in a closed loop, as shown in Figure 2-1. Cells and cell faces in Figure 2-1 have been given absolute numbers to facilitate discussion of full system-equation coupling. In terms of component numbering, cells 1–4 in this figure are considered to be cells 1–4 of PIPE 1, and cells 5–8 in the figure are considered to be cells 1–4 of PIPE 2.

Solution of the 1D Stabilizer Motion Equations

The stabilizer motion equations are purely linear in the unknown stabilizer velocities. If the tilde and superscript are dropped for simplicity, the general form for this linear system for the flow loop in Figure 2-1 is

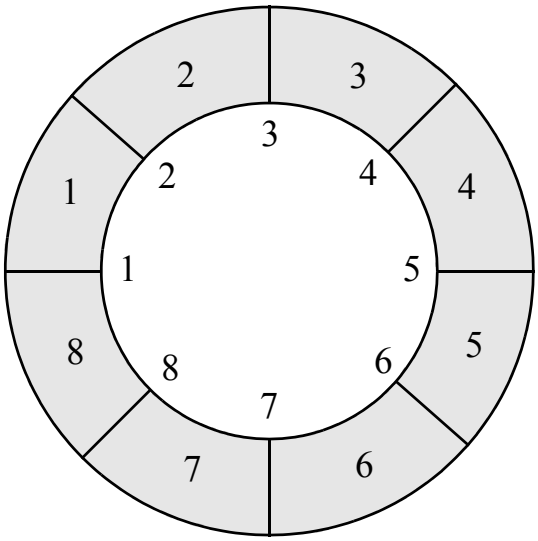

Figure. 2-1. Flow loop for an example of 1D solution.

$$\begin{pmatrix} a_{1,1} & a_{1,2} & 0 & 0 & 0 & 0 & 0 & a_{1,8} \\ a_{2,1} & a_{2,2} & a_{2,3} & 0 & 0 & 0 & 0 & 0 \\ 0 & a_{3,2} & a_{3,3} & a_{3,4} & 0 & 0 & 0 & 0 \\ 0 & 0 & a_{4,3} & a_{4,4} & a_{4,5} & 0 & 0 & 0 \\ 0 & 0 & 0 & a_{5,4} & a_{5,5} & a_{5,6} & 0 & 0 \\ 0 & 0 & 0 & 0 & a_{6,5} & a_{6,6} & a_{6,7} & 0 \\ 0 & 0 & 0 & 0 & 0 & a_{7,6} & a_{7,7} & a_{7,8} \\ a_{8,1} & 0 & 0 & 0 & 0 & 0 & a_{8,7} & a_{8,8} \end{pmatrix} \begin{pmatrix} V_1 \\ V_2 \\ V_3 \\ V_4 \\ V_5 \\ V_6 \\ V_7 \\ V_8 \end{pmatrix} = \begin{pmatrix} b_1 \\ b_2 \\ b_3 \\ b_4 \\ b_5 \\ b_6 \\ b_7 \\ b_8 \end{pmatrix} . \quad (2\text{-}1)$$

One standard linear algebra trick to solve this problem is to break it into blocks that can be more easily solved. One obvious approach would be to isolate the last row and column of the matrix as follows:

$$\left(\begin{array}{ccccccc:c} a_{1,1} & a_{1,2} & 0 & 0 & 0 & 0 & 0 & a_{1,8} \\ a_{2,1} & a_{2,2} & a_{2,3} & 0 & 0 & 0 & 0 & 0 \\ 0 & a_{3,2} & a_{3,3} & a_{3,4} & 0 & 0 & 0 & 0 \\ 0 & 0 & a_{4,3} & a_{4,4} & a_{4,5} & 0 & 0 & 0 \\ 0 & 0 & 0 & a_{5,4} & a_{5,5} & a_{5,6} & 0 & 0 \\ 0 & 0 & 0 & 0 & a_{6,5} & a_{6,6} & a_{6,7} & 0 \\ 0 & 0 & 0 & 0 & 0 & a_{7,6} & a_{7,7} & a_{7,8} \\ \hdashline a_{8,1} & 0 & 0 & 0 & 0 & 0 & a_{8,7} & a_{8,8} \end{array}\right)\left(\begin{array}{c} V_1 \\ V_2 \\ V_3 \\ V_4 \\ V_5 \\ V_6 \\ V_7 \\ V_8 \end{array}\right) = \left(\begin{array}{c} b_1 \\ b_2 \\ b_3 \\ b_4 \\ b_5 \\ b_6 \\ b_7 \\ b_8 \end{array}\right) . \tag{2-2}$$

This can then be written more clearly as the following problem:

$$\left(\begin{array}{ccccccc} a_{1,1} & a_{1,2} & 0 & 0 & 0 & 0 & 0 \\ a_{2,1} & a_{2,2} & a_{2,3} & 0 & 0 & 0 & 0 \\ 0 & a_{3,2} & a_{3,3} & a_{3,4} & 0 & 0 & 0 \\ 0 & 0 & a_{4,3} & a_{4,4} & a_{4,5} & 0 & 0 \\ 0 & 0 & 0 & a_{5,4} & a_{5,5} & a_{5,6} & 0 \\ 0 & 0 & 0 & 0 & a_{6,5} & a_{6,6} & a_{6,7} \\ 0 & 0 & 0 & 0 & 0 & a_{7,6} & a_{7,7} \end{array}\right)\left(\begin{array}{c} V_1 \\ V_2 \\ V_3 \\ V_4 \\ V_5 \\ V_6 \\ V_7 \end{array}\right) = \left(\begin{array}{c} b_1 \\ b_2 \\ b_3 \\ b_4 \\ b_5 \\ b_6 \\ b_7 \end{array}\right) - \left(\begin{array}{c} a_{1,8} \\ 0 \\ 0 \\ 0 \\ 0 \\ 0 \\ a_{7,8} \end{array}\right) V_8 \tag{2-3}$$

and

$$a_{8,1} V_1 + a_{8,7} V_7 + a_{8,8} V_8 = b_8 . \tag{2-4}$$

Equation (2-3) is solved to obtain velocities V_1 through V_7 as linear functions of V_8. The existence of two constant vectors on the right-hand side of the equation means that two solutions of a 7×7 system are required. However, use of an L-U (lower-upper) decomposition method substantially reduces the cost of the second solution. Once these solutions are available, the specific linear expressions for V_1 and V_7 as functions of V_8 are substituted into Eq. (2-4) and a value for V_8 is obtained. Back-substitution of this value into the equations for the other velocities completes the solution.

TRACE is not quite as selective as the previous example in isolating submatrices for solution. When the basic matrix structure is established, all rows are scanned for the presence of those coefficients not on the main (tridiagonal) band. These rows are designated as "network equations" and variables with the same index as "network variables."

$$\left(\begin{array}{c|ccccccc} a_{1,1} & a_{1,2} & 0 & 0 & 0 & 0 & 0 & a_{1,8} \\ \hline a_{2,1} & a_{2,2} & a_{2,3} & 0 & 0 & 0 & 0 & 0 \\ 0 & a_{3,2} & a_{3,3} & a_{3,4} & 0 & 0 & 0 & 0 \\ 0 & 0 & a_{4,3} & a_{4,4} & a_{4,5} & 0 & 0 & 0 \\ 0 & 0 & 0 & a_{5,4} & a_{5,5} & a_{5,6} & 0 & 0 \\ 0 & 0 & 0 & 0 & a_{6,5} & a_{6,6} & a_{6,7} & 0 \\ 0 & 0 & 0 & 0 & 0 & a_{7,6} & a_{7,7} & a_{7,8} \\ \hline a_{8,1} & 0 & 0 & 0 & 0 & 0 & a_{8,7} & a_{8,8} \end{array}\right) \left(\begin{array}{c} V_1 \\ V_2 \\ V_3 \\ V_4 \\ V_5 \\ V_6 \\ V_7 \\ V_8 \end{array}\right) = \left(\begin{array}{c} b_1 \\ b_2 \\ b_3 \\ b_4 \\ b_5 \\ b_6 \\ b_7 \\ b_8 \end{array}\right) . \tag{2-5}$$

Solving Eq. (2-5) is analogous to the steps outlined for Eq. (2-3). In this instance, the central tridiagonal matrix block is reduced to provide velocities V_2 through V_7 as linear functions of V_1 and V_8 (e.g., $V_j = V_{0,j} + c_{j,1} V_1 + c_{j,8} V_8$). The resulting equations are substituted into the two isolated rows of Eq. (2-5) to obtain the following pair of network equations involving only V_1 and V_8 :

$$(a_{1,1} + a_{1,2} c_{2,1}) V_1 + (a_{1,2} c_{2,8} + a_{1,8}) V_8 = b_1 - a_{1,2} V_{0,2} \tag{2-6}$$

and

$$(a_{8,1} + a_{8,7} c_{7,1}) V_1 + (a_{8,7} c_{7,8} + a_{8,8}) V_8 = b_8 - a_{8,7} V_{0,7} . \tag{2-7}$$

This closed system is solved for V_1 and V_8. Back-substitution of these values into the equations for V_2 through V_7 completes the solution of the system.

Solving the SETS Semi-Implicit Step

After the stabilizer motion equations are solved, the version of SETS implemented in TRACE proceeds to solve the semi-implicit (or "basic") equations for motion, mass, and energy. Apart

from the use of stabilizer velocities in the momentum-transport term (and the special flux operator for two-phase flow), these equations are equivalent to the standard semi-implicit method used in old versions of the TRAC series of codes before the SETS methodology was developed. Thus, solving the pure semi-implicit method and solving the semi-implicit step in SETS are identical.

The system solution begins by treating the new-time velocity as a dependent variable, reducing the motion equation at each cell edge to obtain the new-time velocity as a linear function of the pressure difference across that edge. In our single-phase example, Eq. (1-131) is rearranged to the form

$$V_{j+1/2}^{n+1} = \frac{V_{j+1/2}^{n} - \Delta t\left(V_{j+1/2}^{n} \nabla_{j+1/2} \tilde{V}_{j+1/2}^{n+1} - \beta V_{j+1/2}^{n} \nabla_{j+1/2} \tilde{V}_{j+1/2}^{n} + \frac{\tilde{P}_{j+1}^{n+1} - \tilde{P}_{j}^{n+1}}{\langle \rho \rangle_{j+1/2}^{n} \Delta x} \right)}{1 + \Delta t\left(2K_{j+1/2}^{n} \left| V_{j+1/2}^{n} \right| + \beta \nabla_{j+1/2} \tilde{V}_{j+1/2}^{n} \right)} \tag{2-8}$$

For the two-phase equations, the equivalent step requires simultaneous solution of the liquid and gas momentum equations at each face (2 × 2 linear system). At the same time, the following key variable is defined and stored for later use in updating velocities as

$$\left. \frac{dV}{dP} \right|_{j+1/2} = \frac{\Delta t}{\langle \rho \rangle_{j+1/2}^{n} \Delta x \left[1 + \Delta t\left(2K_{j+1/2}^{n} \left| V_{j+1/2}^{n} \right| + \beta \nabla_{j+1/2} \tilde{V}_{j+1/2}^{n} \right) \right]} . \tag{2-9}$$

The mass and energy equations are nonlinear in the independent variables and must be solved with an iterative technique. Here a standard Newton iteration is applied. If the i^{th} approximation to the solution is given, the next level of approximation is written as

$$\tilde{T}_{j}^{n+1,\,i+1} = \tilde{T}_{j}^{n+1,\,i} + \delta T_{j} \tag{2-10}$$

and

$$\tilde{P}_{j}^{n+1,\,i+1} = \tilde{P}_{j}^{n+1,\,i} + \delta P_{j} . \tag{2-11}$$

The pressure definition can be substituted into Eq. (2-8) and simplified with the definition in Eq. (2-9) to give the following expression for the latest approximation to velocity as a linear function of the latest pressure changes:

$$V_{j+1/2}^{n+1,\,i+1} = V_{j+1/2}^{n+1,\,i} + \left.\frac{dV}{dP}\right|_{j+1/2} (\delta P_j - \delta P_{j+1}) \ . \tag{2-12}$$

These expressions are applied to the semi-implicit mass and energy equations [see **Chapter 1** Eqs. (1-120) and (1-121)] through the direct substitutions

$$\tilde{P}_j^{n+1} \Rightarrow \tilde{P}^{n+1,\,i} + \delta P_j \ , \tag{2-13}$$

$$\tilde{T}_j^{n+1} \Rightarrow \tilde{T}_j^{n+1,\,i} + \delta T_j \ , \text{ and} \tag{2-14}$$

$$V_{j+1/2}^{n+1} \Rightarrow V_{j+1/2}^{n+1,\,i} + \left.\frac{dV}{dP}\right|_{j+1/2} (\delta P_j - \delta P_{j+1}) \ . \tag{2-15}$$

Use of the state relationships $[\rho(P\,,\,T)]$ and $[e(P\,,\,T)]$ and a first-order Taylor series expansion produces the linearized mass equation

$$\frac{\left(\left.\frac{\partial \rho}{\partial T}\right|_j^{n+1,\,i} \delta T_j + \left.\frac{\partial \rho}{\partial P}\right|_j^{n+1,\,i} \delta P_j\right)}{\Delta t} \tag{2-16}$$

$$+ \frac{\left[\langle \rho \rangle_{j+\frac{1}{2}}^{n} \left.\frac{dV}{dP}\right|_{j+1/2} (\delta P_j - \delta P_{j+1}) - \langle \rho \rangle_{j-1/2}^{n} \left.\frac{dV}{dP}\right|_{j-1/2} (\delta P_{j-1} - \delta \mathrm{P}_j)\right]}{\Delta x}$$

$$= -\frac{\tilde{\rho}_j^{n+1,\,i} - \rho_j^n}{\Delta t} - \frac{\partial}{\partial x_j}\left(\rho^n V^{n+1,\,i}\right)$$

and the linearized energy equation

$$\frac{\left(\left.\frac{\partial \rho}{\partial T}\right|_j^{n+1,\,i} \tilde{e}_j^{n+1,\,i} + \tilde{\rho}_j^{n+1,\,i} \left.\frac{\partial e}{\partial T}\right|_j^{n+1,\,i}\right)\delta T_j}{\Delta t} + \frac{\left(\left.\frac{\partial \rho}{\partial P}\right|_j^{n+1,\,i} \tilde{e}_j^{n+1,\,i} + \tilde{\rho}_j^{n+1,\,i} \left.\frac{\partial e}{\partial P}\right|_j^{n+1,\,i}\right)\delta P_j}{\Delta t}$$

$$+\frac{\left[\langle\rho e\rangle^{n}_{j+1/2}\left.\frac{dV}{dP}\right|_{j+1/2}(\delta P_j-\delta P_{j+1})-\langle\rho e\rangle^{n}_{j-1/2}\left.\frac{dV}{dP}\right|_{j-1/2}(\delta P_{j-1}-\delta P_j)\right]}{\Delta x}$$

$$+\tilde{P}_j^{n+1,i}\frac{\left[\left.\frac{dV}{dP}\right|_{j+1/2}(\delta P_j-\delta P_{j+1})-\left.\frac{dV}{dP}\right|_{j-1/2}(\delta P_{j-1}-\delta P_j)\right]}{\Delta x}+\delta\tilde{P}_j\frac{V^{n+1,i}_{j+1/2}-V^{n+1,i}_{j-1/2}}{\Delta x}$$

$$=-\frac{\left(\tilde{\rho}_j^{n+1,i}\tilde{e}_j^{n+1,i}-(\rho e)_j^{n}\right)}{\Delta t}-\frac{\partial}{\partial x^j}\left(\rho^n e^n V^{n+1,i}\right)-\tilde{P}_j^{n+1,i}\frac{V^{n+1,i}_{j+1/2}-V^{n+1,i}_{j-1/2}}{\Delta x} \qquad (2\text{-}17)$$

For the particular block-reduction technique used to solve this system of linear equations, an auxiliary variable is defined as

$$\Delta P_{j+1/2}=\delta P_{j+1}-\delta P_j\ . \qquad (2\text{-}18)$$

This results in a set of linear equations for each cell in the form

$$\begin{pmatrix} a_{j,1,1} & a_{j,1,2}\\ a_{j,2,1} & a_{j,2,2}\end{pmatrix}\begin{pmatrix}\delta P_j\\ \delta T_j\end{pmatrix}=\begin{pmatrix} b_{j,1}\\ b_{j,2}\end{pmatrix}-\begin{pmatrix} c_{1j,1}\\ c_{1j,2}\end{pmatrix}\Delta P_{j-1/2}+\begin{pmatrix} c_{rj,1}\\ c_{rj,2}\end{pmatrix}\Delta P_{j+1/2}\ . \qquad (2\text{-}19)$$

The first row in the above linear system can be considered to be the linearized mass conservation equation and the second to be the linearized energy equation. At each cell, this system is solved for the pressure and temperature variations in the form

$$\begin{pmatrix}\delta P_j\\ \delta T_i\end{pmatrix}=\begin{pmatrix} b'_{j,1}\\ b'_{j,2}\end{pmatrix}-\begin{pmatrix} c'_{1j,1}\\ c'_{1j,2}\end{pmatrix}\Delta P_{j-1/2}+\begin{pmatrix} c'_{rj,1}\\ c'_{rj,2}\end{pmatrix}\Delta P_{j+1/2}\ . \qquad (2\text{-}20)$$

At this point, the b' constants represent the linearized predictions of change in pressure and temperature assuming no further velocity changes at the cell faces. The c' coefficients account for contributions due to velocity changes (driven by changes in the pressure gradient).

The solution of the basic equations is completed in two steps. First, for each block represented by Eq. (2-20), the pressure equation is isolated and Eq. (2-18) is substituted to provide a set of 10 equations in the form

$$-c_{1j,1}\delta P_{j-1}+(1+c_{1j,1}+c_{rj,1})\delta P_j-c_{rj,1}\delta P_{j+1}=b_j\ . \tag{2-21}$$

This results in a system with the same form as the stabilizer velocity equations,

$$\left(\begin{array}{c|ccccccc|c}
a_{1,1} & a_{1,2} & 0 & 0 & 0 & 0 & 0 & a_{1,8} \\
\hline
a_{2,1} & a_{2,2} & a_{2,3} & 0 & 0 & 0 & 0 & 0 \\
0 & a_{3,2} & a_{3,3} & a_{3,4} & 0 & 0 & 0 & 0 \\
0 & 0 & a_{4,3} & a_{4,4} & a_{4,5} & 0 & 0 & 0 \\
0 & 0 & 0 & a_{5,4} & a_{5,5} & a_{5,6} & 0 & 0 \\
0 & 0 & 0 & 0 & a_{6,5} & a_{6,6} & a_{6,7} & 0 \\
0 & 0 & 0 & 0 & 0 & a_{7,6} & a_{7,7} & a_{7,8} \\
\hline
a_{8,1} & 0 & 0 & 0 & 0 & 0 & a_{8,7} & a_{8,8}
\end{array}\right)\left(\begin{array}{c}\delta P_1\\ \delta P_2\\ \delta P_3\\ \delta P_4\\ \delta P_5\\ \delta P_6\\ \delta P_7\\ \delta P_8\end{array}\right)=\left(\begin{array}{c}b_1\\ b_2\\ b_3\\ b_4\\ b_5\\ b_6\\ b_7\\ b_8\end{array}\right), \tag{2-22}$$

which is solved with the same procedure outlined for Eq. (2-5). The resulting values of δPs are first substituted into Eq. (2-18) to obtain a set of ΔP values, which are then substituted into the second row of Eq. (2-20) to provide values for temperature changes. The variations in pressure and temperature are substituted into Eq. (2-11) to provide an improved approximation to the new-time variables. The ΔP values are also fed to Eq. (2-12) to obtain new-time velocities, which are consistent with the updated pressure field. If variations in pressure and temperature are small enough, the iteration is terminated. If not, the linearized equations are evaluated again to generate the next approximate solution.

The iteration usually is started by setting the initial guess at the solution to the beginning of time-step values (e.g., $P_j^{n+1,0}=P_j^n$). The only exceptions occur in the full two-phase equations. When the old-time void fraction is zero but a prediction-based flux and phase change indicates appearance of gas, an explicit evaluation of the gas mass equation is used to provide an initial estimate of the new-time void fraction. When the first appearance of noncondensable gas is predicted, information from an explicit noncondensable mass equation is added to provide an estimate of the new-time partial pressure of noncondensable gas.

Use of old-time quantities to start the iteration provides an easy cure to situations in which the initial guess is beyond the convergence radius of the method. The new-time values must approach the old-time values as the time-step size approaches zero. If an iteration fails to converge, the time-step size is reduced and the solution is retried at the new-time-step size. Preemptive action is also taken to minimize convergence problems. If more than five iterations

are required to converge the solution on a given time step, the size of the next step is reduced by the ratio of five divided by the last iteration count.

Solution of the SETS Stabilizer Mass and Energy Equations

The final step in the SETS method is the solution of the stabilizer mass and energy equations. At this point, the new-time velocities have been determined and can be treated as constants in the solution of the equations. The equations vary from the mass and energy equations of the semi-implicit step only in that the densities and energies in flux terms are now evaluated at the new time.

The mass and energy equations are linear in ρ^{n+1} and $(\rho e)^{n+1}$ respectively, with a structure that is basically tridiagonal. For the loop flow problem, the general form of the mass equation can be written as

$$\begin{pmatrix} a_{1,1} & a_{1,2} & 0 & 0 & 0 & 0 & 0 & a_{1,8} \\ a_{2,1} & a_{2,2} & a_{2,3} & 0 & 0 & 0 & 0 & 0 \\ 0 & a_{3,2} & a_{3,3} & a_{3,4} & 0 & 0 & 0 & 0 \\ 0 & 0 & a_{4,3} & a_{4,4} & a_{4,5} & 0 & 0 & 0 \\ 0 & 0 & 0 & a_{5,4} & a_{5,5} & a_{5,6} & 0 & 0 \\ 0 & 0 & 0 & 0 & a_{6,5} & a_{6,6} & a_{6,7} & 0 \\ 0 & 0 & 0 & 0 & 0 & a_{7,6} & a_{7,7} & a_{7,8} \\ a_{8,1} & 0 & 0 & 0 & 0 & 0 & a_{8,7} & a_{8,8} \end{pmatrix} \begin{pmatrix} \rho_1 \\ \rho_2 \\ \rho_3 \\ \rho_4 \\ \rho_5 \\ \rho_6 \\ \rho_7 \\ \rho_8 \end{pmatrix} = \begin{pmatrix} b_1 \\ b_2 \\ b_3 \\ b_4 \\ b_5 \\ b_6 \\ b_7 \\ b_8 \end{pmatrix}, \tag{2-23}$$

where superscripts representing new time $(n+1)$ have been dropped. This can be recognized as identical in form to Eq. (2-5) and is solved with the same procedure.

The linear system produced by the stabilizer energy equation has the same coefficient matrix as that of the mass equation. Time is saved by storing matrix factorization steps used in the mass equation solution and by applying the results during the solution of the energy equation.

Final Solution for a New-Time Void Fraction

Solving the stabilizer mass and energy equations provides new-time values only for macroscopic densities $[\alpha\rho_g, \alpha\rho_a, (1-\alpha)\rho_l]$ and macroscopic energy densities $[\alpha\rho_g e_g, (1-\alpha)\rho_l e_l]$.

Experience with the method has shown that when end-of-time-step values are needed in correlations for variables such as temperature or pressure, the values obtained during the solution of the semi-implicit step are adequate. However, the method is more robust if an attempt is made to obtain a better value of the new-time void fraction.

After the stabilizer solution is completed, an approximate solution is obtained in each computational volume to the following equations:

$$\alpha_j^{n+1}\rho_{g,j}^{n+1} = (\alpha\rho_g)_j^{n+1} , \tag{2-24}$$

$$\alpha_j^{n+1}\rho_{a,j}^{n+1} = (\alpha\rho_a)_j^{n+1} , \tag{2-25}$$

$$(1-\alpha_j^{n+1})\rho_{l,j}^{n+1} = [(1-\alpha)\rho_l]_j^{n+1} , \tag{2-26}$$

$$\alpha_j^{n+1}\rho_{g,j}^{n+1}e_{g,j}^{n+1} = (\alpha\rho_g e_g)_j^{n+1} , \text{ and} \tag{2-27}$$

$$(1-\alpha_j^{n+1})\rho_{l,j}^{n+1}e_{l,j}^{n+1} = [(1-\alpha)\rho_l e_l]_j^{n+1} . \tag{2-28}$$

where the right-hand sides are the known results from the stabilizer equations. These equations are linearized with respect to the independent variables P^{n+1}, T_g^{n+1}, T_l^{n+1}, P_a^{n+1}, and α^{n+1}. The starting point of the linearization is taken to be the values of the corresponding variables obtained after the last iteration of the solution to the semi-implicit step. Thus, the values of the independent variables become

$$T_{g,j}^{n+1} = \tilde{T}_{g,j}^{n+1} + \delta T_{g,j} , \tag{2-29}$$

$$T_{l,j}^{n+1} = \tilde{T}_{l,j}^{n+1} + \delta T_{l,j} , \tag{2-30}$$

$$P_j^{n+1} = \tilde{P}_j^{n+1} + \delta P_j , \tag{2-31}$$

$$P_{a,j}^{n+1} = \tilde{P}_{a,j}^{n+1} + \delta P_{a,j} , \text{ and} \tag{2-32}$$

$$\alpha_j^{n+1} = \tilde{\alpha}_j^{n+1} + \delta\alpha_j . \tag{2-33}$$

These are substituted into Eq. (2-26), and a first-order Taylor expansion is applied. As an example of the results, the linearized macroscopic gas energy density is

$$\left(\tilde{\alpha}_j^{n+1}\left.\frac{\partial\tilde{\rho}_g}{\partial T}\right|_j^{n+1}\tilde{e}_{g,j}^{n+1}+\tilde{\alpha}_j^{n+1}\tilde{\rho}_{g,j}^{n+1}\left.\frac{\partial\tilde{e}_g}{\partial T}\right|_j^{n+1}\right)\delta T_j \tag{2-34}$$
$$+\left(\alpha_j^{n+1}\left.\frac{\partial\tilde{\rho}_g}{\partial P}\right|_j^{n+1}\tilde{e}_{g,j}^{n+1}+\tilde{\alpha}_j^{n+1}\tilde{\rho}_{g,j}^{n+1}\left.\frac{\partial\tilde{e}_g}{\partial P}\right|_j^{n+1}\right)\delta P_j$$
$$+\tilde{\rho}_{g,j}^{n+1}\tilde{e}_{g,j}^{n+1}\delta\alpha_j=(\alpha\rho_g e_g)_j^{n+1}-\tilde{\alpha}_j^{n+1}\tilde{\rho}_{g,j}^{n+1}\tilde{e}_{g,j}^{n+1}$$

This equation, combined with the other four linearized equations, produces a 5 × 5 linear system that is solved by direct Gauss elimination. Although linearized approximations to all new-time variables are available after this solution, only the void fraction is kept for use in the next time step. The other variables are discarded as a result of numerical experiments comparing various approaches. The consistent pressure field resulting from the solution of the semi-implicit step provides the best initial guess for velocities at the next time step. The tendency of temperatures in two-phase problems to follow the saturation temperature makes selection of temperatures consistent with that pressure field a good strategy for the most robust code behavior.

Considerations for 3D Solutions

When VESSEL components are present, the above procedure is followed, with one key exception in each set of equations. When any VESSEL variable (velocity, δP, ρ, or ρe) occurs in a 1D equation, it is moved to the right-hand side with its coefficient and all 1D variables are solved as functions of the unknown VESSEL variables. These results are substituted as needed into the difference equations for the VESSEL to give a closed set of equations that can be solved for all vessel variables. Values for VESSEL variables are back-substituted into the 1D equations, and final values for all 1D unknowns are obtained.

Specific examples of this process are provided here for the system illustrated in Figure 2-2. As in Figure 2-1, cells are given "absolute" numbers rather than a combination of component number and component cell number. For this example, cells numbered 1–5 are in a pipe and cells 6–9 are in a 3D (collapsed to 2D here) VESSEL.

The full system of stabilizer momentum equations for the flow loop in Figure 2-2 is represented by Eq. (2-35). The last block in the coefficient matrix is associated with the radial velocities V_9 and V_{10} and is completely isolated from equations for the axial velocities in the same "3D" region. This reflects the fundamental structure of the 3D stabilizer momentum equations. For example, the axial stabilizer momentum equations evaluate contributions from axial velocities only implicitly. Radial and azimuthal velocities appearing in momentum-transport terms are

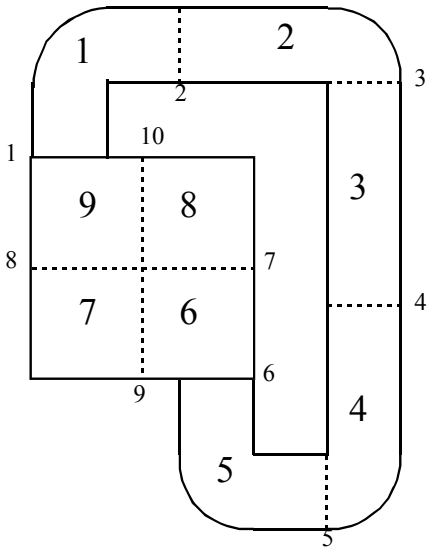

Figure. 2-2. System for 3D solution examples.

evaluated explicitly. This results in no coupling coefficients between velocity variables in the axial momentum block and those in the radial (or azimuthal) blocks. In matrix notation, we have

$$\begin{pmatrix} a_{1,1} & a_{1,2} & 0 & 0 & 0 & 0 & 0 & a_{1,8} & 0 & 0 \\ a_{2,1} & a_{2,2} & a_{2,3} & 0 & 0 & 0 & 0 & 0 & 0 & 0 \\ 0 & a_{3,2} & a_{3,3} & a_{3,4} & 0 & 0 & 0 & 0 & 0 & 0 \\ 0 & 0 & a_{4,3} & a_{4,4} & a_{4,5} & 0 & 0 & 0 & 0 & 0 \\ 0 & 0 & 0 & a_{5,4} & a_{5,5} & a_{5,6} & 0 & 0 & 0 & 0 \\ 0 & 0 & 0 & 0 & a_{6,5} & a_{6,6} & a_{6,7} & 0 & 0 & 0 \\ 0 & 0 & 0 & 0 & 0 & a_{7,6} & a_{7,7} & a_{7,8} & 0 & 0 \\ a_{8,1} & 0 & 0 & 0 & 0 & 0 & a_{8,7} & a_{8,8} & 0 & 0 \\ 0 & 0 & 0 & 0 & 0 & 0 & 0 & 0 & a_{9,9} & a_{9,10} \\ 0 & 0 & 0 & 0 & 0 & 0 & 0 & 0 & a_{10,9} & a_{10,10} \end{pmatrix} \begin{pmatrix} V_1 \\ V_2 \\ V_3 \\ V_4 \\ V_5 \\ V_6 \\ V_7 \\ V_8 \\ V_9 \\ V_{10} \end{pmatrix} = \begin{pmatrix} b_1 \\ b_2 \\ b_3 \\ b_4 \\ b_5 \\ b_6 \\ b_7 \\ b_8 \\ b_9 \\ b_{10} \end{pmatrix} . \quad (2\text{-}35)$$

Solving the 1D portion of this system proceeds as before, isolating the 1D block as

$$\begin{bmatrix} a_{2,2} & a_{2,3} & 0 & 0 \\ a_{3,2} & a_{3,3} & a_{3,4} & 0 \\ 0 & a_{4,3} & a_{4,4} & a_{4,5} \\ 0 & 0 & a_{5,4} & a_{5,5} \end{bmatrix} \begin{bmatrix} V_2 \\ V_3 \\ V_4 \\ V_5 \end{bmatrix} = \begin{bmatrix} b_2 \\ b_3 \\ b_4 \\ b_5 \end{bmatrix} - \begin{bmatrix} a_{2,1} \\ 0 \\ 0 \\ 0 \end{bmatrix} V_1 - \begin{bmatrix} 0 \\ 0 \\ 0 \\ a_{5,6} \end{bmatrix} V_6 \ . \tag{2-36}$$

This is solved to obtain the equation

$$\begin{bmatrix} V_2 \\ V_3 \\ V_4 \\ V_5 \end{bmatrix} = \begin{bmatrix} b'_2 \\ b'_3 \\ b'_4 \\ b'_5 \end{bmatrix} + \begin{bmatrix} c'_{2,1} \\ c'_{3,1} \\ c'_{4,1} \\ c'_{5,1} \end{bmatrix} V_1 + \begin{bmatrix} c'_{2,6} \\ c'_{3,6} \\ c'_{4,6} \\ c'_{5,6} \end{bmatrix} V_6 \ , \tag{2-37}$$

and these results are substituted into the junction equations to obtain

$$(a_{1,1} + a_{1,2} c'_{2,1}) V_1 + a_{1,2} c'_{2,6} V_6 = b_1 - a_{1,2} b'_2 - a_{1,8} V_8 \text{ and} \tag{2-38}$$

$$a_{6,5} c'_{5,1} V_1 + (a_{6,6} + a_{6,5} c'_{5,6}) V_6 = b_6 - a_{6,5} b'_5 - a_{6,7} V_7 \ . \tag{2-39}$$

Solving the previous two equations gives junction velocities as a linear combination of “3D” velocities as

$$\begin{bmatrix} V_1 \\ V_6 \end{bmatrix} = \begin{bmatrix} b'_1 \\ b'_6 \end{bmatrix} + \begin{bmatrix} c'_{1,7} \\ c'_{6,7} \end{bmatrix} V_7 + \begin{bmatrix} c'_{1,8} \\ c'_{6,8} \end{bmatrix} V_8 \ . \tag{2-40}$$

These two expressions are substituted into the 3D axial flow equations to obtain a final closed set of equations for the 3D axial velocities (V_7 and V_8). The current method used to solve this final equation block is described in the next subsection. Once the 3D velocities are known, the 1D network junction velocities (V_1 and V_6) follow by back-substitution of vessel velocities V_7 and V_8 into Eq. (2-40), and the internal component velocities are obtained in a final stage of the back-substitution of V_1 and V_6 into Eq. (2-37).

A similar solution pattern follows for the pressure equation of the semi-implicit (basic) step and for the stabilizer mass and energy equations.

The Capacitance Matrix Method

The capacitance matrix method is applied in TRACE to provide an efficient numerical solution algorithm for solving the multidimensional vessel-matrix equations. Each vessel-matrix equation combines the multidimensional mesh-cell or interface equations of all vessel components in the modeled system. The external or internal connectivity to the VESSEL component(s) of 1D hydro-component loops introduces nonzero elements into the vessel matrix, coupling the vessel mesh cells or interfaces at the loop source connections to the vessel(s). The vessel-matrix equations that are solved are the semi-implicit pressure vessel-matrix equation in the outer-stage solution and the stabilizer motion x- or r-, y- or θ, and z-direction vessel-matrix equations in the prepass stage of the solution and the stabilizer mass and energy vessel-matrix equations in the postpass stage of the solution.

The capacitance matrix method is a direct L-U matrix-decomposition solution algorithm like the direct full-matrix L-U matrix-decomposition solution algorithm used in TRAC-PF1/MOD1, but it does the L-U matrix decomposition on the banded portion of the vessel matrix with a more efficient banded-matrix solver routine. The banded portion of the vessel matrix includes the nonzero coupling elements between a vessel mesh cell or interface and its six adjacent (neighboring) mesh cells or interfaces in 3D geometry. Nonzero elements outside the bandwidth of the matrix that couple vessel mesh cells or interfaces to nonadjacent mesh cells or interfaces of the same vessel or a different vessel component (due to 1D hydro-component loop connectivity) will be referred to as nonzero outlying elements. The effect that the nonzero outlying elements have on the matrix-equation solution is accounted for in the capacitance matrix method by a direct full-matrix L-U matrix decomposition of a lower-order capacitance matrix. That solution is used to modify the banded-matrix equation solution to give the desired solution of the vessel matrix with its nonzero outlying elements. The capacitance matrix method was found in a study to be more efficient than a direct full-matrix L-U matrix-decomposition solution of a vessel-matrix equation when fewer than 20% of the vessel-matrix rows have nonzero outlying elements. For most system models (especially those with more than a hundred vessel mesh cells), only a few percent of the vessel-matrix rows have nonzero outlying elements. Thus, for a four-loop plant model with eight rows on nonzero outlying elements, the capacitance matrix method is faster than a full-matrix method by factors of 2, 4, 8, and 12 for vessel matrices of order 100, 200, 300, and 400, respectively. Similar factors apply to computer memory storage for the vessel-matrix equation by the full-matrix method versus the capacitance matrix method.

We can summarize the above description of the method by noting that the capacitance matrix method is a direct two-stage procedure. In the first stage, the banded-matrix portion of the matrix equation is solved with an efficient banded-matrix solver to determine the solution for the vessel-matrix equation with zero-valued outlying elements. Then, if there are nonzero outlying elements in the vessel matrix (1D hydro-component loops that connect back to a nonadjacent vessel location generate nonzero outlying elements), the second stage evaluates a direct full-matrix L-U matrix-decomposition solution of a much lower-order capacitance-matrix equation. Doing this accounts for the effect the nonzero outlying elements have on the vessel-matrix equation solution. This results in a modification of the banded-matrix solution to determine the solution of the vessel-matrix equation with nonzero outlying elements.

The following derivation determines the working equations and presents the four-step solution procedure programmed into the code. Given the vessel-matrix equation

$$\underline{\underline{A}} \cdot \underline{x} = \underline{b} , \tag{2-41}$$

where $\underline{\underline{A}}$ is a known (vessel) matrix, $\underline{x}$ is an unknown (mass density, velocity, energy, or pressure) vector, and $\underline{b}$ is a known vector, let us partition $\underline{\underline{A}}$ as follows into the sum of its banded matrix $\underline{\underline{B}}$ and a matrix product $\underline{\underline{E}} \cdot \underline{\underline{R}}$ that has only the nonzero elements lying outside the bandwidth:

$$\underline{\underline{A}} \cdot \underline{x} = (\underline{\underline{B}} + \underline{\underline{E}} \cdot \underline{\underline{R}}) \cdot \underline{x} = \underline{b} . \tag{2-42}$$

Consider the following example of how a simple form for $\underline{\underline{A}}$ would appear when partitioned.

$$\text{For } \underline{\underline{A}} = \begin{bmatrix} x & x & O & O & O & O \\ x & x & x & O & t & O \\ O & x & x & x & O & O \\ O & O & x & x & x & O \\ r & O & s & x & x & x \\ O & O & O & O & x & x \end{bmatrix} \text{, a matrix of order } N, \tag{2-43}$$

$$(N \times N)$$

where r, s, t, and x are nonzero elements, $N = 6$ is the total number of rows and columns in $\underline{\underline{A}}$, and $M = 2$ is the number of rows in $\underline{\underline{A}}$ having nonzero elements outside the three-diagonal bandwidth, then define

$$\underline{\underline{A}} = \underline{\underline{B}} + \underline{\underline{E}} \cdot \underline{\underline{R}} \tag{2-44}$$

where

$$\underline{\underline{B}} = \begin{bmatrix} x & x & O & O & O & O \\ x & x & x & O & O & O \\ O & x & x & x & O & O \\ O & O & x & x & x & O \\ O & O & O & x & x & x \\ O & O & O & O & x & x \end{bmatrix} , \quad \underline{\underline{E}} = \begin{bmatrix} O & O \\ O & 1 \\ O & O \\ O & O \\ 1 & O \\ O & O \end{bmatrix}$$

$$(N \times N) \qquad (N \times M)$$

$$\underline{\underline{R}} = \begin{bmatrix} r & O & s & O & O & O \\ O & O & O & O & t & O \end{bmatrix} \quad , \quad \underline{\underline{E}} \cdot \underline{\underline{R}} = \begin{bmatrix} O & O & O & O & O & O \\ O & O & O & O & t & O \\ O & O & O & O & O & O \\ O & O & O & O & O & O \\ r & O & s & O & O & O \\ O & O & O & O & O & O \end{bmatrix} . \tag{2-45}$$

$$(M \times N) \qquad\qquad (N \times N) \tag{2-46}$$

Note that the nonzero elements in $\underline{\underline{E}}$ are unity and in $\underline{\underline{R}}$ are the actual nonzero outlying elements of $\underline{\underline{A}}$. The term $\underline{\underline{A}}$ is an $N \times N$ matrix with M rows having nonzero elements outside its bandwidth, $\underline{\underline{B}}$ is an $N \times N$ banded matrix, $\underline{\underline{E}}$ is an $N \times M$ matrix, and $\underline{\underline{R}}$ is an $M \times N$ matrix.

Multiply Eq. (2-42) by the inverse of the banded matrix, $\underline{\underline{B}}$ to get

$$(\underline{\underline{I}} + \underline{\underline{B}}^{-1} \cdot \underline{\underline{E}} \cdot \underline{\underline{R}}) \cdot \underline{x} = \underline{\underline{B}}^{-1} \cdot \underline{b} . \tag{2-47}$$

Define $\underline{\underline{R}} \cdot \underline{x} = \underline{y}$ and move its term in Eq. (2-47) to the right-hand side of the equation, giving

$$\underline{x} = \underline{\underline{B}}^{-1} \cdot \underline{b} - \underline{\underline{B}}^{-1} \underline{\underline{E}} \cdot \underline{y} . \tag{2-48}$$

Substitute Eq. (2-48) for $\underline{x}$ into Eq. (2-47) to give

$$(\underline{\underline{I}} + \underline{\underline{B}}^{-1} \cdot \underline{\underline{E}} \cdot \underline{\underline{R}}) \cdot (\underline{\underline{B}}^{-1} \cdot \underline{b} - \underline{\underline{B}}^{-1} \cdot \underline{\underline{E}} \cdot \underline{y}) = \underline{\underline{B}}^{-1} \cdot \underline{b} . \tag{2-49}$$

Expand Eq. (2-49), delete the $\underline{\underline{B}}^{-1} \cdot \underline{b}$ term from both sides of the equation, and multiply the equation by $(\underline{\underline{B}}^{-1} \cdot \underline{\underline{E}})^{-1}$ giving

$$(\underline{\underline{I}} + \underline{\underline{R}} \cdot \underline{\underline{B}}^{-1} \cdot \underline{\underline{E}}) \cdot \underline{y} = \underline{\underline{R}} \cdot \underline{\underline{B}}^{-1} \cdot \underline{b} . \tag{2-50}$$

Multiply Eq. (2-50) by the inverse of the matrix on its left-hand side to define $\underline{y}$ as follows:

$$\underline{y} = (\underline{\underline{I}} + \underline{\underline{R}} \cdot \underline{\underline{B}}^{-1} \cdot \underline{\underline{E}})^{-1} \cdot \underline{\underline{R}} \cdot \underline{\underline{B}}^{-1} \cdot \underline{b} . \tag{2-51}$$

To determine $\underline{x} = \underline{\underline{A}}^{-1} \cdot \underline{b}$, evaluate Eq. (2-51) for $\underline{y}$ and substitute $\underline{y}$ into Eq. (2-48) to evaluate $\underline{x}$.

This evaluation procedure appears lengthy until we observe that it involves the following four steps with some intermediate results used several times.

Step 1. Multiply the vector $\underline{b}$ and each of the M columns of $\underline{\underline{E}}$ by the inverse of $\underline{\underline{B}}$.

$$\underline{\hat{x}} = \underline{\underline{B}}^{-1} \cdot \underline{b} \quad \text{and} \quad \underline{\underline{\hat{E}}} = \underline{\underline{B}}^{-1} \cdot \underline{\underline{E}} \tag{2-52}$$

$$(N) \quad (N \text{ x } N) \quad (N) \qquad (N \text{ x } M) \qquad (N \text{ x } N) \qquad (N \text{ x } M)$$

Step 2. Multiply $\hat{\underline{x}}$ and $\hat{\underline{\underline{E}}}$ from Step 1 by $\underline{\underline{R}}$.

$$\underset{(M)}{\hat{\underline{b}}} = \underset{(M \times N)}{\underline{\underline{R}}} \cdot \underset{(N)}{\hat{\underline{x}}} \quad \text{and} \quad \underset{(M \times M)}{\hat{\underline{\underline{R}}}} = \underset{(M \times N)}{\underline{\underline{R}}} \cdot \underset{(N \times M)}{\hat{\underline{\underline{E}}}} \tag{2-53}$$

Step 3. Evaluate Eq. (2-51) for $\underline{y}$ using $\hat{\underline{b}}$ and $\hat{\underline{\underline{R}}}$ from Step 2.

$$\underset{(M)}{\underline{y}} = \underset{(M \times M)}{(\underline{\underline{I}} + \hat{\underline{\underline{R}}})^{-1}} \cdot \underset{(M)}{\hat{\underline{b}}} \tag{2-54}$$

Step 4. Evaluate Eq. (2-48) for the desired solution vector $\underline{x}$ using $\hat{\underline{x}}$ and $\hat{\underline{\underline{E}}}$ from Step 1 and $\underline{y}$ from Step 3.

$$\underset{(N)}{\underline{x}} = \underset{(N)}{\hat{\underline{x}}} - \underset{(N \times M)}{\hat{\underline{\underline{E}}}} \cdot \underset{(M)}{\underline{y}} \tag{2-55}$$

Computationally, Eq. (2-51) is solved by performing a single banded-matrix L-U matrix decomposition to determine $\underline{\underline{B}}^{-1}$. Then $\underline{\underline{B}}^{-1}$ is applied to the $1+M$ column vectors of $\underline{b}$ and $\underline{\underline{E}}$ by a direct forward-elimination and backward-substitution solution procedure. Equation (2-54) requires that a L-U matrix decomposition be applied to the full (nonbanded), but much smaller, capacitance matrix $\underline{\underline{I}}+\hat{\underline{\underline{R}}}$. The method becomes rapidly less efficient as the size of the capacitance matrix $\underline{\underline{I}}+\hat{\underline{\underline{R}}}$ increases. The remainder of the computation involves matrix multiplications that are performed efficiently on a vector computer.

Water Packing

The water-packing logic in the code is triggered under certain conditions (but not all conditions) when the code attempts during a time step to overfill (pack) a liquid-full finite-difference mesh cell or to overextract (stretch) liquid from a liquid-full cell. The physical analog to water-packing event is a water hammer; when cold water surges down a dead-end pipe filled with steam, a large pressure spike occurs when the last steam collapses and the water fills the pipe. This spike has a very short duration because of the low compressibility of liquid water, .

In any Eulerian finite-difference scheme, the boundary of a mesh cell behaves like the dead end of a pipe in a water hammer event. This is especially true when condensation is present. Consider a

1D mesh cell with pure liquid entering from the left and pure vapor flowing in from the right to condense on the liquid. It is not possible for a standard finite-difference momentum equation to produce a liquid-mass flow out of the right cell face that exactly balances the flow in the left cell face at the instant when the cell fills with liquid. In fact, when strong condensation is present, the momentum equation generally will predict a liquid velocity into the cell on the right face. This circumstance produces a numerical dead end for the liquid. Unlike the water hammer, the final solution is not to halt the flow, but to push the liquid on through the right cell face. As with a hammer, this is accomplished with an abrupt increase in pressure.

In TRACE, we have adopted a method for mitigating water-packing that is similar in spirit to shock-fitting techniques. Logic has been installed that detects pressure excursions caused by water-packing. When they occur, it is clear that the finite-difference momentum equation is producing invalid results. Therefore, we modify the equation at those locations and times to obtain a better solution. A standard motion equation at a cell edge can be written as

$$V_{j+1/2}^{n+1} = V_{j+1/2}^{n} + a + b(P_j^{n+1} - P_{j+1}^{n+1}) \ . \tag{2-56}$$

Additional force terms are incorporated in the term *a*, and *b* includes the time-step size and inverse of mesh length and density. If packing is detected in cell *j*, the equation is modified to the form

$$V_{j+1/2}^{n+1} = V_{j+1/2}^{n} + a + b(cP_j^{n+1} - P_{j+1}^{n+1}) \ . \tag{2-57}$$

The constant *c* multiplying P_j^{n+1} is taken to be a large number so that only small changes in the pressure of the j^{th} cell are required to obtain the appropriate velocity for the liquid outflow. To prevent excessively large vapor velocities, the value of the coefficient *b* in the vapor equation is set equal to the corresponding coefficient in the liquid equation.

In a given cell of a 1D component, the code does not consider the water-packing logic if the cell void fraction is greater than 0.08, if the liquid in the cell is superheated, or if the net mass flow is out of the cell. Also, the code cannot make adjustments at a cell interface or test across that interface if the associated flow area is less than or equal to $10^{-10}\mathrm{m}^2$. Further, TRACE does not consider adjacent cells in which the void fraction is less than 0.1. The code predicts the change in the current cell pressure to give a new pressure; if the predicted pressure change is negative, the code transfers to logic to detect stretching. If the pressure rise is greater than or equal to 0, and if this new pressure does not exceed the maximum of its current value and the adjacent-cell pressures by at least 7%, with a minimum increase of 50 kPa (one-half bar), the water-packing logic terminates. The void-fraction tests ensure that the water-packing logic will not smooth out a true water-hammer-type phenomenon in the calculation, while the pressure checks prevent the logic from being triggered too often. If, through the tests, more than one interface of a given cell permits the water-packing correction, the code applies the correction only at the interface across which the void fraction is higher. The code does not permit the water-packing correction at the

interface opposite a FILL component if the velocities at both interfaces have the same sign or at the interface at which the PUMP-component source is applied. Also, the code terminates the water-packing logic for a given cell interface if choking is detected at that interface and if the interface is either the first or last interface of a component.

The stretching logic is similar, although the code looks for a pressure drop in the current cell that reduces its pressure to less than the minimum of 95% of its current value or 95% of the neighboring cells, with the additional constraint that the projected pressure must be less than the saturation pressure corresponding to the current liquid temperature minus 20.0 K. The final constraint for stretching is that the test pressure cannot be below the lower pressure limit for the equation of state (see **Chapter 11**). For a stretch event, the code does not make an adjustment at a given interface if the void fraction on the other side of the interface is less than or equal to 0.1, if the liquid velocity at the interface is into the cell in which the stretch is detected, or if the PUMP-component source is applied at the interface.

The 3D VESSEL water-packing detection logic is very similar. The VESSEL, however, permits packing to occur if the current cell void fraction is greater than 0.1, instead of the 0.08 in the 1D components. Also, in detecting a stretch, the code requires the pressure test to be 0.8 of that in the 1D components.

3

Heat Conduction Equations

The nuclear reaction that takes place in the reactor core generates energy inside the fuel. In a PWR, that energy is then transferred to the primary fluid and crosses the steam-generator tubes to the secondary fluid. In a BWR, that energy is deposited directly into the primary fluid, causing steam to be generated, and ultimately driving the turbines. The code must calculate the heat conduction in the fuel and the steam-generator tubes to simulate correctly the heat-transfer processes involved in thermal-energy transport. Also, the passive solid structures, such as piping walls, vessel walls, and the internal vessel structures, represent significant metal masses that can store or release large amounts of thermal energy depending upon the reactor coolant temperature. Therefore, the code needs to model these additional structures. This chapter describes the underlying theory employed by TRACE in order to model these phenomena.

Nomenclature

The following nomenclature applies to this chapter

A = area in radial direction

A^* = area in axial direction

$\underline{\underline{A}}$ = coefficient matrix

a = nonzero elements of $\underline{\underline{A}}$

$\underline{B}$ = equality vector

b = elements of $\underline{B}$

c_p = specific heat

$\underline{\underline{C}}$, $\underline{\underline{D}}$, $\underline{\underline{E}}$ = nonzero submatrices of $\underline{\underline{A}}$

f_t, f_{ss} = stability flags

HTC = heat transfer coefficient

h = convective HTC

h_{gap} = gap conductance

k = thermal conductivity

NR = number of nodes that segment the radial direction

NZ = number of nodes that segment the axial direction

$\bar{q}$ = heat flux vector

q''' = heat generation rate per unit volume

q_{total} = total heat flux

R = radius

R^+, R^- = variables defined by Eqs. (3-26) and (3-27)

r = radial coordinate

t = time

T = temperature

$\underline{T}$ = temperature vector

V = cell volume

z = axial distance

z_b = bottom of the fuel rod

z_u = top of the fuel rod

Δr = radial increment

Δt = time increment

Δx = slab thickness

Δz = axial increment

ρ = density

Subscripts

g = gas

I = inner surface

i, j = finite-difference indices

l = liquid

max = maximum

o = outer surface

w = wall

Superscripts

j = axial direction

n , $n+1$ = current-time and new-time values

p = predicted new-time values

+, – = refers to material to the right and left of the interface, respectively

′ = new quantities when a fine mesh is added

Governing Equations

Because the heat flux in a solid material is a vector quantity, the following general equation describes the heat-conduction process in an arbitrary geometry:

$$\frac{\partial(\rho c_p T)}{\partial t} + \nabla \cdot \bar{q} = q''' \quad . \tag{3-1}$$

In practice, the product ρc_p is assumed to be constant for purposes of taking the time derivative.

The heat flux $\bar{q}$ can be expressed in terms of the temperature gradient by Fourier's law of conduction (Ref. 3-1) as follows:

$$\bar{q} = -k\nabla T \quad . \tag{3-2}$$

Therefore, Eq. (3-1) becomes

$$\rho c_p \frac{\partial T}{\partial t} = \nabla \cdot (k\nabla T) + q''' \quad . \tag{3-3}$$

The thermal history of the reactor structure is obtained from a solution of the heat-conduction equation applied to different geometries. The next section discusses the coupling of the heat-conduction field equation in any of its many forms to the thermal-hydraulic field equations representing the fluid. Following this discussion, we present the details concerning the various formulations of the heat-conduction equations that represent particular geometries typically found in reactor systems. These geometries include cylindrical walls, slabs, and core fuel rods. The first model analyzes heat conduction within the walls of the 1D loop components, such as pipe walls. The latter two are associated with heat transfer within structural components of the vessel. They are modeled similarly in the code, differing only in the area and volume calculations used in the finite-difference equations.

Coupling of Thermal Hydraulics with the Reactor Structure

The energy transported by convective heat transfer from any structure into the different fluid phases is modeled using Newton's law of cooling to represent the energy exchange rate between the structure and the fluid phase. These terms appear in the energy equations of the different fluid phases. **Chapter 6** discusses the logic used to determine which heat-transfer regime exists between the wall and fluid and which correlations for the wall heat-transfer coefficient (HTC) are used to represent the different regimes. The coupling algorithm (Figure 3-1) is currently implicit in terms of the wall temperature, liquid and vapor phase temperatures and explicit in terms of the heat transfer coefficient. For each new-time step, the wall HTCs (h) of a given structure are evaluated using the surface wall temperatures (T_w) and the fluid conditions obtained for the last time step. The new-time fluid-dynamics equations are solved using these HTCs, the new-time surface temperatures, and the new-time fluid temperatures where the sum of the total energy transported into the fluid cell can be written as

$$q_{\text{total}}^{\,n+1} = h_l^n(T_w^p - T_l^n) + h_g^n(T_w^p - T_g^n) + \left[h_l^n\left(\frac{\partial T_w}{\partial T_l} - 1\right) + h_g^n\frac{\partial T_w}{\partial T_l}\right](T_l^{n+1} - T_l^n) + \left[h_g^n\left(\frac{\partial T_w}{\partial T_g} - 1\right) + h_l^n\frac{\partial T_w}{\partial T_g}\right](T_g^{n+1} - T_g^n) \quad . \quad (3\text{-}4)$$

In general the finite volume approximation for the conduction equation (i.e. Eq. (3-3)) can be written as a set of linear equations for the new time heat structure temperatures:

$$\underline{\underline{A}} \cdot \underline{T} = \underline{B} \quad (3\text{-}5)$$

Given a convective heat transfer boundary condition, then the right-hand side vector $\underline{B}$ is a function of the liquid and vapor phase temperatures for the fluid cell associated with the HS. Therefore, the derivative of Eq. (3-5) with respect to a change in the liquid phase temperature, yields:

$$\underline{\underline{A}} \cdot \frac{\partial \underline{T}}{\partial T_l} = \frac{\partial \underline{B}}{\partial T_l} \quad (3\text{-}6)$$

and the derivative of Eq. (3-5) with respect to a change in the vapor phase temperature, yields,

$$\underline{\underline{A}} \cdot \frac{\partial \underline{T}}{\partial T_g} = \frac{\partial \underline{B}}{\partial T_g} \quad (3\text{-}7)$$

The solution of Eq. (3-5) gives the predicted wall temperatures, T_w^p in Eq. (3-4). The solution of Eq. (3-6) gives how the HS temperatures change given a change in the liquid phase temperatue and the solution of Eq. (3-7) gives how the HS temperatures change given a change in vapor

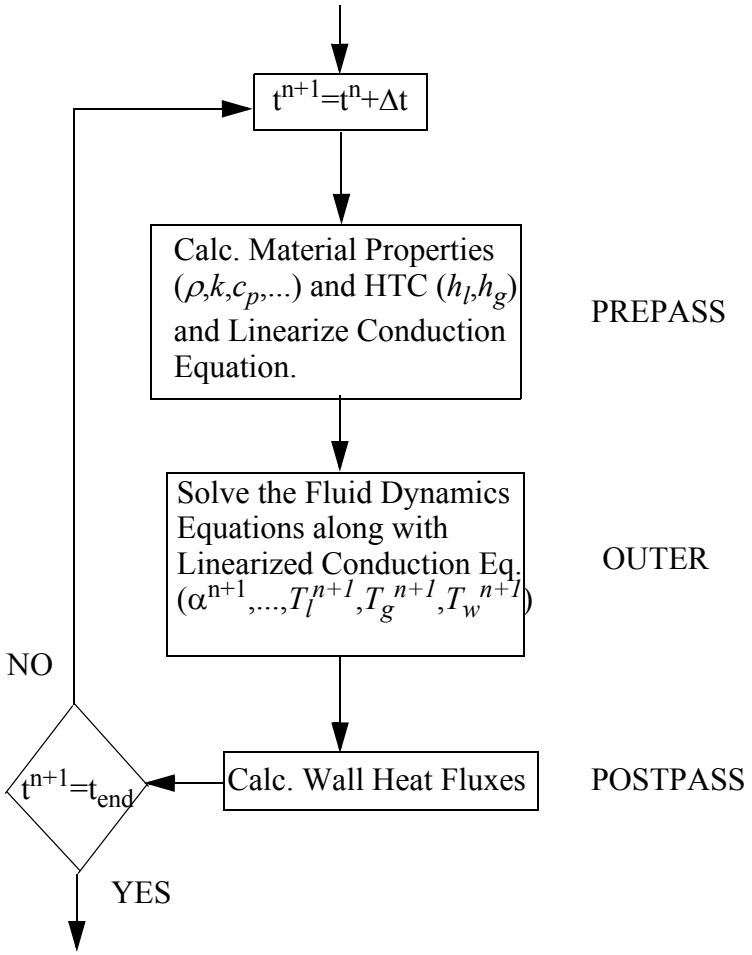

Figure. 3-1. Implicit coupling between hydrodynamics and structural heat transfer.

phase temperatures. The solution of these three equations is the linearization of the conduction equation about the liquid and vapor phase temperatures.

$$\underline{T}^{n+1} = \underline{T}^{n} + \frac{\partial \underline{T}}{\partial T_l}(T_l^{n+1} - T_l^{n}) + \frac{\partial \underline{T}}{\partial T_g}(T_g^{n+1} - T_g^{n}) \ . \tag{3-8}$$

Notice that the coefficient matrix is not a function of the liquid or vapor phase temperatures, therefore, the difference between Eq. (3-5), Eq. (3-6), and Eq. (3-7) is the change in the right-hand side vector. The forward elimination developed for the solution of Eq. (3-5) is saved and used to obtain the linearization derivatives in Eq. (3-6) and Eq. (3-7). From the linearization of the heat conduction equation, the two derivatives $\partial T_w / \partial T_l$ and $\partial T_w / \partial T_g$ are obtained for the radial HS node that is the wall of the HS. These two derivatives of how the HS wall temperature changes given a change in the liquid phase temperature and how the HS wall temperature changes

given a change in the vapor phase temperature together with Eq. (3-4) determines how the wall heat flux changes given a change in the liquid and vapor phase temperatures. This allows the fluid dynamics solution to be consistent with the linearized conduction equation.

Eq. (3-4) and Eq. (3-8) completely describe a single-side heat structure (i.e. a HS with convective heat transfer boundary condition on either the inside or outside surface of the heat structure). For single-sided heat structures Eq. (3-5) through Eq. (3-7) are solved once and the linearization coefficients saved and used to update the HS temperature distribution each outer iteration (see Figure 3-1).

For double-sided heat structures there are additional linearization terms associated with the change in liquid and vapor phase temperatures on the other side of the heat structure. Experimentation with typical double-sided heat structures in a PWR and BWR power plant model indicate that in most cases the derivative of the wall temperature given a change in the fluid temperatures on the other side of the heat structure was small enough that it could be ignored. Therefore, for double-sided HS that derivatives of the phase temperatures on the other side of the heat structure are ignored in Eq. (3-4). However, for double-sided HS's, Eq. (3-8) is not used to update the HS temperature distributions each outer iteration. For double-sided HS's, Eq. (3-5) through Eq. (3-7) are solved for both the inner and outer surface. This ensures that for double-sided HSs the temperature distribution is consistent with the conduction equation and not an approximate linearization of the conduction equation.

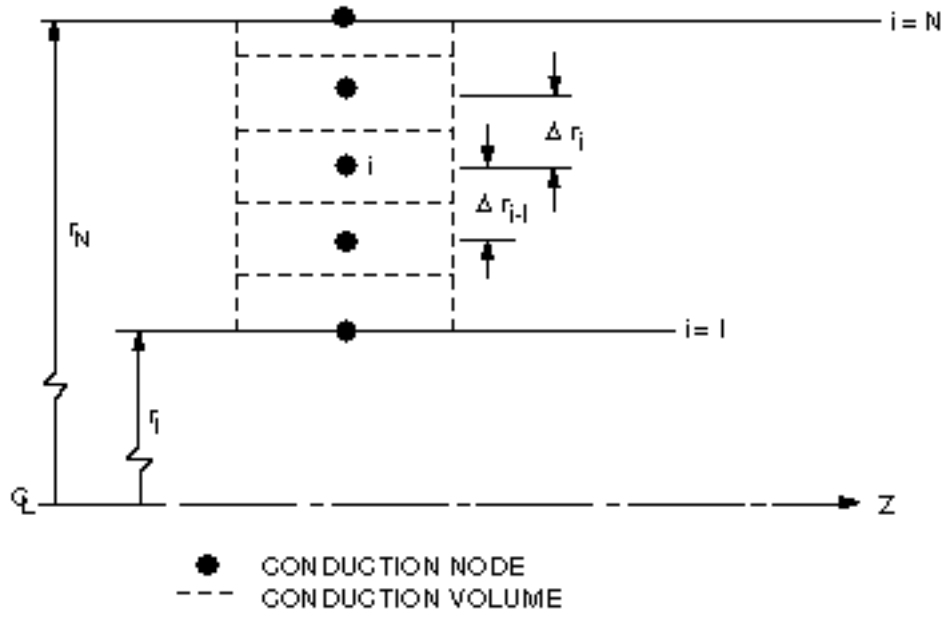

Figure. 3-2. Cylindrical wall geometry.

Cylindrical Wall Heat Conduction

The temperature distribution within the walls of the 1D components is obtained from a finite-difference approximation to the 1D conduction equation,

$$\rho c_p \frac{\partial T}{\partial t} = \frac{1}{r}\left[\frac{\partial}{\partial r}\left(rk\frac{\partial T}{\partial r}\right)\right] + q''' \ . \tag{3-9}$$

The finite-difference equations are derived by applying an integral method (Ref. 3-2) to the elemental volumes shown in Figure 3-2. The general form of the i^{th} volume ($1 < i < N$) is

$$\begin{aligned}
&\frac{r_{i-1/2}\,k_{i-1/2}}{\Delta r_{i-1}} T_{i-1}^{n+1} - \left\{\frac{r_{i-1/2}\,k_{i-1/2}}{\Delta r_{i-1}} + \frac{r_{i+1/2}\,k_{i+1/2}}{\Delta r_i}\right. \\
&\left. + \frac{1}{2\Delta t}\left[\left(r_i\Delta r_{i-1} - \frac{\Delta r_{i-1}^2}{4}\right)(\rho c_p)_{i-1/2} + \left(r_i\Delta r_i + \frac{\Delta r_i^2}{4}\right)(\rho c_p)_{i+1/2}\right]\right\} T_i^{n+1} \\
&+ \frac{r_{i+1/2}\,k_{i+1/2}}{\Delta r_i} T_{i+1}^{n+1} = -\frac{1}{2}\left\{\left(r_i\Delta r_{i-1} - \frac{\Delta r_{i-1}^2}{4}\right)\left[\frac{(\rho c_p)_{i-1/2}}{\Delta t} T_i^n + q'''\right]\right. \\
&\left. + \left(r_i\Delta r_i + \frac{\Delta r_i^2}{4}\right)\left[\frac{(\rho c_p)_{i+1/2}}{\Delta t} T_i^n + q'''\right]\right\}
\end{aligned} \tag{3-10}$$

where

$$f_i^n = f(t^n, r_i) \ . \tag{3-11}$$

This formulation positions nodal points on material interfaces. Material properties are evaluated between nodes. The boundary conditions applied to the inner ($i = 1$) and outer ($i = N$) surfaces are

$$-k\frac{\partial T}{\partial r}\bigg|_{i=1,N} = \pm[h_l(T_l - T_i) + h_g(T_g - T_i)] \ . \tag{3-12}$$

For example, application of this boundary condition to the inner surface ($i = 1$) yields

$$-\left\{\frac{r_{3/2}k_{3/2}}{\Delta r_1}+\frac{1}{2}\left[r_1\Delta r_1+\frac{\Delta r_1^2}{4}\right]\frac{(\rho c_p)_{3/2}}{\Delta t}+r_1(h_l+h_g)\right\}T_1^{n+1}+\frac{r_{3/2}k_{3/2}}{\Delta r_1}T_2^{n+1}$$

$$=-\frac{1}{2}\left(r_1\Delta r_1+\frac{\Delta r_1^2}{4}\right)\left[\frac{(\rho c_p)_{3/2}}{\Delta t}T_1^n+q'''\right]-r_1\left[h_lT_l^{n+1}+h_gT_g^{n+1}\right]$$

$$-\ r_1[h_lT_l^{n+1}+h_gT_g^{n+1}]\ . \qquad (3\text{-}13)$$

The resulting linear equations are solved in a sequential fashion in the axial z-direction. For each axial position, a solution is achieved using Gaussian elimination.

A lumped-parameter solution is available to the user if the number of nodes is set equal to one. For this option the wall temperature is obtained from the equation,

$$T^{n+1}=\left\{\frac{1}{2}\left(2\Delta r+\frac{\Delta r^2}{R_I}\right)\left(\frac{\rho c_p}{\Delta t}T^n+q'''\right)+h_{l_I}T_{l_I}^{n+1}\right. \qquad . \qquad (3\text{-}14)$$

$$\left.+h_{g_I}T_{g_I}^{n+1}+\left(1+\frac{\Delta r}{R_I}\right)[h_{l_o}T_{l_o}^{n+1}+h_{g_o}T_{g_o}^{n+1}]\right\}$$

$$+\left\{\frac{1}{2}\left(2\Delta r+\frac{\Delta r^2}{R_I}\right)\left(\frac{\rho c_p}{\Delta t}\right)+\left[h_{l_I}+h_{g_I}+\left(1+\frac{\Delta r}{R_I}\right)(h_{l_o}+h_{g_o})\right]\right\}^{-1}$$

The subscripts I and o refer to the inner and outer radii, respectively.

Slab and Rod Heat Conduction

Structures that can exchange heat with the fluid in a reactor vessel include downcomer walls and support plates, modeled as slabs, and vessel rods. These elements are referred to as heat-structure components. Both nuclear and electrically heated rods or slabs can be analyzed. The effects of gap conduction, metal-water reaction, and variable material properties are included (these models are documented in **Chapter 8**).

Only one rod within a cell may have hydro-cell coupling. This “average” rod is coupled to the fluid by Newton’s law of cooling. Any number of additional user-specified rods may be included in each segment. The rod power factors (that is, relative to the average rod located within each segment) are specified by the user for these supplemental rods. The supplemental rods allow the

user to include hot rods in the reactor vessel. Such rods do not affect the fluid-dynamics calculation because their contributions are already represented by average rods. They are included separately only for the purpose of determining their temperature response.

More than one slab may be located within a cell. Each slab is coupled to the fluid by Newton's law of cooling.

The user has four numerical calculation options for computing temperature distribution in slabs and rods. For thin slabs or rods of small diameter where the radial temperature profile is flat and axial conduction is negligible, the user may choose the "lumped-parameter" solution. This option gives the best calculational efficiency and should be used whenever it can be justified.

The second option is a 1D solution with implicit differencing in the radial direction and no conduction in the axial direction. This option is appropriate when steep axial profiles do not exist.

The third option is a 2D solution with implicit differencing in the radial direction and explicit differencing in the axial direction. This allows the very small radial node spacing required by the large radial power variations without severely limiting the time step. The explicit differencing in the axial direction does limit the maximum time-step size for axial spacing. In many cases, however, this maximum time-step size is much greater than that used for the fluid-dynamics calculation and is not restrictive. For those cases, the semi-implicit calculation gives good computational efficiency.

The fourth option is the fully implicit, 2D finite-difference calculation. This is the best choice for cases where the axial temperature gradient is very large, such as in the vicinity of a quench front. Then the very fine axial noding that is required would cause the time step to be severely limited if the semi-implicit calculation was used. These methods are discussed in the following sections.

The Lumped-Parameter Solution.

The lumped-parameter equation for cylindrical coordinates is Eq. (3-14). If we choose $f_t = 0$ and $f_{ss} = 1$ for maximum stability, that equation reduces to

$$T^{n+1} = \left\{ \frac{1}{2}\left(2\Delta r + \frac{\Delta r^2}{R_I} \right)\left(\frac{\rho c_p}{\Delta t} T^n + q''' \right) + h_{l_I} T_{l_I}^{n+1} + h_{g_I} T_{g_I}^{n+1} \right.$$

$$\left. + \left(1 + \frac{\Delta r}{R_I} \right)\left[h_{l_o} T_{l_o}^{n+1} + h_{g_o} T_{g_o}^{n+1} \right] \right\}$$

$$\left\{ \frac{1}{2}\left(2\Delta r + \frac{\Delta r^2}{R_I} \right)\left(\frac{\rho c_p}{\Delta t} \right) + \left[h_{l_I} + h_{g_I} + \left(1 + \frac{\Delta r}{R_I} \right)(h_{l_o} + h_{g_o}) \right] \right\}^{-1} \quad . \tag{3-15}$$

For a solid rod, the axial temperatures are

$$T^{n+1} = \left\{ \frac{\Delta r}{2}\left[\frac{\rho c_p}{\Delta t} T^n + q'''\right] + h_{l_o} T_{l_o}^{n+1} + h_{g_o} T_{g_o}^{n+1} \right\} \left\{ \frac{\Delta r \rho c_p}{2\Delta t} + h_{l_o} + h_{g_o} \right\}^{-1} . \tag{3-16}$$

The lumped-parameter equation for the temperature of a slab is

$$T^{n+1} = \frac{\frac{\rho c_p \Delta x}{\Delta t} T^n + q'''\Delta x + h_{l_o} T_{l_o}^{n+1} + h_{g_o} T_{g_o}^{n+1} + h_{l_I} T_{l_I}^{n+1} + h_{g_I} T_{g_I}^{n+1}}{\frac{\rho c_p \Delta x}{\Delta t} + h_{l_o} + h_{g_o} + h_{l_I} + h_{g_I}} , \tag{3-17}$$

where Δx is the slab thickness.

The Semi-Implicit Calculation.

Finite-difference equations are obtained by applying an integral method (Ref. 3-3) to appropriate differential volumes. The axial noding within a rod (see Figure 3-3) is typically the same or at a finer axial noding than the fluid component axial noding.

Consider a general differential volume (that is, the volume labeled i, j in Figure 3-3). Using explicit differencing in the axial direction and implicit differencing in the radial direction, the finite-difference equation for this volume is

$$\left\{ (\rho c_p)_{ij} \frac{T_{ij}^{n+1} - T_{ij}^n}{\Delta t} - q'''_{ij} \right\} \frac{1}{2}\left[\left(r_i \Delta r_i + \frac{\Delta r_i^2}{4} \right) + \left(r_i \Delta r_{i-1} - \frac{\Delta r_{i-1}^2}{4} \right)\right]\left[\frac{\Delta z_j + \Delta z_{j-1}}{2}\right] \tag{3-18}$$

$$= \left\{ r_{i+1/2} k_{i+1/2, j} \left(\frac{T_{i+1, j}^{n+1} - T_{ij}^{n+1}}{\Delta r_i} \right) + r_{i-1/2} k_{i-1/2, j} \left(\frac{T_{i-1, j}^{n+1} - T_{ij}^{n+1}}{\Delta r_{i-1}} \right) \right\}$$

$$\times \left[\frac{\Delta z_j + \Delta z_{j-1}}{2}\right] + \left\{ k_{i, j+1/2} \left(\frac{T_{i, j+1}^{n} - T_{ij}^{n}}{\Delta z_j} \right) + k_{i, j-1/2} \left(\frac{T_{i, j-1}^{n} - T_{ij}^{n}}{\Delta z_{j-1}} \right) \right\}$$

$$\times \frac{1}{2}\left[\left(r_i \Delta r_i + \frac{\Delta r_i^2}{4} \right) + \left(r_i \Delta r_{i-1} - \frac{\Delta r_{i-1}^2}{4} \right)\right]$$

where $f_{ij}^{n} = f(t^{n}, r_i, z_j)$. In Figure 3-3, the locations of nodes within the volumes located at the boundaries differ (i.e. boundary nodes are typically located at the volume edge, while interior nodes are located in the middle of the volume. This difference should be considered when values are assigned for the relative power densities at each node.

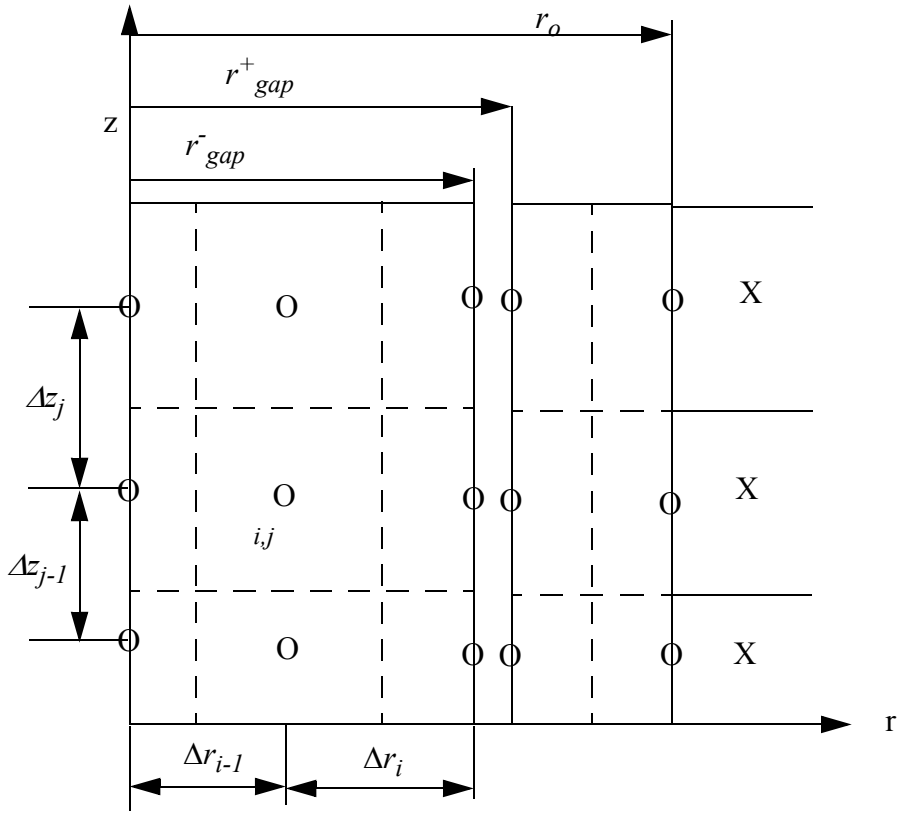

O Conduction Nodes X Fluid-Dynamic Nodes ---- Conduction Volumes

Figure. 3-3. Rod geometry.

The boundary conditions normally applied to the fuel rods are

- the top ($z = z_u$) and bottom ($z = z_b$) of the rods are assumed to be insulated,

$$k\frac{\partial T}{\partial z}\bigg|_{z = z_b,\, z_u} = 0\,; \tag{3-19}$$

- the rod centerline ($r = 0$) is a line of symmetry,

$$\left.\frac{\partial T}{\partial r}\right|_{r=0} = 0\,; \tag{3-20}$$

- heat transfer at the inner and outer gap surfaces ($r = r_{gap}^{-}$, r_{gap}^{+}) and at the cladding surface ($r = r_o$) is specified using Newton's law,

$$k\left.\frac{\partial T}{\partial r}\right|_{r=r_{gap}^{\pm}} = -h_{gap}^{\pm}(T_{r_{gap}^{-}} - T_{r_{gap}^{+}}), \text{ and} \tag{3-21}$$

$$k\left.\frac{\partial T}{\partial r}\right|_{r=r_0} = -h_{fluid}(T_{r_0} - T_{fluid}), \tag{3-22}$$

where $h_{gap}^{+} = h_{gap}^{-}(r_{gap}^{-}/r_{gap}^{+})$ to conserve energy.

All properties (that is, ρ, c_p, and k) required by the difference equations are stored at the node locations. Linear interpolation is used to obtain properties between nodes (that is, at cell surfaces). A node located at the interface between two dissimilar materials requires two sets of properties. Application of an integral technique to the differential volume in Figure 3-4 results in the differential equation (after dividing through by the volume),

$$\overline{(\rho c_p)}_{ij}\left(\frac{T_{ij}^{n+1} - T_{ij}^{n}}{\Delta t}\right) - q_{ij}''' = \left\{ r_{i+1/2} k_{i+1/2,\,j}\left(\frac{T_{i+1j}^{n+1} - T_{ij}^{n+1}}{\Delta r_i}\right) + r_{i-1/2} k_{i-1/2,\,j} \right.$$

$$\left. \times \left(\frac{T_{i-1,\,j}^{n+1} - T_{ij}^{n+1}}{\Delta r_{i-1}}\right) \right\} \times \left[\frac{\left(r_i \Delta r_i + \frac{\Delta r_i^2}{4}\right) + \left(r_i \Delta r_{i-1} + \frac{\Delta r_{i-1}^2}{4}\right)}{2} \right]^{-1}$$

$$+ \left\{ \bar{k}_{i,\,j+1/2}\left(\frac{T_{i,\,j+1}^{n} - T_{ij}^{n}}{\Delta z_j}\right) + \bar{k}_{i,\,j-1/2}\left(\frac{T_{i,\,j-1}^{n} - T_{ij}^{n}}{\Delta z_{j-1}}\right) \right\} \left[\frac{\Delta z_j + \Delta z_{j-1}}{2} \right]^{-1}, \tag{3-23}$$

where

$$\overline{(\rho c_p)}_{ij} \equiv \frac{\left[(\rho c_p)_{i^+,j} R^+ + (\rho c_p)_{i^-,j} R^-\right]}{R^+ + R^-} \tag{3-24}$$

and

$$\bar{k}_{i,j+1/2} \equiv \frac{\left[k_{i^+,j+1/2} R^+ + k_{i^-,j+1/2} R^-\right]}{[R^+ + R^-]} \quad . \tag{3-25}$$

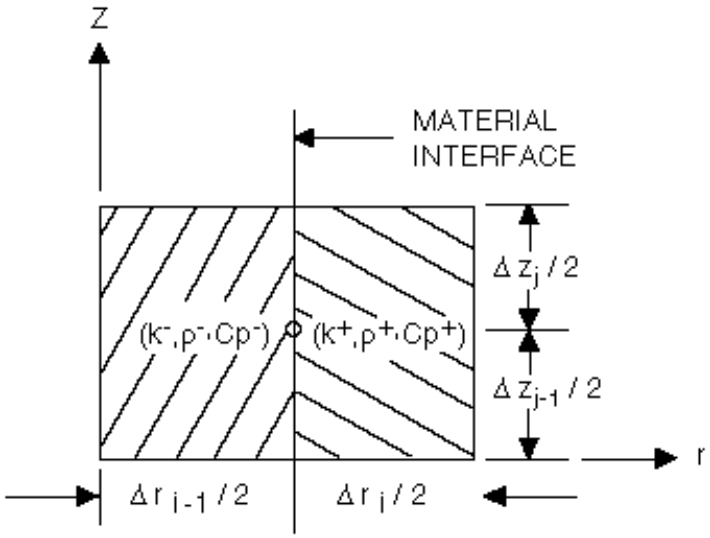

Figure. 3-4. Node located at the interface between two dissimilar materials.

In the above equations,

$$R^+ \equiv \left(r_i + \frac{\Delta r_i}{4}\right)\frac{\Delta r_i}{2} \tag{3-26}$$

and

$$R^- \equiv \left(r_i - \frac{\Delta r_{i-1}}{4}\right)\frac{\Delta r_{i-1}}{2} \quad . \tag{3-27}$$

The superscripts "+" and "–" refer to the material to the right and left of the interface.

The semi-implicit finite-difference formulation for the slab is identical to that of the rod except for the obvious geometric differences.

The Fully Implicit Calculation.

With the cell noding shown in Figure 3-3, the fully implicit finite-difference equation for 2D heat conduction is (Ref. 3-4)

$$
\begin{aligned}
&(\rho c_p)_{i,j}\left(\left(T_{i,j}^{n+1}-T_{i,j}^{n}\right)/\Delta t\right)V_{i,j}\\
&\quad=q_{ij}'''V_{ij}+k_{i+1/2,j}\left(\left(T_{i+1,j}^{n+1}C-T_{i,j}^{n+1}\right)/\Delta r_i\right)A_{i+1/2}\\
&\quad+k_{i-1/2,j}\left(\left(T_{i-1,j}^{n+1}-T_{i,j}^{n+1}\right)/\Delta r_{i-1}\right)A_{i-1/2}\\
&\quad+k_{i,j+1/2}\left(\left(T_{i,j+1}^{n+1}-T_{i,j}^{n+1}\right)/\Delta z_j\right)A_i^j\\
&\quad+k_{i,j-1/2}\left(\left(T_{i,j-1}^{n+1}-T_{i,j}^{n+1}\right)/\Delta z_{j-1}\right)A_i^j,
\end{aligned}
\tag{3-28}
$$

where V = cell volume, A = area in radial direction, A^j = area in axial direction, and Δr = cell length in radial or *x* direction.

Note that this equation applies to both the slab and rod geometries, providing the areas and volumes of the cells are calculated correctly. Eq. (3-28) can be written (Ref. 3-4) as

$$
a_{1,i,j}T_{i-1,j}^{n+1}+a_{2,i,j}T_{i,j}^{n+1}+a_{3,i,j}T_{i+1,j}^{n+1}+a_{4,i,j}T_{i,j-1}^{n+1}+a_{5,i,j}T_{i,j+1}^{n+1}=b_{i,j}, \tag{3-29}
$$

where

$$
a_{1,i,j}=\frac{-k_{i-1/2,j}A_{i-1/2}}{\Delta r_{i-1}}, \tag{3-30}
$$

$$
\begin{aligned}
a_{2,i,j}=&\frac{(\rho c_p)_{i,j}V_{i,j}}{\Delta t}+\frac{k_{i+1/2,j}A_{i+1/2}}{\Delta r_i}+\frac{k_{i-1/2,j}A_{i-1/2}}{\Delta r_{i-1}}\\
&+\frac{k_{i,j+1,j}A_i^j}{\Delta z_j}+\frac{k_{i,j-1/2,j}A_i^j}{\Delta z_{j-1}}
\end{aligned}
\quad , \tag{3-31}
$$

$$a_{3,i,j} = \frac{-k_{i+1/2,j} A_{i+1/2}}{\Delta r_i}, \tag{3-32}$$

$$a_{4,i,j} = \frac{k_{i,j-1/2} A_i^j}{\Delta z_{j-1}}, \tag{3-33}$$

$$a_{5,i,j} = \frac{-k_{i,j+1/2} A_i^j}{\Delta z_j}, \text{ and} \tag{3-34}$$

$$b_{i,j} = \left\{ q'''_{i,j} + \frac{(\rho c_p)_{i,j} T^n_{i,j}}{\Delta t} \right\} V_{i,j} . \tag{3-35}$$

Eq. (3-29) is rewritten in matrix notation as

$$\underline{\underline{A}} \cdot \underline{T} = \underline{B} \tag{3-36}$$

or

$$\begin{pmatrix} \underline{D}(1) & \underline{E}(1) & & & & \\ \underline{C}(2) & \underline{D}(2) & \underline{E}(2) & & & 0 \\ & \underline{C}(3) & \underline{D}(3) & \underline{E}(3) & & \\ & & \ddots & & & \\ 0 & & & & & \\ & & \underline{C}(NZ-1) & \underline{D}(NZ-1) & \underline{E}(NZ-1) & \\ & & & \underline{C}(NZ) & \underline{D}(NZ) & \end{pmatrix} \begin{pmatrix} \underline{T}(1) \\ \underline{T}(2) \\ \underline{T}(3) \\ \vdots \\ \vdots \\ \underline{T}(NZ-1) \\ \underline{T}(NZ)) \end{pmatrix} = \begin{pmatrix} \underline{B}(1) \\ \underline{B}(2) \\ \underline{B}(3) \\ \vdots \\ \vdots \\ \underline{B}(NZ-1) \\ \underline{B}(NZ) \end{pmatrix}, \tag{3-37}$$

where

$$\underline{T}^{(j)} = \begin{pmatrix} T_{1,j} \\ T_{2,j} \\ \vdots \\ T_{NR,j} \end{pmatrix} \quad (j = 1, NZ), \qquad \underline{B}^{(j)} = \begin{pmatrix} b_{1,j} \\ b_{2,j} \\ \vdots \\ b_{NR,j} \end{pmatrix} \quad (j = 1, NZ) \tag{3-38}$$

$$\underline{\underline{C}}^{(j)} = \begin{pmatrix} a_{4,1,j} & & & 0 \\ & a_{4,2,j} & & \\ & & \ddots & \\ 0 & & & a_{4,NR,j} \end{pmatrix} \quad (j = 2, NZ), \tag{3-39}$$

$$\underline{\underline{D}}^{(j)} = \begin{pmatrix} a_{2,1,j} & a_{3,1,j} & & & \\ a_{1,2,j} & a_{2,2,j} & a_{3,2,j} & & \\ & a_{1,3,j} & a_{2,3,j} & a_{3,3,j} & \\ & & \ddots & & \\ & 0 & & a_{1,NR,j} & a_{2,NR,j} \end{pmatrix} \quad (j = 1, NZ), \text{ and} \tag{3-40}$$

$$\underline{\underline{E}}^{(j)} = \begin{pmatrix} a_{5,1,j} & & & 0 \\ & a_{5,2,j} & & \\ & & \ddots & \\ 0 & & & a_{5,NR,j} \end{pmatrix} \quad (j = 1, NZ-1). \tag{3-41}$$

Matrix $\underline{\underline{A}}$ is a symmetrical banded matrix. To solve for the temperatures, matrix $\underline{\underline{A}}$ is inverted by a modified Cholesky method. Then the temperatures are computed from

$$\underline{T} = \underline{\underline{A}}^{-1} \underline{B}. \tag{3-42}$$

Note that Eq. (3-42) yields the predicted temperature distribution for the fully implicit 2D HS that appears in Eq. (3-4). The linearization coefficients for the fully implicit 2D HS are:

$$\frac{\partial \underline{T}}{\partial T_l} = \underline{\underline{A}}^{-1} \frac{\partial \underline{B}}{\partial T_l}. \tag{3-43}$$

$$\frac{\partial \underline{T}}{\partial T_g} = \underline{\underline{A}}^{-1} \frac{\partial \underline{B}}{\partial T_g}. \tag{3-44}$$

Fine-Mesh Algorithm.

The reflood phase of a postulated LOCA is characterized by a sequence of heat-transfer and two-phase-flow regimes advancing rapidly through the vessel core. A correctly predicted thermal response from the fuel/heater rods during reflood requires a numerical technique that can model the quenching phenomena associated with the quench-front motion.

The leading edge of the quenching region is characterized by large variations of temperatures and heat fluxes within small axial distances ($\Delta z \sim 1$ mm) (Ref. 3-5). The front advancement is controlled by two heat-removal mechanisms, the first being axial conduction from the post-CHF region ahead of the quenched region to the nucleate-boiling region behind the advancing film. The rod conduction model contains the necessary physics to analyze such phenomena. The second is the precursory rod cooling associated with heat transfer to the slugs and droplets entrained in the vapor field downstream of the quench front. The convective heat transfer discussed in **Chapter 6** contains the physics necessary to describe this phenomenon.

To model the inherently nonstationary, Lagrangian quench-front motion and to resolve the related thermal gradients, a fine-mesh rezoning technique (Ref. 3-6) is used during the reflood conduction calculations. The axial gradients encountered within the quenching region are resolved by the insertion of rows of transitory nodes (see Figure 3-5). These nodes are added whenever the surface temperature difference between adjacent nodes exceeds a heat transfer regime dependent value (ΔT_{max}). If the heat transfer regime is film boiling, then ΔT_{max} is given by:

$$\Delta T_{max} = Max\left(25\ ,\ 5 + 0.067\Delta T_s + 0.000028(\Delta T_s)^2\right)\ , \tag{3-45}$$

If the heat transfer regime is transition boiling, then ΔT_{max} is given by:

$$\Delta T_{max} = Min\,(25\ ,\ 5 + 0.067\Delta T_s)\ , \tag{3-46}$$

If the heat transfer regime is nucleate boiling, then ΔT_{max} is given by:

$$\Delta T_{max} = Min\left(5\ ,\ \frac{25}{\Delta T_s}\right)\ , \tag{3-47}$$

For all other heat transfer regimes, ΔT_{max} is given by:

$$\Delta T_{max} = 25\ , \tag{3-48}$$

The number of permanent rows inserted within each fluid level is specified by the user. The rows are uniformly spaced (that is, Δz is constant) within each fluid level. The temperature values at the supplemental nodes are determined from linear interpolation. The permanent nodes added in this fashion remain during the entire TRACE calculation, since reflood is either on or off at the beginning of a TRACE calculation.

Insertion of a fine mesh axial node row is illustrated in Figure 3-6. If the surface temperatuer axial gradient exceeds ΔT_{max} given by Eq. (3-45) through Eq. (3-48), then a new transitory node row is inserted. If the original two axial levels j_o and $j_o + 1$ are within the same coarse mesh node, then the temperature of the node row at $j' = j_o + 2$ is equal to the old temperature at $j_o + 1$ and $j' = j_o$ temperature is equal to the old temperature at j_o. The new temperature at $j' = j_o + 1$ is given by Eq. (3-49), which conserves energy assuming heat structure densities do not vary significantly in the axial direction.

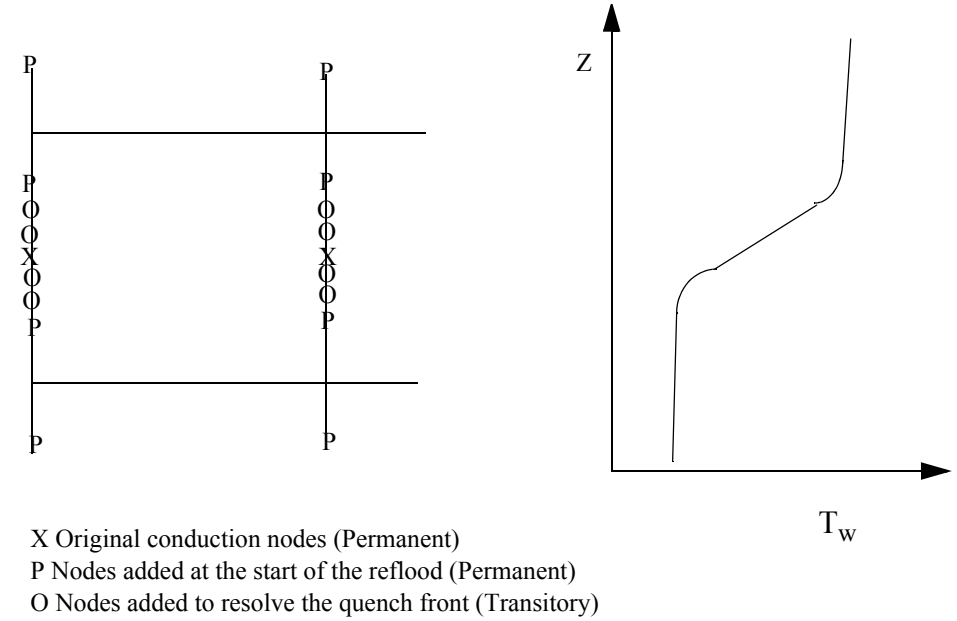

Figure. 3-5. Fine-mesh rezoning.

$$T_{i,j+1} = \frac{c_{p(i,j)} T_{i,j} + c_{p(i,j+2)} T_{i,j+2}}{c_{p(i,j)} + c_{p(i,j+2)}}, \tag{3-49}$$

When the two old conduction node rows are in different coarse mesh axial levels, then the cell edge between the coarse mesh axial levels cannot move. For this case, either the node row below the coarse mesh cell edge will be split according to 2/3 and 1/3 or the node row above the coarse mesh cell edge will be split according to 1/3 and 2/3. The fine mesh logic picks the largest axial

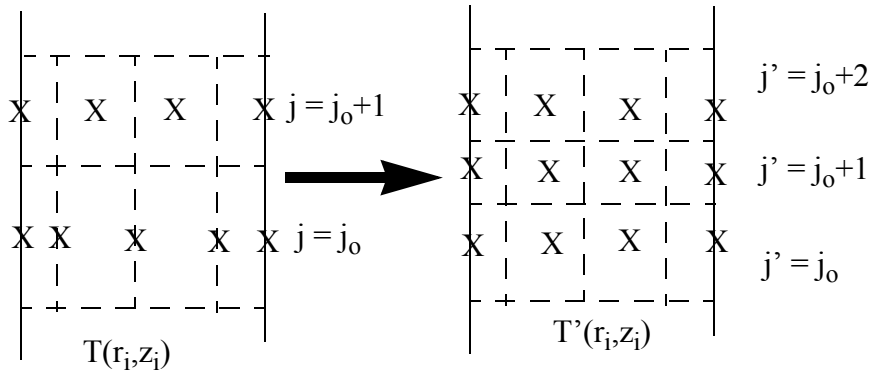

Figure. 3-6. Insertion of conduction nodes during reflood.

level of the two axial levels at the coarse mesh boundary to split into two axial node rows. For this case the new temperatures are based on the linear interpolation based on the original un-modified noding and temperatures. Since it is a single axial level that is split into two axial levels (i.e. one at 1/3 the height of the original axial level and the other at 2/3 the height of the original axial level), it is not necessary to do any averaging to ensure that energy is conserved with the new noding.

When the axial surface temperature gradient between two node rows becomes less than one-half of ΔT_{max} given by Eqs. (3-45) through (3-47), then two node rows are merged into one node row. Inserting an axial node row based on ΔT_{max} and removing an axial node row based on $(\Delta T_{max})/2$ ensures that the fine mesh logic will not consistently insert and remove the same transitory axial level every time step.

The above algorithm can analyze multiple quench fronts simultaneously. Both quenching and dryout are modeled automatically.

During the reflood phase, a number of surface conduction nodes are located within each fluid cell. Therefore, total heat transfer rate is obtained by summing the surface heat flux for each fine mesh axial level associated with a fluid cell.

$$Q = \sum_j \left(q_j + \frac{\partial q_j}{\partial T_l}(T_l^{n+1} - T_l^n) + \frac{\partial q_j}{\partial T_g}(T_g^{n+1} - T_g^n) \right) A_j \tag{3-50}$$

It already has been noted that, for a given time step (Δt), a minimum spacing (Δz) between rows of conduction nodes exists because of the explicit axial differencing. For reflood

calculations, this axial spacing can be violated, resulting in stability problems. To avoid such problems, the time step is limited internally by a diffusion number. The user also can specify minimum spacing (Δz_{min}) beyond which supplemental rows of conduction nodes will not be added. This additional advantage can prevent excessively large computer costs.

References

3-1 G. B. Wallis, *One Dimensional Two-Phase Flow* (McGraw-Hill, Inc., New York, 1969).

3-2 Frank P. Incropera and David P. DeWitt, *Fundamentals of Heat Transfer* (John Wiley & Sons, New York, 1981).

3-3 P. J. Roache, *Computational Fluid Dynamics* (Hermosa Publishers, Albuquerque, New Mexico, 1972).

3-4 H. Akimoto, Y. Abe, and Y. Murao, "Implementation of an Implicit Method into Heat Conduction Calculation of TRAC-PF1/MOD2 Code," JAERI-memo 01-008 (February 1989).

3-5 G. Yadigaroglu, "The Reflooding Phase of the LOCA in PWRs. Part I: Core Heat Transfer and Fluid Flow," *Nuclear Safety* 19 (1978).

3-6 Reactor Safety Research Program, "Quarterly Report for the Period July 1–September 30, 1978," Battelle Pacific Northwest Laboratories report PNL-2653-3 (NUREG/CR-0546) (1978).

4

Drag Models

As shown in **Chapter 1**, the liquid- and gas-field momentum equations each include terms for the interfacial shear force and the wall drag force. Closure of these equations thus requires that we specify the interfacial drag coefficient, C_i, and the phasic wall drag coefficients, C_{wl} and C_{wg}, for wall-liquid and wall-gas shear respectively. Typically, only one of the wall drag coefficients has a non-zero value. For example, in either bubbly/slug or annular/mist flow, all of the wall drag is applied to the liquid phase and C_{wg} is set to zero. Both the models for the interfacial drag coefficient and the wall drag coefficients are dependent upon the flow regime. These flow regime dependent closure models are discussed below, first for the interfacial drag and then for the wall drag.

Nomenclature

The following nomenclature applies to this chapter:

a = minor radius of prolate ellipsoid

A = flow area (m^2)

A_k = flow area of phase k in stratified flow (m^2)

A_i''' = interfacial area per unit volume (m^{-1})

A_p''' = projected area per unit volume (m^{-1})

b = major radius of prolate ellipsoid

C_D = particle drag coefficient

C_i = Interfacial drag coefficient

C_0 = distribution parameter used in drift flux model

C_{wk} = wall drag coefficient for phase k

d = particle diameter, either bubble or drop, (m)

D = pipe diameter (m)

D_h = hydraulic diameter (m)

E = entrainment fraction

f_i = interfacial friction factor

f_Q = fraction of a cell that is quenched, i.e., in the pre-CHF flow regime

f_{wk} = wall friction factor for phase k

F_i''' = interfacial drag force per unit volume

g = gravitational acceleration (m/s^2)

G = mass flux (kg/m^2/s)

h_l = height of liquid layer (m) in stratified flow

j = volumetric flux (m/s)

j_k = superficial velocity of phase k (m/s)

j_k* = non-dimensional superficial velocity of phase k

La = Laplace no., equal to $(\sigma / g\Delta\rho)^{1/2}$

$N_{\mu k}$ = viscosity no. for phase k, $N_{\mu k} = \mu_k / \left[\rho_k \sigma \sqrt{\frac{\sigma}{g\Delta\rho}}\right]^{1/2}$

P = pressure

P_s = profile slip factor

r = drop radius

r^* = non-dimensional drop radius

Re = Reynolds no.

S_g = perimeter of pipe in contact with gas phase in stratified flow

S_i = width of gas-liquid interface in stratified flow

T_k = temperature (K) of phase k

T_{sat} = saturation temperature at the total pressure

$\overline{v}_{gj}$ = weighted area-average value of the drift flux velocity

V = velocity (m/s)

$\overline{V}_k$ = void-weighted area average velocity for phase k

V_r = relative velocity (m/s)

V_∞ = terminal velocity in infinite medium (m/s)

V_∞^* = non-dimensional terminal velocity

We = Weber no.

wf = weighting factor

Greek

α = void fraction

α_k = volume fraction of phase k

δ = film thickness (m)

δ* = non-dimensional gas film thickness defined by Eq. (4-116)

$\Delta\rho$ = density difference between liquid and gas phases (kg/m^3)

ρ = density (kg/m^3)

ε = surface roughness

Γ_f = liquid film flow rate per unit wetted perimeter (kg/s-m)

μ = viscosity (Ns/m^2)

ν = dynamic viscosity (m/s^2), $\nu = \mu/\rho$

$\pi_1\pi_2$ = non-dimensional gas velocities (see Eq. (4-54) and Eq. (4-56))

θ = pipe inclination angle (0 = horizontal)

ϕ_k^2 = two-phase multiplier for phase k flowing alone

σ = surface tension (N/m)

τ = shear stress (N/m^2)

Subcripts

AM = annular/mist flow regime

B = bubble

BS = bubbly/slug flow regime

c = core region in annular/mist flow

$crit$ = critical value

$CCFL$ = counter-current flow limit

CT = churn-turbulent bubbly flow

$C-W$ = Choe-Weisman (see Eq. (4-99))

d = drop

DF = dispersed flow regime

f = liquid film

$film$ = the liquid film or a value at a reference "film" temperature

g = vapor-gas mixture

i = interface

IA = inverted annular

IS = inverted slug

KI = Kataoka-Ishii drift flux model

l = liquid

lam = laminar

m = mixture value

$\max$ = maximum value

MP = multi-particle

ns = non-stratified

NC = non-condensable gas

NB = nucleate boiling

p = projected or particle

$post-CHF$ = value for film boiling or post-CHF regime

$pre-CHF$ = value for normal pre-CHF regime

r = relative

$R-T$ = value from Rayleigh-Taylor instability

s = smooth

sat = value at saturated conditions

$smooth$ = value for laminar-smooth inverted annular regime

$strat$ = stratified flow regime

SM = Sauter mean value

SP = single-particle

$T-D$ = Taitel-Dukler (see Eq. (4-96))

v = vapor

vm = volume median

w = wall

$wavy$ = value for rough-wavy inverted annular regime

wet = in contact with liquid phase

We = value from Kelvin-Helmholtz instability, that is, the Weber no. criterion.

∞ = infinite medium or fully-developed

Interfacial Drag

The two-phase flow model employed by TRACE is what is commonly referred to as the "six equation" two-fluid model. This representation of the two-phase flow provides two characteristic velocities in each coordinate direction. So, for example, for flow in a 1-D component, there are two velocities at every junction: one for the liquid phase, and another for the combined gas/vapor mixture. The equations of motion for these two velocities are coupled by two interfacial terms: one resulting from the interfacial drag force between the phases and the other from the momentum transfer associated with mass transfer (see **Chapter 1**). It is the former, the interfacial drag force arising from shear between the phases, that is the subject of this section.

The interfacial drag force per unit volume is given by

$$F_i''' = C_i V_r |V_r| \tag{4-1}$$

where F_i''' is the interfacial drag force per unit volume, C_i is the interfacial drag coefficient, and V_r is the relative velocity.

The interfacial drag coefficient is dependent upon the flow regime selected by the code. In TRACE, there are three distinct classes of flow regimes:

- Pre-CHF: these consist of the bubbly/slug and the annular/mist regimes as explained below in ***Bubbly/Slug Flow Regime*** and ***Annular/Mist Flow Regime***.
- Stratified: the horizontal stratified flow regime is available for 1-D components that are either horizontal or inclined as explained in ***Stratified Flow Interfacial Drag Models***.
- Post-CHF: this encompasses the "inverted" flow regimes that occur when the wall is too hot for liquid-wall contact, see ***Post-CHF Interfacial Drag Models*** .

Pre-CHF Interfacial Drag Models

In TRACE, four principal flow regimes are considered for vertical flow as depicted in Figure 4-1 below. The three "bubbly" flow regimes — dispersed bubble, slug flow, and Taylor cap bubble — are collectively referred to as the "bubbly/slug" flow regime. The models used for the interfacial drag in the bubbly/slug and annular/mist flow regimes are applied to both vertical and horizontal geometries. However, for the horizontal case, a special horizontal stratification model is introduced as described in ***Stratified Flow Interfacial Drag Models***.

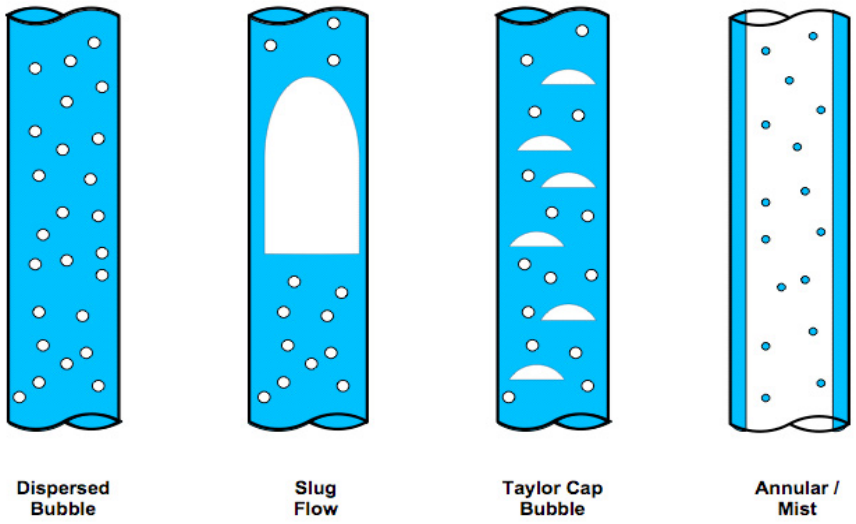

Figure. 4-1. Schematic representation of vertical flow regimes.

In TRACE, there is no explicit flow regime map for the determination of interfacial shear. Rather, the two primary regimes, bubbly/slug and annular/mist, are individually considered and then combined. The interfacial drag for the bubbly/slug flow regime is based on a drift flux formulation and includes specific correlations for both pipes and rod bundles as explained in ***Bubbly/Slug Flow Regime***. The annular/mist flow regime combines the interfacial drag for an annular film with that for entrained droplets as explained in ***Annular/Mist Flow Regime***. Finally, the transition between these two primary flow regimes is discussed in ***Transition from Bubbly/ Slug to Annular/Mist***.

Bubbly/Slug Flow Regime

To improve the accuracy of the void fraction predictions for the bubbly/slug regime, a drift flux based model was implemented with separate correlations for pipes and rod bundles. These models are detailed in ***Pipes*** and ***Rod Bundles*** respectively. First, however, it is necessary to describe the procedure for translating a drift flux correlation into an interfacial drag model.

Equating the magnitude of the interfacial drag force per unit volume to the buoyancy force yields

$$\alpha(1-\alpha)g\Delta\rho = C_i V_r^2 \tag{4-2}$$

so that the interfacial drag coefficient becomes

$$C_i = \frac{\alpha(1-\alpha)g\Delta\rho}{V_r^2} \tag{4-3}$$

To translate equation Eq. (4-3)[A-4] into a correlation for the interfacial drag coefficient, it remains to substitute for the relative velocity from the appropriate drift flux correlation. Then, the interfacial drag coefficient, C_i, will be a function of the weighted drift flux velocity, $\overline{v}_{gj}$, and the distribution parameter, C_0.

To continue, a few definitions are necessary. A value averaged over the cross-sectional area is denoted by the $\langle\ \rangle$'s and defined by

$$\langle X \rangle = \frac{1}{A}\int X dA \tag{4-4}$$

where X is any locally varying quantity and A is the cross-sectional area. Of particular interest are the void-weighted area-averaged velocities, defined by

$$\overline{V}_k = \frac{\langle \alpha_k V_k \rangle}{\langle \alpha_k \rangle} \tag{4-5}$$

where the subscript k indicates the phase (l for liquid and g for the vapor/gas mixture). The void-weighted area-averaged phase velocities are the velocities used in the field equations by TRACE. So, the relative velocity used by TRACE is then a "void-weighted area-averaged" value given by

$$V_r = \overline{V}_g - \overline{V}_l \tag{4-6}$$

Next, the local drift velocity is given by

$$v_{gj} = V_g - j \tag{4-7}$$

where j is the volumetric flux and the weighted area-average value of the drift velocity, as defined by Zuber and Findlay (Ref. 4-1), is then

$$\overline{v}_{gj} = \frac{\langle \alpha v_{gj} \rangle}{\langle \alpha \rangle} \tag{4-8}$$

Zuber and Findlay also introduced the distribution coefficient, C_0, to account for phase distribution effects, where

$$C_0 = \frac{\langle \alpha j \rangle}{\langle \alpha \rangle \langle j \rangle} \tag{4-9}$$

Next, the void-weighted area-averaged relative velocity, as used by TRACE, must be put in terms of these two drift flux parameters. Ishii and Mishima (Ref. 4-5) show that the area-averaged relative velocity can be approximated by

$$\langle V_g - V_l \rangle \approx \frac{\overline{v}_{gj}}{1 - \langle \alpha \rangle} \tag{4-10}$$

where it is important to realize that

$$\langle V_g - V_l \rangle \neq \overline{V}_g - \overline{V}_l \tag{4-11}$$

Rewrite equation [A-4] as

$$C_i = \frac{\alpha(1-\alpha) g \Delta\rho}{\langle V_g - V_l \rangle^2} \cdot \frac{\langle V_g - V_l \rangle^2}{V_r^2} \tag{4-12}$$

and substitute equation Eq. (4-10) to give

$$C_i = \frac{\alpha(1-\alpha)^3 g \Delta\rho}{\overline{v}_{gj}^2} \cdot \frac{\langle V_g - V_l \rangle^2}{V_r^2} \tag{4-13}$$

The last term on the right-hand-side of equation Eq. (4-13) will be denoted as the "profile slip factor"

$$P_s = \frac{\langle V_g - V_l \rangle^2}{V_r^2} \tag{4-14}$$

so equation Eq. (4-13) yields

$$C_i = \frac{\alpha(1-\alpha)^3 g \Delta\rho}{\overline{v}_{gj}^2} \cdot P_s \tag{4-15}$$

for the interfacial drag coefficient.

To evaluate the profile slip factor, it is necessary to relate the area-averaged relative velocity to the void-weighted area-averaged phase velocities used by TRACE. Again from Ishii and Mishima (Ref. 4-5), we have

$$\langle V_g - V_l \rangle = \frac{1 - C_0 \langle \alpha \rangle}{1 - \langle \alpha \rangle} \overline{V}_g - C_0 \overline{V}_l \tag{4-16}$$

so that the profile slip factor becomes

$$P_s = \frac{\left(\frac{1 - C_0 \langle \alpha \rangle}{1 - \langle \alpha \rangle} \overline{V}_g - C_0 \overline{V}_l \right)^2}{V_r^2}. \tag{4-17}$$

The profile slip factor can be considerably less than unity and, for many situations, is much more important in the calculation of the void fraction than is the drift flux velocity. For numerical reasons, its value is limited to be greater than 0.05.

To convert a drift flux model into an interfacial drag coefficient then requires the specification of two parameters: $\overline{v}_{gj}$ and C_0. The drift flux velocity is specified uniquely for each of the bubbly/slug flow regimes as described below, whereas, one formulation is used for the distribution coefficient for all of the bubbly/slug regimes (see Eq. (4-19)).

Pipes

For two-phase flow in pipes, two characteristic flow regimes are treated for the bubbly/slug region. They are:

- Dispersed Bubbly Flow: bubbles are relatively small and may be spherical or distorted.
- Slug Flow or Taylor Cap Bubbly Flow: agglomeration has progressed to the extent that most of the gas phase is transported in large structures that are either slugs (for small diameter pipes) or Taylor cap bubbles (large diameter pipes).

For the dispersed bubbly flow regime, only one type of bubbly flow is considered: churn-turbulent flow. The churn-turbulent flow regime, according to Wallis (Ref. 4-2), represents a transition region between "ideal bubbly flow," in which bubbles rise uniformly and steadily, and slug flow in which large bubbles fill the tube and flow entirely in each other's wakes. The flow pattern is somewhat agitated and unsteady; agglomeration is important, and there is significant entrainment of bubbles in each other's wakes. The result is an increase in the relative velocity with an increase in the number of bubbles present.

For the churn-turbulent regime, the correlation proposed by Ishii was selected (see Reference 4-3). The weighted drift flux velocity is given by

$$\bar{v}_{gj} = \sqrt{2}\left(\frac{\sigma g \Delta\rho}{\rho_l^{\,2}}\right)^{1/4} \tag{4-18}$$

and the distribution parameter by

$$C_0 = 1.2 - 0.2\sqrt{\frac{\rho_g}{\rho_l}} \tag{4-19}$$

For small diameter pipes, the drift flux velocity given by Eq. (4-18) can exceed that for the slug flow regime (see Eq. (4-20)). To prevent this unrealistic situation, the churn-turbulent drift flux velocity is limited to always be less than that for slug flow.

As the void fraction increases, agglomeration becomes progressively more important and the bubbles grow to form either Taylor cap or slug bubbles. This regime will be referred to as the "cap/slug" regime in what follows. For this regime, Kataoka and Ishii (Ref. 4-4) developed one correlation with two parts to handle both the cases of cap bubble and slug flow. This model was selected for the cap/slug regime in TRACE.

As presented by Kataoka and Ishii, the model has two formulations, one for low viscosity fluids and another for high viscosity fluids. As the low viscosity formulation applies to fluids such as water, it was implemented in TRACE. For relatively small diameter pipes, slug flow is possible and the governing characteristic dimension becomes the pipe diameter. For this case, the weighted drift velocity is given by:

$$\bar{v}_{gj}^{+} = 0.0019\,(D_h^*)^{0.809}\left(\frac{\rho_g}{\rho_l}\right)^{-0.157}(N_{\mu l})^{-0.562}, \text{ for } \quad D_h^* \le 30 \tag{4-20}$$

where the non-dimensional drift velocity is defined

$$\bar{v}_{gj}^{+} = \frac{\bar{v}_{gj}}{\left(\frac{\sigma g \Delta\rho}{\rho_l^{\,2}}\right)^{1/4}}, \tag{4-21}$$

the non-dimensional hydraulic diameter is given by

$$D_h^* = \frac{D_h}{\sqrt{\sigma / g\Delta\rho}}, \tag{4-22}$$

and the liquid viscosity number is

$$N_{\mu l} = \frac{\mu_l}{\left(\rho_l \sigma \sqrt{\sigma / g\Delta\rho}\right)^{1/2}} \tag{4-23}$$

In relatively large diameter pipes, $D_h^* > 30$, slug bubbles cannot be sustained due to surface instability, and they are disintegrated into cap bubbles. For this regime, Kataoka and Ishii gave

$$\bar{v}_{gj}^{+} = 0.030 \left(\frac{\rho_g}{\rho_l}\right)^{-0.157} (N_{\mu l})^{-0.562}, \text{ for } D_h^* \geq 30 \tag{4-24}$$

Eq. (4-20) and Eq. (4-24) are continuous with respect to pipe diameter and are programmed as

$$\bar{v}_{gj}^{+} = 0.0019 \cdot Min\left[30 , D_h^*\right]^{0.809} \left(\frac{\rho_g}{\rho_l}\right)^{-0.157} (N_{\mu l})^{-0.562} \tag{4-25}$$

For both the cap bubble and slug formula, Kataoka and Ishii recommend using the same distribution coefficient, C_0, as for the churn-turbulent regime (see Eq. (4-19)).

It remains to specify how the transition between the dispersed bubble and the cap/slug bubble regimes is handled. Air-water two-phase flow data indicate a clear transition for this transition in the void fraction range from 20 to 30%. For values of the void fraction less than about 20%, the flow regime is dispersed bubble, and the data is well represented by the churn-turbulent model (Eq. (4-18) and Eq. (4-19)). As the void fraction increases, a transition to the Taylor cap bubble regime occurs for void fractions greater than about 30% as represented by the Kataoka-Ishii model (Eq. (4-25) and Eq. (4-19)).

A simple linear ramp on the calculated drift flux velocity as a function of void fraction between the limits of 20% to 30% provides a good fit to this transition region. The transition is then effected by

$$\bar{v}_{gj} = wf_{CT} \cdot \left(\bar{v}_{gj}\right)_{CT} + (1 - wf_{CT}) \cdot (\bar{v}_{gj})_{KI} \quad \text{for} \quad 0.2 \leq \alpha \leq 0.3 \tag{4-26}$$

where the linear ramp is

$$wf_{CT} = \left(\frac{0.3 - \alpha}{0.3 - 0.2}\right) \tag{4-27}$$

The implementation of this transition is illustrated in Figure 4-2 and Figure 4-3.

For saturated steam-water flows, the bubbly/slug transition developed using air-water data results in a significant over-prediction of the void fraction for the bubbly flow region. Indeed, even for low values of the void fraction, $\alpha \sim 10\%$, the cap bubble model of Kataoka-Ishii provides a more reasonable prediction of the void fraction than the churn-turbulent drift flux model.

This tendency for adiabatic steam-water data to be better fit by a cap bubble model than by a dispersed bubbly flow model was first noted by Zuber and Findlay (Ref. 4-1). They attributed the difference between the air-water data and the steam-water data to the manner in which bubbles were introduced into the test section based upon an analysis of the perforated plate used to break up the steam flow into bubbles.

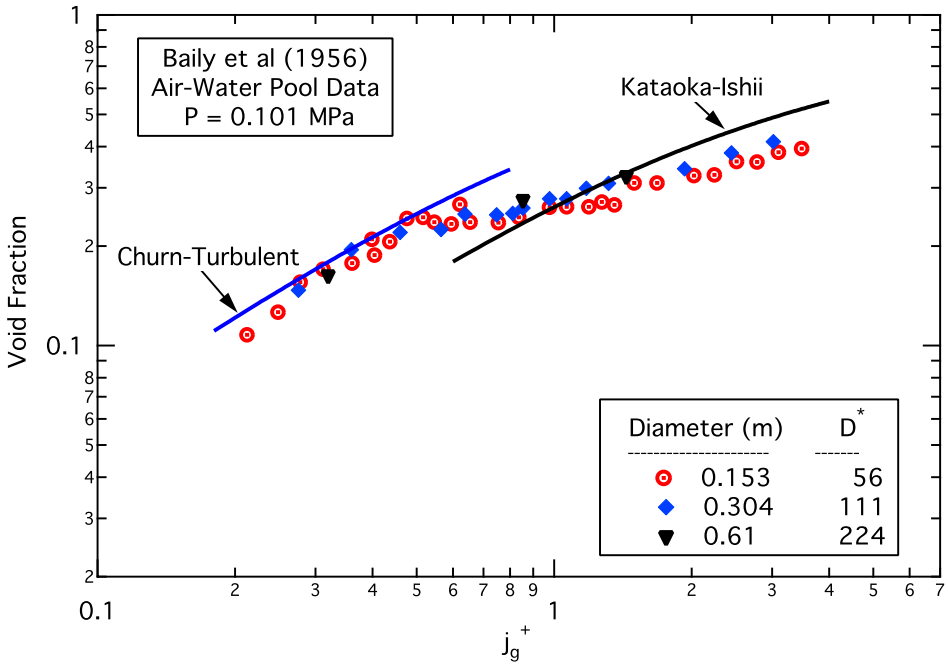

Figure. 4-2. Void fraction versus non-dimensional gas velocity for air-water pool data of Baily et al. (Ref. 4-10) illustrating the bubbly/slug transition.

However, in selecting a model for TRACE, all of the steam-water data examined, both for pools and for cocurrent upflow, exhibited the same behavior for void fraction down to about 10%. That is, the data was better fit using the slug/cap bubble model rather than the churn-turbulent bubbly flow model. Also, visual observations of boiling two-phase flows indicate that a dramatic transition in bubble size occurs at the point where subcooling is lost. The relatively small bubbles produced by subcooled boiling would almost instantaneously grow larger at the point where the bulk fluid became saturated. Consequently, a tentative conclusion was reached that for saturated two-phase mixtures, the bubbly/slug transition should occur at a much lower value than that observed for air-water flows. Subcooled two-phase flows, however, would be expected to behave more like their air-water counterparts.

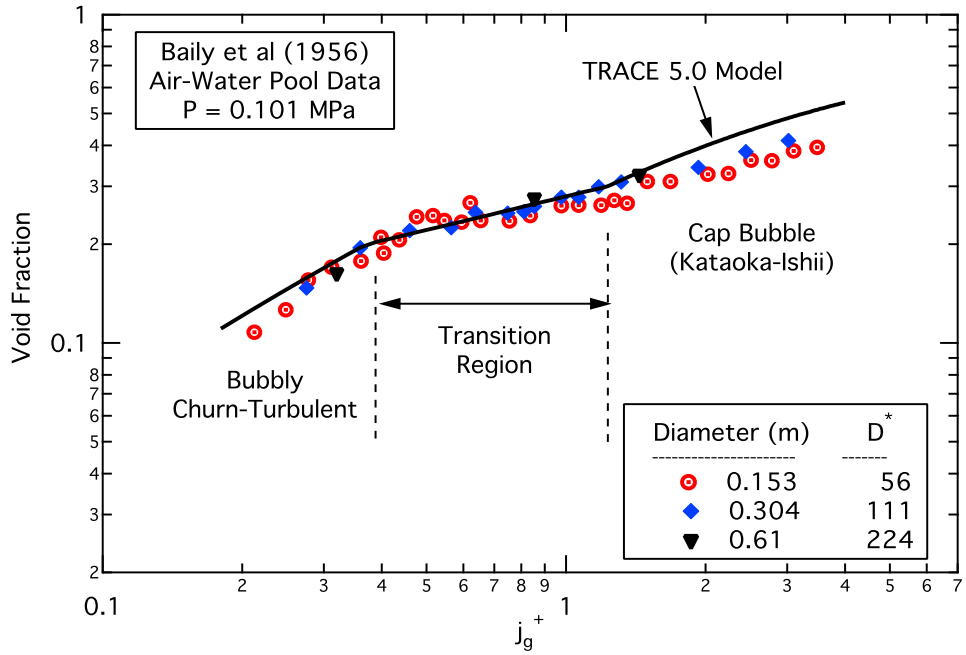

Figure. 4-3. The TRACE bubbly/slug transition model for the air-water pool data of Baily et al. (Ref. 4-10).

Therefore, the values of the void fraction over which the bubbly/slug transition is applied were made a function of the liquid subcooling. This is an ad hoc approach that serves to match the data in the current investigation. However, it should be re-examined as subsequent improvements to the interfacial drag package of the TRACE code are made.

The bubbly/slug transition is then given by

$$wf_{CT} = \left(\frac{\alpha_{KI} - \alpha}{\alpha_{KI} - \alpha_{CT}} \right) \tag{4-28}$$

where

$$\alpha_{CT} = 0.2 \cdot Min\left[1 , \left(\frac{T_{sat} - T_l}{5} \right) \right], \text{ and} \tag{4-29}$$

$$\alpha_{KI} = \alpha_{CT} + 0.1 \tag{4-30}$$

An example of the efficacy of this approach, for the data considered, is given by comparing the calculated void fractions for the steam-water data of Behringer (Ref. 4-11). In Figure 4-4, the transition regime is calculated using the "air-water" transition as given in Eq. (4-26), while for

Figure 4-5, the transition regime is calculated using the "steam-water" transition as given by Eq. (4-29) and Eq. (4-30). The improvement is obvious as the "bump" present in Figure 4-5 has now disappeared.

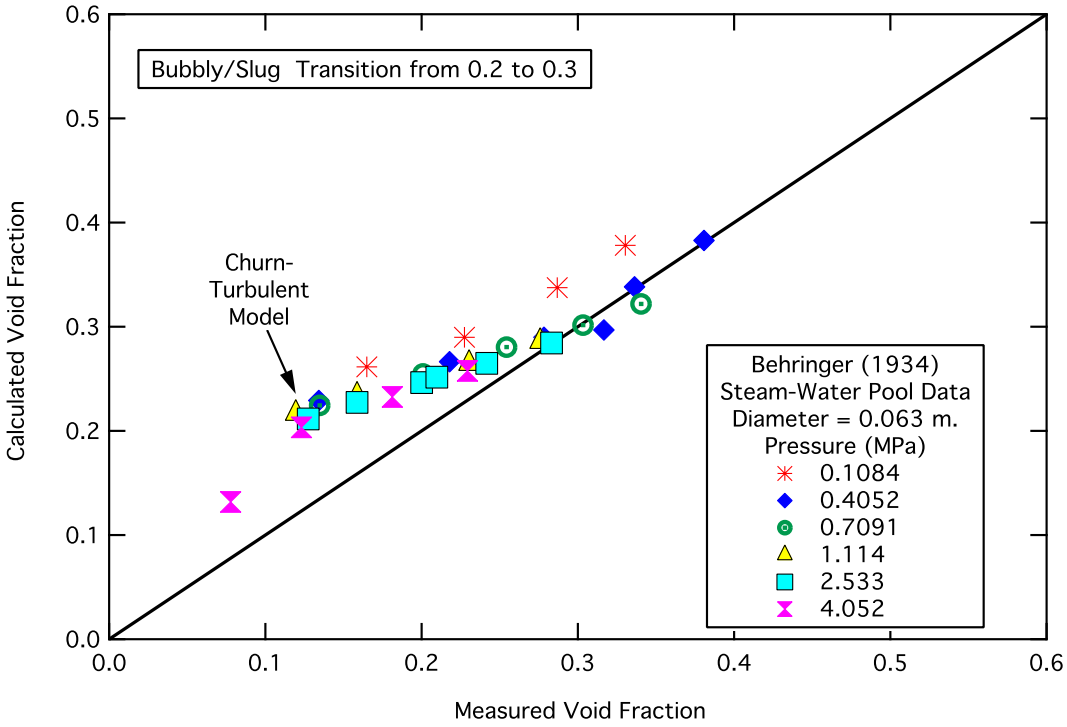

Figure. 4-4. Illustration of the problem with the air-water bubbly/slug transition model for the steam-water pool data of Behringer (Ref. 4-11).

Finally, for high flow rate conditions, turbulent shear stresses act to break up the bubbles thereby extending the dispersed bubbly regime to a much higher void fraction range. For such cases, the above bubbly/slug transition would not be appropriate. However, the void fraction for high flow conditions is almost entirely determined by the distribution parameter, C_0, and is unaffected by the specification of the drift flux velocity. Therefore, no special treatment for high mass flux conditions is needed.

Rod Bundles

The usage of pipe interfacial drag models for rod bundle geometries, as was done previously in TRAC-PF1/MOD2, resulted in core void fractions that were consistently over-predicted. To improve the accuracy of void fraction calculations, and hence core inventory, the Bestion (Ref. 4-6) drift flux model was implemented into TRACE. This model is used for the calculation of the interfacial drag coefficient in the core region of the 3-D vessel component and for the 1-D CHAN component.

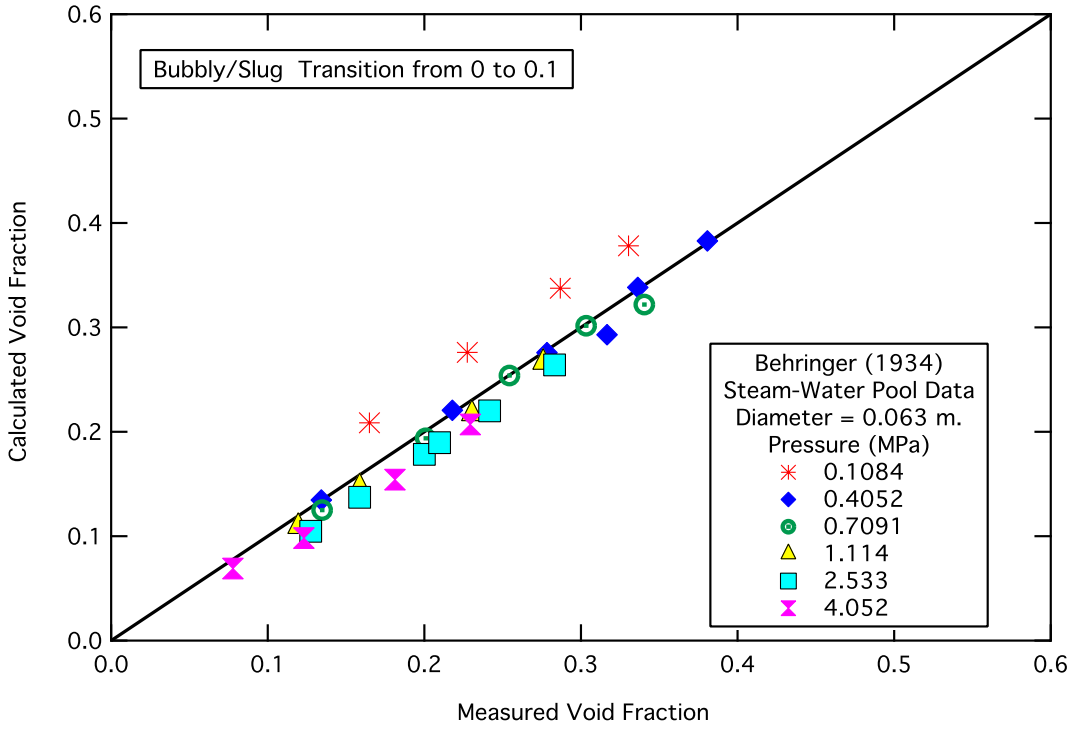

Figure. 4-5. Illustration of the improved bubbly/slug transition model for the steam-water pool data of Behringer (Ref. 4-11).

Based on previous experience, it was known that the Bestion model did a reasonably good job for low-flow low-pressure conditions. Also, a study by Salay (Ref. 4-7) compared the predictive capability of five drift flux models for high-pressure boil-off conditions and recommended the implementation of the Bestion correlation in TRACE. This recommendation, in addition to the good low-pressure performance of the Bestion model led to its adoption as the interfacial drag model for rod bundles.

The Bestion model is simply given by

$$\bar{v}_{gj} = 0.188\sqrt{g\Delta\rho D_h/\rho_g} \tag{4-31}$$

and was originally specified with a constant distribution parameter, $C_0 = 1.2$. In TRACE, it was implemented using the same distribution parameter as Ishii recommended for pipe flow. That is,

$$C_0 = 1.2 - 0.2\sqrt{\frac{\rho_g}{\rho_l}} \tag{4-32}$$

At low pressure, these are essentially equivalent, and the dependence upon density ratio provides the proper behavior as the pressure increases to the critical point.

However, assessment of TRACE for boiling water reactor conditions revealed a marked tendency to under-predict the void fraction for values above about 40%. Consequently, the value of the distribution parameter for rod bundles was set to unity, as recommended by Coddington and Macian (Ref. 4-12). With this change, the comparison with the FRIGG void fraction data (Ref. 4-13) is much improved, see Figure 4-6. Indeed, the average void fraction error was reduced from -5.0% to only 0.2%, and the RMS error was reduced from 6.0% to 2.7%.

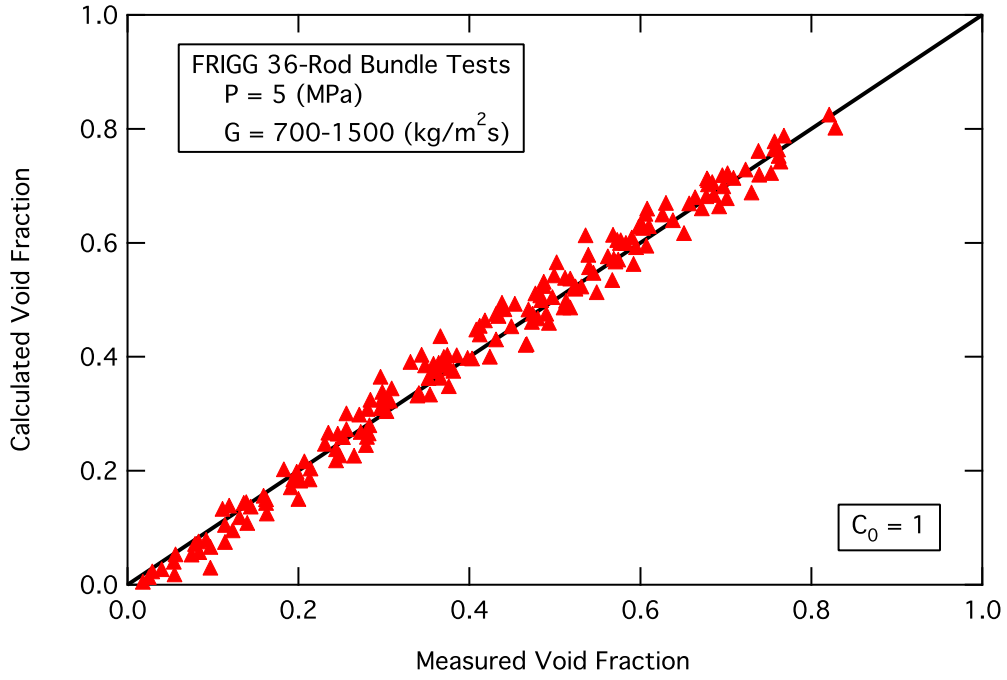

Figure. 4-6. Comparison of calculated and measured values of the void fraction for the FRIGG experiments (Ref. 4-13) with the distribution parameter set to unity.

Annular/Mist Flow Regime

The annular/mist flow regime in the TRACE code is treated as a superposition of interfacial drag on a liquid film and on entrained droplets. To complete this model, in addition to interfacial drag formulations for films and droplets, an entrainment model is needed to determine the fraction of liquid flowing as droplets and a weighting scheme is needed to combine the individual contributions. The following four sections describe each of these in turn.

Annular Film Models

For the annular flow regime, the interfacial drag force per unit volume for the liquid film is given by

$$F'''_{i,film} = f_{i,film} A'''_{i,film} \cdot \frac{1}{2}\rho_g |V_r| V_r \tag{4-33}$$

where $f_{i,film}$ is the interfacial friction factor and $A'''_{i,film}$ is the interfacial area per unit volume for the liquid film. The interfacial friction coefficient from Eq. (4-1) is then defined as

$$C_{i,film} = f_{i,film} A'''_{i,film} \cdot \frac{1}{2}\rho_g \tag{4-34}$$

The correlations used to evaluate the interfacial friction factor, $f_{i,film}$, are detailed below. The interfacial area per unit volume is computed from

$$A'''_{i,film} = \frac{4}{D_h}\sqrt{\alpha} \tag{4-35}$$

which assumes that the volume fraction of the entrained droplets is much less than that of the gas/ vapor mixture. That is,

$$\sqrt{\alpha} \approx \sqrt{\alpha + \alpha_d} \tag{4-36}$$

which is a good approximation for annular/mist flow.

The TRAC-PF1/MOD2 model for the annular flow interfacial friction factor was that proposed by Wallis (Ref. 4-8). Due to its general applicability, simple formulation and reasonably accurate predictions, this model was retained in the TRACE code. However, for the special case of cocurrent downflow, important for downflow tube condensation, the model of Wallis was found to significantly over-predict the interfacial friction and hence under-predict the film thickness. Consequently, a modified form of the Asali-Hanratty correlation (Ref. 4-14) was implemented for this regime.

The Wallis model (Ref. 4-8) treats the interfacial friction in annular flow as if the wavy film represented an equivalent "sand roughness" for turbulent pipe flow. Thus, the friction factor was given as a function of a dimensionless film thickness

$$f_{i,film} = 0.005\left[1 + 300\frac{\delta}{D}\right] \tag{4-37}$$

and approximated by

$$f_{i,film} = 0.005\left[1 + 75(1-\alpha)\right] \tag{4-38}$$

There are two principal assumptions built into this model:

- The flow is fully turbulent, i.e., $f_g \approx 0.005$, and
- The film surface is wavy, so that the wall roughness analogy applies.

These two assumptions are usually valid for vertical upflows but may not always be accurate for downflow. As Wallis states, in horizontal or downflow at low gas velocities, the liquid film is smooth and the interfacial friction factor approaches the smooth pipe value.

Tube condensers are being proposed as safety equipment in the advanced passive reactor designs, so the TRACE code has been modified to enable accurate predictions of their heat removal capacity. Both the wall and interfacial heat transfer coefficients in the annular flow regime use the liquid film thickness as the characteristic length scale. So, to calculate pure-steam condensation heat transfer with reasonable agreement, a good prediction of the film thickness is needed. Therefore, an assessment of this capability was conducted for TRACE and led to two code improvements:

- Wall Drag: an annular flow wall drag model was implemented (see the section titled ***Wall Drag*** below), and
- Interfacial Drag: a special correlation for cocurrent downflow (Asali and Hanratty, (Ref. 4-14)) was implemented.

The model of Asali and Hanratty for cocurrent downflow with entrainment was selected for TRACE, based on data comparisons with the downflow data of Andreussi and Zanelli (Ref. 4-15). The original form of the Asali and Hanratty correlation is

$$\frac{f_i}{f_s} - 1 = 0.45 \cdot Re_g^{-0.2} \cdot (\delta_g^+ - \ 5.9) \tag{4-39}$$

where f_s is the smooth tube friction factor as a function of the gas Reynolds no. and the non-dimensional film thickness is

$$\delta_g^+ = \delta \cdot \frac{\sqrt{\tau_i/\rho_g}}{\nu_g} \tag{4-40}$$

Note that the non-dimensional film thickness formula uses a friction velocity characterized by the interfacial shear stress. This makes δ_g^+ a function of the interfacial shear stress and hence of the interfacial friction factor itself. That is, Eq. (4-39) is an implicit formulation and, as such, is unsuitable for implementation into the TRACE code as it would require an iterative solution.

However, the definition of the interfacial shear stress

$$\tau_i = f_i \cdot \frac{1}{2} \cdot \rho_g \cdot V_r^2 \tag{4-41}$$

can be substituted into Eq. (4-40) so that, making use of the quadratic formula, Eq. (4-39) can be solved to yield an explicit formulation. This explicit formulation is given by

$$f_i = \left\{ \frac{-b + \sqrt{b^2 - 4 \cdot c}}{2} \right\}^2 \tag{4-42}$$

where the coefficients are

$$b = -\frac{0.45 \cdot f_s \cdot \delta \cdot V_r}{\sqrt{2} \cdot Re_g^{0.2} \cdot \nu_g}, \text{ and} \tag{4-43}$$

$$c = f_s \cdot \left(-1 + 5.9 \cdot \frac{0.45}{Re_g^{0.2}} \right) \tag{4-44}$$

Note that the coefficient, c, must be constrained to have a negative value.

Although not as accurate as the original implicit formulation, Eq. (4-42) still predicts the downflow data of Andreussi and Zanelli well. Indeed, it is more accurate than any of the eight annular flow models tested except the original implicit formulation. For example, the average RMS values for the relative error in the interfacial friction factor were -17.6% and 51.7%, respectively for the Wallis correlation but were reduced to -12.0% and 5.5% for the explicit formulation of the Asali-Hanratty model.

Entrainment Models

For the estimation of the interfacial drag coefficient in the annular/mist flow regime, as detailed in ***Annular/Mist Interfacial Drag Coefficient***, it is necessary to know the fraction of the liquid flow that is composed of droplets. TRAC-PF1/Mod2 employed the Ishii-Mishima (Ref. 4-16) correlation to determine the mass fraction of liquid flowing as entrained droplets. Due to its large database, reasonable accuracy and usage in other thermal-hydraulic codes such as RELAP5, this model has been retained in TRACE.

However, during the developmental assessment process, significant problems were observed when the Ishii-Mishima correlation was used outside the range of its database. Most specifically, one of the correlating variables that Ishii and Mishima used is the liquid film Reynolds no. The

correlation's database covers a film Reynolds no. range of $370 < Re_f < 6400$, which is usually adequate for annular flow in small diameter pipes.

For large diameter pipes, such as the cold and hot legs of a PWR, the film Reynolds no. can be on the order of $10^5 - 10^6$. Consequently, the Ishii-Mishima correlation would be far outside the range of its database and significantly over-predict the entrainment fraction. Indeed, the correlation was found to predict nearly full entrainment at gas velocities below that necessary for the initiation of entrainment. To remedy this problem, the Steen-Wallis entrainment correlation was implemented for large diameter pipes while Ishii-Mishima was retained for geometries with small hydraulic diameters, such as steam generator tubes and rod bundles. Both of these correlations are detailed below.

Ishii and Mishima developed a semi-empirical correlation for the fraction of the liquid flux flowing as entrained drops. The theoretical basis came from a consideration of the roll wave entrainment mechanism. Using the entrainment inception criterion of Ishii and Grolmes (Ref. 4-17) as a starting point, they determined a critical film flow and assumed that all liquid flow in excess of this critical value would be entrained. Refinements to this theory were then made to account for droplet deposition effects and to better match experimental data.

The entrained fraction was correlated as

$$E_\infty = \tanh\left[7.25\times10^{-7}(j_g^*)^{2.5}(D^*)^{1.25}Re_f^{0.25}\right] \tag{4-45}$$

where the subscript, ∞, indicates the value for fully developed flow. In Eq. (4-45), the non-dimensional gas superficial velocity is defined by

$$j_g^* = \frac{j_g}{\left[\dfrac{\sigma(g\Delta\rho)}{\rho_g^{\,2}(\Delta\rho/\rho_g)^{2/3}}\right]^{1/4}}, \tag{4-46}$$

the non-dimensional tube diameter is scaled by the Taylor wavelength and given by

$$D^* = D_h\sqrt{g\Delta\rho/\sigma}\ , \tag{4-47}$$

and the film Reynolds no. is defined

$$Re_f = \frac{(1-\alpha)\rho_l V_l D_h}{\mu_l} \tag{4-48}$$

which is equivalent to the usual definition for film flow,

$$Re_f = \frac{4 \cdot \Gamma_f}{\mu_l} \tag{4-49}$$

where Γ_f is the film flow rate per unit wetted perimeter.

Finally, the non-dimensional gas flux and diameter were combined to define an effective Weber no. for entrainment,

$$We_g = \frac{\rho_g \; j_g^2 \; D_h}{\sigma} \left(\frac{\Delta\rho}{\rho_g} \right)^{1/3} \tag{4-50}$$

yielding

$$E_\infty = \tanh\left[7.25 \times 10^{-7} \, We_g^{\,1.25} Re_f^{0.25} \right] \tag{4-51}$$

Ishii and Mishima compared their correlation for the entrained fraction in fully developed annular/mist flow, given by Eq. (4-51), to an extensive set of experimental data in air-water systems for the ranges:

1	<	P	< 4	(atm)
0.95	<	D	< 3.2	(cm)
370	<	Re_f	< 6400	
		j_g	< 100	(m/s)

Despite its semi-theoretical basis, the Ishii-Mishima correlation, as is the case for all empirical formulations, should be used with caution outside the range of its database.

Furthermore, the behavior of the Ishii-Mishima correlation when extrapolated outside its database was considered to be unrealistic. Consequently, two changes were made to TRACE. First, the film Reynolds no. used in the Ishii-Mishima correlation was limited to the upper limit of the database. That is,

$$E_\infty = \tanh\left[7.25 \times 10^{-7} \, We_g^{\,1.25} \cdot Min\left\{ 6400 \, , \, Re_f \right\}^{0.25} \right] \tag{4-52}$$

Also, the Steen-Wallis entrainment correlation (Ref. 4-18) was implemented for usage in large diameter pipes. Here the definition of "large diameter" is simply taken to be the upper limit of the database used by Ishii and Mishima, that is $D_h > 3.2 \quad (\mathrm{cm})$.

The Steen-Wallis correlation is a simple recasting of the formula presented by Paleev and Filippovich (Ref. 4-19) to better represent the property dependence upon liquid viscosity and explicitly take into account the non-dimensional critical gas velocity introduced by Steen (Ref. 4-20). Paleev and Filippovich correlated the entrained fraction as

$$E_\infty = 0.015 + 0.44 \log_{10} [\pi_1 \cdot 10^4] \tag{4-53}$$

where the non-dimensional group, π_1 , is defined

$$\pi_1 = \frac{\bar{\rho}}{\rho_l}\left(\frac{j_g \mu_l}{\sigma}\right)^2 \tag{4-54}$$

and $\bar{\rho}$ is the mean density of the gas-droplet flow.

In his comments on the paper of Paleev and Filippovich, Wallis (Ref. 4-18) states that their proposed entrainment correlation [Eq. (4-53)] agrees substantially with the results obtained by Wallis (Ref. 4-21) and Steen and Wallis (Refs. 4-20 and 4-22) as far as the effects of gas density, surface tension, and liquid density are concerned. However, their results were not in agreement with the viscosity dependence reported by Steen who found that a change of a factor of 100 in liquid viscosity did not change the entrainment characteristics as long as the liquid flow rate was high enough. Consequently, Wallis proposed modifying the correlation of Paleev and Filippovich to

$$E_\infty = 0.015 + 0.44 \log_{10} [2.77 \times 10^7 \cdot \pi_2^2] \tag{4-55}$$

where the non-dimensional gas velocity, π_2 , is that proposed by Steen to correlate the onset of entrainment. Namely,

$$\pi_2 = \frac{j_g \mu_g}{\sigma}\sqrt{\frac{\rho_g}{\rho_l}} \tag{4-56}$$

Steen found that the critical gas velocity for the onset of entrainment could be expressed by

$$\pi_{2\,,\,crit} \sim 2.46 \times 10^{-4} \tag{4-57}$$

However, Eq. (4-55) implies that the onset of entrainment begins at

$$\pi_{2,crit} \sim 1.83\times10^{-4} \tag{4-58}$$

Consequently, in TRACE, Eq. (4-55) has been rewritten as an explicit function of the critical non-dimensional gas velocity, $\pi_{2,crit}$:

$$E_{\infty} = 0.015 + 0.44\log_{10}\left[0.9245 \cdot \left(\frac{\pi_2}{\pi_{2,crit}}\right)^2\right] \tag{4-59}$$

and the inception criteria of Steen is used, (i.e., $\pi_{2,crit} = 2.46\times10^{-4}$).

Droplet Drag

The droplet drag force per unit volume is given by:

$$F_d''' = C_D A_d''' \cdot \frac{1}{2}\rho_g V_{r,d}^2 \tag{4-60}$$

where C_D is the drop drag coefficient, A_d''' is the drop projected area per unit volume (m^{-1}), and $V_{r,d}$ is the drop relative velocity (m/s). Each of these quantities needed to compute the droplet drag are described below.

First, the drop drag coefficient is taken from a correlation recommended by Ishii and Chawla (Ref. 4-23). The correlation is given by

$$C_D = \frac{24}{Re_d}\left(1 + 0.1\,Re_d^{0.75}\right) \tag{4-61}$$

and is an approximation to the drag curve for a solid sphere. In Eq. (4-61), the drop Reynolds no. is defined as a function of the relative velocity

$$Re_d = \frac{\rho_g \left| V_g - V_d \right| d_d}{\mu_m} \tag{4-62}$$

where d_d is the droplet Sauter mean diameter and the mixture viscosity is given by

$$\mu_m = \frac{\mu_g}{(1-\alpha_d)^{2.5}} \tag{4-63}$$

Next, to compute the droplet projected area per unit volume, A_d''', it is necessary to obtain an estimate of the fraction of the annular core occupied by the droplets, α_d[1]. From the definition of the entrained fraction, we have

$$\alpha_d = \frac{E_\infty\ (1-\alpha)\ V_l}{\alpha_c\ V_d} \approx \frac{E_\infty\ (1-\alpha)\ V_l}{\alpha\ V_d} \tag{4-64}$$

where α_c is the volume fraction of the annular core region (gas + drops), the product $\alpha_c\ \alpha_d$ is the drop volume fraction, and it has been assumed that, $\alpha_c \approx \alpha$.

There is one unknown on the right-hand-side of Eq. (4-64) — the drop velocity, V_d. Because TRACE employs a six-equation two-fluid model, the drop velocity is not directly calculated but must be inferred. For the purpose of estimating the drop fraction, it is assumed that the droplet relative velocity is small compared to the gas velocity, thus

$$V_d \approx V_g \tag{4-65}$$

and

$$\alpha_d \approx \frac{E_\infty\ (1-\alpha)\ V_l}{\alpha\ V_g} = E_\infty \frac{j_l}{j_g} \tag{4-66}$$

The value of the droplet fraction calculated from Eq. (4-66) is then limited, so that

$$\alpha_d \le E_\infty\ (1-\alpha) \tag{4-67}$$

to protect against an unphysical result for a case where the gas velocity is low but the entrainment fraction is non-zero.

From the definition of the Sauter mean diameter, the drop projected area per unit volume, is then

$$A_d''' = \frac{6}{4}\frac{\alpha_c\ \alpha_d}{d_d} = \frac{3}{2}\frac{\alpha\ \ \alpha_d}{(1-\ \alpha_d)\,d_d} \tag{4-68}$$

The next step is to determine the drop Sauter mean diameter that appears in the denominator of Eq. (4-68). In TRACE, this is accomplished through the evaluation of an empirical correlation based on the local flow conditions and is calculated using the correlation of Kataoka, Ishii, and Mishima (Ref. 4-24). They assumed that the mechanism for the generation of the droplets is that

1. Note that this droplet fraction is relative to the area of the annular core and not to the total cross-section. This terminology complicates the discussion but is retained here so that the model description will be consistent with the actual coding.

of shearing from wave crests and proposed that the droplet diameter should be correlated as a function of the film Reynolds no. in addition to the gas Reynolds no. and gas superficial velocity. The full form of their correlation is given by

$$d_{d,vm} = 0.028\left(\frac{\sigma}{\rho_g j_g^2}\right) Re_f^{-1/6} Re_g^{2/3} \left(\frac{\mu_g}{\mu_l}\right)^{2/3} \left(\frac{\rho_g}{\rho_l}\right)^{-1/3} \tag{4-69}$$

where the gas Reynolds no. is defined

$$Re_g = \frac{\rho_g j_g D_h}{\mu_g} \tag{4-70}$$

and the second subscript on the drop diameter, vm, indicates that the diameter is a volume median value. However, for the data used in developing this correlation, the film Reynolds no. range only varied from 100 to 4700. This corresponds to a range in $Re_f^{-1/6}$ of 0.46 to 0.24. Consequently, they proposed a simplified form of the correlation where the dependency upon film Reynolds no. has been removed. The volume median diameter is then

$$d_{d,vm} = 0.01\left(\frac{\sigma}{\rho_g j_g^2}\right) Re_g^{2/3} \left(\frac{\mu_g}{\mu_l}\right)^{2/3} \left(\frac{\rho_g}{\rho_l}\right)^{-1/3}, \tag{4-71}$$

and it is this simplified form that is used in TRACE.

The droplet diameter used in TRACE for the calculation of both interfacial drag and heat transfer is taken to be the Sauter mean diameter, that is, the drop diameter that has the same ratio of interfacial area to volume as that of the entire population. Kataoka et al. (Ref. 4-24) also developed an expression for the droplet size distribution. They fitted the data to the upper limit log-normal distribution proposed by Mugele and Evans (Ref. 4-25). For the fitting parameters that Kataoka et. al. used, the ratio of the Sauter mean to the volume median diameter is

$$\frac{d_{d,SM}}{d_{d,vm}} = 0.796 \tag{4-72}$$

Thus, Eq. (4-71) yields

$$d_d = 0.008\left(\frac{\sigma}{\rho_g j_g^2}\right) Re_g^{2/3} \left(\frac{\mu_g}{\mu_l}\right)^{2/3} \left(\frac{\rho_g}{\rho_l}\right)^{-1/3} \tag{4-73}$$

for the Sauter mean diameter, where the subscript, SM , has been dropped.

Finally, the drop diameter calculated from Eq. (4-73) is limited to be in the range

$$84\ \mu m \leq d_d \leq 4mm\ \ . . \tag{4-74}$$

According to Cappiello (Ref. 4-26), this droplet diameter range was selected because it matched the range of the experimental data used in developing the correlation.

The final quantity in Eq. (4-60) left to be defined is the drop relative velocity, $V_{r,d}$. As explained below, the drop relative velocity is much less than the computed phasic velocity difference. That is,

$$V_{r,d} \ll \left| V_g - V_l \right|, \tag{4-75}$$

because the computed liquid velocity represents both the film and the droplets. Consequently, the drop terminal velocity is used to approximate the drop relative velocity.

The drop terminal velocity is taken from Ishii (Ref. 4-3). For spherical droplets in the Newton regime, the relative velocity is given by:

$$V_{r,d} = 1.718\sqrt{d_d}\left[\frac{g\Delta\rho}{\rho_g}\right]^{1/2}(1-\alpha_d)^{1.5} \tag{4-76}$$

For larger distorted drops, where the relative velocity is independent of the drop diameter, Ishii gives

$$V_{r,d} = \sqrt{2}\left[\frac{\sigma g\Delta\rho}{\rho_g^2}\right]^{1/4}(1-\alpha_d)^{1.5}. \tag{4-77}$$

A criterion for the transition from the Newton to the distorted particle regime that is both simple and physically meaningful is to simply limit the drop relative velocity given by Eq. (4-76) to be less than that for a distorted particle. The Newton regime would then be used for

$$d_d \leq 0.678\sqrt{\frac{\sigma}{g\Delta\rho}} \tag{4-78}$$

Finally, the drop relative velocity estimated by either Eq. (4-76) or Eq. (4-77) is limited to be less than the value calculated for the phasic velocity difference by the solution of the two-fluid momentum equations. That is,

$$V_{r,d} \leq |V_g - V_l| . \tag{4-79}$$

From Eq. (4-60), the interfacial drag force per unit volume on the drops is

$$F_d''' = C_D A_d''' \cdot \frac{1}{2} \rho_g V_{r,d}^2 \tag{4-80}$$

or, in terms of the drop interfacial drag coefficient,

$$F_d''' = C_{i,drop} \cdot V_{r,d}^2 \tag{4-81}$$

The drop interfacial drag coefficient, $C_{i,drop}$, is then defined by

$$C_{i,drop} = C_D A_d''' \cdot \frac{1}{2} \rho_g \tag{4-82}$$

Substituting for the drop projected area per unit volume, A_d''', from Eq. (4-68), the final form the drop interfacial drag coefficient is

$$C_{i,drop} = C_D \cdot \rho_g \cdot \frac{3\alpha_c \alpha_d}{4 d_d} \tag{4-83}$$

It remains to explain the procedure for superposing the interfacial drag forces for the drops and the film. This is the subject of the following section.

Annular/Mist Interfacial Drag Coefficient

For the annular/mist flow regime, when the gas velocity is high enough, the liquid phase is comprised of two distinct forms, the annular film and droplets carried in the gaseous core region. These two liquid forms interact with each other through the processes of entrainment and de-entrainment and have their own distinctly different characteristic velocity; indeed the droplets and the liquid film can even flow counter-current to each other. Future versions of the TRACE code will model each of these liquid forms with its own set of field equations thereby providing separate velocities for the droplets and the annular film. However, in TRACE version 5.0, only one liquid field is available to model the combined droplet and annular film flows necessitating a modeling compromise.

Consequently, the drag forces between the gas-to-droplets and the gas-to-film are superposed. In TRAC-PF1/MOD1, this was done in the following simplified manner:

$$C_{i,AM} = C_{i,film} + C_{i,drop} \tag{4-84}$$

That is, the interfacial drag coefficients for the two liquid forms were simply added. The drag force between the gas and the liquid was then

$$F'''_{i,AM} = \left(C_{i,film} + C_{i,drop}\right)(V_g - V_l)^2 \tag{4-85}$$

The result of this approach is that, as entrainment becomes significant, the drag force between the gas and liquid fields far exceeds that for the gas-to-film of annular flow. The calculated liquid fraction is then much too small and the calculated liquid velocity is much larger than is appropriate for a liquid film,

$$V_f \ll V_l < V_d, \tag{4-86}$$

which in turn causes the wall drag to be over-estimated.

To improve this situation, a significant modification was made to the model for the annular/mist flow regime in the development of the TRAC-PF1/Mod2 code. Here, the drag forces were superposed rather than just the coefficients. So,

$$F'''_{i,AM} = C_{i,film}(V_g - V_f)^2 + C_{i,drop}(V_g - V_d)^2 \tag{4-87}$$

and then

$$C_{i,AM} = \frac{\left[C_{i,film}(V_g - V_f)^2 + C_{i,drop}(V_g - V_d)^2\right]}{(V_g - V_l)^2} \tag{4-88}$$

The evaluation of Eq. (4-88) requires that relative velocities for both the gas-drops and the gas-film be specified in addition to the drag coefficients. In Eq. (4-76) and Eq. (4-77), we have seen how the drop terminal velocity, corrected for multi-particle effects, is used to estimate the gas-drop relative velocity. It remains to specify the relative velocity between the gas core and the annular film. In TRACE, it is assumed that

$$V_g - V_f \approx V_g - V_l \tag{4-89}$$

so Eq. (4-88) becomes

$$C_{i,AM} = C_{i,film} + C_{i,drop}\frac{V_{r,d}^2}{(V_g - V_l)^2} \quad (4\text{-}90)$$

This completes the description for the annular/mist flow regime, the following section describes how the transition between the bubbly/slug and the annular/mist regimes is treated.

Transition from Bubbly/Slug to Annular/Mist

The replacement of the original TRAC-PF1/MOD2 interfacial drag model for the bubbly/slug regime with a drift flux based approach was done to:

- Improve accuracy of void fraction predictions, and
- Reduce void fraction oscillations at low-pressure conditions.

The improved accuracy is demonstrated during the developmental assessment, both for pipes and for rod bundle geometries. Also, the root cause of the calculated void fraction oscillations was determined to be the linear interpolation of the interfacial friction coefficient between the bubbly/slug and the annular/mist flow regimes that were used in TRAC-PF1/MOD2. This section describes the procedure adopted to resolve this oscillation problem.

The magnitude of the interfacial friction coefficient varies by orders of magnitude between the bubbly/slug and the annular/mist flow regime as illustrated below in Figure 4-7. In this figure, the bubbly/slug interfacial drag coefficient was calculated using the drift flux model for pipe geometry. It has a peak value in the void fraction range of 20% to 25%, as expected, and then decreases dramatically as the annular flow regime is approached[1].

Because of this large difference in magnitude of the interfacial friction coefficient for these two regimes, a natural transition is provided by a simple power law weighting scheme. That is:

$$C_i = \sqrt{C_{i,BS}^2 + C_{i,AM}^2} \quad (4\text{-}91)$$

An example of this transition is provided in Figure 4-8 for these low-pressure low-flow conditions. The key point is that the flow regime transition is consistent with the interfacial drag models. Thus, the transition void fraction will change as the flow conditions change unlike the static transition of TRAC-PF1/MOD2. The result of the implementation of this power law weighting flow regime transition in TRACE is the almost complete elimination of the void fraction oscillation that was observed for low-pressure low-flow conditions.

1. The inflection that occurs in the bubbly/slug curve of Figure 4-7 at a void fraction of about 75% is due to the limitation on the profile slip factor, $P_s \geq 0.05$.

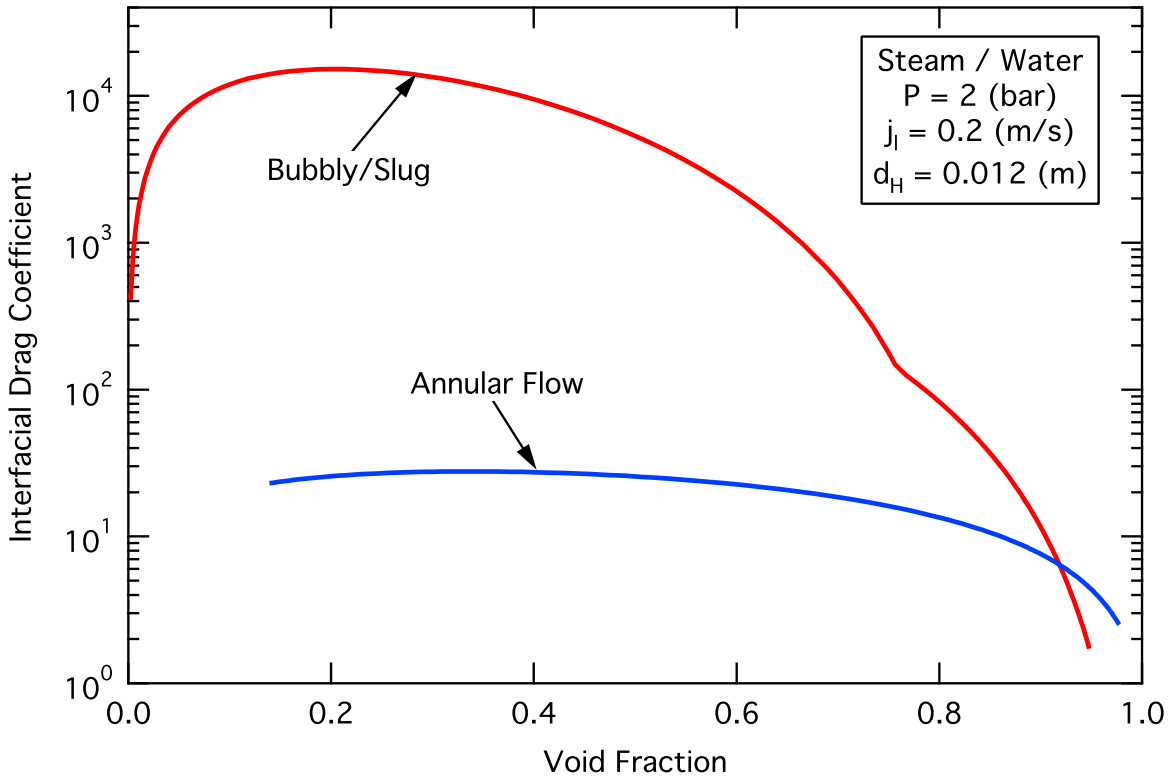

Figure. 4-7. Comparison of the interfacial friction coefficient for the bubbly/slug and annular/ mist flow regimes for low-pressure low-flow conditions.

This completes the description of the interfacial drag models for the normal pre-CHF flow regimes. The specialized models for stratified flow and for post-CHF regimes are described in the following sections.

Stratified Flow Interfacial Drag Models

For horizontal and inclined pipes, there exists the possibility for the flow to become stratified at low velocity conditions as gravity causes the phases to separate. Figure 4-9 gives a schematic representation of some of the commonly recognized horizontal flow regimes.

A brief description of each regime is given below:

1) Stratified Smooth: this pattern only occurs at low liquid and gas velocities, the two phases flow separately with a relatively smooth interface.

2) Stratified Wavy: as the gas velocity is increased, the interface becomes disturbed by waves traveling in the direction of the flow.

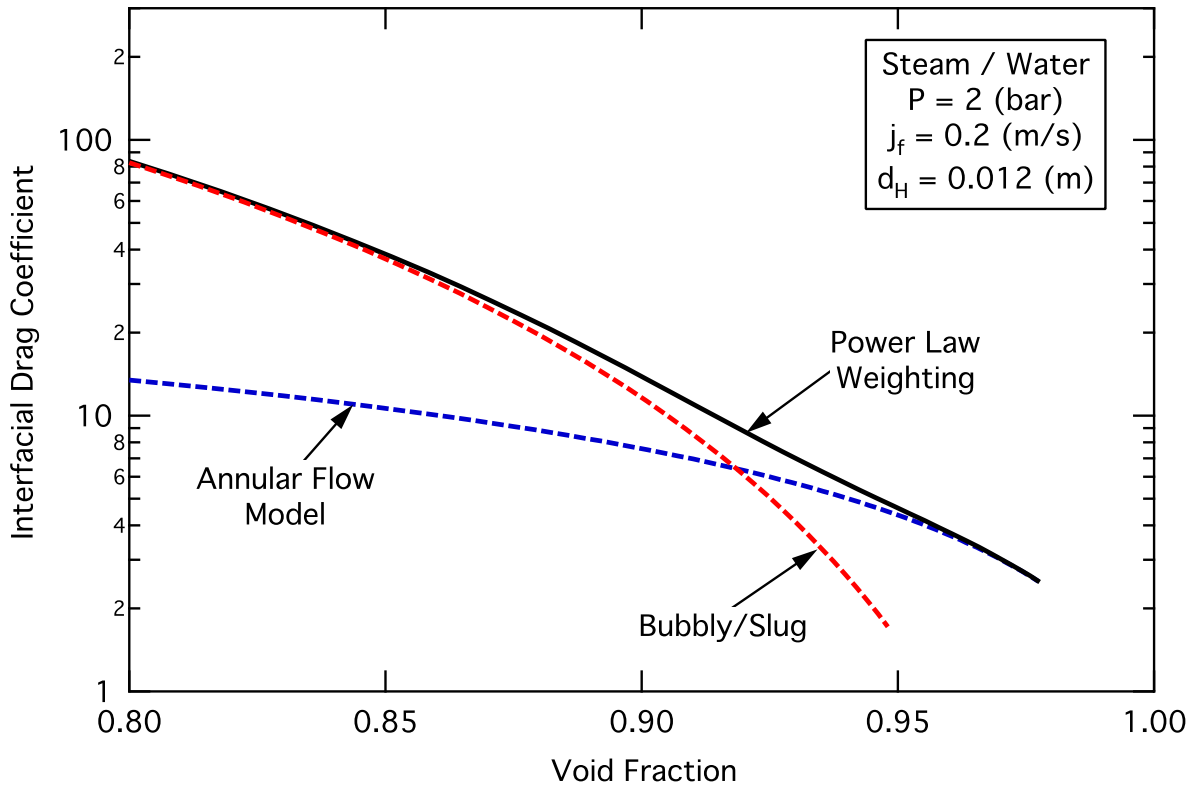

Figure. 4-8. Close-up of interfacial drag curve giving an example of the bubbly/slug to annular/ mist transition using a power law weighting scheme.

3) Plug/Slug Flow: a further increase in the gas velocity causes the waves at the interface to bridge the channel and form a frothy slug that is propagated with a high velocity.

4) Annular/Dispersed: a still higher gas velocity results in the formation of a gas core with a liquid film around the periphery of the pipe. This regime is usually accompanied by the presence of entrained droplets due to the high gas velocity.

5) Dispersed Bubble: this flow pattern is similar to that of vertical flow; at low liquid velocities the gas bubbles tend to travel in the upper half of the pipe, whereas at high liquid velocities the bubbles are dispersed.

Not all of these horizontal flow regimes are explicitly considered by TRACE. The "dispersed bubble" and "annular/dispersed" regimes are treated by their vertical flow analogs, that is, by the bubbly/slug and annular/mist flow regimes described in ***Bubbly/Slug Flow Regime*** and ***Annular/ Mist Flow Regime*** respectively. No special alterations to these regimes are made for differences that might occur in horizontal flow. The "stratified smooth" regime is explicitly considered as described in ***Interfacial Friction for Stratified Flow***. However, the other two regimes, "stratified wavy" and "plug/slug flow" are not explicitly considered but rather are treated as transition regimes that occur as the flow regime is transitioning from stratified flow to a non-stratified flow pattern.

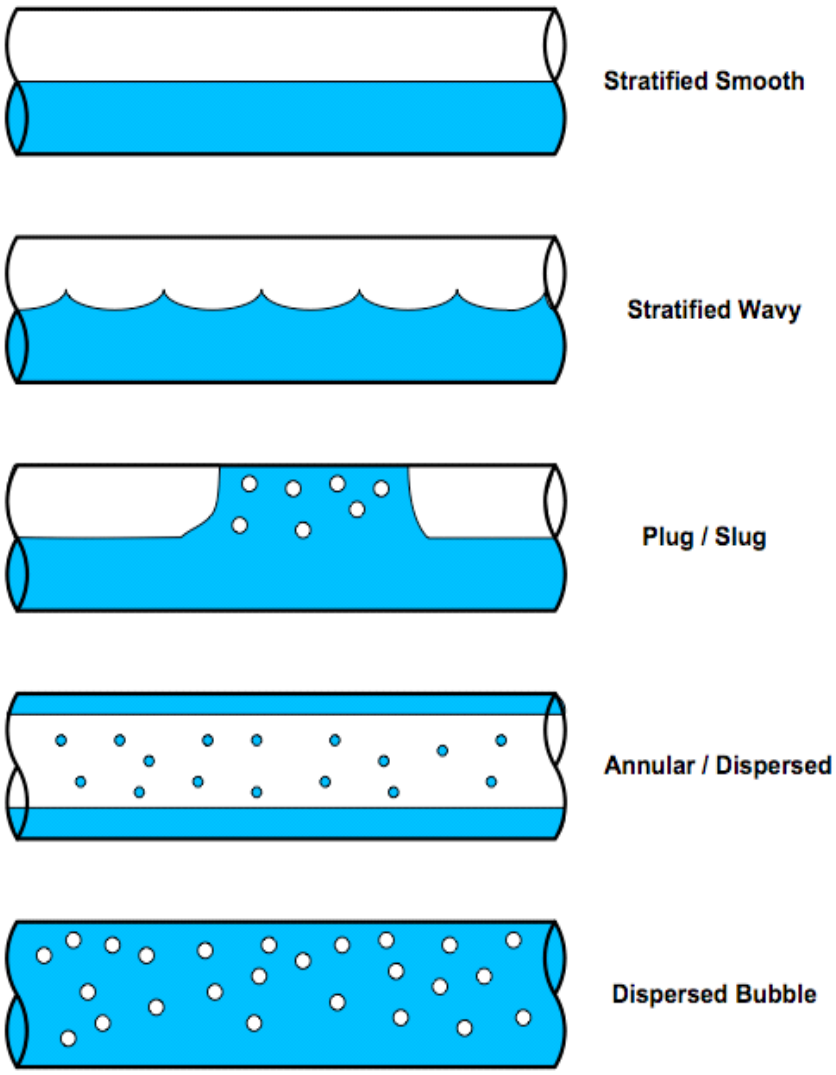

Figure. 4-9. Schematic representation of horizontal flow regimes.

The purpose of this section is then to detail the models used to determine if the flow is stratified, the interfacial friction for stratified flow, and how the transition to non-stratified flow is treated. Each of these three topics is covered in turn in ***Stratification Criteria*** through ***Transition to Non-Stratified Flow*** respectively.

Stratification Criteria

In TRACE, a check for stratified flow conditions is performed for all junctions of 1-D components that:

- have an inclination of less than 80 degrees, and
- do not have vertical junctions on both sides.

For downflow, Barnea (Ref. 4-27) presents flow regime maps that indicate significant regions of stratified flow can exist at inclination angles of up to 80 degrees and so this value has been selected as the upper limit for this regime. Barnea also observes that for slight upwards inclinations ($\theta \sim 1°$), the region of stratified flow shrinks substantially and practically vanishes at intermediate angles of inclination ($\theta \sim 30°$). However, a specific upflow criterion is not needed because the stratified flow interfacial friction is not large enough to carry the liquid up against gravity as the inclination angle increases.

The second limitation on the application of the stratified flow regime, namely that the junction not have vertical junctions on both sides, is to prevent a problem encountered in a special case. Specifically, it prevents a cross-flow junction between vertical components from being in the stratified flow regime and hence having a vastly different interfacial drag coefficient from that of the vertical components.

The primary criterion used to determine the boundary between stratified and non-stratified flow is that of Taitel-Dukler (Ref. 4-28) as suggested by Barnea. The Taitel-Dukler criterion for the transition from stratified flow is given by

$$j_g > \left(1 - \frac{h_l}{D}\right)\left[\frac{g\Delta\rho\cos\theta A_g}{\rho_g(dA_l/dh_l)}\right]^{1/2} \tag{4-92}$$

where h_l is the height of liquid layer (m), A_g is the flow area of the gas phase ($A_g = \alpha A$), θ is the pipe inclination angle (0 = horizontal), dA_l/dh_l is the derivative of liquid flow area with respect to height and can be expressed by the following relationship:

$$\frac{dA_l}{dh_l} = \left[1 - \left(2\frac{h_l}{D} - 1\right)^2\right]^{1/2} D. \tag{4-93}$$

Note that both the calculation of the liquid height, h_l , and the above derivative of the liquid flow area with respect to the liquid height, Eq. (4-93), assumes that the geometry is that of a circular pipe. At this time, TRACE does not have an option to specify that a 1-D component should be treated as a rectangular channel. Also, to prevent a division by zero, the magnitude of the derivative, evaluated using Eq. (4-93), is limited so that

$$\frac{dA_l}{dh_l} \geq 0.001\,D \ . \tag{4-94}$$

Based on data comparisons for stratified flow in relatively large diameter pipes using data from the TPTF[1] facility (see Reference 4-29), the Taitel-Dukler criterion was modified as suggested by

Anoda et. al. (Ref. 4-30). That is, the superficial gas velocity in Eq. (4-92) was replaced by the relative velocity, so that the criterion becomes

$$V_{r,crit} = \left(1 - \frac{h_l}{D}\right)\left[\frac{g\Delta\rho\cos\theta A_g}{\rho_g(dA_l/dh_l)}\right]^{1/2} \tag{4-95}$$

Using the value of the critical relative velocity from Eq. (4-95), a weighting factor for the Taitel-Dukler transition from stratified flow is defined

$$wf_{T-D} = Max\left[0\ ,\ Min\left(1\ ,\ 2-\frac{V_r}{V_{r,crit}}\right)\right] \tag{4-96}$$

where a value of unity indicates that stratification is possible and zero that the flow is non-stratified. The usage of the stratified flow weighting factor is explained in ***Transition to Non-Stratified Flow***, and its effectiveness in predicting the void fraction for co-current horizontal flow is illustrated in Figure 4-10. This figure presents the results of a TRACE assessment case against the TPTF horizontal flow tests (Ref. 4-29) for a pipe with a diameter of 0.18 m.

Two additional criteria are used to determine whether the flow can be stratified:

- the flow regime transition criterion for dispersed bubbly flow, and
- the counter-current flow limit (CCFL) for inclined pipes.

Each of these criteria and its TRACE implementation are described below.

For high liquid flow rates, liquid phase turbulence can break-up the gas phase into small dispersed bubbles. Choe et. al. (Ref. 4-31) gave the criterion for this transition to homogeneous dispersed bubbly flow as a simple mass flux limit. They concluded that homogeneous flow begins at

$$G = 2\times10^6\ \ (\mathrm{lbm/ft^2\ hr}) \tag{4-97}$$

or

$$G \approx 2700\ \ (\mathrm{kg/m^2 s}) \tag{4-98}$$

The implementation of this criterion is taken from the TRAC-PF1/Mod2 flow regime map (Ref. 4-32) and the corresponding weighting factor is defined by

1. TPTF - the Two-Phase Test Facility operated in conjunction with the ROSA program by the Japan Atomic Energy Research Institute, located in Tokai, Japan.

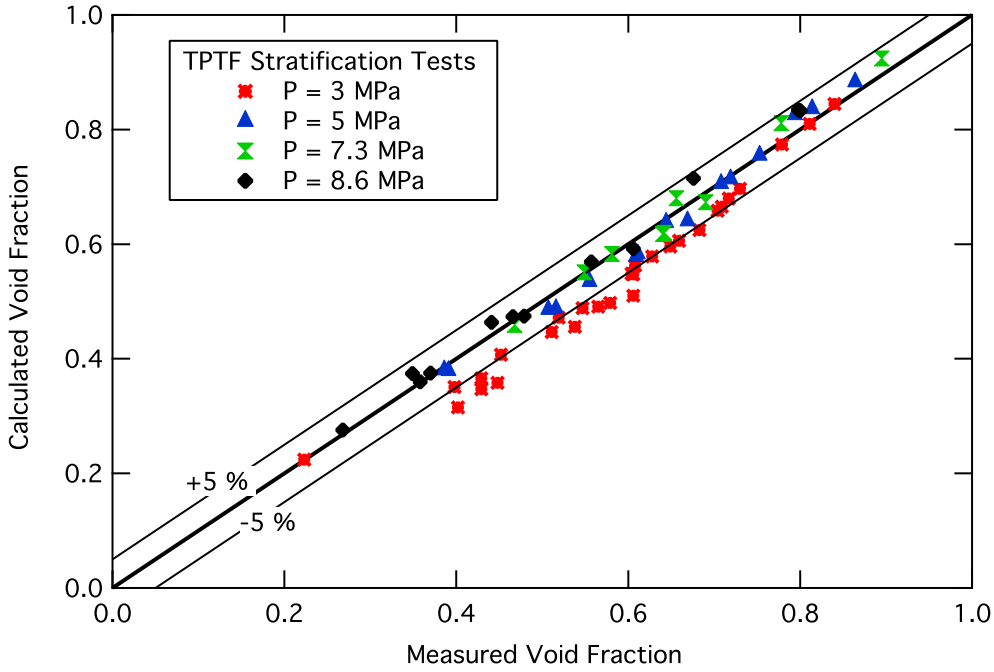

Figure. 4-10. Comparison of calculated and measured void fractions for the TPTF co-current horizontal flow tests (Ref. 4-29).

$$wf_{C-W} = Max\left[0\ ,\ Min\left(1\ ,\ \frac{2700 - G}{2700 - 2000}\right)\right] \tag{4-99}$$

In building a TRACE input model, the user has the responsibility of specifying geometry dependent CCFL model coefficients at all significant flow area restrictions where CCFL is expected to occur. However, CCFL can also occur, and be important, for components such as the hot leg of a PWR that do not have any significant flow area restrictions. To handle such geometries, without placing a needless burden on the user, the Richter CCFL model (Ref. 4-33) for inclined pipes was built into the stratification criteria of TRACE. Basically, the idea is that if the flooding criteria are exceeded, then the flow cannot be stratified and the increased interfacial drag of the non-stratified regime will be sufficient to prevent counter-current flow.

The Richter CCFL model (Ref. 4-33) for inclined pipes was selected for implementation in TRACE due to its good representation of the full-scale hot leg CCFL tests in the UPTF[1] facility (see Reference 4-34). It is expressed by:

1. The Upper Plenum Test Facility, for investigating three-dimensional flow phenomena at full-scale, modeled the upper plenum, loops and downcomer of a PWR and was the German contribution to the 2D/3D project.

$$j_g^{*1/2} + j_l^{*1/2} = 0.7 \tag{4-100}$$

where

$$j_g^* = j_g \left(\frac{\rho_g}{g \Delta \rho D} \right)^{1/2}, \text{ and} \tag{4-101}$$

$$j_l^* = j_l \left(\frac{\rho_l}{g \Delta \rho D} \right)^{1/2} \tag{4-102}$$

To implement this model in TRACE, a stratified weighting factor is defined as

$$wf_{CCFL} = Max \left\{ 0 \, , \, Min \left[1 \, , \, \frac{1.2 - \left(j_g^{*1/2} + j_l^{*1/2} \right)}{1.2 - 0.65} \right] \right\} \tag{4-103}$$

This weighting factor is used to turn stratification off gradually as the sum, $\left(j_g^{*1/2} + j_l^{*1/2} \right)$, increases from 0.65 to 1.2 and was found to give a good representation of the flooding curve for the UPTF hot leg tests as illustrated in Figure 4-11.

In Eq. (4-100) and Eq. (4-103), it is assumed that the flow is counter-current and so it is the magnitude of the liquid superficial velocity that is used in Eq. (4-102). For co-current flow situations, for the evaluation of the CCFL weighting factor, the liquid superficial velocity is taken to be zero, and so Eq. (4-100) effectively becomes

$$j_g^{*1/2} = 0.7 \tag{4-104}$$

and is applied as an upper limit for the gas velocity in co-current stratified flow. This approach was adopted to provide a continuous treatment at the flooding point.

In summary, three separate criteria are used to determine whether or not the flow can be stratified:

- it must first satisfy the modified form of the Taitel-Dukler criterion (Eq. (4-95)) that represents the transition from stratified to intermittent flow,
- the mass flux must be low enough, see Eq. (4-98), so that the flow is not in the dispersed bubble regime, and

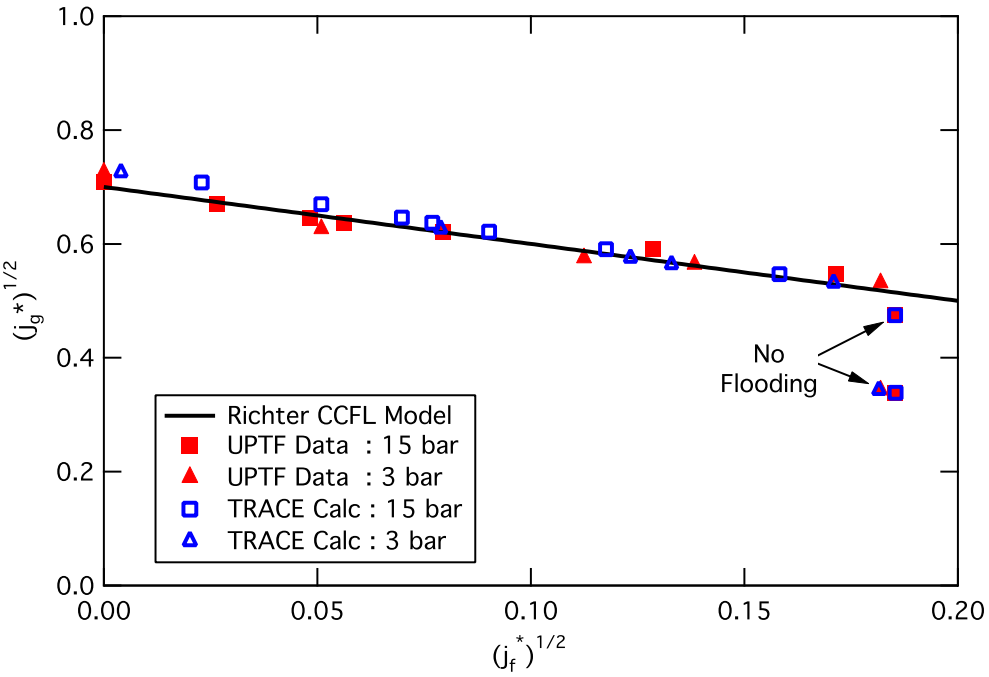

Figure. 4-11. Comparison of calculated and measured flooding curve for counter-current flow in the hot leg of a PWR using the full-scale UPTF test data (Ref. 4-34).

- the flow must not be flooded, that is, the CCFL criterion given by Eq. (4-100) must be satisfied.

These three criteria are implemented as stratification weighting factors, see Eq. (4-96), Eq. (4-99) and Eq. (4-103). To provide a smooth continuous transition from stratified to non-stratified flow, these weighting factors are combined multiplicatively

$$wf_{strat} = wf_{T-D} \cdot wf_{C-W} \cdot wf_{CCFL} \tag{4-105}$$

This combined stratification weighting factor, wf_{strat}, is used to weight the interfacial drag coefficient between that of stratified and non-stratified flow as described in ***Transition to Non-Stratified Flow***.

Interfacial Friction for Stratified Flow

For stratified flow, the interfacial drag coefficient is given by

$$C_{i,strat} = \frac{1}{2}\rho_g f_i A_i''' \tag{4-106}$$

where the interfacial area per unit volume is

$$A_i''' = \frac{S_i}{A} \tag{4-107}$$

and S_i is the width of the stratified two-phase interface as depicted in Figure 4-12.

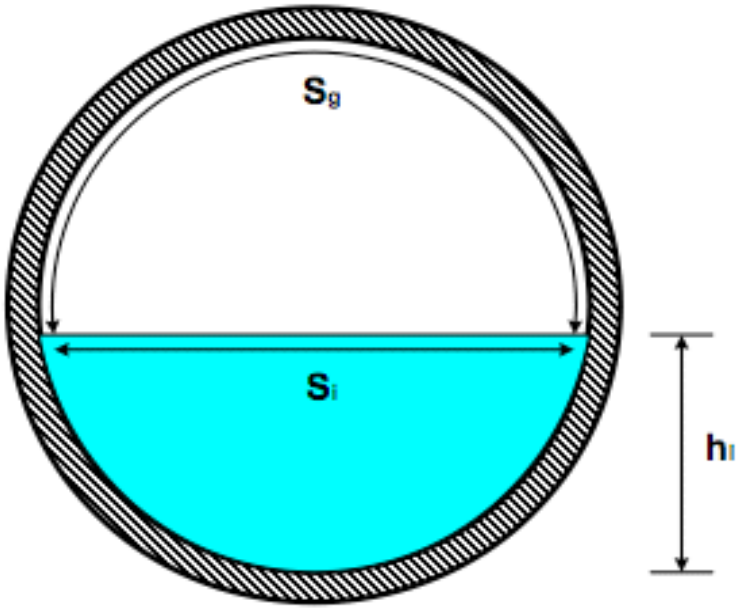

Figure. 4-12. Schematic of stratified flow in a horizontal pipe.

The only stratified flow regime that is explicitly modeled is the "stratified smooth" regime where the phases flow separately with a relatively smooth interface. To specify the interfacial friction factor for this regime, the correlation of Ohnuki et. al. (Ref. 4-35) that was used in TRAC-PF1/ Mod2 is retained. The interfacial friction factor is then given by

$$f_i = 1.84 \cdot f_{wg} \tag{4-108}$$

where f_{wg} is the single-phase wall drag friction factor for the gas phase. The wall-gas friction factor is evaluated as a function of the gas Reynolds no. using the formula of Churchill (Ref. 4-36). This is given in the section ***Single-Phase Friction Factor*** below. The gas phase Reynolds no. is computed from

$$Re_g = \frac{\rho_g V_g D_g}{\mu_g}, \tag{4-109}$$

where D_g is a special hydraulic diameter for the gas-phase computed for stratified flow as suggested by Agrawal et. al. (Ref. 4-37):

$$D_g = \frac{4 A_g}{(S_g + S_i)} \tag{4-110}$$

where S_g is the perimeter of the pipe in the gas region (see Figure 4-12).

Transition to Non-Stratified Flow

The stratified flow weighting factor, wf_{strat}, introduced in Eq. (4-105), is used to weight the contributions to the interfacial drag from the stratified and non-stratified flow regimes. Because the respective interfacial drag coefficients for these disparate regimes can vary by several orders of magnitude, an exponential weighting scheme is used. Thus, when the stratified flow weighting factor is greater than zero, the interfacial drag coefficient is given by

$$C_i = C_{i,\,strat}^{n} \cdot C_{i,\,ns}^{(1-n)} \tag{4-111}$$

where the exponent, n, is set equal to wf_{strat}.

Post-CHF Interfacial Drag Models

When the temperature of a surface is above the Leidenfrost[1] point, the liquid phase cannot contact the hot surface. This gives rise to a family of "inverted" flow regimes with the gas phase in contact with the wall as depicted schematically in Figure 4-13. The determination between the normal pre-CHF flow regimes and the inverted post-CHF flow regimes is made using the axial locations of the bottom and top quench fronts. For momentum cells that are completely quenched, the normal pre-CHF regimes are used. Whereas, for momentum cells whose heat transfer surface is in film boiling, (i.e., they are located entirely between the top and bottom quench fronts), the inverted post-CHF flow regimes are used. Finally, for cells that are partially quenched, an interpolation between the interfacial drag coefficients for the pre- and post-CHF values is performed as explained in ***Transition to Pre-CHF Regimes***.

Three principal inverted flow regimes are modeled in TRACE for post-CHF conditions: inverted annular, inverted slug, and dispersed flow. The region over which each of these post-CHF flow regimes is applied is shown in Figure 4-14. This post-CHF flow regime map is primarily a function of the void fraction with the gas superficial velocity governing the entrainment fraction

1. This temperature is also commonly known as T_{min}, which is short for the "minimum stable film boiling temperature".

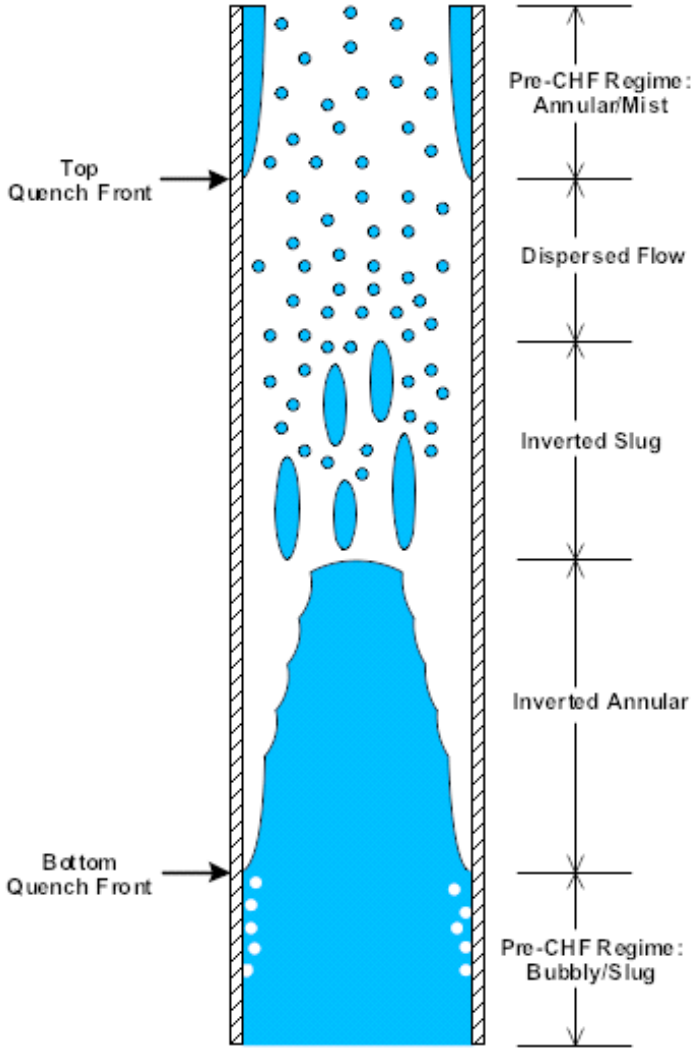

Figure. 4-13. Schematic of the inverted flow regimes that occur for post-CHF conditions.

and hence the transition to dispersed flow. The models used for the evaluation of the interfacial drag coefficient for each of these flow regimes, as well as the flow regime transition criteria are described in the following sections.

Inverted Annular

The inverted annular flow regime typically occurs when subcooled liquid flows past the quench front. Just downstream of the quench front, a thin vapor film separates the liquid core from the hot wall. Initially, the vapor velocity is low so that the flow is laminar and the gas-liquid interface is smooth. Further downstream of the quench front, as the subcooling of the liquid core is

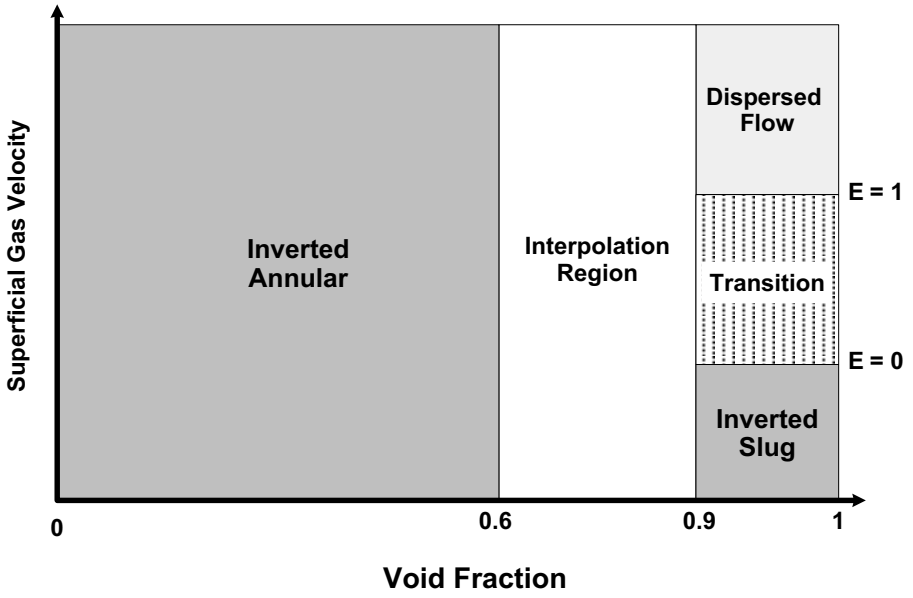

Figure. 4-14. Post-CHF flow regime map.

reduced, the vapor flow increases causing the interface to first become wavy and then oscillate violently until breakup occurs at about the point where the liquid becomes saturated. Experimental data indicate that the inverted annular regime persists up to void fractions of 60-70% and that a smooth transition, in so far as the wall heat transfer is concerned, is made to the dispersed flow regime. In TRACE, the inverted annular regime is assumed to exist for void fractions up to 60%.

For the inverted annular regime, the interfacial drag coefficient is given by

$$C_{i,IA} = \frac{1}{2}\rho_g f_i A_i''' \tag{4-112}$$

where the interfacial area per unit volume is computed from the void fraction assuming that the liquid core is circular, that is

$$A_i''' = 4\frac{\sqrt{(1-\alpha)}}{D_h} \tag{4-113}$$

When the gas film flow is laminar, the interfacial friction factor is assumed equal to that for flow between parallel plates, namely

$$f_i = \frac{24}{Re_g} \tag{4-114}$$

where the gas phase Reynolds no. is defined by

$$Re_g = \frac{\alpha \rho_g \ V_g D_h}{\mu_g} \tag{4-115}$$

Cachard (Ref. 4-38) introduced a non-dimensional gas film thickness for the analysis of inverted annular film boiling, given by

$$\delta^* = \delta \left[\frac{\rho_g g \Delta \rho}{\mu_g^2} \right]^{1/3} \tag{4-116}$$

and used it as the correlating parameter for the interfacial friction factor. For laminar flow with a smooth interface, Eq. (4-114) can then be recast as

$$f_{i,\,smooth} = \frac{144}{(\delta^*)^3} \tag{4-117}$$

and it is this formulation that is used in TRACE.

As the gas flow increases, the flow becomes turbulent and the interface becomes wavy or irregular causing the friction factor to increase. To complete the specification for the interfacial friction factor for the inverted annular regime, it remains to define the friction factor for this wavy regime.

Although void fraction measurements exist for inverted annular flow, because the flow quality is negative, the actual phasic velocities are unknown and it is impossible to directly determine the interfacial friction from this data. Consequently, a simple model has been developed that describes the correct qualitative behavior. This model is an inverted analog to that for annular flow. Specifically, the interfacial friction factor is taken to be a function of the interface roughness and this roughness is assumed to be proportional to the thickness of the gas film.

From observations on ducts with grooved or wavy walls, the friction factor follows that of smooth parallel plates up to a Reynolds no. of about 200-400. With further increases in the Reynolds no., significant flow separation is observed and the friction factor versus Reynolds no. curve takes on the appearance of that for fully rough turbulent flow. That is, it is nearly a constant value with the magnitude of that value dependent upon the amplitude/wavelength ratio. From this observation, and that of Andritsos and Hanratty (Ref. 4-39) that the interfacial friction factor for horizontal stratified flow is dependent on the wave amplitude and consequently is linearly proportional to the vapor Reynolds no., the following model was developed:

$$f_{i,\,wavy} = 0.35 \left(\frac{\delta}{La} \right)^{0.72} . \tag{4-118}$$

The exponent in the above formula was selected so that the interfacial friction factor, when waves govern its value, is linearly proportional to the vapor Reynolds no. The Laplace no., given by

$$La = \sqrt{\frac{\sigma}{g\Delta\rho}} \tag{4-119}$$

was used to non-dimensionalize the gas film thickness in order to provide a continuous treatment with that for the inverted slug regime. Finally, the approximate value of the coefficient in Eq. (4-118) was determined from data comparisons with FLECHT-SEASET high flooding rate reflood data.

Rather than try to specify a criterion for the transition from smooth to wavy inverted annular flow, a power law weighting was used. Specifically,

$$f_{i,IA} = \left[f_{i,smooth}^{2} + f_{i,wavy}^{2} \right]^{1/2} \tag{4-120}$$

The resulting model for the interfacial friction factor in the inverted annular flow regime is depicted in Figure 4-15. The minimum value of the friction factor occurs at a gas Reynolds no. of about 350 followed by an increase that is linearly proportional to the Reynolds no.

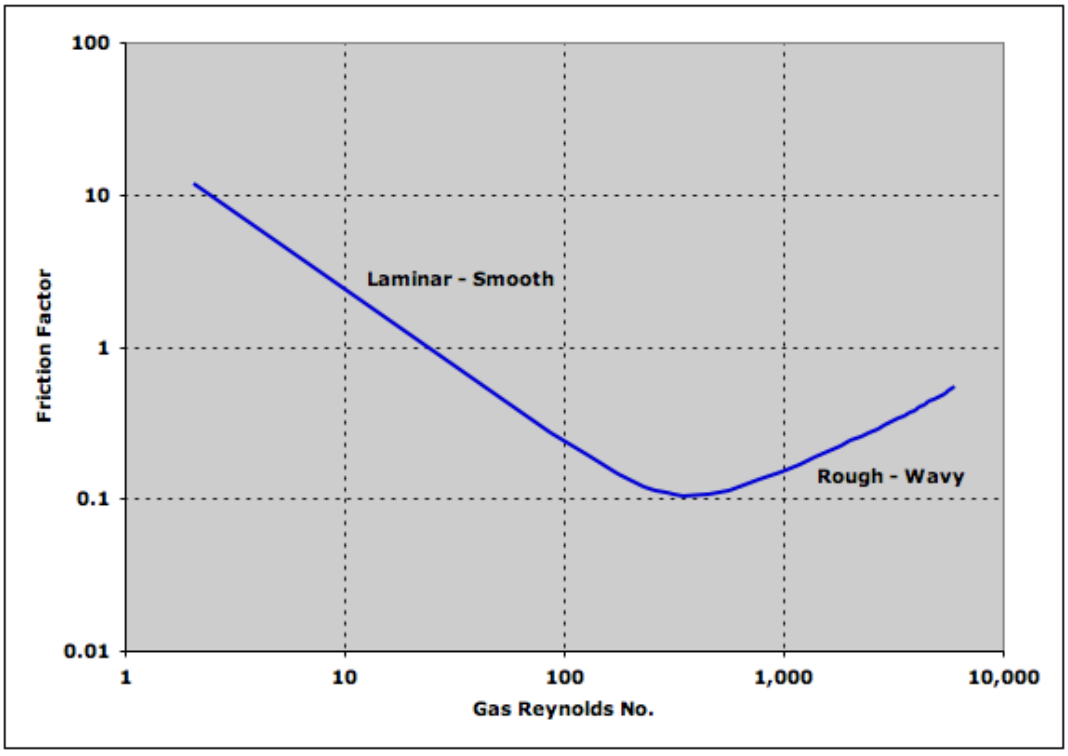

Figure. 4-15. Interfacial friction factor for the inverted annular flow regime as a function of the gas Reynolds no.

Inverted Slug Regime

Further downstream of the quench front, as the subcooling of the liquid core is reduced, the vapor flow increases causing the interface to first become wavy and then oscillate violently until breakup occurs at about the point where the liquid becomes saturated. Kawaji and Banerjee (see Reference 4-40) observed that the wavelength of maximum growth rate was about 4.5 times the diameter of the liquid column. Therefore, they proposed that the ligaments formed by the disintegration of the inverted annular core could be modeled as prolate ellipsoids with the length of the semi-major axis larger than that of the semi-minor axis by a factor of 4.5. This proposal, coupled with the fluidized bed concept, form the basis for the inverted slug flow regime model in TRACE.

For the inverted slug regime, the interfacial drag coefficient is given by

$$C_{i,IS} = \frac{1}{2}\rho_g C_{D,MP} A_p''' \tag{4-121}$$

where $C_{D,MP}$ is the drag coefficient corrected for multi-particle effects and A_p''' is the projected area per unit volume. Based on the assumption that the ligaments can be represented as prolate ellipsoids, the projected area of a ligament would be

$$A_p = \pi a^2 \tag{4-122}$$

and its volume would be

$$V = \frac{4}{3}\pi a^2 b \tag{4-123}$$

where a and b are the minor and major radii of the ellipsoid respectively. With an aspect ratio of 4.5, the projected area per unit volume becomes

$$A_p''' = \frac{(1-\alpha)}{3\,d_{IS}} \tag{4-124}$$

where d_{IS} is the diameter of the ligament, that is twice the minor radius.

To estimate the drag coefficient for a ligament, the formula for a distorted droplet given by Clift, Grace and Weber (Ref. 4-41) is used. The single particle drag coefficient is then

$$C_{D,SP} = \frac{1}{3}\left(\frac{d_{IS}}{La}\right) \tag{4-125}$$

The multi-particle effect is taken to be that of the inertial regime from Richardson and Zaki (Ref. 4-42), that is

$$C_{D,MP} = \frac{C_{D,SP}}{\alpha^{1.8}} \tag{4-126}$$

Combining Eq. (4-124) through Eq. (4-126), we have

$$C_{i,IS} = \frac{1}{18}\frac{\rho_g}{La}\frac{(1-\alpha)}{\alpha^{1.8}} \tag{4-127}$$

In TRACE, the above interfacial drag coefficient has been reduced by a factor of ¾ to better match FLECHT-SEASET high flooding rate reflood data, so that

$$C_{i,IS} = \frac{1}{24}\frac{\rho_g}{La}\frac{(1-\alpha)}{\alpha^{1.8}} \tag{4-128}$$

As indicated in Figure 4-14, an interpolation region is applied between the inverted annular and inverted slug flow regimes. The rationale for this interpolation region is that film boiling heat transfer data indicates a smooth transition between these two regimes. Consequently, an interpolation region was used for the wall heat transfer coefficient and the same interpolation scheme is used here for consistency.

For void fractions less than 60%, the flow regime is inverted annular, whereas for void fractions above 90%, the flow regime is inverted slug. At void fractions between these limits, the interfacial drag coefficient is computed from

$$C_i = wf_{IA} \cdot C_{i,IA} + (1 - wf_{IA}) \cdot C_{i,IS} \tag{4-129}$$

where wf_{IA} is a spline weighting factor for inverted annular flow. This weighting factor is given by

$$wf_{IA} = x\,(2 - x) \tag{4-130}$$

where

$$x = \frac{(0.9 - \alpha)}{(0.9 - 0.6)} \tag{4-131}$$

This completes the description of the models used for the inverted slug flow regime. As the gas velocity increases, entrainment becomes important and a transition to the dispersed flow regime occurs as described in the following section.

Dispersed Flow

After the breakup of the inverted annular core, the liquid phase is assumed to consist of ligaments and droplets. The ligaments are treated as prolate ellipsoids as described in ***Inverted Slug Regime***. The droplets are relatively small and nearly spherical, so they are treated using models appropriate for spheres.

The interfacial drag coefficient for the dispersed flow regime is

$$C_{i,DF} = \frac{1}{2}\,\rho_g C_{D,MP} A_p''' \tag{4-132}$$

where the projected area per unit volume is calculated from the droplet Sauter mean diameter by

$$A_p''' = \frac{6(1-\alpha)}{4\,d_{SM}} \tag{4-133}$$

Four specific constitutive models are needed to evaluate $C_{i,DF}$ of the dispersed flow regime:

- Droplet diameter,
- Droplet drag coefficient,
- Multiple particle effect, and
- Entrained fraction.

Each of these four models is detailed below, along with the interpolation scheme used for the transition from inverted slug to dispersed flow.

As the gas velocity increases and ligaments shatter, both large liquid fragments and small droplets are formed. It is assumed that the creation of these small droplets is due to the Kelvin-Helmholtz instability, and hence a Weber no. criterion is used to estimate their initial diameter. The maximum droplet diameter is then

$$d_{\max} = \frac{12\sigma}{\rho_g V_r^2} \tag{4-134}$$

where a critical value of 12 was chosen for the Weber no. The relative velocity in the denominator of Eq. (4-134) is evaluated using the droplet terminal velocity. Wallis (Ref. 4-43) gives the terminal velocity for large spherical drops (Region 2B in (Ref. 4-43)) as

$$V_\infty^* = 0.693(r^*)^{0.858} \tag{4-135}$$

where the non-dimensional values of the velocity and droplet radius are defined as

$$V_\infty^* = V_\infty \left[\frac{\rho_g^2}{\mu_g g \Delta\rho} \right]^{1/3}, \text{ and} \tag{4-136}$$

$$r^* = r \left[\frac{\rho_g g \Delta\rho}{\mu_g^2} \right]^{1/3} \tag{4-137}$$

Eq. (4-135) is valid for the range, $10 < r^* < 36$, which covers the expected size range for drop diameters during reflood. Combining Eq. (4-134) and Eq. (4-135) yields

$$d_{\max} = 5.07 \cdot La \cdot N_{\mu g}^{0.176} \tag{4-138}$$

for the initial maximum droplet diameter as a function of the Laplace and Viscosity nos.

Further downstream, as the gas velocity increases, additional droplet breakup due to the Kelvin-Helmholtz instability may occur. Here, it is assumed that the largest drops are only just levitated by the gas stream and that for the dispersed flow region the void fraction is near unity, so the relative velocity is approximated by the gas superficial velocity,

$$V_r \approx j_g \tag{4-139}$$

The critical Weber no. criterion then becomes

$$d_{We} = \frac{We_{crit}\ \sigma}{\rho_g\ j_g^2} \tag{4-140}$$

In TRACE, for the subsequent breakup of drops in the dispersed flow regime, the value of the critical Weber no., We_{crit}, was set to 18 to better match dispersed flow film boiling heat transfer data in the THTF upflow film boiling tests. Thus,

$$d_{We} = \frac{18\sigma}{\rho_g\ j_g^2} \tag{4-141}$$

The local value for the maximum drop diameter is then taken as the minimum of the two values given by Eq. (4-138) and Eq. (4-141), that is

$$d_{\max} = Min \left[5.07 \cdot La \cdot N_{\mu g}^{0.176}\ , \left(\frac{18\sigma}{\rho_g\ j_g^2} \right) \right] \tag{4-142}$$

Eq. (4-142) is used for the maximum drop diameter for upflow cases, $j_g > 0$.

For downflow, $j_g < 0$, the assumptions used to estimate the drop relative velocity in Eq. (4-138) and Eq. (4-141) do not apply, as the drops can fall freely with the gas stream. Consequently, a different criterion is used for the maximum droplet diameter, that is, the drop size is assumed to be governed by the Rayleigh-Taylor instability and the physical dimensions of the flow channel. Kitscha and Kocamustafaogullari (Ref. 4-44) give the Rayleigh-Taylor limit, for freely falling drops in a gaseous media, as

$$d_{R-T} = 3.52 La \tag{4-143}$$

and, since the largest drop cannot be larger than the flow channel,

$$d_{\max} = Min \left[3.52 La \, , D_h \right] \tag{4-144}$$

For upflow conditions, the maximum diameter given by Eq. (4-142) should always be significantly smaller than that given by Eq. (4-144). However, for consistency, the value from Eq. (4-144) is also applied as an upper limit on the drop size.

Finally, for the estimation of the projected area per unit volume, the relationship between the maximum diameter and the Sauter mean diameter is needed. Ardron and Hall (Ref. 4-45) observed that for their experimental droplet size distributions, the Sauter mean diameter was typically about one-third of the maximum diameter and this ratio is used in TRACE. Thus,

$$d_{SM} = \frac{1}{3} d_{\max} \tag{4-145}$$

The second step is to evaluate the droplet drag coefficient. As stated above, the dispersed droplets are relatively small and nearly spherical, so the standard drag curve for spheres can be used. Clift, Grace and Weber (Ref. 4-46), provide a table of formulas that approximate the rigid sphere drag curve. From this table, the formula of Schiller and Nauman was selected due to its high accuracy for drop Reynolds nos. less than 800. The single-particle drag coefficient is then

$$C_{D,SP} = \frac{24}{Re_d} \left(1 + 0.15 Re_d^{0.687} \right) \tag{4-146}$$

where the drop Reynolds no. is defined by

$$Re_d = \frac{\rho_g V_r d_{SM}}{\mu_{g,film}} \tag{4-147}$$

The relative velocity used in Eq. (4-147) is simply the magnitude of the difference between the phasic velocities, $|V_g - V_l|$, but with the two modifications described below.

First, the phasic relative velocity results from the solution of the velocity equations using the multi-particle drag coefficient. To make it consistent with the Richardson and Zaki (Ref. 4-42) formulation, this relative velocity must be translated to that which would occur for a single particle in an infinite medium. Thus,

$$V_r = \frac{|V_g - V_l|}{\alpha^{1.4}} \tag{4-148}$$

Then, to prevent unrealistically high values of the drag coefficient, this relative velocity is limited to be larger than that given by Eq. (4-135) for the single-particle terminal velocity.

Note also that the gas viscosity in Eq. (4-147) is evaluated at a "film" temperature. This is to account for the mass transfer effect upon the drag coefficient as suggested by Renksizbulut and Yuen (Ref. 4-47). The film temperature is defined by

$$T_{film} = \frac{1}{2}(T_g + T_{sat}) \tag{4-149}$$

to account for the surface of the droplet being at the saturation temperature and the variation of properties from the free stream value.

Finally, for drop Reynolds nos. greater than about 1000, the drag coefficient approaches a constant value and may be approximated by

$$C_{D,SP} \approx 0.44 \tag{4-150}$$

To provide a continuous treatment, the maximum of Eq. (4-146) and Eq. (4-150) is taken.

For the multi-particle effect, the inertial regime from Richardson and Zaki (Ref. 4-42) is used. To implement this model requires two modifications. The first was described above and modifies the drop Reynolds no. used in the computation of the single-particle drag coefficient. The second directly modifies the drag coefficient in the same manner as was done for the inverted slug regime, that is

$$C_{D,MP} = \frac{C_{D,SP}}{\alpha^{1.8}} \tag{4-151}$$

The transition from the inverted slug to the dispersed flow regime is governed by the entrainment fraction, that is, the fraction of the liquid determined to be entrained is treated as droplets while

the remainder of the liquid is considered to be inverted slugs. To effect this transition, a simple linear weighting scheme is employed,

$$C_i = E \cdot C_{i,DF} + (1 - E) \cdot C_{i,IS} \tag{4-152}$$

where E is the entrainment fraction.

The first step in determining the entrainment fraction is to specify a critical gas velocity for the onset of entrainment. This critical gas velocity is computed from Eq. (4-135) to be consistent with the formula for the drop diameter. The critical gas superficial velocity is then that which is just sufficient to levitate a drop with the Sauter mean diameter given by Eq. (4-138) and Eq. (4-145). Thus,

$$j_{g,crit} = 0.6\left[\frac{\sigma^{0.316}(g\Delta\rho)^{0.228}}{\rho_g^{0.456}\,\mu_g^{0.0879}}\right] \tag{4-153}$$

For superficial gas velocities less than this value, the entrainment fraction will be zero and the flow regime will be inverted slug.

For higher gas velocities, the entrainment fraction is estimated using a modified form of the pool entrainment correlation of Kataoka and Ishii (Ref. 4-48). They express the entrained liquid mass flux as a function of a critical non-dimensional gas velocity and the gas mass flux by

$$G_d = 0.002\; j_g^{*3} N_{\mu g}^{1/2} \left(\frac{\Delta\rho}{\rho_g}\right) G_g \tag{4-154}$$

where the non-dimensional gas superficial velocity is defined

$$j_g^* = j_g \left(\frac{\rho_g^2}{\sigma\, g\Delta\rho}\right)^{1/4} \tag{4-155}$$

To make Eq. (4-154) consistent with the criterion for the onset of entrainment, two modifications are made. First, it is recast in terms of the critical gas velocity as

$$G_d = 4.32\times10^{-4}\left(\frac{j_g}{j_{g,crit}}\right)^3 N_{\mu g}^{0.236} \left(\frac{\Delta\rho}{\rho_g}\right) G_g \tag{4-156}$$

which does not affect the magnitude of the entrained liquid mass flux. Then, to force the entrained fraction to zero at the critical value for the onset of entrainment, Eq. (4-156) is modified to

$$G_d = 4.32\times10^{-4}\left[\left(\frac{j_g}{j_{g,crit}}\right)^3 - 1\right] N_{\mu g}^{0.236} \left(\frac{\Delta\rho}{\rho_g}\right) G_g \tag{4-157}$$

or more simply to

$$G_d = 4.32\times10^{-4}\left[\left(\frac{j_g}{j_{g,crit}}\right)^3 - 1\right] N_{\mu g}^{0.236} \Delta\rho j_g \tag{4-158}$$

Based on reflood data comparisons with TRACE, the value for the entrained mass flux given by Eq. (4-158) above is reduced by a factor of two. So,

$$G_d = 2.16\times10^{-4}\left[\left(\frac{j_g}{j_{g,crit}}\right)^3 - 1\right] N_{\mu g}^{0.236} \Delta\rho j_g \tag{4-159}$$

The last step is to convert the entrained mass flux into the entrainment fraction and by definition

$$E = \frac{G_d}{G_l} \tag{4-160}$$

which is expressed in TRACE as

$$E = \frac{\alpha_d}{(1-\alpha)} \tag{4-161}$$

where the droplet volume fraction is estimated from

$$\alpha_d \approx \frac{G_d}{\rho_l \cdot Max(0.01\ ,\ V_l)} \tag{4-162}$$

This completes the description of the models necessary to determine the interfacial drag coefficient for the dispersed flow regime and for the transition regime between dispersed flow and inverted slug flow. The following section describes the transition from the post-CHF regimes to the normal pre-CHF flow regimes.

Transition to Pre-CHF Regimes

The determination between the normal pre-CHF flow regimes and the inverted post-CHF flow regimes is made using the axial locations of the bottom and top quench fronts. For momentum

cells that are completely quenched, the normal pre-CHF regimes are used. Whereas, for momentum cells whose heat transfer surface is in film boiling, (i.e., they are located entirely between the top and bottom quench fronts), the inverted post-CHF flow regimes are used. Finally, for cells that are partially quenched, an exponential interpolation between the interfacial drag coefficients for the pre- and post-CHF values is performed.

Let f_Q represent the fraction of the momentum cell that is quenched. Then,

$$C_i = (C_i)^{f_Q}_{pre-CHF} \cdot (C_i)^{(1-f_Q)}_{post-CHF} \tag{4-163}$$

where the exponential interpolation is used because of the large difference in the magnitude of the pre- and post-CHF interfacial drag coefficients. This helps to reduce the perturbation that occurs as the quench front crosses a cell boundary.

The description of the interfacial drag models is complete, the single-phase and two-phase wall drag models are described next.

Wall Drag

Two types of frictional pressure losses are modeled in TRACE:

- Wall Drag: models the fluid-wall shear using a friction factor approach, and
- Form Drag: models geometry specific pressure losses through user specification of additive loss coefficients" for irreversible form losses due to abrupt or semi-abrupt flow-area expansions and contractions, thin-plate-orifice-type flow restrictions, and flow redirection (turning) at an elbow or tee.

The models for both single- and two-phase wall drag are described in the following sections. The TRACE model for additive loss coefficients is described in **Chapter 7**.

In the TRACE formulation, the frictional pressure gradient due to wall drag is given by:

$$\left.\frac{dP}{dz}\right|_f = - \ C_{wl} \cdot \left|V_l\right| \cdot V_l - \ C_{wg} \cdot \left|V_g\right| \cdot V_g \tag{4-164}$$

where C_{wl} and C_{wg} are the wall drag coefficients for wall-liquid and wall-gas shear respectively. Typically, only one of these coefficients has a non-zero value. For example, in either bubbly/slug or annular/mist flow, all of the wall drag is applied to the liquid phase and C_{wg} is set to zero.

For TRACE, the wall drag model from TRAC-PF1/MOD2 was substantially modified to:

- Improve accuracy in the annular flow regime so that film thickness can be calculated accurately, especially for applications in downflow condensers, and

- Explicitly account for the post-CHF "inverted" flow regimes where the only wall-fluid contact is to the gas phase.

Four specific areas of application for the wall drag model are discussed below: single-phase fraction factor, pre-CHF regimes, horizontal stratified flow, and post-CHF regimes.

Single-Phase Friction Factor

For single-phase flow, the wall drag coefficient is defined by

$$C_{wk} = f_{wk} \cdot \frac{4}{D_h} \cdot \frac{1}{2}\rho_k = f_{wk} \cdot \frac{2\rho_k}{D_h} \tag{4-165}$$

where the subscript k indicates the fluid phase (l or g) and f_w is the Fanning friction factor[1] . The Churchill formula (see Reference 4-36) for the friction factor is used in TRACE because it applies to all three flow regimes - laminar, transition, and turbulent.

The Churchill friction factor formula is given by

$$f_w = 2\left[\left(\frac{8}{Re}\right)^{12} + \frac{1}{(a+b)^{3/2}}\right]^{1/12} \tag{4-166}$$

where

$$a = \left\{2.475 \cdot \ln\left[\frac{1}{\left(\frac{7}{Re}\right)^{0.9} + 0.27\left(\frac{\epsilon}{D_h}\right)}\right]\right\}^{16} \tag{4-167}$$

and

$$b = \left(\frac{3.753\times10^{4}}{\mathrm{Re}}\right)^{16} \tag{4-168}$$

1. The Darcy friction factor is four times larger than the Fanning friction factor.

Its predictions for the laminar regime are in agreement with $f_w = 16/Re$, as expected. The predictions for transition flow are subject to some uncertainty (as indeed is the experimental data for this regime). However, according to Reference 4-49, its accuracy for turbulent flow shows a maximum deviation from the Colebrook-White equation of about 3.2% for $4000 < Re < 10^8$ and $10^{-8} < \epsilon/D < 0.05$. A simplified Moody diagram created using the Churchill equation is presented in Figure 4-16.

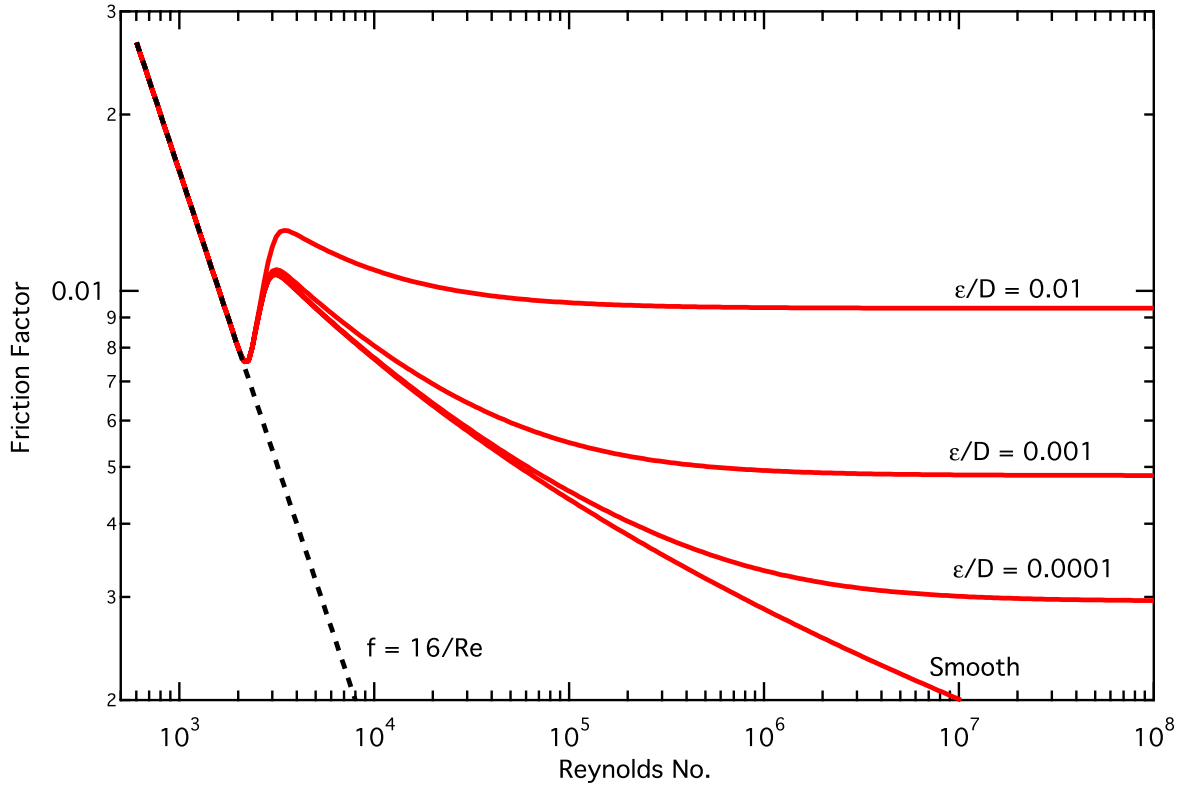

Figure. 4-16. Representation of the Moody diagram using the Churchill friction factor formula Eq. (4-166).

In Eq. (4-166), the Reynolds no. is computed for the phase of interest by

$$Re_k = \frac{\rho_k |V_k| D_h}{\mu_k} \tag{4-169}$$

and, to eliminate very large values for nearly stagnant conditions, is limited to be greater than 10.

In TRACE, there is no specific test for single-phase liquid wall drag. Instead, the two-phase model for the bubbly/slug regime devolves into the single-phase value as the limit of zero void fraction is approached. In contrast, as the void fraction approaches unity, an explicit ramp is

applied to switch the wall drag from the liquid to the gas phase. This ramp is explained in ***Annular Flow Regime***.

Pre-CHF Regimes: Two-Phase Multiplier

For the normal pre-CHF flow regimes, bubbly/slug and annular/mist, all of the wall drag is applied to the liquid phase alone. Thus,

$$\left.\frac{dP}{dz}\right|_f = -\,\mathrm{C}_{wl}\cdot\left|V_l\right| V_l \tag{4-170}$$

or, in terms of the two-phase multiplier for the liquid phase considered to flow alone in the channel,

$$\left.\frac{dP}{dz}\right|_f = -\Phi_l^2\left[\frac{2f_{2\Phi,l}\left|G_l\right| G_l}{D_h\,\rho_l}\right] \tag{4-171}$$

where the friction factor, $f_{2\Phi,l}$, is the Fanning friction factor[1] calculated with

$$Re_{2\Phi,\,l} = \frac{\left|G_l\right| D_h}{\mu_l} = \frac{(1-\alpha)\rho_l\left|V_l\right| D_h}{\mu_l} \tag{4-172}$$

The wall drag coefficient is then

$$C_{wl} = \Phi_l^2\left[\frac{2f_{2\Phi,\,l}(1-\alpha)^2\rho_l}{D_h}\right] \tag{4-173}$$

To complete the specification of the wall drag for the pre-CHF regimes, it remains to specify the two-phase multiplier, Φ_l^2, and the friction factor, $f_{2\Phi,\,l}$. The annular flow regime is treated first because:

1. Note, the double subscript, "$2\Phi, l$", is used to differentiate the liquid friction factor for two-phase conditions for the liquid phase considered to flow alone in the channel, $f_{2\Phi,\,l}$, from the single-phase liquid friction factor, f_{wl}. The primary difference between these two is the definition of the liquid Reynolds no. (see Eq. (4-169) and Eq. (4-172)) used to evaluate them.

- improving accuracy for this regime was the reason for the modification to the wall drag model of TRACE, and
- its derivation is more straightforward than that for the bubbly/slug regime.

Following the description of the annular flow regime, the model for the bubbly/slug regime and the transition between these two regimes are described.

Annular Flow Regime

The two-phase multiplier for the annular flow regime will be described first, followed by the determination of the friction factor for both the laminar and turbulent regimes. Finally, the modifications to account for the transition to single-phase gas flow as the void fraction approaches unity are described.

Annular flow theory (see References 4-50 and 4-51) gives the two-phase multiplier as

$$\Phi_l^2 = \frac{1}{(1-\alpha)^2} \tag{4-174}$$

Eq. (4-174) has been shown to give excellent predictions of the frictional pressure gradient when the friction coefficient is adjusted in the transition regime, as depicted in Figure 4-18. For example, see Figure 4-17 for a comparison of the annular flow two-phase multiplier, Φ_l, used by TRACE with data both for co-current upflow and downflow.

Substituting Eq. (4-174) into Eq. (4-173) simplifies the wall drag coefficient to:

$$C_{wl} = f_{film} \cdot \frac{2\rho_l}{D_h} \tag{4-175}$$

The only difference between Eq. (4-165) for single-phase liquid flow and Eq. (4-175) for annular flow is the evaluation of the friction factor.

In Figure 4-18, the friction factor for the annular flow regime is given by a power law combination of the laminar and turbulent values:

$$f_{film} = \left(f_{lam}^3 + f_{turb}^3 \right)^{1/3} \tag{4-176}$$

where the laminar value is that for pipe flow

$$f_{lam} = \frac{16}{Re_{2\Phi,\,l}} \tag{4-177}$$

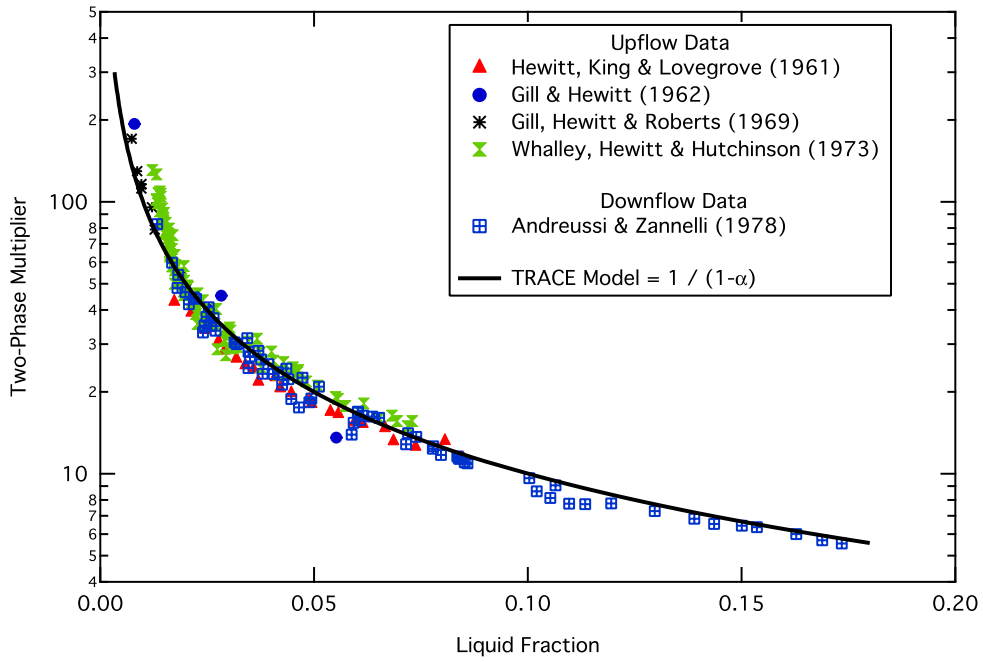

Figure. 4-17. Comparison of the TRACE annular flow model versus data.

and the turbulent value is given by Haaland's explicit approximation (Ref. 4-52) to the Colebrook equation

$$f_{turb} = \frac{1}{\left\{ 3.6 \cdot \log_{10}\left[\frac{6.9}{Re_{2\Phi,\,l}} + \left(\frac{\epsilon / D}{3.7} \right)^{1.11} \right] \right\}^2} \tag{4-178}$$

Note that the roughness effect has not been established conclusively for annular flow, it is included here to provide a continuous description with that for single-phase flow.

For laminar flow, Eq. (4-177) is appropriate for pipe flow. However, as the film thins, the friction factor is better approximated by that for a parallel plate, namely

$$f_{lam} = \frac{24}{Re_{2\Phi,\,l}} \tag{4-179}$$

Therefore, in TRACE, a simple void fraction ramp[1] is used between the formulas given by Eq. (4-177) and Eq. (4-179). Specifically, for void fractions greater than 99%, the parallel plate formula is used and for void fractions less than 95%, the pipe formula is used. In between these values, the laminar friction factor is computed from

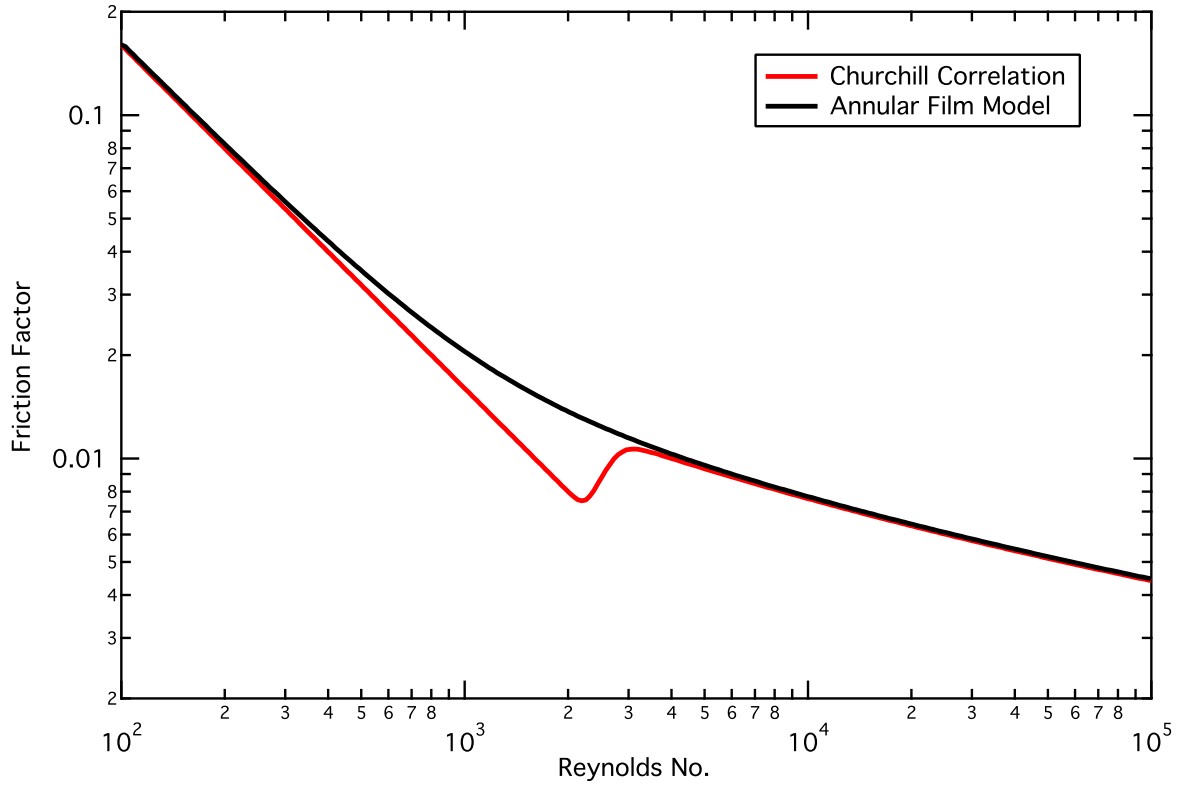

Figure. 4-18. Comparison of friction factor for a film with that for a smooth pipe.

$$f_{lam} = \frac{\left[16 + 8\left(\frac{\alpha - 0.95}{0.99 - 0.95}\right)\right]}{Re_{2\Phi,l}} \tag{4-180}$$

The accuracy of the TRACE model to calculate liquid film thickness is demonstrated in Figure 4-19 for falling liquid films.

The transition to single-phase gas flow is handled by considering the breakdown of the film into rivulets. Film breakdown is assumed to occur when the film thickness becomes less than a critical value. Many different models of varying complexity are available to predict this minimum film thickness depending upon flow orientation, and whether evaporation or condensation is occurring. In TRACE, a simple constant value of 25 microns is used. The resulting rivulets are further assumed to have a thickness equal to this critical value, so that the fraction of the surface in contact with the liquid phase is estimated by

1. Note, there is no theoretical basis for Eq. (4-180), the actual laminar friction factor depends on the velocity profile within the liquid film and is a function of the gravitational and interfacial shear forces. This ramp merely forces it to the correct limiting values.

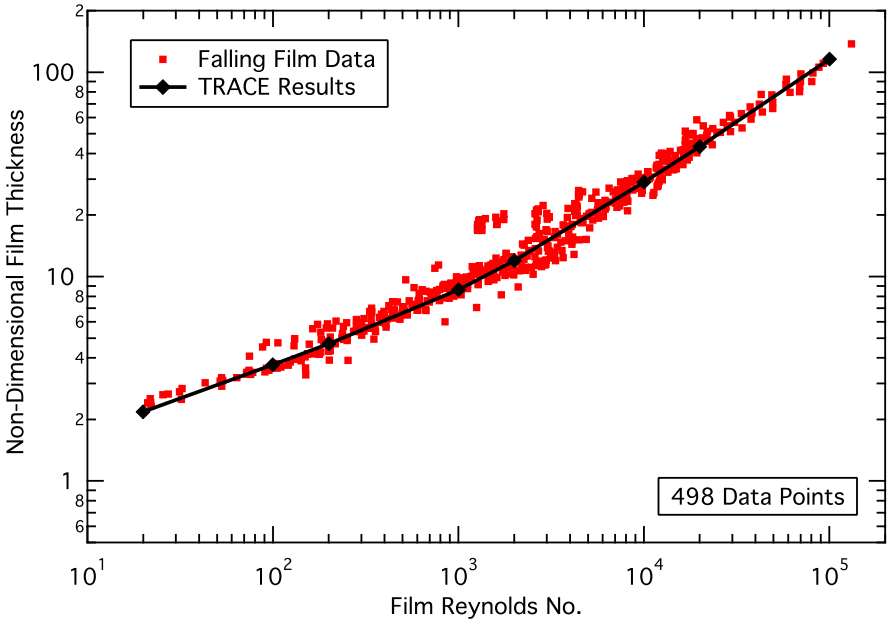

Figure. 4-19. Comparison of TRACE calculated values for film thickness with falling film data.

$$f_{wet} \approx \frac{(1-\alpha)D_h}{4(25\times10^{-6})} \tag{4-181}$$

where the thin film approximation has been used. The wall-liquid drag coefficient then becomes

$$C_{wl} = f_{wet} \cdot f_{film} \cdot \frac{2\rho_l}{D_h} \tag{4-182}$$

For the fraction of the surface not covered by rivulets, wall drag is applied to the gas phase using the friction factor from Eq. (4-166) and

$$\mathrm{C}_{wl} = (1-f_{wet}) \cdot \ f_{2\Phi\,,\,g} \cdot \frac{2\rho_g}{D_h} \tag{4-183}$$

This completes the description for the annular flow regime, a similar "void fraction based" two-phase multiplier is used for the bubbly/slug flow regime as detailed below.

Bubbly/Slug Flow Regime

To also improve the accuracy of TRACE's wall drag model for the bubbly/slug regime, a two-phase multiplier was implemented as described below. Most correlations from the literature use the flow quality as the primary correlating variable. However, as flow quality is undefined or meaningless for a number of situations encountered in transient reactor analysis, such as counter-current flow and pool boiling, it is not an ideal correlating variable for a model in TRACE. Consequently, a "void fraction based" two-phase multiplier model was developed.

First, it was observed that the original Lockhart and Martinelli model (Ref. 4-53) tabulated values for Φ_l^2, almost exactly reproduce Eq. (4-174). However, in comparisons with two-phase pressure drop data, it was found that this expression over-estimated the two-phase multiplier. Indeed, using the adiabatic steam-water data of Ferrell & McGee (Ref. 4-54), one obtains

$$\Phi_l^2 \approx \frac{1}{(1-\alpha)^{1.72}} \tag{4-184}$$

as shown in Figure 4-20.

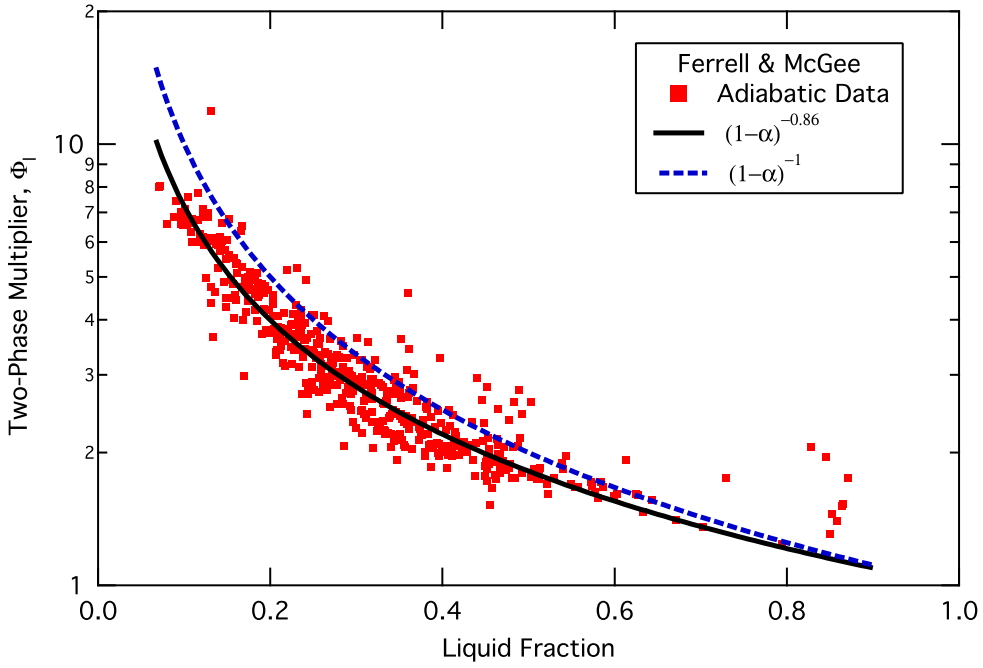

Figure. 4-20. Liquid-only two-phase multipliers inferred from the adiabatic steam-water data of Ferrel-McGee (Ref. 4-54)

This behavior of the two-phase multiplier with respect to the liquid fraction given by Eq. (4-184) is very similar to values reported by Yamazaki & Shiba (Ref. 4-55) and Yamazaki & Yamaguchi

(Ref. 4-56) who suggested exponents of -1.75 for upflow and -1.8 for downflow. Especially notable is that when the data are represented this way there is no noticeable effect of mass flux, pressure or tube diameter.

Recall that for turbulent pipe flow, the friction factor varies roughly as $Re^{-0.25}$ to $Re^{-0.2}$. Then, using the model for single-phase liquid flow Eq. (4-165) and Eq. (4-166) and a Reynolds no. defined by Eq. (4-169), gives an effective two-phase multiplier of

$$\Phi_l^2 \sim \frac{1}{(1-\alpha)^{1.75}} \text{ to } \frac{1}{(1-\alpha)^{1.8}} \tag{4-185}$$

in line with experimental observations for adiabatic two-phase flow. This simple model for the two-phase multiplier was adopted for use in TRACE for the bubbly-slug flow regime.

For two-phase flows with nucleate boiling, the situation is more complicated than that discerned above for adiabatic flows. The pressure drop data of Ferrell & Bylund (Ref. 4-57) show that the two-phase multiplier when boiling is present is both significantly higher and contains a pronounced mass flux effect, as shown in Figure 4-21. No available model for the two-phase multiplier specifically addresses the enhancement due to wall nucleation evident in this data. Collier (Ref. 4-58) does discuss a surface roughness effect for subcooled boiling and suggests that it might be correlated in terms of the bubble departure diameter but does not extend this concept into the saturated boiling regime. Ferrell & Bylund's data covers both subcooled and saturated boiling, yet there is no evident discontinuity in the behavior of the two-phase multiplier versus liquid fraction as the saturation line is crossed.

Consequently, a simple correction factor to the two-phase multiplier for adiabatic two-phase flow has been developed using the data of Ferrell & Bylund in the form:

$$\Phi_l' = \Phi_l \cdot \left(1 + C_{NB}\right) \tag{4-186}$$

As suggested by Collier, it was postulated that this correction factor would be a function of the bubble departure diameter. Collier also suggests using the model developed by Levy (Ref. 4-59) that balances surface tension and drag forces to give

$$\frac{d_g}{D_h} = 0.015 \cdot \left[\frac{\sigma}{\tau_w \cdot D_h}\right]^{\frac{1}{2}} \tag{4-187}$$

where the wall shear stress is computed without the enhancement due to wall nucleation. Thus,

$$\tau_w = \frac{f_{2\Phi,l}}{2} \cdot \rho_l \cdot V_l^2 \tag{4-188}$$

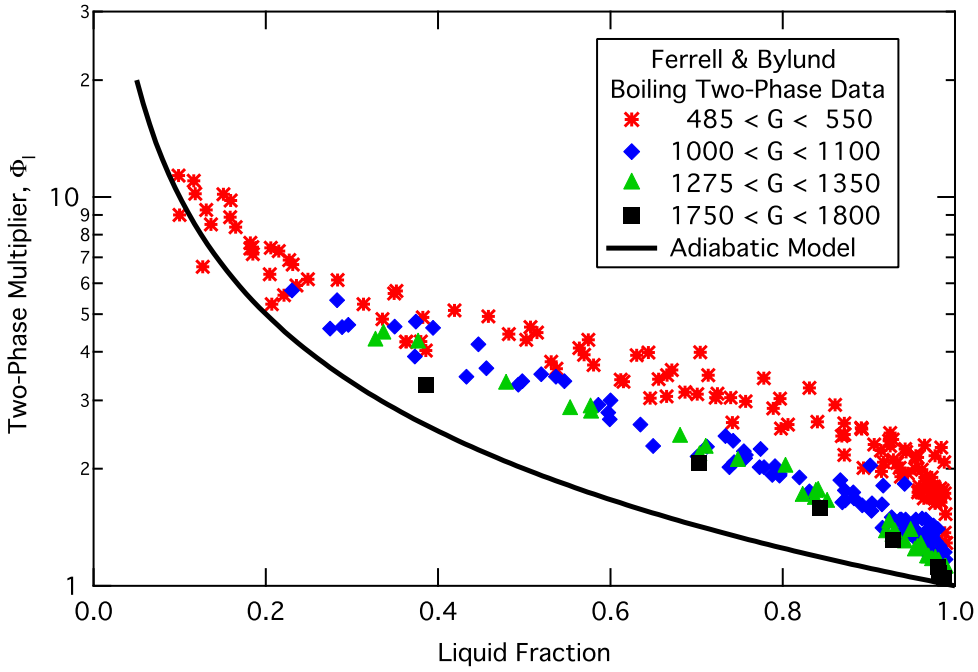

Figure. 4-21. Effect of nucleate boiling on the two-phase multiplier.

and the bubble diameter becomes a function of mass flux in addition to pressure.

From an examination of Ferrell & Bylund's data, it was determined that in addition to the bubble diameter this correction factor would also have to be a function of void fraction. The resulting model employs a curve fit for the void fraction dependence and should be considered empirical in nature. The model is then given by

$$C_{NB} = 155 \cdot \left(\frac{d_B}{D_h}\right) \cdot \left[\alpha \cdot (1-\alpha)\right]^{0.62} \tag{4-189}$$

The two-phase multipliers computed using this empirical model are compared to the data of Ferrell & Bylund in Figure 4-22. The average error is essentially zero, while the standard deviation is less than 11%.

As with any empirical model, it is necessary to assure reasonable behavior when it is extrapolated outside of its database (as will happen during a transient system calculation). With respect to pressure, the database extends from about 4 to 17 bar, so most of the extrapolation is to higher pressures. As the pressure increases, the surface tension, and hence the bubble diameter, decreases thereby driving the correction factor to zero as the critical point is approached. This behavior is reasonable and so no explicit limit is needed.

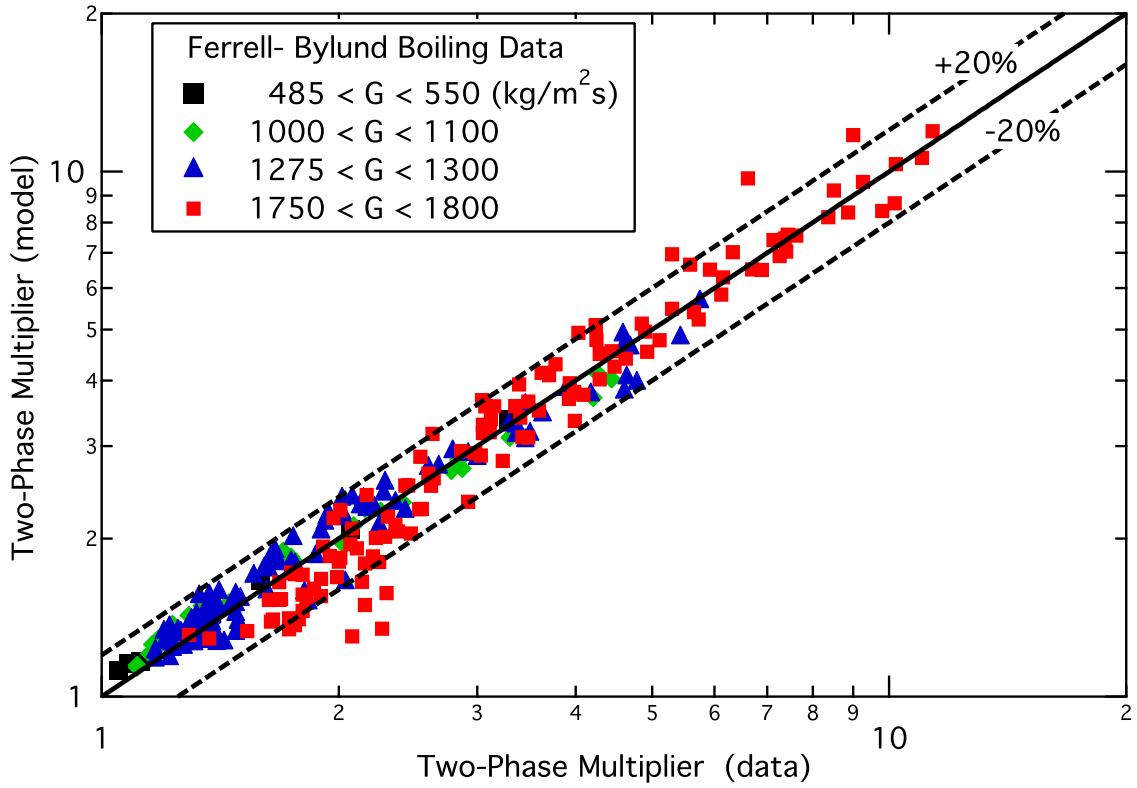

Figure. 4-22. Comparison of calculated and measured two-phase multiplier with the empirical correction factor for the wall nucleation effect.

The bubble diameter also is a strong function of the liquid mass flux and the database extends only from about 500 to 1800 (kg/m^2-s). With respect to the upper limit, as the mass flux increases significantly above 1800 (kg/m^2-s), the bubble diameter decreases and the wall nucleation effect disappears so that the two-phase multiplier approaches that for adiabatic flow. Again, this is reasonable behavior and no limit need be imposed. However, as the mass flux decreases below 500 (kg/m^2-s), the bubble diameter rapidly increases. As the correction factor is directly proportional to the bubble diameter, this introduces the possibility that unreasonably large two-phase multipliers will be calculated. It is possible to place limits on either the mass flux or the bubble diameter to ensure that this does not occur. The simplest approach, and the one implemented in TRACE, is to directly limit the correction factor itself, that is

$$C_{NB} = Min\left\{2\ ,\ 155\cdot\left(\frac{d_B}{D_h}\right)\cdot[\alpha\cdot(1-\alpha)]^{0.62}\right\} \tag{4-190}$$

Finally, the wall drag coefficient for the bubbly/slug regime with wall nucleation is:

$$C_{wl} = f_{wl} \cdot \frac{2\rho_l}{D_h} \cdot (1 + C_{NB})^2 \tag{4-191}$$

Transition from Bubbly/Slug to Annular/Mist

For the computation of interfacial drag, the transition between the bubbly/slug and the annular/mist regimes was handled by a power-law combination. (See the counterpart section titled ***Transition from Bubbly/Slug to Annular/Mist*** in ***Interfacial Drag***.) However, as the magnitude of the two-phase multipliers for these regimes is similar over the entire range of liquid fractions, a power-law combination is unsuitable for the wall drag. Consequently, an explicit ramp as a function of void fraction was introduced to provide a continuous definition of the wall drag coefficient. Based on observations of the data used to develop the model, the model for the bubbly/slug wall drag is applied up to a void fraction of 80%, and above void fractions of 90%, the annular flow model is applied. For values of the void fraction between 80% and 90%,

$$C_{wl} = wf_{BS} \cdot C_{wl,BS} + (1 - wf_{BS}) \cdot C_{wl,AM} \tag{4-192}$$

where the bubbly/slug weighting factor is

$$wf_{BS} = \left(\frac{0.9 - \alpha}{0.9 - 0.8} \right) \tag{4-193}$$

This completes the description of the wall drag models for the normal pre-CHF flow regimes. The next two sections describe the models for horizontal stratified flow and for the post-CHF flow regimes respectively.

Horizontal Stratified Flow Model

In horizontal stratified flow (see Figure 4-12), both the liquid and gas phases are in contact with the pipe wall, so the wall drag coefficient is specified for both phases. Taitel and Dukler (Ref. 4-28) gave the wall shear stresses as

$$\tau_{wl} = f_{wl} \frac{\rho_l V_l^2}{2} \tag{4-194}$$

$$\tau_{wg} = f_{wg} \frac{\rho_g V_g^2}{2}$$

where the friction factors are evaluated using

$$f_{wk} = \frac{0.046}{Re_k^{0.2}} \tag{4-195}$$

for turbulent flow, and

$$f_{wk} = \frac{16}{Re_k} \tag{4-196}$$

for laminar flow. The phasic Reynolds nos. are calculated from

$$Re_l = \frac{\rho_l V_l D_l}{\mu_l} \tag{4-197}$$

$$Re_g = \frac{\rho_g V_g D_g}{\mu_g}$$

with the phasic hydraulic diameters evaluated in the manner suggested by Agrawal et. al. (Ref. 4-37):

$$D_l = \frac{4A_l}{S_l} \tag{4-198}$$

$$D_g = \frac{4A_g}{(S_g + S_i)}$$

Note that this definition of the phasic hydraulic diameters implies that the wall drag to the liquid is similar to that for open channel flow and that of the gas phase to closed-duct flow.

From Eq. (4-194) and considering the surface area of the wall in contact with each phase, the wall drag coefficients are:

$$C_{wl} = f_{wl}\frac{P_l}{2} \cdot \frac{S_l}{A} \tag{4-199}$$

$$C_{wg} = f_{wg}\frac{P_g}{2} \cdot \frac{S_g}{A}$$

As the friction factors used by Taitel and Dukler, Eq. (4-195) and Eq. (4-196), are simply those for a pipe, the formula of Churchill, Eq. (4-166), is used in TRACE.

The determination of whether or not the flow is stratified is made using the criteria described in ***Stratification Criteria***. Should the flow regime be in the transition region, the wall drag coefficients are evaluated by a simple linear interpolation between the values calculated for stratified and non-stratified flow using the weighting factor given by Eq. (4-105),

$$C_{wk} = wf_{strat} \cdot C_{wk,\,strat} + (1 - wf_{strat}) \cdot C_{wk,\,ns} \tag{4-200}$$

This completes the description of the wall drag for the horizontal stratified flow regime. The following section describes the wall drag models for the inverted post-CHF flow regimes.

Post-CHF Flow Regimes

For the "inverted" post-CHF flow regimes, the wall surface temperature is beyond the Leidenfrost point and so only the gas phase is in contact with the wall. Consequently, wall-fluid shear only occurs for the gas phase and C_{wl} should be zero. As described below, the inverted annular regime is treated as a direct analog to the annular regime while the dispersed flow regime is treated using a model for particle-laden flows.

Inverted Annular

The inverted annular regime is treated as a direct "inverse" analog to the annular flow regime. That is, the frictional pressure gradient is computed from

$$\left.\frac{dP}{dz}\right|_f = -\Phi_g^2 \left[\frac{2f_{2\Phi,\,g}\,|G_g|\,G_g}{D_h \rho_g}\right] \tag{4-201}$$

in terms of the two-phase multiplier for the gas phase considered to flow alone in the channel, Φ_g^2. The friction factor, $f_{2\Phi,\,g}$, is the Fanning friction factor for the gas phase calculated from the Churchill formula with

$$Re_{2\Phi,\,g} = \frac{|G_g| D_h}{\mu_g} = \frac{\alpha\ \rho_g |V_g| D_h}{\mu_g} \tag{4-202}$$

The wall drag coefficient is then

$$C_{wg} = \Phi_g^2 \left[\frac{2f_{2\Phi,\,g}\,\alpha^2 \rho_g}{D_h}\right] \tag{4-203}$$

From the analogy with annular flow, the two-phase multiplier is simply

$$\Phi_g^2 = \frac{1}{\alpha^2} \tag{4-204}$$

and so the wall drag coefficient reduces to

$$C_{wg} = f_{2\Phi,g} \cdot \frac{2\rho_g}{D_h} \tag{4-205}$$

Dispersed Flow

The frictional pressure gradient for the dispersed flow regime is calculated using an empirical model for particle-laden gas flows developed by Pfeffer et. al. (Ref. 4-60). The pressure gradient is given by the formula for single-phase gas flow

$$\left.\frac{dP}{dz}\right|_f = -\frac{2f_{pg}|G_g|G_g}{D_h\rho_g} \tag{4-206}$$

with the gas phase friction factor replaced by the equivalent friction factor, f_{pg} , for a gas-particle mixture. The ratio of the friction factor for dilute suspensions was found to be a function of the loading ratio only. No significant dependence was found upon the gas Reynolds no., particle diameter, or particle density. They correlated this effective friction factor for dilute suspensions as

$$\frac{f_{pg}}{f_{wg}} = (1 + LF)^{0.3} \tag{4-207}$$

where LF is the loading factor and is given by

$$LF = \frac{\dot{m}_p}{\dot{m}_g} \tag{4-208}$$

For the case of dispersed flow, the loading factor becomes the ratio of the liquid to gas flow rate, so

$$LF = \frac{(1-\alpha)\ \rho_l\ V_l}{\alpha\ \rho_g\ V_g} \tag{4-209}$$

The TRACE implementation of this model uses the Churchill formula for the gas friction factor and limits the loading factor to be less than 12, the maximum value in the database used to develop the correlation. Then, the effective friction factor is

$$f_{pg} = f_{wg} \cdot \left[1 \; + \; Min\left(12 \, , \, LF\right) \right]^{0.3} \tag{4-210}$$

and the wall drag coefficient for dispersed flow is

$$C_{wg} = f_{pg} \cdot \frac{2\rho_g}{D_h} \tag{4-211}$$

As discussed above in ***Inverted Annular*** and ***Dispersed Flow***, the inverted annular regime is applied for void fractions less than 60%, while the dispersed flow regime is applied for void fractions greater than 90%. For intermediate values of the void fraction, a dispersed flow weighting factor is defined,

$$wf_{DF} = \left(\frac{\alpha - 0.6}{0.9 - 0.6} \right) \tag{4-212}$$

and a linear interpolation scheme is used, so

$$C_{wg} = (1 - wf_{DF}) \cdot C_{wg\,,\,IA} \; + wf_{DF} \cdot C_{wg\,,\,DF} \tag{4-213}$$

Transition to Pre-CHF Regimes

As was done for interfacial drag, the determination between the normal pre-CHF flow regimes and the inverted post-CHF flow regimes for wall drag is made using the axial locations of the bottom and top quench fronts. For momentum cells that are completely quenched, the normal pre-CHF regimes are used. Whereas, for momentum cells whose heat transfer surface is in film boiling, (i.e., they are located entirely between the top and bottom quench fronts), the inverted post-CHF flow regimes are used. Finally, for cells that are partially quenched, a linear interpolation between the wall drag coefficients for the pre- and post-CHF values is performed.

Let f_Q represent the fraction of the momentum cell that is quenched. Then,

$$C_{wl} = f_Q \cdot C_{wl}\big|_{pre-CHF} \tag{4-214}$$

$$C_{wg} = (1 - f_Q) \cdot C_{wg}\big|_{post-CHF} + f_Q \cdot C_{wg}\big|_{pre-CHF}$$

Note, the wall-gas drag coefficient for the pre-CHF regime may be non-zero (for example, during the transition from annular/mist to single-phase gas flow) and so is included in Eq. (4-214).

References

4-1 N. Zuber and J. Findlay, "Average Volumetric Concentration in Two-Phase Flow Systems," Trans. ASME J. of Heat Trans., series C, 87, 453-468 (1965).

4-2 G. B. Wallis, "One-Dimensional Two-Phase Flow," Chapter 9, McGraw-Hill, New York, NY (1969).

4-3 M. Ishii, "One-Dimensional Drift-Flux Model and Constitutive Equations for Relative Motion Between Phases in Various Flow Regimes," Argonne National Laboratory report ANL-77-47 (1977).

4-4 I. Kataoka and M. Ishii, "Drift Flux Model for Large Diameter Pipe and New Correlation for Pool Void Fraction," Int. J. Heat Mass Transfer, 30, 1927-1939 (1987).

4-5 M. Ishii and K. Mishima, "Two-Fluid Model and Hydrodynamic Constitutive Relations," Nucl. Eng. and Design, 82, 107-126 (1984).

4-6 D. Bestion, "Interfacial Friction Determination for the 1-D Six Equation Two-Fluid Model Used in the CATHARE Code," European Two-Phase Flow Group Meeting, Marchwood, 3-7 June 1985.

4-7 M. A. Salay, "Evaluation of Interfacial Drag Models for Use in TRAC-M Rod Bundle Compoents with Validation Against Steady-State and Transient Boil-Off Experiments," Ph.D. Thesis, Univ. of Maryland, 2001.

4-8 G. B. Wallis, "Annular Two-Phase Flow, Part 1: A Simple Theory," J. of Basic Eng., 59-72, 1970.

4-9 I. Kataoka and M. Ishii, "Prediction of Pool Void Fraction by New Drift Flux Correlation," Argonne National Laboratory Report ANL-86-29 (NUREG/CR-4657), (1986).

4-10 R. V. Baily, P. C. Zmola, F. M. Taylor and R. J. Planchet, "Transport of Gases Through Liquid-Gas Mixture," paper presented at the AIChE New Orleans Meeting (1956). Taken from secondary reference (4-9).

4-11 P. Behringer, "Steiggeshwindigheit von Dampfblasen in Kesselrohrev," V.D.I. Forschungsheft, 365 (1934). Taken from secondary reference (4-9).

4-12 P. Coddington and R. Macian, "A Study of the Performance of Void Fraction Correlations Used in the Context of Drift-Flux Two-Phase Flow Models," Nucl. Eng. Design, 215, 199-216, 2002.

4-13 O. Nylund, et al., "Hydrodynamic and Heat Transfer Measurements on a Full-Scale Simulated 36-Rod Marviken Fuel Element with Uniform Heat Flux Distribution," FRIGG Loop Project, FRIGG-2, 1968.

4-14 C. Asali, T.J. Hanratty and P. Andreussi, "Interfacial Drag and Film Height for Vertical Annular Flow," AIChE J., 31 (6), 895-902, 1985.

4-15 Andreussi and S. Zanelli, "Downward Annular and Annular-Mist Flow of Air-Water Mixtures," from Two-Phase Momentum, Heat and Mass Transfer in Chemical, Process, and Energy Engineering Systems, Volume 1, Hemisphere Publishing, 1978.

4-16 M. Ishii and K. Mishima, "Droplet Entrainment Correlation in Annular Two-Phase Flow," Int. J. Heat Mass Transf., 32(10),1835-1845, 1989.

4-17 M. Ishii and M. A. Grolmes, "Inception Criteria for Droplet Entrainment in Two-Phase Concurrent Film Flow," AIChE Journal, 21 (2), 308-318, 1975.

4-18 G. B. Wallis, letter to the editor on "Phenomena of Liquid Transfer in Two-Phase Dispersed Annular Flow," Int. J. Heat Mass Transfer, 11, 783-785, 1968.

4-19 I. I. Paleev and B. S. Filippovich, "Phenomena of Liquid Transfer in Two-Phase Dispersed Annular Flow," Int. J. Heat Mass Transfer, 9, 1089-1093, 1966.

4-20 D. A. Steen, M. S. Thesis, Dartmouth College, 1964.

4-21 G. B. Wallis, "The Onset of Droplet Entrainment in Annular Gas-Liquid Flow," Report no. 62GL127, General Electric Co., Schenectady, N.Y., 1962.

4-22 D. A. Steen and G. B. Wallis, "The Transition from Annular to Annular-Mist Concurrent Two-Phase Down Flow," AEC Report NYO-3114-2, 1964.

4-23 M. Ishii and T.C. Chawla, "Local Drag Laws in Dispersed Two-Phase Flow," Argonne National Laboratory Report ANL-79-105 (NUREG/CR-1230), December 1979.

4-24 I. Kataoka, M. Ishii, and K. Mishima, "Generation and Size Distribution of Droplets in Annular Two-Phase Flow," Transactions of the ASME, 105, 230-238, June 1983.

4-25 R. A. Mugele and H. D. Evans, "Droplet Size Distribution in Sprays," Ind. Eng. Chem., 43, p. 1317, 1951.

4-26 M. W. Cappiello, "A Model for the Interfacial Shear in Vertical, Adiabatic, Annular-Mist Flow," Los Alamos National Laboratory Report, LA-CP-89-392, October 1989.

4-27 D. Barnea, "A Unified Model for Predicting Flow-Pattern Transitions for the Whole Range of Pipe Inclinations," Int. J. Multiphase Flow, 13 (1), 1-12, 1987.

4-28 Y. Taitel and A.E. Dukler, "A Model for Predicting Flow Regime Transitions in Horizontal And Near Horizontal Gas-Liquid Flow," AIChE Journal, 22 (1), 47-55, 1976.

4-29 H. Nakamura, "Slug Flow Transition in Horizontal Gas/Liquid Two-Phase Flows," Japan Atomic Energy Research Institute Report, JAERI-Research 96-022, May 1996.

4-30 Y. Anoda et. al., "Flow Regime Transition in High-Pressure Large-Diameter Horizontal Two-Phase Flow," 26th ASME/AIChE/ANS National Heat Transfer Conference, Philadelphia, 1989.

4-31 W.G. Choe, L. Weinberg and J. Weisman, "Observation and Correlation of Flow Pattern Transition in Horizontal, Co-Current Gas-Liquid Flow," in Two-Phase Transport and Reactor Safety (Edited by T.N. Veziroglu & S. Kakac), Hemisphere, Washington, 1978.

4-32 J.W. Spore et. al., "TRAC-PF1/Mod2: Volume I. Theory Manual," NUREG/CR-5673, 1993.

4-33 H.J. Richter et. al., "De-entrainment and Counter-Current Air-Water Flow in a Model PWR Hot Leg," NRC-0193-9, 1978.

4-34 MPR Associates, Inc., "Summary of Results from the UPTF Hot Leg Separate Effects Test, Comparison to Scaled Tests and Application to U.S. Pressurized Water Reactors," MPR Report MPR-1024, September 1987.

4-35 A. Ohnuki, H. Adachi and Y. Murao, "Scale Effects on Countercurrent Gas-Liquid Flow in Horizontal Tube Connected to Inclined Riser," ANS National Heat Transfer Conference, Pittsburgh, Pennsylvania, pp. 40-49, 1987.

4-36 S.W. Churchill, "Friction Factor Equations Spans All Fluid-Flow Regimes," Chemical Eng., November, 91-92, 1977.

4-37 S.S. Agrawal, G.A. Gregory and G.W. Govier, "An Analysis of Horizontal Stratified Two-Phase Flow in Pipes," Can. J. Chem. Eng., 51, 280-286, 1973.

4-38 F. de Cachard, "Development, Implementation, and Assessment of Specific Closure laws for Inverted-Annular Film-Boiling in a Two-Fluid Model," USNRC International Agreement Report, NUREG/IA-0133, 1996.

4-39 N. Andritsos and T.J. Hanratty, "Influence of Interfacial Waves in Stratified Gas-Liquid Flows," AIChE Journal, 33 (3), 444-454, 1987.

4-40 M. Kawaji and S. Banerjee, "Application of a Multifield Model to Reflooding of a Hot Vertical Tube: Part II - Analysis of Experimental Results," J. of Heat Transfer, 110, 710-720, 1988.

4-41 R. Clift, J.R. Grace and M.E. Weber, Bubbles, Drops, and Particles, Chapter 7, p. 179, Equation [7-14], Academic Press, New York, 1978.

4-42 J.F Richardson and W.N. Zaki, "Sedimentation and Fluidisation, Part 1," Trans. Instn. Chem. Engrs., 32, 35-53, 1954.

4-43 G.B. Wallis, "The Terminal Speed of Single Drops or Bubbles in an Infinite Medium," Int. J. Multiphase Flow, 1, 491-511, 1974.

4-44 J. Kitscha and G. Kocamustafaogullari, "Breakup Criteria for Fluid Particles," Int. J. Multiphase Flow, 15 (4), 573-588, 1989.

4-45 K.H. Ardron and P.C. Hall, "Droplet Hydrodynamics in the Dispersed Flow Regime in Bottom Flooding," in Transient Two-Phase Flow: Proceedings of the Third CSNI Specialist Meeting, edited by M.S. Plesset, N. Zuber, and I. Catton, Hemisphere Publishing Corp., pp. 205-225, 1983.

4-46 R. Clift, J.R. Grace and M.E. Weber, Bubbles, Drops, and Particles, Chapter 5, p. 111, Table 5.1, Academic Press, New York, 1978.

4-47 M. Rensizbulut and M.C. Yuen, "Numerical Study of Droplet Evaporation in a High-Temperature Stream," J. of Heat Transfer, 105, 389-397, 1983.

4-48 I. Kataoka and M. Ishii, "Mechanistic Modeling of Pool Entrainment Phenomenon," Int. J. of Heat Mass Transfer, 27 (11), 1999-2014, 1984.

4-49 M.A.Ebadian and Z.F. Dong, "Forced Convection, Internal Flow in Ducts," Chapter 5 of the Handbook of Heat Transfer, edited by W.M. Rohsenow, J.P. Hartnett and Y.I. Cho, 3rd edition, McGraw Hill, 1998.

4-50 G.B. Wallis, One-Dimensional Two-Phase Flow, Chapter 11, pp. 323-329, McGraw-Hill, New York, 1969.

4-51 G.F. Hewitt and N.S. Hall-Taylor, Annular Two-Phase Flow, Chapter 5, p. 79, Equation [5.4], Pergamon Press, Oxford, 1970.

4-52 S.E. Haaland, "Simple and Explicit Formulas for the Friction Factor in Turbulent Pipe Flow," J. Fluids Eng., 105, 89-90, 1983.

4-53 R.W. Lockhart and R.C. Martinelli, "Proposed Correlation of Data for Isothermal Two-Phase, Two-Component Flow in Pipes," Chem. Eng. Prog., 45 (1), 39-48, 1949.

4-54 J.K. Ferrell and D.M. Bylund, "A Study of Convection Boiling Inside Channels," Final Report, Volume II, North Carolina State University, Dept. of Chemical Eng., June 1966.

4-55 Y. Yamazaki and M. Shiba, "A Comparative Study on the Pressure Drop of Air-Water and Steam-Water Flows," in Cocurrent Gas-Liquid Flow, Proceedings of an International Symposium on Research in Cocurrent Gas-Liquid Flow at the University of Waterloo, pp. 359-380, Plenum Press, New York, 1969.

4-56 Y. Yamazaki and K. Yamaguchi, "Characteristics of Cocurrent Two-Phase Downflow in Tubes," J. Nuclear Science and Technolgy, 16 (4), 245-255, 1979.

4-57 J.K. Ferrell and J.W. McGee, "A Study of Convection Boiling Inside Channels," Final Report, Volume III, North Carolina State University, Dept. of Chemical Eng., June 1966.

4-58 J.G. Collier, Convective Boiling and Condensation, Chapter 6, pp. 186-188, McGraw-Hill, London, 1972.

4-59 S. Levy, "Forced Convection Subcooled Boiling Prediction of Vapor Volumetric Fraction," Int. J. Heat Mass Transfer, 10, 951-965, 1967.

4-60 R. Pfeffer, S. Rossetti and S. Lieblein, "Analysis and Correlation of Heat Transfer Coefficients and Friction Factor Data for Dilute Gas-Solid Suspensions," NASA TN D-3603, September 1966.

4-61 G. F. Hewitt, R. D. King and P. C. Lovegrove, "Techniques for Liquid Film and Pressure Drop Studies in Annular Two-Phase Flow," AERE-R3921, United Kingdom Atomic Energy Authority, Harwell, England, 1962.

4-62 L. E. Gill and G. F. Hewitt, "Further Data on the Upwards Annular Flow of Air-Water Mixtures," AERE-R3935, United Kingdom Atomic Energy Authority, Harwell, England, 1962.

4-63 L. E. Gill, G. F. Hewitt and D. N. Roberts, "Studies of the Behaviour of Disturbance Waves in Annular Flow in a Long Vertical Tube," AERE-R6012, United Kingdom Atomic Energy Authority, Harwell, England, 1969.

4-64 P. B. Whalley, G. F. Hewitt and P. Hutchinson, "Experimental Wave and Entrainment Measurements in Vertical Annular Two-Phase Flow," AERE-R7521, United Kingdom Atomic Energy Authority, Harwell, England, 1973.

5

Interfacial Heat Transfer Models

This chapter describes the TRACE interfacial heat transfer package.

Nomenclature

a = minor radius of prolate ellipsoid

A = flow area (m^2)

A_k = flow area of phase k in stratified flow (m^2)

A_i = interfacial (m^2)

A_i''' = interfacial area per unit volume (m^{-1})

b = major radius of prolate ellipsoid or the mass transfer driving potential

B_f = "blowing factor" for effect of mass transfer upon heat transfer

c_p = specific heat (J/kg-K)

C = concentration (kg/m3)

C^* = coefficient in formula for bubbly/slug interfacial area, see Eq. (5-29)

d = particle diameter, either bubble or drop, (m).

D = pipe diameter (m)

D_h = hydraulic diameter (m)

D^* = diameter used in bubbly/slug flow regime, see Eq. (5-30)

D_0 = diffusion coefficient (m^2/s)

e = ellipticity, see Eq. (5-96)

E = entrainment fraction

f_{fog} = "fog factor" to account for increase of sensible heat transfer due to mist formation

f_Q = fraction of a cell that is quenched, i.e., in the pre-CHF flow regime.

f_{wet} = fraction of the surface covered by a liquid film

g = gravitational acceleration (m/s^2)

G = mass flux (kg/m^2-s)

Gr = Grashof no., $[= (L^3 \cdot g \cdot \Delta\rho)/(\rho \cdot V^2)]$

h = heat transfer coefficient (W/m^2-K)

h_{ki} = interfacial heat transfer coefficient for phase k to interface (W/m^2-K)

h_{fg} = latent heat of evaporation (J/kg)

h_k = enthalpy of phase k (J/kg)

h_M = mass transfer coefficient (m/s)

H_0 = empirical constant in Eq. (5-38)

k = thermal conductivity (W/m-K)

La = Laplace no., equal to $\sqrt{\sigma / g\Delta\rho}$

M_W = molecular weight (kg/mole)

$N_{\mu k}$ = viscosity no. for phase k, $N_{\mu k} = \mu_k/(\rho_k \sigma La)^{1/2}$

Nu = Nusselt no., $(= h \cdot d/k)$

P = pressure (Pa)

P_{NC} = partial pressure of the non-condensable gas in the gas-vapor mixture (Pa)

P_v = vapor partial pressure of gas-vapor mixture (Pa)

P/D_r = pitch-to-diameter ratio for a rod bundle

Pe = Peclet no., $(= Re \cdot Pr)$

Pr = Prandtl no., $(= c_p \mu/k)$

q_{ki}'' = interfacial heat flux from phase k to the interface (W/m^2)

q_{ki}''' = interfacial heat transfer rate per unit volume from phase k (W/m^3)

R_s = gas constant for steam (J/kg-K)

Re = Reynolds no.

S = surface area (m^2)

S_i = width of gas-liquid interface in stratified flow

Sc = Schmidt no., $(= \nu / D_0)$

Sh = Sherwood no., $(= h_M \cdot d / D_0)$

T = temperature (K)

T_{sat} = saturation temperature at the total pressure (K)

T_{sv} = saturation temperature at the bulk vapor partial pressure (K)

V = velocity (m/s)

V_r = relative velocity (m/s)

V_∞ = terminal velocity in infinite medium (m/s)

V^*_{max} = maximum dimensionless circulation velocity at drop surface

wf = weighting factor

x_v = vapor mass fraction in gas-vapor mixture

Greek

α = void fraction (volume fraction of gas phase α_g)

α_k = volume fraction of phase k

δ = film thickness (m)

$\Delta\rho$ = density difference between liquid and gas phases (kg/m^3)

ρ = density (kg/m^3)

Γ = mass transfer rate per unit volume, negative for condensation, positive for evaporation (kg/m^3-s)

Γ_f = liquid film flow rate per unit wetted perimeter (kg/s-m)

Γ_i = mass transfer rate per unit volume due to interfacial heat transfer

Γ_{sub} = mass transfer rate per unit volume due to subcooled boiling

Γ'' = mass flux at interface due to condensation or evaporation (kg/m^2-s)

Γ''_0 = condensation mass flux calculated without variable property correction (kg/m^2-s)

λ_t = turbulent length scale

μ = viscosity (Ns/m^2)

ν = dynamic viscosity (m/s^2), $\nu = \mu / \rho$

σ = surface tension (N/m)

Subscripts

a = air

AM = annular/mist flow regime

b = bubble

c = condensation or the core region in annular/mist or inverted annular flow

$cond$ = condensation

$crit$ = critical value

d = drop

DB = dispersed-bubble

DF = dispersed flow regime

$drop$ = drop

$evap$ = evaporation

f = film

$film$ = the liquid film or a value at a reference "film" temperature

$flash$ = flashing

FC = forced convection

gl = gas-to-liquid

$Gnielinski$ = evaluated using Gnielinski correlation for turbulent forced convection

g = vapor-gas mixture

i = interface

IA = inverted annular

IS = inverted slug

k = phase index, l = liquid, and g = gas/vapor mixture

l = liquid

lam = laminar

li = liquid-to-interface

LB = large bubble (e.g., slug or Taylor cap bubbles)

ns = non-stratified

NC = non-condensable or natural convection

rad = component due to thermal radiation

$R-T$ = value from Rayleigh-Taylor instability

s = steam

sat = value at saturation

$sens$ = sensible heat component

$strat$ = stratified

sub = subcooled or subcooled boiling

sup = superheat

sv = saturation at the vapor partial pressure

SB = subcooled boiling

t = turbulent

$term$ = terminal

$turb$ = turbulent

v = vapor

vi = vapor-to-interface

V = based on equivalent volume

w = wall

Introduction

Interfacial heat transfer models are required for closure of both the mass and energy equations. In TRACE, the interfacial mass transfer rate per unit volume, Γ , is defined as the sum of the mass transfer rates from interfacial heat transfer and from subcooled boiling, as

$$\Gamma = \Gamma_i + \Gamma_{sub} \tag{5-1}$$

where Γ_i is the mass transfer rate per unit volume due to interfacial heat transfer, and Γ_{sub} is the mass transfer rate per unit volume due to subcooled boiling.

The mass transfer rate due to subcooled boiling will be described in **Chapter 6,** *Subcooled Boiling Model*. The mass transfer rate caused by interfacial heat transfer is evaluated from the thermal energy jump relation

$$\Gamma_i = \frac{q'''_{li} + q'''_{vi}}{(h_v^* - h_l^*)} \tag{5-2}$$

where q'''_{li} and q'''_{vi} are the interfacial heat transfer rates per unit volume for the liquid-to-interface and vapor-to-interface respectively. The denominator of Eq. (5-2) is not simply the latent heat, h_{fg}, but rather is given by

$$(h_v^* - h_l^*) = \begin{cases} (h_{v,sat} - h_l) \; ; \; \Gamma > 0 \\ (h_v - h_{l,sat}) \; ; \; \Gamma < 0 \end{cases} \tag{5-3}$$

where the second subscript *"sat"* denotes that the phase enthalpy is evaluated at saturation. This formulation correctly accounts for the sensible heat that is first required to bring the disappearing phase to saturation and that the generated phase appears at saturation.

In the TRACE numerical scheme, the liquid-gas interface is assumed to be at the saturation temperature corresponding to the bulk vapor partial pressure for the mass-energy computational cell. This temperature is denoted by T_{sv} where

$$T_{sv} = T_{sat}(P_v) \tag{5-4}$$

and is distinct from the saturation temperature, T_{sat}, computed from the total pressure,

$$T_{sat} = T_{sat}(P) \tag{5-5}$$

that is especially important for wall heat transfer processes such as nucleate boiling.

The interfacial heat transfer rates are then given by

$$q'''_{li} = h_{li} \cdot A'''_i \cdot (T_l - T_{sv}) \tag{5-6}$$

for the liquid-side heat transfer and by

$$q'''_{vi} = h_{vi} \cdot A'''_i \cdot (T_g - T_{sv}) \tag{5-7}$$

for the gas-side heat transfer. For the special case where the liquid is superheated with respect to saturation at the total pressure, $T_l > T_{sat}$, rapid nucleation will occur at any surface and the resulting interfacial heat transfer coefficient will increase dramatically as the level of liquid superheat increases. Under these conditions, Eq. (5-6) is modified to add an additional term for flashing, that is,

$$q'''_{li} = h_{li} \cdot A_i''' \cdot (T_l - T_{sv}) + h_{flash} \cdot A_i''' \cdot (T_l - T_{sat}) \tag{5-8}$$

When non-condensable gases are present, several modifications are made to the above equations. First, as discussed below in ***Default Model for Condensation***, the additional heat transfer resistance associated with the diffusion of the non-condensable gas either to or from the interface is added to that for the liquid-side heat transfer. Thus, Eq. (5-6) becomes

$$q_{li}''' = h_{li,NC} \cdot A_i''' \cdot (T_l - T_{sv}) \tag{5-9}$$

where the second subscript "*NC*" indicates that the non-condensable gas effect has been added.

Second, for the effect of non-condensable gases upon the gas-side heat transfer, the interfacial heat transfer coefficient determined using the models described below is multiplied by the relative partial pressure in the energy equation. Thus,

$$q_{vi}'' = \frac{P_v}{P} \cdot h_{vi} \cdot (T_g - T_{sv}) \tag{5-10}$$

which forces the vapor-interface heat transfer to zero as the vapor is depleted. Finally, allowance is made for the sensible heat transfer between the gas mixture and the liquid phase. The gas-liquid heat transfer coefficients described below are similarly multiplied by the relative partial pressure of the non-condensable gas, so that

$$q_{gl}'' = \frac{P_{NC}}{P} \cdot h_{gl} \cdot (T_g - T_l) \tag{5-11}$$

and the sensible heat transfer goes to zero as pure-steam conditions are approached.

Therefore, models need to be specified for the four heat transfer coefficients, h_{li}, h_{vi}, h_{flash}, and h_{gl}, and the associated interfacial area. These interfacial heat transfer coefficients are dependent upon the flow regime selected by the code. As explained above for the interfacial drag coefficient, TRACE considers three distinct classes of flow regimes:

- Pre-CHF: these consist of the bubbly/slug and the annular/mist regimes as explained in **Chapter 4,** *Pre-CHF Interfacial Drag Models*.
- Stratified: the horizontal stratified flow regime is available for 1-D components that are either horizontal or inclined as explained in **Chapter 4,** *Stratified Flow Interfacial Drag Models*.
- Post-CHF: this encompasses the "inverted" flow regimes that occur when the wall is too hot for liquid-wall contact, see **Chapter 4,** *Post-CHF Interfacial Drag Models*.

The interfacial heat transfer models used by TRACE for these flow regimes are detailed below in ***Pre-CHF Interfacial Heat Transfer Models***, ***Stratified Flow Interfacial Heat Transfer Models*** and ***Post-CHF Interfacial Heat Transfer Models***. In addition, a special section is added to describe the models for the effect on non-condensable gases upon condensation and evaporation.

Pre-CHF Interfacial Heat Transfer Models

In TRACE, as discussed previously for the evaluation of the interfacial drag coefficient, four principal flow regimes are considered for vertical flow as depicted in Figure 4-1 The three "bubbly" flow regimes, i.e., dispersed bubble, slug flow and Taylor cap bubble, are collectively referred to as the "bubbly/slug" flow regime. The models used for the interfacial heat transfer in the bubbly/slug and annular/mist flow regimes are applied to both vertical and horizontal geometries. However, for the horizontal case, a special horizontal stratification model is introduced as described in ***Stratified Flow Interfacial Heat Transfer Models*** below.

The pre-CHF flow regime map used for interfacial heat transfer is that of TRAC-PF1/MOD2, as depicted in Figure 5-1. The flow regime determination is primarily based on void fraction with the mass flux range for the Taylor cap or slug bubble flow regime limited. Both the region over which a flow regime is applied and the corresponding models for interfacial area and heat transfer coefficient are detailed below. Also, the churn regime, that is, the transition regime between the bubbly/slug and the annular/mist flow regimes, where the nature of the two-phase interface is not clearly defined, is approximated by interpolation between the values for the other regimes.

Bubbly Flow Regime

The upper limit of the void fraction for the dispersed bubble flow regime is nominally given a value of 30%. This value was chosen as it roughly corresponds to bubble concentrations where coalescence rates rapidly drive the regime towards either Taylor cap or slug flow. For high liquid flow rates, however, liquid phase turbulence can break-up the gas phase into small, dispersed

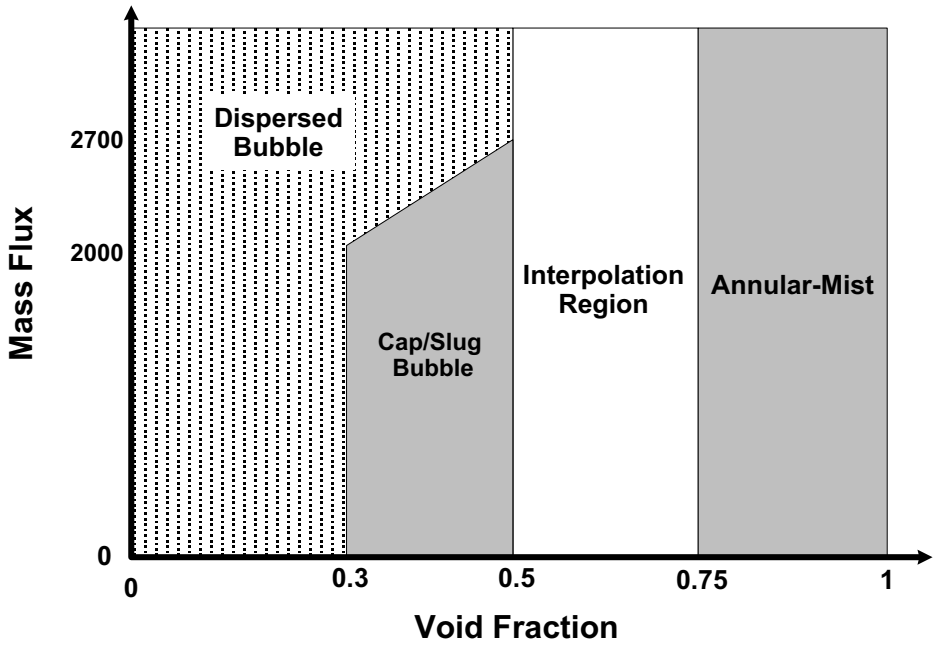

Figure. 5-1. Pre-CHF flow regime map for interfacial heat transfer.

bubbles. Choe et. al. (Ref. 4-31) give the criterion for this transition to homogeneous dispersed bubbly flow as a simple mass flux limit, specifically, that homogeneous flow exists for mass fluxes greater than about 2700 kg/m^2-s.

In TRACE, the Choe-Weisman mass flux criterion for the transition to dispersed bubble flow is implemented by a linear ramp on the maximum allowable volume fraction for the dispersed bubbles. That is,

$$\alpha_{DB} = \begin{cases} 0.3 & ; \quad G \leq 2000 (kg/m^2 s) \\ 0.3 + 0.2 \cdot \left(\dfrac{G - 2000}{2700 - 2000} \right) & ; \; 2000 < G < 2700 (kg/m^2 s) \\ 0.5 & ; \quad G \geq 2700 (kg/m^2 s) \end{cases} \tag{5-12}$$

The diameter of the dispersed bubbles is approximated by that for a distorted bubble and is a function of the Laplace coefficient, namely

$$d_{DB} = 2 \cdot La = 2 \cdot \sqrt{\sigma / g \Delta \rho} \tag{5-13}$$

and is constrained to be in the range

$$1.0 \times 10^{-4}(m) \leq d_{DB} \leq 0.9 \cdot D_h \tag{5-14}$$

If the void fraction is less than α_{DB} , the interfacial area for the dispersed bubbles is simply

$$A'''_{i,DB} = \frac{6 \cdot \alpha}{d_{DB}} \tag{5-15}$$

However, for larger values of the void fraction, a combination of small dispersed bubbles and large slug or cap bubbles is assumed to exist. For this case, Ishii and Mishima (Ref. 5-1) give the interfacial area concentration due to small bubbles as a function of the average void fraction within the liquid slug, so that

$$A'''_{i,DB} = \frac{6 \cdot \alpha_{DB}}{d_{DB}} \cdot \left(\frac{1-\alpha}{1-\alpha_{DB}}\right) \tag{5-16}$$

The interfacial area and heat transfer associated with the large slug or cap bubbles is described in the following section. It remains to calculate the interfacial heat transfer coefficient for the dispersed bubbles as it is the product, hA_i , that is needed for the energy equation.

For both evaporation and condensation, the heat transfer between the liquid and the bubble interface is modeled using the Ranz-Marshall correlation (Ref. 5-2) as recommended by Warrier et. al. (Ref. 5-3). The heat transfer coefficient is then

$$h_{li,DB} = \frac{k_l}{d_{DB}} \cdot Nu_{DB} \tag{5-17}$$

where the Nusselt no. is given by

$$Nu_{DB} = 2.0 + 0.6 \cdot Re_{DB}^{1/2} \cdot Pr_l^{1/3} \tag{5-18}$$

For high bubble Reynolds no. conditions, the values of the Nusselt no. given by the Ranz-Marshall correlation are similar but somewhat lower than those of the Chen-Mayinger correlation (Ref. 5-4) that was used in TRAC-PF1/MOD2. However, for low Reynolds no. conditions, the behavior of the Ranz-Marshall correlation is clearly superior as it correctly reduces to the steady state conduction solution for a sphere immersed in an infinite fluid (Ref. 5-5).

The bubble Reynolds no. used in Eq. (5-18) is a function of the dispersed bubble relative velocity and is defined

$$Re_{DB} = \frac{\rho_l \cdot V_{r,DB} \cdot d_{DB}}{\mu_l} \tag{5-19}$$

In practice, the dispersed bubble relative velocity cannot simply be assumed to be given by the phasic relative velocity, $|V_g - V_l|$, that results from the solution of the two-fluid momentum equations. This is because the gas field in TRACE can represent a combination of large and small bubbles, and so

$$V_{r,DB} \ll |V_g - V_l|$$

is generally true. To get a more accurate estimate of the dispersed bubble relative velocity, the bubble terminal velocity is used as an upper limit. Thus,

$$V_{r,DB} = Min\left[|V_g - V_l| , V_{DB,term} \right] \tag{5-20}$$

where the dispersed bubble terminal velocity is calculated for a distorted particle with the multi-particle correction of Richardson & Zaki (Ref. 4-42). For a single distorted particle, Wallis' formula (Ref. 4-43) gives

$$V_{r,\infty} = \sqrt{2}\left(\frac{\sigma \cdot g \cdot \Delta\rho}{\rho_l^2} \right)^{1/4} \tag{5-21}$$

and, applying the Richardson-Zaki correction, the multi-particle terminal velocity is

$$V_{DB,term} = V_{r,\infty} \cdot (1-\alpha)^{2.39} \tag{5-22}$$

Note – The exponent in Eq. (5-22) is incorrect in TRACE V5.0. It should be 1.39. This will be corrected in a follow-on bug fix release.

Normally, due both to its high values of heat transfer coefficient and interfacial area, the dispersed bubble component of the interfacial heat transfer dominates over that of the Taylor cap/slug bubble described below.

Eq. (5-18) gives the formula for the Nusselt no. for the liquid-side interfacial heat transfer. To complete the description, models are also needed for the gas-side heat transfer and, when non-condensable gases are present, for the sensible heat transfer between the gas and the liquid. In

TRACE, these heat transfer coefficients are simply set to the constant values that were used previously in TRAC-PF1/MOD2. That is,

$$h_{vi} = h_{gl} = 1000(\,W/m^2 K) \tag{5-23}$$

The vapor-interface heat transfer coefficient, h_{vi} , is seldom important in governing the mass transfer rate for bubbly flow and it is thought adequate to keep it at a constant value that is sufficiently high enough to prevent large departures from thermal equilibrium. For the sensible heat transfer when non-condensable gases are present, however, this argument does not hold. This is especially true as using Eq. (5-23) for h_{gl} ignores the heat transfer resistance on the liquid-side. A future update to TRACE 5.0 will correct this oversight.

When subcooled boiling is present, the liquid-side interfacial heat transfer for bubbly flow is modified to account for near-wall condensation. The TRACE model for this is described below in ***Modifications for Subcooled Boiling***. The following section describes the models for the large bubbles that occur in the cap bubble/slug flow regimes.

Cap Bubble/Slug Flow Regime

For void fractions greater than the dispersed bubble limit, α_{DB}, but less than 50%, the flow regime for interfacial heat transfer is considered to be either cap bubble or slug flow. In either case, the bubble diameter is much larger than for the dispersed bubbly regime, so that both the interfacial area and heat transfer coefficient are much smaller. Consequently, the component of the interfacial heat transfer due to these large bubbles is dwarfed by that of the smaller dispersed bubbles contained within the liquid slugs. Nevertheless, for completeness, the large bubble component is calculated and added to that of the dispersed bubbles, so that

$$(h_{li} \cdot A_i) = (h_{li} \cdot A_i)_{DB} + (h_{li} \cdot A_i)_{LB} \tag{5-24}$$

The approach taken to describe the interfacial heat transfer for cap and slug bubbles is similar to that used above for dispersed bubbles with the primary differences being the estimation of the bubble diameter, the interfacial area, and the limiting value of the relative velocity. To estimate the interfacial area, the first step is to determine whether the flow regime is cap bubble or slug flow. Kataoka and Ishii (Ref. 4-4) state that slug bubbles cannot be sustained for channels with a diameter much larger than $40La$. Similarly, the interface stability analysis of Kitscha and Kocamustafaogullari (Ref. 4-44) yields

$$d_{b,V} = 27.07 \cdot (1 + N_{\mu l})^{0.83} La \tag{5-25}$$

for the maximum stable bubble diameter, where $d_{b,V}$ is the volume equivalent diameter. For water, the liquid viscosity number is much less than unity and so,

$$d_{b,V} \approx 27 \cdot La \tag{5-26}$$

Using the geometry of an idealized cap bubble with a wake angle of 55°, the diameter of the base of a cap bubble would then be about $45La$. Further, assuming that a cap bubble will grow into a slug bubble when its diameter reaches about $0.9D_h$, the channel critical diameter for the transition to slug flow is then

$$D_{h,crit} \approx 50 \cdot La \tag{5-27}$$

So, for channels having a hydraulic diameter less than $D_{h,crit}$, large bubbles will be treated as slugs, while for larger diameter channels they will be Taylor cap bubbles.

For the cap bubble/slug regime, the interfacial area associated with the large bubbles is computed using the formula of Ishii and Mishima (Ref. 5-1), specifically

$$A'''_{i,LB} = \frac{C^*}{D^*} \cdot \left(\frac{\alpha - \alpha_{DB}}{1 - \alpha_{DB}} \right) \tag{5-28}$$

where the values of the coefficient C^* and the diameter D^* depend on whether or not the flow regime is slug or cap bubble and is a function of the channel hydraulic diameter. Namely,

$$C^* = \begin{cases} 4.5 \ ; \ D_h < D_{h,crit} \\ 16 \ ; \ D_h \geq D_{h,crit} \end{cases} \tag{5-29}$$

and

$$D^* = \begin{cases} D_h \ ; \ D_h < D_{h,crit} \\ D_{h,crit} \ ; \ D_h \geq D_{h,crit} \end{cases} \tag{5-30}$$

The liquid-side heat transfer coefficient for these large bubbles is

$$h_{li,LB} = \frac{k_l}{D^*} \cdot Nu_{LB} \tag{5-31}$$

where the Nusselt no. is computed using the Ranz-Marshall correlation Eq. (5-18) and the bubble Reynolds no. is

$$Re_{LB} = \frac{\rho_l \cdot V_{r,LB} \cdot D^*}{\mu_l} \tag{5-32}$$

As was the case for small dispersed bubbles, the relative velocity for the large bubbles cannot simply be taken to be the phasic velocity difference, $|V_g - V_l|$. Thus,

$$V_{r,LB} = Min\left\{ |V_g - V_l| , V_{LB,term} \right\} \tag{5-33}$$

An upper limit on the relative velocity for cap and slug bubbles is estimated using the formulas from Wallis (Ref. 4-43) for the terminal velocity of his "region 5" bubbles with the correction factor for tube radius. Define the non-dimensional bubble diameter as

$$d^*_{LB} = \frac{D^*}{D_h} \tag{5-34}$$

and a relative velocity in an infinite medium by

$$V_{r,\infty} = \frac{\sqrt{2}}{2} \cdot \frac{\sqrt{g \cdot \Delta\rho \cdot D^*}}{\rho_l} \tag{5-35}$$

Then, the limiting value of the relative velocity is

$$V_{LB,term} = \begin{cases} V_{r,\infty} & ; \quad d^*_{LB} < 0.125 \\ 1.13 \cdot V_{r,\infty} \cdot e^{-d^*_{LB}} & ; \; 0.125 < d^*_{LB} < 0.6 \\ 0.496 \cdot V_{r,\infty} / \sqrt{d^*_{LB}} & ; \quad d^*_{LB} \geq 0.6 \end{cases} \tag{5-36}$$

This completes the description for the liquid-side interfacial heat transfer for the large bubbles in the cap bubble/slug flow regimes. For both the gas-side, h_{vi} , and sensible heat transfer, h_{gl} , the constant values used for the dispersed bubbles are retained. The small bubble interfacial area is simply augmented by that for the large bubbles, e.g.,

$$(h_{vi} \cdot A_i) = h_{vi} \cdot (A_{i,DB} + A_{i,LB}) \tag{5-37}$$

Modifications for Subcooled Boiling

When subcooled boiling is present, the liquid-side interfacial heat transfer for bubbly flow is modified to account for near-wall condensation. For this effect, TRACE uses the model suggested by Lahey and Moody (see Eq. 5.174 in Reference 5-6), which is given by

$$q''_{cond} = H_0 \cdot \frac{D_h}{4} \cdot h_{fg} \cdot \frac{\rho_l \rho_g}{\Delta\rho} \cdot \alpha \cdot (T_l - T_{sv}) \tag{5-38}$$

where H_0 is an empirical constant and q''_{cond} is the interfacial heat flux due to near-wall condensation. The product of the interfacial heat transfer coefficient and interfacial area concentration for subcooled boiling is then

$$(h_{li} A'''_i)_{SB} = H_0 \cdot h_{fg} \cdot \frac{\rho_l \rho_g}{\Delta\rho} \cdot \alpha \tag{5-39}$$

Lahey and Moody suggest that

$$H_0 = 0.075(s - K)^{-1} \tag{5-40}$$

and this is the value used in TRACE. Also, to provide a reasonable value as the void fraction approaches zero, Eq. (5-39) is rewritten as

$$(h_{li} A'''_i)_{SB} = 0.075 \cdot h_{fg} \cdot \frac{\rho_l \rho_g}{\Delta\rho} \cdot Max[0.0001, \alpha] \tag{5-41}$$

This model is applied only when subcooled boiling is occurring, that is

$$\Gamma_{sub} > 0$$

and

$$T_l < T_{sv} .$$

Finally, as the condition of bulk boiling is approached, a smooth transition between the subcooled boiling model and that for normal bubbly flow is necessary. This is accomplished by using a simple void fraction ramp between values of 10% and 20%. The subcooled boiling weighting factor is defined

$$wf_{SB} = Max\{0\ ,\ Min[1\ ,\ 10 \cdot (0.2 - \alpha)]\} \tag{5-42}$$

and the interfacial heat transfer for bubbly flow is given by

$$(h_{li}A_i)_{DB} = (1 - wf_{SB}) \cdot (h_{li}A_i)_{DB} + wf_{SB} \cdot (h_{li}A_i)_{SB} \tag{5-43}$$

Interfacial Heat Transfer Models for the Annular/Mist Flow Regime

For void fractions in excess of 75%, the flow regime for interfacial heat transfer is assumed to be annular/mist. As was the case for the computation of interfacial drag, components for both an annular film and entrained droplets are calculated separately and then combined. For example,

$$(h_{li}A_i)_{AM} = (h_{li}A_i)_{film} + (h_{li}A_i)_{drops} \tag{5-44}$$

The models used for annular films are discussed first, followed by those for the entrained droplets.

Annular Film Models

For annular films, the most important quantity is the film thickness as it is the characteristic length for heat transfer. In TRACE, this characteristic length results directly from the solution of the two-fluid momentum equations that yield the void fraction as a function of wall drag, interfacial shear, and gravity. The film thickness is then calculated from the void fraction based on the geometry. For most components, the film thickness is computed using the formula for tube geometry, that is,

$$\delta = \frac{D_h}{2} \cdot (1 - \sqrt{\alpha}) \tag{5-45}$$

A special case is made for the downcomer region of the 3-D vessel component, here the film thickness is computed assuming the geometry of an annulus. So,

$$\delta = \frac{D_h}{2} \cdot (1 - \alpha) \tag{5-46}$$

In both cases, the film thickness is constrained to be greater than 10 μm. This value was selected as a limiting value because a film with that thickness gives a heat transfer coefficient of about the same magnitude as dropwise condensation.

The interfacial area is similarly calculated directly from the void fraction and hydraulic diameter,

$$A_i''' = \frac{4}{D_h} \cdot \sqrt{\alpha} \tag{5-47}$$

For cases where the surface is considered to be only partially wetted by the liquid film, this interfacial area is modified by the fraction of the surface wetted, as

$$A_i''' = \frac{4}{D_h} \cdot \sqrt{\alpha} \cdot f_{wet} \tag{5-48}$$

The fraction of the surface wetted by the film, f_{wet} , is estimated using Eq. (4-181).

The model for the liquid-side film interfacial heat transfer, $h_{li,film}$, has to be valid over a wide range of film Reynolds numbers: from a laminar falling film during condensation to a highly sheared turbulent film during forced convection evaporation. To accomplish this, models for both the turbulent and laminar regimes were implemented and are combined using power-law weighting as

$$h_{li,film} = \left[(h_{li,lam})^2 + (h_{li,turb})^2 \right]^{1/2} \tag{5-49}$$

For the laminar film, the condensation correlation of Kuhn et. al. (Ref. 5-7) was selected. This is an empirical correlation fitted to their pure steam condensation data for co-current downflow by Kuhn, Schrock and Peterson. It is given by

$$Nu_{cond} = 1 + 1.83 \times 10^{-4} \cdot Re_f \tag{5-50}$$

where the Nusselt no. is based on the film thickness,

$$Nu_{cond} = \frac{h_c \cdot \delta}{k_l} \tag{5-51}$$

and the film Reynolds no. is calculated from

$$Re_f = \frac{4 \cdot \Gamma_f}{\mu_l} = \frac{G_l \cdot D_h}{\mu_l} \tag{5-52}$$

The Kuhn-Schrock-Peterson empirical correlation is compared to its database in Figure 5-2 and to the well-known Kutateladze model (Ref. 5-8). From the form of Eq. (5-50), it is obvious that the Nusselt no. reduces to the correct value of one for conduction through a film as the film Reynolds no. goes to zero. The enhancement as the film Reynolds no. increases is attributed to the onset of

ripples though this enhancement is less than that of the Kutateladze model. From its database, the K-S-P correlation is applicable to films with Reynolds nos. in the range $50 \leq Re_f \leq 2000$. .

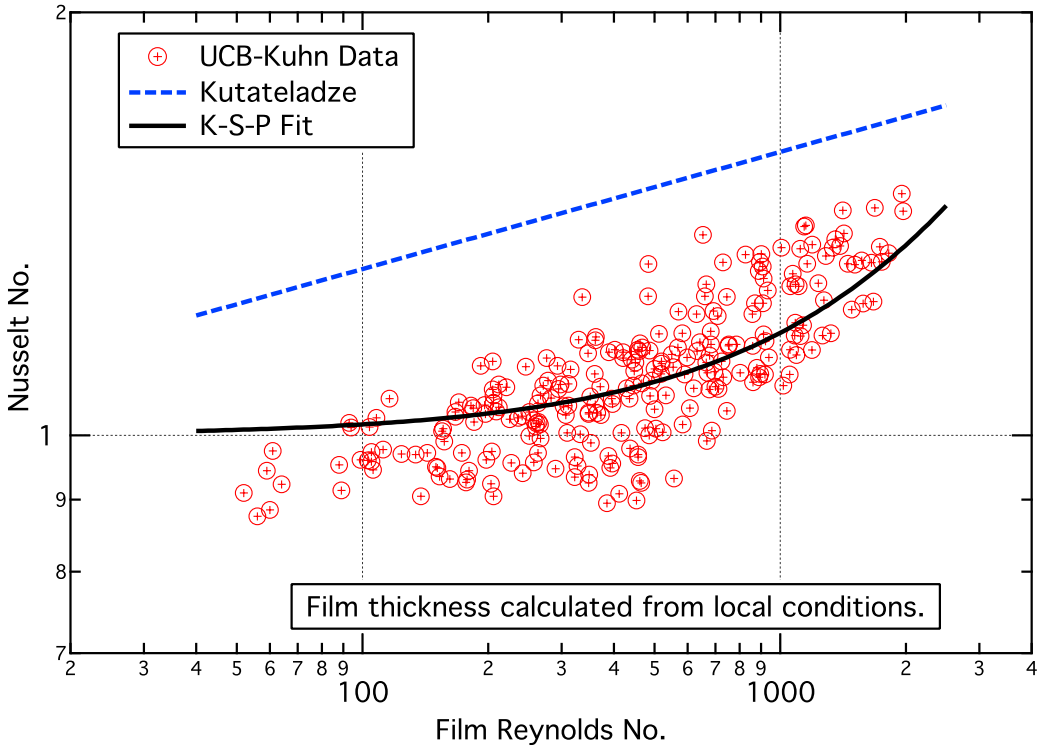

Figure. 5-2. Comparison of Kuhn-Schrock-Peterson correlation for laminar film condensation with its database.

In its original form, this correlation was for the Nusselt no. across a film during condensation and hence included heat transfer resistances for both the wall-liquid and liquid-interface. To translate it into a correlation for interfacial heat transfer, it is necessary to make an assumption regarding the apportioning of these two resistances. As the wall heat transfer package also uses the K-S-P correlation for laminar films (see **Chapter 6,** *Laminar Film Heat Transfer*), exactly how the resistances are apportioned is of little consequence as the total heat transfer resistance will remain the same. Consequently, it was decided to simply divide the total heat transfer resistance into two equal parts. Then, the K-S-P correlation, when used for interfacial heat transfer becomes

$$Nu_{li,\,lam} = 2 \cdot (1 + 1.83 \times 10^{-4} \cdot Re_f) \tag{5-53}$$

For turbulent films, the "turbulence-centered method" of Bankoff (Ref. 5-9) was initially selected due to its simplicity, its reasonable estimation of the Northwestern University interfacial condensation data (Ref. 5-10), and its semi-theoretical basis [Banerjee (Ref. 5-11), and Theofanus (Ref. 5-12)]. This model is simply given by

$$Nu_t = 0.25 \cdot Re_t^{3/4} \cdot Pr_l^{1/2} \tag{5-54}$$

where the Nusselt no. is defined using a turbulent length scale,

$$Nu_t = \frac{h \cdot \lambda_t}{k_l}$$

and the Reynolds no. is defined using turbulent length and velocity scales,

$$Re_t = \frac{V_t \cdot \lambda_t}{\nu_l}$$

Bankoff (Ref. 5-9) chose the film thickness for the length scale and 0.3 times the film velocity for the velocity scale. Substituting these into Eq. (5-54) yields

$$Nu_{li,\,turb} = 0.036 \cdot Re_f^{3/4} \cdot Pr_l^{1/2} \tag{5-55}$$

for the Nusselt no. as a function of the film Reynolds no. Further comparisons with the Northwestern University condensation data revealed that the values of the Nusselt no. from Eq. (5-55) were inflated somewhat due to the inclusion of data points with significant inlet effects. Omitting these data points resulted in a "modified Bankoff" model given by

$$Nu_{li,\,turb} = 0.027 \cdot Re_f^{3/4} \cdot Pr_l^{1/2} \tag{5-56}$$

During the developmental assessment of TRACE for tube condensation with pure steam, it was determined that using Eq. (5-56) resulted in a significant over-prediction of the heat transfer for films with Reynolds nos. in the transition region. To remedy this problem, the single-phase forced convection heat transfer correlation of Gnielinski (see **Chapter 6,** *Single-Phase Liquid Convection*) was adapted for use as an interfacial heat transfer model. As the modified Bankoff model is considered to be reasonably accurate over the range of its database, $10,000 < Re_f < 50,000$, a multiplier was put on the Gnielinski correlation so that it would match the values given by the modified Bankoff model in this range. Thus,

$$Nu_{li,\,turb} = 0.7 \cdot Nu_{Gnielinski} \tag{5-57}$$

The results of this adaptation are shown in Figure 5-3. As can been seen from this figure, using a multiplier of 0.7 on the Gnielinski correlation does a good job of matching the modified Bankoff model for high Reynolds no. conditions. Also, the large over-prediction of the Nusselt no. in the transition region is corrected.

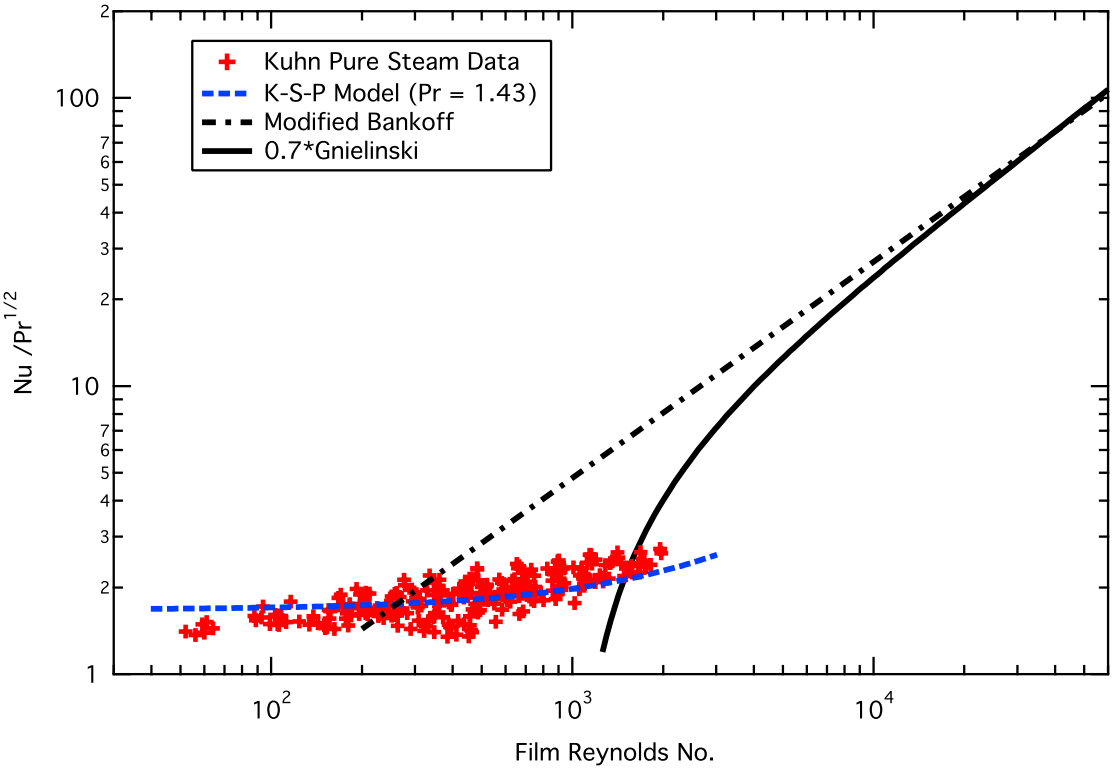

Figure. 5-3. Illustration of transition region for the Bankoff and Gnielinski models.

For the annular/mist flow regime, the gas-side interfacial heat transfer is considered to be of secondary importance. Consequently, no changes were made to the legacy TRAC-PF1/MOD2 models. Thus, for the vapor-interface heat transfer coefficient, we have

$$h_{vi} = \frac{k_g}{D_c} \cdot Nu_{vi} \tag{5-58}$$

where D_c is the diameter of the annular core approximated by

$$D_c \approx \sqrt{\alpha} \cdot D_h \tag{5-59}$$

The vapor-interface Nusselt no. is taken to be the maximum of that given by the Dittus-Boelter correlation (Ref. 5-13) for turbulent convection and a constant value of 4 for laminar flow in a tube. That is,

$$Nu_{vi} = Max\{4\ ,\ 0.23 \cdot Re_c^{0.8} \cdot Pr_g^{0.4}\} \tag{5-60}$$

where the Reynolds no. for the annular core is

$$Re_c = \frac{G_g \cdot D_c}{\mu_g} \tag{5-61}$$

For the sensible heat transfer between the gas and the liquid that occurs when non-condensable gases are present, Eq. (5-60) is also used. Though, as in the case for bubbly flow discussed above, this approach ignores the heat transfer resistance associated with the liquid film, this is not significant as

$$h_{li} \gg h_{vi}$$

for annular flow, and so

$$h_{gi} \approx h_{vi}$$

is a reasonable approximation. This completes the description of the interfacial heat transfer models for the annular film region. Those for heat transfer to/from the entrained droplets are described below.

Entrained Droplet Models

For droplet heat transfer, the characteristic length is the droplet diameter. To estimate the Sauter mean diameter for the droplets in the annular/mist flow regime, Eq. (4-73) is used, as detailed previously in **Chapter 4,** *Annular/Mist Flow Regime*. Similarly, the droplet interfacial area concentration is given by Eq. (4-68) except that the droplet projected area is translated to its surface area. Thus,

$$A'''_{i,drop} = \frac{6 \cdot \alpha \cdot \alpha_d}{(1-\alpha_d) \cdot d_d} \tag{5-62}$$

where α_d is the fraction of the annular core region occupied by the droplets. To estimate this quantity requires both the knowledge of the entrained fraction and the droplet velocity. The entrained fraction is calculated using either Eq. (4-52) or Eq. (4-59) depending upon the channel hydraulic diameter. As was done for the calculation of the droplet interfacial drag, the assumption is made to approximate the droplet velocity by that of the gas in the annular core region, thus Eq. (4-66) is again used to evaluate α_d .

With the droplet diameter and interfacial area thus specified, it remains to describe the models for the interfacial heat transfer coefficients $h_{li,d}$ and $h_{vi,d}$, and for the sensible heat transfer, $h_{gl,d}$. For the liquid-side, the rate of heat transfer between the drop and its surface is governed

by parameters such as the exposure time of the droplet and the internal circulation within the droplet. As both of these are highly uncertain, a simple model has been selected, namely the asymptotic value given by Kronig and Brink (Ref. 5-14). Thus,

$$h_{li,d} = 2 \cdot \pi^2 \cdot \frac{k_l}{d_d} \tag{5-63}$$

During both condensation and evaporation, the vapor-side heat transfer coefficient is calculated using the correlation developed by Ryskin (Ref. 5-15),

$$Nu_{vi,d} = 2 + \sqrt{V^*_{max} \cdot Pe} \tag{5-64}$$

where the Nusselt and Peclet nos. are defined as

$$Nu_{vi,d} = \frac{h_{vi,d} \cdot d_d}{k_g} \tag{5-65}$$

and

$$Pe = \frac{\rho_g \cdot c_{P,g} \cdot d_d \cdot V_r}{k_g} \tag{5-66}$$

respectively. The drop relative velocity appearing in Eq. (5-65) and Eq. (5-66) is calculated from a force balance between gravity and interfacial drag using a drop drag coefficient of 0.44, which yields

$$V_r = 2.462 \sqrt{\frac{g \cdot \Delta\rho}{\rho_g} \frac{d_d}{2}} \tag{5-67}$$

In Eq. (5-64), V^*_{max} is the maximum dimensionless circulation velocity at the surface of the drop. Ryskin (Ref. 5-15) defines this as

$$V^*_{max} = \frac{1.5}{1 + \frac{2.8(1+2\lambda)(2+3\kappa)}{(2+3\lambda)\sqrt{Re_d}}} \tag{5-68}$$

where

$$Re_d = \frac{\rho_g \cdot V_r \cdot d_d}{\mu_g} , \tag{5-69}$$

$$\lambda = \sqrt{\frac{\rho_l \mu_l}{\rho_g \mu_g}} , \tag{5-70}$$

and

$$\kappa = \mu_l / \mu_g . \tag{5-71}$$

In the evaluation of Eq. (5-68), the drop Reynolds no. is first constrained to be in the range $0.5 \leq Re_d \leq 200$, and the resulting value of the maximum dimensionless circulation velocity to be in the range $0.0001 \leq V^*_{max} \leq 1.0$.

The same model defined by Eqs. (5-64) through (5-71) for the droplet gas-side interfacial heat transfer are also used for the direct sensible heat transfer when non-condensable gases are present. That is,

$$h_{gl,d} = h_{vi,d} .$$

Interpolation Region

The interfacial heat transfer coefficients for the churn regime, that is, the transition regime between the bubbly/slug and the annular/mist flow regimes, where the nature of the two-phase interface is not clearly defined, are approximated by interpolation between the values for the other two regimes. In TRACE, this interpolation region covers the void fraction range from 50% to 75%. The procedure to effect this interpolation is described below.

First, the interfacial heat transfer coefficients are evaluated for the bubbly/slug regime with the void fraction set to the maximum value for that regime, that is, $\alpha_{BS} = 0.5$. Then, the values for the annular/mist regime are calculated with the void fraction set to the minimum value for that regime, i.e., $\alpha_{AM} = 0.75$. A weighting factor is then defined by

$$wf_{AM} = \left(\frac{\alpha - 0.5}{0.75 - 0.5} \right) \tag{5-72}$$

Both the interfacial and sensible heat transfer coefficients are then calculated using linear interpolation as

$$h_{ki} \cdot A_i = wf_{AM} \cdot (h_{ki} \cdot A_i)_{AM} + (1 - wf_{AM}) \cdot (h_{ki} \cdot A_i)_{BS} \ . \tag{5-73}$$

Flashing Model

When the liquid is superheated relative to the saturation temperature at the total pressure, i.e., $T_l > T_{sat}$, a special flashing model is invoked. Namely,

$$(h_{li} \cdot A_i''')_{flash} = 1 \times 10^7 \cdot Max\left\{1 \ , \ Min\left[20 \ , \ 20(T_l - T_{sat})\right]\right\} \tag{5-74}$$

The basis for this model is its high magnitude, which prevents the liquid phase from becoming highly super-heated. This model is flow regime independent and is used for all flow patterns.

Stratified Flow Interfacial Heat Transfer Models

For horizontal and inclined pipes, there exists the possibility for the flow to become stratified at low velocity conditions as gravity causes the phases to separate. Figure 4-9 gives a schematic representation of some of the commonly recognized horizontal flow regimes. This section will describe the model used for the "stratified smooth" and "stratified wavy" flow regimes for the liquid-side interfacial heat transfer. Also, the interpolation between stratified and non-stratified regimes is given.

The interfacial area concentration is the same as that given by Eq. (4-107) for interfacial drag. That is,

$$A_i''' = \frac{S_i}{A} \tag{4-107}$$

where S_i is the width of the stratified two-phase interface as depicted in Figure 4-12.

The critical length for the liquid-side heat transfer is the height of the liquid layer, h_l . This height is calculated from the void fraction assuming that the pipe has a cylindrical cross-section. To facilitate this calculation, a curve-fit to the geometrical formula is used. So, for the case where the pipe is more than half full, i.e., $0.001 \leq \alpha \leq 0.5$, the curve-fit is given by

$$\frac{h_l}{D} = 1 - 0.70269591 \cdot \alpha^{2/3} - 0.34146667 \cdot \alpha - 0.161023911 \cdot \alpha^2 \tag{5-75}$$

and if $\alpha < 0.001$,

$$\frac{h_l}{D} = 1 - 7.612668 \cdot \alpha \tag{5-76}$$

Conversely, for the case where the pipe is more than half empty, i.e., $\alpha > 0.5$, Eq. (5-75) and Eq. (5-76) are rewritten as a function of the liquid volume fraction:

$$\frac{h_l}{D} = 0.70269591 \cdot \alpha_l^{2/3} + 0.034146667 \cdot \alpha_l + 0.161023911 \cdot \alpha_l^2 \tag{5-77}$$

and if $\alpha_l < 0.001$,

$$\frac{h_l}{D} = 7.612668 \cdot \alpha_l \tag{5-78}$$

For the liquid-side interfacial heat transfer coefficient, we have

$$h_{li} = \frac{k_l}{h_l} \cdot Nu_{li} \ , \tag{5-79}$$

where the Nusselt no. is given by the same models as were used for the liquid film in annular flow [see Eqs. (5-49), (5-53), and (5-57)]. For stratified flow, however, the Reynolds no. is calculated using Eq. (4-197) which makes use of the "liquid-phase hydraulic diameter" defined by Eq. (4-198).

For stratified flow, no data on interfacial condensation for the laminar flow regime was found. Though the K-S-P correlation was developed for condensation on slightly sheared falling films, it yields values only slightly greater than for steady conduction in laminar flow and thus should provide a reasonable lower bound for the heat transfer.

For turbulent stratified flow, we have the data produced in the series of condensation experiments conducted at Northwestern University. These experiments included test configurations for co-current horizontal flow (Ref. 5-10), counter-current horizontal flow (Ref. 5-16) with a pipe inclination angle of 4^o, and counter-current vertical flow (Ref. 5-16) with a pipe inclination angle of 87^o. Figure 5-4 compares all of the data from these three experiments to the models used in TRACE. For the co-current horizontal data, either the modified Bankoff or the adaptation of the Gnielinski correlation used in TRACE, provides a reasonable lower bound to the data. As

explained above in ***Interfacial Heat Transfer Models for the Annular/Mist Flow Regime***, a significant entrance length effect was found in this data and the Bankoff correlation was reduced by 25% to better fit the data in the fully-developed region. Consequently, the data points corresponding to the inlet region are under-predicted.

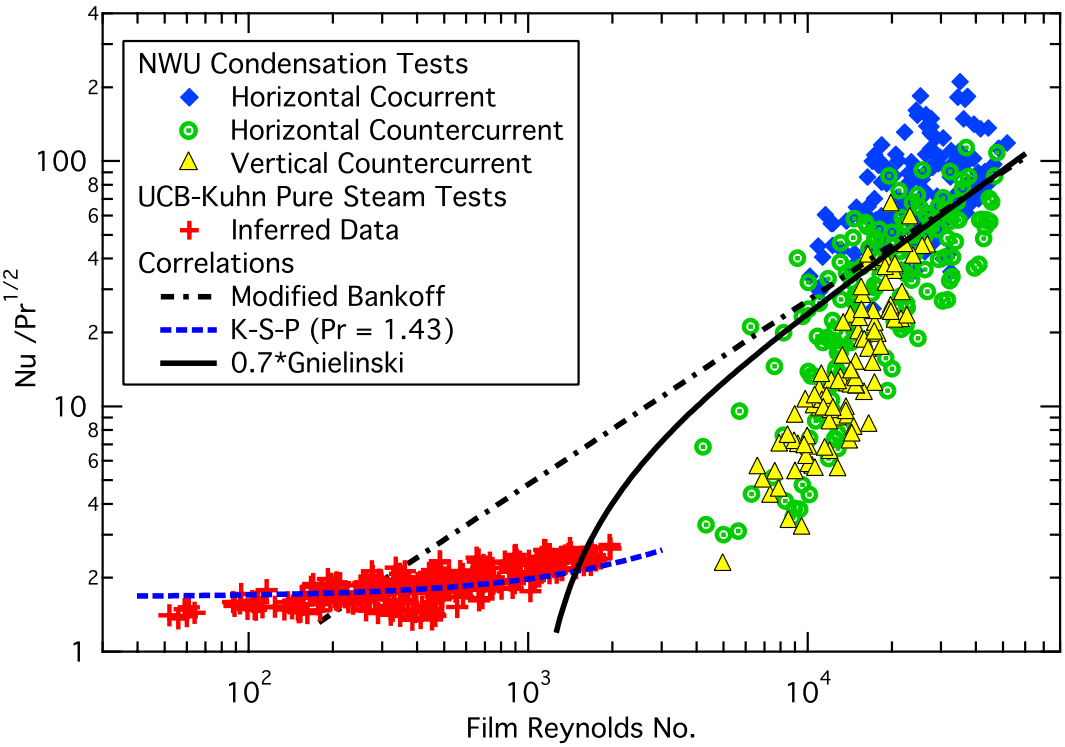

Figure. 5-4. Comparison of Bankoff and Gnielinski correlations with the Northwestern University condensation data.

The counter-current horizontal flow data are also reasonably well represented by the TRACE model as long as the film Reynolds no. has a value greater than about 10^4. However, for the transition region, $2,000 < Re_f < 10,000$, the TRACE model consistently over-predicts the heat transfer for both the horizontal and vertical counter-current flow data.

Of more concern than the apparent over-prediction in the transition region is the capability of the model to scale to larger Reynolds no. conditions. The maximum value in the NWU database is only about 5×10^4, whereas in a PWR cold leg during ECC injection the Reynolds no. can range from about 4×10^5 during LPCI to about 4×10^6 during accumulator injection for LBLOCA conditions. Consequently, due to the large amount of extrapolation that could be expected, the interfacial heat transfer coefficient from Eq. (5-79) is limited to the maximum value present in the NWU database, namely

$$h_{li} = Min\{2.5\times10^{4}\ ,\ h_{li}\} \tag{5-80}$$

Additionally, it should be noted that all of the NWU data was taken at atmospheric conditions and so pressure scaling could not be established.

Transition to Non-Stratified Flow

As was the case for the interfacial drag coefficients, there exists the potential for order-of-magnitude differences between the interfacial heat transfer for the stratified and non-stratified flow regimes. The section ***Stratified Flow Interfacial Drag Models*** in **Chapter 4** detailed the criteria used to determine whether or not the flow is stratified. The weighting factor for stratified flow, wf_{strat}, determined in the calculation of the interfacial drag is also used for the interfacial heat transfer and is not repeated here [see Eq. (4-95) through Eq. (4-105)].

When the stratified flow weighting factor is greater than zero, the interfacial heat transfer coefficient is calculated from

$$h_{li}\cdot A_i = (h_{li}\cdot A_i)^{n}_{strat}\cdot(h_{li}\cdot A_i)^{(1-n)}_{ns} \tag{5-81}$$

where the exponent, n , is set equal to wf_{strat} .

Post-CHF Interfacial Heat Transfer Models

The post-CHF models are used to describe the interfacial heat transfer for the "inverted" flow regimes that occur when the surface temperature is too hot for the liquid phase to contact the wall. These regimes are shown schematically in Figure 4-13 and are the same as those described in **Chapter 4,** *Post-CHF Interfacial Drag Models*.

The determination between the normal pre-CHF flow regimes and the inverted post-CHF flow regimes is made using the axial locations of the bottom and top quench fronts. For mass/energy computational volumes that are completely quenched, the normal pre-CHF regimes are used. Whereas, for computational volumes whose heat transfer surface is in film boiling, (i.e., they are located entirely between the top and bottom quench fronts), the inverted post-CHF regimes are used. Finally, for computational volumes that are partially quenched, an interpolation between the interfacial heat transfer for pre- and post-CHF values is performed as explained in ***Transition to Pre-CHF Regimes***.

Three principal inverted flow regimes are modeled in TRACE for post-CHF conditions: inverted annular, inverted slug, and dispersed flow. The region over which each of these post-CHF regimes is applied is shown in Figure 4-14. The models used for the evaluation of the interfacial

heat transfer for each of these flow regimes are described in the following sections along with the transition to pre-CHF regimes.

Inverted Annular

During film boiling, when the liquid phase is significantly subcooled, only a thin vapor film separates the hot surface from the subcooled liquid core. This regime is called inverted annular film boiling and the heat transfer paths are as depicted in Figure 5-5. Most of the heat transfer from the wall is across the vapor film to the saturated liquid interface and thence into the subcooled liquid core. Experimental data indicate that the inverted annular regime persists up to void fractions of 60-70% and that a smooth transition is made to the dispersed flow regime. In TRACE, the inverted annular regime is assumed to exist for void fractions up to 60%. This section describes the models used for the two interfacial heat transfer paths: vapor-interface and interface-liquid.

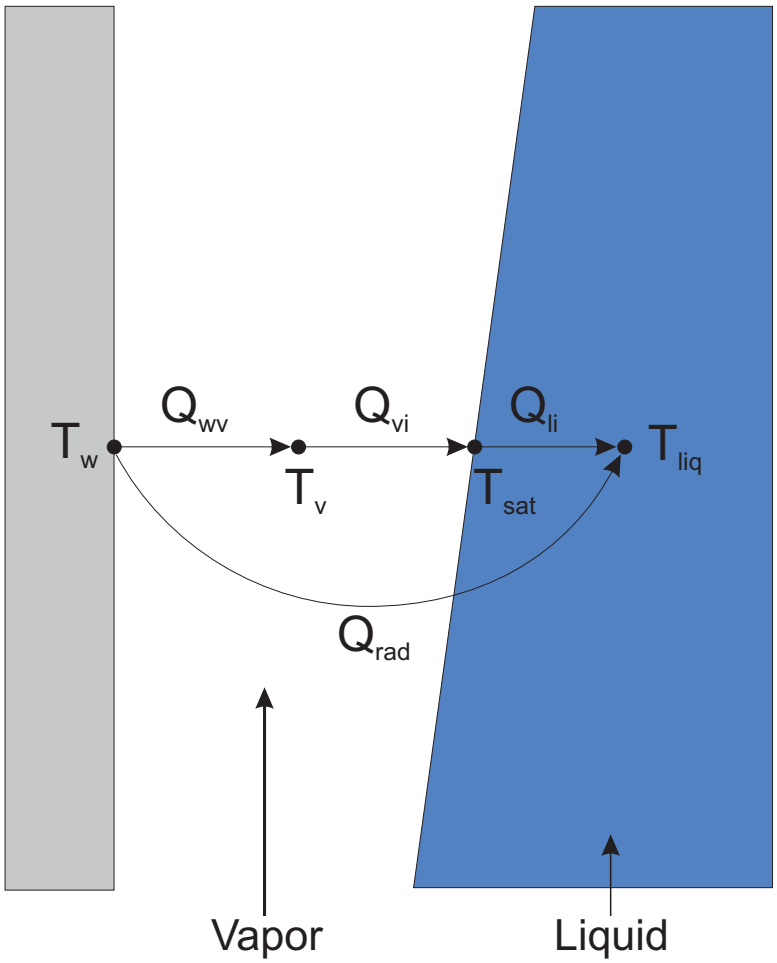

Figure. 5-5. Schematic of heat transfer paths for inverted annular film boiling.

In this regime, the limiting heat transfer resistance is that from the interface to the subcooled liquid core. The width of the vapor film simply adjusts so that the heat transfer rate across the film matches the maximum that can be convected into the liquid core region.

The models available in the literature for the interface-liquid heat transfer are more supposition in nature than data based. For example, Hammouda et. al. (Ref. 5-17) propose that the liquid core is turbulent and that the Dittus-Boelter correlation can be used with an entrance length effect modifier applied. Conversely, Denham (Ref. 5-18) treats it as a transient conduction problem with the characteristic time scale being the time since the liquid passed the quench front. Due to this disparity of approaches, an effort was made to infer what this interfacial heat transfer should be based on film boiling data.

The steady state low-quality film boiling data of Fung et. al. (Ref. 5-19) was used to get an estimate of the magnitude of the liquid-interface heat transfer coefficient. First, the interfacial area was calculated from the measured value of the void fraction assuming a cylindrical geometry for the liquid core. That is,

$$A_i''' = \sqrt{1-\alpha} \cdot \frac{4}{D_h} \tag{5-82}$$

with the diameter of the inverted liquid core given by

$$D_c = \sqrt{1-\alpha} \cdot D_h \tag{5-83}$$

The Nusselt no. would then be calculated from

$$Nu_{li} = \frac{q_{li}''}{\Delta T_{sub}} \cdot \frac{D_c}{k_l} \tag{5-84}$$

However, in these experiments, neither the liquid-interface heat flux, q_{li}'' , nor the liquid subcooling, ΔT_{sub} , were measured. Therefore, in reducing this data, two assumptions were made:

- The liquid-interface heat flux was approximated by that of the wall with a correction for radiation subtracted, and
- The liquid subcooling was calculated from the equilibrium quality.

The first assumption, that

$$q_{li}'' \approx q_w'' - q_{rad}'' \tag{5-85}$$

is good for highly subcooled conditions where the vapor generation rate is small but becomes increasingly worse as the subcooling decreases.

Figure 5-6 shows the results of this data analysis for the experiments of Fung (Ref. 5-19) using the above two assumptions. The first thing to note is that there is little if any dependence upon the mass flux, so using a model for turbulent forced convection, such as Dittus-Boelter, is probably not correct. Second, at high values of the liquid subcooling, where the assumption given by Eq. (5-85) is considered valid, it appears that the inferred Nusselt no. approaches an asymptotic value. This leads then to the proposed model,

$$Nu_{li} \approx 200 \tag{5-86}$$

that is similar to that of Saha and Zuber (Ref. 5-20) for subcooled boiling at low Peclet nos., namely

$$Nu_{li} \approx 455 \tag{5-87}$$

This simple constant value for the liquid-interface Nusselt no. was chosen as the model for TRACE. However, in simulations of FLECHT-SEASET high flooding rate tests, this value appeared to be too large and thus was reduced to

$$Nu_{li} \approx 100 \ . \tag{5-88}$$

Also, in Figure 5-6, a large increase in the liquid-interface Nusselt no. is indicated as the subcooling decreases to zero. At least part of this large increase results from the assumption given by Eq. (5-85) becoming invalid. However, as the liquid core approaches saturation and vapor generation increases dramatically, the surface of the core becomes rough and the entire core can oscillate. So, it is possible that some of this apparent enhancement is real though no attempt to model it is made in TRACE.

For the vapor-interface heat transfer, the model chosen was laminar convection in a thin film. That is,

$$h_{vi} = 2 \cdot \frac{k_g}{\delta} \tag{5-89}$$

The characteristic length, δ, is the vapor film thickness, which is computed from the void fraction using geometric formula either for a tube or a rod bundle. For the rod bundle case, the film thickness is then

$$\delta = \frac{D_h}{2} \cdot \left\{ \sqrt{1 + \alpha \cdot \left[\frac{4}{\pi} \left(\frac{P}{D_r} \right)^2 - 1 \right]} - 1 \right\} \tag{5-90}$$

where (P/D_r) is the pitch-to-diameter ratio, and for a tube geometry

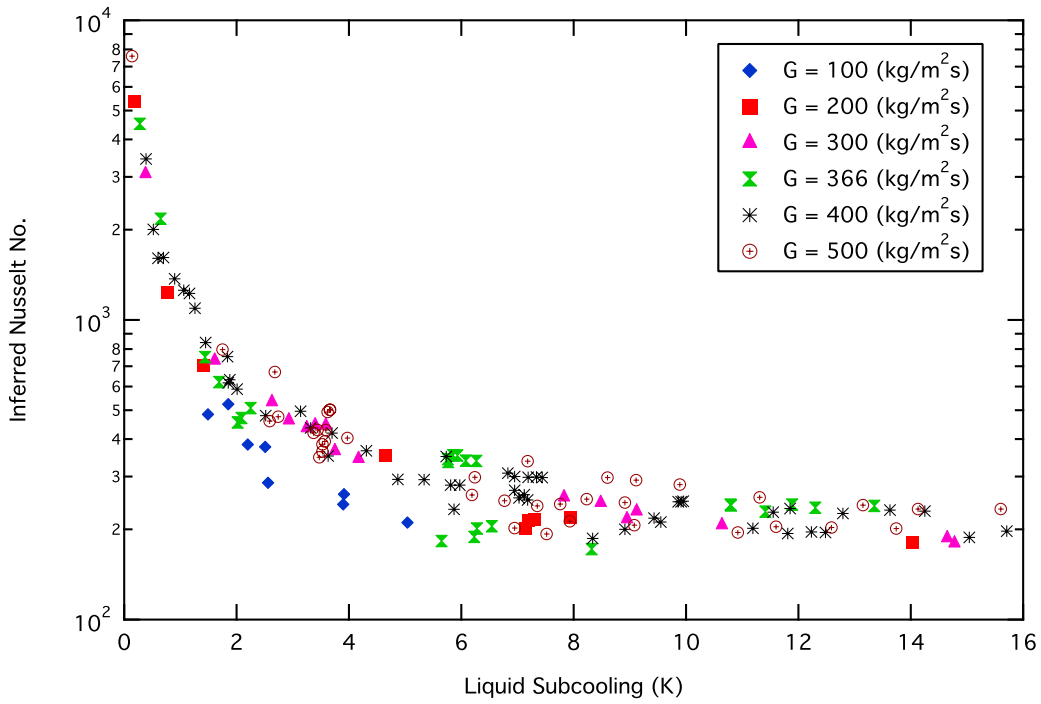

Figure. 5-6. Inferred values of the Nusselt no. for liquid-interface heat transfer for the low-quality film boiling data of Fung.

$$\delta = \frac{D_h}{2} \cdot (1 - \sqrt{1-\alpha}) \tag{5-91}$$

In both Eq. (5-90) and Eq. (5-91), the void fraction is limited to be greater than 0.01 to keep the magnitude of the resulting heat transfer coefficient from getting unreasonably large.

Two heat transfer coefficients remain to be specified: that for gas-liquid sensible heat transfer and that for flashing. Neither of these is considered to be important for inverted annular film boiling, but both must be specified to complete the mathematical model. First, for the case of sensible heat transfer, the gas-liquid heat transfer coefficient is taken to be the same as that for the vapor-interface,

$$h_{gl} = h_{vi} \tag{5-92}$$

which assumes that the liquid-side heat transfer resistance is negligible.

Flashing occurs when the liquid temperature exceeds saturation. This is not expected to occur in inverted annular film boiling as the associated large vapor generation rate would rapidly lead to breakup and entrainment of the liquid core. However, to ensure that unreasonably large values of liquid superheat do not occur, the interfacial heat transfer coefficient given by Eq. (5-88) is

ramped to a large value as a function of liquid superheat. The so-called "F12" multiplier of the RELAP5 code (Ref. 5-21) is used to accomplish this ramping. Thus,

$$(h_{li})_{flash} = h_{li} \cdot \left[1 + \Delta T_{sup} \cdot (250 + 50 \cdot \Delta T_{sup})\right] \tag{5-93}$$

where ΔT_{sup} is the liquid superheat.

This completes the description for the models used in the inverted annular film boiling regime. Film boiling data indicates that there is a smooth transition from inverted annular film boiling to dispersed flow. As no models were available for this "transition region", a simple interpolation procedure is used as discussed below in ***Interpolation Region***. First, the models for inverted slugs and dispersed droplets that provide the other point for the interpolation scheme are described.

Inverted Slug

As the liquid core approaches saturation and the vapor generation rate increases, the liquid core disintegrates into a mixture of ligaments and droplets. In TRACE, breakup of the inverted annular liquid core is assumed to begin at a void fraction of 60% and to be complete at a void fraction of 90%. Between these two values, an "interpolation region" is used to provide a smooth transition as described below. For void fractions above 90%, the liquid phase is assumed to be composed entirely of a mixture of small, dispersed droplets and large liquid fragments, or "inverted slugs" with the determination between these two forms being given by the entrainment fraction. This section describes the interfacial heat transfer models for the liquid considered to be in the form of inverted slugs.

The fraction of the liquid considered to be in the form of dispersed droplets is given by the entrained fraction and is computed using Eqs. (4-159) and (4-160), while the remainder of the liquid is treated as inverted slugs. The interfacial heat transfer is then calculated using a simple linear weighting scheme, for example,

$$h_{li} \cdot A_i = (1 - E) \cdot (h_{li} \cdot A_i)_{IS} + E \cdot (h_{li} \cdot A_i)_{DF} \tag{5-94}$$

where E is the entrainment fraction.

As discussed for interfacial drag in **Chapter 4,** *Inverted Slug Regime*, the inverted slugs are idealized as prolate ellipsoids with an aspect ratio of 4.5. The surface area of a prolate ellipsoid is given by

$$S = 2\pi \cdot a^2 + 2\pi \cdot \frac{a \cdot b}{e} \cdot \operatorname{asin}(e) \tag{5-95}$$

where a and b are respectively the minor and major radii and e is the ellipticity defined by

$$e = \sqrt{1 - \left(\frac{a}{b}\right)^2} \tag{5-96}$$

For a ligament with an aspect ratio of 4.5, the ellipticity is then equal to 0.975 and the surface area reduces to

$$S = 7.2156 \cdot 2\pi \cdot a^2 \tag{5-97}$$

Then, using Eq. (4-123) for the ligament volume, the surface area per unit volume is

$$(A_i''')_{IS} = \frac{4.8104 \cdot (1-\alpha)}{d_{IS}} \tag{5-98}$$

where d_{IS} is the diameter of the ligament, that is, twice the minor radius.

To evaluate the interfacial area, it remains to specify the ligament diameter. As a first approximation, the diameter of the inverted annular core at breakup is used. Then, using a void fraction of 60% as the upper limit for the inverted annular regime, we have

$$d_{IS} \approx 0.6325 \cdot D_h \tag{5-99}$$

To compute the interfacial heat transfer coefficients, the models described below for dispersed flow are used. For large droplets, such as an inverted slug, one modification to the dispersed droplet models is made. Specifically, the liquid-side heat transfer coefficient is increased by up to a factor of 4 for large drops in order to account for the effects of shape oscillation as noted by Hijikata et. al. (Ref. 5-22). In practice, this enhancement helps to eliminate any residual subcooling that might exist from the inverted slugs in a region close to where they are formed. This enhancement factor is an engineering approximation and is given by

$$h_{li}' = h_{li} \cdot 4 \cdot Min\left[1\ , \left(\frac{d_{IS}}{d_{RT}}\right)^2\right] \tag{5-100}$$

where d_{RT} is the Sauter mean diameter for a distribution having a maximum diameter that is stable against the Rayleigh-Taylor instability. Using the formula of Kitsch and Kocamustafaogullari (Ref. 4-44), then gives

$$d_{RT} = \frac{3.52}{4} \cdot \sqrt{\frac{\sigma}{g \cdot \Delta\rho}} \tag{5-101}$$

The following section details all of the droplet heat transfer models used in TRACE for post-CHF conditions.

Dispersed Flow

The fraction of the liquid that is entrained is treated as dispersed droplets that are relatively small and nearly spherical. The droplet diameter for interfacial heat transfer is calculated from the same models as previously described for post-CHF interfacial drag in **Chapter 4,** *Post-CHF Flow Regimes* (see Eqs. (4-134) through (4-145)). The interfacial area concentration is then

$$A_i''' = \frac{6 \cdot (1-\alpha)}{d_{SM}} \tag{5-102}$$

in terms of the droplet Sauter mean diameter.

For post-CHF conditions, the most important interfacial heat transfer process is that for the gas-side as it limits the steam superheat and thereby directly affects the peak clad temperature. The gas-side heat transfer coefficient is given by

$$h_{vi} = \frac{k_g}{d_{SM}} \cdot Nu_d \tag{5-103}$$

For the gas-side drop Nusselt no., the model of Renksizbulut & Yuen (Ref. 5-23) was chosen giving

$$Nu_{d,f} \cdot [1 + B_f]^{0.7} = 2 + 0.57 \cdot Re_{d,f}^{1/2} \cdot Pr_{g,f}^{1/2} \tag{5-104}$$

as a function of the droplet Reynolds no. This correlation is stated to be valid for the range

$$25 \le Re_{d,f} \le 2000$$

$$0.07 \le B_f \le 2.79$$

$$150 \le (T_g - T_{sat}) \le 700^\circ C$$

The major difference between Eq. (5-104) and the model of Ranz-Marshall is the inclusion of a "blowing factor", B_f, to account for the effects of mass transfer upon heat transfer. In addition, the vapor transport properties used in Eq. (5-104) are evaluated at a reference film temperature as indicated by the second "f" subscript. However, in TRACE, we have elected to simply use the

vapor properties evaluated at the bulk steam temperature. This simplification results in a small decrease in the consequent heat transfer coefficient. Then, Eq. (5-104) becomes

$$Nu_d \cdot [1 + B_f]^{0.7} = 2 + 0.57 \cdot Re_d^{1/2} \cdot Pr_g^{1/3} \tag{5-105}$$

where the drop Reynolds no. is given by

$$Re_d = \frac{\rho_g \cdot V_r \cdot d_{SM}}{\mu_g} \tag{5-106}$$

and the "blowing factor" by

$$B_f = \left(\frac{c_{P,g} \cdot (T_g - T_{sat})}{h_{fg}} \right) \cdot \left(1 + \frac{q_r''}{q_c''} \right) \tag{5-107}$$

where q_r'' and q_c'' are respectively the radiative and convective heat fluxes to the drop. In TRACE, we have made the assumption that

$$\frac{q_r''}{q_r''} \ll 1$$

so that the blowing factor simplifies to

$$B_f = \left(\frac{c_{P,g} \cdot (T_g - T_{sat})}{h_{fg}} \right) = \left(\frac{h_g - h_{g,sat}}{h_{fg}} \right) \tag{5-108}$$

In the evaluation of the drop Reynolds no., the problem of using the magnitude of the phase velocity difference, $|V_g - V_l|$, that results from the solution of the two-fluid momentum equations for the drop relative velocity that was discussed previously resurfaces. Especially when the void fraction is in the transition region between inverted annular and dispersed flow, the calculated relative velocity can be much larger than what would be expected for droplets. Consequently, the drop relative velocity used in Eq. (5-106) is taken to be the minimum of the phasic velocity difference and the terminal velocity for a spherical drop with the multi-particle correction factor applied, thus

$$V_r = Min\left[|V_g - V_l| , V_\infty \cdot \alpha^{1.4} \right] \tag{5-109}$$

For the single-particle terminal velocity, V_∞, the formula of Wallis given in Eq. (4-135) is used again. Also, the reflood Sauter mean drop diameter from Eq. (4-138) and Eq. (4-145) was substituted into Eq. (4-135) to yield

$$V_\infty = 0.6 \cdot \frac{\sigma^{0.316} (g \cdot \Delta\rho)^{0.228}}{\rho_g^{0.456} \mu_g^{0.0879}} \tag{5-110}$$

For the liquid-side heat transfer, h_{li}, the asymptotic value of Kronig & Brink (Ref. 5-14) given by Eq. (5-63) is used. For the gas-liquid sensible heat transfer, we assume that the liquid-side heat transfer resistance is much smaller than the gas-side, and so the gas-side interfacial heat transfer coefficient from Eq. (5-105) is used. That is,

$$h_{gl} = h_{vi} \tag{5-111}$$

Finally, as was done for the inverted annular regime, see Eq. (5-93), the flashing interfacial heat transfer is computed by applying the "F12" multiplier from RELAP5 to the liquid-side heat transfer coefficient.

Interpolation Region

Experimental data indicate that the inverted annular regime persists up to void fractions of 60-70% and that a smooth transition is made to the dispersed flow regime. The role of the interpolation region is to provide this smooth transition. As shown in Figure 4-14, the inverted annular regime is assumed for void fractions less than 60%, while for void fractions greater than 90%, the flow consists of a mixture of inverted slugs and droplets. Between these two limits, the following interpolation scheme is used.

First, the interfacial heat transfer for the inverted annular regime is calculated, as denoted by the subscript "*IA*". Next, the interfacial heat transfer is re-calculated treating the liquid phase as a mixture of dispersed droplets and inverted slugs with the subscripts "*DF*" and "*IS*" denoting the values for dispersed flow and inverted slugs respectively. Then, the weighting factor for inverted annular flow is calculated from

$$wf_{IA} = 2 \cdot x_{IA} - x_{IA}^2 \tag{5-112}$$

where

$$x_{IA} = \left(\frac{0.9 - \alpha}{0.9 - 0.6} \right) \tag{5-113}$$

Finally, the contributions from the inverted annular and the dispersed flow or inverted slug regimes are combined as illustrated for the case of the liquid-side heat transfer by

$$h_{li} \cdot A_i = wf_{IA} \cdot (h_{li} \cdot A_i)_{IA} + (1 - wf_{IA})[E \cdot (h_{li} \cdot A_i)_{DF} + (1 - E) \cdot (h_{li} \cdot A_i)_{IS}] \quad (5\text{-}114)$$

This same interpolation formula is used for the other interfacial heat transfer coefficients and for the wall heat transfer coefficient (see **Chapter 6,** *Inverted Slug Film Boiling*).

Transition to Pre-CHF Regimes

The determination between the normal pre-CHF flow regimes and the inverted post-CHF flow regimes is made using the axial locations of the bottom and top quench fronts. For mass/energy computational volumes that are completely quenched, the normal pre-CHF regimes are used. Whereas, for computational volumes whose heat transfer surface is in film boiling, (i.e., they are located entirely between the top and bottom quench fronts), the inverted post-CHF regimes are used. Finally, for computational volumes that are partially quenched, an interpolation between the interfacial heat transfer for pre- and post-CHF values is performed.

Let f_Q represent the fraction of the mass/energy computational volume that is quenched. The interfacial heat transfer coefficients are then computed using a simple linear interpolation scheme. For example, for the liquid-side heat transfer,

$$h_{li} \cdot A_i = f_Q \cdot (h_{li} \cdot A_i)_{pre-CHF} + (1 - f_Q) \cdot (h_{li} \cdot A_i)_{post-CHF} \quad (5\text{-}115)$$

This same linear interpolation is used for all of interfacial heat transfer coefficients.

However, before Eq. (5-115) is applied to the liquid-side heat transfer, one modification is made. Specifically, the liquid-side heat transfer coefficient for the pre-CHF regime is constrained to be greater than that for the post-CHF regime as would be expected.

Non-Condensable Gas Effects

When non-condensable gases are present, the mass transfer processes of condensation and evaporation are both affected in two ways. First, the driving temperature difference is reduced in the case of condensation, as

$$T_{sv} - T_l \leq T_{sat} - T_l$$

or, increased in the case of evaporation, as

$$T_l - T_{sv} \geq T_l - T_{sat}$$

where T_{sv} is the saturation temperature at the vapor bulk partial pressure for the mass/energy computational cell. Secondly, the mass transfer rate can become limited by the rate at which the non-condensable gas can diffuse either away from (condensation) or towards the interface (evaporation).

The models used by TRACE to modify the liquid-side interfacial heat transfer when non-condensable gases are present are described below. Both the default model for condensation and the model for evaporation were retained from the TRAC-PF1/MOD2 code. However, to improve TRACE's predictive capability for both in-tube condensation for the PCCS component and for wall condensation in the drywell of the proposed ESBWR design, a new model for the effects of non-condensable gases upon film condensation was added to the TRACE code. This new model is described in ***Special Model for Film Condensation*** below and is expected to replace the default model in a future code release after more testing has been completed.

For the effect of non-condensable gases upon the gas-side heat transfer, the interfacial heat transfer coefficient determined using the models described above is multiplied by the relative partial pressure in the energy equation. Thus,

$$q_{vi}'' = \frac{P_v}{P} \cdot h_{vi} \cdot (T_g - T_{sv}) \tag{5-116}$$

which forces the vapor-interface heat transfer to zero as the vapor is depleted.

Also, when non-condensable gases are present, allowance is made for the sensible heat transfer between the gas mixture and the liquid phase. The gas-liquid heat transfer coefficients described above are similarly multiplied by the relative partial pressure of the non-condensable gas, so that

$$q_{gl}'' = \frac{P_{NC}}{P} \cdot h_{gl} \cdot (T_g - T_l) \tag{5-117}$$

and the sensible heat transfer goes to zero as pure-steam conditions are approached.

Default Model for Condensation

During condensation driven by interfacial heat transfer for pure-steam conditions, the limiting heat transfer resistance is usually that between the interface and the subcooled liquid. When non-condensable gases are present, the concentration of the non-condensable gas builds up at the interface, thereby lowering the local vapor partial pressure and hence the temperature of the interface below that for saturation of the bulk gas mixture. That is,

$$T_i \leq T_{sv}$$

and so the driving potential for condensation is reduced even further and the condensation rate can become limited by the rate at which the non-condensable gas can diffuse away from the interface.

The two-fluid numerical scheme of TRACE includes a non-condensable gas field and so the bulk vapor partial pressure is calculated for every mass/energy computational volume. The interfacial heat transfer rates that drive mass transfer, are then defined in terms of the cell's bulk conditions, for example

$$q''_{li} = h_{li} \cdot (T_l - T_{sv}) \tag{5-118}$$

rather than in terms of the local interface temperature. The non-condensable gas effect described above then must be added as an effective heat transfer resistance on the liquid-side heat transfer, so that

$$q''_{li} = h_{li,\,NC} \cdot (T_l - T_{sv}) = h_{li} \cdot (T_l - T_i) \tag{5-119}$$

where the second subscript "*NC*" indicates that the additional resistance due to diffusion of the non-condensable gas away from the interface has been added to that of the liquid-side heat transfer.

The TRACE default model is the empirical correlation of Sklover and Rodivilin (Ref. 5-24) and it is invoked whenever $\left| T_l \leq T_{sv} \right|$ and the special film condensation model is not selected (see below). The original form of this correlation was developed for subcooled water jets with an air-steam crossflow and was given by

$$\frac{h_{li,\,NC}}{h_{li}} = 0.366 \cdot \left(\frac{G_a G_l}{G_s^2} \right)^{-0.2} \tag{5-120}$$

where $h_{li,\,NC}$ is the liquid-side heat transfer coefficient in the presence of non-condensables, and G_a, G_l, and G_s are the air, water, and steam mass fluxes, respectively. The experimental basis for the Sklover and Rodivilin correlation covered the following liquid and steam mass flux ranges,

$$3000 \leq G_l \leq 18000 \ \ (kg/m^2 s)$$

$$100 \leq G_s \leq 710 \ \ (kg/m^2 s)$$

but the range for the air mass flux was not specified.

In TRACE, the mixture of condensable and non-condensable gases flows with the same velocity. Thus, Eq. (5-120) reduces to

$$\frac{h_{li,NC}}{h_{li}} = 0.366 \cdot \left(\frac{\rho_s}{\rho_{NC}}\right)^{0.2} \cdot \left(\frac{G_s}{G_l}\right)^{0.2} \tag{5-121}$$

which is finally rewritten in terms of the gas mixture density and non-condensable gas density as

$$\frac{h_{li,NC}}{h_{li}} = 0.366 \cdot \left(\frac{\rho_g - \rho_{NC}}{\rho_{NC}}\right)^{0.2} \cdot \left(\frac{G_s}{G_l}\right)^{0.2} \tag{5-122}$$

In the evaluation of Eq. (5-122), the mass fluxes are limited to be in the ranges,

$$3000 \leq G_l \leq 18000 \ \ (kg/m^2 s)$$

$$0 \leq G_s \leq 640 \ \ (kg/m^2 s) \tag{5-123}$$

and the reduction factor is limited to the range

$$0.1 \leq \frac{h_{li,NC}}{h_{li}} \leq 1.0 \tag{5-124}$$

The above model is strictly applicable only to the specific configuration for which it was developed, that is, a subcooled liquid jet in an air-steam crossflow. It is not applicable to other configurations and being highly empirical, extrapolation beyond its database will lead to questionable results. This model will be replaced in a future TRACE update by he mass transfer based model described below in ***Special Model for Film Condensation*** as soon as sufficient testing has been conducted to assure the accuracy and robustness of the new model.

Special Model for Film Condensation

For the proposed ESBWR design, a critical component is the Passive Containment Cooling System (PCCS) that removes decay heat from the drywell via in-tube condensation of a steam-gas mixture. To improve the predictive capability of the TRACE code for the PCCS component, a new model for condensation in the presence of non-condensable gases was developed as described below. Later, this model was extended to also be applicable to condensation on the walls of the drywell itself. It is intended that this new model will become the default in TRACE replacing the Sklover-Rodivilin correlation in a future update once it has been extended to the other flow regimes and sufficient testing has been completed. For this code release though, the "special film condensation model" has to be invoked for each component using the "PipeType" or "VessType" input parameters as described in the user's guide.

This new model for film condensation in the presence of non-condensable gases employs the mass transfer conductance approach as developed by Kuhn et. al. (Ref. 5-7). This approach is similar to the classical model of Colburn & Hougen (Ref. 5-25) that computes the heat flow through the liquid film and equates it to the sum of the heat flow due to latent and sensible heat transfer on the film surface. Both the heat flows to and away from the interface are dependent upon the conditions at the film surface as represented by the interface temperature, T_i . Consequently, this approach requires an iterative solution as described below.

For the heat flux from the steam-gas mixture to the film interface, we have

$$q''_{mix} = q''_{cond} + q''_{sens} \tag{5-125}$$

where q''_{cond} is the heat flux to the film surface associated with the latent heat release of the condensing vapor, and q''_{sens} is the heat flux due to sensible heat transfer. Then, substituting for the latent[1] and sensible heat transfer rates,

$$q''_{mix} = -\Gamma'' \cdot h_{fg} + h_{sens} \cdot (T_g - T_i) \tag{5-126}$$

For the heat flux from the interface to the subcooled liquid, we have

$$q''_{li} = h_{li} \cdot (T_i - T_l) \tag{5-127}$$

and equating the heat fluxes to/from the interface yields,

$$-\Gamma'' \cdot h_{fg} + h_{sens} \cdot (T_g - T_i) = h_{li} \cdot (T_i - T_l) \tag{5-128}$$

An iterative solution is then used to find the interface temperature that satisfies the equality expressed by Eq. (5-128). Also, in this equation, the liquid-side interfacial heat transfer coefficient, h_{li} , is computed using the models for film flow described above. To complete the model description, it remains to provide the formulation for the condensation mass flux and the correlations used for the mass transfer and sensible heat transfer.

The condensation mass flux is determined from

$$\Gamma'' = \left(\frac{\rho_g \cdot D_0}{d} \right) \cdot B_f \cdot Sh \cdot b \tag{5-129}$$

1. Note, the sign convention used in TRACE has the vapor generation rate negative for condensation, that is, $\Gamma < 0$.

where ρ_g is the density of the gas-steam mixture at free-stream conditions, D_0 is the diffusion coefficient, and d is the characteristic length. The mass transfer driving potential, b, is given by

$$b = \frac{\left(x_{v,\infty} - x_{v,i}\right)}{\left(x_{v,i} - 1\right)} \tag{5-130}$$

in terms of the vapor mass fraction for the interface, $x_{v,i}$, and for the free-stream, $x_{v,\infty}$. The vapor mass fraction at the interface is

$$x_{v,i} = \frac{\rho_{v,i}}{(\rho_v + \rho_{NC})_i} \tag{5-131}$$

where the vapor density is computed for saturation conditions at a partial pressure corresponding to the interface temperature. That is,

$$P_{v,i} = P_{v,sat}(T_i) \tag{5-132}$$

and

$$\rho_{v,i} = \rho_{v,sat}\left(P_{v,i}\right) \tag{5-133}$$

The density of the non-condensable gas is similarly evaluated as a function of its partial pressure and the interface temperature.

The Sherwood no., Sh, will be evaluated from standard heat transfer correlations using the heat-mass transfer analogy as discussed below. Finally, B_f, is the "blowing factor" that accounts for the effects of mass transfer upon the diffusion of steam towards the interface and is given by

$$B_f = \frac{\ln(1+b)}{b} \tag{5-134}$$

according to Eq. (18-9) of Reference 5-26.

The sensible heat flux is given by

$$q''_{sens} = f_{fog} \cdot \left(\frac{k_g}{d}\right) \cdot B_f \cdot Nu \cdot (T_g - T_l) \tag{5-135}$$

where f_{fog} is the "fog factor" that accounts for the augmentation of the sensible heat transfer due to the formation of mist in the boundary layer for the vapor/gas mixture. Mori and Hijikata (Ref. 5-27) found this augmentation to have a value of approximately 2, while Kageyama et. al. (Ref. 5-28) inferred a value of 7 in their analysis. In TRACE, we have chosen to use the smaller value, and so

$$f_{fog} = 2 \tag{5-136}$$

The initial implementation of this model was for the conditions in the PCCS condenser tubes, thus the correlations chosen for the evaluation of the Sherwood and Nusselt numbers were those appropriate for fully developed flow in a tube. Specifically, a power-law combination of the values for laminar flow and turbulent flow was used,

$$Nu = \left[(3.66)^3 + (Nu_{Gnielinski})^3\right]^{1/3} \tag{5-137}$$

The laminar flow value is that for a uniform surface temperature boundary condition, while that for turbulent flow is calculated from the correlation of Gnielinski (see **Chapter 6,** *Single-Phase Liquid Convection*). Also, the characteristic length in Eqs. (5-129) and (5-135) is set to the diameter of the annular core.

For the Sherwood no., the heat-mass transfer analogy is applied so that

$$Sh = \left[(3.66)^3 + (Sh_{Gnielinski})^3\right]^{1/3} \tag{5-138}$$

where the Gnielinski correlation is evaluated using the Schmidt no. in place of the Prandtl no. One additional modification is made as suggested by Kays & Crawford (Ref. 5-26). As both the gas temperature and concentration can vary significantly across the boundary layer, a correction for variable properties is needed. For mass transfer, Kays & Crawford suggest using a property ratio scheme based upon the molecular weight of the gas-steam mixture. They state that the density variation associated with the concentration and temperature gradients across the boundary layer is primarily responsible for the variable property influence and that is why correlation can be approximately obtained by use of a molecular-weight ratio. For turbulent forced convection, they give

$$\Gamma'' = \Gamma''_0 \cdot \left(\frac{M_{W,i}}{M_{W,\infty}}\right)^{0.4} \tag{5-139}$$

where Γ_0'' is the condensation mass flux for constant properties evaluated at free-stream conditions.

Once the iterative solution for the interface temperature has converged, the condensation rate is known and the resulting interfacial heat transfer coefficients can be determined. In terms of the interface temperature, the condensation rate is then

$$\Gamma'' \cdot h_{fg} = h_{li} \cdot (T_l - T_i) \tag{5-140}$$

and so the liquid-side interfacial heat transfer coefficient in the presence of non-condensable gases becomes

$$h_{li,NC} = \frac{\Gamma'' \cdot h_{fg}}{(T_l - T_{sv})} = h_{li} \cdot \frac{(T_l - T_i)}{(T_l - T_{sv})} \tag{5-141}$$

Similarly, the heat flux associated with the sensible heat transfer from the gas mixture to the interface is translated into a heat transfer coefficient using the gas-liquid temperature difference as the driving potential. Namely,

$$h_{gl} = h_{sens} \cdot \frac{(T_g - T_i)}{(T_g - T_l)} \tag{5-142}$$

The choice was made to use a more mechanistic approach, i.e., a mass transfer conductance model, for the effect of non-condensable gases upon condensation not only because it is more philosophically appealing but because it also has the potential to be more accurate. For example, Kuhn et. al. (Ref. 5-7) noted that for their database, the mass transfer conductance model was more accurate than a purely empirical model developed from that same data. We compared the above TRACE model to all of the air-steam and helium-steam data in the experiments of Kuhn. There were 72 air-steam tests giving a total of 571 data points, the TRACE model calculated the heat transfer coefficient for these with an average error of 12.5% and an RMS error of 20.5%. Similarly, there were 25 helium-steam tests giving a total of 192 data points, the TRACE model calculated the heat transfer coefficient for these with an average error of 0.9% and an RMS error of 16.3%. These values are considered to be within the error bands associated with this data.

Later, it was decided to extend this film condensation model to also be applicable for the conditions of the drywell walls in the ESBWR design. For large containment volumes, the correlations used for turbulent forced convection to evaluate the Nusselt and Sherwood numbers needed to be replaced by something more appropriate. For this purpose, the correlation for turbulent free convection on a vertical plate given by McAdams (Ref. 5-29) was chosen. That is,

$$Nu_L = 0.13 \cdot (Gr_L \cdot Pr_g)^{1/3}$$

$$Sh_L = 0.13 \cdot (Gr_L \cdot Sc_g)^{1/3} \tag{5-143}$$

where the subscript *L* indicates that it is the average over a plate of that length. The Grashof no. is calculated from the density difference between the interface and the free-stream. Thus,

$$Gr_L = \frac{L^3 \cdot g \cdot \left| \rho_g - \rho_{g,i} \right|}{\rho_g \cdot \nu_g^2} \tag{5-144}$$

Note that because the characteristic length scale, L, in Eq. (5-144) is cubed, and the Grashof no. is taken to the one-third power, the dependence upon the length scale is absent from the resulting heat and mass transfer coefficients. Consequently, in TRACE, the hydraulic diameter is used for this length scale but has no effect upon the results.

Similar to the situation for turbulent forced convection, a correction for variable properties is also needed for the free convection case. Failing to find a suitable correction factor in the literature, a model was derived along the lines of that proposed by Kays and Crawford (Ref. 5-26) for the forced convection case. The resulting correction yields

$$\Gamma'' = \Gamma_0'' \cdot \left(\frac{M_{W,i}}{M_{W,\infty}} \right)^{0.57} \tag{5-145}$$

for the case of turbulent free convection.

A comparison of this model was made to both the Uchida correlation (Ref. 5-30) and the Dehbi data (Ref. 5-31) with excellent results. Figure 5-7 presents this comparison to the Uchida correlation over a wide range of non-condensable gas mass fraction for atmospheric pressure conditions.

Finally, to eliminate the need for the user to select either "tube" or "wall" condensation, the correlations used to evaluate the Sherwood and Nusselt numbers for free and forced convection were combined. Simply stated, the maximum value for either free or forced convection is used. For example,

$$Nu = Max\left[Nu_{NC}, Nu_{FC} \right] \tag{5-146}$$

As stated above, this model is invoked by the user through the specification of the PIPETYPE or VESSTYPE input variables for 1-D and 3-D components, respectively. When this model has been extended to the remaining flow regimes and sufficiently tested, it will become the default model for the effects of non-condensable gases upon condensation. At present, its application is limited to the annular flow regime.

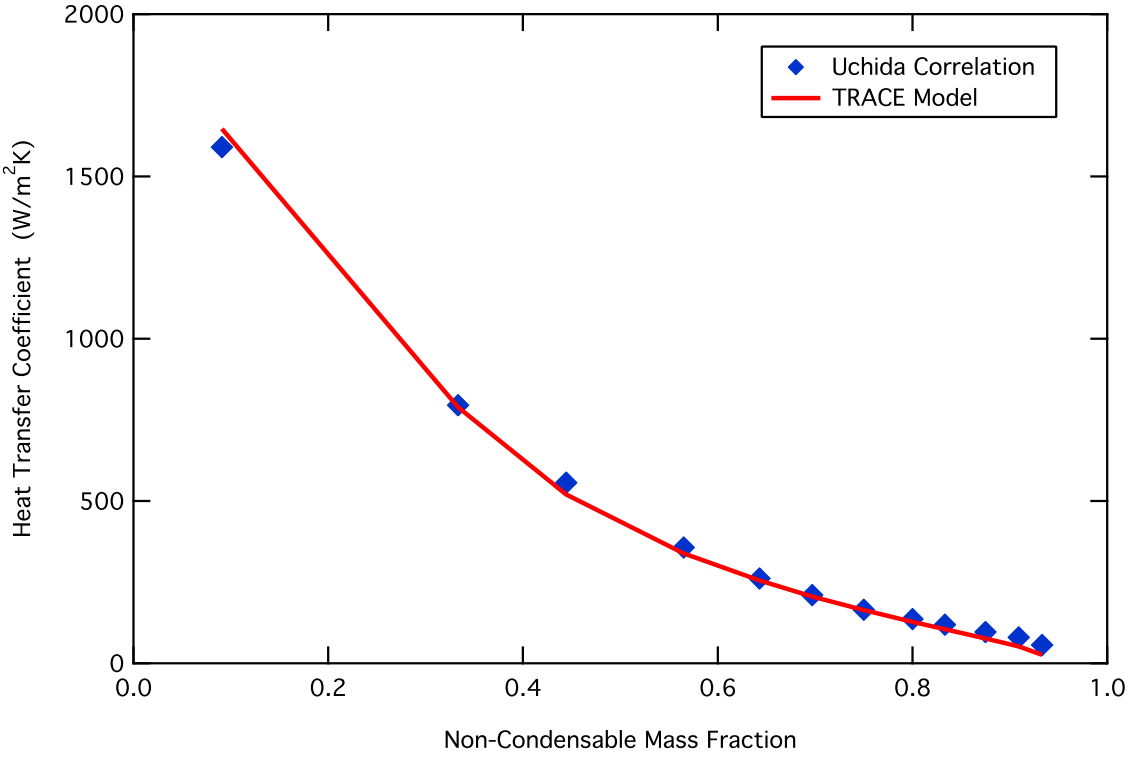

Figure. 5-7. Comparison of the TRACE model for wall condensation in the presence of non-condensable gases with the Uchida correlation at atmospheric pressure.

Model for Evaporation

When non-condensable gases are present, $T_{sv} < T_{sat}$, and evaporation due to interfacial heat transfer can occur whenever $T_l \geq T_{sv}$. For this case, the vapor generation increases the concentration of steam at the interface, thereby increasing the local interface temperature and decreasing the evaporation rate. When a significant fraction of non-condensable gases are present, evaporation can then be governed by the rate at which the non-condensable gas can diffuse towards the interface. In TRACE, this is modeled by adding the resistance to heat transfer associated with this diffusion to that of the heat transfer within the liquid phase. That is,

$$h_{li,NC} = \left[\frac{1}{h_{li}} + \frac{1}{h_{evap}} \right]^{-1} \tag{5-147}$$

where $1/h_{evap}$ denotes the effective interfacial heat transfer resistance associated with the diffusion process.

To provide a reasonable estimate for h_{evap}, a simple diffusion model is used. The mass transfer coefficient is obtained from

$$Sh = \begin{cases} 3.66 & ; \quad Re_g \leq 2300 \\ 0.023 \cdot Re_g^{0.8} \cdot Sc_g^{1/3} & ; \quad Re_g > 2300 \end{cases} \tag{5-148}$$

where the Sherwood, Schmidt, and Reynolds numbers are defined respectively as

$$Sh = \frac{h_M D_h}{D_0}$$

$$Sc_g = \frac{\mu_g}{\rho_g D_0}$$

$$Re_g = \frac{G_g D_h}{\mu_g} \tag{5-149}$$

Eq. (5-148) was given by Skelland (Ref. 5-32) for the mass transfer coefficient, h_M, in fully developed pipe flow with constant concentration on the wall. This is simply the heat-mass transfer analogy with the Dittus-Boelter correlation used for turbulent flow.

The diffusion coefficient, D_0, is obtained from a curve fit to a theoretical equation for the diffusion of steam in air[1]. The curve fit is given by

$$D_0 = \frac{1 \times 10^{-3}}{P} \cdot \left[-699.2438 + 4.9249 \cdot T_g + 0.0171 \cdot T_g^2 \right] \tag{5-150}$$

where the diffusion coefficient is in (m/s), the gas temperature is in (K), and the total pressure is in (Pa). The curve fit was obtained for $273 \leq T_g \leq 600 K$.

With the mass transfer coefficient from Eq. (5-148), the evaporative mass flux is computed from

$$\Gamma''_{evap} = h_M (C_i - C_\infty) \tag{5-151}$$

where C_i and C_∞ are the steam concentration at the interface and for the free-stream respectively. We assume that the interface temperature is equal to that of the liquid, and hence the

1. This is one of the limitations implicit in using this model. A future update to TRACE will use the correct diffusivity for whatever non-condensable gas is present.

interface concentration is the density of pure steam with the vapor pressure corresponding to saturation at the liquid temperature, that is

$$P_v = P_{v,sat}(T_l) \tag{5-152}$$

Using an ideal gas approximation for the vapor phase, the interface concentration is

$$C_i = \rho_{v,i} \approx \frac{P_{v,sat}(T_l)}{R_s \cdot T_l} , \tag{5-153}$$

where R_s is the ideal gas constant for steam and has the value 462 (J/kg-K). For the free-stream conditions, the steam density is simply that computed for the bulk conditions in the computational volume, and hence

$$C_\infty = \rho_g - \rho_{NC} \tag{5-154}$$

where ρ_g and ρ_{NC} are the mixture and non-condensable gas densities, respectively. Substituting into Eq. (5-151), the evaporative mass flux is

$$\Gamma''_{evap} = h_M(\rho_{v,i} - \rho_g + \rho_{NC}) \tag{5-155}$$

and the associated heat transfer resistance is

$$\frac{1}{h_{evap}} = \frac{(T_l - T_{sv})}{h_{fg} \cdot h_M(\rho_{v,i} - \rho_g + \rho_{NC})} \tag{5-156}$$

In addition to the diffusivity in this model being that of steam in air, this model is further limited by its usage of a Sherwood no. appropriate for fully developed flow in a pipe. Though this assumption is good for annular flow, this model is used for all flow regimes.

This completes the description of the interfacial heat transfer models used in TRACE, the next section describes the models for wall heat transfer.

References

5-1 M. Ishii and K. Mishima, "Study of Two-Fluid Model and Interfacial Area," Argonne National Laboratory Report, ANL-80-111 (NUREG/CR-1873), 1980.

5-2 E. Ranz and W.R. Marshall, "Evaporation from Droplets: part I and II," Chemical Engineering Progress, 48, 141-146 and 173-180, 1952.

5-3 G.R. Warrier, N. Basu and V.K. Dhir, "Subcooled Boiling at Low Pressures, Progress Report for USNRC Task Order No. 5," UCLA ENG-01-224, September, 2001.

5-4 Y.M. Chen and F. Mayinger, "Measurement of Heat Transfer at the Phase Interface of Condensing Bubbles," ANS Proc. 1989 National Heat Transfer Conf. (Philadelphia, Pa., August 6-9, 1989), HTC-Vol. 4, 147-152, 1989.

5-5 S. Whitaker, "Forced Convection Heat Transfer Correlations for Flow in Pipes, Past Flat Plates, Single Cylinders, Single Spheres, and for Flow in Packed Beds and Tube Bundles," AIChE Journal, 18, 361-371, 1972.

5-6 R.T. Lahey, Jr. and F.J. Moody, The Thermal-Hydraulics of a Boiling Water Nuclear Reactor, ANS monograph, 1977.

5-7 S.Z. Kuhn, V.E. Schrock and P.F. Peterson, "Final Report on U. C. Berkeley Single Tube Condensation Studies," UCB-NE-4201, August 1994.

5-8 S.S. Kutateladze, "Semi-Empirical Theory of Film Condensation of Pure Vapours," Int. J. Heat Mass Transfer, 25, 653-660, 1982.

5-9 S.G. Bankoff, "Some Condensation Studies Pertinent to LWR Safety," Int. J. Multiphase Flow, 6, 51-67, 1980.

5-10 I.S. Lim et. al., "Cocurrent Steam/Water Flow in a Horizontal Channel," NUREG/CR-2289, 1981.

5-11 S. Banerjee, D.S. Scott and E. Rhodes, "Mass Transfer to Falling Wavy Liquid Films in Turbulent Flow," I&EC Fundamentals, 7, 22-27, 1968.

5-12 T.G. Theofanus, R.N. Houze and L.K. Brumfield, "Turbulent Mass Transfer at Free Gas-Liquid Interfaces, with Applications to Open-Channel, Bubble and Jet Flows," Int. J. Heat Mass Transfer, 19, 613-624, 1976.

5-13 P.W. Dittus and L.M.K. Boelter, "Heat Transfer in Automobile Radiators of the Tubular Type," Univ. Calif. Pub. Eng., 2/13, 443-461, 1930; reprinted in Int. Comm. Heat mass Transfer, 12, 3-22, 1985.

5-14 R. Kronig and J. Brink, "On the Theory of Extraction From Falling Droplets," Applied Scientific Research, Vol. A2, 142-154, 1950.

5-15 G. Ryskin, "Heat and Mass Transfer from a Moving Drop - Some Approximate Relations for the Nusselt Number," *Int. Comm. Heat Mass Transfer*. **14**, 741-749, 1987.

5-16 H.J. Kim, "Local Properties of Countercurrent Stratified Steam-Water Flow," NUREG/CR-4417, 1985.

5-17 N. Hammouda, D.C. Groeneveld and S.C. Cheng, "Two-Fluid Modelling of Inverted Annular Film Boiling," Int. J. Heat Mass Transfer, 40, 2655-2670, 1997.

5-18 M.K. Denham, "Inverted Annular Film Boiling and the Bromley Model," Winfrith UKAEA Report, AEEW-R 1590, 1983.

5-19 K.K. Fung, "Subcooled and Low Quality Film Boiling of Water in Vertical Flow at Atmospheric Pressure," Ph.D. Thesis, University of Ottawa, 1981.

5-20 P. Saha and N. Zuber, "Point of Net Vapor Generation and Vapor Void Fraction in Subcooled Boiling," Proc. 5th Int. Heat Transfer Conf., Tokyo, Japan, Paper B4.7, 1974.

5-21 "RELAP5/Mod3.3 Code Manual, Volume IV: Models and Correlations," NUREG/CR-5535, Vol. IV, 2001.

5-22 K. Hijikata, Y. Mori and S. Kawaguchi, "Direct Contact Condensation of Vapor to Falling Cooled Droplets," Int. J. Heat Mass Transfer, 27, 1631-1640, 1984.

5-23 M. Renksizbulut and M.C. Yuen, "Experimental Study of Droplet Evaporation in a High-Temperature Air Stream," J. Heat Transfer, 105, 384-388, 1983.

5-24 G.G. Sklover and M.D. Rodivilin, "Condensation on Water Jets with a Cross Flow of Steam," Teploenergetika, 23, 48-51, 1976.

5-25 A.P. Colburn and O.A. Hougen, "Design of Cooler Condensers for Mixtures of Vapors with Noncondensing Gases," Ind. And Eng. Chemistry, 26, 1178-1182, 1934.

5-26 W.M. Kays and M.E. Crawford, Convective Heat and Mass Transfer, 2nd Edition, Chapter 18, McGraw-Hill Book Co., New York, NY, 1980.

5-27 Y. Mori and K. Hijikata, "Free Convective Condensation Heat Transfer with Noncondensable Gas on a Vertical Surface," *Int. J. Heat Mass Transfer*, **16**, 2229-2240, 1973.

5-28 T. Kageyama, P. F. Peterson and V. E. Schrock, "Diffusion Layer Modeling for Condensation in Vertical Tubes with Noncondensable Gases," *Nucl. Eng. Design*, **141**, 289-302, 1993

5-29 W.H. McAdams, Heat Transmission, 3rd Edition, Chapter 7, Eq. (7-4a), McGraw-Hill Book Co., New York, NY, 1954.

5-30 H. Uchida, A. Oyama and Y. Togo, "Evaluation of Post-Incident Cooling Systems of Light-Water Power Reactors," Proc. Of the Third International Conference on the Peaceful uses of Atomic Energy, 13, 93-104, 1965.

5-31 A.A. Dehbi, "Analytical and Experimental Investigation of the Effects of Noncondensable Gases on Steam Condensation under Turbulent Natural Convection Conditions," PhD Thesis, Dept of Nuclear Engineering, MIT, Jan 1991.

5-32 A.H.P. Skelland, Diffusional Mass Transfer, Robert E. Kreiger Publishing Co, Malabar, Fl., 1985.

6

Wall Heat Transfer Models

This chapter describes the TRACE wall heat transfer package. We have grouped the models that are presented into five separate sections:

- ***Pre-CHF Heat Transfer***: models for wall-liquid convection, nucleate boiling, and subcooled boiling.
- ***Critical Heat Flux***: models for the peak heat flux in the nucleate boiling heat transfer regime and the wall temperature at which it occurs.
- ***Minimum Film Boiling Temperature***: the temperature above which wall-liquid contact does not occur.
- ***Post-CHF Heat Transfer***: models for transition and film boiling heat transfer.
- ***Condensation Heat Transfer***: models for film condensation and the non-condensable gas effect.

Nomenclature

A_w''' = wall heat transfer area per unit volume (m^{-1})

c_p = specific heat (J/kg-K)

C_D = drag coefficient

C_{EG}, C_{In}, C_W = constants used for the rod bundle P/D_R effect in the heat transfer correlations of El-Genk, Inayatov, and Weisman, respectively.

d_d = drop diameter (m)

D = pipe diameter (m)

D_c = available cavity diameter (m)

D_h = hydraulic diameter (m)

D_R = rod diameter (m)

f = Fanning friction factor

f_{sub} = fraction of the wall-liquid heat transfer that causes subcooled boiling

f_{wet} = fraction of the surface covered by a liquid film

F = flow factor in Chen nucleate boiling correlation

F''' = force per unit volume (N/m^3)

F_P = pressure effect in Gorenflo correlation

F_{wk} = radiation gray body factor for the wall to phase k

g = gravitational acceleration (m/s^2)

G = mass flux (kg/m^2-s)

Gr = Grashof no.

h_0 = reference heat transfer coefficient in Gorenflo correlation

h_{ki} = interfacial heat transfer coefficient for phase k (W/m^2-K)

h_{wk} = wall heat transfer coefficient for phase k (W/m^2-K)

h_Γ = wall-liquid heat transfer coefficient for subcooled boiling (W/m^2-K)

h_{fg} = latent heat of evaporation (J/kg)

h_{ld} = liquid enthalpy at bubble departure in subcooled boiling (J/kg)

h_l^* = liquid enthalpy, set to the bulk value for boiling and saturation for condensation

h_v^* = vapor enthalpy, set to the bulk value for condensation and saturation for boiling

k = thermal conductivity (W/m-K)

K_1, K_2, K_8 = correction factors in the AECL-IPPE CHF look-up table for tube diameter, rod bundle geometry, and low flow conditions, respectively.

L_B = boiling length $\left(= Z - Z_{sat}\right)$

L/D = development length, i.e., the length-to-diameter ratio

Nu = Nusselt no., $(= h \cdot d/k)$

Nu^* = Nusselt no. with characteristic length based on fluid property group relevant to film flow, $\left(= (h_w / h_l) \cdot \left[\mu_l^2 / (g \cdot \Delta\rho \cdot \rho_l)\right]^{1/3}\right)$

P = pressure (the default units are Pa, but certain correlations may use MPa or psia as indicated in the text)

P^* = non-dimensional pressure used in AECL-IPPE CHF look-up table (see Eq. (6-98))

P_{crit} = critical pressure (Pa)

P_h = heated perimeter (m)

P_w = wetted perimeter (m)

P_r = reduced pressure $\left(= P / P_{crit}\right)$

P / D_R = pitch-to-diameter ratio for a rod bundle

Pe = Peclet no. $(= Re \cdot Pr)$

Pr = Prandtl no., $(= c_p \, \mu / k)$

q''_0 = reference heat flux in Gorenflo correlation

q''_{wk} = heat flux from the wall to phase k (W/m^2)

q'''_{wk} = wall heat transfer rate per unit volume to phase k (W/m^3)

R_f = radial peaking factor for critical quality correlations

R_P = surface roughness (μm)

Re = Reynolds no.

Ri = Richardson no. $\left(= Gr / Re^2\right)$

s = rod bundle pitch (m)

S = suppression factor in Chen nucleate boiling correlation

St = Stanton no. $\left(= Nu / (Re \cdot Pr)\right)$

T = temperature (K)

T_{sat} = saturation temperature at the total pressure (K)

T_{sv} = saturation temperature at the bulk vapor partial pressure (K)

ΔT_{sat} = wall superheat $\left(= T_w - T_{sat}\right)$

ΔT_{sub} = subcooling $\left(= T_{sat} - T_l\right)$

V_{rel} = relative velocity (m/s)

wf = weighting factor

x = flow quality

x_{crit} = critical quality, i.e., the quality at which annular film dryout occurs.

x_{static} = "static" quality used for low flow conditions (see Eqs. (6-101) to (6-107))

X_{tt} = Martinelli parameter (see Eq. (6-42))

Z_{QF} = axial location of the quench front (m)

Greek

α = void fraction (volume fraction of gas phase α_g)

α_k = volume fraction of phase k

β = thermal expansion coefficient $\left(= -\frac{1}{\rho} \cdot \left.\frac{\partial \rho}{\partial t}\right|_P\right)$

δ = gas or liquid film thickness (m)

δ^* = non-dimensional gas or liquid film thickness, $\left(= \delta / \left[\mu_k^2 / (g \cdot \Delta\rho \cdot \rho_k)\right]^{1/3}\right)$

ε = emissivity

Γ_f = film flow rate per unit of wetted perimeter (kg/s-m)

Γ_i = mass transfer rate per unit volume due to interfacial heat transfer

Γ_{sub} = mass transfer rate per unit volume due to subcooled boiling

μ = viscosity (Ns/m^2)

ν = dynamic viscosity (m/s^2), $\nu = \mu / \rho$

ϕ = liquid-solid contact angle (radians)

$\Delta\rho$ = density difference between liquid and gas phases (kg/m^3)

ρ = density (kg/m^3)

σ = surface tension (N/m)

σ_{SB} = Stefan-Boltzman constant (= 5.670×10^{-8} W/m^2-K)

$\Psi_{2\Phi}$ = two-phase convective enhancement factor for dispersed flow film boiling

Ψ_s, Ψ_t = correction factors for rod bundle geometry and variable fluid properties in heat transfer correlation of Inayatov.

Subscripts

0 = constant property value

1Φ = single-phase

2Φ = two-phase

ann = annular flow regime

b = evaluated at the "bulk" fluid condition

BI = boiling initiation

CHF = critical heat flux

$cond$ = condensation

cp = constant property value, i.e., evaluated at the bulk fluid conditions.

DB = Dittus-Boelter

$DFFB$ = dispersed flow film boiling

DW = dropwise

EG = El-Genk

f = film

FB = film boiling

FC = forced convection

$film$ = the liquid or gas film, or a value at a reference "film" temperature

g = vapor-gas mixture[1]

$Gnielinski$ = evaluated using Gnielinski correlation for turbulent forced convection

i = interface

$IAFB$ = inverted annular film boiling

1. For brevity, the vapor-gas mixture is simply referred to as the gas phase. When the vapor phase alone or the non-condensable gas alone are referenced, their individual subscripts, v and NC, are used.

In = Inayatov

k = phase index, l = liquid, and g = gas/vapor mixture

KL = Kim & Li

l = liquid

lam = laminar

m = mixture

min = value at the minimum film boiling point

NB = nucleate or flow boiling

NC = natural convection or non-condensable

ONB = onset of nucleate boiling

PB = pool boiling

rad = radiation

$rough$ = value for rough wall

sat = value at saturation

$sens$ = sensible heat

$smooth$ = value for smooth wall

sub = subcooled or subcooled boiling

sv = saturation at the vapor partial pressure

TB = transition boiling

$turb$ = turbulent

v = vapor

vp = variable property value

w = wall

W = Weisman

Γ = component that causes subcooled vapor generation

Introduction

Wall heat transfer models are required for closure of both the mass and energy equations. The phasic energy equations contain the terms, q_{wl}''' and q_{wg}''', that represent the heat transfer rate

per unit volume from the wall to the liquid and from the wall to the gas-vapor mixture respectively. These heat transfer rates are computed from

$$q_{wl}''' = h_{wl} \cdot (T_w - T_l) \cdot A_w'''$$

$$q_{wg}''' = h_{wg} \cdot (T_w - T_g) \cdot A_w''' \tag{6-1}$$

where h_{wl} is the wall-to-liquid heat transfer coefficient, h_{wg} is the wall-to-gas heat transfer coefficient, and the wall heat transfer surface area per unit volume is given by

$$A_w''' = \frac{4}{D_h} \tag{6-2}$$

Normally, only one of these phasic wall heat transfer coefficients is non-zero as only one phase is in contact with the wall. For example, in pre-CHF heat transfer, the wall-to-gas component is zero.

In addition, the mass equations contain a term, Γ_{sub} , for the vapor generation rate at the wall due to subcooled nucleate boiling as explained below in the section ***Subcooled Boiling Model***. In TRACE, the subcooled vapor generation rate is computed from

$$\Gamma_{sub} = \frac{h_\Gamma \cdot (T_w - T_l) \cdot A_w'''}{h_{fg}} \tag{6-3}$$

which can be restated as

$$\Gamma_{sub} = \frac{f_{sub} \cdot h_{wl} \cdot (T_w - T_l) \cdot A_w'''}{h_{fg}} \tag{6-4}$$

where f_{sub} is the fraction of the wall-to-liquid heat transfer that results in vapor generation when the bulk liquid temperature is subcooled. Also note that the latent heat in the denominator of Eq. (6-4) is defined by Eq. (5-3).

To calculate these phasic heat transfer coefficients, the wall heat transfer package used in TRACE consists of a library of heat transfer correlations and a selection logic algorithm. Together these produce a continuous heat transfer surface that is used to determine the phasic heat fluxes and hence heat transfer coefficients. For a fixed set of fluid conditions, a boiling curve can be produced to illustrate how these correlations work together, for example, see Figure 6-1. The resultant boiling curve is continuous and has the expected shape with inflection points denoted as: T_{ONB} (onset of nucleate boiling), T_{CHF} (critical heat flux), and T_{min} (minimum film boiling temperature).

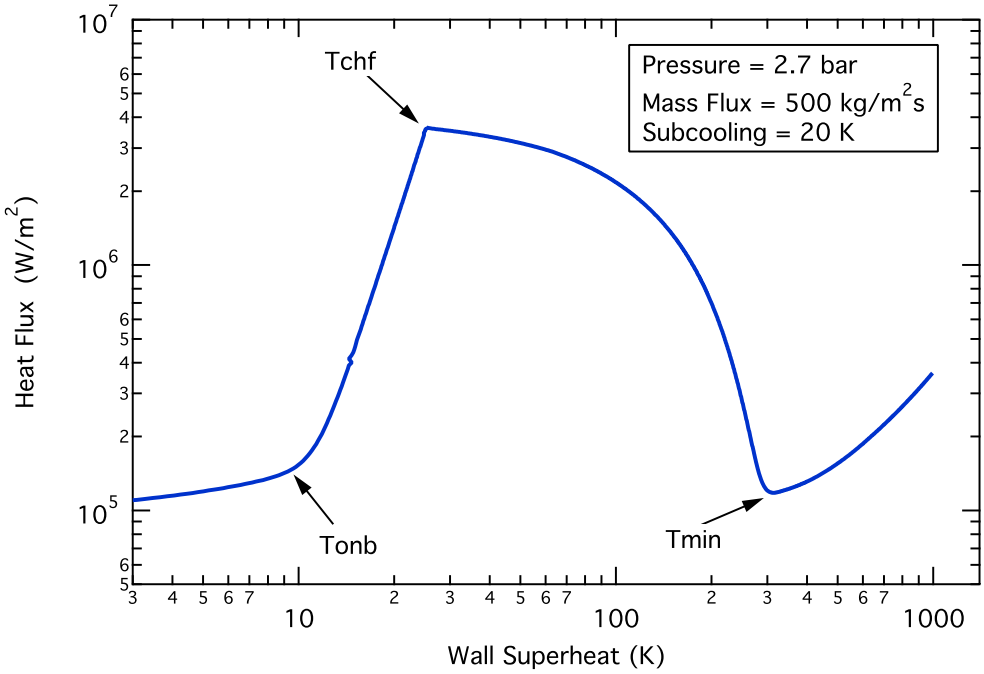

Figure. 6-1. Example of boiling curve calculated using the TRACE wall heat transfer package.

Each region (mode of heat transfer) defined by the boiling curve is described in turn below.

Pre-CHF Heat Transfer

The pre-CHF heat transfer regimes are characterized by wall-to-liquid contact and consist of both convection and nucleate boiling. The selection logic used to determine the pre-CHF heat transfer regime is given in Figure 6-2. For forced convection, correlations specific to both tube and rod bundle geometries are included.

Single-Phase Liquid Convection

This section describes the models used for convective heat transfer to single-phase liquid. Some of the same models are also used for convection to single-phase gases, however, the details of these models are given later in the section ***Dispersed Flow Film Boiling***. In addition to standard models for tube geometry, models specific to rod bundle geometry are available in TRACE. Models for rod bundles are invoked for the core region of a vessel and for the fuel rods in a CHAN component. In either case, correlations are provided for the laminar and turbulent forced convection regimes and for natural convection.

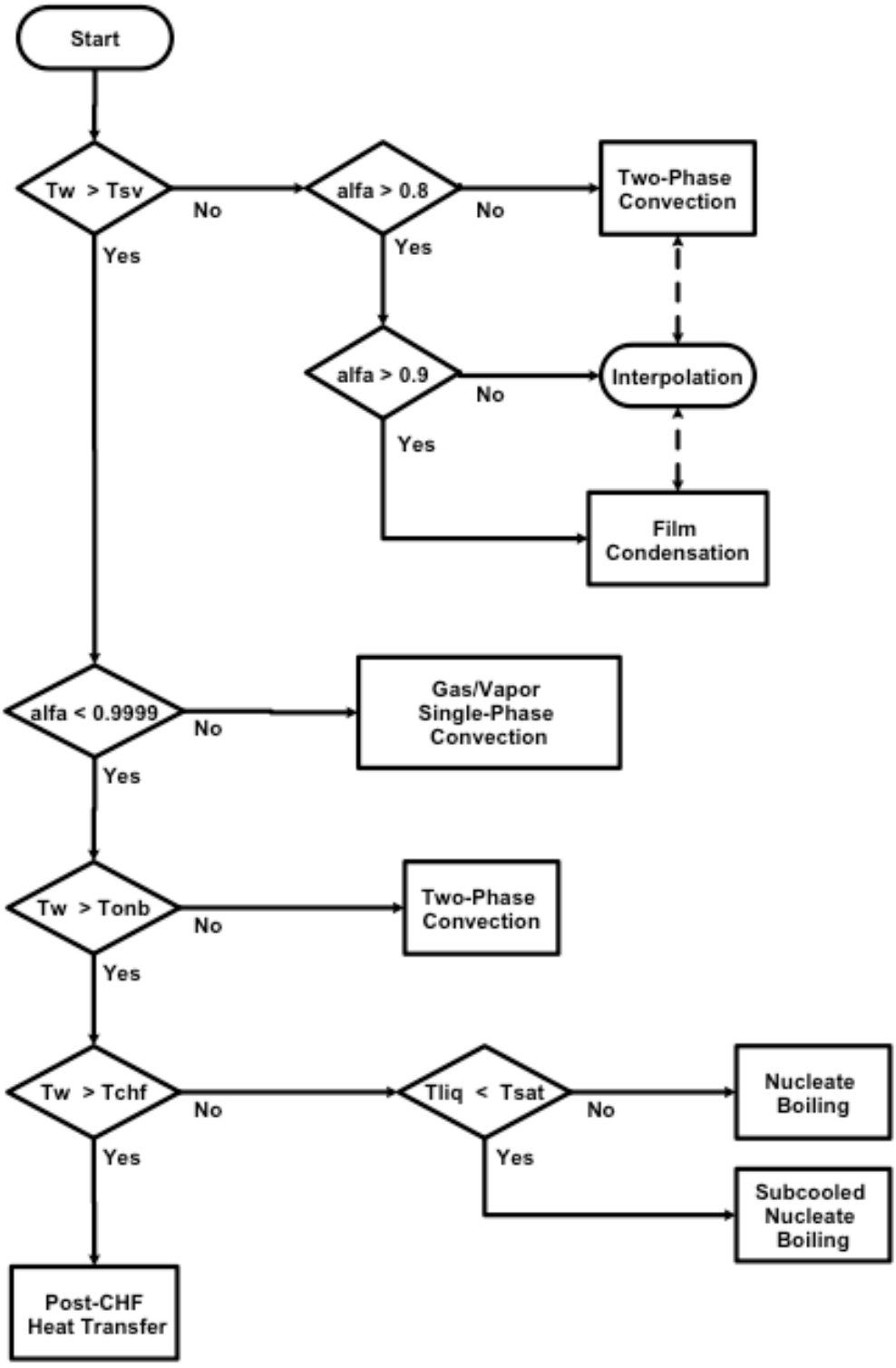

Figure. 6-2. Heat transfer regime selection logic for the pre-CHF and condensation regimes.

The wall heat transfer coefficient for single-phase liquid convection is taken as the maximum of the values for laminar and turbulent forced convection and natural convection. That is,

$$h_{wl} = Max\left\{ h_{lam} , h_{turb} , h_{NC} \right\} \tag{6-5}$$

where h_{NC} is the wall heat transfer coefficient for natural convection, h_{lam} is the wall heat transfer coefficient for laminar forced convection, and h_{turb} is the wall heat transfer coefficient for turbulent forced convection.

The models used for tube geometry are described first, followed by those for a rod bundle geometry.

Tube Geometry

For laminar forced convection, the Nusselt no. is set to the analytical value for fully developed flow with a constant heat flux boundary condition. Thus,

$$Nu_{lam} = 4.36 \tag{6-6}$$

Laminar forced convection typically has long development lengths, however, these are not considered in TRACE. Instead, the fully developed laminar Nusselt no. given by Eq. (6-6) is used as a lower limit on the wall forced convection heat transfer. Also, the effect of variable fluid properties upon the heat transfer coefficient in laminar flow is neglected. Therefore, the liquid thermal conductivity is evaluated at the bulk fluid temperature, and so,

$$h_{lam} = 4.36 \cdot \frac{k_l}{D_h} \tag{6-7}$$

For turbulent forced convection, the legacy TRAC-PF1/MOD2 code used the classic correlation of Dittus-Boelter (Ref. 5-13) for heating, given by

$$Nu_{DB} = 0.023 \cdot Re_l^{0.8} \cdot Pr_l^{0.4} \tag{6-8}$$

Equation (6-8) gives a reasonably accurate value for the Nusselt no. in fully developed turbulent flow at moderate values of the Prandtl no. Bhatti and Shah (Ref. 6-1) state that for the Reynolds no. range, $10^4 \le Re \le 1.24 \times 10^5$, the Dittus-Boelter correlation gives values for air ($Pr = 0.7$) that are 13.5% to 17% too high. Conversely, for heat transfer to water, $3 \le Pr \le 10$, it over-predicts by about 7%. However, if extended into the transition regime, it

seriously over-predicts the heat transfer coefficient and was judged to be unacceptable for Reynolds numbers less than about 10^4. This leaves a large gap between the region where the laminar value is appropriate and that where the accuracy of the Dittus-Boelter correlation is acceptable.

Consequently, it was decided to use a more modern heat transfer correlation for turbulent forced convection that would also be applicable to the transition region. As recommended by both Bhatti and Shah (Ref. 6-1) and Incropera and De Witt (Ref. 6-2), we selected the Gnielinski correlation (Ref. 6-3) for implementation in TRACE. For fully developed turbulent flow with constant properties, the Gnielinski correlation is given by

$$Nu_{turb} = \frac{(f/2)(Re - 1000) \cdot Pr}{1 + 12.7 \cdot (f/2)^{1/2}\left(Pr^{2/3} - 1\right)} \tag{6-9}$$

where the friction factor is evaluated using the smooth tube formula of Filonenko (Ref. 6-4),

$$f = [1.58 \cdot 1n(Re) - 3.28]^{-2} \tag{6-10}$$

The above formulation for the Nusselt no. is valid over the range

$$2300 \leq Re \leq 5 \times 10^6$$

$$0.5 \leq Pr \leq 2000$$

but yields negative values for Reynolds numbers less than 1000. So, the liquid Reynolds no. is limited to be greater than 1000, and is defined for single-phase flow by

$$Re_l = \frac{G_l \cdot D_h}{\mu_l} \tag{6-11}$$

For similar reasons, the Prandtl no. in Eq. (6-9) is constrained to have a value greater than 0.15.

A comparison of the Gnielinski correlation to the classic correlation of Dittus-Boelter is given in Figure 6-3. Also plotted in this figure is experimental data for the average Nusselt no. for atmospheric air flowing through a long heated tube (Ref. 6-5). The superior performance of the Gnielinski correlation for the transition region is clearly evident in this figure.

Note that the data presented in Figure 6-3 are taken from the textbook of Kreith and Bohn (Ref. 6-5) which cites them without reference. For this data, the Nusselt no. in the laminar region appears to decrease proportional to $Re^{0.3}$ and falls below the laminar value for fully developed flow for either a constant heat flux boundary condition, $Nu = 4.36$, or for a constant temperature

boundary condition, $Nu = 3.66$. The reason for this discrepancy between laminar theory and data is not known.

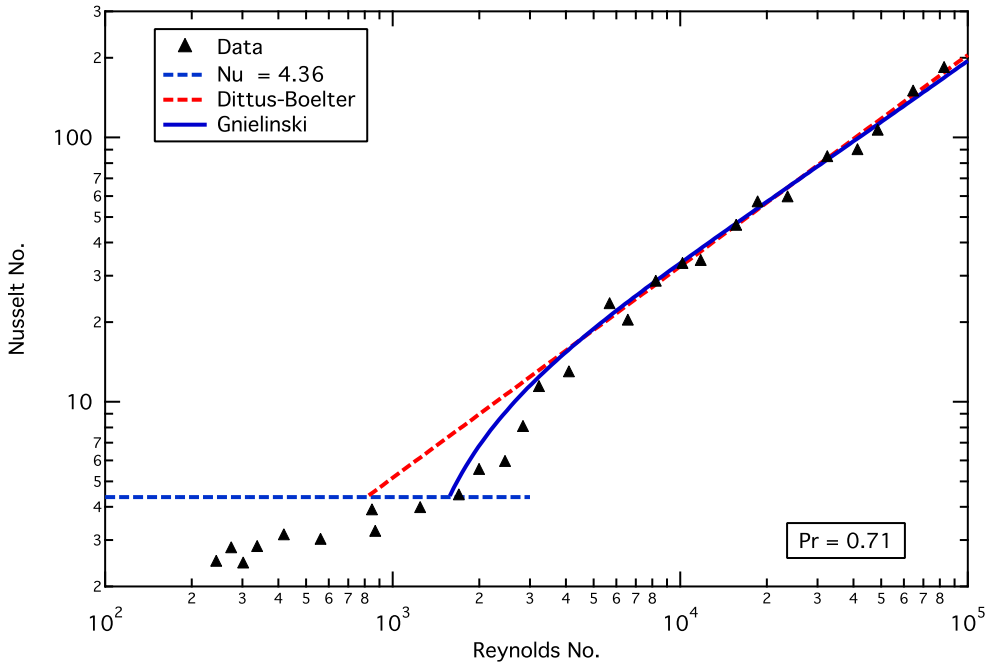

Figure. 6-3. Comparison of the Gnielinski and Dittus-Boelter correlations versus heat transfer data for air in a long heated tube.

The correction factor for temperature dependent property effects for single-phase liquid heat transfer is that of Hufschmidt and Burck (Ref. 6-6) as given in the original paper of Gnielinski. Namely,

$$Nu = Nu_0 \cdot \left(\frac{Pr_l}{Pr_w}\right)^{0.11} \tag{6-12}$$

where Nu_0 is the constant property value from Eq. (6-9), Pr_l is the liquid Prandtl no. evaluated at the liquid bulk temperature, and Pr_w is the liquid Prandtl no. evaluated at the wall surface temperature. This correction is valid for Prandtl no. ratios in the range

$$0.05 \le \frac{Pr_l}{Pr_w} \le 20$$

and for heating of the fluid, $T_w > T_b$. Note that although the above variable property correction factor for forced convection heat transfer to liquids was developed for tube data, it will also be applied for heat transfer in rod bundles.

Finally, for heat transfer due to natural convection, the correlations used in TRAC-PF1/MOD2 were retained (Ref. 6-7). Correlations for both the laminar and turbulent regimes are provided and a simple maximum of the two values is used to ensure continuity. The heat transfer coefficient is computed from

$$h_{NC} = \frac{k_l}{D_h} \cdot Nu_{NC} \tag{6-13}$$

where the liquid thermal conductivity is evaluated at the bulk fluid temperature and the characteristic length is the hydraulic diameter.

The Nusselt no. is then given by

$$Nu_{NC} = Max\left\{ Nu_{NC,\,lam}\,,\, Nu_{NC,\,turb} \right\} \tag{6-14}$$

where

$$Nu_{NC,\,turb} = 0.1 \cdot (Gr_l \cdot Pr_l)^{1/3} \tag{6-15}$$

is used for turbulent natural convection, and

$$Nu_{NC,\,lam} = 0.59 \cdot (Gr_l \cdot Pr_l)^{1/4} \tag{6-16}$$

for laminar natural convection. The Grashof no. appearing in Equations Eq. (6-15) and Eq. (6-16) is calculated using the hydraulic diameter as the characteristic length from

$$Gr_l = \frac{g \cdot \beta_l \cdot \Delta T \cdot D_h^3}{\left(\mu_l / \rho_{l,\,film}\right)^2} \tag{6-17}$$

where

$$\Delta T = \left| T_w - T_l \right| \tag{6-18}$$

and $\rho_{l,\,film}$ is the liquid density evaluated at a reference "film" temperature,

$$T_{film} = \frac{1}{2} \cdot (T_w + T_l) \tag{6-19}$$

With respect to the Nusselt no. formulations given above in Eq. (6-15) and Eq. (6-16), a few comments are in order. First, both of these formulas were developed for vertical plates. Also, the formula for turbulent natural convection, Eq. (6-15), is that for the local value on a plate, whereas the formula for laminar natural convection, Eq. (6-16), is that for the average value. To be consistent, the average value should also be used for the turbulent formula, that is,

$$Nu_{NC,\,turb} = 0.13 \cdot (Gr_l \cdot Pr_l)^{1/3} \tag{6-20}$$

Next, both of these formulas were originally developed with all of the fluid properties evaluated at the reference film temperature, while in TRACE all of the properties except the liquid density are evaluated at the bulk liquid temperature. This approach was chosen in the TRAC-PF1/MOD2 code to avoid extra calls to the thermodynamic properties subroutine and has been retained for this version of TRACE.

Finally, there is the question of the appropriateness of using the hydraulic diameter as the characteristic length whereas the correct length scale is the height of the vertical plate. For turbulent natural convection, this apparent discrepancy is moot because the length scale is cancelled out. That is,

$$h_{NC,\,turb} = 0.1 \cdot \frac{k_l}{D_h} \cdot \left[\frac{g \cdot \beta_l \cdot \Delta T \cdot D_h^3}{\left(\mu_l / \rho_{l,\,film}\right)^2} \right]^{1/3} \cdot Pr_l^{1/3} \tag{6-21}$$

which simplifies to,

$$h_{NC,\,turb} = 0.1 \cdot k_l \cdot \left[\frac{g \cdot \beta_l \cdot \Delta T}{\left(\mu_l / \rho_{l,\,film}\right)^2} \right]^{1/3} \cdot Pr_l^{1/3} \tag{6-22}$$

and so the dependence upon the hydraulic diameter disappears. However, for laminar natural convection, this is not the case and

$$h_{NC,\,lam} \propto D_h^{-1/4} \tag{6-23}$$

Although the dependency indicated by Eq. (6-23) is not correct, the resulting error is small. First, the ¼ power dependency reduces the effect. More importantly, for convection to liquid, the wall-liquid temperature difference in the Grashof no. seldom gets large enough for natural convection to be used because increases of the wall temperature result in a transition to nucleate boiling.

Rod Bundle Geometry

Although it has been standard practice to use tube correlations for forced convection heat transfer in a rod bundle, this tends to under-estimate the wall heat transfer coefficient. Consequently, it was decided to implement heat transfer correlations specific to rod bundle geometry in TRACE as described below.

Perhaps the best-known rod bundle heat transfer correlation is that of Weisman (Ref. 6-8) for fully developed turbulent flow. It is given by,

$$Nu_{turb} = C_W \cdot Re^{0.8} \cdot Pr^{1/3} \tag{6-24}$$

where the coefficient, C_W , is a function of the rod bundle pitch-to-diameter ratio as

$$C_W = 0.042 \cdot \left(\frac{P}{D_R}\right) - 0.024 \tag{6-25}$$

and the fluid properties are evaluated at the bulk fluid temperature. A similar formulation proposed by Inayatov (Ref. 6-9) is

$$Nu_{turb} = \Psi_t \cdot \Psi_s \cdot 0.023 \cdot Re^{0.8} \cdot Pr^{0.4} \tag{6-26}$$

where Ψ_t is a correction factor to account for the effect of variable fluid properties and Ψ_s is the factor to account for rod bundle geometry. Specifically, for liquid heat transfer, the variable property effect is that of Hufschmidt & Burck (Ref. 6-6) seen previously,

$$\Psi_t = \left(\frac{Pr_l}{Pr_w}\right)^{0.11} \tag{6-27}$$

and the rod bundle geometry is correlated by

$$\Psi_s = \sqrt{\frac{s_1 \cdot s_2}{D_R^2}} \tag{6-28}$$

where s_1 and s_2 are the pitches for a rectangular tube bundle. For liquid convection in a square rod bundle, the correlation of Inayatov then reduces to

$$Nu_{turb} = 0.023 \cdot \left(\frac{P}{D_R}\right) \cdot Re^{0.8} \cdot Pr^{0.4} \cdot \left(\frac{Pr}{Pr_w}\right)^{0.11} \tag{6-29}$$

or equivalently,

$$Nu_{turb} = C_{In} \cdot Re^{0.8} \cdot Pr^{0.4} \cdot \left(\frac{Pr}{Pr_w}\right)^{0.11} \tag{6-30}$$

with

$$C_{\mathrm{In}} = 0.023 \cdot \left(\frac{P}{D_R}\right) \tag{6-31}$$

Finally, a more recent correlation is that of El-Genk et al. (Ref. 6-10), which for fully developed turbulent flow in a bare rod bundle is also based on the Dittus-Boelter correlation and is given by

$$Nu_{turb} = C_{EG} \cdot Re^{0.8} \cdot Pr^{0.33} \tag{6-32}$$

where

$$C_{EG} = 0.028 \cdot \left(\frac{P}{D_R}\right) - 0.006 \tag{6-33}$$

and the fluid properties are evaluated at the bulk fluid temperature.

Figure 6-4 compares the above three expressions for C_W, C_{In}, and C_{EG}, for the rod bundle geometry effect. Especially in the range, $P/D_R \sim 1.33$, common for operating BWRs and PWRs, there is little to choose from as

$$C_W = 0.03186 \ ,$$
$$C_l = 0.03059 \ ,$$

and

$$C_{EG} = 0.03124$$

So, for the conditions of most interest, the correlation of El-Genk is intermediate in value being about 2% above that of Inayatov and 2% below that of Weisman and was selected for TRACE. Note that in the current TRACE version, the pitch-to-diameter ratio is fixed at a value of 1.33. Future code versions will include the pitch-to-diameter ratio as part of the heat structure input.

In addition to developing a correlation for turbulent forced convection, El-Genk et al. (Ref. 6-10) also investigated the transition and laminar regimes. Consequently, their model provides two

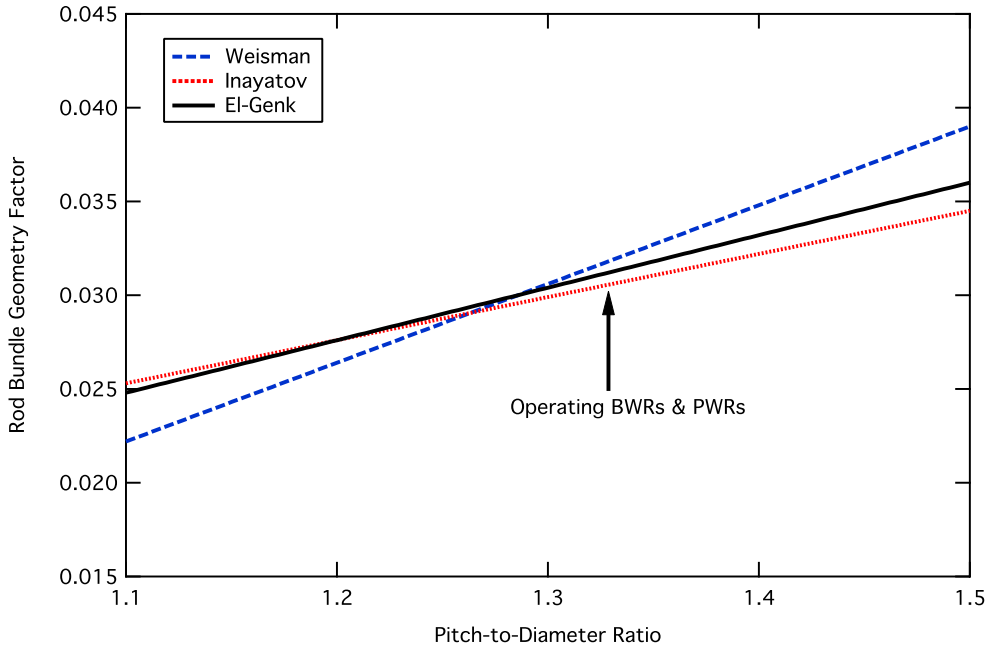

Figure. 6-4. Comparison of rod bundle geometry factor for turbulent convection heat transfer correlations of Weisman, Inayatov and El-Genk.

correlations, the turbulent formula given by Eq. (6-32) and Eq. (6-33), and the laminar formula given by

$$Nu_{lam} = A \cdot Re^{B} \cdot Pr^{0.33} \tag{6-34}$$

where

$$\begin{aligned} A &= 2.97 - 1.76 \cdot (P/D_R) \\ B &= 0.56 \cdot (P/D_R) - 0.30 \end{aligned} \tag{6-35}$$

The laminar and turbulent correlations of El-Genk, Eq. (6-32) through Eq. (6-35), were developed from an experimental database that covered the range:

$$P/D_R = 1.25\ ,\ 1.38\ ,\ and\ 1.50$$

$$250 \le Re \le 30000$$

$$3 \le Pr \le 9$$

As the correlation of El-Genk is the only one to provide coverage of the laminar and transition regimes in addition to the turbulent regime, it was selected for implementation in TRACE. Also,

for the turbulent correlation, the variable property effect of Hufschmidt & Burck (Ref. 6-6) for heat transfer to liquid is included as proposed by Inayatov. Thus,

$$Nu_{turb} = C_{EG} \cdot Re^{0.8} \cdot Pr^{0.33} \cdot \left(\frac{Pr}{Pr_w}\right)^{0.11} \tag{6-36}$$

One potential problem with the laminar correlation of El-Genk is that it goes to zero as the Reynolds no. decreases rather than approaching the expected constant value. Consequently, the analytical results presented by Kim & Li (Ref. 6-11) for fully developed laminar flow in a rod bundle with constant heat flux boundary condition are used as a lower limit. Kim & Li presented their results in a tabular format as shown in Table 6-1.

Table 6-1. Fully developed laminar Nusselt no. for square array rod bundles, Kim & Li (Ref. 6-11).

Pitch-to-Diameter	Nusselt no.
1.02	1.618
1.10	2.845
1.2	4.600
1.3	6.377
1.5	9.448
1.8	12.99
2	15.06

Rather than use tabular interpolation, their results are implemented in TRACE as a curvefit over the region, $1.1 \leq P/D_R \leq 2$, by

$$Nu_{KL} = -5.6605 \cdot \left(\frac{P}{D_R}\right)^2 + 31.061 \cdot \left(\frac{P}{D_R}\right) - 24.473 \tag{6-37}$$

which gives a value of 6.825 for a pitch-to-diameter ratio of 1.33.

To ensure continuity, the Nusselt no. for forced convection to liquid in a rod bundle geometry is taken as the maximum of the three values given by the analytical lower limit of Kim & Li, and the laminar and turbulent correlations of El-Genk. That is,

$$Nu_{FC} = Max\left\{ Nu_{KL} , Nu_{lam} , Nu_{turb} \right\} \tag{6-38}$$

The resulting model for forced convective heat transfer in a rod bundle is compared to that for a tube in Figure 6-5. In the fully turbulent regime, the rod bundle Nusselt no. is about 12% greater than that for a tube. However, in the laminar regime, the results are drastically different. Finally, recall that the correlations of El-Genk and the analytical result of Kim & Li are both for bare rod bundles. Thus, any heat transfer enhancement due to the presence of spacer grids should be superposed upon this.

Similar to the heat transfer model for convection to single-phase liquid in tubes, the Nusselt no. for liquid convection in a rod bundle is taken as the maximum of the values for forced and natural convection. That is,

$$Nu = Max\left\{ Nu_{FC} , Nu_{NC} \right\} \tag{6-39}$$

For the Nusselt no. due to natural convection, Nu_{NC}, TRACE needs a "local condition" model that correlates the wall heat transfer in terms of the local wall-to-fluid temperature difference. Most natural convection heat transfer models, however, use either an isothermal condition for the entire heat transfer surface or a constant power boundary condition and neither of these boundary conditions is appropriate for our application.

One local-condition correlation for natural convection in vertical tubes was found in the literature [Sarma et al., (Ref. 6-12)] and was implemented in TRACE. Sarma's correlation was developed expressly for mixed convection and is given by

$$Nu_{NC} = 0.7 \cdot (Gr_D \cdot Pr_l)^{1/4} \tag{6-40}$$

where the Grashof no. is defined in terms of the tube diameter using Eq. (6-17). As was the case for heat transfer in tubes, the liquid density is evaluated at the reference film temperature but all other properties are at the bulk liquid temperature. The values for the natural convection Nusselt no. from Eq. (6-40) are approximately three times higher than those for a vertical flat plate.

Two-Phase Forced Convection

As illustrated in Figure 6-2, the two-phase forced convection heat transfer regime is invoked whenever the fluid is two-phase and the wall temperature is below that necessary for the onset of nucleate boiling. Thus, it occurs both for fluid heating, $T_{ONB} > T_w > T_l$, and for condensing

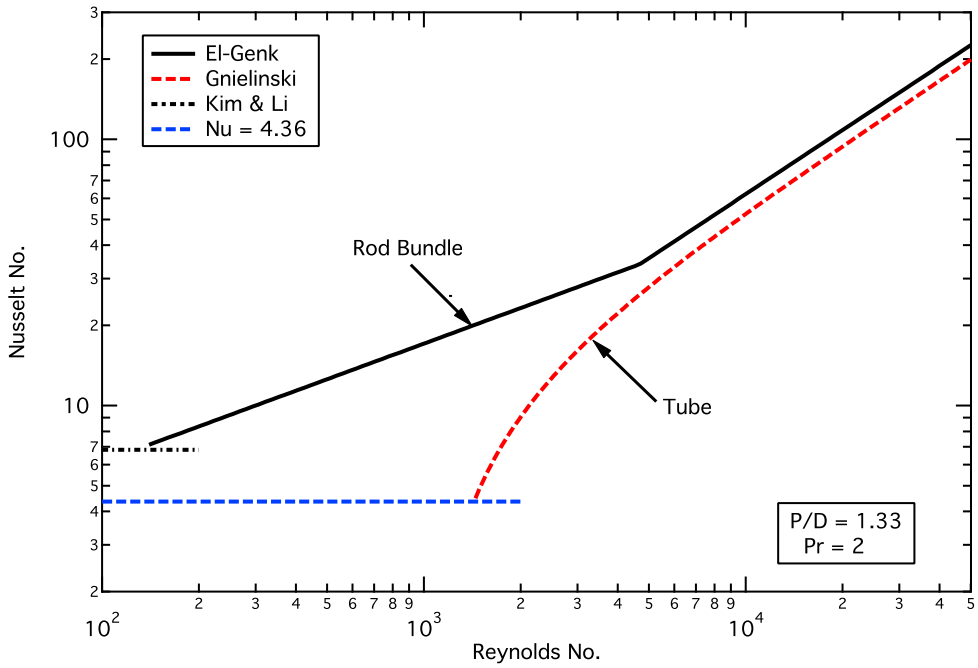

Figure. 6-5. Comparison of models for forced convection heat transfer in tube and rod bundle geometries.

flows, $T_w < T_{sv}$. In addition, as explained in the section ***Nucleate Boiling***, the models presented below for two-phase convective heat transfer are also used for the forced convection evaporation component when boiling is occurring.

When the fluid condition is two-phase and forced convection heat transfer is occurring, either with or without the presence of nucleate boiling, the forced convection heat transfer is significantly enhanced above that for single-phase flow. The approach developed here will be to use the single-phase heat transfer correlations described above with an appropriate multiplier to account for two-phase effects.

In TRAC-PF1/MOD2, this two-phase enhancement was accounted for by using the flow factor of the Chen nucleate boiling correlation (Ref. 6-13). The wall-liquid forced convection heat transfer coefficient is given by

$$h_{FC,2\Phi} = 0.023 \cdot \frac{k_l}{D_h} \cdot Re_l^{0.8} \cdot Pr_l^{0.4} \cdot F \tag{6-41}$$

The first part of the above equation is recognizable as the Dittus-Boelter correlation, the last term is Chen's flow factor. The flow factor, or "F factor", is a function of the Martinelli parameter, defined by

$$X_{tt} = \left(\frac{1-x}{x}\right)^{0.9} \cdot \left(\frac{\rho_g}{\rho_l}\right)^{0.5} \cdot \left(\frac{\mu_l}{\mu_g}\right)^{0.1} \tag{6-42}$$

The ratio involving the flow quality in X_{tt} can vary significantly from time-step to time-step for low flow conditions where the flow quality is ill-defined. This was one of the root causes of oscillations in RELAP5 for AP-600 calculations due to its usage in both the flow factor (which can vary by two orders of magnitude) and in the suppression factor of the nucleate boiling component of the Chen correlation. Consequently, another approach, one that is less likely to generate unphysical oscillations was selected for TRACE. That is, the two-phase multiplier for convective heat transfer should be a function of the void fraction rather than of flow quality.

Recently, Kim et al. (Ref. 6-14) critically reviewed twenty different heat transfer correlations for two-phase forced convection by comparing them against seven sets of experimental data. Two of the correlations consistently recommended were those of Aggour (Ref. 6-15) and Rezkallah & Sims (Ref. 6-16). Both of these correlations have their two-phase enhancement factor based on the void fraction and hence would be suitable for our application.

The correlation of Aggour (Ref. 6-15) is given by

$$\frac{h_{2\Phi}}{h_l} = (1-\alpha)^{-\frac{1}{3}} \tag{6-43}$$

$$Nu_l = 1.615 \cdot \left(Re_l \cdot Pr_l \cdot \frac{D_h}{L}\right)^{\frac{1}{3}} \cdot \left(\frac{\mu_b}{\mu_w}\right)^{0.14}$$

for laminar flow, and by

$$\frac{h_{2\Phi}}{h_l} = (1-\alpha)^{-0.83}$$

$$Nu_l = 0.0155 \cdot Re_l^{0.83} \cdot Pr_l^{0.5} \cdot \left(\frac{\mu_b}{\mu_w}\right)^{0.33} \tag{6-44}$$

for turbulent flow in tubes with the liquid Reynolds no. defined by

$$Re_l = \frac{G_l \cdot D_h}{\mu_l} = \frac{\rho_l \cdot (1-\alpha) \cdot V_l \cdot D_h}{\mu_l} \tag{6-45}$$

In both the above formulations, it is apparent that the role of the two-phase multiplier is to simply correct the liquid Reynolds no. so that it is based on the actual liquid velocity rather than the superficial liquid velocity. This is in accordance with Collier's (Ref. 6-17) observation that:

> "It would appear that in the bubbly and slug flow regimes, the mechanism of heat transfer is by the normal convective process to the liquid phase and that the enhancement over the single-phase liquid heat transfer coefficient is due, in general, to the increase in the liquid phase velocity in the two-phase case."

For turbulent flow, Rezkallah and Sims (Ref. 6-16) found that an excellent method of correlating the two-phase convective heat transfer coefficient was what they termed the "Liquid-Acceleration Model." In this model, it is implied that the role of the gas phase is to accelerate the liquid phase while the heat transfer coefficient is predicted using a conventional single-phase correlation with the liquid properties and an adjusted liquid velocity. The equation describing this model is

$$\frac{h_{2\Phi}}{h_l} = (1-\alpha)^{-n} \tag{6-46}$$

where the n is the exponent on the Reynolds no. for single-phase heat transfer.

Again, it is seen that the primary role of the enhancement factor is to correct the liquid Reynolds no. so that it is based on the actual liquid velocity rather than the superficial liquid velocity. Therefore, for implementation in TRACE, this is accomplished by defining a two-phase Reynolds no. as

$$Re_{2\Phi} = \frac{G_l \cdot D_h}{(1-\alpha)\cdot \mu_l} = \frac{\rho_l \cdot V_l \cdot D_h}{\mu_l} \tag{6-47}$$

and using it in the evaluation of the forced convection Nusselt no. This approach should work reasonably well (and is certainly simple) for turbulent forced convection in tubes, and for both laminar and turbulent convection in rod bundles using the correlations given in ***Single-Phase Liquid Convection***, above.

For laminar convection in tubes, where the Nusselt no. is not a function of the Reynolds no., this approach is not applicable. For the bubbly flow and slug regimes, as per Collier's observation, it is probably sufficient to simply leave the laminar Nusselt no. unmodified and that is the case in the TRACE model.

However, for annular flow, it is obvious that the characteristic length that should be used with the Nusselt no. is not the tube diameter but rather the thickness of the annular film. This is the approach followed in TRACE, and the heat transfer models used for convection in the annular flow regime are detailed below in ***Film Condensation***. To ensure continuity between the two-phase convection models and those for the annular flow regime, a simple linear interpolation in void fraction is used between the values of 80% to 90%. Specifically,

$$h_{wl} = wf_{ann} \cdot h_{ann} + (1 - wf_{ann}) \cdot h_{2\Phi} \tag{6-48}$$

where the weighting factor for annular flow is given by

$$wf_{ann} = \frac{(\alpha - 0.8)}{(0.9 - 0.8)} \tag{6-49}$$

and is limited to values between zero and unity.

Onset of Nucleate Boiling

As the wall temperature increases above the saturation temperature corresponding to the total pressure, nucleate boiling heat transfer can be initiated if the wall superheat is sufficient to activate nucleation sites present on the surface. The wall surface temperature at which nucleate boiling heat transfer begins is denoted as the "temperature for the onset of nucleate boiling", T_{ONB}. This temperature is used as part of the heat transfer regime selection logic as depicted in Figure 6-2 for the pre-CHF heat transfer regimes.

Recently, Basu et al. (Ref. 6-18) have proposed a correlation for ΔT_{ONB} , the wall superheat at the onset of nucleate boiling, that includes the effects of material surface properties by expressing the available cavity size as a function of the fluid-surface contact angle. Included in the database for this model is a 9-rod bundle with Zircaloy-4 cladding.

The wall superheat is then

$$\Delta T_{ONB} = \frac{4 \cdot \sigma \cdot T_{sat}}{D_c \cdot \rho_v \cdot h_{fg}} \tag{6-50}$$

where the available cavity size, D_c, is given by

$$D_c = F(\phi) \cdot D_c^0 \tag{6-51}$$

with $F(\phi)$ being a correction factor that depends on contact angle, and D_c^0 is the cavity diameter corresponding to the tangency condition. From the available data, the contact angle correction factor was determined to be

$$F(\phi) = 1 - \exp(-\phi^3 - 0.5 \cdot \phi) \tag{6-52}$$

where the contact angle, ϕ , is measured in radians. D_c^0 is obtained by invoking the minimum superheat criteria as

$$D_c^0 = \left(\frac{8 \cdot \sigma \cdot T_{sat} \cdot k_l}{\rho_v \cdot h_{fg} \cdot q''_w} \right)^{\frac{1}{2}} \tag{6-53}$$

Combining these equations, the wall superheat at the onset of nucleate boiling is then

$$\Delta T_{ONB} = \frac{\sqrt{2}}{F(\phi)} \cdot \left(\frac{\sigma \cdot T_{sat} \cdot q''_{ONB}}{\rho_v \cdot h_{fg} \cdot k_l} \right)^{\frac{1}{2}} \tag{6-54}$$

Figure 6-6 compares the values for the wall superheat at the onset of nucleate boiling calculated using the model of Basu et al. (Ref. 6-18) [Eq. (6-54)] with that of the empirical correlation of Bergles & Rohsenow (Ref. 6-19) and with that of the analytical model of Davis & Anderson (Ref. 6-20) for two different heat flux levels. At the modest wall heat flux level, $q''_{ONB} = 10^5 (W/m^2)$, the values given by all three models are nearly identical. For the higher heat flux level, $q''_{ONB} = 10^6 (W/m^2)$, such as might be encountered in subcooled boiling at high flow conditions, there is a small difference between the predicted values with those given by the models of Basu et al. being the highest and those of Bergles & Rohsenow the lowest. However, the maximum difference, that occurs at low pressure, is only about 1 Kelvin degree.

From the above comparison, any one of these models would be suitable, however, only the model of Basu et al. (Ref. 6-18) includes the surface material effect. Consequently, it was selected for use in TRACE. An example of the dependence upon the surface material is given in Figure 6-7 which compares the values for stainless steel with those for Zircaloy-4.

Equation (6-54) is an implicit relationship as the wall heat flux, appearing on the right-hand-side, is a function of ΔT_{ONB} . As the value of T_{ONB} is needed for the determination of the heat transfer regime, and an implicit formula would require an iterative solution, a procedure to translate this implicit formula into an explicit one was developed as detailed below.

Prior to the onset of nucleate boiling, single-phase heat transfer prevails on the heater surface. Thus, the associated wall heat flux can be expressed in terms of the single-phase convective heat transfer coefficient as

$$q''_{ONB} = h_{FC} \cdot (T_{ONB} - T_l) = h_{FC} \cdot (\Delta T_{ONB} + \Delta T_{sub}) \tag{6-55}$$

where h_{FC} is the forced convection heat transfer coefficient, and

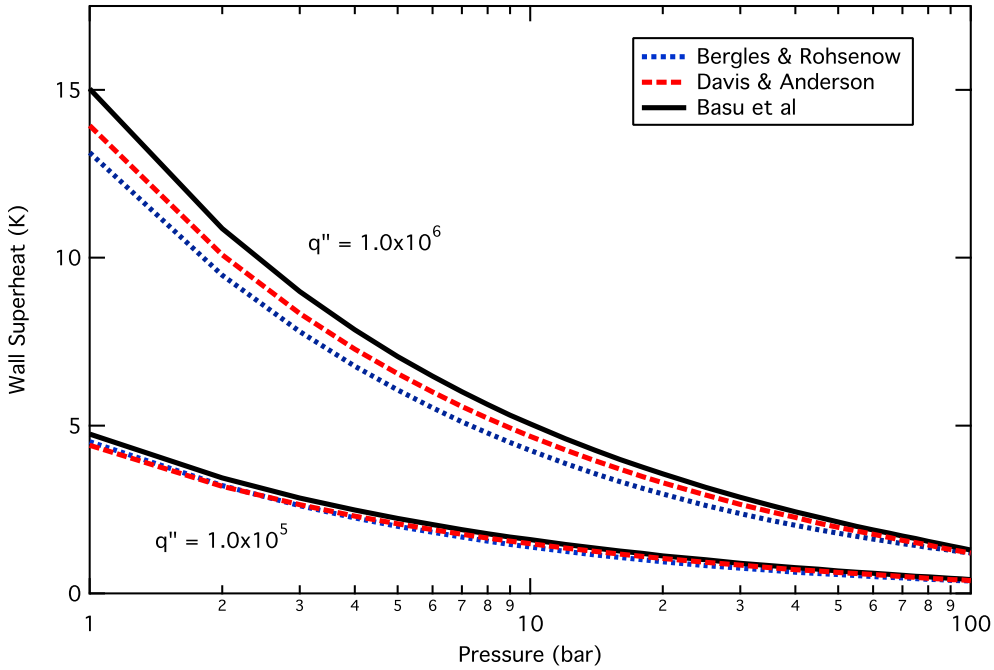

Figure. 6-6. Comparison of wall superheat values at the onset of nucleate boiling for three different models for water-stainless steel.

$$\Delta T_{ONB} = T_{ONB} - T_{sat}$$

$$\Delta T_{sub} = T_{sat} - T_l$$

Substitute Eq. (6-54) into Eq. (6-55) to yield,

$$q''_{ONB} = \frac{\sqrt{2} \cdot h_{FC}}{F(\phi)} \cdot \left(\frac{\sigma \cdot T_{sat} \cdot q''_{ONB}}{\rho_v \cdot h_{fg} \cdot k_l} \right)^{\frac{1}{2}} + h_{FC} \cdot \Delta T_{sub} \tag{6-56}$$

Equation (6-56) is implicit in q''_{ONB} but can be solved using the quadratic equation as

$$q''_{ONB} = \left[\frac{1}{2} \cdot \left(\sqrt{h_{FC} \cdot \Delta T_{ONB,\,sat}} + \sqrt{h_{FC} \cdot \Delta T_{ONB,\,sat} + 4 \cdot h_{FC} \cdot \Delta T_{sub}} \right) \right]^2 \tag{6-57}$$

where to simplify the notation, the quantity, $\Delta T_{ONB,\,sat}$, the wall superheat necessary for the onset of nucleate boiling when the liquid is at saturation, has been introduced and is given by

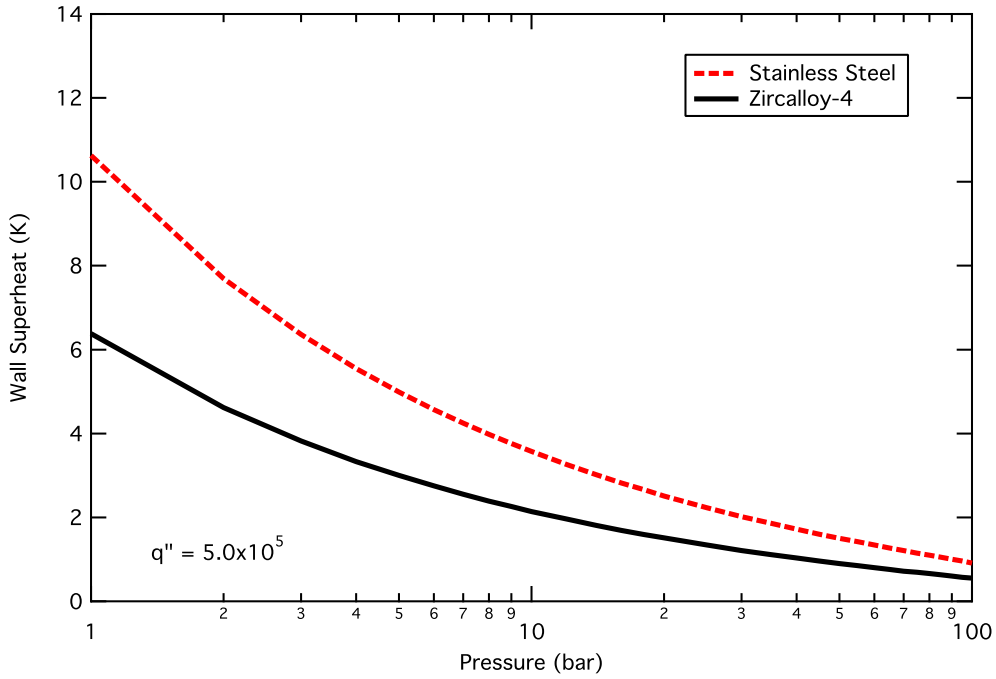

Figure. 6-7. Comparison of wall superheat values at the onset of nucleate boiling for stainless steel and Zircalloy-4 using the model of Basu et al. (Ref. 6-18) with water as the working fluid.

$$\Delta T_{ONB,\,sat} = \frac{\sqrt{2}}{F(\phi)} \cdot \left(\frac{\sigma \cdot T_{sat} \cdot h_{FC} \cdot \Delta T_{ONB,\,sat}}{\rho_v \cdot h_{fg} \cdot k_l} \right)^{\frac{1}{2}} \tag{6-58}$$

which yields

$$\Delta T_{ONB,\,sat} = \frac{2 \cdot h_{FC}}{F^2(\phi)} \cdot \frac{\sigma \cdot T_{sat}}{\rho_v \cdot h_{fg} \cdot k_l} \tag{6-59}$$

The wall-liquid temperature difference is then

$$T_w - T_l = \frac{q''_{ONB}}{h_{FC}} = \frac{1}{4} \cdot \left[\left(\sqrt{\Delta T_{ONB,\,sat}} + \sqrt{\Delta T_{ONB,\,sat} + 4 \cdot \Delta T_{sub}} \right) \right]^2 \tag{6-60}$$

and finally

$$T_{ONB} = T_l + \frac{1}{4} \cdot \left[\left(\sqrt{\Delta T_{ONB,\,sat}} + \sqrt{\Delta T_{ONB,\,sat} + 4 \cdot \Delta T_{sub}} \right) \right]^2 \tag{6-61}$$

This formula for T_{ONB} will be used to determine whether or not the heat transfer regime is forced convection or nucleate boiling. To use this model, we need the contact angle for the particular surface-fluid combination. From Basu et al., the contact angle for water and stainless steel is ~38º and for water and zircaloy-4 it is ~57º. At present, TRACE uses the value for stainless steel. A future code update will introduce the effect of surface material upon T_{ONB} .

Nucleate Boiling

The model for nucleate boiling must be suitable for pool boiling and for flow boiling at both saturated and subcooled conditions. The model traditionally selected for this, and the one used in TRAC-PF1/MOD2, is the Chen correlation (Ref. 6-21). The Chen correlation is a straightforward linear superposition of forced convection and pool boiling heat transfer components

$$h_{NB} = F \cdot h_{FC} + S \cdot h_{PB} \tag{6-62}$$

where F is the flow factor discussed in ***Two-Phase Forced Convection*** above and S is the suppression factor[1].

As noted above, the flow factor is a function of the Martinelli parameter that in turn is a function of the flow quality. The suppression factor is likewise a function of the Martinelli parameter and serves to turn off the nucleate boiling component of the wall heat flux as the flow quality increases. Consequently, for low flow conditions where the flow quality is ill-defined, the heat transfer coefficients calculated by the Chen correlation can vary wildly from time-step to time-step producing unphysical oscillations in the numerical solution. Although there are numerous more modern nucleate boiling heat transfer correlations that claim higher accuracy, the Chen correlation might be accurate enough for our purposes, however, the potential for poor numerical behavior led to its replacement in the TRACE code.

A second reason for choosing a more modern nucleate boiling correlation is the dependency of the boiling heat flux upon the wall superheat. That is,

$$q''_{PB} \propto \Delta T_{sat}^{n} \tag{6-63}$$

1. It would be preferable to use the subscript "FB" to indicate flow boiling instead of "NB". However, to avoid confusion with film boiling, "NB" will be used to indicate flow boiling.

where the exponent n is generally agreed upon to have a value between 3 and 4 (e.g., McAdams (Ref. 6-29)). However, for the Chen correlation, the value of n is only about 2. For a comparison with other correlations, both modern and classical, refer to Table 6-2.

Table 6-2. Comparison of wall superheat exponent in nucleate boiling.

Correlation	Year Published	Pressure (bar)	
		2.7	70
Chen (Ref. 6-21)	1963	2.16	2.07
Cooper (Ref. 6-22)	1984	3.03	3.03
Gorenflo (Ref. 6-23)	1993	3.92	2.84
Jens-Lottes (Ref. 6-24)	1951	4	4
Levy (Ref. 6-25)	1959	-	3
McAdams (Ref. 6-26)	1949	3.96	-
Steiner & Taborek (Ref. 6-27)	1992	3.31	2.67
Thom (Ref. 6-28)	1965	2	2

Also, to minimize the potential for unphysical oscillations caused by large fluctuations in the forced convective component that are especially troublesome for the low-pressure, low-flow conditions prevalent in passive plants during the long-term cooling phase, the model for the two-phase multiplier should be void fraction based rather than a function of flow quality. Consequently, the model discussed above in ***Two-Phase Forced Convection*** is retained for the forced convection component of the flow boiling regime.

Then, to complete the model for flow boiling, we need to:

1) Identify a suitable superposition method for the forced convection and nucleate boiling components.
2) Select a heat transfer correlation for the nucleate boiling component.
3) Determine an appropriate form for the nucleate boiling suppression factor.
4) Ensure continuity in the wall heat flux at the onset of nucleate boiling.

Each of these four items is discussed in the subsections below. Following this is a subsection on the implementation of the selected pool boiling model.

Flow Boiling Additive Approach

The super-position method is treated first. Steiner and Taborek (Ref. 6-27) proposed a flow boiling correlation where each of the components (forced convection and nucleate boiling) were correlated independently. The superposition method was an "asymptotic" or "power-type" addition model of the type proposed by Kutateladze (Ref. 6-30) and formalized by Churchill (Ref. 6-31) to represent the transition between two regimes, each dominated by different limiting phenomena. In generalized form, the asymptotic addition method for flow boiling is

$$h_{NB} = \left[h_{FC}^{n} + \left(S \cdot h_{PB} \right)^{n} \right]^{\frac{1}{n}} \tag{6-64}$$

From a regression analysis using the Karlsruhe heat transfer databank, Steiner and Taborek determined that the value of the exponent, n, should be ≈ 3 so that is the value that will be used here. Thus,

$$h_{NB} = \left[h_{FC}^{3} + \left(S \cdot h_{PB} \right)^{3} \right]^{\frac{1}{3}} \tag{6-65}$$

However, as we intend to use this model for both saturated and subcooled boiling where the sink temperatures are different, the asymptotic addition method will be applied to the heat flux components rather than to the heat transfer coefficients. That is,

$$q''_{NB} = \left[q''^{3}_{FC} + q''^{3}_{PB} \right]^{\frac{1}{3}} \tag{6-66}$$

and the wall-to-liquid heat transfer coefficient becomes

$$h_{wl} = \frac{q''_{NB}}{\left(T_w - T_l \right)} \tag{6-67}$$

Pool Boiling Model

To select a heat transfer correlation for the nucleate boiling component, three of the more modern boiling correlations were investigated: Steiner & Taborek (Ref. 6-27), Cooper (Ref. 6-22) and Gorenflo (Ref. 6-23). As a large nucleate boiling database was not readily available, the candidate correlations were evaluated through comparison with each other and with well-known classical models. For saturated pool boiling conditions, these three models were evaluated at pressures of 2.7 bar (typical of reflood and passive cooling conditions) and 70 bar (typical of BWR operating conditions and PWR SBLOCA pressure) and compared to the McAdam's

correlation (low pressure) and the Levy correlation (high pressure) as recommended by Holman (Ref. 6-32). The results of these comparisons are given in Figure 6-8 and Figure 6-9 where the nucleate boiling component of the Chen correlation has been included.

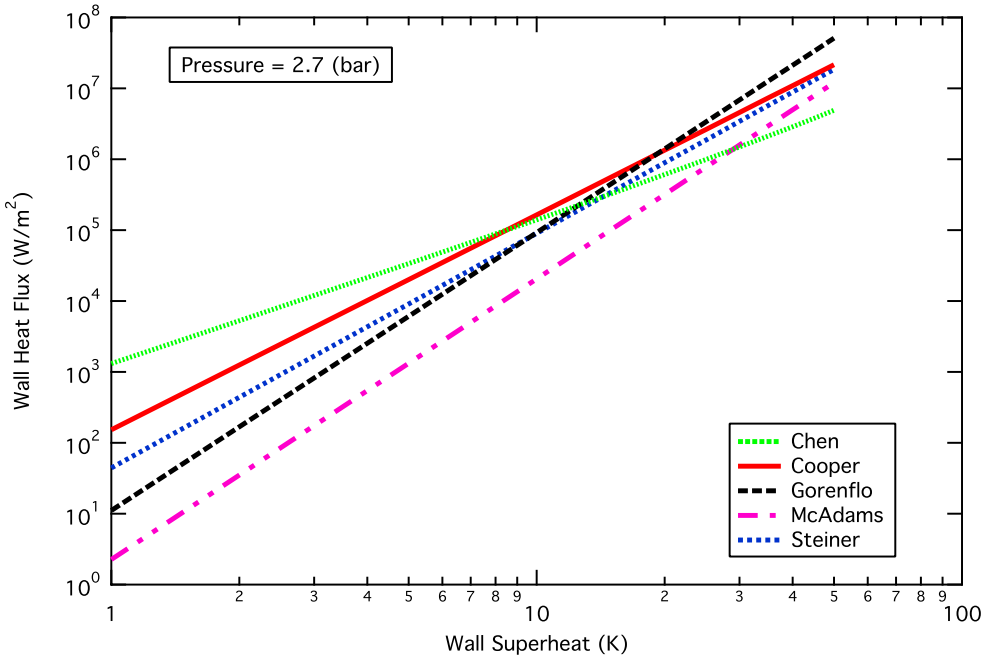

Figure. 6-8. Comparison of pool boiling correlations at low pressure.

For low pressure conditions, all of the modern correlations predict larger values of the saturated pool boiling heat flux than the correlation of McAdams. The model of Gorenflo has a similar slope to that of McAdams, that is, its dependence upon wall superheat has approximately the same power (3.92 versus 3.96), while the models of both Cooper and Steiner & Taborek have shallower slopes (exponents of 3.03 and 3.31 respectively). At high pressure conditions, the models of Gorenflo and Cooper give values of the wall heat flux very close to that of Levy while the values given by Steiner & Taborek are clearly too low. The dependence upon the wall superheat has an exponent of 3 for Levy's correlation, 2.67 for Steiner & Taborek, 3.03 for Cooper, and 2.84 for Gorenflo. Based on these comparisons, the model of Steiner & Taborek was eliminated from consideration.

Based on these comparisons, no definitive conclusions can be made as to the superiority of one correlation over another for the models of Cooper and Gorenflo. Also, implementation complexity is about the same for both models. Therefore, the model of Gorenflo was selected because of its lower predicted value of the nucleate boiling heat transfer coefficient at low superheats for low pressure conditions. The rationale for this choice is that during reflood simulations, for the region below the quench front where the boiling component should simply be removing the decay heat and wall superheats are only a few degrees, the model of Gorenflo will be less likely to produce large wall heat flux variations in response to small pressure oscillations.

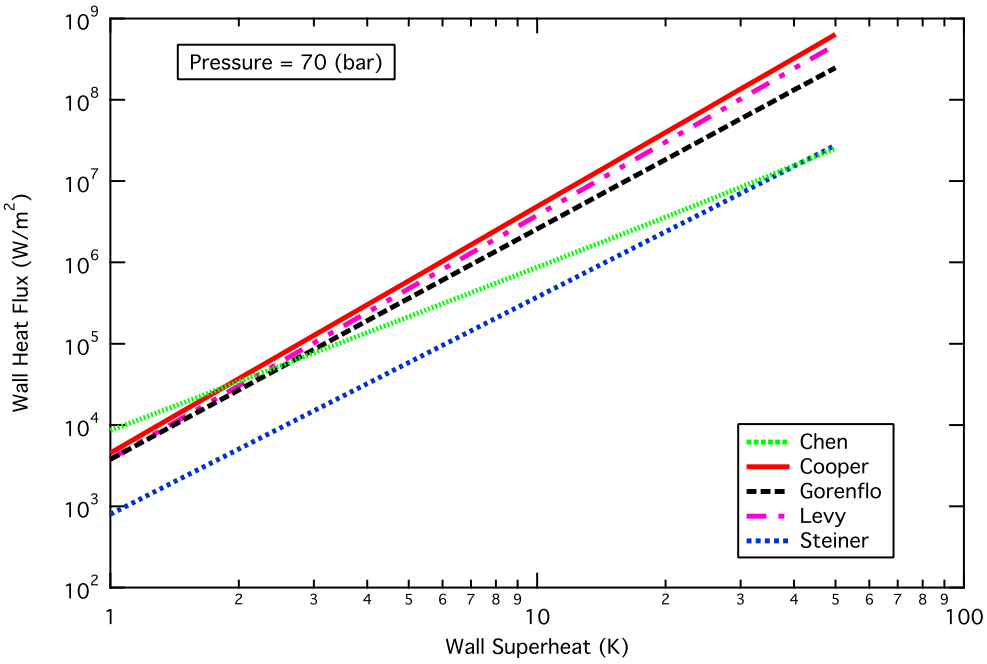

Figure. 6-9. Comparison of pool boiling correlations at high pressure.

The pool boiling model of Gorenflo uses a reference point formulation and is given by

$$h_{PB} = h_0 \cdot F_P \cdot (q''/q''_0)^n \cdot (R_P/R_{P0})^{0.133} \tag{6-68}$$

where, for water,

$$h_0 = 5600 \ \text{(W/m}^2\text{ - C)}$$

$$q''_0 = 20000 \ \text{(W/m}^2\text{)}$$

$$F_P = 1.73 \cdot P_r^{0.27} + \left(6.1 + \frac{0.68}{1 - P_r}\right) \cdot P_r^2$$

$$n = 0.9 - 0.3 \cdot P_r^{0.15} \tag{6-69}$$

with P_r being the reduced pressure,

$$P_r = \frac{P}{P_{crit}}$$

and the surface roughness having the reference value

$$R_{P0} = 0.4 \ \mu m$$

For boiling surfaces that have not been characterized, it is recommended that the roughness be taken to be $0.4 \ \mu m$, so that the surface roughness term is unity and this is the approach used in TRACE.

Nucleate Boiling Suppression Factor

The role of the nucleate boiling suppression factor is to "turn off" the nucleate boiling heat flux component as the flow regime becomes annular and the heat transfer regime switches to forced convection evaporation. That is, as the annular film becomes thin, the heat transfer mode becomes convection through the film causing evaporation at the interface rather than nucleation at the wall. The suppression factor, due to its dependence upon the film thickness, is also usually correlated in terms of the Martinelli parameter. Consequently, the numerical problems encountered for the "F factor" at low flow conditions also occur for the suppression factor.

A number of recent flow boiling models, see Steiner & Taborek (Ref. 6-27) or Bjorge et al. (Ref. 6-33), omit the suppression factor. Indeed, the appendix to Steiner & Taborek's paper makes the argument that the suppression factor doesn't exist. To avoid the numerical difficulties at low flow conditions observed with the Chen correlation, the approach used here will follow that which does not provide an explicit suppression factor. While an explicit suppression factor has not been included in the TRACE model, the effect of the two-phase forced convection heat transfer coefficient upon ΔT_{ONB} provides an implicit suppression of the nucleate boiling component of the wall heat flux.

Continuity at the Onset of Nucleate Boiling

The power-law combination used for the super-position of the forced convection and the nucleate boiling heat transfer components, that is,

$$q''_{NB} = \left[q''^{3}_{FC} + q''^{3}_{PB} \right]^{\frac{1}{3}} \tag{6-66}$$

leads to a jump in the wall heat flux at the point of ONB as the value of q''_{PB} abruptly changes from zero to a finite value. Though this discontinuity is usually small, it is best to remove it and the approach of Bjorge et al. (Ref. 6-33) is adopted to accomplish this. Namely,

$$q''_{NB} = \left[q''_{FC} + \left(q''_{PB} - q''_{BI} \right)^{3} \right]^{\frac{1}{3}} \tag{6-70}$$

where q''_{Bl} is the fully developed boiling heat flux at the point of boiling initiation,

$$q''_{BI} = q''_{PB}\,(T_{ONB}) \tag{6-71}$$

which forces the boiling component to be zero at T_{ONB}. Furthermore, as noted above, this approach provides an implicit suppression factor. For example, as the forced convection component increases, T_{ONB} increases, so that q''_{BI} increases and the nucleate boiling component of the total heat flux decreases.

Implementation of the Gorenflo Correlation

The Gorenflo correlation for the pool boiling heat transfer coefficient, with the roughness factor taken as unity, is

$$h_{PB} = h_0 \cdot F_P \cdot (q''/q''_0)^n \tag{6-72}$$

where the exponent is a function of pressure only. When only pool boiling is to be considered, the pool boiling heat flux is given by the implicit relationship

$$q''_{PB} = h_{PB} \cdot (T_w - T_{sat}) = h_0 \cdot F_P\,(q''_{PB}/q''_0)^n \cdot (T_w - T_{sat}) \tag{6-73}$$

This can be expressed explicitly as

$$q''_{PB} = \left(h_0 \cdot F_P / q''^n_0\right)^{\frac{1}{1-n}} \cdot \left(T_w - T_{sat}\right)^{\frac{1}{1-n}} \tag{6-74}$$

where the first term on the right hand side is a function of pressure and second term gives the dependence upon the wall superheat.

When the Gorenflo pool boiling correlation is used as part of a flow boiling correlation, where the total heat flux is given as the sum of forced convection and pool boiling components,

$$q''_{NB} = \left[q''_{FC} + (q''_{PB} - q''_{BI})^3\right]^{\frac{1}{3}} \tag{6-70}$$

an ambiguity occurs with respect to what heat flux should be used in the evaluation of the pool boiling heat transfer coefficient. That is, should we use

$$h_{PB} = h_0 \cdot F_P \cdot (q''_{PB}/q''_o)^n \tag{6-75}$$

or

$$h_{PB} = h_0 \cdot F_P \cdot (q''_{NB} / q''_o)^n \tag{6-76}$$

where the subscript "PB" indicates the pool boiling component only and the subscript "NB" indicates the total flow boiling heat flux. If the latter expression, i.e., Eq. (6-76), is used, and the wall superheat is the independent variable, an iterative procedure is required to evaluate the pool boiling component.

Except near the point for the onset of nucleate boiling, there is very little difference between these two approaches. Therefore, we have decided to use the approach that is the simplest to implement and the most computationally efficient. Thus, the pool boiling heat flux is used so that an explicit formula for the pool boiling heat transfer coefficient is

$$h_{PB} = (h_0 \cdot F_P / q''^n_0)^{\frac{1}{1-n}} \cdot (T_w - T_{sat})^{\frac{n}{1-n}} \tag{6-77}$$

This completes the description of the models used for pool and flow boiling in the TRACE code.

Subcooled Boiling Model

When the wall temperature exceeds that necessary for the onset of nucleate boiling, $T_w > T_{ONB}$, but the bulk liquid temperature is subcooled, $T_l < T_{sv}$, the wall heat transfer regime is subcooled nucleate boiling. In this regime, despite the subcooling of the liquid, significant levels of void fraction exist and are important to calculate accurately due to their effects on reactor kinetics, gravity heads in passive plants, and two-phase friction losses.

Recall from the Interfacial Heat Transfer chapter that the mass transfer rate per unit volume due to interfacial heat transfer is

$$\Gamma_i = \frac{q'''_{li} + q'''_{vi}}{(h_v^* - h_l^*)} \tag{6-78}$$

with the interfacial heat transfer rates given by

$$q'''_{li} = h_{li} \cdot A'''_i \cdot (T_l - T_{sv}) \tag{6-79}$$

for the liquid-side heat transfer and by

$$q'''_{vi} = h_{vi} \cdot A'''_i \cdot (T_g - T_{sv}) \tag{6-80}$$

for the gas-side heat transfer. With the liquid subcooled, the liquid-side heat transfer will be negative indicating the presence of condensation for the bulk flow conditions. Also, the gas-side heat transfer is usually negligible as the gas temperature is typically close to saturation. Consequently, to provide a mechanism for the generation of vapor during subcooled boiling, a special source term, Γ_{sub}, the mass transfer rate per unit volume due to subcooled boiling, was introduced. Thus, the net mass transfer is

$$\Gamma = \Gamma_i + \Gamma_{sub} \tag{6-81}$$

where for subcooled boiling, Γ_i would represent bulk condensation and Γ_{sub} the net vapor generation rate at the wall. It is the role of this section to describe the models used to calculate Γ_{sub} . The wall heat transfer coefficient in the subcooled nucleate boiling regime is calculated using the models described above in ***Nucleate Boiling*** and is not repeated here.

During subcooled boiling, vapor bubbles are generated at the wall due to nucleate boiling. Some of these bubbles immediately collapse due to condensation in the "near wall" region while others detach and become part of the bulk two-phase flow. Still other bubbles may slide along the heated surface before either condensing or growing large enough to detach. The details of these micro-processes are too complicated to be modeled explicitly in a reactor system analysis code such as TRACE. Instead, a constitutive model is provided that specifies the net vapor generation rate resulting from the competing processes of vapor generation and condensation in this near wall region.

In the nucleate boiling regime, the wall heat flux is comprised of both forced convection and pool boiling components. The fraction of the wall heat flux that results in subcooled vapor generation only derives from the pool boiling component as the forced convection component should only result in a change in the sensible heat. Recall that the total flow boiling heat flux is given by

$$q''_{NB} = \left[q''_{FC} + (q''_{PB} - q''_{BI})^3 \right]^{\frac{1}{3}} \tag{6-70}$$

This power-law additive scheme makes it difficult to determine what the actual pool boiling component is. Consequently, we will consider all of the wall heat flux in excess of forced convection as available to generate vapor, that is,

$$q''_{PB} \approx q''_{NB} - q''_{FC} \tag{6-82}$$

The net vapor generation rate due to subcooled boiling is then specified as a fraction of this boiling heat flux by

$$\Gamma_{sub} = \frac{f_{sub} \cdot (q''_{NB} - q''_{FC}) \cdot A'''_w}{(h_{v,sat} - h_l)} \tag{6-83}$$

where f_{sub} is the fraction that results in subcooled vapor generation and A'''_w is the surface area of the heat transfer surface per unit volume.

The fraction of the boiling heat flux that results in subcooled vapor generation is taken from the Lahey mechanistic subcooled boiling model (Ref. 6-34) and takes the form

$$f_{sub} = Max\left[0, \frac{(h_l - h_{ld})}{(h_{l,sat} - h_{ld})}\right] \tag{6-84}$$

where h_{ld} is the liquid enthalpy at which bubble detachment occurs.

Saha and Zuber (Ref. 6-35) give two separate formulations for h_{ld} based on the Peclet no. depending upon whether the subcooled boiling regime is thermally or hydrodynamically controlled. At low mass fluxes, it was found that the point of net vapor generation is dependent only on local thermal conditions, which determine the rates of vapor condensation and evaporation at the wall. To make an estimate of these two rates it was assumed that the rate of evaporation at the wall was proportional to the wall heat flux, whereas the rate of condensation was proportional to the local subcooling. Thus, the similarity parameter was taken to be the local Nusselt number defined by

$$Nu = \frac{q''_{NB} \cdot D_h}{k_l \cdot (T_{sat} - T_l)} \tag{6-85}$$

For high mass flux conditions, the phenomenon is hydrodynamically controlled, and the appropriate similarity parameter is the local Stanton number defined as

$$St = \frac{q''_{NB}}{G \cdot c_{p,l} \cdot (T_{sat} - T_l)} \tag{6-86}$$

The Peclet number, which by definition is the ratio of the Nusselt number and the Stanton number, is then

$$Pe = \frac{Nu}{St} = \frac{G \cdot D_h \cdot c_{p,l}}{k_l}, \tag{6-87}$$

was selected to be the correlation-independent parameter with the Stanton number as the dependent parameter. Data from 10 different sources were plotted as shown in Figure 6-10. The two distinct regions can easily be identified. Up to a Peclet number of 70000, the data fall in a straight line having the slope of minus one, which implies a constant value for the local Nusselt number. This is the thermally controlled region. Beyond a Peclet number of 70000, the data fall on a constant Stanton number, which is referred to as the hydrodynamically controlled region. The entire correlation for the point of net vapor generation is then expressed as

$$\begin{aligned} Nu &= 455 \quad : \quad Pe \leq 70000 \\ St &= 0.0065 \quad : \quad Pe > 70000 \end{aligned} \tag{6-88}$$

These two formulas can be written simply as

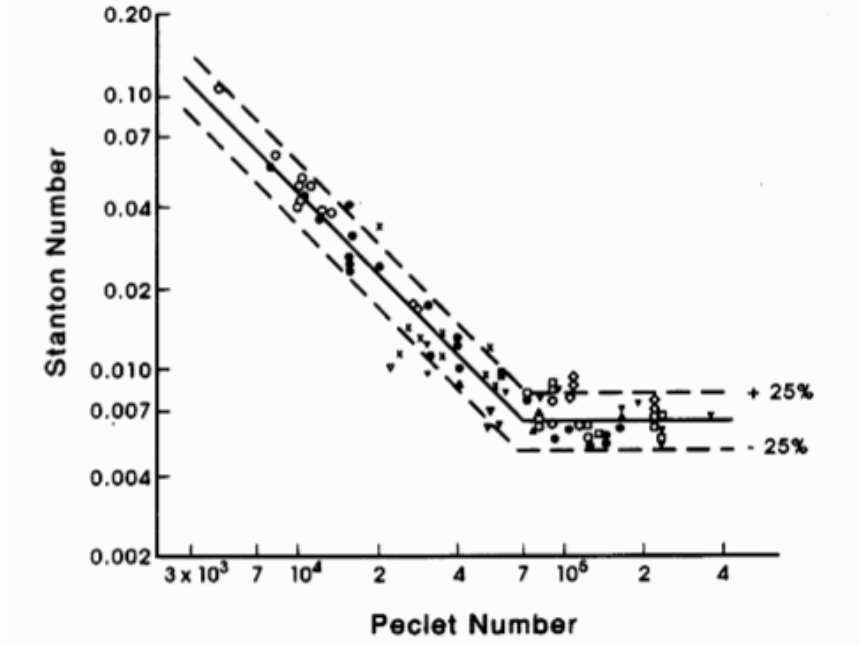

Figure. 6-10. Original database of the Saha-Zuber correlation.

$$(h_f - h_{ld}) = \frac{q''_{NB} \cdot D_h \cdot C_{p,l}}{Pe \cdot St} \tag{6-89}$$

where the Peclet no. is constrained to be larger than the critical value of 7.0×10^4. The Peclet no. is then

$$Pe = Max\left[7.0 \times 10^4 , \frac{G \cdot D_h \cdot c_{p,l}}{k_l}\right] \tag{6-90}$$

or

$$Pe = Max\left[7.0 \times 10^4 , Re_l \cdot Pr_l\right] \tag{6-91}$$

and the Stanton no. has a constant value of 0.0065.

Finally, the implementation of this model can be made a bit simpler by writing the subcooled vapor generation fraction in terms of temperature rather than enthalpy. Thus,

$$f_{sub} = Max\left[0 , \frac{(T_l - T_{ld})}{(T_{sat} - T_{ld})}\right] \tag{6-92}$$

and

$$(T_{sat} - T_{ld}) = \frac{q''_{NB} \cdot D_h}{Pe \cdot St} \tag{6-93}$$

where the Peclet no. is evaluated from Eq. (6-91) and the Stanton no. has a constant value of 0.0065.

Critical Heat Flux

The point where the maximum heat flux occurs in the idealized boiling curve shown in Figure 6-1 will be denoted as the CHF point, (q''_{CHF} , T_{CHF}) , and is characterized by both the critical heat flux and the wall temperature at which it occurs. This is the point where the heat transfer regime transitions from that where the liquid phase wets the wall (i.e., nucleate boiling), to the post-CHF regimes where liquid-wall contact is either transient (transition boiling) or non-existent (film boiling).

In TRACE, the role of the CHF model is two-fold:

1) Determine the transition point for the heat transfer regime, and
2) Serve as the anchor point for the transition boiling wall heat flux (see ***Transition Boiling*** below).

To serve both these roles, the CHF model in TRACE must provide a continuous estimate of the CHF over a wide range of conditions with reasonable accuracy. This range of conditions must extend from the high pressure, high-flow conditions typical of operating PWRs and BWRs, to the low pressure, low-flow conditions existing after a LBLOCA or for a passive plant in the long term cooling phase.

For the analysis of anticipated transients, such as a perturbation in the core flow or inlet subcooling, the metric is the departure from nucleate boiling (DNB) margin. DNB is one of the types of CHF and for each fuel type there are specific DNB correlations with high accuracy. Most of these correlations employ the boiling length concept, in which the core inlet quality or enthalpy explicitly appears in the correlation. During many transients and postulated accidents, however, the use of boiling length correlations is not appropriate. For example, during a cold-leg-break LOCA, the core experiences a flow reversal thereby rendering the definition of the core inlet ambiguous. In addition, these correlations are unsuited for general use in TRACE because they are highly empirical with a limited range of validity, and are unreliable when extrapolated outside their original database.

Therefore, for the default CHF model in TRACE the 1995 AECL-IPPE CHF look-up table (Ref. 6-36) was selected. It is based on an extensive database of CHF values obtained in tubes with a vertical upflow of a steam-water mixture and provides the value of the critical heat flux as a function of the local conditions. As described below, a correction factor is included to improve the accuracy of this table when applied to rod bundles. This look-up table allows for a reasonably accurate prediction of CHF based on the local flow conditions for a much wider range of conditions than would be possible with either empirical correlations or phenomena based models.

To define the CHF point, the wall temperature at which the critical heat flux occurs must be determined. This is accomplished by solving the equation

$$q''_{NB}(T_{CHF}) = q''_{CHF} \tag{6-94}$$

which requires an iterative solution due to the non-linearities associated with the flow boiling heat flux as a function of wall temperature. As shown above in Figure 6-2, the critical heat flux temperature, T_{CHF} , is used to determine whether the heat transfer regime is pre- or post-CHF. Also, both q''_{CHF} and T_{CHF} are used in the formulation for the wall heat flux in the transition boiling regime.

For BWRs, the high-quality, high mass flux conditions may introduce memory effects that limit the accuracy of a local condition CHF model such as the default look-up table. Therefore, as part of the consolidation of the TRAC-B code's capabilities into TRACE, two critical quality correlations were implemented as well and are described below. Either of these critical quality correlations can be selected by the user via input through the "ICHF" parameter in the heat structure input. In TRACE, the role of these critical quality correlations is limited to that of determining the transition point from nucleate to transition boiling. That is, if the local flow quality exceeds the value of x_{crit} , the heat transfer regime switches to post-CHF. For the wall

heat flux in the transition boiling regime, however, the CHF point calculated using the look-up table is used.

AECL-IPPE CHF Table

Groeneveld et al. (Ref. 6-36) published an updated look-up table for CHF that was developed jointly by AECL[1] Research (Canada) and IPPE[2] (Russia). This method of determining the value of the critical heat flux was selected for TRACE because of its reasonably good accuracy and wide range of applicability. The AECL-IPPE CHF table is based upon an extensive database of CHF values obtained in tubes for a vertical upward flow of a steam-water mixture. While the database covers a wide range of flow conditions, the look-up table was designed to provide CHF values for 8 mm tubes at discrete values of pressure, mass flux, and dryout quality. Three-dimensional linear interpolation is used to determine the CHF for conditions between tabulated values and is implemented as a direct-indexing scheme to reduce the computational burden associated with a table look-up.

The database used to develop the AECL-IPPE look-up table contains 22,946 unique data points covering the following range of conditions:

$3 \leq D \leq 40$ (mm)

$0.1 \leq P \leq 20$ (MPa)

$6 \leq G \leq 8000$ (kg/m^{2}s)

$-0.5 \leq x \leq 1$

$80 \leq L/D \leq 2485$

Despite the large number of data points in this database, the data population density at some flow conditions remains relatively low thereby contributing to greater uncertainty, especially for low flow conditions where CHF is very difficult to measure due to unstable flow conditions. The resulting table was constructed to provide CHF values for 8 mm tubes at discrete values of pressure, mass flux, and dryout quality, and includes empirical correction factors to extend the table to other tube diameters and for rod bundles. Details of the table's derivation and accuracy are given in the original reference (Ref. 6-36) by Groeneveld and are not repeated here. Compared against the combined AECL-IPPE CHF databank, the 1995 look-up table predicts the

1. AECL: Atomic Energy of Canada Limited.
2. IPPE: Institute of Power and Physics, Obninsk, Russia.

data with overall average and root-mean-squared errors of 0.69% and 7.82% respectively. The implementation of the look-up table in TRACE is described below.

The value of the critical heat flux is given by

$$q''_{CHF} = K_1 \cdot K_2 \cdot K_8 \cdot fn\{P, G, x\} \tag{6-95}$$

where K_1 is the correction factor for tube diameter, K_2 is the correction factor for rod bundle geometry, K_8 is the correction factor for low flow conditions and $fn\{P, G, x\}$ is the table look-up value.

These correction factors and the procedures used to extrapolate outside the table boundaries are given below. In addition to the above correction factors, Groeneveld (Ref. 6-37) provides other factors for effects such as that of axial flux shape, heated length and grid spacers. However, these factors were not implemented in this version of TRACE.

The first parameter used in the table look-up is the total pressure. As the table values cover the range, $0.1 \leq P \leq 20$ (MPa) , extrapolation outside this range is seldom encountered. In TRACE, no provision is made for extrapolation to sub-atmospheric conditions; however, the procedure recommended by Groeneveld (Ref. 6-37) is used to extrapolate to pressures above this range. Specifically, the pool boiling relationship is used, so that

$$q''_{CHF}(P, G, x) = q''_{CHF}(P_{20}, G, x) \cdot \frac{\left(\rho_g^{1/2} h_{fg} [\sigma \cdot \Delta\rho]^{1/4}\right)\Big|_P}{\left(\rho_g^{1/2} h_{fg} [\sigma \cdot \Delta\rho]^{1/4}\right)\Big|_{P_{20}}} \tag{6-96}$$

where $q''_{CHF}(P_{20}, G, x)$ indicates the table look-up value at a pressure of 20 MPa. To avoid the extra computational burden associated with the fluid property calls necessary to evaluate the last term in Eq. (6-96), a curve-fit is used in TRACE. Thus,

$$\frac{q''_{CHF}(P, G, x)}{q''_{CHF}(P_{20}, G, x)} = 1.546 \cdot P^* - 1.6108 \cdot P^{*2} + 1.7818 \cdot P^{*3} - 0.7199 \cdot P^{*4} \tag{6-97}$$

where the non-dimensional pressure is defined by

$$P^* = \frac{P_{crit} - P}{P_{crit} - P_{20}} \tag{6-98}$$

The second parameter used in the table look-up is the mass flux, G. For co-current flow conditions, either upflow or downflow, the mass flux is taken to be the sum of the individual phasic liquid and gas mass fluxes as expected. However, for counter-current flow conditions, for which the table is not strictly applicable, the mass flux is set to that of the liquid phase alone. That is,

$$G = \begin{cases} G_l + G_g & : \quad (G_l \cdot G_g) > 0 \\ G_l & : \quad (G_l \cdot G_g) \leq 0 \end{cases} \tag{6-99}$$

For mass flux values greater than the table upper limit, no extrapolation is made. The mass flux is simply set to the maximum value,

$$G = Min\left\{8000\ ,\ G\right\} \tag{6-100}$$

as recommended by Groeneveld (Ref. 6-37). Finally, for two-phase low mass flux conditions, $-400 \leq G \leq 100$ (kg/m^{2}s) , the low flow correction factor, K_8, is applied as described below.

The final parameter used in the table look-up is the quality, x, defined as

$$x = \frac{h_m - h_{l,\,sat}}{h_g - h_{l,\,sat}} \tag{6-101}$$

where h_m is the flowing mixture enthalpy given by

$$h_m = \frac{G_l \cdot h_l + G_g \cdot h_g}{G_l + G_g} \tag{6-102}$$

Substitution of Eq. (6-102) into Eq. (6-101) yields

$$x = \frac{G_g}{G} + \frac{G}{G} \cdot \left(\frac{h_l - h_{l,\,sat}}{h_g - h_{l,\,sat}} \right) \tag{6-103}$$

Examination of Eq. (6-103) reveals that for co-current flow with saturated liquid, the expression reduces to the expected value for the flow quality,

$$x = \frac{G_g}{G} \tag{6-104}$$

Similarly, for single-phase liquid conditions, Eq. (6-103) becomes the familiar

$$x = \frac{h_l - h_{l,sat}}{h_{g,sat} - h_{l,sat}} \tag{6-105}$$

The definition of quality given by Eq. (6-101) and Eq. (6-102) is meaningless for counter-current flow. Consequently, a "static" quality is introduced to account for this special case. The static quality, x_{static}, is calculated from the void fraction using Eq. (6-101) and a mixture enthalpy given by

$$h_m = \frac{(1-\alpha)\cdot\rho_l\cdot h_l + \alpha\cdot\rho_g\cdot h_g}{(1-\alpha)\cdot\rho_l + \alpha\cdot\rho_g} \tag{6-106}$$

With both phases at saturation, this reduces to

$$x_{static} = 1/\left[1 + \frac{(1-\alpha)\rho_l}{(\alpha\rho_g)}\right] \tag{6-107}$$

This static quality is used both for counter-current flow conditions and for the special case of low flow in the evaluation of the K_8 correction factor.

The CHF look-up table is constructed so that the CHF value for a quality of unity is set to zero. As the maximum dryout quality is 1.0, no need for extrapolation beyond this point is needed. At the lower end, table values for subcooled conditions are supplied for values down to a quality of -0.5. For high-pressure conditions, it is possible for the liquid subcooling to be large enough that this lower bound is exceeded. For this case, a linear extrapolation is used as recommended by Groeneveld (Ref. 6-37).

The three correction factors used in TRACE are described next. First, the diameter factor, K_1, is

$$K_1 = \sqrt{0.008/D_h} \tag{6-108}$$

and is based on data for a range of tube diameters from 0.62 mm to 92.4 mm. For large diameter tubes, Groeneveld (Ref. 6-36) observed that the value of K_1 seems to approach a constant value of about 0.6. Thus,

$$K_1 = Max\left\{0.6\ ,\ \sqrt{0.008/D_h}\right\} \tag{6-109}$$

Also, Groeneveld notes that the CHF for small diameter tubes is more difficult to estimate due to the small amount of data and that the effect of diameter on CHF is more likely to be affected by flow conditions. So, caution should be used when applying this correction factor to tubes with a diameter of less than 3 mm. This caveat has little relevance to reactor safety applications where the characteristic dimension is much larger than this value.

For rod bundle geometries, Groeneveld et al. (Ref. 6-38) recommend

$$K_2 = \left[2 \cdot \left(\frac{P}{D_R}\right) - 1.5\right] \cdot \exp\left(-\frac{x^{1/3}}{2}\right) \tag{6-110}$$

where (P/D_R) is the pitch-to-diameter ratio for the bundle, as the simplest one available and one that exhibits the correct asymptotic trends. Furthermore, the value of K_2 is constrained to be less than unity. Thus, for a typical rod bundle with $P/D_R = 1.33$, the ratio of the CHF value for the rod bundle to that of an 8 mm diameter tube is within the range $0.7339 \le K_2 \le 1$. In the evaluation of this rod bundle correction factor, note that the quality is limited to positive values and that the diameter factor, K_1, is set to unity.

For two-phase low mass flux conditions, Eq. (6-95) includes a correction factor denoted as K_8. Although indicated as a multiplicative correction factor, the low flow correction is actually implemented through an interpolation procedure. First, the procedure used to construct the pool boiling, $G = 0$, part of the look-up table is briefly described, followed by an explanation of the recommended interpolation procedure that was implemented in TRACE.

Due to the scarcity of reliable CHF data for low flow conditions, Groeneveld (Ref. 6-36) used the pool boiling CHF model of Zuber (Ref. 6-39) as the basis for the table values at zero mass flux. Two modifications were then made to improve the accuracy of the pool boiling CHF model for subcooled and two-phase conditions. For subcooled pool boiling, the increase in the CHF with subcooling was modeled using the correlation of Ivey & Morris (Ref. 6-40). For negative values of the quality, the CHF table was then computed from

$$q''_{CHF}\ (P\ ,\ G = 0\ ,\ x < 0) = q''_{CHF}\ (P\ ,\ G = 0\ ,\ x = 0) \cdot [1 + B \cdot \Delta T_{sub}] \tag{6-111}$$

where $q''_{CHF}\ (P\ ,\ G = 0\ ,\ x = 0)$ is the CHF value from the Zuber pool boiling model and

$$B = 0.1 \cdot \left(\frac{\rho_l}{\rho_g}\right)^{0.75} \left(\frac{c_{P,l}}{h_{fg}}\right) \tag{6-112}$$

For low flow two-phase conditions, Griffith (Ref. 6-41) showed that the value of the pool boiling CHF decreased in an approximately linear manner with the decrease in the liquid fraction. This approach was built into the CHF look-up table with the provision that the value of the quality used for the table look-up be computed using the static value given above in Eq. (6-107). Thus,

$$q''_{CHF}\ (P\ ,\ G = 0\ ,\ x > 0) = q''_{CHF}\ (P\ ,\ G = 0\ ,\ x_{static}) \tag{6-113}$$

The mass flux boundaries of the low flow region for the AECL-IPPE CHF look-up table are defined as $-400 \le G \le 100$ (kg/m^2-s). Within this region, a linear extrapolation is performed between the look-up table value at the limit and the pool boiling value with the quality set to the static value. For positive flow, $0 \le G < 100$ (kg/m^2-s), this gives

$$\begin{aligned} q''_{CHF}\ (P\ ,\ G\ ,\ x) = {} & wf \cdot q''_{CHF}\ (P\ ,\ G = 100\ ,\ x) \\ & + (1 - wf) \cdot q''_{CHF}\ (P\ ,\ G = 0\ ,\ x_{static}) \end{aligned} \tag{6-114}$$

where the weighting factor is

$$wf = G/100 \tag{6-115}$$

and for negative flow, $-400 \le G < 0$ $(kg/m^2 s)$,

$$\begin{aligned} q''_{CHF}\ (P\ ,\ G\ ,\ x) = {} & wf \cdot q''_{CHF}\ (P\ ,\ G = 400\ ,\ x) \\ & + (1 - wf) \cdot q''_{CHF}\ (P\ ,\ G = 0\ ,\ x_{static}) \end{aligned} \tag{6-116}$$

with the weighting factor given by

$$wf = -G/400 \tag{6-117}$$

In addition to providing a much wider range of applicability than that of the Biasi CHF correlation (Ref. 6-42), the default model in the TRAC-PF1/MOD2 code, the selection of the AECL-IPPE look-up table for TRACE also provides gains in accuracy. Figure 6-11 and Figure 6-12 show examples of the behavior of the predicted CHF values from the look-up table and from the Biasi correlation for high-pressure high-flow case and a low-pressure low-flow case respectively.

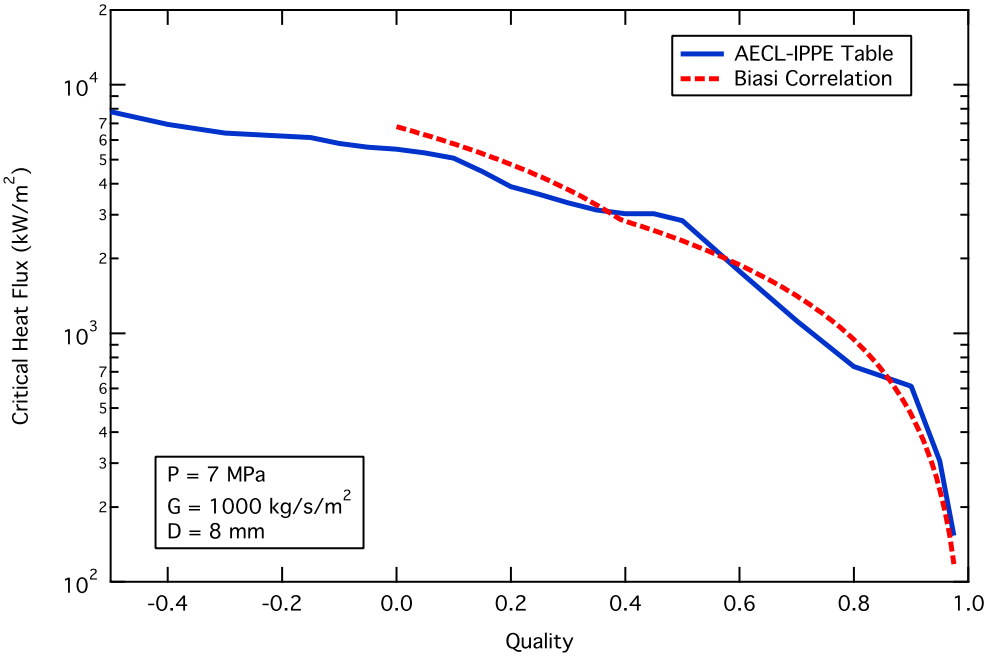

Figure. 6-11. Comparison of the AECL-IPPE CHF table and the Biasi correlation for high-pressure high-flow conditions.

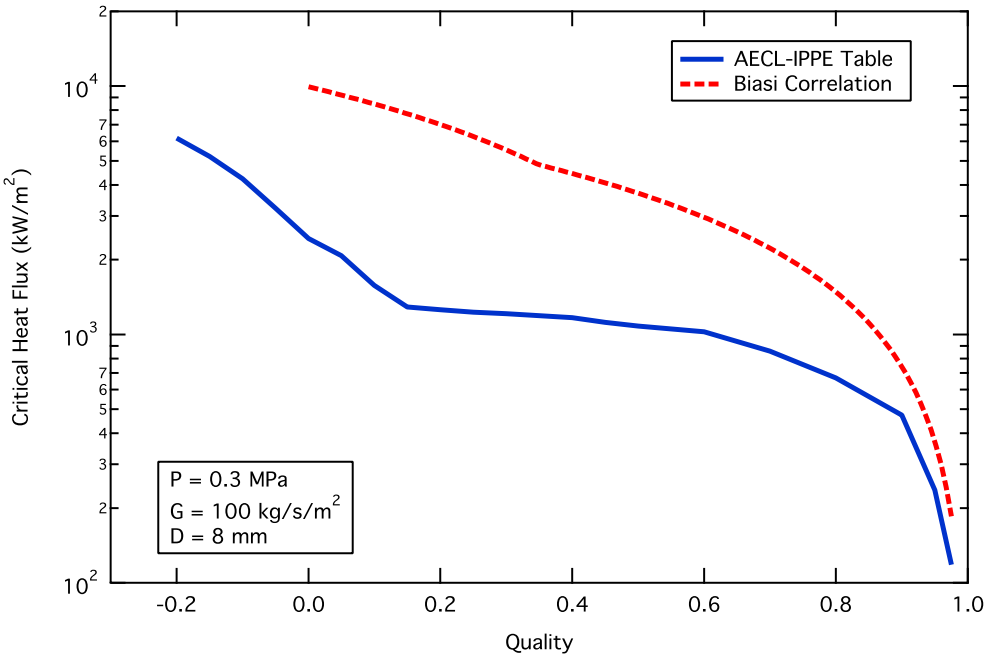

Figure. 6-12. Comparison of the AECL-IPPE CHF table and the Biasi correlation for low-pressure low-flow conditions.

From these figures, the applicability of the CHF table to subcooled conditions, whereas the Biasi correlation is limited to two-phase conditions, is readily apparent. Also, in Figure 6-11, the CHF values for the high-pressure high-flow comparison are remarkably similar, as is to be expected, as the database used to develop the Biasi correlation is included in that used for the lookup table. Conversely, in Figure 6-12, the CHF values for the low-pressure low-flow comparison are quite different. Indeed, comparing the two figures reveals that the predicted CHF values from the Biasi correlation for the low-pressure low-flow case exceed those for the high-pressure high-flow case. This low-flow behavior of the Biasi correlation is contrary to experimental evidence and reveals a limitation of the correlation even though these conditions are within its stated range of applicability.

In both Figure 6-11 and Figure 6-12, the curves of CHF versus quality from the look-up table are not smooth. Groeneveld (Ref. 6-36) notes that this undesirable behavior is present in all three parametric directions: pressure, mass flux, and quality. These fluctuations are attributed to data scatter, systematic differences between different data sets, and possible effects of such second-order parameters as the heated length, surface conditions and flow instability. Future revisions to the CHF look-up table, in addition to improving accuracy, may also improve the smoothing algorithm used to create the table.

Finally, a quantitative comparison of the accuracy of the CHF look-up table versus the Biasi correlation is given in Reference (Ref. 6-36). The database used was that of AECL-IPPE but only the data points within the recommended range of the Biasi correlation were used in the comparison. This reduced the number of data values from 22,946 to 14,977. For this reduced data set, the overall average and RMS errors for the look-up table were 0.38% and 8.17% respectively, compared to errors of 6.48% and 14.38% for the Biasi correlation.

In summary, the wider range of applicability and improved accuracy of the AECL-IPPE look-up table over that of the Biasi correlation led to its selection as the default model in the TRACE code. However, as stated above, for transient DNB analysis, where the flow conditions do not deviate drastically from their nominal values, highly accurate DNB correlations for specific fuel types are available and should be used when the estimation of the DNB margin is paramount. Such fuel type specific DNB correlations have not been incorporated in TRACE due to their limited range of applicability and their proprietary nature.

For BWR conditions, as part of the consolidation of TRAC-B's capabilities within the TRACE code, a pair of critical quality correlations were implemented in TRACE and are described in the following two sections. The user, through the heat structure input "ICHF" parameter, can select either of these critical quality correlations. When one of these critical quality correlations is selected, its value is used in determining the transition point from pre- to post-CHF heat transfer as illustrated in Figure 6-19 below. However, even in this case, the values of the CHF point, (q''_{CHF}, T_{CHF}), used in the determination of the wall heat flux for the transition boiling regime are calculated using the CHF look-up table.

CISE-GE Critical Quality

In a boiling water reactor, the core exit under normal operating conditions is in the annular/mist flow regime. Consequently, the transition from flow boiling to post-CHF heat transfer is governed by annular film dryout. The dryout of the liquid film on the wall is determined by a balance between losses due to vaporization and entrainment and gains due to droplet deposition. In future versions of TRACE, a droplet field will be included and these processes can be modeled directly. However, in the present two-fluid version, it is necessary to provide a constitutive model to predict the location of film dryout and hence the point of boiling transition.

The most widely used empirical approach for the computation of the dryout point is the "critical quality-boiling length" approach. The inclusion of the boiling length - the axial distance from the location where the bulk fluid enthalpy reaches saturation to the dryout point - in this approach gives a measure of the upstream history that is important to the prediction of film dryout that is not available in a local conditions approach such as the AECL-IPPE look-up table. Two critical quality correlations were available in the TRAC-B code and have been incorporated into TRACE as part of the code consolidation process: the CISE-GE correlation (the subject of this section), and a model derived from the Biasi CHF correlation (the subject of the next section). Either of these models may be selected through the specification of the "ICHF" parameter in the heat structure input.

The critical quality-boiling length approach was introduced by Bertoletti et al. (Ref. 6-43) and has the general form

$$x_{crit} = \frac{A \cdot L_B}{B + L_B} \tag{6-118}$$

where L_B is the boiling length and

$$A = fn\left\{ P\,,\ G \right\}$$

$$B = fn\left\{ P\,,\ G\,,\ D \right\}$$

The CISE-GE correlation (Ref. 6-44) is a modified form of the original CISE (Ref. 6-43) tube correlation that was derived from blowdown heat transfer experiments performed by the General Electric Corporation (GE). It is therefore based on data from rod bundle experiments and includes the effect of local peaking factors. The database from which it was derived is limited and the correlation is adequate only for mass fluxes in the range $300 \leq G \leq 1400$ (kg/m^2-s) . Note that in its TRACE implementation, the critical quality is set to unity if the mass flux is outside this range or if the boiling length is less than one meter.

In TRACE, the modified CISE-GE correlation from TRAC-BF1/MOD1 (Ref. 6-44) is used, so that

$$x_{crit} = \frac{A \cdot L_B}{B + L_B} \cdot \left(\frac{1.24}{R_f} \right) \tag{6-119}$$

where the last term is a correction factor for the effect of the radial peaking factor, R_f. In the formulas given below, the functions A and B are expressed in British units, specifically, the mass flux has the units ($Mlb_m/ft^2/hr$), the pressure is in psia, and the boiling length in inches. Then,

$$A = 1.055 - 0.013 \left(\frac{P - 600}{400} \right)^2 - 1.233 \cdot G + 0.907 \cdot G^2 - 0.285 \cdot G^3 \tag{6-120}$$

and

$$B = 17.98 + 78.873 \cdot G \cdot -35.464 \cdot G^2 \tag{6-121}$$

Also, for the case of an 8x8 rod bundle,

$$B = B / 1.12 \tag{6-122}$$

which corrects for the effect of the difference between the heated perimeter for the 8x8 bundle versus a 7x7 bundle for which the correlation was originally derived.

Biasi Critical Quality

In addition to the CISE-GE critical quality correlation, a form of the Biasi CHF correlation (Ref. 6-42) transformed into a critical quality correlation has been included. Phillips et al. (Ref. 6-45) developed this correlation and it was selected for inclusion in TRAC-B due to its large database and greater mass flux range, i.e., $100 \leq G \leq 6000$ (kg/m^2s) .

The original Biasi CHF correlation has two separate formulas for the CHF value. Consequently, the transformed critical quality correlation also has two formulas for the critical quality and the maximum value of the two is used. Thus,

$$x_{crit} = Max \left\{ x_{crit,1}, x_{crit,2} \right\} \tag{6-123}$$

The general form of the Biasi critical quality correlation is

$$x_{crit,k} = \frac{A_k \cdot L_B}{B_k + L_B} \cdot \left(\frac{P_h}{P_w}\right) \cdot \left(\frac{1}{R_f}\right)^{1/2} \tag{6-124}$$

where the subscript k indicates the formula, P_h is the heated perimeter, and P_w is the wetted perimeter. The functions A and B are then specified for each formula as

$$A_1 = 1.0$$

$$B_1 = \frac{1.048 \times 10^{-8} \cdot G^{1.6} \cdot D_h^{1.4} \cdot h_{fg}}{H(P)} \tag{6-125}$$

and

$$A_2 = F(P) / G^{1/6}$$

$$B_2 = 5.707 \times 10^{-8} \cdot G^{7/6} \cdot D_h^{1/4} \cdot h_{fg} \tag{6-126}$$

The functions of pressure, $F(P)$ and $H(P)$, used in the above formulas are written in terms of the pressure in bars and are given by

$$F(P) = 0.7249 + 0.099 \cdot P \cdot \exp\{-0.032 \cdot P\}$$

$$H(P) = -1.159 + 0.149 \cdot P \cdot \exp\{-0.019 \cdot P\} + \frac{8.99 \cdot P}{(10 + P^2)} \tag{6-127}$$

The Biasi critical quality correlation was implemented the TRAC-B code due to its larger database and greater mass flux range compared to the CISE-GE correlation. However, unlike the CISE-GE correlation, it is not based on rod bundle data and is also subject to the assumptions used in converting it from a local CHF correlation into a critical quality correlation (Ref. 6-45). The TRAC-B code manual notes that the Biasi x_{crit} correlation gives larger values of the critical quality than the CISE-GE correlation. An example of this is given in Figure 6-13. The over-prediction of the Biasi correlation vis-à-vis CISE-GE is considerable and indicates that the Biasi form should be used with caution due to its potential for non-conservatism.

In its TRACE implementation, due to poor performance at low mass fluxes, the Biasi x_{crit} correlation is only evaluated for mass fluxes greater than 300 (kg/m^2-s) . For values of the mass

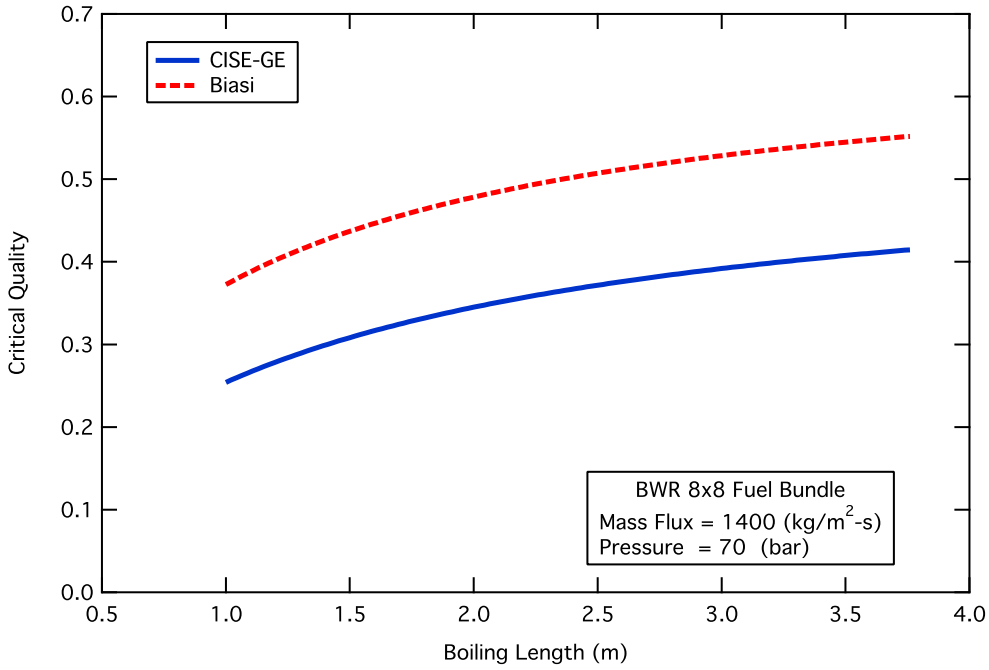

Figure. 6-13. Comparison of predicted critical quality for the CISE-GE and Biasi correlations for high-pressure high-flow conditions.

flux less than this, or if the boiling length is less than one meter, the critical quality is set to unity. Also, negative mass fluxes (i.e., downflow) are computed using the absolute value of the mass flux.

Minimum Film Boiling Temperature

The temperature where the minimum post-CHF heat flux occurs in the idealized boiling curve shown in Figure 6-1 will be denoted as the minimum film boiling temperature, i.e., T_{min}. In the literature, this point is referred to by many other names according to the specific circumstances under which it is observed. For example, during the high-pressure high-flow conditions associated with blowdown during a LBLOCA, it is referred to as the "rewet temperature", during low-pressure bottom reflood as the "quench temperature", during quenching of a rod by a falling liquid film as the "sputtering temperature", and, of course, classically as the "Leidenfrost point". For all of these cases, this temperature designates the point at which the heat transfer regime switches from transition boiling to film boiling or vice-versa and corresponds to the point at which the wall superheat is high enough that no appreciable liquid-wall contact occurs. This section describes the model selected for this transition temperature. In what follows, T_{min} will be used in lieu of the other names mentioned above with the one exception that a distinction will be drawn between T_{min} and the "quench temperature" as discussed below.

There is a general consensus that T_{min} is governed by hydrodynamic stability for low pressure conditions and then by the maximum liquid superheat condition as the pressure increases. If hydrodynamic stability governs (e.g., the well-known Berenson model (Ref. 6-46)), then liquid subcooling is an important parameter. Material properties (e.g., thermal conductivity) of the heater surface have little impact as the surface is insulated from the liquid by a relatively thick vapor film. Surface roughness, if sufficiently rough, can be a factor though, as the vapor film must blanket the highest peaks on the surface.

At higher pressures (perhaps as low as 2-3 bar for water), the governing process appears to switch to that of the maximum liquid superheat condition. Basically, this states that for liquid-wall contact to occur the wall temperature must be low enough that the liquid will not exceed its maximum superheat value, that is the liquid temperature must remain below that at which homogeneous nucleation would occur. When transient conduction effects are considered, in effect taking the instantaneous "contact temperature" to be equal to the homogeneous nucleation temperature, then material property effects can be included and are substantial for a surface with a sufficiently thick coating of a low conductivity material such as zircaloy dioxide.

Indeed, in early reactor system analysis codes such as COBRA-TRAC (Ref. 6-47) the model for T_{min} used the minimum of the values given by the Berenson model and the homogeneous nucleation temperature with a contact temperature correction applied. These two models are plotted in Figure 6-14 against data from both the Winfrith (Ref. 6-48) and Groeneveld-Stewart (Ref. 6-49) "hot patch" film boiling tests. Also included in this figure is the correlation of Groeneveld and Stewart (Ref. 6-49). The conditions of these tests were such that subcooling was negligible and, as the tubes were Inconel, the contact temperature correction is also minimal. Furthermore, the tests were conducted so that the reported T_{min} is more representative of a "spontaneous collapse" of film boiling rather than the "quench temperature" associated with a propagating quench front.

As can be seen in Figure 6-14, the Berenson model, which is based on hydrodynamic stability of the vapor film, is close to the data at only very low pressure (2 bar or less) and rapidly goes to unrealistically high values as the pressure increases. Obviously, the approach of taking the minimum of the values given by the Berenson model and the homogeneous nucleation temperature with a contact temperature correction provides a more reasonable approximation for T_{min} over the entire pressure range than using Berenson alone. However, compared to the data, it appears that this approach could over-predict T_{min} for pressures of a few bar and under-predict it significantly for higher pressures. In addition, this approach does not capture the subcooling effect evident in other data.

The Groeneveld-Stewart correlation (Ref. 6-49) is an empirical relation for the minimum film boiling temperature valid over a wide range of pressure (1-90 bar) that includes the subcooling effect and consequently was selected as the model for T_{min} in TRACE. This correlation is based on vapor film collapse data that is purported to be unaffected by a propagating quench front. The reason that this distinction is made is that the "quench temperature" is somewhat higher than the

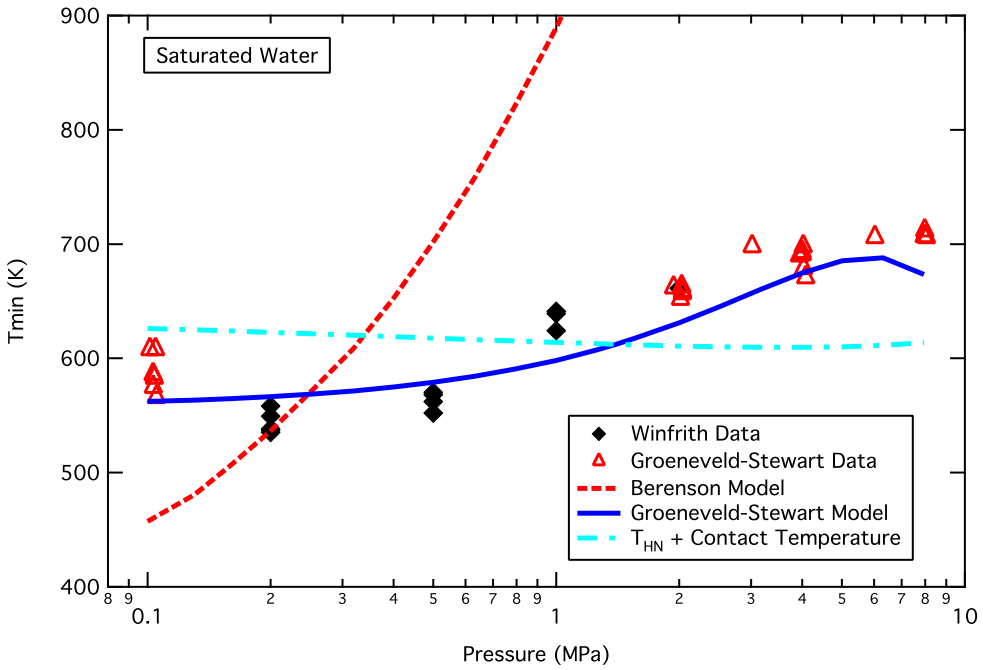

Figure. 6-14. Comparison of data and models for the minimum film temperature for saturated water and Inconel surface as a function of pressure.

actual minimum film boiling temperature due to the axial conduction effects present at a quench front. The Groeneveld-Stewart correlation for saturated water (or positive quality conditions) is given by

$$T_{min,sat} = 557.85 + 44.1 \cdot P - 3.72 \cdot P^2 \tag{6-128}$$

for pressures less than 9 MPa where $T_{min,sat}$ is in K and P is in MPa. In their database, both the effects of mass flux and quality (for positive values) were deemed negligible.

A significant effect of subcooling was observed and was correlated by

$$T_{min} = T_{min,sat} - \frac{x \cdot 10^4}{(2.82 + 1.22 \cdot P)} \tag{6-129}$$

where x is the subcooled quality. This can be rewritten in terms of liquid enthalpy as

$$T_{min} = T_{min,sat} + \frac{\left(h_{l,sat} - h_l\right)}{h_{fg}} \cdot \frac{10^4}{(2.82 + 1.22 \cdot P)} \tag{6-130}$$

For pressures in excess of this correlation's database, the authors recommend that T_{min} be calculated by

$$T_{min} = \Delta T_{min}(9\,MPa) \cdot \frac{(P_{crit} - P)}{(P_{crit} - 9)} + T_{sat} \tag{6-131}$$

where $\Delta T_{min}(9\,MPa)$ is the wall superheat corresponding to T_{min} at a system pressure of 9 MPa. The effect of Eq. (6-131) is to ramp the calculated value for T_{min} to the critical temperature as the pressure approaches the critical point.

In Figure 6-14, the Groeneveld-Stewart correlation was plotted against both their own data and the Winfrith data and gave a more reasonable behavior with pressure than the approach that used Berenson and the homogeneous nucleation temperature. The inclusion of the Winfrith data in this figure, which were not part of the database used to develop the correlation, serves to verify its predicted behavior for T_{min} with pressure and support its selection for TRACE.

In many simple film boiling experiments, it has been observed that the minimum film boiling temperature is greatly increased as the liquid subcooling increases. For example, Dhir and Purohit (Ref. 6-50), for subcooled forced convection film boiling on spheres in water at atmospheric pressure, observed that T_{min} increased about 80 K for every 10 degree K increase in liquid subcooling. They further observed that the effects of liquid mass flux and surface material properties were minimal. Note, however, that their experiment was at low pressure and so should be controlled by hydrodynamic stability and that the materials they tested (steel, copper, and silver) all had relatively high thermal conductivities. The subcooling effect of the Groeneveld-Stewart correlation is in good agreement with this trend at atmospheric pressure, namely, it gives an increase of about 63 K for every 10 degree K increase in liquid subcooling.

At high pressure, it is expected that T_{min} will be governed by the maximum superheat limit of the liquid and that subcooling would not be a major factor. Yet, the subcooling effect given by the Groeneveld-Stewart correlation for high-pressure conditions is still considerable. For example, at a pressure of 9 MPa, the Groeneveld-Stewart correlation predicts an increase in T_{min} of about 28 K for every 10 degree K increase in liquid subcooling. This result is somewhat surprising as the controlling mechanism is no longer that of hydrodynamic stability. However, this trend is well supported by their database as shown in Figure 6-15 for a pressure of 9 MPa.

Figure 6-14 compared the behavior of the Groeneveld-Stewart correlation with pressure for data associated with the vapor film collapse mechanism up to values of 9 MPa for the system pressure. To examine its behavior both at higher pressures and for quench conditions, the high-pressure quench data taken at the ROSA-TPTF facility (a 5x5 rod bundle, (Ref. 6-51)) and for a single-rod reflood experiment conducted by JAERI (Ref. 6-52) will be used. For both series of tests, the

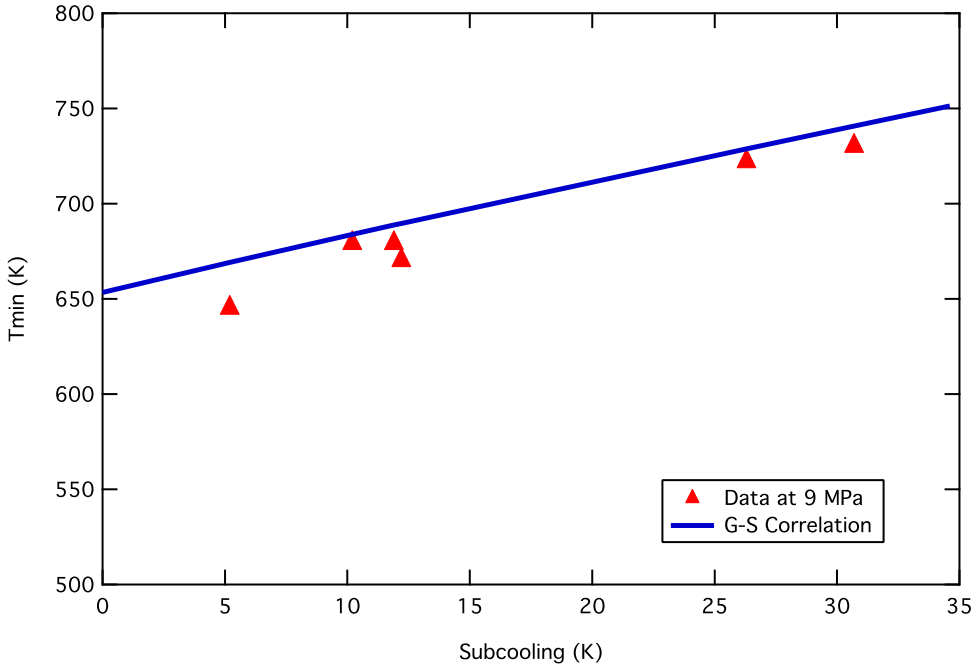

Figure. 6-15. Comparison of the subcooling effect in the Groeneveld-Stewart correlation with high-pressure data.

liquid inlet was saturated, so no subcooling effect is present. Also, for both experiments, the heater rods were clad with Inconel 600, so material property effects, due for example to the presence of a low-conductivity surface oxide, are expected to be minimal. However, both of these experiments were quenching tests and it is expected that the observed value of the quench temperature would be somewhat in excess of T_{min} due to the aforementioned effects of axial conduction at the quench front. Given this expectation, Groeneveld-Stewart does a reasonable job of predicting the behavior of the data with pressure as shown in Figure 6-16.

In Figure 6-16, each data point represents the mean value for all of the thermocouples in the rod bundle (9 instrumented rods with a total of about 57 thermocouples per test). The errors bars in the figure then represent the range of measured quench temperatures, that is, the maximum and minimum observed values, for each test. The first observation from this data is that, in agreement with the Groeneveld-Stewart correlation, there is no effect of the mass flux upon the quench temperature. Second, it is clear that the value of T_{min} from the Groeneveld-Stewart correlation consistently under-predicts the high-pressure quench data by 20 to 70 degrees K. Finally, though the general prediction of the behavior with respect to pressure is reasonably good, the extrapolation procedure employed for pressures above 9 MPa leads to a discontinuity in the slope. It appears that the relatively rapid decrease in T_{min} given by Groeneveld-Stewart for pressures greater than about 6 MPa is primarily a result of the data fitting procedure used and the limitations of their database.

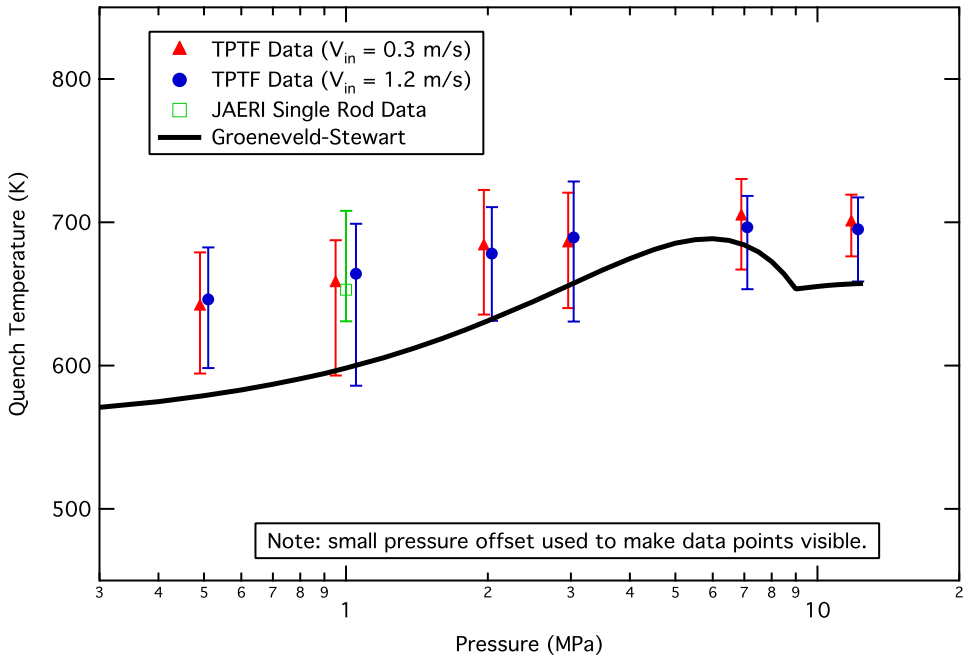

Figure. 6-16. Comparison of Groeneveld-Stewart correlation to JAERI high-pressure rod bundle and single-rod quench data for inconel clad rods.

Based on the consistent under-prediction of the quench temperature by the correlation of Groeneveld-Stewart as indicated in Figure 6-16, further investigation is warranted. As shown in Figure 6-17, for a low-pressure reflood test conducted in the FLECHT-SEASET facility, the quench temperature can be identified as that which coincides with the "knee" of the clad temperature curve thereby indicating the switch from film boiling to transition boiling. This transition from film boiling through transition boiling to nucleate boiling is very abrupt in both time and space having an axial extent of only about 1 cm of the heater rod surface. Mathematically, the quench temperature point can be specified as that where the curvature of the clad temperature trace reaches its maximum negative value.

For the thermocouple trace in Figure 6-17, the inferred quench temperature is about 800 K whereas the Groeneveld-Stewart correlation gives a value of only 570 K. Some fraction of this 230 K under-prediction is probably due to surface property effects as the FLECHT-SEASET rods are clad with stainless steel that will oxidize more heavily than Inconel rods. However, the majority of the discrepancy is probably due to differences between the "spontaneous film collapse" mechanism upon which the Groeneveld-Stewart correlation is based and what occurs at the location of a quench front. Therefore, a modification to the value of T_{min} in the vicinity of a quench front is made in TRACE to improve its performance for the prediction of reflood tests.

Quench temperature data from a total of seven FLECHT-SEASET low-pressure reflood tests (Ref. 6-53) and nine THTF high-pressure reflood tests (Refs. 6-54 and 6-55) were compiled to form the database shown in Figure 6-18. For the FLECHT-SEASET tests, a total of 763 data points were collected and indicated a wide spread of quench temperatures with the distribution

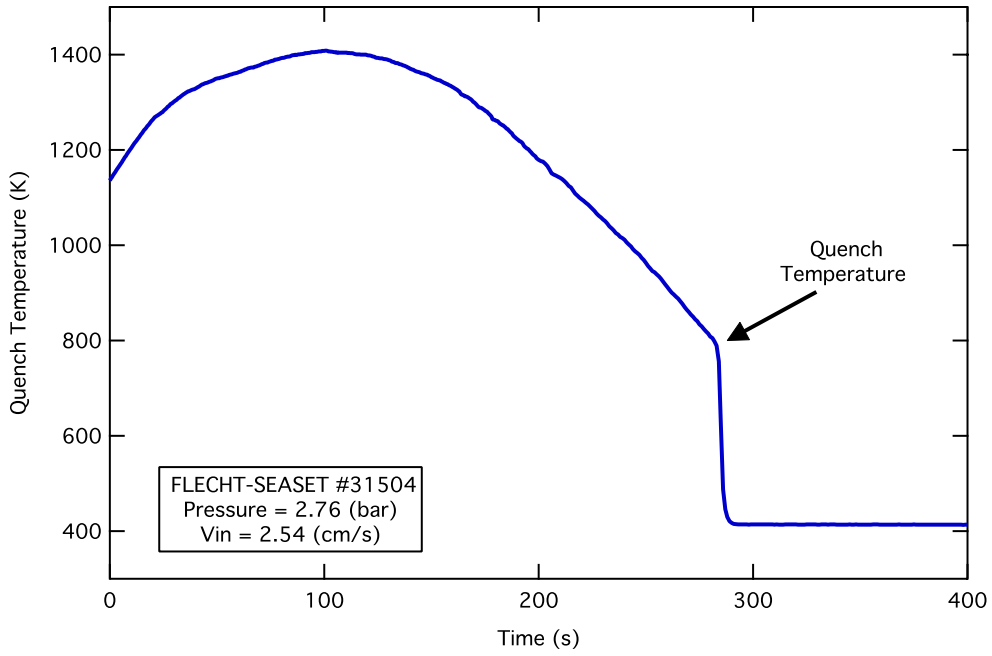

Figure. 6-17. Clad temperature history for a thermocouple at the core mid-plane in FLECHT-SEASET test #31504 showing the quench temperature.

having a mean value of 728 K and a standard deviation of 65 K. For the THTF tests, a total of 539 data points were collected with a much narrower spread of quench temperatures with the distribution having a mean value of 752 K and a standard deviation of 23 K. Consequently, in the TRACE code, the value of T_{min} is set to the maximum of that given by the Groeneveld-Stewart correlation and a value of 725 K for the region within 15 cm of a quench front.

In summary, the selected model for T_{min} is the Groeneveld-Stewart correlation (Ref. 6-49). The one significant deficiency of this correlation is that it applies to Inconel only and does not predict the effect of low conductivity oxide layers on T_{min}. For example, Dhir et al. (Ref. 6-56) report that for zircaloy rods the quench temperature increases as the rods become oxidized to about 50-80 K higher than the value for fresh rods. For the present, the Groeneveld-Stewart correlation should be viewed as giving a reasonable but conservative estimate of T_{min}. Future efforts will be directed towards the inclusion of material property effects. Finally, to improve the predictive capability of this model for reflood simulations, based on data from FLECHT-SEASET and THTF reflood tests, the value of T_{min} is limited to be greater than 725 K for regions within 15 cm of a quench front.

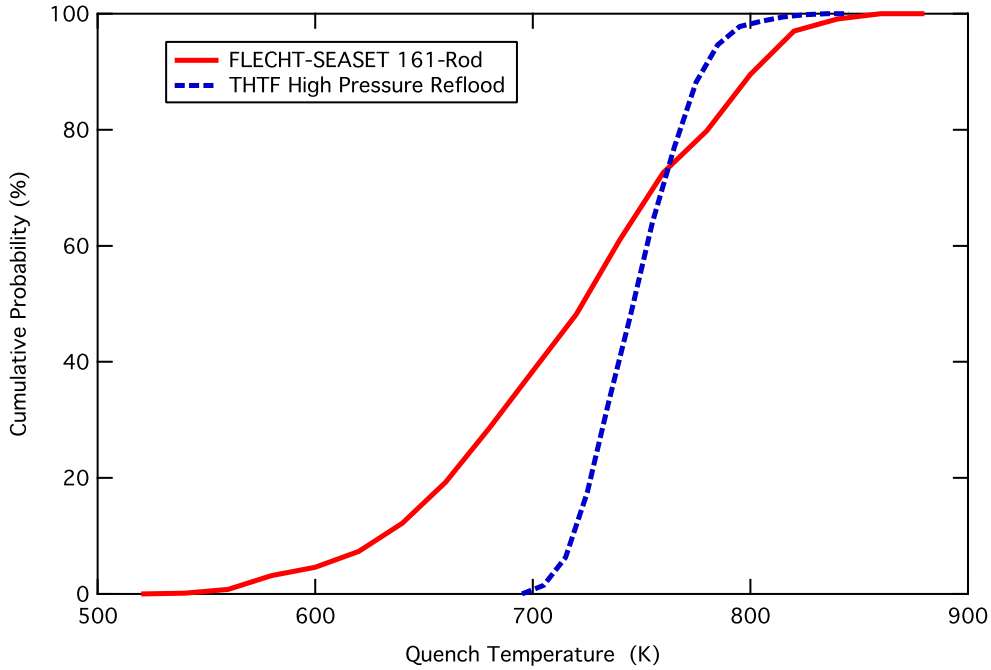

Figure. 6-18. Cumulative distributions for the quench temperature at both low- and high-pressure reflood conditions for stainless steel clad rods.

Post-CHF Heat Transfer

The post-CHF heat transfer regimes consist of transition and film boiling and are selected as illustrated in Figure 6-19 below. The transition boiling regime literally provides a "transition" from the wet-wall heat transfer of the nucleate boiling regime to that of "dry-wall" heat transfer in the film boiling regime. The film boiling regime models are used to describe the wall heat transfer for the "inverted" flow regimes that occur when the surface temperature is too hot for the liquid phase to contact the wall. These regimes are described in **Chapter 4,** *Post-CHF Interfacial Drag Models* and are shown schematically in Figure 4-13. Three principal inverted flow regimes are modeled in TRACE for post-CHF conditions: inverted annular, inverted slug, and dispersed flow. The heat transfer models used for each of these regimes are described in the following sections.

Transition Boiling

The transition boiling regime provides the transition between the "wet wall" heat transfer of the nucleate boiling regime and the "dry wall" heat transfer of the film boiling regime. There are many correlations for the transition boiling heat transfer coefficient available in the literature, however, there is no general consensus on a best correlation. Nor is there much consistency between different correlations. Furthermore, oscillatory behavior in some system thermal-

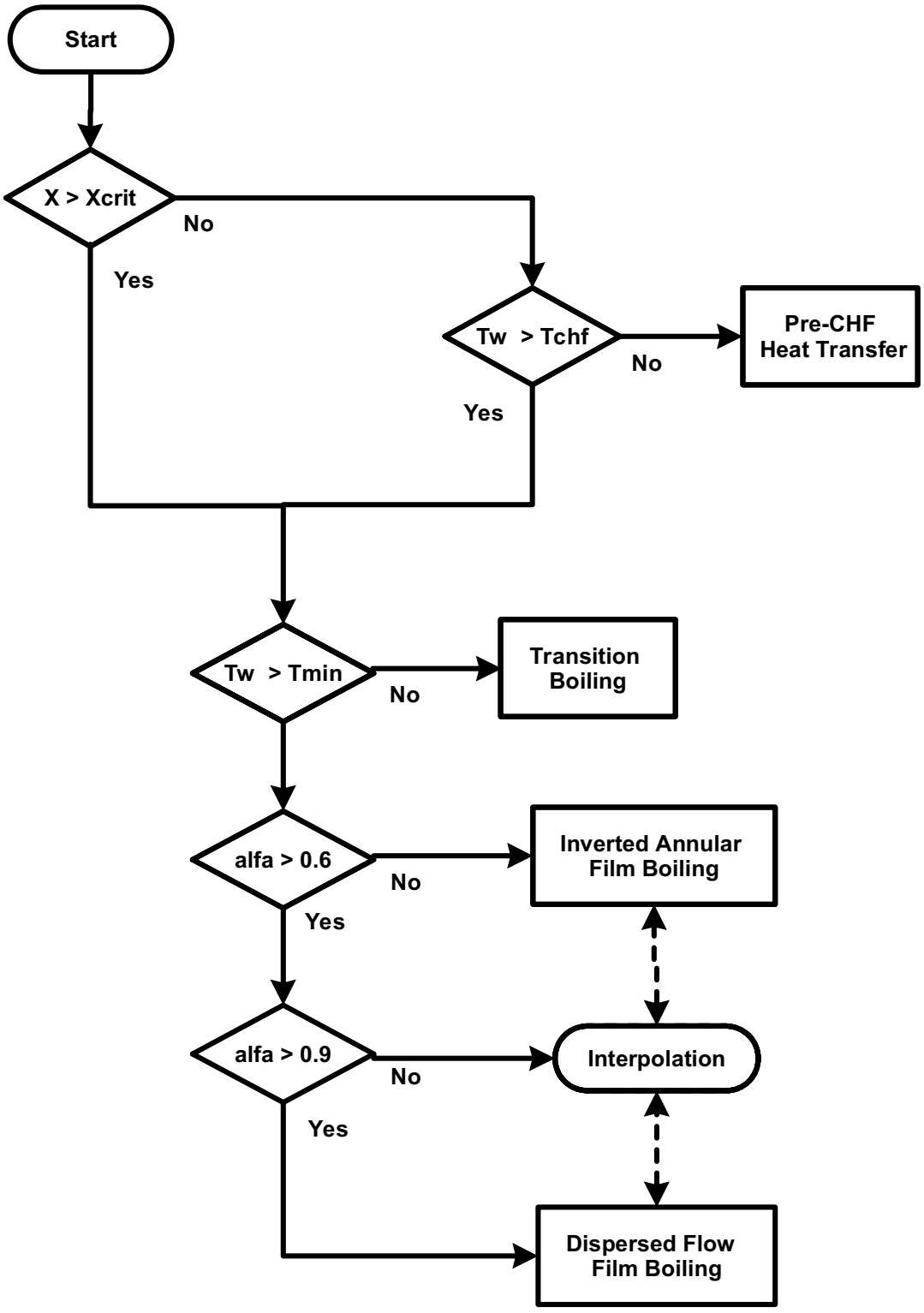

Figure. 6-19. Post-CHF Heat Transfer Regime Selection Logic.

hydraulic analysis codes has been traced to the choice of transition boiling correlation, e.g., the Chen transition boiling correlation as it was implemented in RELAP5 (Ref. 6-57).

For the TRACE code, we have made the decision to use the minimum film boiling temperature as the regime transition criteria between film boiling and transition boiling. The wall heat flux at this point, q''_{min} , is simply the film boiling heat flux calculated for the wall superheat corresponding to T_{min}. That is,

$$q''_{min} = q''_{FB}\ (T_{min}) \tag{6-132}$$

where the film boiling heat transfer can be either that for dispersed flow film boiling or inverted annular film boiling. For our boiling curve specification to be continuous with respect to wall superheat, it must pass through this minimum film boiling (MFB) point, (q''_{min} , T_{min}) .

Similarly, the above described CHF point, (q''_{CHF} , T_{CHF}) , provides the lower wall superheat boundary for the transition boiling regime. Again, for our boiling curve specification to be continuous with respect to wall superheat, it must pass through this CHF point. Consequently, both ends of the transition boiling regime have been specified and no empirical correlation could be expected to match these two points. Instead, an interpolation between these two points based on wall superheat will be implemented as the transition boiling heat transfer model.

This interpolation approach has been used with some success in the past, notably in the TRAC-PF1/MOD1 (Ref. 6-58) and COBRA/TRAC (Ref. 6-47) codes. Considering that the normal schematic representation of the boiling curve portrays the transition boiling regime as a straight line in log-log coordinates connecting the CHF and MFB points, one such scheme is logarithmic interpolation as described in Kirchner (Ref. 6-59). The wall heat flux in the transition boiling regime would then be

$$q''_{TB} = q''_{CHF} \cdot \left(\frac{T_w}{T_{CHF}} \right)^n \tag{6-133}$$

where the exponent is calculated from

$$n = \frac{\ln(q''_{CHF} / q''_{min})}{\ln(T_{CHF} / T_{min})} \tag{6-134}$$

The resulting curve is displayed on Figure 6-20 and is denoted by the label "Log Interpolation".

A second interpolation approach is that suggested by Bjornard and Griffith (Ref. 6-60) as implemented in both TRAC-PF1/MOD1 and COBRA/TRAC, that is

$$q''_{TB} = wf_{TB} \cdot q''_{CHF} + (1 - wf_{TB}) \cdot q''_{min} \tag{6-135}$$

where

$$wf_{TB} = \left(\frac{T_w - T_{min}}{T_{CHF} - T_{min}} \right)^2 \tag{6-136}$$

This formula is also displayed on Figure 6-20 and is denoted by the label "TRAC-PF1/MOD1". In effect, the interpolation weighting factor, wf_{TB}, represents the fraction of the surface considered to have "wet-wall" heat transfer and decreases from a value of unity at the CHF point to zero when the wall temperature reaches T_{min} .

The last interpolation scheme to be considered is a cubic spline fit with the additional constraints that the derivative of the heat flux with respect to wall superheat is zero at both the CHF and MFB points. This cubic spline fit is given by

$$q''_{TB} = q''_{CHF} \cdot (c_0 + c_1 \cdot \theta + c_2 \cdot \theta^2 + c_3 \cdot \theta^3) \tag{6-137}$$

where

$$\theta = \left(\frac{T_w - T_{CHF}}{T_{min} - T_{CHF}} \right) \tag{6-138}$$

and

$$c_0 = 1$$

$$c_1 = 0$$

$$c_2 = -3 \cdot (1 - q''_{min} \,/\, q''_{CHF})$$

$$c_3 = -\frac{2}{3} \cdot c_2 \tag{6-139}$$

Figure 6-20 compares the results of all three interpolation schemes with the transition boiling data of Johannsen et al. (Ref. 6-61) for a case with

Pressure = 2.5 (bar)
Mass Flux = 50 (kg/m2-s)
Inlet Subcooling = 21.7 (K)

According to their data report, the shape of the boiling curve depicted for this particular test (Run 025-050-23) is representative of that observed in all of their tests.

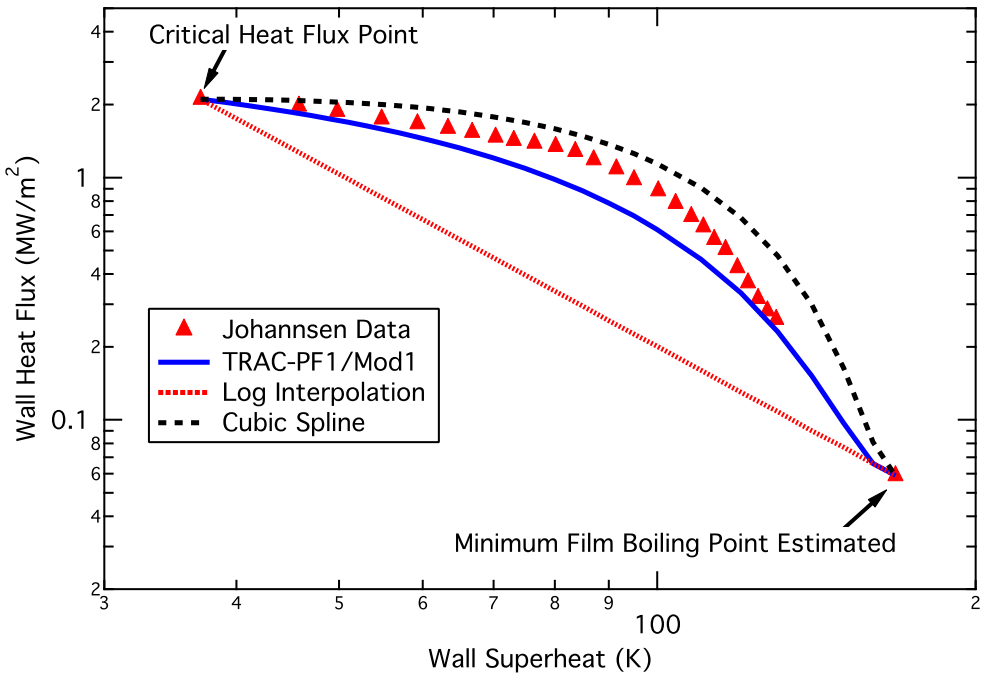

Figure. 6-20. Example of transition boiling interpolation schemes for Run 025-050-23 of Johannsen et al. (Ref. 6-61).

In Figure 6-20, the CHF point is that given by the data but the MFB point is estimated based on T_{min} calculated using the Groeneveld-Stewart correlation and a film boiling heat transfer coefficient of 350 (W/m^2-K) which is representative of the inverted annular film boiling regime with a moderate subcooling. It was necessary to estimate the MFB point because it was not measured for the test used to obtain the transition boiling data depicted in the figure. All three interpolation schemes connect the CHF and MFB points as they should, however, the resulting shape of the curves are quite different.

The log interpolation scheme gives a straight line connecting the CHF and MFB points and clearly gives a poor representation of the actual boiling curve. Both the TRAC-PF1/MOD1 and the cubic spline interpolation schemes give a reasonable approximation of the measured boiling curve shape. No firm conclusions with respect to accuracy can be drawn due to the MFB point being estimated. For example, for the same T_{min}, a higher value of the wall heat transfer coefficient at the MFB point would give a higher value of q''_{min} and hence make the TRAC-PF1/MOD1 interpolation scheme appear to be more accurate. Conversely, a lower estimate of the wall heat transfer coefficient at the MFB point would cause the cubic spline fit appear to be more accurate. For TRACE, we chose the TRAC-PF1/MOD1 interpolation scheme over that of the

cubic spline because it is simpler and should provide a slight under-estimate of the heat flux whereas the spline interpolation is expected to slightly over-predict.

Using the TRAC-PF1/MOD1 interpolation scheme described above, the boiling curve illustrated in Figure 6-1 was generated using the TRACE models for pre- and post-CHF heat transfer for the indicated conditions. When used in reflood simulations, this simple interpolation scheme for the transition boiling region resulted in overly rapid quenching of the bottom portion of the heater rod. It was found that this too rapid quenching was the consequence of the transition boiling heat flux not having a dependence upon the local value of the void fraction. Therefore, the transition boiling weighting factor was modified to include a void fraction multiplier, namely

$$wf_{TB} = \sqrt{1-\alpha} \cdot \left(\frac{T_w - T_{min}}{T_{CHF} - T_{min}} \right)^2 \tag{6-140}$$

The above void fraction multiplier is an ad hoc approach to address the specific problem of too rapid quenching at the bottom of heater rods during reflood simulations. It has the undesirable consequence of introducing a sharp decrease in the wall heat flux as the CHF point is exceeded as illustrated in the boiling curve of Figure 6-21. Also, this approach will under-predict the transition boiling heat flux for high void fraction dispersed flow conditions such as those encountered at the top of a fuel rod during reflood. Consequently, during reflood simulations, the top down quenching of the rods is expected to be under-predicted. Nevertheless, this approach has been adopted for this first version of TRACE.

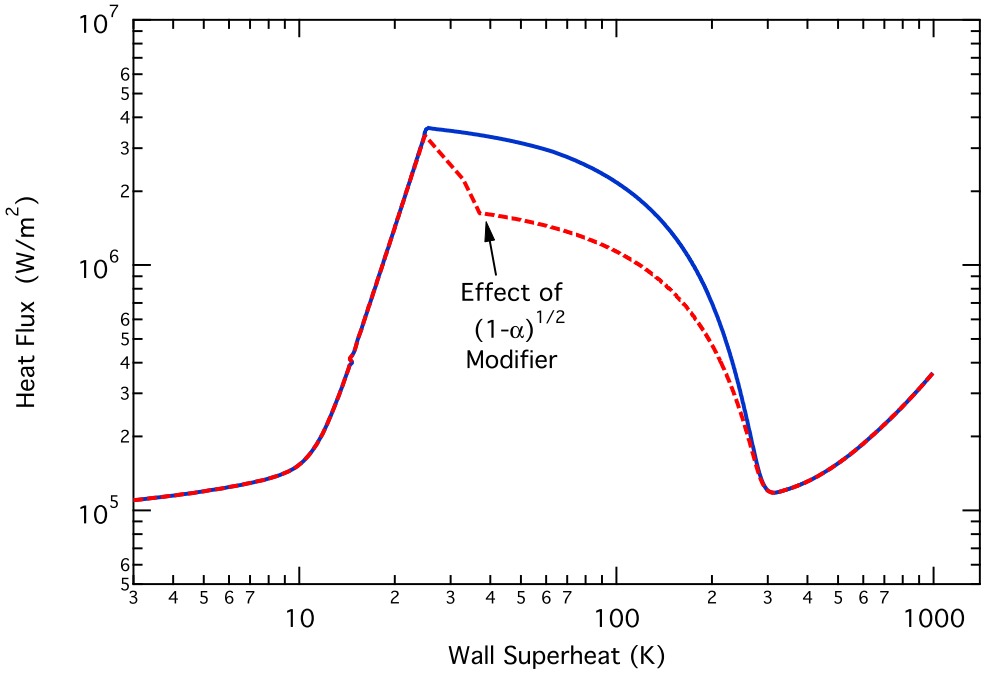

Figure. 6-21. Effect of the void fraction multiplier upon the boiling curve.

It remains to specify the heat transfer coefficients for the wall-liquid and wall-gas for the transition boiling regime. First, the "wet wall" component of the transition boiling heat flux is assumed to be entirely transmitted to the liquid phase and is designated with a second subscript of "TB". Thus,

$$q''_{wl,\,TB} = wf_{TB} \cdot q''_{CHF} \tag{6-141}$$

where wf_{TB} is given by Eq. (6-140). The corresponding heat transfer coefficient is computed as

$$h_{wl,\,TB} = \frac{q''_{wl,\,TB}}{(T_w - T_l)} = \frac{wf_{TB} \cdot q''_{CHF}}{(T_w - T_l)} \tag{6-142}$$

Also, as this "wet wall" heat flux is due to boiling heat transfer, all of it is assumed to result in vapor generation. Therefore,

$$h_{\Gamma,\,TB} = h_{wl,\,TB} \tag{6-143}$$

Next, the "dry wall" component of the transition boiling heat flux is calculated by evaluating the heat transfer coefficients for the film boiling regime (see below) with the wall temperature set to T_{min}. These will be designated with the addition of "FB" as a second subscript, i.e., $h_{wl,\,FB}$, $h_{\Gamma,\,FB}$ and $h_{wg,\,FB}$. Finally, these "dry wall" components are weighted with the transition boiling interpolation parameter and added to the "wet wall" components, yielding

$$h_{wl} = h_{wl,\,TB} + (1 - wf_{TB}) \cdot h_{wl,\,FB} \tag{6-144}$$

$$h_{\Gamma} = h_{\Gamma,\,TB} + (1 - wf_{TB}) \cdot h_{h,\,FB}$$

$$h_{wg} = (1 - wf_{TB}) \cdot h_{wg,\,FB}$$

The following three subsections describe the film boiling heat transfer models used for the inverted annular, dispersed flow, and inverted slug regimes. The inverted slug regime is treated via interpolation as indicated in Figure 6-19.

Inverted Annular Film Boiling

During film boiling, when the liquid phase is significantly subcooled, only a thin vapor film separates the hot surface from the subcooled liquid core. This regime is called inverted annular film boiling and the heat transfer paths are as depicted in Figure 6-22 below. Most of the heat transfer from the wall is across the vapor film to the saturated liquid interface. Here, part of the

heat is transferred into the subcooled liquid core with the remainder resulting in vapor generation. Experimental data indicate that the inverted annular regime persists up to void fractions of 60-70% and that a smooth transition is made to the dispersed flow regime. In TRACE, the inverted annular regime is assumed to exist for void fractions up to 60%. This section describes both the convective and radiation heat transfer models used for inverted annular film boiling regime.

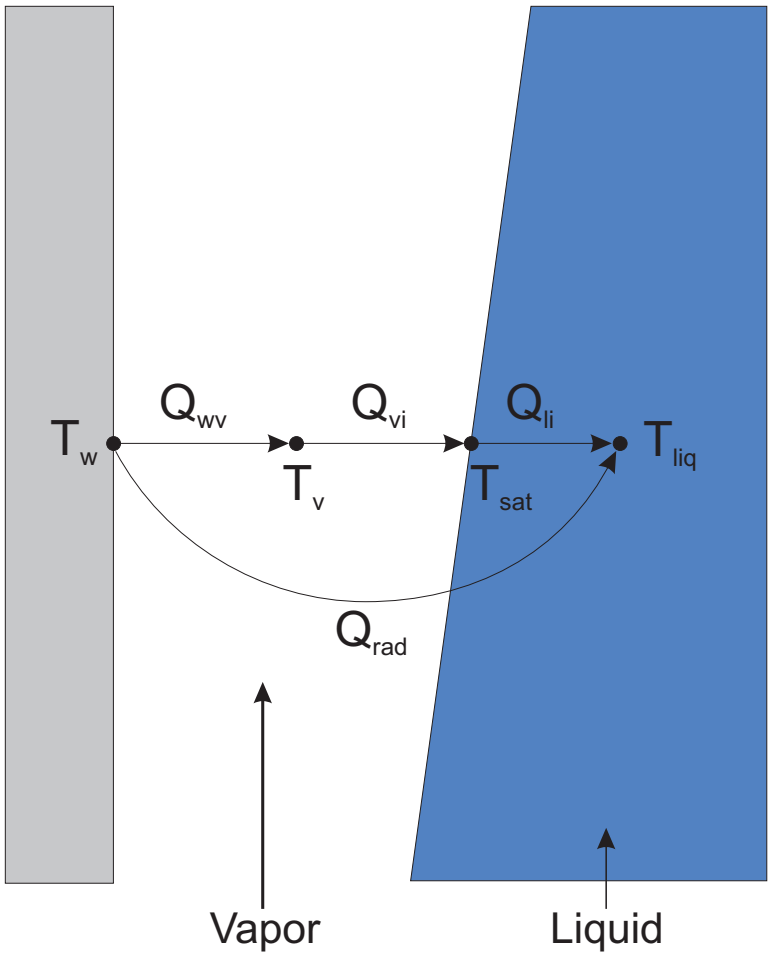

Figure. 6-22. Schematic of heat transfer paths for inverted annular film boiling.

As indicated in Figure 6-22, the convective heat transfer between the wall and the liquid interface has two components: the wall-vapor and the vapor-interface heat transfer. No experimental information exists as to the expected value of the vapor superheat in this regime and hence the relative magnitude of these two heat transfer resistances cannot be determined. Thus, it will be assumed that these two resistances are equal which is equivalent to assuming that the vapor temperature is halfway between that of the wall and the saturated interface.

If the vapor-liquid interface were smooth and the vapor flow laminar, then the wall heat transfer coefficient (referenced to the saturation temperature) would simply be

$$h_w = \frac{k_g}{\delta} \tag{6-145}$$

where k_g is the vapor thermal conductivity and δ is the vapor film thickness. However, as the measured void fraction increases, the heat transfer coefficient does not decrease as rapidly as would be predicted by the above equation, see Figure 6-23. Considerable qualitative experimental evidence exists that suggests this enhancement is a result of the waviness of the interface and/or oscillation of the liquid core thereby bringing the liquid much closer to the hot surface than indicated by the time-averaged void fraction. Therefore, to develop an accurate model for heat transfer in the inverted annular film boiling regime, an empirical correction factor is needed to account for this heat transfer enhancement.

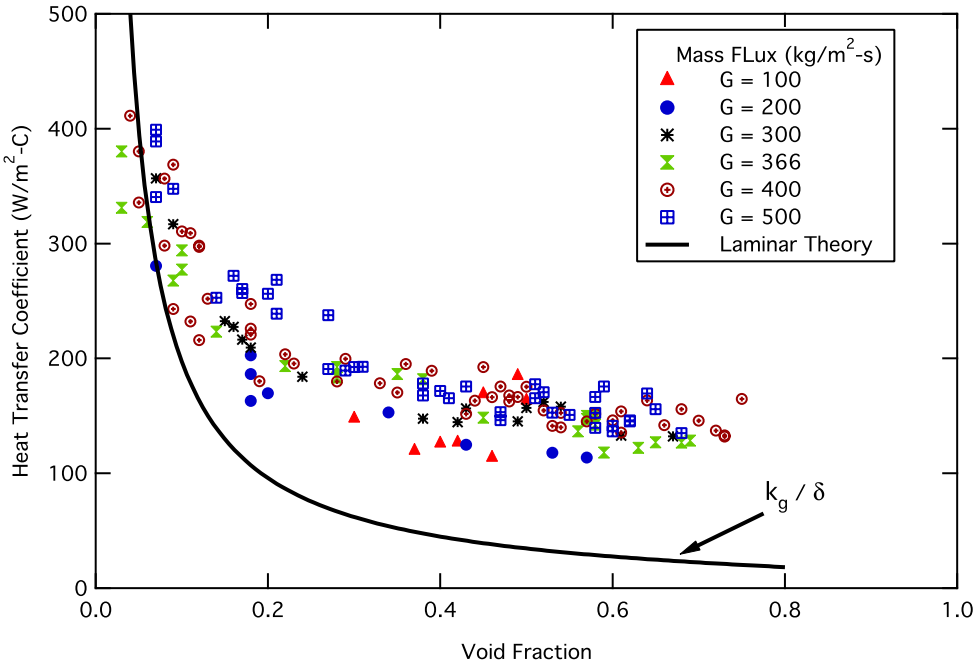

Figure. 6-23. Fung's (Ref. 6-62) low-pressure subcooled film boiling data illustrating void fraction dependence for the inverted annular film boiling regime.

Figure 6-23 presents the low-pressure (near atmospheric) low-quality steady state film boiling data of Fung (Ref. 6-62). This data was taken for a heated tube using the "hot patch" technique to freeze the quench front so that steady state film boiling data could be taken. The plotted value of the heat transfer coefficient is referenced to the saturation temperature,

$$h_w = \frac{q''_w}{(T_w - T_{sat})} \tag{6-146}$$

and has the radiative heat transfer component subtracted from it, so that

$$h_w = \frac{q''_w - q''_{rad}}{(T_w - T_{sat})} \tag{6-147}$$

where the radiation heat flux, q''_{rad} , is estimated using Eq. (6-158) below.

The void fraction was measured using a gamma densitometer at discrete axial elevations. Only the data for which bulk subcooling is present is plotted in this figure and indicates that inverted annular film boiling may exist up to void fractions of 60% to 70%. For void fractions less than about 10%, the laminar theory matches the data well. For values above this, the measured heat transfer increasingly exceeds that of the laminar theory.

Also of note in Figure 6-23 is the marked lack of dependence of the heat transfer coefficient upon the mass flux. This suggests that a simple empirical correlation as a function of the void fraction would be suitable for characterizing the heat transfer in this regime. However, all of Fung's data (Ref. 6-62) were taken at nearly atmospheric pressure and so a pressure effect cannot be determined from this data alone.

To investigate a possible pressure effect, the steady state film boiling data generated at Winfrith (Ref. 6-48) was used as illustrated in Figure 6-24. The experimental technique was virtually the same as that of Fung but with the extension to higher pressures. Only a few points with bulk subcooling, and hence inverted annular film boiling, were available. The behavior of the heat transfer coefficient with void fraction is similar to that of Fung's data but a pronounced pressure effect is clearly evident. Therefore, the empirical model for the heat transfer enhancement effect must take into account this pressure effect in addition to that of the void fraction.

The model that we developed for TRACE uses a suggestion of Cachard (Ref. 6-63) that this enhancement can be correlated as a function of a non-dimensional vapor film thickness. From the solution for a buoyancy driven laminar vapor film, Cachard gave the non-dimensional film thickness as

$$\delta^* = \delta \cdot \left(\frac{\rho_g \cdot g \cdot \Delta\rho}{\mu_g^2} \right)^{1/3} \tag{6-148}$$

where for a tube, the film thickness is deduced from the void fraction by the geometric relation,

$$\delta = \frac{D}{2} \cdot (1 - \sqrt{1-\alpha}) \tag{6-149}$$

Then, using the data of Fung, a simple empirical model was developed as

$$Nu_w = 1 + (0.268 \cdot \delta^{*0.77} - 0.34) \tag{6-150}$$

where the wall Nusselt no. is defined by

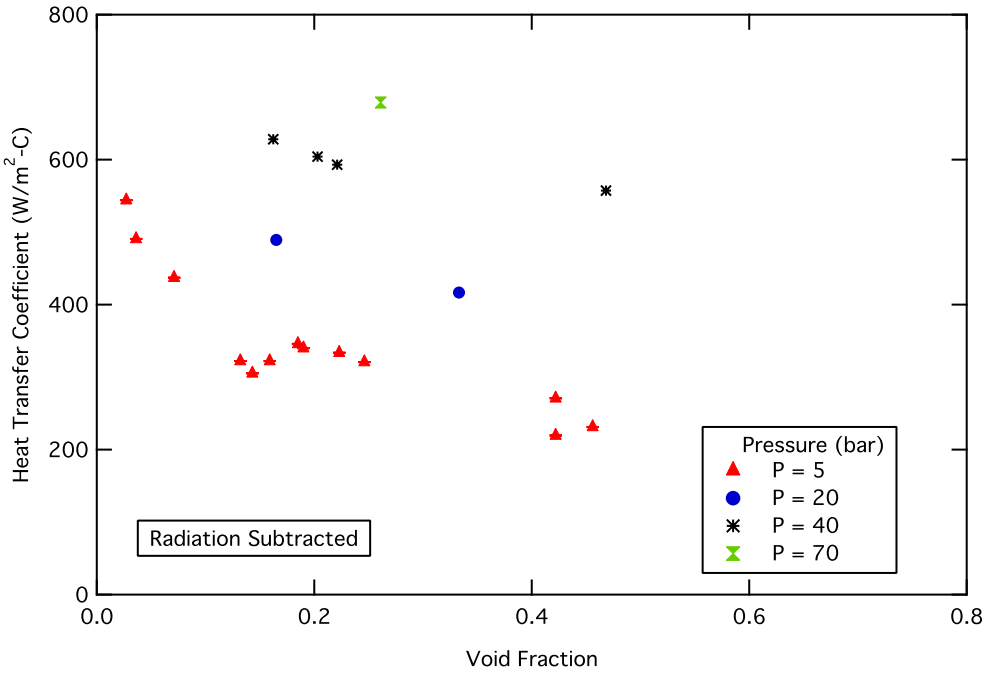

Figure. 6-24. Winfrith subcooled film boiling data showing pressure dependence of the heat transfer coefficient in the inverted annular film boiling regime.

$$Nu_w = \frac{h_w \cdot \delta}{k_g} \tag{6-151}$$

and has a minimum value of unity so that it devolves into the laminar theory. In Eq. (6-150) the term in parentheses is the enhancement factor due to the waviness or oscillatory behavior of the liquid core. Note, in developing this model, an estimate of the heat transfer due to thermal radiation [see Eq. (6-158)] was subtracted from the total heat transfer before the data was correlated.

In TRACE, the heat transfer rate corresponding to that of the laminar theory is represented by a wall-gas component while the heat transfer enhancement is modeled as a wall-interface component. That is,

$$h_{wg} = 2 \cdot \frac{k_g}{\delta} \tag{6-152}$$

and

$$h_\Gamma = h_{wl} = \frac{k_g}{\delta} \cdot Nu_{wl} \cdot \frac{(T_w - T_{sat})}{(T_w - T_l)} \tag{6-153}$$

where the liquid Nusselt no. is given by

$$Nu_{wl} = Max\left\{0\ ,\ 0.268 \cdot \delta^{*0.77} - 0.34\right\} \tag{6-154}$$

In Eq. (6-152), the factor of 2 was added because the wall-gas heat transfer coefficient is referenced to the gas temperature and this has been assumed to be halfway between that of the wall and the saturated interface, consistent with the model used for the interfacial heat transfer. Eq. (6-153), for the wall-liquid heat transfer coefficient, is referenced to the liquid temperature as opposed to the saturation temperature thereby necessitating the final term in this formula, which is usually not far from unity.

This simple, wholly empirical, model provides a good estimate of the wall heat transfer coefficient for Fung's subcooled data as depicted in Figure 6-25. It also does a reasonable job of correlating the pressure effect observed in the Winfrith data as shown in Figure 6-26 though some under-prediction of the high-pressure data for thick vapor films is evident.

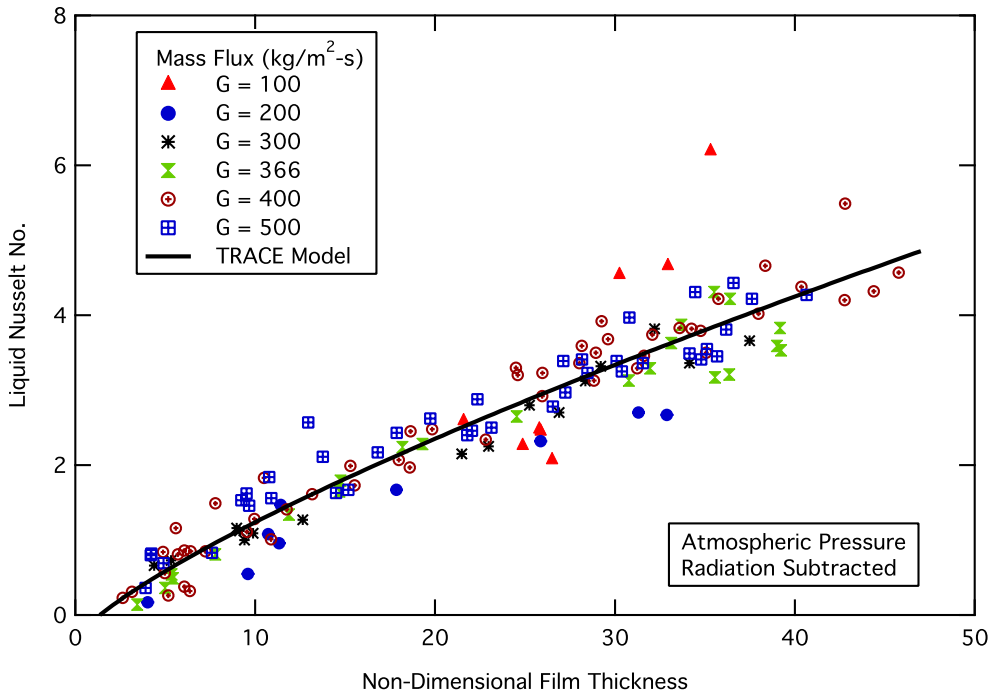

Figure. 6-25. Comparison of TRACE empirical model for the IAFB enhancement factor versus the subcooled data of Fung (Ref. 6-62).

The model for the inverted annular film boiling heat transfer enhancement given by Eq. (6-150) is strictly only applicable to tube geometry. To investigate its possible validity to rod bundle geometry, a database of film boiling heat transfer coefficient versus void fraction was generated using the forced-feed reflood data of the FLECHT-SEASET 161-Rod tests (Ref. 6-53). To accomplish this, at specific times in the reflood transient, axial profiles of both the heat transfer

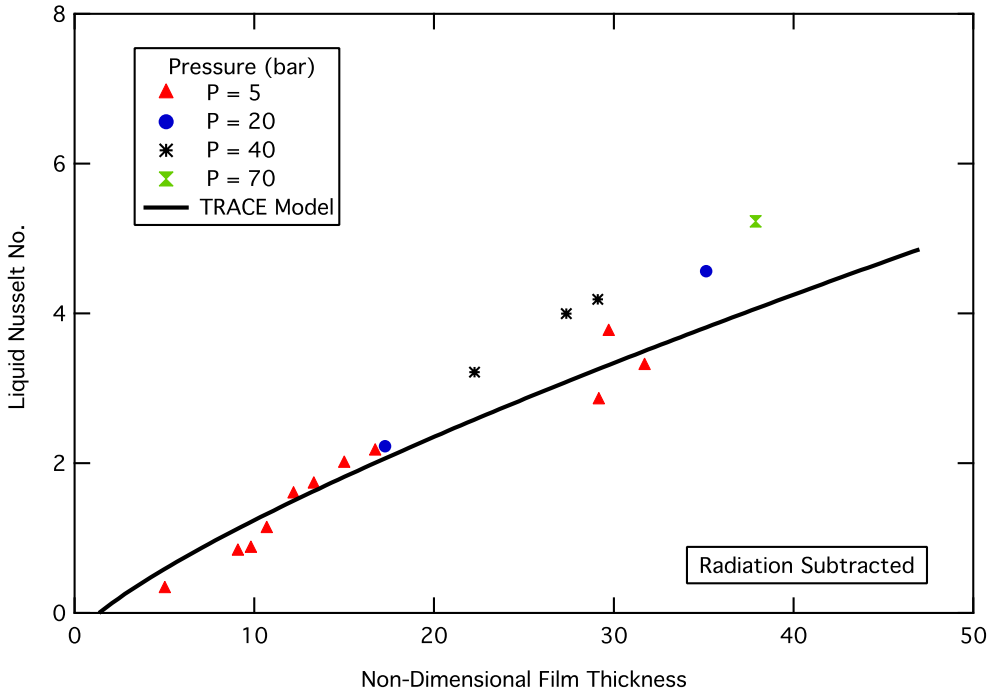

Figure. 6-26. Comparison of TRACE empirical model for the IAFB enhancement factor versus the subcooled data of Winfrith (Ref. 6-48).

coefficient and the void fraction were made. The void fraction, inferred from delta-P cells with a 30.48 cm spacing, was then interpolated to the axial location of the thermocouples so that a plot of heat transfer coefficient versus void fraction could be made.

For a rod bundle geometry, the vapor film thickness is calculated from the void fraction using the geometrical formula

$$\delta = \frac{D_h}{2} \cdot \left\{ \left[1 + \alpha \cdot \left(\frac{4}{\pi} \cdot \left(\frac{P}{D_R} \right)^2 - 1 \right) \right]^{1/2} - 1 \right\} \tag{6-155}$$

that assumes the film is uniformly distributed around the rod. The results for FLECHT-SEASET Test # 31302 (2.76 bar, 7.6 cm/s) are given in Figure 6-27. The functional form for the Nusselt no. as a function of the vapor film non-dimensional thickness is the same as that previously found for the tube data of Fung. However, the magnitude of the enhancement had to be increased by 30%. Thus, for rod bundle geometries, the TRACE model is given by

$$Nu_w = 1 + 1.3 \cdot (0.268 \cdot \delta^{*0.77} - 0.34) \tag{6-156}$$

so that the liquid Nusselt no. becomes

$$Nu_{wl} = Max\left\{0\ ,\ 1.3 \cdot (0.268 \cdot \delta^{*^{0.77}} - 0.34)\right\} \tag{6-157}$$

as depicted in Figure 6-27.

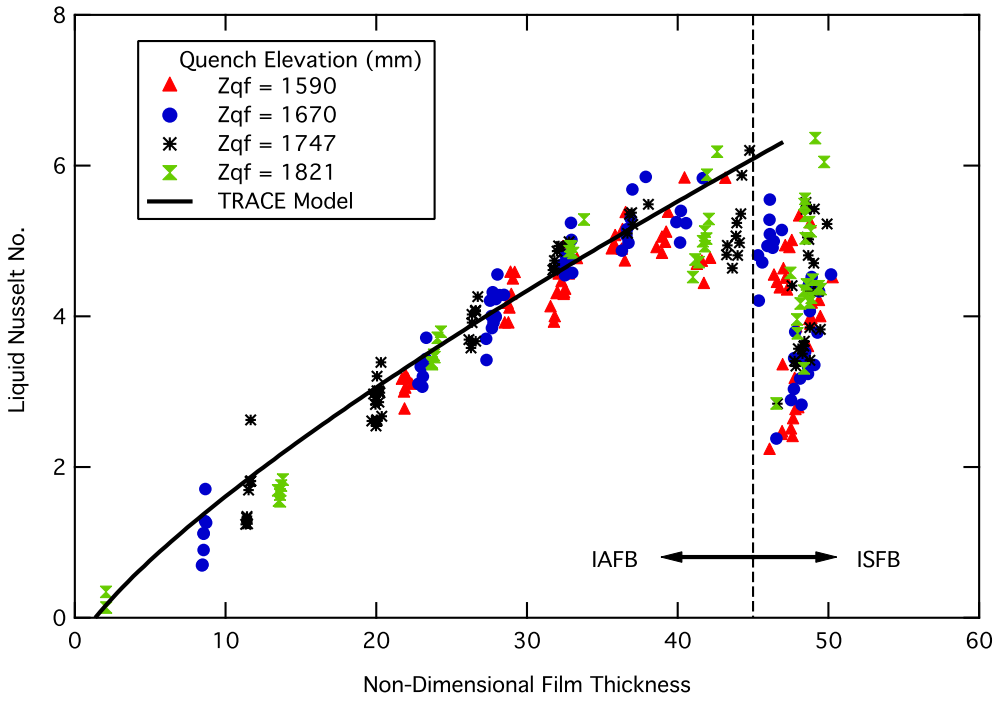

Figure. 6-27. Comparison of TRACE empirical model for the IAFB enhancement factor versus rod bundle data from FLECHT-SEASET Test #31302.

For void fractions greater than about 60%, equivalent to a non-dimensional vapor film thickness greater than about 45, the wall heat transfer coefficient decreases as the heat transfer regime transitions to that of dispersed flow. This transition regime is denoted as inverted slug film boiling and is discussed in the section ***Inverted Slug Film Boiling***.

Due to the elevated temperatures encountered in film boiling, it is necessary to consider thermal radiation in addition to the convective heat transfer discussed above. For the inverted annular film boiling regime, the radiative component is almost entirely from the wall to the liquid, and is approximated (Ref. 6-64) by

$$q''_{wl,\,rad} = \frac{\sigma_{SB} \cdot (T_w^4 - T_l^4)}{\dfrac{1}{\varepsilon_l \cdot \sqrt{1-\alpha}} + \left(\dfrac{1}{\varepsilon_w} - 1\right)} \tag{6-158}$$

where ε_l and ε_w are the liquid and the wall emissivities respectively. The radiation from the wall to the vapor phase is ignored. As the wall-liquid radiation is absorbed within the liquid, as opposed to occurring at the surface, it can be considered as a sensible heat input. The wall-liquid radiation heat transfer coefficient is then

$$h_{wl,rad} = \frac{q''_{wl,rad}}{(T_w - T_l)} = \frac{\sigma_{SB} \cdot (T_w^2 + T_{sat}^2)(T_w + T_{sat})}{\frac{1}{\varepsilon_l \cdot \sqrt{1-\alpha}} + \left(\frac{1}{\varepsilon_w} - 1\right)} \tag{6-159}$$

and is added to that for the convective heat transfer.

In summary, the heat transfer coefficients for the inverted annular film boiling regime are

$$h_{wg} = 2 \cdot \frac{k_g}{\delta} \tag{6-152}$$

for the wall-gas component,

$$h_{wl} = \frac{k_g}{\delta} \cdot Nu_{wl} \cdot \frac{(T_w - T_{sat})}{(T_w - T_l)} + h_{wl,rad} \tag{6-160}$$

for the wall-liquid component, and

$$h_{\Gamma} = \frac{k_g}{\delta} \cdot Nu_{wl} \cdot \frac{(T_w - T_{sat})}{(T_w - T_l)} \tag{6-153}$$

for the wall-interface heat transfer that results in subcooled vapor generation. The wall-liquid Nusselt no. in Eq. (6-160) and Eq. (6-153) is given by either Eq. (6-154) for tube geometries or Eq. (6-157) for rod bundles.

Dispersed Flow Film Boiling

In TRACE, the dispersed flow film boiling regime is assumed to exist for void fractions greater than 90%. This regime consists of a finely dispersed droplet mixture with the continuous phase being superheated vapor. The void fraction, especially for low-pressure conditions, is generally in excess of 99% though the quality is often 50% or even lower. The two primary components of the wall heat transfer are forced convection to the superheated vapor and thermal radiation to the liquid droplets. In dispersed flow film boiling, droplet-to-wall contact heat transfer is commonly added to the convective heat transfer, usually through some variant of the Forslund-Rohsenow correlation (Ref. 6-65). However, for wall temperatures in excess of the Leidenfrost point, this

drop contact heat transfer is small compared to the uncertainty in the convective component and so it is not treated in TRACE.

The primary heat transfer mode is usually convection from the wall to the superheated steam with the consequent level of superheat being governed by the interfacial heat transfer between the steam and the droplet mixture. Dispersed flow film boiling is then modeled as a superposition of radiative and convective components with the heat transfer equivalent of a two-phase multiplier on the convective term, that is

$$q''_{DFFB} = q''_{wg,FC} + q''_{wl,rad} + q''_{wg,rad} \tag{6-161}$$

where

$$q''_{wg,FC} = \frac{k_g}{D_h} \cdot Nu_{wg,FC} \cdot \Psi_{2\Phi} \cdot (T_w - T_g) \tag{6-162}$$

The two-phase enhancement factor, $\Psi_{2\Phi}$, accounts for the enhancement of the convective component of the wall-vapor heat transfer due to the presence of the dispersed droplets in the superheated vapor flow. The single-phase vapor Nusselt no., $Nu_{wg,FC}$, is calculated using the normal single-phase forced convection heat transfer correlations for the gas phase as if it were flowing alone.

The heat transfer correlations used for the wall-gas convective heat transfer are essentially those described above in ***Single-Phase Liquid Convection*** with modifications for property and development length effects as described below. Next, the model developed for the two-phase convective enhancement effect is described. Finally, the radiation heat transfer models for dispersed flow film boiling are discussed.

Convective Heat Transfer Models

This section describes the models used for wall-gas convective heat transfer for single-phase and for dispersed flow. Most of these correlations are essentially the same as those described above for single-phase liquid convective heat transfer with some changes to incorporate variable property effects for the gas and development length effects. In addition to standard models for tube geometry, models specific to rod bundle geometry are available in TRACE. Models for rod bundles are invoked for the core region of a vessel and for the fuel rods in a CHAN component. In either case, correlations are provided for the laminar and turbulent forced convection regimes and mixed convection effects are considered.

For both tubes and rod bundles, the wall heat transfer coefficient for single-phase gas convection is taken as the maximum of the values for laminar and turbulent forced convection. That is,

$$h_{wg} = Max\left\{ h_{lam}\,,\, h_{turb} \right\} \tag{6-163}$$

where h_{lam} is the wall heat transfer coefficient for laminar or mixed convection and h_{turb} is the wall heat transfer coefficient for turbulent forced convection

The characteristic length used for the convective heat transfer regimes is the hydraulic diameter; consequently the wall-gas heat transfer coefficient is given by

$$h_{wg} = \frac{k_g}{D_h} \cdot Nu_{wg} \tag{6-164}$$

where the gas thermal conductivity is evaluated at the bulk fluid temperature.

The forced convection heat transfer models used for tube geometry are described first, followed by those for rod bundle geometry. For low flow conditions, the temperature differential between the wall and the gas can be large enough that mixed or natural convection becomes important. TRACE also considers mixed convection effects for the laminar flow regime as detailed below in the ***Mixed Convection Effects*** subsection.

Tube Geometry

For laminar forced convection, the Nusselt no. is set to the analytical value for fully developed flow with a constant heat flux boundary condition. Thus,

$$Nu_{lam} = 4.36 \tag{6-6}$$

Laminar forced convection typically has long development lengths, however, these are not considered in TRACE. Instead, the fully developed laminar Nusselt no. given by Eq. (6-6) is used as a lower limit on the wall forced convection heat transfer. Also, the effect of variable fluid properties upon the heat transfer coefficient in laminar flow is neglected.

For turbulent forced convection, it was decided to use a modern heat transfer correlation that would also be applicable to the transition region. As recommended by both Bhatti and Shah (Ref. 6-1) and Incropera and De Witt (Ref. 6-2), we selected the Gnielinski correlation (Ref. 6-3) for implementation in TRACE. For fully developed turbulent flow with constant properties, the Gnielinski correlation is

$$Nu_{turb} = \frac{(f/2)(Re - 1000) \cdot Pr}{1 + 12.7 \cdot (f/2)^{1/2}\left(Pr^{2/3} - 1\right)} \tag{6-9}$$

where the friction factor is evaluated using the smooth tube formula of Filonenko (Ref. 6-4), see Eq. (6-10).

The above formulation for the Nusselt no. is valid over the range

$$2300 \le Re \le 5 \times 10^6$$
$$0.5 \le Pr \le 2000$$

but yields negative values for Reynolds numbers less than 1000. So, the gas Reynolds no. is limited to be greater than 1000, and is defined by

$$Re_g = \frac{\rho_g \cdot V_g \cdot D_h}{\mu_g} \tag{6-165}$$

For similar reasons, the Prandtl no. in Eq. (6-9) is constrained to have a value greater than 0.15.

The effect of variable properties upon the Nusselt no., due to the large temperature difference across the boundary layer, can be significant. For turbulent forced convection to a gas in a tube, Gnielinski uses the temperature ratio factor

$$\frac{Nu_{vp}}{Nu_{cp}} = \left(\frac{T_w}{T_g}\right)^{-0.45} \tag{6-166}$$

which is valid for

$$0.67 \le \frac{T_w}{T_g} \le 2$$

where the subscripts vp and cp designate variable and constant properties respectively. This temperature ratio range is quite limited, therefore TRACE uses the variable property correction factor proposed by Sleicher & Rouse (Ref. 6-66), which has the form

$$\frac{Nu_{vp}}{Nu_{cp}} = \left(\frac{T_w}{T_g}\right)^{n} \tag{6-167}$$

where the exponent n is

$$n = -\left[\log_{10}(T_w / T_g)\right]^{\frac{1}{4}} + 0.3 \tag{6-168}$$

The Sleicher & Rouse correction factor is valid for the range

$$1 < \frac{T_w}{T_g} < 5$$

which implies that the fluid is being heated. For dispersed flow film boiling during reflood, however, there arises the possibility for the condition of reverse heat transfer, that is, $T_w < T_g$. For this case, the formula for the exponent n is undefined and TRACE uses the value of -0.36 initially suggested by Petukhov (Ref. 6-67) for cooling of the fluid.

In fully turbulent flow, entrance effects are generally negligible for development lengths greater than about 60 L/D's. However, at the moderate Reynolds nos. typical of dispersed flow film boiling, entrance length effects can enhance the wall heat transfer by up to 15% for L/D's as large as 50, see Figure 6-28. In a reactor system thermal-hydraulic code such as TRACE, correction factors for entrance effects are difficult to apply, as the "entrance" is not always clearly defined, especially in the case of reverse flow. For large break LOCA analysis, the peak clad temperature usually occurs during the reflood phase of the transient in the dispersed flow film boiling regime. Therefore, in TRACE, a provision is made to include entrance effects for this special case, namely where a quench front exists, the flow is positive and the heat transfer regime is either single-phase forced convection or dispersed flow film boiling. For this case, the entrance length is defined as the distance downstream of the bottom quench front, i.e.,

$$\frac{L}{D} = \frac{Z - Z_{QF}}{D_h} \tag{6-169}$$

Molki & Sparrow (Ref. 6-68) proposed an empirical correction factor for the entrance length effect in turbulent forced convection that is a function of both the entrance length and the Reynolds no., see Figure 6-28. For implementation in TRACE, we have selected the simpler formula of Bhatti & Shah (Ref. 6-1) that is only a function of the entrance length. The correlation Bhatti & Shah is based on the experimental data of Mills (Ref. 6-69) for an abrupt contraction and is given by

$$\frac{Nu_L}{Nu_0} = 1 + \frac{2.4254}{(L/D)^{0.676}} \tag{6-170}$$

where the subscript L on the Nusselt no. indicates that it is the average value over that development length. As shown in Figure 6-28, the simpler correlation of Bhatti & Shah is in good agreement with that of Molki & Sparrow for moderate Reynolds nos. Bhatti & Shah state that this formula is valid for $L/D > 3$; so to stay within its database and avoid unreasonably large values for this effect, the value of L/D is constrained to be larger than 3 in TRACE.

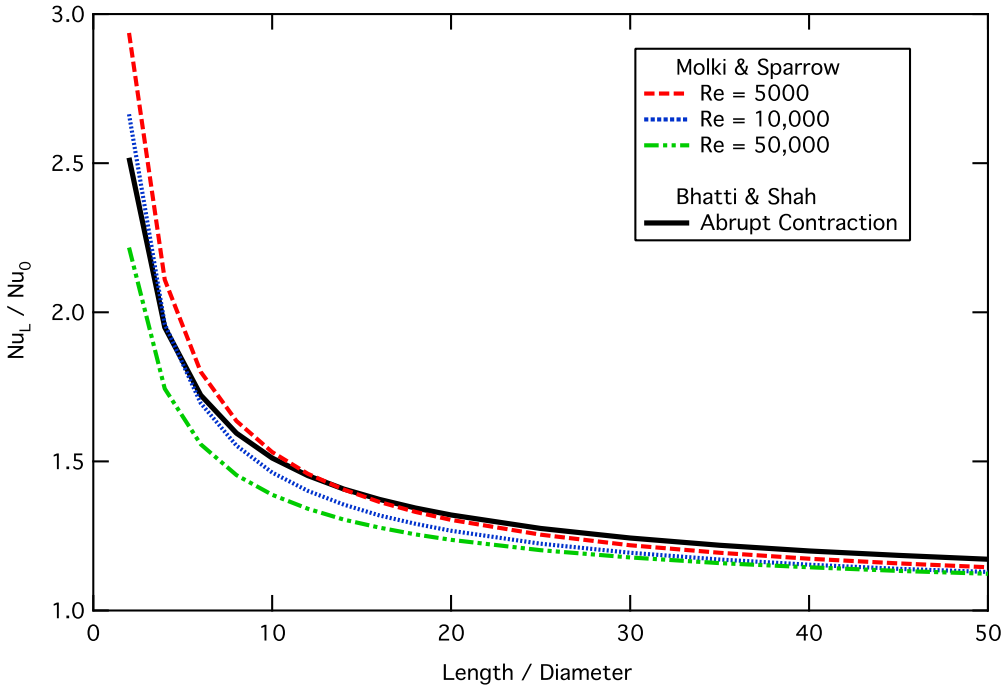

Figure. 6-28. Comparison of models for the entrance length effect in turbulent forced convection.

Note that although the above correction factors for variable properties and entrance length effects were developed for tube data, they are also applied for heat transfer in rod bundles in TRACE. Likewise, the treatment for mixed convection is the same for tubes and rod bundles (as detailed below in the ***Mixed Convection Effects*** subsection).

Rod Bundle Geometry

Although it has been standard practice to use tube correlations for forced convection heat transfer in a rod bundle, this tends to under-estimate the wall heat transfer coefficient. Consequently, it was decided to implement heat transfer correlations specific to rod bundle geometry in TRACE as described below.

As explained above in the section ***Single-Phase Liquid Convection***, the correlation of El-Genk et al. (Ref. 6-10) provides coverage of the laminar and transition regimes in addition to the turbulent regime, and was selected for implementation in TRACE. For fully developed turbulent flow in a bare rod bundle their correlation is based on that of Dittus-Boelter correlation and is given by

$$Nu_{turb} = C_{EG} \cdot Re^{0.8} \cdot Pr^{0.33} \tag{6-32}$$

where

$$C_{EG} = 0.028 \cdot \left(\frac{P}{D_R}\right) - 0.006 \tag{6-33}$$

and the fluid properties are evaluated at the bulk fluid temperature.

The effect of variable fluid properties is treated using the relation of Sleicher & Rouse (Ref. 6-66) as described above. So,

$$Nu_{turb} = C_{EG} \cdot Re_g^{0.8} \cdot Pr_g^{0.33} \cdot \left(\frac{T_w}{T_g}\right)^n \tag{6-171}$$

where the exponent n is given by Eq. (6-168). Also, for turbulent convection, the entrance length effect of Bhatti & Shah (Ref. 6-1) is added using Eq. (6-170).

For the transition and laminar regimes El-Genk et al. correlate the Nusselt no. by

$$Nu_{lam} = A \cdot Re^B \cdot Pr^{0.33} \tag{6-34}$$

where

$$\begin{aligned} A &= 2.97 - 1.76 \cdot (P/D_R) \\ B &= 0.56 \cdot (P/D_R) - 0.30 \end{aligned} \tag{6-35}$$

As was the case for laminar convection in tubes, no correction factors for variable property or entrance length effects are applied to Eq. (6-34).

The laminar and turbulent correlations of El-Genk, Eq. (6-32) through Eq. (6-35), were developed from an experimental database that covered the range:

$$P/D_R = 1.25 \text{ , } 1.38 \text{ , } and \text{ } 1.50$$

$$250 \le Re \le 30000$$

$$3 \le Pr \le 9$$

One potential problem with the laminar correlation of El-Genk is that it goes to zero as the Reynolds no. decreases rather than approaching the expected constant value. Consequently, the analytical results presented by Kim & Li (Ref. 6-11) for fully developed laminar flow in a rod bundle with constant heat flux boundary condition are used as a lower limit, see Table 6-1 and Eq. (6-37). For low flow conditions, mixed convection effects can become significant and are treated as described in the following section.

Mixed Convection Effects

When the wall-to-fluid temperature difference is large and the velocity low, the potential for buoyancy forces to influence the heat transfer arises. For laminar flow with the buoyancy force aiding the flow (i.e., heated upflow or cooled downflow), the resultant acceleration of the fluid near the wall leads to an increase of the wall heat transfer coefficient. Also, according to Worsoe-Schmidt and Leppert (Ref. 6-70), when the buoyancy force acts in opposition to the flow (e.g., heated down flow) in laminar flow, instability tends to develop at quite low values of the natural convection parameter and transition to turbulent flow occurs at Reynolds numbers far below the usual critical value. The result is an enhancement of the wall heat transfer above that for forced convection alone. So, for laminar flow, mixed convection effects always serve to increase the heat transfer coefficient.

To account for the effect of mixed convection in dispersed flow film boiling, TRACE uses the superposition method of Churchill (Ref. 6-31) to modify the laminar Nusselt no.,

$$Nu_{lam} = \left[Nu^3_{lam\,,\,FC} + Nu^3_{NC} \right]^{1/3} \tag{6-172}$$

The forced convection Nusselt no. for laminar flow, $Nu_{lam\,,\,FC}$, is evaluated by the formulas given above for tubes and rod bundles. For the Nusselt no. due to natural convection, Nu_{NC}, TRACE needs a "local condition" model that correlates the wall heat transfer in terms of the local wall-to-fluid temperature difference. Most natural convection heat transfer models, however, use either an isothermal condition for the entire heat transfer surface or a constant power boundary condition and neither of these boundary conditions is appropriate for our application.

One local-condition correlation for natural convection in vertical tubes was proposed by Sarma et al. (Ref. 6-12) and was tested for use in TRACE. Sarma's correlation is

$$Nu_{NC} = 0.7 \cdot (Gr_D \cdot Pr_g)^{1/4} \tag{6-173}$$

where the Grashof no. is defined in terms of the tube diameter and wall-to-fluid temperature difference as

$$Gr_D = g \cdot \beta_g \cdot (T_w - T_g) \cdot D^3 / \nu_g^2 \tag{6-174}$$

where β is the thermal expansion coefficient and ν is the dynamic viscosity. During simulations with TRACE, it was found that Eq. (6-173) over-estimated the core heat transfer for low-flow conditions. Indeed, for the range of Rayleigh numbers encountered in the core during low flooding rate reflood tests, the correlation of Sarma et al. gave values of the Nusselt no. about three times larger than those calculated using the formula of McAdams (Ref. 6-71) as illustrated in Figure 6-29.

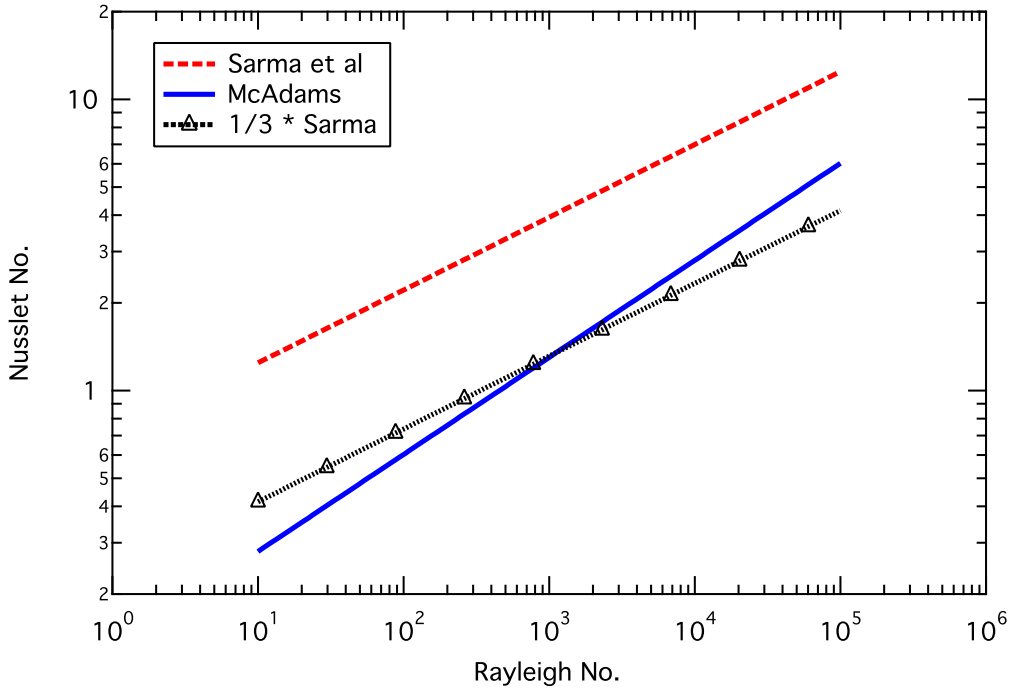

Figure. 6-29. Comparison of natural convection heat transfer models for the range of Rayleigh nos. encountered in the core during low flooding rate reflood tests.

Consequently, the correlation of Sarma was replaced in TRACE by that of McAdams for turbulent natural convection from a vertical flat plate, given by

$$Nu_{NC} = 0.13 \cdot (Gr_L \cdot Pr_g)^{1/3} \tag{6-175}$$

In the McAdams correlation, the length scale in the Grashof no. is the total height of the plate whereas in TRACE, the length scale is taken to be the hydraulic diameter. This discrepancy is inconsequential because when the Nusselt no. is converted to a heat transfer coefficient the length scale dependence is removed. That is,

$$Nu_{NC} = 0.13 \cdot \left[\frac{g \cdot \beta_g \cdot (T_w - T_g) \cdot D_h^3}{\nu_g^2} \cdot Pr_g \right]^{1/3} \tag{6-176}$$

becomes

$$h_{wg,NC} = 0.13 \cdot k_g \cdot \left[\frac{g \cdot \beta_g \cdot (T_w - T_g)}{\nu_g^2} \cdot Pr_g \right]^{1/3} \tag{6-177}$$

In TRACE, the natural convection Nusselt no. given by Eq. (6-176) is always added to that of forced convection for laminar flow using the superposition method of Churchill as shown in Eq. (6-172). This accounts for the heat transfer enhancement evident in both buoyancy-aided and buoyancy-opposed laminar flows.

Mixed convection effects also exist for turbulent flow conditions. As for laminar flow, buoyancy-opposed flows lead to an enhancement of heat transfer. However, for buoyancy-aided flows, if the buoyancy force is large enough with respect to the forced convection, the flow can "re-laminarize" with the result that the heat transfer coefficient is somewhat decreased. For TRACE applications, e.g., reflood heat transfer, these effects are considered to be of secondary import and no mixed convection effects are considered for turbulent flow.

For stagnant flow conditions, the usage of the Nusselt no. for fully-developed laminar flow in Eq. (6-172) leads to an over-prediction of the wall heat transfer. For example, the fully-developed laminar Nusselt no. is 4.36 for a tube and 6.825 for a rod bundle with a pitch-to-diameter ratio of 1.33, whereas the Nusselt no. for natural convection, appropriate for stagnation conditions, would have a value perhaps as low as 1 or 2. Consequently, a procedure to "turn off" the laminar forced convection component is needed as the flow goes to zero.

The Eckert-Metais map (Ref. 6-72), see Figure 6-30, indicates the regions of forced, mixed and natural convection for flow in a vertical tube. The vertical axis is the Reynolds no. and the horizontal axis is the product of the Rayleigh no. and the ratio of tube diameter to length. This map is valid for the range $0.01 \leq (Pr \cdot D/L) \leq 1$, but is not directly applicable in TRACE because of the usage of the tube diameter-to-length ratio that can be ambiguous during a transient simulation. Therefore, we decided to use a procedure based on a constant value of the Richardson no. instead of directly applying the Eckert-Metais map.

The Richardson no. is given by

$$Ri = \frac{Gr_D}{Re_D^2} \tag{6-178}$$

and provides a measure of the importance of the buoyancy forces to those associated with forced convection. In general, buoyancy forces become non-negligible when the Richardson no. exceeds a value of unity. As the Richardson no. increases further, the effects of forced convection eventually become negligible and the heat transfer can be modeled by free convection only.

In TRACE, we have selected a value of 100 for the Richardson no. at which only free convection is considered. Then, a logarithmic ramp is used to gradually turn off laminar forced convection as the Richardson no. ranges from 1 to 100. That is,

$$wf_{FC} = \frac{\log_{10}(100) - \log_{10}(Ri)}{\log_{10}(100) - \log_{10}(1)} = \frac{2 - \log_{10}(Ri)}{2} \tag{6-179}$$

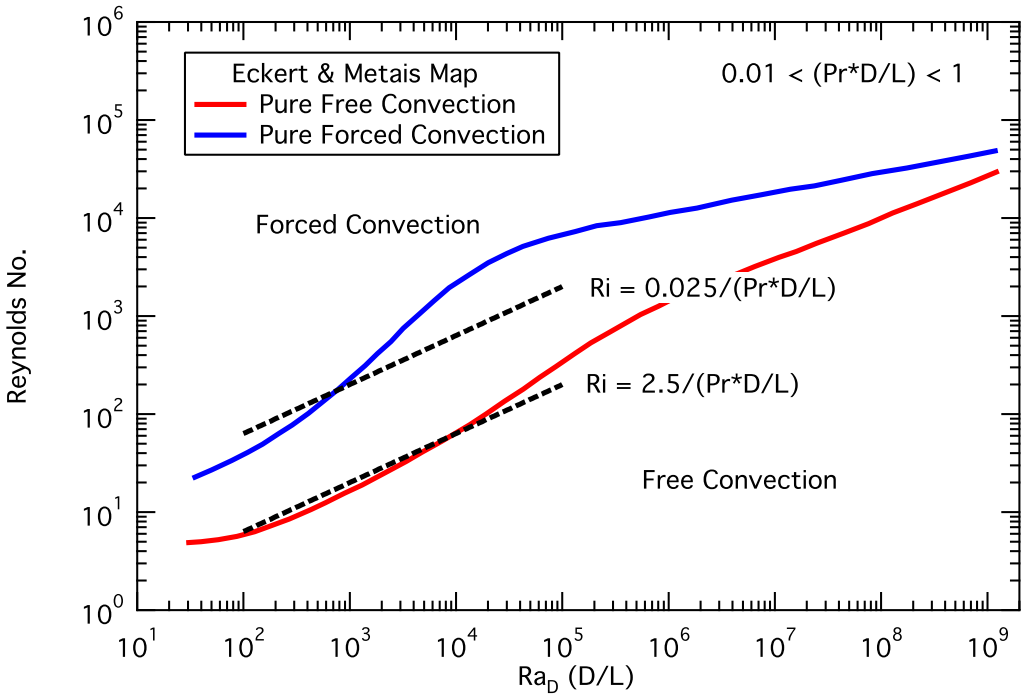

Figure. 6-30. The Eckert-Metais (Ref. 6-72) map for mixed convection in vertical tubes.

and

$$Nu_{lam,FC} = wf_{FC} \cdot Nu_{lam,FC} \tag{6-180}$$

where the weighting factor is only evaluated for values of the Richardson no. between 1 and 100.

To relate the procedure used in TRACE to the Eckert-Metais map, two lines of constant Richardson no. were plotted in Figure 6-30. For laminar flow conditions, the mixed-free convection boundary line, below which only free convection is important, is reasonably well approximated by

$$Ri_{max} = \frac{2.5}{Pr \cdot (D/L)} \tag{6-181}$$

Taking this maximum value of the Richardson no. equal to be 100 corresponds to a length-to-diameter ratio of about 40 for superheated steam. For a rod bundle in an operating PWR, the distance between grid spacers gives an L/D of about 44. So, the mixed-free convection boundary for a PWR rod bundle for low-flow steam conditions is reasonably well represented by a Richardson no. of 100.

Also shown in Figure 6-30 is a line for

$$Ri_{min} = \frac{0.025}{Pr \cdot (D/L)} \tag{6-182}$$

that roughly corresponds to the forced-mixed convection boundary. Again, for a PWR rod bundle in low-flow steam conditions, this line is approximately equal to a Richardson no. of unity and provides some basis for ramping the laminar forced convection Nusselt no. to zero as the Richardson no. increases from a value of 1 to 100 as given by Eq. (6-179) and Eq. (6-180).

Two-Phase Enhancement of Convective Heat Transfer

The wall-to-gas convective heat flux for dispersed flow film boiling is given by

$$q''_{wg,FC} = \frac{k_g}{D_h} \cdot Nu_{wg,FC} \cdot \Psi_{2\Phi} \cdot (T_w - T_g) \tag{6-162}$$

where $\Psi_{2\Phi}$ is the two-phase enhancement factor and the single-phase vapor Nusselt no., $Nu_{wg,FC}$, is calculated using the normal single-phase forced convection heat transfer correlations for the vapor phase as if it were flowing alone. $\Psi_{2\Phi}$ accounts for the enhancement of the convective component of the wall-gas heat transfer due to the presence of the dispersed droplets in the superheated vapor flow.

An example of two-phase convective enhancement is given in Figure 6-31 as a plot of the convective Nusselt no. versus vapor Reynolds no. for dispersed flow film boiling in a tube. For the data, the two-phase Nusselt no. was calculated from

$$Nu_{wg,2\Phi} = \frac{D_h}{k_g} \cdot \frac{(q''_{meas} - q''_{rad})}{(T_w - T_g)} \tag{6-183}$$

where the gas temperature was measured but the radiative heat flux was estimated using the models described in the section below. The curve labeled "Gnielinski" represents the single-phase Nusselt no. for turbulent forced convection calculated with a Prandtl no. of 0.91. The data shown in Figure 6-31 is highly uncertain due to the experimental difficulties encountered in performing steady-state film boiling experiments and in measuring the temperature of the superheated steam in a dispersed flow. Nevertheless, it is apparent that as the vapor Reynolds no. decreases into the transition region, the observed enhancement over the single-phase value increases dramatically. It is for this enhancement that a model was implemented in TRACE.

Two separate film boiling heat transfer databases were used in the model selection process. The first database consists of tests from the following experiments:

- Lehigh Tube Steady State [Nijhawan, (Ref. 6-73)]

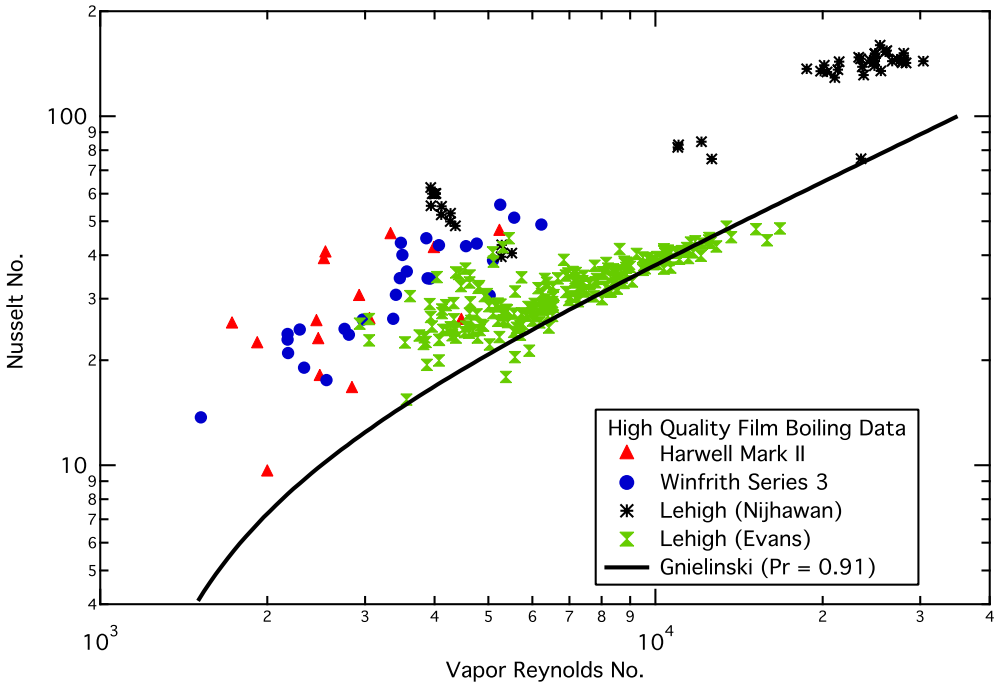

Figure. 6-31. Example of two-phase convective enhancement for high-quality dispersed flow film boiling in a tube.

- Lehigh Tube Quasi-Steady State [Evans et al., (Ref. 6-74)]
- Winfrith Test Series 3 (Ref. 6-48)
- Harwell Mark II Experiments (Ref. 6-75)

and has a total of 301 data points. In the above tests, either a "hot patch" was used to freeze the quench front at the test section inlet or the quench front was allowed to propagate into the test section and the data was analyzed as a series of quasi-steady axial "snapshots". For the above experiments, either an aspirated steam probe or bare fluid thermocouples were used to measure the superheated vapor temperature. As only data points where the vapor temperature measurement was judged by the experimenters to be of high quality were included in this database, the resulting fluid conditions tended to be in the highly dispersed flow regime and hence at relatively high values of the flow quality. For this reason, this database will be referred to as the "high quality" database.

The reasonably accurate measure of vapor superheat in the high quality database allowed for a straightforward calculation of the actual flow quality and derived quantities such as the vapor Reynolds no. and single-phase Nusselt no. However, critical parameters such as the entrained liquid volume fraction and droplet diameter, necessary for the development of a model for the enhancement, had to be inferred from the data using the TRACE models for drop diameter and interfacial drag described in **Chapter 4,** *Post-CHF Interfacial Drag Models*. Consequently, the uncertainty in this database is even larger than the experimental uncertainty in quantities such as the wall heat flux, the actual quality and the steam temperature.

The second database consisted of the following experiments:

- Winfrith Test Series 3 (Ref. 6-48)
- Winfrith Test Series 4 (Ref. 6-76)
- Harwell Mark II Experiments (Ref. 6-75)
- Fung Low-Pressure Film Boiling (Ref. 6-62)

and has a total of 368 data points. All of these experiments utilized a tube test section and a hot patch to freeze the quench front at the inlet. For these tests, the void fraction was measured by a gamma densitometer at several axial elevations. These same tests were used in the development of the inverted annular film boiling model described above. The difference here is that only data points where the equilibrium quality is positive are considered (the data used in the inverted annular film boiling model development all were at subcooled conditions). The addition of this second database added flow conditions where significant liquid fractions existed such as are expected for the transition region between inverted annular and dispersed flow.

However, for these liquid rich flows, it was not possible to measure the vapor temperature, therefore to back calculate the vapor heat transfer coefficient from the wall heat flux, the vapor temperature has to be inferred from the fluid conditions. This was accomplished by performing a heat balance between the imposed wall heat flux and the interfacial heat transfer with the key assumption being that all of the wall heat flux (minus the radiative component) was assumed to be transferred to the liquid droplets via interfacial heat transfer. This assumption tended to over-estimate the vapor temperature and hence indicate higher than actual values for the two-phase enhancement. The data points in this database tend to be at lower quality and higher liquid fraction conditions than the "high quality" database and will be referred to as the "low quality" database.

Once the local fluid conditions were inferred for both of these databases, a comparison was made between the experimental value of the wall heat flux and that calculated assuming single-phase forced convection to vapor and thermal radiation. Figure 6-32 makes this comparison and illustrates the large enhancement over single-phase forced convection that results from the presence of the liquid droplets within the vapor stream. For the high quality data, labeled as "Tvap Measured", the average value of the two-phase enhancement is ~70% while the maximum value is almost a factor of four times larger than the single-phase heat transfer alone. For the low quality database, labeled as "Void Fraction Measured", the average value of the two-phase enhancement is about 5.5 while the maximum is almost 30. The large enhancement values seen for the low quality data are somewhat inflated due to the assumptions used in our analysis procedure (see comment above). Nevertheless, both these results illustrate the importance of modeling this enhancement factor, without which significant under-predictions of the dispersed flow film boiling heat transfer are likely to occur.

Two separate mechanisms have been proposed for the heat transfer enhancement observed in dispersed flow film boiling: 1) turbulence enhancement, and 2) distributed heat sinks. In the first, it is proposed that the wake turbulence caused by droplet drag increases the overall free stream turbulence level and thereby enhances the wall heat transfer. In the second, it is supposed that the

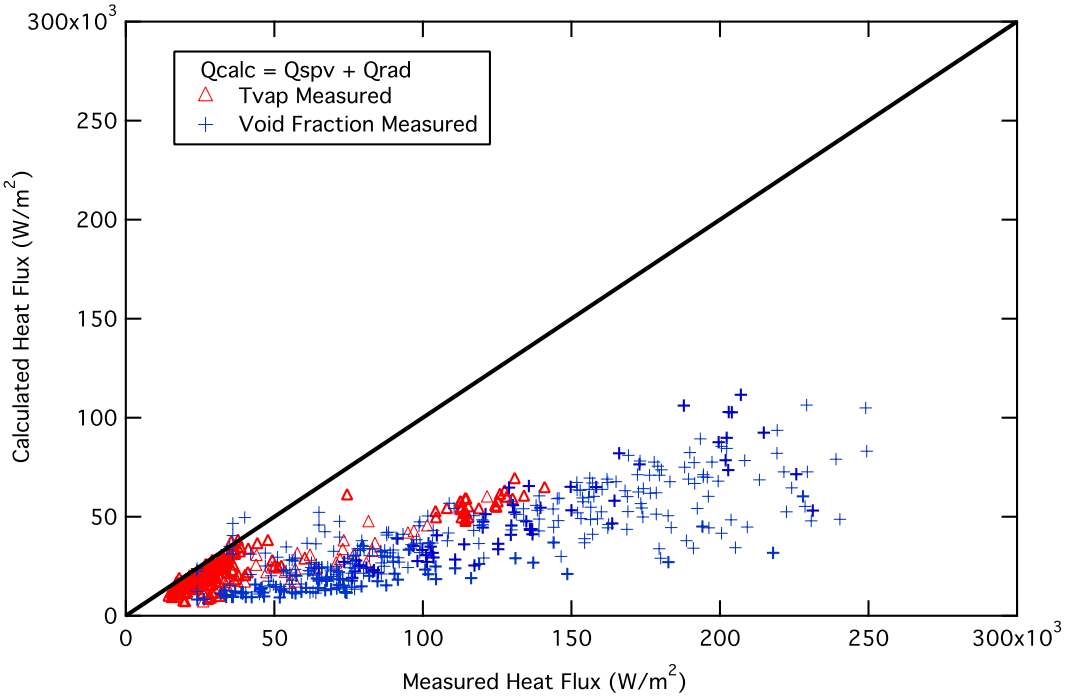

Figure. 6-32. Comparison of calculated versus measured heat flux for dispersed flow film boiling database assuming single-phase vapor convection and thermal radiation only.

droplets act as heat sinks distributed throughout the superheated vapor changing the radial temperature profile and hence the heat transfer. Models from the literature based on the distributed heat sink approach (see Refs. 6-77 and 6-78) were compared to this database but caused large over-predictions of the heat transfer coefficient under reflood conditions. Consequently, the model chosen for TRACE is based on turbulent enhancement and was modified to provide a conservative estimate of the two-phase enhancement.

For the high quality database, the majority of the data points are in the dispersed flow film boiling regime and have void fractions in excess of 95%. Whereas, for the low quality database, the void fractions range from about 70-90% and indicate that the flow regime is primarily inverted slug. Other than this obvious difference in void fraction level, the high quality data tend to be at higher values of the vapor superficial velocity, which in turn implies that the drop diameter is smaller than that of the low quality data. For the low quality data, the larger drops and higher drop volume fractions would make a model based on wake induced turbulence enhancement more likely.

Clare and Fairbairn (Ref. 6-79) proposed two similar two-phase turbulence enhancement models of differing complexity. Their "complex" model was compared to our database but the scatter was unacceptably large. Their "simple" model was based on the observation that, for a rough wall, the heat transfer coefficient is approximately equal to that for a smooth wall multiplied by the square root of the ratio of the rough-wall to smooth-wall friction factors, that is

$$\frac{h_{rough}}{h_{smooth}} = \sqrt{\frac{f_{rough}}{f_{smooth}}} \tag{6-184}$$

Using this "rough wall" analogy, they proposed that the two-phase heat transfer coefficient could be represented by

$$\frac{h_{2\Phi}}{h_{1\Phi}} = \sqrt{\frac{f_{2\Phi}}{f_w}} \tag{6-185}$$

where $f_{2\Phi}$ is an equivalent "friction factor" for two-phase dispersed flow. This equivalent two-phase friction factor was defined by

$$f_{2\Phi} = \frac{D_h \cdot (F_w''' + F_i''')}{2 \cdot \rho_g \cdot V_g^2} \tag{6-186}$$

where F_w''' is the wall drag force per unit volume and F_i''' is the interfacial drag force per unit volume given by

$$F_w''' = f_w \cdot \frac{\rho_g \cdot V_g^2}{2} \cdot \frac{4}{D_h} \tag{6-187}$$

and

$$F_i''' = C_D \cdot \frac{3 \cdot \rho_g \cdot V_{rel}^2}{4} \cdot \frac{(1-\alpha)}{d_d} \tag{6-188}$$

respectively.

Then, for steady dispersed flow, the interfacial drag force can be approximated by the buoyancy force, yielding

$$F_i''' = (1-\alpha) \cdot g \cdot \Delta\rho \tag{6-189}$$

The two-phase enhancement factor then becomes

$$\Psi_{2\Phi} = \left[1 + \frac{(1-\alpha) \cdot g \cdot \Delta\rho \cdot D_h}{2 \cdot f_w \cdot \rho_g \cdot V_g^2}\right]^{1/2} \tag{6-190}$$

Equation (6-190) can be rewritten in terms of a two-phase Grashof no. and the gas Reynolds no. as

$$\Psi_{2\Phi} = \left[1 + \frac{(1-\alpha)\cdot Gr_{2\Phi}}{2\cdot f_w \cdot Re_g^2}\right]^{1/2} \tag{6-191}$$

where

$$Gr_{2\Phi} = \frac{\rho_g \cdot g \cdot \Delta\rho \cdot D_h^3}{\mu_g^2} \tag{6-192}$$

If we assume that the wall friction factor has its fully developed value for a smooth pipe of 0.005 (as suggested by Drucker et al. (Ref. 6-80)), then

$$\Psi_{2\Phi} = \left[1 + 100 \cdot \frac{(1-\alpha)\cdot Gr_{2\Phi}}{Re_g^2}\right]^{1/2}. \tag{6-193}$$

Equation (6-193) does a reasonable job of correlating the "low quality" data but caused the peak clad temperature in reflood simulations to be under-predicted. Therefore, the magnitude of the enhancement factor was reduced to

$$\Psi_{2\Phi} = \left[1 + 25 \cdot \frac{(1-\alpha)\cdot Gr_{2\Phi}}{Re_g^2}\right]^{1/2} \tag{6-194}$$

for implementation in TRACE. Also, to eliminate unreasonably large values for this enhancement factor at low Reynolds no. conditions, $\Psi_{2\Phi}$ is limited to have a value no greater than 5.

The correlating group that we have chosen is the same as that used by Kianjah et al. (Ref. 6-81) to correlate their heat transfer data for air-particle dispersed flows using 30 and 100 μm glass spheres. Their data was correlated by

$$\Psi_{2\Phi} = 1 + 71.5 \cdot \left[\frac{(1-\alpha)\cdot Gr_{2\Phi}}{Re_g^2}\right]^{0.85} \tag{6-195}$$

and

$$\Psi_{2\Phi} = 1 + 2.6 \cdot \left[\frac{(1-\alpha) \cdot Gr_{2\Phi}}{Re_g^2} \right]^{1/2} \tag{6-196}$$

for the 30 and 100 μm particles respectively. The TRACE model, given by Eq. (6-194), produces very similar results for the enhancement as the empirical correlation of Kianjah for a 100 μm diameter spheres as shown in Figure 6-33. The original form of this model, as given by Eq. (6-193), would produce values for the enhancement about halfway between those for the 30 and 100 μm glass spheres.

Both of the air-particle mixtures that Kianjah et al. (Ref. 6-81) tested were mono-dispersed and they noted a sizable particle diameter effect as evidenced by their usage of two different correlations and as shown in Figure 6-33. However, for a poly-dispersed mixture containing both 30 and 100 μm spheres, the observed heat transfer enhancement was close to that for the 30 μm spheres alone. The poly-dispersed result is probably more realistic for dispersed droplet flow as the droplet diameter range covers a continuous spectrum. Consequently, the model implemented in TRACE would be expected to yield a conservative estimate of the two-phase enhancement.

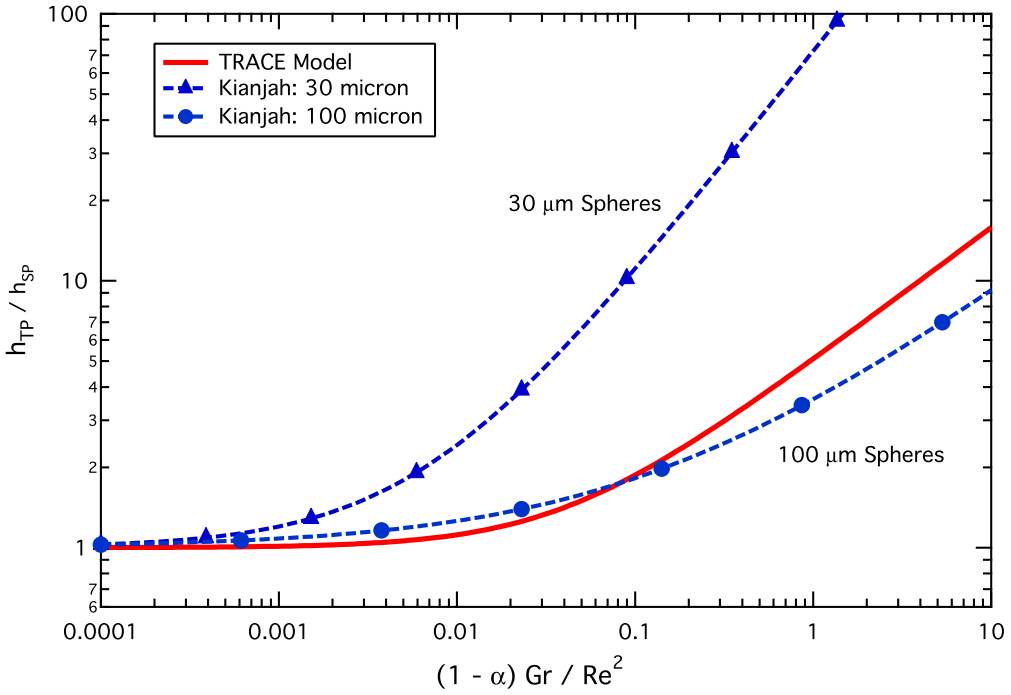

Figure. 6-33. Comparison of two-phase enhancement calculated using the TRACE model [Eq. (6-194)] to the empirical results of Kianjah et al. (Ref. 6-81) for spherical particles in air.

The TRACE model is compared to both the high-quality (indicated by the data points labeled "Tvap Measured) and the low-quality (indicated by the data points labeled "Void Fraction

Measured) databases in Figure 6-34. As expected, the majority of the data points are under-predicted because the TRACE model was given a conservative bias to avoid under-predicting the peak clad temperature during reflood. For the high-quality database, the wall heat flux was under-predicted by an average of 28% and had an RMS error of 34%. For the low-quality database, the wall heat flux was under-predicted by an average of 33% and had an RMS error of 47%.

The large scatter in this comparison and the model's conservative bias, necessary for TRACE during reflood calculations, point to inaccuracies in this modeling approach. These inaccuracies are due to the uncertainties in the experimental data, to the larger uncertainties associated with the analysis technique to infer local flow conditions, and to the correlation itself. Resolving this two-phase convective enhancement, in addition to improving the models for droplet diameter, is necessary for future improvement in the code's predictive capability for dispersed flow heat transfer.

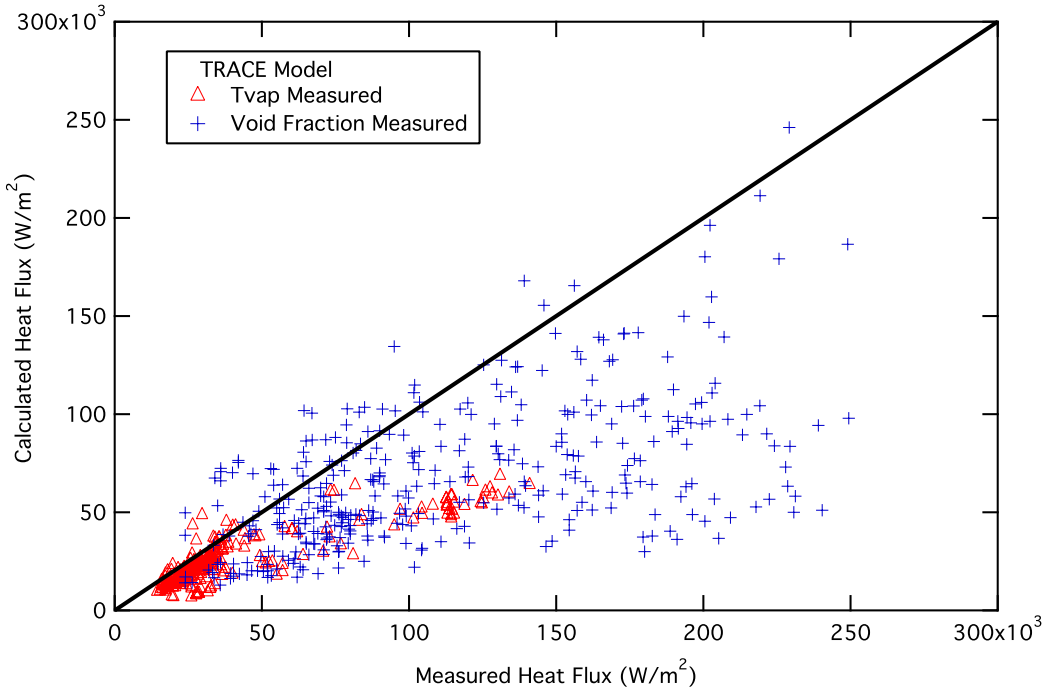

Figure. 6-34. Comparison of calculated versus measured heat flux for dispersed flow film boiling database using the TRACE model for two-phase convective enhancement.

Radiation Heat Transfer Models

The final component in the model for dispersed flow film boiling heat transfer is the addition of radiation heat transfer. Two models are provided for this: 1) the default model (described below), and 2) a radiation enclosure model (see the descriptions of the CHAN and RADENC components in Volume 2 of the TRACE User's Guide, as well as Reference 6-94 for details of the actual physical model). The radiation enclosure model includes rod-to-rod and rod-to-wall radiation

heat transfer in addition to wall-to-fluid. This enclosure model is automatically invoked for the CHAN component (BWR fuel bundles) and can be selected as a user option for other heat structures. The default model, however, only includes wall-fluid radiation as described below.

The default radiation model for the dispersed flow regime is that developed by Sun, Gonzalez, and Tien (Ref. 6-82). They demonstrated that if the dispersed flow regime is "optically thin", then the wall, vapor, and liquid droplets could be treated as single nodes in a conventional network analysis of radiation heat transfer. Surface-to-surface radiation is not included and the assumption that the vapor-droplet mixture is optically thin means that the liquid and vapor do not self-absorb emitted radiation. In their network model, radiation energy exchange between the wall and the droplets, the wall and the gas, and the gas and the droplets were considered. In TRACE, the gas-to-droplet radiation is not modeled as it is negligible in comparison to the interfacial heat transfer.

The wall-to-fluid radiation heat fluxes were expressed by Sun et al. (Ref. 6-82) as

$$q''_{wl,rad} = F_{wl} \cdot \sigma_{SB} \cdot \left(T_w^4 - T_{sv}^4\right) \tag{6-197}$$

$$q''_{wg,rad} = F_{wg} \cdot \sigma_{SB} \cdot (T_w^4 - T_g^4)$$

where F_{wl} and F_{wg} are the wall-to-liquid and wall-to-gas gray body factors respectively, and σ_{SB} is the Stefan-Boltzman constant (5.670×10^{-8} W/m^2-K). The gray body factors are

$$F_{wl} = 1 \Big/ \left[R_2 \left(1 + \frac{R_3}{R_1} + \frac{R_3}{R_2} \right) \right] \tag{6-198}$$

$$F_{wg} = 1 \Big/ \left[R_1 \left(1 + \frac{R_3}{R_1} + \frac{R_3}{R_2} \right) \right]$$

where

$$R_1 = \frac{1-\varepsilon_g}{\varepsilon_g(1-\varepsilon_g\varepsilon_l)}$$

$$R_2 = \frac{1-\varepsilon_l}{\varepsilon_l(1-\varepsilon_g\varepsilon_l)} \tag{6-199}$$

$$R_3 = \frac{1}{(1-\varepsilon_g\varepsilon_l)} + \frac{1-\varepsilon_w}{\varepsilon_w}$$

The emissivities for the gas and liquid droplets, ε_g and ε_l, used in Eq. (6-199) are calculated using the method described in Reference 6-94. Both ε_g and ε_l are functions of the average beam length and this has been taken to be equal to 0.9 times the hydraulic diameter as recommended in (Ref. 6-82). The emissivity for the wall, ε_w, would be a function of the temperature and possibly of time as the surface undergoes oxidation. For simplicity, it is set to a fixed value of 0.7 as recommended in the RELAP5 Manual (Ref. 6-57) for Zircaloy.

Finally, in TRACE, the wall-to-droplet heat flux is modified from that given in Eq. (6-197) to

$$q''_{wl,\,rad} = F_{wl} \cdot \sigma_{SB} \cdot (T_w^4 - T_l^4) \tag{6-200}$$

This modification simplifies the necessary conversion to a heat transfer coefficient referenced to the liquid temperature as required by the phasic energy equations. Also, when radiation heat transfer is significant, there is little difference in the values of the wall-droplet radiation heat flux calculated using either Eq. (6-197) or Eq. (6-200).

Inverted Slug Film Boiling

The inverted annular flow regime typically occurs when subcooled liquid flows past the quench front. Just downstream of the quench front, a thin vapor film separates this subcooled liquid core from the hot wall. The vapor velocity is low so that the flow is laminar and the gas-liquid interface is smooth. Further downstream of the quench front, as the subcooling of the liquid core is reduced, the vapor flow increases causing the interface to first become wavy and then oscillate violently until breakup occurs at about the point where the liquid becomes saturated. Experimental data indicate that the inverted annular regime persists up to void fractions of 60-70% and that a smooth transition is made to the dispersed flow regime. In TRACE, the inverted annular regime is assumed to exist for void fractions up to 60%. For void fractions greater than about 60%, equivalent to a non-dimensional vapor film thickness greater than about 45, the wall heat transfer coefficient decreases as the heat transfer regime transitions to that of dispersed flow. This transition regime is denoted as inverted slug film boiling.

To ensure a smooth transition for the wall heat transfer coefficient between inverted annular film boiling ($\alpha \leq 0.6$) and dispersed flow film boiling ($\alpha \geq 0.9$), the TRACE model employs interpolation as illustrated in Figure 6-35. This is accomplished by using a spline interpolation function to ramp the inverted annular heat transfer to zero at a void fraction of 90% and that has a zero derivative at a void fraction of 60%. The wall heat transfer coefficients for the inverted slug regime are then

$$h_{wl} = wf \cdot h_{wl,\,IAFB} + (1 - wf) \cdot h_{wl,\,DFFB}$$

$$h_{wg} = wf \cdot h_{wg,\,IAFB} + (1 - wf) \cdot h_{wg,\,DFFB} \qquad (6\text{-}201)$$

$$h_{\Gamma} = wf \cdot h_{\Gamma,\,IAFB}$$

where the weighting function is calculated from

$$wf = x \cdot (2 - x) \qquad (6\text{-}202)$$

with

$$x = \frac{0.9 - \alpha}{0.9 - 0.6} \qquad (6\text{-}203)$$

As can be seen in Figure 6-35, this interpolation function provides a reasonable representation of the heat transfer in this regime.

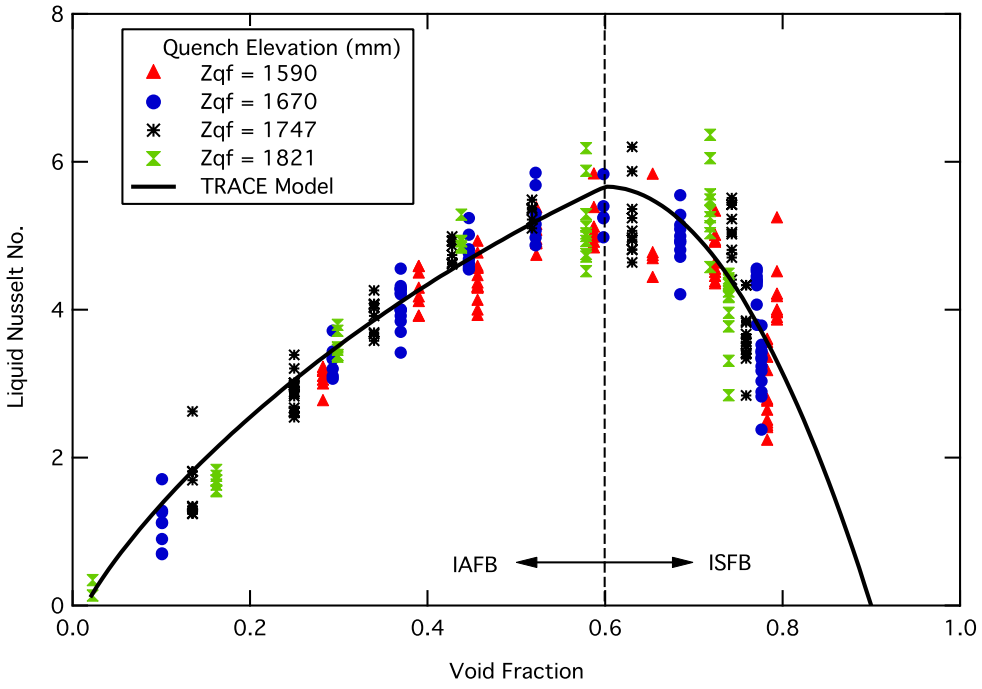

Figure. 6-35. Wall-liquid Nusselt no. versus void fraction for FLECHT-SEASET Test #31302 illustrating the ramp used by TRACE for the inverted slug regime.

Condensation Heat Transfer

Whenever the surface temperature of a heat structure is less than the saturation temperature corresponding to the vapor partial pressure, i.e., $T_w < T_{sv}$, condensation will occur. In TRACE, models for condensation heat transfer either with or without non-condensable gases have been implemented and are invoked whenever the above wall temperature criterion is met and the void fraction is greater than 90%. As illustrated in the pre-CHF heat transfer regime selection map, see Figure 6-2, condensation heat transfer that occurs when the void fraction is less than 80% is handled using the normal models for two-phase convection. Also, for void fraction values between these two limits, $0.8 < \alpha < 0.9$, interpolation is used as given in Eq. (6-48) and Eq. (6-49). This section describes the models that are used for the wall heat transfer coefficient when condensation is occurring and the void fraction is greater than 90%.

During filmwise condensation, condensation occurs at the liquid-vapor interface. As depicted in Figure 6-36, this heat transfer occurs in a two-step process, whereby heat is removed from the two-phase interface by interfacial heat transfer, Q_{li}, and then from the subcooled liquid to the wall, Q_{wl}. The models used by TRACE for interfacial heat transfer were previously described in **Chapter 5**, this section describes the models used for the wall heat transfer coefficient. The primary mode of condensation is filmwise, and for this mode the heat transfer coefficient is that from the wall to the liquid phase, h_{wl}, and the corresponding models are given in ***Film Condensation*** below. However, especially during transient calculations, wall condensation can occur when there is not enough liquid present to cover the wall with a film. For this case, it is necessary to specify a wall-to-gas heat transfer coefficient as described in ***Dropwise Condensation***. Finally, the section ***Non-Condensible Gas Effects*** describes the modifications used when non-condensable gases are present.

Film Condensation

The primary mode for condensation heat transfer is filmwise as depicted above in Figure 6-36. This section describes the models used for the heat transfer coefficient between the liquid and the wall, defined by

$$h_{wl} = \frac{k_l}{\delta} \cdot Nu_{wl} \tag{6-204}$$

where δ is the film thickness. One of the requirements for the TRACE condensation model was that it must be applicable to both falling films (such as occur on containment structures) and sheared films (e.g., high velocity flows in condenser tubes). Using the film thickness as the characteristic length allows for both cases as the primary effect of interfacial shear is film thinning. Likewise, the TRACE condensation model must be applicable over a wide range of

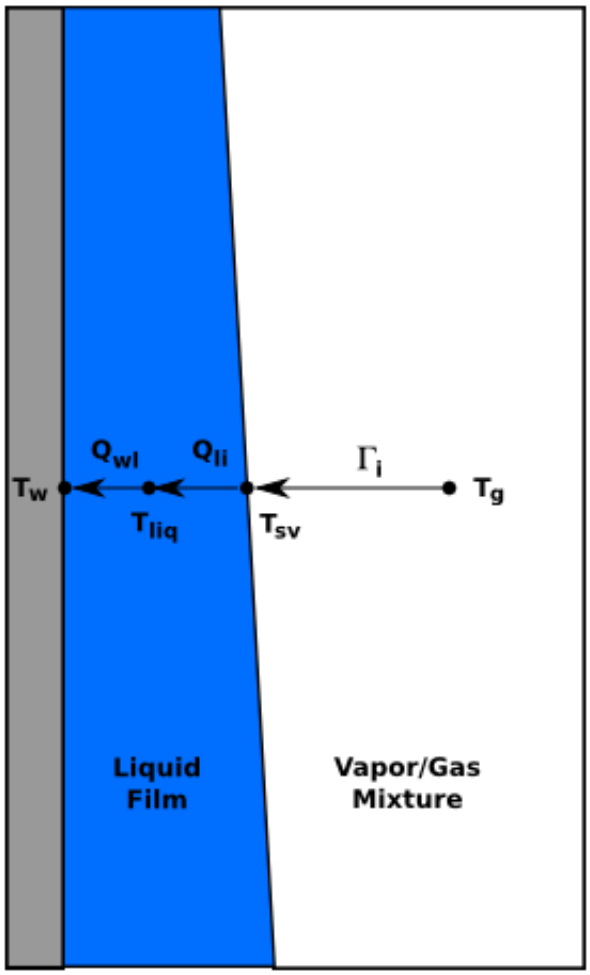

Figure. 6-36. Schematic of heat flow paths during filmwise condensation.

film Reynolds numbers. To accomplish this, the wall-liquid Nusselt no., Nu_{wl}, is computed using a power-law weighting of values for laminar and turbulent film flow as

$$Nu_{wl} = (Nu_{lam}^2 + Nu_{turb}^2)^{1/2} \tag{6-205}$$

The models used to evaluate the Nusselt no. for laminar and turbulent films are given in the following subsections.

For heat transfer in liquid films, the characteristic length is the film thickness. In TRACE, this characteristic length results directly from the solution of the two-fluid momentum equations that

yield the void fraction as a function of wall drag, interfacial shear, and gravity. The film thickness is then calculated from the void fraction by the formula

$$\delta = \frac{D_h}{2} \cdot (1 - \sqrt{\alpha}) \tag{6-206}$$

and is constrained to be greater than 10 μm. This limiting value was selected because a film with that thickness gives a heat transfer coefficient of about the same magnitude as dropwise condensation.

Laminar Film Heat Transfer

For a smooth laminar film, the Nusselt no. for heat transfer across the film[1] is simply unity, so that

$$h_{cond} = \frac{k_l}{\delta} \tag{6-207}$$

corresponding to conduction through the film. The Reynolds no. for a film is defined by

$$Re_f = \frac{4 \cdot \Gamma_f}{\mu_l} \tag{6-208}$$

where Γ_f is the film flow rate per unit width of the wetted perimeter. Thus, using the definition of the hydraulic diameter,

$$Re_f = \frac{4 \cdot \Gamma_f}{\mu_l} = \frac{G_l \cdot D_h}{\mu_l} \tag{6-209}$$

and so the Reynolds no. is the same as that for single-phase pipe flow. As the film Reynolds no. increases above a value of about 20, (see Ref. 6-83), ripples develop on the film surface and enhance the heat transfer primarily by the film thinning that occurs in the troughs. At sufficiently high Reynolds no. values, roll waves appear leading to further heat transfer enhancement.

There are many correlations in the literature to account for the wave-induced enhancement of heat transfer in laminar-wavy falling films. For example, Kutateladze (Ref. 5-8) recommended

$$Nu_{cond} = 0.895 \cdot Re_f^{1/12} \tag{6-210}$$

1. Note that the subscript 'cond', for condensation, will be used for heat transfer across a liquid film that includes both the wall-liquid and liquid interface heat transfer resistances.

However, when compared to the UCB pure steam condensation tests for cocurrent downflow in a tube (Ref. 5-7), correlations such as that given by Eq. (6-210) over-predicted the data significantly. Therefore, the empirical correlation of Kuhn, Schrock and Peterson (Ref. 5-7) given by

$$Nu_{cond} = 1 + 1.83\times10^{-4} \cdot Re_f \tag{6-211}$$

was selected for implementation in TRACE.

The Kuhn-Schrock-Peterson (K-S-P) empirical correlation is compared to its database in Figure 6-37 and to the Kutateladze model (Ref. 5-8). From the form of Eq. (6-211), it is obvious that the Nusselt no. reduces to the correct value of one for conduction through a film as the film Reynolds no. goes to zero. The enhancement as the film Reynolds no. increases is attributed to the onset of ripples though this enhancement is less than that of the Kutateladze model. From its database, the K-S-P correlation is applicable to films with Reynolds nos. in the range: $50 \leq Re_f \leq 2000$.

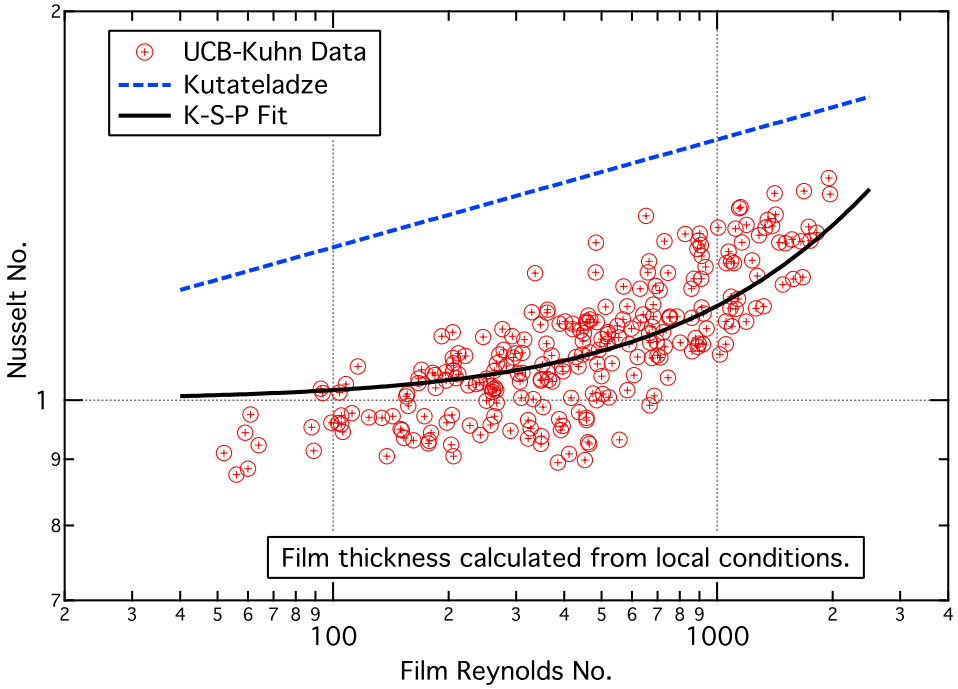

Figure. 6-37. Comparison of Kuhn-Schrock-Peterson correlation for laminar film condensation with its database.

In its original form, the K-S-P correlation was for the Nusselt no. across a film during condensation and hence included heat transfer resistances for both the wall-liquid and liquid-interface. To translate it into a correlation for interfacial heat transfer, it is necessary to make an assumption regarding the apportioning of these two resistances. As, the interfacial heat transfer package also uses the K-S-P correlation for laminar films (see **Chapter 5**), exactly how the

resistances are apportioned is of little consequence as the total heat transfer resistance will remain the same. Consequently, it was decided to simply divide the total heat transfer resistance into two equal parts. Then, the K-S-P correlation, when used for wall heat transfer becomes

$$Nu_{lam} = 2 \cdot (1 + 1.83\times10^{-4} \cdot Re_f) \tag{6-212}$$

and this is the form used in the TRACE wall heat transfer package for laminar-wavy film condensation.

Turbulent Film Heat Transfer

For heat transfer between the wall and a turbulent liquid film, we wanted a model that would be applicable both to the turbulent and the transition regimes. In selecting such a model, it was very difficult to use falling film condensation data. The reason for this is that the experimental values of the heat transfer coefficient were averaged over the entire heat transfer surface and thus included integration over both the laminar and turbulent regions. Consequently, this data could not be used in a straightforward model selection process.

Instead, we elected to use turbulent film heating data for the model selection process as the experimental technique allowed for better determination of the wall-liquid heat transfer coefficient as a function of the film Reynolds no. First, three candidate correlations were identified: Wilke (Ref. 6-84), Gimbutis (Ref. 6-85), and a modified form of the Gnielinski (Ref. 6-3) tube correlation. Both the Wilke and Gimbutis correlations were developed from film heating data and their usual forms are given as

$$Nu^* = \frac{h_{wl}}{k_l} \cdot \left(\frac{\mu_l^2}{g \cdot \Delta\rho \cdot \rho_l} \right)^{1/3} \tag{6-213}$$

where the property group on the right-hand-side has taken the place of the film thickness as the length scale.

While Nusselt no. correlations in the form given by Eq. (6-213) would be applicable to heat transfer for falling films, they would not include the effect of interfacial shear upon the film thickness. So, for implementation in TRACE, it was required that these correlations be translated into the Nusselt no. definition that directly employs the film thickness, see Eq. (6-207). The Wilke correlation was available in both forms and is given in a piece-wise fashion by

$$Nu_{film} = \begin{cases} Max\left[1.88\,,\,0.0293\cdot Re_f^{8/15}\cdot Pr_l^{0.344}\right] & : \quad Re_f < 1600 \\ 2.122\times10^{-4}\cdot Re_f^{6/5}\cdot Pr_l^{0.344} & : \quad 1600 < Re_f < 3200 \\ 0.00181\cdot Re_f^{14/15}\cdot Pr_l^{0.344} & : \quad Re_f > 3200 \end{cases} \tag{6-214}$$

The Gimbutis correlation (Ref. 6-85) was only available in terms of Nu* as

$$Nu^* = (0.165\cdot Re_f^{0.16} - 0.4)\cdot Pr_l^{0.34} \tag{6-215}$$

However, a correlation for the non-dimensional film thickness,

$$\delta^* = \frac{\delta}{\left[\mu_l^2/(g\cdot\Delta\rho\cdot\rho_l)\right]^{1/3}} = (0.03175\cdot Re_f^{0.92} + 8)^{2/3} \tag{6-216}$$

was also provided so that the Nusselt no. could be converted to the usual form. That is,

$$Nu_{film} = Nu^*\cdot\delta^* \tag{6-217}$$

A third candidate correlation was generated by modifying Gnielinski's correlation for turbulent convection in a tube to be applicable for film heat transfer. Specifically, it was recognized that the "hydraulic diameter" for a thin liquid film is simply four times the film thickness. Thus,

$$Nu_{film} \approx \frac{1}{4}\cdot Nu_{Gnielinski} \tag{6-218}$$

These three candidate correlations are compared to one another in Figure 6-38.

From Figure 6-38, it is evident that all three candidate models produce very similar values for the film Nusselt no. and that any one of them would be suitable for TRACE. Figure 6-39 and Figure 6-40 compare the Wilke and modified Gnieliski correlations to different sets of film heating data so that both the Reynolds no. and Prandtl no. dependencies could be checked. In these figures, the vertical axis uses Nu* that is based on a property group instead of the film thickness. To compare the Gnielinski correlation to this data, it was necessary to calculate the falling film thickness. This was accomplished using the wall-film friction factors described in **Chapter 4**.

Both correlations do a good job of reproducing the data with the Wilke's correlation being a little more accurate in the transition region but tending to over-predict for highly turbulent films. For TRACE, the Gnielinski film correlation was chosen for its better performance at higher film

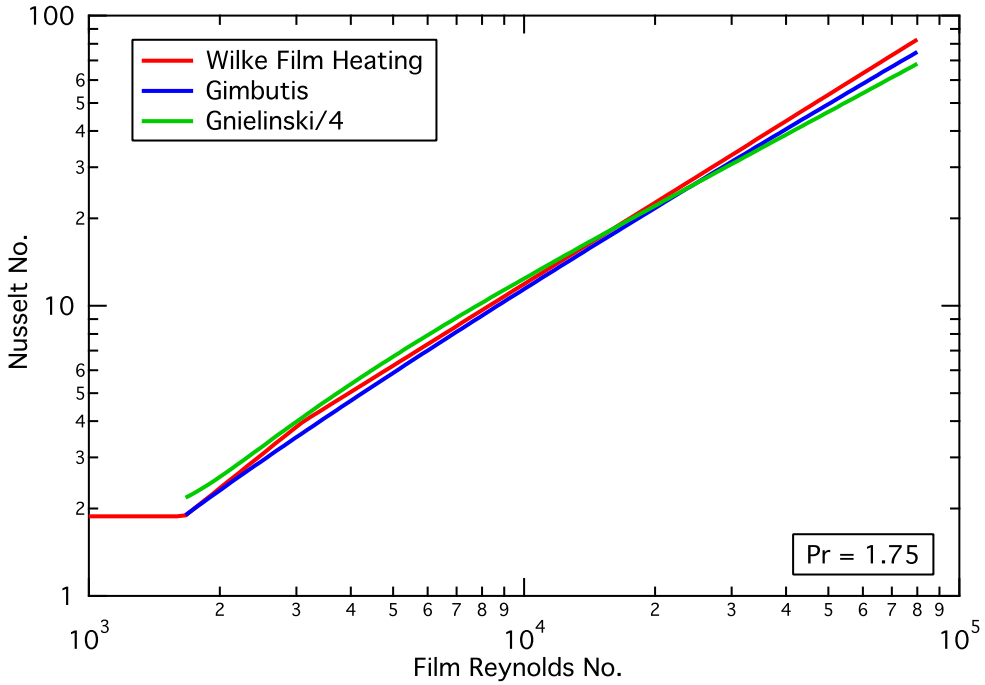

Figure. 6-38. Comparison of turbulent film heat transfer models.

Reynolds numbers and because it was already implemented as part of the wall and interfacial heat transfer packages.

The above comparisons validate the selection of the modified Gnielinski correlation for the wall-liquid heat transfer coefficient for the case of film heating. However, the intended application is for film condensation. As stated above, it was difficult to use falling film condensation data for the model selection as the data values were averaged over the entire heat transfer surface and thus included both the laminar and turbulent regimes. Consequently, we have compared the TRACE model to a selection of correlations for turbulent falling film condensation. As shown in Figure 6-41, a wide variety of correlations were used, ranging from the classical Colburn (Ref. 6-88) and Kutateladze (Ref. 6-89) correlations to more modern correlations such as those of Soliman et al. (Ref. 6-90) and Chen et al. (Ref. 6-91).

To make this comparison, both the heat transfer resistances for the wall-liquid [Eq. (6-218)] and for the liquid-interface [Eq. (5-57)] were combined to generate a Nusselt no. for heat transfer across the liquid film. Then, the TRACE wall friction models were used to calculate the film thickness as a function of Reynolds no. so that the Nusselt no. could be transformed into the Nu* form as described above. From Figure 6-41, a few observations are obvious. First, there is a wide degree of scatter between the literature correlations for film condensation, which is not too surprising given the difficulties in performing condensation experiments. Second, the TRACE model does a good job of approximating the mean value of the other models. Finally, for turbulent flow conditions, the TRACE model virtually reproduces the values given by the Labuntsov (Ref. 6-92) correlation. This comparison validates that the TRACE models for wall

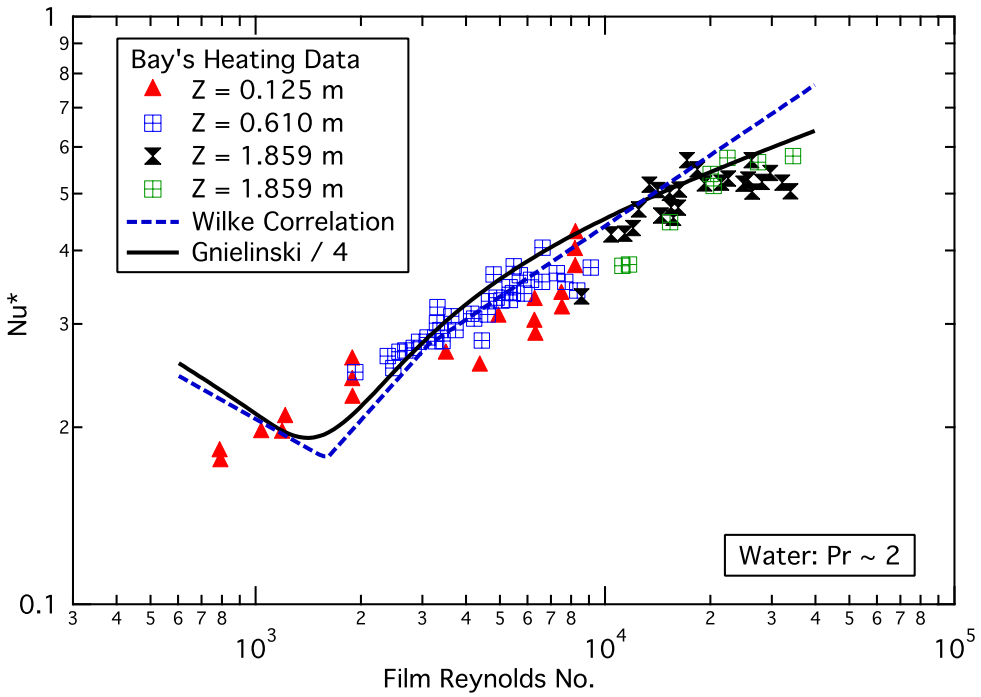

Figure. 6-39. Comparison of candidate film heat transfer models with the falling film heating data of Bays (Ref. 6-86) for water.

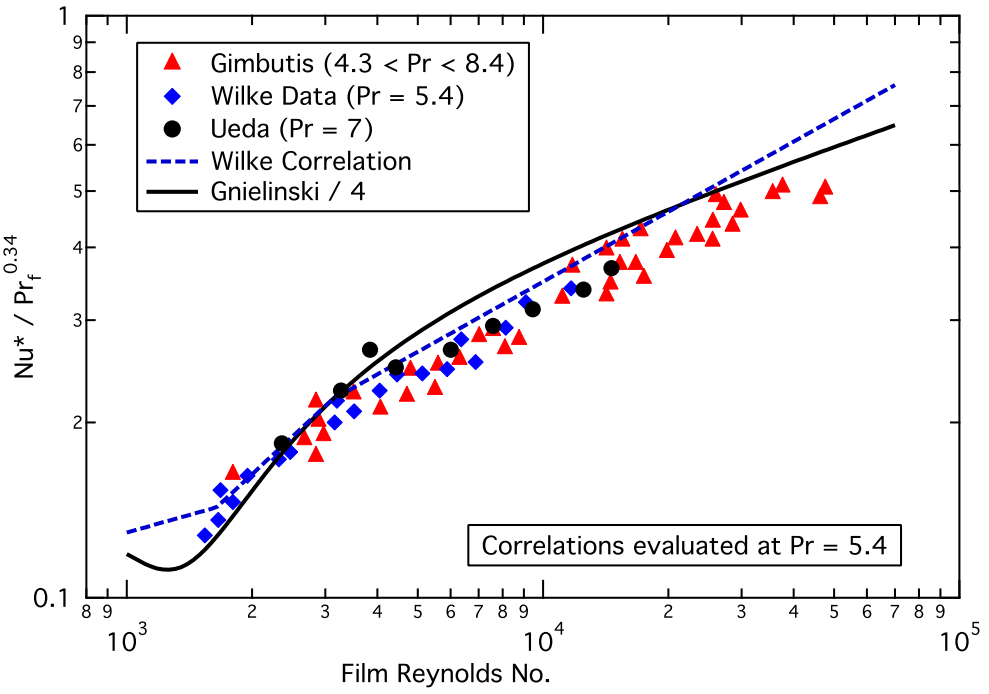

Figure. 6-40. Comparison of candidate film heat transfer models with the falling film heating data of Gimbutis (Ref. 6-85), Wilke (Ref. 6-84), and Ueda (Ref. 6-87).

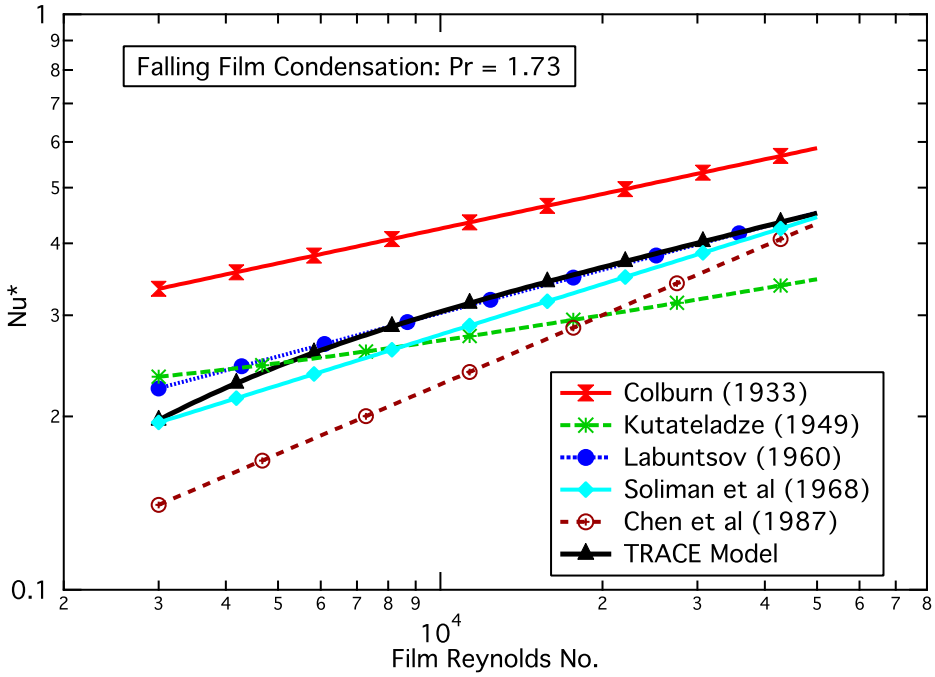

Figure. 6-41. Comparison of TRACE model with literature correlations for falling film condensation.

drag, wall-liquid heat transfer, and interfacial heat transfer all work together correctly to provide a good estimate for film condensation heat transfer in turbulent flow.

Dropwise Condensation

There is no explicit dropwise condensation model in the TRACE code as dropwise condensation usually only occurs for non-wettable surfaces. During TRACE simulations, however, conditions can arise where the heat transfer mode is condensation but there is not enough liquid present to wet the surface. Such a condition occurs, for example, during a transient when condensation is just beginning so that a film has not yet had time to form. Similarly, for a vertical heat transfer surface undergoing condensation, the top-most node is often only partially wetted for the same reason. For such conditions, where only a fraction of the surface is covered with a liquid film, a condensation model is needed for the fraction of the surface that is "dry".

For film condensation, as described above, heat transfer occurs in a two-step process[1]; condensation occurs at the film surface with heat being removed first by interfacial heat transfer to the liquid and thence to the wall. However, if there is not enough liquid present for a film to form, then the condensation heat flux must be removed directly from the vapor. That is,

1. It is a two-step process for pure-steam conditions, but a three-step process for condensation with non-condensable gases with the additional step being the mass transfer that occurs in the steam-gas mixture.

$$q''_{DW} = q''_{wg} = h_{wg} \cdot (T_w - T_g) \tag{6-219}$$

where the subscript "*DW*" is used to indicate dropwise condensation. As dropwise condensation only occurs for either a short period of time or for a small fraction of a heat transfer surface, an accurate model is not required for TRACE. Indeed, there is no such thing as an accurate model for dropwise condensation. Instead, a model is required that simply provides a heat transfer coefficient that is large enough to get condensation started but not so large as to cause computational difficulties.

To realize this in TRACE, the wall-gas heat transfer coefficient is simply set equal to the maximal value used for a liquid film. Thus, for pure-steam condensation,

$$h_{wg} = \frac{k_l}{\delta_{min}} \tag{6-220}$$

where δ_{min} is the value for the minimum liquid film thickness. The value for δ_{min} was taken to be 10 μm, so that the resulting condensation heat transfer coefficient would have the right order of magnitude for dropwise condensation. This approach provides a degree of continuity as condensation progresses and the surface becomes covered with a liquid film. Note, however, that this approach is only appropriate for pure-steam condensation. When non-condensable gases are present, the additional heat transfer resistance associated with the mass transfer process must be added. This will be described in the next section.

The fraction of the heat transfer surface that is covered by a liquid film is estimated from the void fraction using the thin film approximation,

$$f_{wet} = \frac{(1-\alpha) \cdot D_h}{4 \cdot \delta_{min}} \tag{6-221}$$

Then, for the fraction of the wall that is wetted, the wall-liquid heat transfer is used,

$$h_{wl} = f_{wet} \cdot h_{wl} \tag{6-222}$$

and for the non-wetted fraction,

$$h_{wg} = (1 - f_{wet}) \cdot h_{wg} \tag{6-223}$$

Non-Condensible Gas Effects

As described by Collier and Thome (Ref. 6-93), the presence of even a small quantity of non-condensable gas in the condensing vapor has a profound influence on the overall heat transfer

resistance during condensation. The non-condensable gas is carried with the vapor towards the interface where it accumulates so that the partial pressure of the vapor at the interface decreases thereby decreasing the driving potential for heat transfer across the liquid film. The process limiting the heat transfer rate then becomes the mass transfer rate for the vapor diffusing through the gas-vapor mixture to the interface. Indeed, as shown in Figure 10.4 of Reference 6-93, reductions of more than 50% in the heat transfer can be caused by air mass fractions as low as 0.5% for a stagnant air-steam mixture.

To improve the predictive capability of the TRACE code for the Passive Containment Cooling System (PCCS) of the proposed ESBWR design, a new model for condensation in the presence of non-condensable gases was developed. Later, this model was extended to also be applicable to condensation on the walls of the drywell itself. This new model for film condensation in the presence of non-condensable gases employs the mass transfer conductance approach as developed by Kuhn et al. (Ref. 5-7) and was described previously in **Chapter 5,** *Special Model for Film Condensation*.

During film condensation, the wall heat transfer coefficient is calculated using the models for wall-to-liquid heat transfer for laminar and turbulent films given by Eq. (6-212) and Eq. (6-218). The non-condensable gas effect, that normally controls the condensation rate, is calculated using the mass transfer model described previously in **Chapter 5** and serves to augment the interfacial heat transfer resistance between the liquid and the gas-vapor mixture. This description of this model will not be repeated here but a comparison of its predicted heat transfer coefficients with those of the UCB-Kuhn (Ref. 5-7) condensation experiments is given below.

Kuhn et al. (Ref. 5-7) conducted condensation experiments for cocurrent downflow in a tube with the same diameter as that proposed for the PCCS condenser of the ESBWR design. In addition to the pure-steam tests used above for the laminar film condensation model, they conducted both air-steam and helium-steam tests. We compared the TRACE model to all of the air-steam and helium-steam data in the experiments of Kuhn. In these comparisons, the "total" heat transfer coefficient is defined as

$$h_{cond} = \frac{q''_w}{(T_w - T_{sv})} \tag{6-224}$$

There were 72 air-steam tests giving a total of 571 data points, the TRACE model calculated the heat transfer coefficient for these with an average error of 7.7% and an RMS error of 16.1% (see Figure 6-42). Similarly, there were 25 helium-steam tests giving a total of 192 data points, the TRACE model calculated the heat transfer coefficient for these with an average error of 0.9% and an RMS error of 16.3% (see Figure 6-43). These values are considered to be within the error bands associated with this data.

This film condensation model was extended to also be applicable for the conditions of the drywell walls in the ESBWR design. For large containment volumes, the correlations used for turbulent forced convection in the mass transfer model needed to be replaced by something more appropriate. For this purpose, the correlation for turbulent free convection on a vertical plate

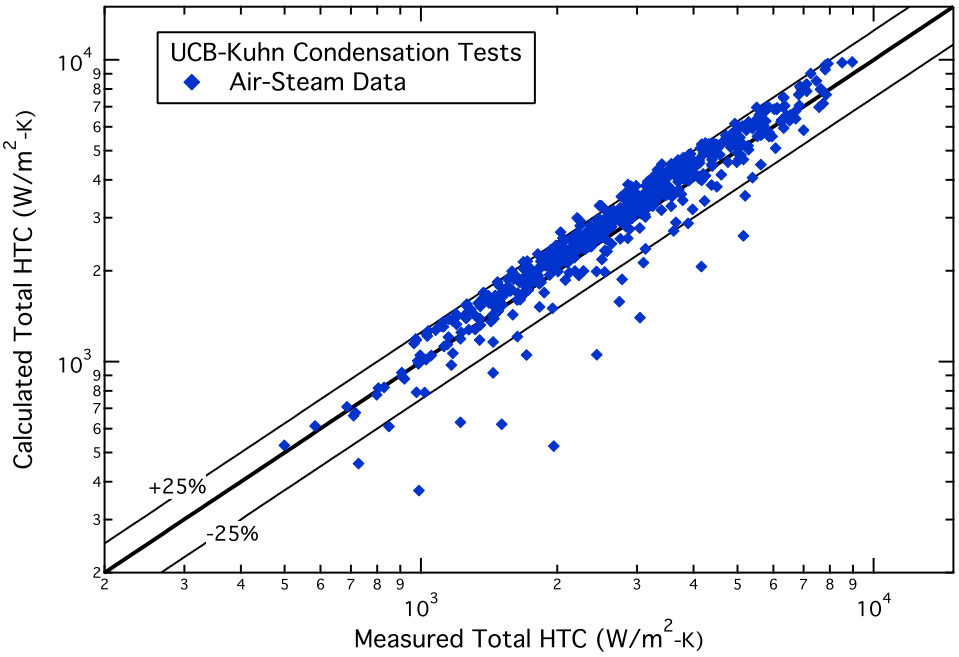

Figure. 6-42. Comparison of condensation heat transfer coefficients calculated using the TRACE model with the air-steam data of Kuhn et al. (Ref. 5-7).

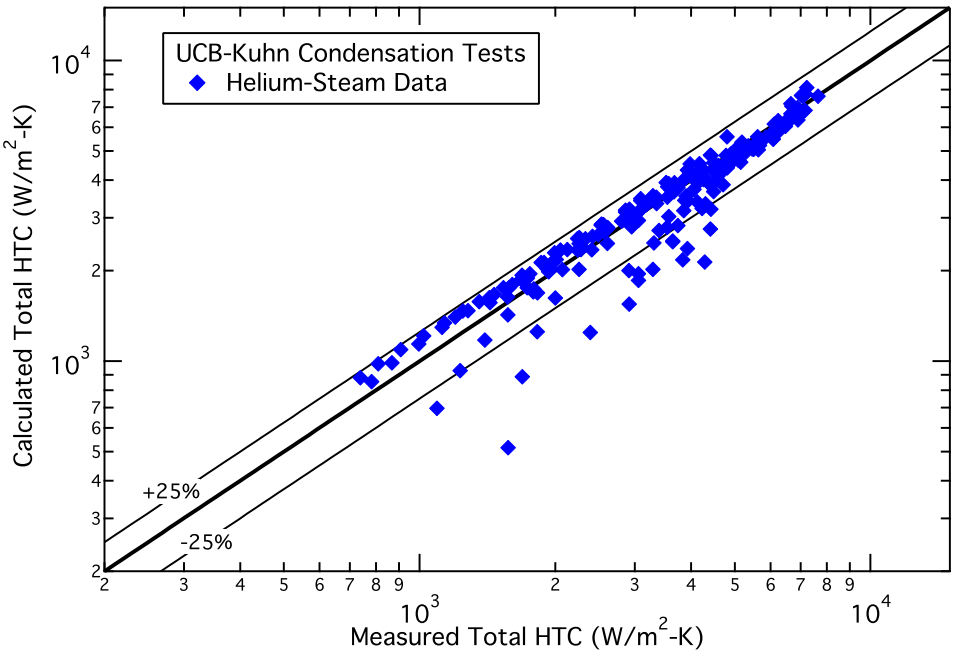

Figure. 6-43. Comparison of condensation heat transfer coefficients calculated using the TRACE model with the helium-steam data of Kuhn et al. (Ref. 5-7).

given by McAdams (Ref. 5-29) was chosen as detailed in **Chapter 5,** *Special Model for Film Condensation*. Again, this model description will not be repeated here.

For the case of "dropwise" condensation, that is, when not enough liquid is present to cover the surface with a film, the non-condensable gas effect must be applied directly to the wall-gas heat transfer coefficient. To accomplish this, the mass transfer and gas-side interfacial heat transfer models described previously are used to compute the condensation and sensible heat fluxes that would occur if the liquid-side heat transfer resistance was negligible. Simply put, the iterative procedure for the liquid-gas interface temperature is bypassed so that $T_i \approx T_w$. Then, the wall-gas heat flux is computed from

$$q''_{wg} = q''_{cond} + q''_{sens} \tag{6-225}$$

and the heat transfer coefficient becomes

$$h_{wg} = \frac{(q''_{cond} + q''_{sens})}{(T_w - T_g)} \tag{6-226}$$

A comparison of this model was made to both the Uchida correlation (Ref. 5-30) and the Dehbi data (Ref. 5-31) with excellent results. Figure 6-44 presents this comparison to the Uchida correlation over a wide range of non-condensable gas mass fraction for atmospheric pressure conditions.

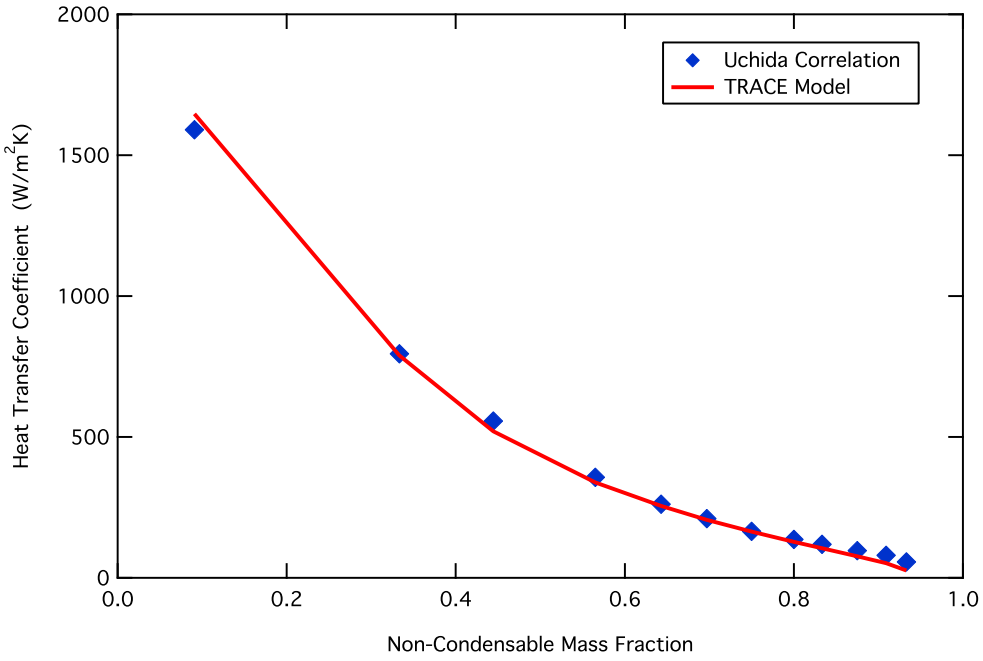

Figure. 6-44. Comparison of the TRACE model for wall condensation in the presence of non-condensable gases with the Uchida correlation at atmospheric pressure.

This completes the description of the TRACE wall heat transfer models.

References

6-1 M.S. Bhatti and R.K. Shah, "Turbulent and Transition Flow Convective Heat Transfer in Ducts," *Handbook of Single-Phase Convective Heat Transfer*, eds. S. Kakac, R.K. Shah, and W. Aung, Chapter 4, Wiley-Interscience, New York, 1987.

6-2 F.P. Incropera and D.P. De Witt, *Introduction to Heat Transfer*, 2nd edition, Chapter 8, John Wiley & Sons, New York, 1990.

6-3 V. Gnielinski, "New Equations flow regime Heat and Mass Transfer in Turbulent Pipe and Channel Flow," *Int. Chem. Eng.*, 16, 359-368, 1976.

6-4 G.K. Filonenko, "Hydraulic Resistance in Pipes," (in Russian), *Teplonergetika*, 1, 40-44, 1954.

6-5 F. Kreith and M.S. Bohn, *Principles of Heat Transfer*, 4th edition, Chapter 6, page 289-290, Harper-Collins Publishers, New York, 1986.

6-6 W. Huschmidt and E. Burck, "The Effect of Temperature-Dependent Properties of Materials on Heat Transfer in the Turbulent Flow of Liquids in Tubes at High Heat Fluxes and Prandtl Numbers," *Int. J. Heat Mass Transfer*, 11, 1041-1048, 1968.

6-7 J.P Holman, *Heat Transfer*, 5th edition, Table 7.1, McGraw-Hill Book Co., Inc., New York, 1981.

6-8 J. Weisman, "Heat Transfer to Water Flowing Parallel to Tube Bundles," *Nuclear Science and Engineering*, 6, 78-79, 1959.

6-9 A. Ya. Inayatov, "Correlation of Data on Heat Transfer. Flow Parallel to Tube Bundles at Relative Tube Pitches of $1.1 < s/d < 1.6$," *Heat Transfer - Soviet Research*, 7, 84-88, 1975.

6-10 M.S. El-Genk, B. Su, and Z. Guo, "Experimental Studies of Forced, Combined and Natural Convection of Water in Vertical Nine-Rod Bundles with a Square Lattice," I*nt. J. Heat Mass Transfer*, 36, 2359-2374, 1993.

6-11 J.H. Kim and W.-H. Li, "Heat Transfer in Laminar Flow Along Circular Rods in Infinite Square Arrays," *J. Heat Transfer*, 110, 252-257, 1988.

6-12 P.K. Sarma, C.V.N. Sastry, and V.N. Murthy, "Experimental Investigation of Combined Forced and Free Convective Heat Transfer Rates in a Vertical U-Tube with One Leg Heated," Proceedings of the 7th International Heat Transfer Conference, Vol. 3, 471-476, 1982.

6-13 J. C. Chen, "A Correlation for Boiling Heat Transfer to Saturated Fluids in Convective Flow," presented to 6th National Heat Transfer Conference, Boston, 11-14 Aug., ASME preprint 63-HT-34, 1963.

6-14 D. Kim et al, "Comparison of 20 Two-Phase Heat Transfer Correlations with Seven Sets of Experimental Data, Including Flow Pattern and Tube Inclination Effects," *Heat Transfer Engineering*, 20, 15-40, 1999.

6-15 M.A. Aggour, M.M. Vijay, and G.E. Sims, "A Correlation of Mean Heat Transfer Coefficients for Two-Phase Two-Component Flow in a Vertical Tube," Proceedings of the 7th International Heat Transfer Conference, Vol. 5, 367-372, 1982.

6-16 K.S. Rezkallah and G.E. Sims, "An Examination of Correlations of Mean Heat Transfer Coefficients in Two-Phase Two-Component Flow in Vertical Tubes," *AIChE Symposium Series*, 83 (257), 109-114, 1987.

6-17 J.G. Collier, *Convective Boiling and Condensation*, p. 382-406, McGraw-Hill, London, 1972.

6-18 N. Basu, G.R. Warrier, and V.K. Dhir, "Onset of Nucleate Boiling and Active Nucleation Site Density During Subcooled Flow Boiling," *J. Heat Transfer*, **124**, 717-728, 2002.

6-19 A. E. Bergles and W. M. Rohsenow, "The Determination of Forced Convection Surface Boiling Heat Transfer," *J. Heat Transfer*, **86**, 365-372, 1964.

6-20 E. J. Davis and G. H. Anderson, "The Incipience of Nucleate Boiling in Forced Convection Flow," *AIChE Journal*, **12**(4), 774-780, 1966

6-21 J.C. Chen, "A Correlation for Boiling Heat Transfer to Saturated Fluids in Convective Flow," ASME preprint 63-HT-34 presented at 6th National Heat Transfer Conference, Boston, 11-14 August, 1963.

6-22 M. G. Cooper, "Heat Flow Rates in Saturated Nucleate Boiling - a Wide-Ranging Examination Using Reduced Properties," *Adv. Heat Transfer*, **16**, 157-239, 1984.

6-23 D. Gorenflo, "Pool Boiling," VDI-Heat Atlas, Sect. Ha, VDI-Verlag, Dusseldorf, 1993. Obtained from secondary reference: J.G. Collier and J. R. Thome, *Convective Boiling and Condensation*, 3rd Edition, p. 155-158, Oxford University Press, Oxford, 1994.

6-24 W. H. Jens and P. A. Lottes, "Analysis of Heat Transfer Burnout, Pressure Drop and Density Data for High Pressure Water," ANL-4627, May 1951.

6-25 S. Levy, "Generalized Correlation of Boiling Heat Transfer," *J. Heat Transfer*, **81C**, 37-42, 1959.

6-26 W. H. McAdams, et al., "Heat Transfer at High Rates to Water with Surface Boiling," I*nd. Eng. Chem.*, **41**, 1945-1955, 1949.

6-27 D. Steiner and J. Taborek, "Flow Boiling Heat Transfer in Vertical Tubes Correlated by an Asymptotic Model," *Heat Transfer Engng.*, **13**(2), 43-69, 1992.

6-28 J. R. S. Thom, et al., "Boiling in Subcooled Water During Flow Up Heated Tubes or Annuli," Paper 6 presented at the Symposium on Boiling Heat Transfer in Steam Generation Units and Heat Exchangers held in Manchester, IMechE (London) 15-16 September, 1965.

6-29 W.H. McAdams, *Heat Transmission*, 3rd Edition, p. 378, McGraw-Hill, New York, 1954.

6-30 S. S. Kutateladze, "Boiling Heat Transfer," *Int. J. Heat Mass Transfer*, **4**, 3-45, 1961

6-31 S. W. Churchill, *The Interpretation and Use of Rate Data*, Hemisphere, New York, 1974.

6-32 J. P. Holman, *Heat Transfer*, 8th Edition, McGraw-Hill, New York, p. 536, 1997.

6-33 R. W. Bjorge, G. R. Hall and W. M. Rohsenow, "Correlation of Forced Convection Boiling Heat Transfer Data," I*nt. J. Heat Mass Transfer*, **25**(6), 753-757, 1982.

6-34 R. T. Lahey, Jr., "A Mechanistic Subcooled Boiling Model," *Heat Transfer 1978*, Proceedings of the 6th International Heat Transfer Conference, Toronto, Canada, Vol. 1, 293-297, 1978.

6-35 P. Saha and N. Zuber, "Point of Net Vapor Generation and Vapor Void Fraction in Subcooled Boiling," Heat Transfer 1974, Proceedings of the 5th International Heat Transfer Conference, Tokyo, Japan, Vol. 4, 175-179, 1974.

6-36 D. C. Groeneveld, et al., "The 1995 Look-Up Table for Critical heat Flux in Tubes," *Nucl. Eng. Des.*, **163**, 1-23, 1996.

6-37 D. C. Groeneveld, S. C. Cheng and T. Doan, "1986 AECL-UO Critical Heat Flux Lookup Table," *Heat Trans. Eng.*, **7**, 46-62, 1986.

6-38 D. C. Groeneveld, et al., "A General Method of Predicting Critical Heat Flux in Advanced Water-Cooled Reactors," Proceedings of the 9th International Topical Meeting on Nuclear Reactor Thermal Hydraulics (NURETH-9), San Francisco, California, October 1999.

6-39 N. Zuber, "Hydrodynamic Aspects of Boiling Heat Transfer," AECU-4439, Atomic Energy Commission, 1959

6-40 H. J. Ivey and D. J. Morris, "On the Relevance of the Vapour-Liquid Exchange Mechanism for Subcooled Boiling Heat Transfer at High Pressure," AEEW-R-137, United Kingdom Atomic Energy Authority Research Group, 1962.

6-41 P. Griffith, C. T. Avedisian and J. P. Walkush, "Counterflow Critical Heat Flux," AIChE Symposium Series, No. 174, Vol. 74, 149-155, 1978.

6-42 L. Biasi et al., "Studies in Burnout, Part 3: A New Correlation for Round Ducts and Uniform Heating and Its Comparison with World Data," *Energ. Nucl.*, **14**, 530-536, 1967.

6-43 S. Bertoletti et al., "Heat Transfer Crisis with Steam-Water Mixtures," *Energ. Nucl.*, **12**(3), 1965.

6-44 J. A. Borkowski and N. L. Wade, editors, "TRAC-BF1/MOD1 Models and Correlations," NUREG/CR-4391, Section 4.2.12, 1992.

6-45 R. E. Phillips, R. W. Shumway and K. H. Chu, "Improvements to the Prediction of Boiling Transition in BWR Transient Calculations," Proceedings of the 20th ASME/AIChE National Heat Transfer Conference, Milwaukee, WI, August 1981.

6-46 P. J. Berenson, "Film Boiling Heat Transfer from a Horizontal Surface," *J. Heat Transfer*, p. 351-358, August 1961.

6-47 M. J. Thurgood et al., "COBRA/TRAC - A Thermal-Hydraulics Code for Transient Analysis of Nuclear Reactor Vessels and Primary Coolant Systems," Vol. 1, NUREG/CR-3046, 1983.

6-48 D. Swinnerton, K. G. Pearson, and M. L. Hood, "Steady State Post Dryout Experiments at Low Quality and Medium Pressure," United Kingdom Atomic Energy Authority, AEEW-R 2192, 1988.

6-49 J. C. Stewart and D. C. Groeneveld, "Low-Quality and Subcooled Film Boiling of Water at Elevated Pressures," *Nucl. Eng. Des.*, **67**, 259-272, 1981.

6-50 V. K. Dhir and G. P. Purohit, "Subcooled Film Boiling Heat Transfer from Spheres," *Nucl. Eng. Des.*, **47**, 49-66, 1978.

6-51 Y. Koizumi, et al., "High-Pressure Reflooding Experiments of Multi-Rod Bundle at ROSA-IV TPTF," *Nucl. Eng. Design*, **120**, 301-310, 1990.

6-52 G. Xu, H. Kumamaru, and K. Tasaka, "Reflood Experiments in Single Rod Channel Under High-Pressure Condition," Japan Atomic Energy Research Institute, JAERI-M 89-178, 1989.

6-53 M. J. Loftus et al., "PWR FLECHT-SEASET Unblocked Bundle, Forced and Gravity Reflood Task Data Report," NUREG/CR-1532, 1981.

6-54 T. M. Anklam, "ORNL Small-Break LOCA Heat Transfer Test Series I: High-Pressure Reflood Analysis," NUREG/CR-2114, 1981.

6-55 C. R. Hyman, T. M. Anklam and M. D. White "Experimental Investigations of Bundle Boiloff and Reflood Under High-Pressure Low Heat Flux Conditions," NUREG/CR-2455, 1982.

6-56 V. K. Dhir, R. B. Duffey, and I. Catton, "Quenching Studies on a Zircaloy Rod Bundle," J. *Heat Transfer*, **103**, 293-299, 1981.

6-57 "RELAP5/Mod3.3 Code Manual, Volume IV: Models and Correlations," NUREG/CR-5535, Rev. 1, Vol. IV, 2001.

6-58 D. R. Liles et al., "TRAC-PF1/MOD1: Correlations and Models," NUREG/CR-5069, 1988.

6-59 W. L. Kirchner, "Reflood Heat Transfer in a Light Water Reactor," Ph.D Thesis, Massachusetts Institute of Technology, NUREG-0106, 1976.

6-60 T. A. Bjornard and P. Griffith, "PWR Blowdown Heat Transfer," *Thermal and Hydraulic Aspects of Nuclear Reactor Safety*, American Society of Mechanical Engineers, New York, Vol. 1, 17-41, 1977.

6-61 K. Johannsen, P. Weber, and Q. Feng, "Experimental Investigation of Heat Transfer in the Transition Region," Commission of the European Communities, EUR 13235 EN, 1990.

6-62 K. K. Fung, "Subcooled and Low Quality Film Boiling of Water in Vertical Flow at Atmospheric Pressure," NUREG/CR-2461, 1981.

6-63 F. de Cachard, "Development, Implementation, and Assessment of Specific Closure Laws for Inverted-Annular Film-Boiling in a Two-Fluid Model," NUREG/IA-0133, 1996.

6-64 N. Hammouda, D. C. Groeneveld and S. C. Cheng, "Two-Fluid Modeling of Inverted Annular Film Boiling," *Int. J. Heat Mass Transfer*, **40**(11), 2655-2670, 1997.

6-65 R. P. Forslund and W. M Rohsenow, "Dispersed Flow Film Boiling," *J. Heat Transfer*, **90**(6), 399-407, 1968.

6-66 C. A. Sleicher and M. W. Rouse, "A Convenient Correlation for Heat Transfer to Constant and Variable Property Fluids in Turbulent Pipe Flow," *Int. J. Heat Mass Transfer*, 18, 677-683, 1975.

6-67 B. S. Petukhov, "Turbulent Heat Transfer in Tubes with Variable Fluid Properties," Chapter 9, *Heat Exchanger Sourcebook*, edited by J. W. Palen, Hemisphere, Washington, 1986.

6-68 M. Molki and E. M. Sparrow, "An Empirical Correlation for the Average Heat Transfer Coefficient in Circular Tubes," *J. Heat Transfer*, **108**, 482-484, 1986.

6-69 A. F. Mills, "Experimental Investigation of Turbulent Heat Transfer in the Entrance Region of a Circular Conduit," *J. Mech. Eng. Sci*., **4**, 63-77, 1962.

6-70 P. M. Worsoe-Schmidt and G. Leppert, "Heat Transfer and Friction for Laminar Flow of a Gas in a Circular Tube at High Heating Rate," *Int. J. Heat Mass Transfer*, **8**, 1281-1301, 1965.

6-71 W.H. McAdams, *Heat Transmission*, 3rd Edition, Chapter 7, Eq. (7-4a), McGraw-Hill Book Co., New York, NY, 1954.

6-72 B. Metais and E. R. G. Eckert, "Forced, Mixed, and Free Convection Regimes," *J. Heat Transfer*, 295-296, May 1964.

6-73 S. M. Nijhawan, "Experimental Investigation of Thermal Non-Equilibrium in Post-Dryout Steam-Water Flow," Ph.D Thesis, Lehigh University, 1980.

6-74 D. G. Evans, S. W. Webb, and J. C. Chen, "Measurement of Axially Varying Nonequilibrium in Post-Critical-Heat-Flux Boiling in a Vertical Tube," NUREG/CR-3363, Vol. 2, 1983.

6-75 D. P. Frankum, J. C. Ralph, and C. D. Wade, "Post Dryout Heat Transfer and Void Fraction Measurements at Low Flow and 2-4 Bar Pressure," United Kingdom Atomic Energy Authority, Harwell, PWR/HTWG/P(90)777 and G-5415, 1990.

6-76 R. A. Savage, D. Swinnerton, and K. G. Pearson, "Steady State Post Dryout Experiments at Low Quality and Medium Pressure," United Kingdom Atomic Energy Authority, AEEW-R 2486, 1989.

6-77 A. N. Bhaskarwar and M. S. Phanikumar, "On Heat Transfer Augmentation Using Dilute Gas-Solid Suspensions," *J. Heat Transfer*, **117**, 1091-1094, 1995.

6-78 S. W. Webb and J. C. Chen, "A Two-Region Vapor Generation Rate Model for Convective Film Boiling," Proceedings of the 1st International Workshop on Fundamental Aspects of Post-Dryout Heat Transfer, Salt Lake City, NUREG/CP-0060, p 485-508, 1984.

6-79 A. J. Clare and S. A. Fairbairn, "Droplet Dynamics and Heat Transfer in Dispersed Two-Phase Flow," Proceedings of the 1st International Workshop on Fundamental Aspects of Post-Dryout Heat Transfer, Salt Lake City, NUREG/CP-0060, p 373-396, 1984.

6-80 M. I. Drucker, V. K. Dhir, and R. B. Duffey, "Two-Phase Heat Transfer for Flow in Tubes and Over Rod Bundles with Blockages," *J. Heat Transfer*, **106**, 856-864, 1984.

6-81 H. Kianjah, V. K. Dhir, and A. Singh, "An Experimental Study of Heat Transfer Enhancement in Disperse Flow in Rod Bundles," Proceedings of the 1st International Workshop on Fundamental Aspects of Post-Dryout Heat Transfer, Salt Lake City, NUREG/CP-0060, p 397-415, 1984.

6-82 K. H. Sun, J. M. Gonzalez-Santalo, and C. L. Tien, "Calculations of Combined Radiation and Convection Heat Transfer in Rod Bundles Under Emergency Cooling Conditions," *J. Heat Transfer*, 414-420, August 1976.

6-83 S. Z. Kuhn, P. F. Peterson, and V. E. Schrock, "Interfacial Shear and Waviness Effects on Laminar Film Flow Heat Transfer in Vertical Tubes," Proceedings of the 31st National Heat Transfer Conference, Houston, **4**, 79-89, 1996.

6-84 W. Wilke, "Heat Transfer in Rippling Films," *Ver. Deut. Ingr. Forshungsh*., 490, 1962.

6-85 G. J. Gimbutis, "Heat Transfer of a Turbulent Vertically Falling Film," Heat Transfer 1974, Proceedings of the 5th International Heat Transfer Conference, Tokyo, Vol. **2**, 85-89, 1974.

6-86 G. S. Bays and W. H. McAdams, "Heat Transfer Coefficients in Falling Film Heaters: Streamline Flow," *Ind. Eng. and Chem*., **29** (11), 1240-1246, 1937.

6-87 T. Ueda, et al., "Heat Transfer and Pressure Drop for Flow Condensation Inside a Vertical Tube," *Bulletin of the JSME*, **15**, No. 88, 1267-1277, 1972.

6-88 A. P. Colburn, "The Calculation of Condensation Where a Portion of the Condensate Layer is in Turbulent Flow," *Trans. AIChE*, **30**, 187-193, 1933.

6-89 S. S. Kutateladze, *Fundamentals of Heat Transfer*, p. 307, Academic Press, New York, 1963.

6-90 M. Soliman, J. R. Schuster, and P. J. Berenson, "A General Heat Transfer Correlation for Annular Flow Condensation," *J. Heat Transfer*, **90**, 267-276, 1968.

6-91 S. L. Chen, F. M. Gerner, and C. L. Tien, "General Film Condensation Correlations," *Experimental Heat Tranfer*, **1**, 93-107, 1987.

6-92 D. A. Labuntsov, "Condensation of Steam on a Vertical Surface with Turbulent Condensate Film," *Inzh. Fiz. Zhur*,, **3**(8), 3-8, 1960.

6-93 J.G. Collier and J. R. Thome, *Convective Boiling and Condensation*, 3rd Edition, p. 439-445, Oxford University Press, Oxford, 1994.

6-94 R. Shumway, "Consolidation of TRAC Codes: Task CHAN," Scientech Internal Report SCIE-NRC-375-99, NRC ADAMS Accession No. ML071710042, (January 12, 1999).

7

Flow Process Models

Special models play an important role in the overall performance of TRACE. In the following sections, four special models are described:

- models for critical flow,
- countercurrent flow,
- offtake flow from a large pipe in horizontal stratified flow,
- form loss, and

Nomenclature

The nomenclature that applies to this section follows:

a_{HE} = homogeneous equilibrium sound speed

A = flow area

A_j = flow area before the abrupt expansion

A_{j+1} = flow area after the abrupt expansion

C = virtual mass coefficient

C_B = abscissa intercept in Bankoff CCFL correlation

C_i = interfacial drag coefficient

C_1, C_2 = correlation constants in offtake model

D = diameter

$\overline{\mathrm{E}}$ = interpolation constant used in the CCFL model

g = gravitational acceleration constant

h = characteristic height from liquid surface to offtake entrance plane

h_b = critical entrainment height

h_{fg} = latent heat of vaporization

H_g = dimensionless gas flux

H_l = dimensionless liquid delivery

j = superficial velocity

k_c = critical wave number

K = additive loss factor or kinetic energy (in level tracking model)

L = length or water level height (in level tracking model)

L^* = Bond number

M_B = slope in the Bankoff CCFL correlation

n = number of holes in the tie plate

P = pressure

P_c = pressure at the choking plane

P_{up} = pressure upstream of the choking plane

q_{il} = heat flux from the saturation interface to the liquid field

q_{ig} = heat flux from the saturation interface to the gas field

q_{dl} = flux of direct sensible heat to the liquid field

q_{dg} = flux of direct sensible heat to the gas field

R = gas constant or nondimensional height ratio for offtake model

s = entropy

t = time

t_p = thickness of the tie plate

T = temperature

T_o = stagnation temperature

V = velocity

V_{cg} = critical velocity for single-phase vapor

V_{cl} = subcooled-liquid choking velocity

V_{up} = velocity upstream of the choking plane

Vol = volume

W = mass flow rate in offtake model

x = distance or offtake flow quality

Greek

α = gas volume fraction

γ = specific heat ratio or mass, energy and volume flux time weighting factor

ΔT = temperature difference

Δt = time step size

Δx = cell height

Γ_i = interfacial mass exchange term

λ_i = characteristic roots

λ_E = distance between liquid-gas interface and cell boundaries

ρ = density

$\Delta\rho$ = difference between the phasic densities

ϕ = mass flux

ζ = energy flux

Φ = potential energy

σ = surface tension

η = ratio of the area of the holes in the tie plate to the total area of the tie plate

ω = volume flux

Subscripts

a = noncondensable gas

c = cell-centered value

cut = a cutoff value

E = edge variables

g = combined-gas mixture

j = denotes a cell index location (could also be $j+1$, $j+1/2$, $j-1/2$, etc)

k = phase index (liquid or gas)

L = applies to the water level

l = liquid

lev = denotes the cell that contains the water level

m = total mixture

up = conditions upstream of the choking plane

v = vapor

e = edge-based value (may be accompanied by a + or - superscript to indicate which side of cell center the edge is on)

Superscripts

L = applies to the water level

n = current-time quantity

$n+1$ = new-time quantity

p = predicted quantity

$+$ = above the water level

- = below the water level

Critical Flow

Critical (or "choked") flow occurs when the mass flow in a pipe becomes independent of the downstream conditions. Therefore, a further reduction in the downstream pressure will not change the mass flow rate. The reason choking occurs is that acoustic signals can no longer propagate upstream to affect the boundary conditions that determine the mass flow rate at the choke plane. There are numerous examples in the operation of a nuclear power plant where the presence of critical flow can play a large role in how the plant responds during some hypothetical transient. Predicting such phenomena during reactor safety simulations can therefore be key to achieving an accurate overall understanding of the scenario being simulated.

Because the TRACE fluid-dynamics equations for one-dimensional components use a multi-step procedure that allows the material Courant condition to be violated, the presence of critical flow can be predicted for components with smooth area changes simply by using a sufficiently fine nodalization. The computational efficiency of models that employ this technique, however, generally makes this approach cost prohibitive. For 1-D components with abrupt area changes, this technique can also be problematic as a fine nodalization can cause erroneous natural choking results. As a result, a separate choking model that will allow TRACE to predict critical flow is almost a necessity (Ref. 7-1).

The basic thrust of the critical flow model is to predict, for a given cell edge, the conditions for which choked flow would be expected to occur. Then, by comparing the momentum solution

predictions against these conditions, TRACE can determine whether the flow is actually choked at a particular cell edge, and adjust the velocity and associated pressure derivatives accordingly. Because the predictions of the choking criteria are highly dependent upon the nature of the flow field at the cell-edge and upstream cell-center, the critical flow model is really three separate models in one:

- a subcooled-liquid choked-flow model
- a two-phase, two-component choked-flow model
- a single-phase vapor choked-flow model

Each of these models will be addressed separately in the sub-sections that follow.

The critical flow model in TRACE is implemented as a modeling option that you may turn on or off at individual cell edges in each 1D component. Each edge location may also have associated with it, one of four pairs of user-defined subcooled and two-phase choked-flow multipliers. Depending on which choking model is used (either subcooled-liquid, two-phase two-component fluid, or superheated vapor), these multipliers allow you to adjust the predicted liquid, steam/gas-mixture, or both, choking velocities to account for break or nozzle geometry effects. The use of these multipliers is described more completely in the TRACE User's Guide.

Subcooled Liquid

The subcooled choked-flow model is a modified form of the Burnell model (Ref. 7-2) and is essentially the same as that used in RELAP5 (Ref. 7-3). The physical process that occurs during the subcooled blowdown phase is described in the following paragraphs. Much of the discussion presented here has simply been repeated directly from Reference 7-3.

Initially, and in the early phase of blowdown , the flow approaching the break or break nozzle will be subcooled liquid. Under most conditions of interest in LWR systems, the fluid changes phase at the break because the downstream pressure is much lower than the saturation pressure corresponding to the system fluid temperature. The transition from single- to two-phase flow, which is accompanied by a nearly discontinuous change in the fluid bulk modulus (measure of its compressibility), leads to a large discontinuity in the sound speed at the break. This is especially true for the liquid to liquid-vapor transition (for example, at 600 kPa, the ratio of single- to two-phase sound speed at the liquid boundary is 339.4. An effective discontinuity is also present at the vapor boundary, but the ratio is only 1.069). Thus considerable care must be exercised when analyzing a flow having transitions to or from a pure phase.

To understand the physical process that occurs for subcooled upstream conditions, consider the flow through a converging/diverging nozzle connected to an upstream plenum with subcooled water at a high pressure. For a downstream pressure only slightly lower than the upstream pressure, subcooled liquid flow will exist throughout the nozzle. Under these conditions, the flow can be analyzed using Bernoulli's equation, which predicts a minimum pressure, P_t, at the throat[1]. As the downstream pressure is lowered further, a point is reached where the throat

pressure equals the local saturation pressure, P_{sat}. If the downstream pressure is lowered further, vaporization will take place at the throat[1]. When this happens, the fluid sound speed lowers drastically; but continuity considerations dictate that the velocity, v_t, of the two-phase mixture (at the point of minuscule void fraction) just equals the velocity of the subcooled water slightly upstream of the throat. When this occurs, v_t in the subcooled region is less than the water sound speed, a_{liq}; but in the two-phase region, v_t can be greater than the two-phase sound speed, a_{HE}. Hence, the subcooled water has a Mach number (M) < 1, whereas the two-phase mixture at the throat has $M > 1$. Under these conditions ($M > 1$ in the two-phase region), downstream pressure effects cannot be propagated upstream, so the flow is considered to be choked. In particular, the supersonic two-phase fluid at the throat must increase in velocity and the pressure must drop as it expands in the diverging section[2]. We should be careful to note, however, that transition back to subsonic flow can occur in the nozzle as a result of a shock wave. This choked condition is shown in Figure 7-1, along with the corresponding sound speed and velocity profiles. Contrary to the usual single-phase choked flow in a converging/diverging nozzle, there is no point in the flow field where $M = 1$. This is because in the homogeneous equilibrium model the fluid undergoes a discontinuous change in sound speed from single-phase subcooled conditions to two-phase conditions, although the fluid properties are continuous through the transition point.

The liquid velocity at the throat can be calculated from Bernoulli's equation, assuming steady, frictionless, incompressible flow, such that

$$V_t = \left[V_{up}^2 + \frac{2(p_{up} - p_t)}{\rho_l} \right]^{\frac{1}{2}}, \tag{7-1}$$

where the subscript t refers to values at the throat and the subscript up refers to the upstream values. The throat pressure, p_t, is equal to the nucleation pressure, p_{nuc}, and can be considerably lower than the local saturation pressure, p_{sat}, because thermal nonequilibrium effects can cause nucleation delay.

Any further reduction in the downstream pressure does not affect the flow because the disturbance cannot move upstream where the flow is supersonic in the diverging section. Thus, Eq. (7-1) gives the liquid throat velocity for any downstream pressure lower than the pressure necessary to cause the subcooled liquid to begin flashing at the throat (which is the case for most problems of interest in LWR applications).

1. For all practical cases of choking, the subcooled water can be considered incompressible with infinite sound speed.

1. An idealized one-dimensional homogeneous equilibrium model is assumed.
2. In a supersonic flow, a diverging nozzle implies an increase in velocity.

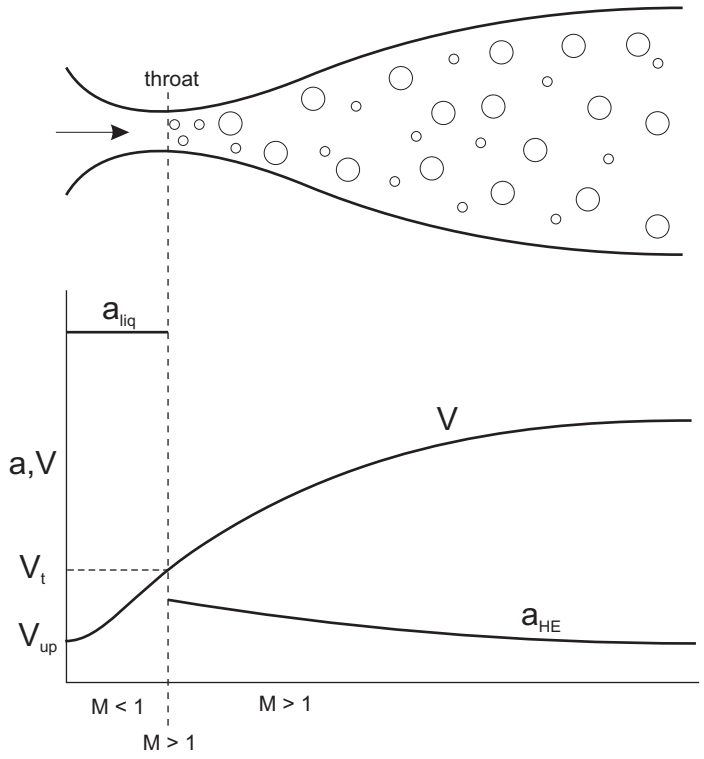

Figure. 7-1. Subcooled choking process when nucleation begins at the throat.

Now, consider the situation in which the subcooled choked flow, as described above, exists initially (with a very low downstream pressure), and the upstream pressure is lowered. As the upstream pressure, p_{up}, decreases, the pressure at the throat remains equal to p_{nuc}, and Bernoulli's equation (Eq. (7-1)) will give a smaller subcooled liquid velocity, V_t, at the throat. As the upstream pressure is lowered further, a point will be reached at which the liquid throat velocity is just equal to the two-phase homogeneous equilibrium sound speed, that is,

$$V_t = a_{HE} \tag{7-2}$$

and $M = 1$ on the two-phase side of the throat (the Mach number in the subcooled portion upstream of the throat is much less than 1).

As the upstream pressure is lowered further, the point where $p = p_{nuc}$ must move upstream. The subcooled liquid velocity at the p_{nuc} location is smaller that the two-phase sound speed, so the flow will be subsonic. In the two-phase region between the point at which p_{nuc} is reached and the throat, the Mach number is less than 1, but increases to $M = 1$ at the throat; that is, the two-phase sonic velocity, $V_t = a_{HE}$, is reached at the throat (as in the case of choked flow having a

continuous variation of sound speed with pressure). As the upstream pressure is reduced even further, the p_{nuc} point moves upstream until complete two-phase flow exists. Therefore, the maximum of the Burnell expression and the homogeneous equilibrium sound speed give the subcooled choking criterion. Thus,

$$V_t = Max\left\{ a_{HE} , \left[V_{up}^2 + \frac{2(p_{up} - p_t)}{\rho_l} \right]^{\frac{1}{2}} \right\} . \tag{7-3}$$

In TRACE, a nucleation delay model, developed by Alamgir and Leinhard (Ref. 7-4) and improved upon by Jones (Ref. 7-5) and Abuaf (Ref. 7-6), determines the cell-edge pressure, p_t, from the saturation pressure, p_{sat} (corresponding to the upstream liquid temperature, T_l), such that

$$p_t = p_{nuc} = p_{sat} - Max\left[0.0 , 0.258 \frac{\sigma^{1.5}\left(\frac{T_l}{T_c}\right)^{13.76} \sqrt{1 + 13.25\left(-\frac{1}{1.01325\times10^{11}} \frac{Dp}{Dt} \right)^{0.8}}}{(kT_c)^{0.5}\left(1 - \frac{\rho_g}{\rho_l}\right)} \right.$$

$$\left. -27(0.072)^2 \left(\frac{A_t}{A_{up}}\right)^2 \frac{\rho_l V_t^2}{2} \right] \tag{7-4}$$

where σ is the surface tension, T_l is the upstream liquid temperature, T_c is the critical temperature, Dp/Dt is the substantial derivative of the pressure, k is the Boltzmann constant, ρ_l and ρ_g are cell-edge phasic densities, V_t is the throat (cell-edge) velocity, and A_t and A_{up} are throat and upstream (nozzle inlet) flow areas.

Equations (7-3) and (7-4) form a set of coupled equations that, through iteration, can be solved to determine the throat velocity that will result when the flow is choked. By comparing the velocity, as calculated by the momentum solution, against this predicted choke velocity, TRACE is able to determine whether, in fact, choked flow has occurred and thereby take the necessary steps to account for this in the time solution procedure. The calculational sequence for the TRACE subcooled-liquid choking model is described in **Appendix C**.

Two-Phase, Two-Component Fluid

The two-phase, two-component, choked-flow model was developed from first principles using the characteristic analysis approach. The TRACE model is an extension of a model developed by Ransom and Trapp (Ref. 7-7) that incorporates an additional inert-gas component and nonequilibrium effects. As suggested by Ransom and Trapp, we assume that thermal equilibrium exists between the phases. The validity of this assumption has not been investigated in the presence of an inert gas. This assumption, however, is not an inherent feature of the TRACE model and can be changed easily, if necessary.

The two-fluid field under thermal equilibrium is described by the overall continuity equation, two-phasic momentum equations, the mixture energy equation, and the inert-gas continuity equation. When the nondifferential source terms are omitted (because they do not enter into characteristic analysis), the equations are

$$\frac{\partial \rho_m}{\partial t} + \frac{\partial}{\partial x}(\rho_m V_m) = 0 \tag{7-5}$$

$$\alpha\rho_g\left[\frac{\partial V_g}{\partial t} + V_g\frac{\partial V_g}{\partial x}\right] + \alpha\frac{\partial p}{\partial x} + C\alpha(1-\alpha)\rho_m\left[\frac{\partial V_g}{\partial t} + V_l\frac{\partial V_g}{\partial x} - \frac{\partial V_l}{\partial t} - V_g\frac{\partial V_l}{\partial x}\right] = 0 \tag{7-6}$$

$$(1-\alpha)\rho_l\left[\frac{\partial V_l}{\partial t} + V_l\frac{\partial V_l}{\partial x}\right] + (1-\alpha)\frac{\partial p}{\partial x} + C\alpha(1-\alpha)\rho_m\left[\frac{\partial V_l}{\partial t} + V_g\frac{\partial V_l}{\partial x} - \frac{\partial V_g}{\partial t} - V_l\frac{\partial V_g}{\partial x}\right] = 0 \tag{7-7}$$

$$\frac{\partial}{\partial t}(\rho_m s_m) + \frac{\partial}{\partial x}[\alpha\rho_g V_g s_g + (1-\alpha)\rho_l V_l s_l] = 0 \tag{7-8}$$

and

$$\frac{\partial}{\partial t}(\alpha\rho_a) + \frac{\partial}{\partial x}(\alpha\rho_a V_g) = 0 \tag{7-9}$$

where C is the virtual mass coefficient; s is the entropy; and subscripts a, g, l, and m refer to the noncondensable gas, steam/gas mixture, liquid, and total mixture, respectively. The last terms in Eqs. (7-6) and (7-7) represent interphasic force terms caused by relative acceleration. These terms are discussed in detail in References 7-2 and 7-7. Following Ransom and Trapp's formulation, the energy equation is written in the form of the mixture-specific entropy that is conserved for adiabatic flow (with the irreversibilities associated with interphasic mass transfer

and relative phase acceleration neglected). No basic difficulty in the analysis is experienced, however, if the mixture energy equation is written in terms of the internal energy or enthalpy.

In the thermal-equilibrium case, ρ_v, ρ_l, s_g, s_l, and ρ_a are known functions of p_a and p_v. If we assume that Dalton's law of partial pressures applies, Eqs. (7-5) through (7-9) can be written in terms of the five unknowns p_v, α, V_g, V_l, and p_a. The matrix representation of these equations is of the form

$$A(\overline{U})\frac{\partial \overline{U}}{\partial t} + B(\overline{U})\frac{\partial \overline{U}}{\partial x} = 0 \tag{7-10}$$

where the $\overline{U}$ consists of p_v, α, V_g, V_l, and p_a.

An example of one of the equations in the system given by Eq. (7-10) is the mixture or overall continuity equation, Eq. (7-5). We will provide here the details of the derivation of that equation, then merely list the other equations. Under equilibrium, we know that

$$\begin{aligned} T_l &= T_g = T, \\ \rho_a &= f(p_a, T), \\ \rho_v &= f(p_v), \text{ and} \\ \rho_l &= f(p, T) \end{aligned} \tag{7-11}$$

which results in

$$\begin{aligned} d\rho_a &= \left(\frac{\partial \rho_a}{\partial p_a}\right)_T dp_a + \left(\frac{\partial \rho_a}{\partial T}\right)_{p_a} dT \\ &= \left(\frac{\partial \rho_a}{\partial p_a}\right)_T dp_a + \left(\frac{\partial \rho_a}{\partial T}\right)_{p_a} \frac{dT}{dp_v} dp_v \end{aligned} \tag{7-12}$$

$$\begin{aligned} d\rho_l &= \left(\frac{\partial \rho_l}{\partial p}\right)_T dp + \left(\frac{\partial \rho_l}{\partial T}\right)_p dT \\ &= \left(\frac{\partial \rho_l}{\partial p}\right)_T (dp_a + dp_v) + \left(\frac{\partial \rho_l}{\partial T}\right)_p \frac{dT}{dp_v} dp_v \\ &= \left(\frac{\partial \rho_l}{\partial p}\right)_T dp_a + \left[\left(\frac{\partial \rho_l}{\partial p}\right)_T + \left(\frac{\partial \rho_l}{\partial T}\right)_p \frac{dT}{dp_v}\right] dp_v \\ &\approx \left(\frac{\partial \rho_l}{\partial p}\right)_T dp_a + \rho_l^* dp_v \end{aligned} \tag{7-13}$$

$$d\rho_v = \left(\frac{\partial \rho_v}{\partial p_v}\right)_T dp_v + \left(\frac{\partial \rho_v}{\partial T}\right)_{p_v} dT \tag{7-14}$$
$$= \left(\frac{\partial \rho_v}{\partial p_v}\right)_T dp_v + \left(\frac{\partial \rho_v}{\partial T}\right)_{p_v} \frac{dT}{dp_v} dp_v$$
$$\approx \rho_v^* dp_v$$

Expanding the differential terms of Eq. (7-5), we get

$$d\rho_m = \alpha\, d\rho_a + \alpha\, d\rho_v + \rho_g d\alpha + (1-\alpha)\, d\rho_l - \rho_l d\alpha \tag{7-15}$$

and

$$d(\rho_m V_m) = \alpha \rho_g d V_g + \alpha\, V_g (d\rho_a + d\rho_v) + \rho_g V_g d\alpha \tag{7-16}$$
$$+ (1-\alpha)\rho_l d V_l + (1-\alpha)\, V_l d\rho_l - \rho_l V_l d\alpha$$

Using the relationships derived above and rearranging terms, Eq. (7-5) can be written as

$$\left\{\alpha\left[\left(\frac{\partial \rho_a}{\partial T}\right)_{p_a} \frac{dT}{dp_v} + \rho_v^*\right] + (1-\alpha)\rho_l^*\right\}\frac{\partial p_v}{\partial t} + (\rho_g - \rho_l)\frac{\partial \alpha}{\partial t} \tag{7-17}$$
$$+ 0 \cdot \frac{\partial V_g}{\partial t} + 0 \cdot \frac{\partial V_l}{\partial t} + \left[\alpha\left(\frac{\partial \rho_a}{\partial p}\right)_T + (1-\alpha)\left(\frac{\partial \rho_l}{\partial p}\right)_T\right]\frac{\partial p_a}{\partial t}$$
$$+ \left\{ V_g \alpha\left[\left(\frac{\partial \rho_a}{\partial T}\right)_{p_a} \frac{dT}{dp_v} + \rho_v^*\right] + V_l(1-\alpha)\rho_v^*\right\}\frac{\partial p_v}{\partial x} + (\rho_g V_g - \rho_l V_l)\frac{\partial \alpha}{\partial x}$$
$$+ \alpha \rho_g \frac{\partial V_g}{\partial x} + (1-\alpha)\rho_l \frac{\partial V_l}{\partial x} + \left[V_g \alpha\left(\frac{\partial \rho_a}{\partial p}\right)_T + V_l(1-\alpha)\left(\frac{\partial \rho_l}{\partial p}\right)_T\right]\frac{\partial p_a}{\partial x}$$

$$= 0$$

The complete matrices for the system are provided in Equations (7-18) through (7-38) ,

$$\underline{\underline{A}} = \begin{bmatrix} A_{1,1} & \rho_g - \rho_l & 0 & 0 & A_{1,5} \\ 0 & 0 & A_{2,3} & -C\alpha(1-\alpha)\rho_m & 0 \\ 0 & 0 & -C\alpha(1-\alpha)\rho_m & A_{3,4} & 0 \\ A_{4,1} & \rho_g s_g - \rho_l s_l & 0 & 0 & A_{4,5} \\ \alpha\left(\frac{\partial \rho_a}{\partial T}\right)_{p_a} \frac{dT}{dp_v} & \rho_a & 0 & 0 & \alpha\left(\frac{\partial \rho_a}{\partial p_a}\right)_T \end{bmatrix} \begin{bmatrix} \frac{\partial p_v}{\partial t} \\ \frac{\partial \alpha}{\partial t} \\ \frac{\partial V_g}{\partial t} \\ \frac{\partial V_l}{\partial t} \\ \frac{\partial p_g}{\partial t} \end{bmatrix} \tag{7-18}$$

where

$$A_{1,1} = \alpha\left[\left(\frac{\partial \rho_a}{\partial T}\right)_{p_a} \frac{dT}{dp_v} + \rho_v^*\right] + (1-\alpha)\rho_l^* \tag{7-19}$$

$$A_{1,5} = \alpha\left(\frac{\partial \rho_a}{\partial p}\right)_T + (1-\alpha)\left(\frac{\partial \rho_l}{\partial p}\right)_T \tag{7-20}$$

$$A_{2,3} = \alpha\rho_g + C\alpha(1-\alpha)\rho_m \tag{7-21}$$

$$A_{3,4} = (1-\alpha)\rho_l + C\alpha(1-\alpha)\rho_m \tag{7-22}$$

$$A_{4,1} = \alpha\left[-\rho_v s_v^* + s_v \rho_v^* + \frac{dT}{dp_v}\left(\rho_a\left(\frac{\partial s_a}{\partial T}\right)_{p_a} + s_a\left(\frac{\partial \rho_a}{\partial T}\right)_{p_a}\right)\right] + (1-\alpha)[\rho_l s_l^* + s_l \rho_l^*] \tag{7-23}$$

$$A_{4,5} = \alpha\left[\rho_a\left(\frac{\partial s_a}{\partial p_a}\right)_T + s_a\left(\frac{\partial \rho_a}{\partial p_a}\right)_T\right] + (1-\alpha)\left[\rho_l\left(\frac{\partial s_l}{\partial p}\right)_T + s_l\left(\frac{\partial \rho_l}{\partial p}\right)_T\right] \tag{7-24}$$

and

$$\underline{\underline{B}} = \begin{bmatrix} B_{1,1} & B_{1,2} & \alpha\rho_g & (1-\alpha)\rho_l & B_{1,5} \\ \alpha & 0 & B_{2,3} & -V_g C\alpha(1-\alpha)\rho_m & \alpha \\ (1-\alpha) & 0 & -V_l C\alpha(1-\alpha)\rho_m & B_{3,4} & (1-\alpha) \\ B_{4,1} & B_{4,2} & \alpha\rho_g s_g & (1-\alpha)\rho_l s_l & B_{4,5} \\ B_{5,1} & V_g\rho_a & \alpha\rho_a & 0 & V_g\alpha\left(\frac{\partial\rho_a}{\partial p_a}\right)_T \end{bmatrix} \begin{bmatrix} \frac{\partial p_v}{\partial x} \\ \frac{\partial\alpha}{\partial x} \\ \frac{\partial V_g}{\partial x} \\ \frac{\partial V_l}{\partial x} \\ \frac{\partial p_g}{\partial x} \end{bmatrix} \tag{7-25}$$

where

$$B_{1,1} = V_g\left[\left(\frac{\partial\rho_a}{\partial T}\right)_{p_a}\frac{dT}{dp_v} + \rho_v^*\right] + V_l(1-\alpha)\rho_l^* \tag{7-26}$$

$$B_{1,2} = \rho_g V_g - \rho_l V_l \tag{7-27}$$

$$B_{1,5} = V_g\alpha\left(\frac{\partial\rho_a}{\partial p_a}\right)_T + V_l(1-\alpha)\left(\frac{\partial\rho_l}{\partial p}\right)_T \tag{7-28}$$

$$B_{2,3} = V_g\alpha\rho_g + V_l C\alpha(1-\alpha)\rho_m \tag{7-29}$$

$$B_{3,4} = V_g C\alpha(1-\alpha)\rho_m + V_l(1-\alpha)\rho_l \tag{7-30}$$

$$B_{4,1} = V_g\alpha\left[-\rho_v s_v^* + s_v\rho_v^* + \frac{dT}{dp_v}\left(\rho_a\left(\frac{\partial s_a}{\partial T}\right)_{p_a} + s_a\left(\frac{\partial\rho_a}{\partial T}\right)_{p_a}\right)\right] + V_l(1-\alpha)[\rho_l s_l^* + s_l\rho_l^*] \tag{7-31}$$

$$B_{4,2} = V_g\rho_g s_g - V_l\rho_l s_l \tag{7-32}$$

$$B_{4,5} = V_g \alpha \left[\rho_a \left(\frac{\partial s_a}{\partial p_a} \right)_T + s_a \left(\frac{\partial \rho_a}{\partial p_a} \right)_T \right] + V_l (1-\alpha) \left[\rho_l \left(\frac{\partial s_l}{\partial p} \right)_T + s_l \left(\frac{\partial \rho_l}{\partial p} \right)_T \right] \tag{7-33}$$

$$B_{5,1} = V_g \alpha \left(\frac{\partial \rho_a}{\partial T} \right)_{p_a} \frac{dT}{dp_v} \tag{7-34}$$

The starred terms are given by the following relationships

$$\rho_v^* = \left(\frac{\partial \rho_v}{\partial p_v} \right)_T + \left(\frac{\partial \rho_v}{\partial T} \right)_{p_v} \frac{dT}{dp_v} \tag{7-35}$$

$$s_v^* = \frac{1}{T} \left[\left(\frac{\partial e_v}{\partial p_v} \right)_T + \left(\frac{\partial e_v}{\partial T} \right)_{p_v} \frac{dT}{dp_v} \right] - \frac{p_v}{p_v^2 T} \left[\left(\frac{\partial \rho_v}{\partial p_v} \right)_T + \left(\frac{\partial \rho_v}{\partial T} \right)_{p_v} \frac{dT}{dp_v} \right] \tag{7-36}$$

and

$$\rho_v^* = \left(\frac{\partial \rho_l}{\partial p} \right)_T + \left(\frac{\partial \rho_l}{\partial T} \right)_p \frac{dT}{dp_v} \tag{7-37}$$

$$s_l^* = \frac{1}{T} \left[\left(\frac{\partial e_l}{\partial p} \right)_T + \left(\frac{\partial e_l}{\partial T} \right)_p \frac{dT}{dp_v} \right] - \frac{p}{\rho_l^2 T} \left[\left(\frac{\partial \rho_l}{\partial p} \right)_T + \left(\frac{\partial \rho_l}{\partial T} \right)_p \frac{dT}{dp_v} \right] . \tag{7-38}$$

With p, p_a, and T known, all of the thermodynamic partial derivatives used in the above equations are obtained by a call to the equation of state package.

The characteristic roots, λ_i, of the above system of equations are defined as the roots of the fifth-order polynomial,

$$\text{determinant } (\underline{\underline{A}} \lambda - \underline{\underline{B}}) = 0 . \tag{7-39}$$

Choking occurs when the signal propagating with the largest velocity relative to the fluid is stationary; that is, the maximum value of the real part of a characteristic root, $\lambda_{i,re,max}$, is zero.

Eq. (7-39) is extremely difficult to solve analytically. Thus, TRACE obtains the characteristic roots of Eq. (7-39) numerically. This method advantageously maintains generality and facilitates computations under different assumptions. The calculational sequence for the TRACE two-phase choking model is described in **Appendix C**.

Single-Phase Vapor

The single-phase vapor choked-flow model is based on isentropic expansion of an ideal gas (see Reference 7-8). A throat pressure, p_e, is calculated from the stagnation pressure, p_o, such that

$$p_e = p_o\left(\frac{2}{\gamma+1}\right)^{\gamma/\gamma-1} \tag{7-40}$$

where γ is the specific-heat ratio. A downstream throat temperature, T_e, is calculated from the stagnation temperature, T_o, using the ideal-gas relation

$$T_e = T_o\left(\frac{2}{\gamma+1}\right) \tag{7-41}$$

When T_e is greater than the saturation temperature at p_e, the fluid flow at the throat is predicted to be superheated by the ideal-gas relations. The continuity equation, in conjunction with the ideal-gas relations, yields a fluid choking velocity,

$$V_{ge} = \sqrt{\frac{2\gamma}{\gamma+1} R T_o} \tag{7-42}$$

where R is the gas constant.

If T_e is less than or equal to the saturation temperature at p_e, then the fluid flow at the throat is not predicted to be superheated by the ideal-gas relations, and the choking velocity is calculated using iterations to maximize mass flux along the isentrope that extends from the superheated conditions upstream of the throat to the two-phase conditions at the throat. This method assumes that no delay in condensation occurs as the steam expands to the saturated two-phase state at the throat.

The calculational sequence for the TRACE single-phase vapor choking model is described in **Appendix C**.

Transition Regions

Because there is a discontinuity in the sound speed during the transition from liquid to two-phase flow, the flow during this transition regime must be analyzed carefully. In TRACE, this transition is handled by linear interpolation between the subcooled ($\alpha \leq 1.0\times10^{-8}$) and the two-phase ($\alpha \geq 1.0\times10^{-5}$) regimes. The basis for these limits is somewhat arbitrary and comes from numerical experimentation designed to identify the values that allow the model to perform most

robustly. The calculational sequence for the TRACE transition region is described in **Appendix C**.

The transition from the two-phase to the vapor-phase regime is smooth because the two-phase characteristic solution approaches the homogeneous equilibrium limit as $\alpha \rightarrow 1$. Thus, this transition is made by switching the calculational logic at $\alpha = 0.999$.

Cell-Center Momentum-Solution Velocities

The velocities obtained from the momentum solution are cell-edge values. However, in order to evaluate stagnation conditions, it is necessary to know the phasic velocities at the cell center. This transition between cell edge and cell center is accomplished by averaging the mass flux between cell edges, such that

$$V_{gc} = \frac{\frac{1}{2}[(\rho_g \alpha)_{e^-} V_{g,e^-} A_{e^-} + (\rho_g \alpha)_{e^+} V_{g,e^+} A_{e^+}]}{\rho_{gc} \alpha_c A_c} \tag{7-43}$$

and

$$V_{lc} = \frac{\frac{1}{2}[(\rho_l (1-\alpha))_{e^-} V_{l,e^-} A_{e^-} + (\rho_l (1-\alpha))_{e^+} V_{l,e^+} A_{e^+}]}{\rho_{lc} (1-\alpha)_c A_c}\ , \tag{7-44}$$

where V_{gc} and V_{lc} are the transformed cell-center velocities, ρ_g and ρ_l are the steam/gas-mixture and liquid densities, α is the void fraction, V_l and V_g are the liquid and steam/gas-mixture velocities, and A is the cross-sectional flow area. The subscripts e^- and e^+ refer to upstream cell-edge and downstream cell-edge quantities, while the subscript c refers to cell-center quantities for the particular cell in question. It is assumed that $\rho\alpha$ at the upstream face is equal to the upstream cell product value, whereas $\rho\alpha$ at the downstream face is taken to be equal to the current cell value because densities and void fractions are normally associated with cell-center rather than with cell-edge positions.

New-Time Choking Velocities.

New-time phasic choking velocities are computed by time-averaging the old-time velocities with the predicted choking velocities, such that

$$V_l^{n+1} = 0.1\, V_{le}^{p} + 0.9\, V_l^{n} \tag{7-45}$$

and

$$V_g^{n+1} = 0.1\, V_{ge}^{p} + 0.9\, V_g^{n} \ , \tag{7-46}$$

where V_{le}^{p} and V_{ge}^{p} are the predicted liquid and steam/gas-mixture choking velocities, and V_l^n and V_g^n are the old-time liquid and steam/gas-mixture velocities (either momentum solution or choking). This old-time, new-time method of weighting limits the change in the choking velocity for either phase to only 10% of the actual calculated change and ensures that the choking model lags slightly behind any pressure transients so that the effects of unnatural pressure changes caused by fluid inertia are limited.

Determining the Sound Speed

The evaluation of Eqs. (7-3) and (7-4) in the subcooled-liquid choking model and the solution of Eq. (7-39) in the two-phase, two-component choking model require that conditions at the cell-edge where the choking criterion is applied be known. The homogeneous equilibrium sound speed and an estimate of the corresponding cell-edge conditions are determined, given the conditions at cell center. Three basic calculational sequences are used:

1) If the cell contains pure noncondensable gas, the homogeneous equilibrium sound speed and corresponding cell-edge conditions are computed by assuming an isentropic expansion of an ideal gas.

2) If the cell length-to-hydraulic-diameter ratio, L/D, is greater than or equal to 1.5, or if some noncondensable gas is present in the vapor phase of a two-phase flow at cell center (regardless of the value of L/D), then the conditions at cell center are required to come to equilibrium by means of an isenthalpic process before stagnation conditions are calculated. Once the stagnation conditions have been determined, a homogeneous equilibrium sound speed and the corresponding cell-edge conditions are calculated by first assuming thermal equilibrium and no slip at the cell edge and an isentropic expansion from stagnation to cell edge. We then iterate for the cell-edge pressure, which results in the maximum or critical mass flux at the cell edge (a classical technique used in generating the HEM tables).

3) If the cell length-to-hydraulic-diameter ratio, L/D, is less than 1.5, or if only the superheated vapor phase or the subcooled-liquid phase exists at the cell center, then the stagnation conditions are calculated from the actual cell-center properties, rather than from the effective equilibrium properties as in (2). Once stagnation conditions have been determined, a homogeneous equilibrium sound speed and the corresponding cell-edge conditions are determined either by assuming an isentropic expansion of an ideal gas (for the case of superheated vapor phase at the cell edge) or by iterating for the cell-edge pressure, which gives the maximum mass flux as in (2) above.

The details concerning these models are discussed in **Appendix C**.

Countercurrent Flow

Countercurrent flow and CCFL can occur at any location in the reactor system. For instance, in the case of a reflux-condensation transient associated with a small-break LOCA, countercurrent flow is predicted to exist in the hot leg and in the entrance to the steam-generator inlet plenum. In the reactor vessel, CCFL can occur during blowdown as ECC liquid is attempting to fill the downcomer. During reflood, CCFL can occur at the tie plate, where the upflow of steam prevents or limits the fallback of liquid. This is especially important for those systems that employ upper-plenum ECC injection.

Excluding mass transfer, the accurate prediction of the flow rates is dependent primarily on the interfacial drag between the phases (which is itself dependent on the accurate prediction of the flow regime). In a given flow system, CCFL usually occurs at a flow-area restriction. Typically, without the use of the CCFL model, TRACE will predict the complete turnaround point (zero liquid delivery), but overpredict the amount of liquid downflow in the region of countercurrent flow. To improve the prediction in the countercurrent region, a special model exists in TRACE that allows you to invoke characteristic CCFL correlations at specific locations in the 3D VESSEL component (in the axial direction) or in 1D vertical components.

CCFL in the 3D VESSEL

The CCFL model has been designed primarily for use in the tie-plate region of a PWR. The mechanism for countercurrent flow at this location is very complex. For instance, in a single-bundle experiment, it has been observed that downflow can exist at the periphery of the plate, whereas upflow may occur in the center region. On the average over time, this behavior can be described by a CCFL (or flooding) correlation. CCFL correlations typically provide a superficial mass flux of liquid downflow versus a superficial mass flux of gas upflow. The correlations are developed from the integral over time of the amount of liquid accumulation below the plate for a given gas-injection rate. The correlation therefore provides a 1D empirical model of the time-averaged multidimensional countercurrent-flow behavior. These correlations are geometry-dependent. For tie plates, the plate thickness, hole diameter (or slot dimensions), number of holes, as well as the type of hardware above and below the tie plate can affect the CCFL characteristics. Rather than try to develop a new mechanistic CCFL model that could predict these complex behaviors in a variety of geometrical configurations, we decided to make use of the vast amount of correlated data already available. Therefore, the TRACE CCFL model provides you with the option to implement a CCFL correlation for the specific geometry available and to apply it at specific locations in the VESSEL component. The input has been generalized so that Wallis (Ref. 7-9), Kutateladze (Ref. 7-10), or Bankoff (Ref. 7-11) scaling can be accommodated.

The main point of the CCFL model is that the user supplies the correlation to be used at a specific location. Thus, the database is dependent on user input because the correlation constants are determined either from experimental data or from estimates based on physical dimensions. If the user provides a correlation that represents data that are similar to the cell dimensions in geometry and scale, then the code should adequately predict countercurrent flow. Also, CCFL correlations

normally scale with pressure because the form of the equations includes the effect of the change in density.

The Model

The TRACE CCFL model is designed to provide you with an alternative method for calculating countercurrent flow in geometrically complex reactor hardware. It allows you to input the characteristic flooding curve parameters for a specific geometry applied at a particular location in the vessel. Typically, these parameters have been developed from experimental data for the geometry of interest or for hardware of at least similar dimensions. Bankoff (Ref. 7-11) has shown that the data correlate well with the relationship

$$H_g^{1/2} + M_B H_l^{1/2} = C_B \ , \tag{7-47}$$

where H_g is the dimensionless gas flux, H_l is the dimensionless liquid delivery, C_B is the abscissa intercept, and M_B is the slope.

This relationship is used in the CCFL model because it allows the user to implement either the Wallis scaling (diameter dependence), Kutateladze scaling (surface-tension dependence), or a combination of the two. This is done by defining a variable-length scale in the determination of the dimensionless flux, as follows:

$$H_k = j_k \left(\frac{\rho_k}{g w \Delta\rho} \right)^{1/2} \ , \tag{7-48}$$

$$w = D^{1-\overline{E}} L^{\overline{E}} \ , \tag{7-49}$$

and

$$L = \left(\frac{\sigma}{g \Delta\rho} \right)^{1/2} \ , \tag{7-50}$$

where k refers to the phase (gas or liquid), j is the superficial velocity, D is the diameter of the holes, g is the gravitational constant, σ is the surface tension, ρ is the density, $\Delta\rho$ is the difference between the phasic densities, and $\overline{E}$ is an interpolation constant between 0 and 1.

Note that for $\overline{E}$ = 0, the correlation reverts to the Wallis scaling, and for $\overline{E}$ = 1, it reverts to the Kutateladze scaling. For $\overline{E}$ between 0 and 1, the user can input the scaling proposed by Bankoff.

This scaling can be calculated for tie-plate geometry, even if no experimental data are available, based on the critical wave number (Ref. 7-11),

$$k_c = \frac{2\pi}{t_p} \ , \tag{7-51}$$

so that

$$\overline{E} = \tanh(\eta k_c D) \ , \tag{7-52}$$

where η is the ratio of the area of the holes to the area of the tie plate and t_p is the thickness of the tie plate. Also, Bankoff developed a correlation for C_B based on the Bond number:

$$L^* = n\pi D(g\Delta\rho/\sigma)^{1/2}, \tag{7-53}$$

such that

$$C_B = \begin{cases} 1.07 + 4.33 \times 10^{-3} L^* & \text{, for } L^* \leq 200 \\ 1.94 & \text{, for } L^* > 200 \end{cases} \tag{7-54}$$

where n is the number of holes in the tie plate.

Input Scheme

The user supplies the correlation constants M_B, E, and C_B, and the location where the CCFL model is to be applied. Alternatively, the values of C_B and E can be calculated by the code from thermodynamic properties and the input of n, t_p, h, and D. The void fraction in the cell below the interface is used to calculate the vapor flux. The void fraction in the cell above the interface is used to calculate the liquid flux. The surface tension, liquid density, and vapor density in the cell below the interface are used in the CCFL model.

Level Tracking

Note – The discussion that follows has been pulled, almost entirely verbatim, from the Ph.D. thesis of Birol Aktas (Ref. 7-24), which was partially funded by NRC. We have taken the liberty to eliminate and/or re-order the presentation of certain concepts so as to fit within the scope and framework of a code theory manual. Where necessary, we also made slight modifications to eliminate typos, improve formatting, fix grammatical issues, change usage of 'TRAC' to 'TRACE', etc.

The presence of water levels can severely plague the standard methods of solution to the six-equation model. The use of an average void fraction for a computational volume can lead to an erroneous description of a computational volume when it contains a water level. A short analysis of the initial TRACE simulations of these tests reached a conclusion that such computational volumes indeed had two sub-volumes separated by the interface and each of these sub-volumes had their own distinct flow topology, e.g. the dispersed liquid droplets above the interface and the gas bubbles below. Further conclusion was drawn that for more accurate description of these divided computational volumes, regions above and below the interface ought to be treated separately requiring the use of separate void fractions inside each region as the outcome of closure models strongly depended on the flow regime and the flow regimes were strong functions of the "cell" void fraction.

Not only the void fractions must be known for the regions above and below the interface but also the volumes of each region and the rate at which they change. Only when this additional information is known, one can modify a standard method of solution for the six-equation model such as Semi-Implicit or SETS to accomplish a more accurate description of computational volumes with water levels inside them. This strategy of "tracking" to deal with water levels requires that the location of a water level, the volumes of regions above and below it, and the void fractions inside these regions be known at all times.

The idea of tracking water levels is not new. An example is the method which had been developed for the BWR version of TRAC to track water levels in BWR simulations. This method in TRAC-BWR, which had been applied to the transient simulations of BWRs with some limited success, permitted the use of very large volumes in building computational models of BWR pressure vessels. .

The level tracking method of TRAC-BWR, and of TRACE, consists of two parts: 1) a decision making step to locate and follow the water levels, and 2) modifications to the field equations and closure models to account for the presence of a water level. The presentation in this section is organized around these two parts. First, the method of locating the water levels is presented. Modifications to the field equations and the evaluation of closure models then follow. However, there is a third component necessary for a successful level tracking method, mostly overlooked in the past. This third component is a systematic approach to propagate the water levels across the cell boundaries. The discussions in the following sections present the ideas and approaches critical to a robust method of level tracking. An overview of the first and second components of level tracking will be discussed for 1D components to illustrate the level tracking modifications.

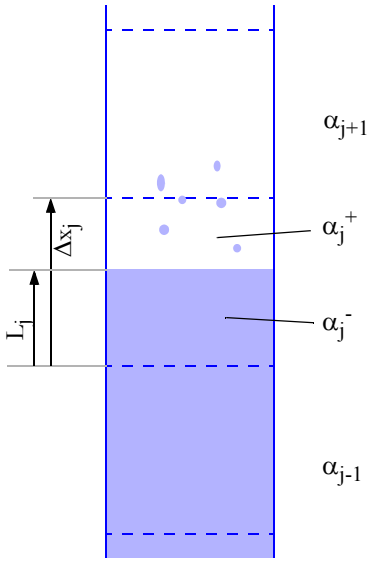

Figure. 7-2. A computational volume with the stratified liquid-gas interface

A detailed discussion of both 1D and 3D level tracking and details of modifications for the field equations, closure model evaluation, and levels crossing cell boundaries will be contained in an Appendix of the manual that will be added in the future.

Level Tracking Method

The search for liquid-gas interfaces is conducted using a series of logical decisions that are based on empirical observations. Once it is determined that an interface exists inside a computational volume, its location inside the volume and its velocity are computed along with the separated sub-volumes. A computational volume that consists of a liquid-gas interface is shown in Figure 7-2. A void fraction profile decreasing with increasing height shown in this figure is the simplest case where a stratified interface must satisfy either of the following conditions:

$$(\alpha_j - \alpha_{j\text{-}1} > \delta\alpha) \wedge (\alpha_{j+1} - \alpha_j > \Delta\alpha_{\text{cut}}) \wedge (\alpha_{j+1} > \alpha_{\text{lev}}) \tag{7-55}$$

$$(\alpha_j - \alpha_{j\text{-}1} > \Delta\alpha_{\text{cut}}) \wedge (\alpha_{j+1} - \alpha_j > \delta\alpha) \wedge (\alpha_{j+1} > \alpha_{\text{lev}}) \tag{7-56}$$

The recommended values for $\Delta\alpha_{\text{cut}}$, $\delta\alpha$, and α_{lev} are 0.2, 0.005, and 0.7, respectively. There are other void fraction profiles, e.g. decreasing with increasing height, reversed void profile above and below obstructions, etc... which the liquid-gas interfaces must satisfy different conditions. The void fractions designated for the regions below and above an interface, and the volumes of these regions can then be correlated from the computational volume and its void fraction.

$$\mathrm{Vol}_j = \mathrm{Vol}_j^- + \mathrm{Vol}_j^+ \tag{7-57}$$

$$\mathrm{Vol}_j \alpha_j = \mathrm{Vol}_j^- \alpha_j^- + \mathrm{Vol}_j^+ \alpha_j^+ \tag{7-58}$$

Subvolumes can be evaluated from Eq. (7-57) and Eq. (7-58).

$$\mathrm{Vol}_j^- = \frac{\alpha_j^+ - \alpha_j}{\alpha_j^+ - \alpha_j^-} \mathrm{Vol}_j \tag{7-59}$$

In a computational volume with constant flow area, the location of the interface can be correlated from Eq. (7-59):

$$L_j = \frac{\alpha_j^+ - \alpha_j}{\alpha_j^+ - \alpha_j^-} \Delta x_j \tag{7-60}$$

Next, the velocity of the liquid-gas interface is formulated by taking the time derivative of Eq. (7-59) as follows:

$$V_{L,j} = \frac{\Delta x_j}{\alpha_j^+ - \alpha_j^-}\left[\frac{d\alpha_j^+}{dt} - \frac{d\alpha_j}{dt}\right] - \frac{L_j}{\alpha_j^+ - \alpha_j^-}\left[\frac{d\alpha_j^+}{dt} - \frac{d\alpha_j^-}{dt}\right] \tag{7-61}$$

$$V_{L,j}^{n+1} = \frac{\Delta x_j}{(\alpha_j^+)^{n+1} - (\alpha_j^-)^{n+1}}\left[\frac{(\alpha_j^+)^{n+1} - (\alpha_j^+)^n}{\Delta t} - \frac{\alpha_j^{n+1} - \alpha_j^n}{\Delta t}\right] - \frac{L_j}{(\alpha_j^+)^{n+1} - (\alpha_j^-)^{n+1}}\left[\frac{(\alpha_j^+)^{n+1} - (\alpha_j^+)^n}{\Delta t} - \frac{(\alpha_j^-)^{n+1} - (\alpha_j^-)^n}{\Delta t}\right] \tag{7-62}$$

In Eq. (7-61), the time derivative of void fractions are first-order approximations. Finally, the location of an interface at the end of a timestep can be projected from its location and velocity at the beginning of a timestep:

$$L_j^{n+1} = L_j^n + \Delta t \; V_{L,j}^{n+1} \tag{7-63}$$

When it is determined that a liquid-gas interface exists in a computational volume, an integer variable is set to one to flag its existence. Otherwise, the same variable is set to zero to flag that no interface is present.

$$\lambda_j = \begin{cases} 1 & \text{, for } 0 < L_j < \Delta x_j \\ 0 & \text{, otherwise} \end{cases} \tag{7-64}$$

Modifications To The Field Equations

Once it is determined that a liquid-gas interface is present in a computational cell, a new variable, λ_E, is defined to specify the distance between the liquid-gas interface and the cell boundaries. A second variable, α_E, is defined to specify the void fraction of the two-phase fluid convected across the boundaries between two adjacent volumes.

$$\lambda_{E,j+1/2} = \begin{cases} L_{j+1} & \text{, if } \lambda_{j+1} = 1 \\ L_j - \Delta x_j & \text{, if } \lambda_j = 1 \\ 0 & \text{, otherwise} \end{cases} \tag{7-65}$$

$$\alpha_{E,j\text{-}1/2} = \begin{cases} \alpha_j^- & \text{, if } \lambda_{E,j\text{-}1/2} > 0 \\ \alpha_{j\text{-}1}^+ & \text{, if } \lambda_{E,j\text{-}1/2} < 0 \\ \langle \alpha \rangle_{j\text{-}1/2} & \text{, if } \lambda_{E,j\text{-}1/2} = 0 \end{cases} \tag{7-66}$$

$$\alpha_{E,j+1/2} = \begin{cases} \alpha_{j+1}^- & \text{, if } \lambda_{E,j+1/2} > 0 \\ \alpha_j^+ & \text{, if } \lambda_{E,j+1/2} < 0 \\ \langle \alpha \rangle_{j+1/2} & \text{, if } \lambda_{E,j+1/2} = 0 \end{cases} \tag{7-67}$$

In the above equations, $\langle \alpha \rangle$ is the void fraction at a boundary defined as an average of void fractions computed for the cells adjacent to a boundary.

Mass and Energy Equations

When a liquid-gas interface is present in a computational cell, its presence must be accounted for by the terms that describe the flux of mass and energy across the cell boundaries. The flux terms

used in the regular solution schemes shown in Equations (1-101), (1-104), (1-105), and (1-106) use an average of properties from adjacent cells as an approximation for the state properties, which are defined and calculated at cell centers by definition, across the cell boundary. Once it is determined that a liquid-gas interface is present adjacent to a cell boundary, averaging of the properties at the boundary must account for the presence of the interface. Accounting for the presence of the interface is accomplished by redefining the flow area at the cell boundary in the following redefined flux terms:

$$\phi_{g,j+1/2} = \langle \alpha \rho_g \rangle^n_{j+1/2} A^{\alpha}_{g,j+1/2} V^{n+1}_{g,j+1/2} \tag{7-68}$$

$$\phi_{l,j+1/2} = \langle (1-\alpha) \rho_l \rangle^n_{j+1/2} A^{\alpha}_{l,j+1/2} V^{n+1}_{l,j+1/2} \tag{7-69}$$

$$\zeta_{g,j+1/2} = \langle \alpha \rho_g e_g \rangle^n_{j+1/2} A^{\alpha}_{g,j+1/2} V^{n+1}_{g,j+1/2} \tag{7-70}$$

$$\zeta_{l,j+1/2} = \langle (1-\alpha) \rho_l e_l \rangle^n_{j+1/2} A^{\alpha}_{l,j+1/2} V^{n+1}_{l,j+1/2} \tag{7-71}$$

$$\omega_{g,j+1/2} = \langle \alpha \rangle^n_{j+1/2} A^{\alpha}_{g,j+1/2} V^{n+1}_{g,j+1/2} \tag{7-72}$$

$$\omega_{l,j+1/2} = \langle 1-\alpha \rangle^n_{j+1/2} A^{\alpha}_{l,j+1/2} V^{n+1}_{l,j+1/2} \tag{7-73}$$

where the new definition of flow area in the gas and liquid terms, i.e. $A^{\alpha}_{g,j+1/2}$ and $A^{\alpha}_{l,j+1/2}$, accounts for the presence of an interface in either cell adjacent to the boundary:

$$A^{\alpha}_{g,j+1/2} = \begin{cases} A_{j+1/2} \dfrac{\alpha_{E,j+1/2}}{\alpha_j} & \text{, if } \left(\lambda_{E,j+1/2} < 0\right) \text{ and } \left(V_{g,j+1/2} > 0\right) \\ A_{j+1/2} \dfrac{\alpha_{E,j+1/2}}{\alpha_{j+1}} & \text{, if } \left(\lambda_{E,j+1/2} > 0\right) \text{ and } \left(V_{g,j+1/2} < 0\right) \\ A_{j+1/2} & \text{, otherwise} \end{cases} \tag{7-74}$$

$$A^{\alpha}_{l,j+1/2} = \begin{cases} A_{j+1/2}\dfrac{1-\alpha_{E,j+1/2}}{1-\alpha_j} & \text{, if } \left(\lambda_{E,j+1/2}<0\right) \text{ and } \left(V_{l,j+1/2}>0\right) \\ A_{j+1/2}\dfrac{1-\alpha_{E,j+1/2}}{1-\alpha_{j+1}} & \text{, if } \left(\lambda_{E,j+1/2}>0\right) \text{ and } \left(V_{l,j+1/2}<0\right) \\ A_{j+1/2} & \text{, otherwise} \end{cases} \tag{7-75}$$

The above equations redefine the flux terms in the mass and energy equations of the basic step, i.e. Equations (1-141), (1-144), (1-145), and (1-146), accurately in terms of void fractions above and below a water level. However, these corrections to the flux terms in the basic step equations do not work for the flux terms in the stabilizer step equations, i.e. Equations (1-149), (1-152), (1-156), and (1-157) as the flux terms in these equations are formulated in terms of $\tilde{\alpha}^{n+1}$ from the basic step, not α^{n} of the previous time step. The following equations further adjust the "phasic" flow areas so that the flux terms in the stabilizer step equations remain consistent with the solution to the basic step equations.

$$A^{\alpha}_{g,j+1/2} \rightarrow \begin{cases} A^{\alpha}_{g,j+1/2}\dfrac{\alpha^{n}_{j}}{\tilde{\alpha}^{n+1}_{j}} & \text{, if } \left(\lambda_{E,j+1/2}<0\right) \text{ and } \left(V_{g,j+1/2}>0\right) \\ A^{\alpha}_{g,j+1/2}\dfrac{\alpha^{n}_{j+1}}{\tilde{\alpha}^{n+1}_{j+1}} & \text{, if } \left(\lambda_{E,j+1/2}>0\right) \text{ and } \left(V_{g,j+1/2}<0\right) \end{cases} \tag{7-76}$$

$$A^{\alpha}_{l,j+1/2} \rightarrow \begin{cases} A^{\alpha}_{l,j+1/2}\dfrac{(1-\alpha^{n}_{j})}{(1-\tilde{\alpha}^{n+1}_{j})} & \text{, if } \left(\lambda_{E,j+1/2}<0\right) \text{ and } \left(V_{l,j+1/2}>0\right) \\ A^{\alpha}_{l,j+1/2}\dfrac{(1-\alpha^{n}_{j+1})}{(1-\tilde{\alpha}^{n+1}_{j+1})} & \text{, if } \left(\lambda_{E,j+1/2}>0\right) \text{ and } \left(V_{l,j+1/2}<0\right) \end{cases} \tag{7-77}$$

Redefining the macroscopic quantities that are convected across the cell boundaries in terms of the void fractions above and below an interface curtails the otherwise inadvertent flux of quantities based on cell average void fraction. The modifications above are necessary but not sufficient for a successful method of level tracking. Additional considerations must be given to the other terms which make up the fluxes, i.e. liquid and gas velocities.

Momentum Equations

The phase velocities at time level n+1 are expressed as linear functions of pressure changes at the adjacent computational volumes:

$$V_{j+1/2}^{n+1} = \tilde{V}_{j+1/2}^{n+1} + \sum_{i} \left\{ \frac{\partial V_{j+1/2}^{n+1}}{\partial P_{j+1}^{n+1}} \delta P_{j+1} + \frac{\partial V_{j+1/2}^{n+1}}{\partial P_{j}^{n+1}} \delta P_{j} \right\} \tag{7-78}$$

$$V_{j-1/2}^{n+1} = \tilde{V}_{j-1/2}^{n+1} + \sum_{i} \left\{ \frac{\partial V_{j-1/2}^{n+1}}{\partial P_{j}^{n+1}} \delta P_{j} + \frac{\partial V_{j-1/2}^{n+1}}{\partial P_{j-1}^{n+1}} \delta P_{j-1} \right\} \tag{7-79}$$

Equations (7-78) and (7-79) are substituted into Eqs. (7-68) to (7-73) eliminating the velocities as unknowns from the flux terms. Thus, the flux terms consists of two components before the iterative solution begins: 1) the known portion in terms of the tilde fluid velocities ($\tilde{V}_{j+1/2}^{n+1}$), and 2) the variable portion in terms of the unknown changes in pressures (δP_j^i). The flux quantities modified by Eqs. (7-74) and (7-75) multiply both the known and the variable portions of flux terms. It should not be overlooked that the product of the tilde velocities and modified flux quantities will be inconsistent unless the momentum equations, i.e. Eq. (1-99) and Eq. (1-100), are also modified to account for the presence of liquid-gas interfaces.

This subtle detail pertinent to Eqs. (1-99) and (1-100) deserves further clarification. Equations (1-99) and (1-100) balance the fluid momentum across a staggered control volume for liquid and gas fields, i.e. the control volume drawn with thick dotted lines in Figure 7-3 that stretches from the center of cell j to the center of cell $j+1$. The use of staggered control volumes allows the expression of the net force due to pressure drop across the fluid enclosed by the staggered volume simply as $P_{j-1} - P_j$ without the need for any further approximation. In the meantime, other variables such as fluid density and void fraction in Eq. (1-99) and Eq. (1-100) are approximations since these variables are defined at cell centers. From the balance of momentum across a staggered cell, Eq. (1-99) and Eq. (1-100) are formulated for the liquid and gas velocities. Later, the product of these velocities and the flux quantities at cell boundaries, depicted by the arrows located at j+½ in Figure 7-3, define the flux of mass and energy across the cell boundary. A solution with the standard upstream donor method defines the flux quantitities at cell boundaries as an average of quantities from the adjacent cells. This picture must be revisited when the fluid enclosed by the staggered control volume is no longer uniform and it consists of two regions divided by an interface.

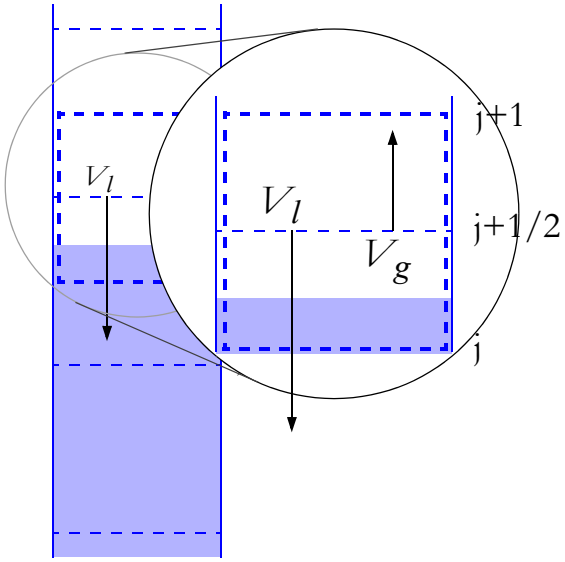

Figure. 7-3. A staggered control volume with the stratified liquid-gas interface

In the presence of a liquid-gas interface, the flux terms at cell boundaries given in Eqs. (7-68) to (7-73) are modified by the newly defined phasic flow areas, i.e. $A^{\alpha}_{g\,,\,j+1/2}$ and $A^{\alpha}_{l\,,\,j+1/2}$. Of the example shown in Figure 7-3, the phasic flow areas correct the flux quantities so that the velocities multiply the quantities only that belong to the region above the interface, i.e. the white region. On the other hand, Eq. (1-99) and Eq. (1-100) will continue to be formulated for an average fluid mixture of regions below and above the interface, i.e. the white and shaded regions, unless properly corrected. Corrections to Eq. (1-99) and Eq. (1-100) must be made so that these equations balance the forces acting on the white region above the interface that prevails at j+1/2 and the velocities from these equations be consistent with the flux quantities that they multiply.

First, the fluid inertia terms in Eq. (1-99) and Eq. (1-100) are redefined using the void fractions below and above an interface:

$$\langle \alpha\rho_g \rangle^n_{j+1/2} = \begin{cases} \alpha_{E\,,\,j+1/2} \langle \rho_g \rangle^n_{j+1/2} \ , \text{ if } \ \lambda_{E\,,\,j+1/2} \neq 0 \\ \alpha_{j+1/2} \langle \rho_g \rangle^n_{j+1/2} \ , \text{ if } \ \lambda_{E\,,\,j+1/2} = 0 \end{cases} \tag{7-80}$$

$$\langle (1-\alpha)\rho_l \rangle_{j+1/2}^{n} = \begin{cases} (1-\alpha_{E,j+1/2})\langle \rho_l \rangle_{j+1/2}^{n} & \text{, if } \lambda_{E,j+1/2} \neq 0 \\ (1-\alpha_{j+1/2})\langle \rho_l \rangle_{j+1/2}^{n} & \text{, if } \lambda_{E,j+1/2} = 0 \end{cases} \tag{7-81}$$

Second, the pressure gradient term in Eq. (1-99) and Eq. (1-100) is redefined as

$$\left.\frac{\partial P}{\partial x}\right|_{j+1/2}^{n+1} = \frac{P_{j+1}^{n+1} - P_{j}^{n+1} + \delta P_{L,j+1/2}}{\Delta x_{j+1/2}} \tag{7-82}$$

where the correction term to account for the presence of a liquid-gas interface is given by the following equation.

$$\delta P_{L,j+1/2} = \begin{cases} (0.5\Delta x_{j+1} - L_{j+1}) \left.\frac{\partial P}{\partial x}\right|_{j\text{-}1/2}^{n+1} & \text{, if } L_{j+1} < 0.5\Delta x_{j+1} \\ (0.5\Delta x_{j} - L_{j}) \left.\frac{\partial P}{\partial x}\right|_{j\text{-}3/2}^{n+1} & \text{, if } L_{j} > 0.5\Delta x_{j} \\ 0 & \text{, otherwise} \end{cases} \tag{7-83}$$

It should be noted that Eq. (7-83) yields an accurate pressure drop from the interface to the cell boundary not only due to the hydrostatic head of fluid but also due to the fluid accelaration. This detail should not be overlooked and it is important for situations in which an interface accelarates. It should also be emphasized that Eq. (7-83) yields to the weight of the fluid below the interface between the interface and the cell boundary in the hydrostatic limit, i.e. when there is no pressure drop due to fluid accelaration $\frac{\partial V}{\partial t} = 0$.

Third, the gradients of liquid and gas velocities across the cell boundary are set to zero based on an assumption that the changes in fluid velocity across the interface will not contribute to the pressure drop across the staggered control volume. For example, the gas bubbles that reach the liquid-gas interface rise at a terminal velocity. The velocity of gas escaping from the interface is generally much smaller than the terminal rise velocity of gas bubbles below the interface. However, this sudden slowdown of gas across the interface, which is due to continuity, should not cause additional pressure changes across the staggered cell. Similarly, the liquid droplets entrained into the region above the interface may have higher velocity than the continuous liquid region below the interface. Any additional pressure drop due to this change of liquid velocity across the staggered cell is incorrect, too. Therefore, the velocity gradient of a field at any cell boundary is set to zero when a liquid-gas interface is present in the upstream direction of that

field. The correction to the gradients of liquid and gas velocities are formulated into Equations Eq. (1-99) and Eq. (1-100) as follows:

$$\left.\frac{\partial V_l}{\partial x}\right|_{j+1/2}^{n} = 0 \text{ when } \begin{cases} \left(\lambda_{E,j+1/2} < 0\right) \text{ and } \left(V^n_{l,j+1/2} > 0\right) \\ \left(\lambda_{E,j+1/2} > 0\right) \text{ and } \left(V^n_{l,j+1/2} < 0\right) \end{cases} \tag{7-84}$$

$$\left.\frac{\partial V_g}{\partial x}\right|_{j+1/2}^{n} = 0 \text{ when } \begin{cases} \left(\lambda_{E,j+1/2} < 0\right) \text{ and } \left(V^n_{g,j+1/2} > 0\right) \\ \left(\lambda_{E,j+1/2} > 0\right) \text{ and } \left(V^n_{g,j+1/2} < 0\right) \end{cases} \tag{7-85}$$

As the level tracking method and the necesary modifications to the field equations described Eq. (7-55) to Eq. (7-85) are incorporated, numerical experiments presented must be simulated to test the method and the modifications to the field equations.

Corrections to Evaluation of the Closure Models

The modifications to the field equations and the extra measures taken to ensure that the water levels cross the cell boundaries without harming the solution are not sufficient alone for a successful level tracking method. Although not discussed in the previous sections, a correction is necessary to the definition of the interfacial drag coefficient in terms of fluid properties at a cell boundary when a liquid-gas interface is present in either cell adjacent to a boundary. This correction to the interfacial drag coefficient is explained here along with another correction to the interfacial heat transfer coefficient.

Interfacial Drag

Let us first consider the interfacial drag coefficient, C_i in Eq. (4-1). This coefficient relates the drag force between the separated field to the relative velocity of one field to another. Therefore, it is a strong function of the flow regime The void fraction that is used to determine the flow regime for any given staggered cell (see Figure 7-3) is an average of void fractions from half-cells that make up the staggered cell. As emphasized in discussions on modifications to the momentum equations, the use of an average void fraction for the entire staggered is not consistent with the corrections made to the flux terms of conservation equations. The conclusion from these discussions is that the balance of forces acting on the fluid should represent the conditions prevailing at cell boundaries, i.e. the center of staggered cell. In view of this conclusion, the

interfacial drag coefficient in Eq. (4-1) is evaluated in terms of fluid conditions that prevail at the cell boundary when a liquid-gas interface is present in either of cells adjacent to the boundary.

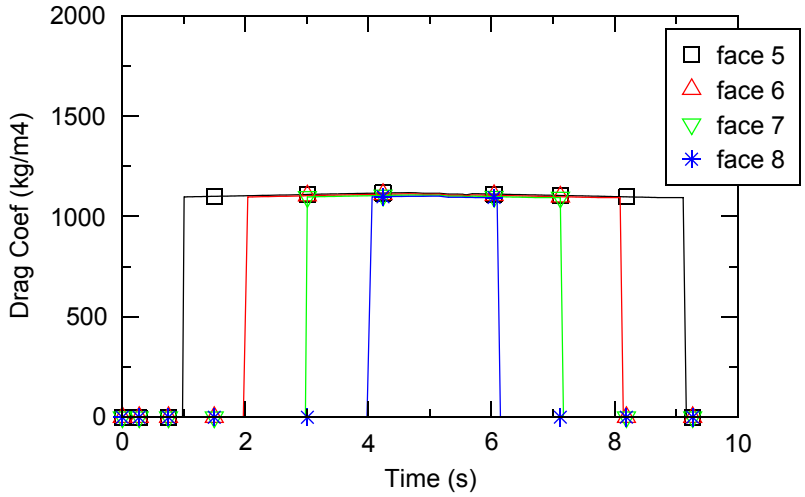

Figure. 7-4. Interfacial drag coefficients at cell boundaries of the single-phase fill and drain test (simulated with the level tracking method)

$$C_{i,j+1/2} = \begin{cases} C(\alpha_{E,j+1/2}) & , \quad \text{if} \quad \lambda_{E,j+1/2} \neq 0 \\ C(\langle \alpha \rangle_{j+1/2}) & , \quad \text{if} \quad \lambda_{E,j+1/2} = 0 \end{cases} \tag{7-86}$$

Figure 7-4 shows the interface drag coefficients at cell boundaries (i.e. cell faces) along the test pipe of the single-phase rising and falling test. The sharp change in the drag coefficient is expected as the water level crosses the cell boundaries. It should be noted here that it is a common practice among the methods like semi-implicit to impose limits on the rate at which drag coefficients change. Such limits are set to prevent numerical instabilities due to explicit nature of these coefficients. In the case of an interface crossing the cell boundary, however, no limit should be imposed on the interfacial drag coefficient since a sharp change is expected and the remainder of equations are already preconditioned to account for sharp changes and to remain stable. Contrary to the other cases, imposing any such limit renders the solution unstable in this case.

The interfacial drag coefficients at cell faces along the test pipe of the two-phase rising and falling test exhibit sharp changes, as expected, as the mixture level crosses the cell boundaries. In addition to the expected sharp changes, the interfacial drag coefficients in Figure 7-5 also show how strongly the drag coefficient depends on the void fraction that prevails at the cell boundary along with the relative motion of fields against each other. In this figure, the decreasing drag coefficient at a cell boundary realizes the slight depression of void fraction in the adjacent cells, as is also shown later in Figure 7-13, as the column of bubbly liquid and gas mixture rises above a

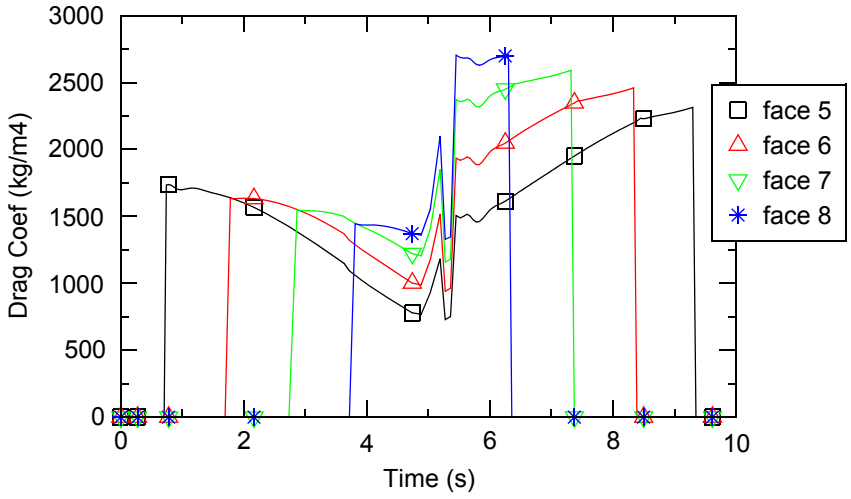

Figure. 7-5. Interfacial drag coefficients at cell boundaries of the two-phase fill and drain test (simulated with the level tracking method)

cell boundary. This behavior is physically sensible since the void fraction of a bubbly liquid-gas mixture is expected to decrease under an increasing weight of the rising mixture column.

Interfacial Heat and Mass Transfer

The closure model for the interfacial heat transfer (IHT) between the liquid and gas fields must account for the presence of water levels in computational cells. A brief description of the IHT model in TRACE is therefore appropriate here before discussing how the IHT model should be adjusted. The following two equations describe the heat transfer to and from liquid and gas at the phase interface

$$\begin{aligned} q_g &= q_{ig} + q_{dg} \\ &= \frac{P_s}{P} H_{\mathrm{CHTI}} (T_g - T_{sv}) + \frac{P_a}{P} H_{\mathrm{CHTA}} (T_g - T_l) \end{aligned} \tag{7-87}$$

$$\begin{aligned} q_l &= q_{il} + q_{dl} \\ &= [H_{\mathrm{ALVE}} (T_l - T_{sv}) + H_{\mathrm{ALV}} \langle T_l - T_{sat} \rangle^{\dagger}] + \frac{P_a}{P} H_{\mathrm{CHTA}} (T_l - T_g) \end{aligned} \tag{7-88}$$

where

$$\langle T_l - T_{sat} \rangle^{\dagger} = \begin{cases} 0 & \text{if } T_l \le T_{sat} \\ T_l - T_{sat} & \text{if } T_l > T_{sat} \end{cases}. \tag{7-89}$$

Eq. (7-87) assumes that the gas field is a homogeneous mixture of water vapor and noncondensable gas in thermodynamic equilibrium. The first term in Eq. (7-87) accounts for heat transfer to or from the interface (q_{ig}) and is converted to or released as latent heat through phase change. The second term in Eq. (7-87) is the direct sensible heat exchange between the liquid and the gas fields. Similarly, the first term in Eq. (7-88) corresponds to the sensible heat transferred to or from the interface, which is converted to or released as latent heat. The second term in Eq. (7-88) is the direct sensible heat exchange between the liquid and the gas fields. It should be noted that the liquid to interface has two heat transfer coefficients, H_{ALV} and H_{ALVE}, for condensation and evaporation. Evaporation occurs if $T_{sv} < T_l < T_{sat}$ and flashing occurs if $T_l > T_{sat}$. Equations (7-87) and (7-88) are added to calculate the total rate of heat exchange at the phase interface where the direct sensible heat transfer terms, q_{dg} and q_{dl}, cancel out.

$$Vol\ h_{fg} \cdot \Gamma_i = q_{ig} + q_{il} \tag{7-90}$$

When there is a water level inside a computational cell, the IHT coefficients must be determined for each region above and below the level along with the coefficients that describe the heat transfer at the level as follows:

$$q_g = (q_{ig}^{-} + q_{dg}^{-}) + (q_{ig}^{\mathrm{L}} + q_{dg}^{\mathrm{L}}) + (q_{ig}^{+} + q_{dg}^{+}) \tag{7-91}$$

$$q_l = (q_{il}^{-} + q_{dl}^{-}) + (q_{il}^{\mathrm{L}} + q_{dl}^{\mathrm{L}}) + (q_{il}^{+} + q_{dl}^{+}). \tag{7-92}$$

The heat transfer coefficients for regions above and below the interfaces can be easily determined using the same procedures that apply to an entire computational cells. However, it should be noted that the field temperatures are assumed identical above and below the interface. This is an assumption which may lead to significant errors. Another area of concern is the description heat transfer at the level. In the presence of a strong condensation, the temperature of stratified liquid near the level may be very close to the saturation temperature, and thus, create a resistance to further condensation. As this may sound like a subtle detail, it is a situation which should be considered very carefully and accounted for by the IHT terms "from" and "to" the saturation interface at the water level, i.e. q_{ig}^{L} and q_{il}^{L}. For the purpose of this discussion, these two terms will be determined using TRACE's special treatment for the computational volumes that represent the accumulator or pressurizer of a nuclear plant while it is noted that evaluating these two terms accurately requires an investigation of its own.

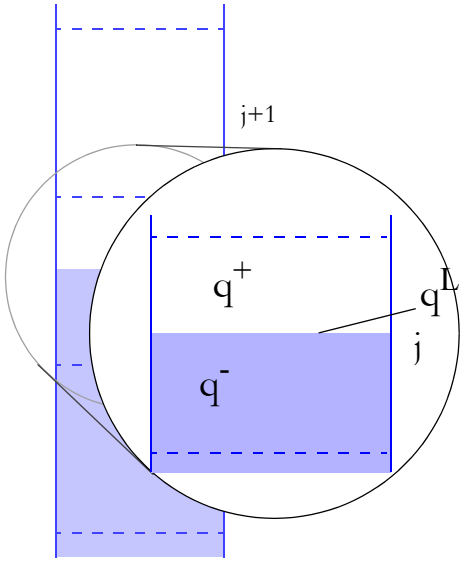

Figure. 7-6. Interfacial HT terms designated for a computational volume with the stratified liquid-gas interface

Numerical Experiments

As the level tracking method and the necesary modifications to the field equations described Eq. (7-55) to Eq. (7-85) are incorporated, numerical experiments presented must be simulated to test the method and the modifications to the field equations. A thorough testing is critical to a successful implementation of the level tracking method. Several simple problems were run to show the problems with the regular solution scheme and how level tracking improves the results.

Fill and Drain Test

A schematic diagram of the test problem is shown in Figure 7-7. The model consists of a vertical pipe with 1.0 m^2 axial flow area and 10.0 m height. A "T" branch with 0.5 m^2 axial flow area and 3.0 m height is connected to the bottom of the test pipe. There are two variations to this test problem. In the first case, liquid water is injected, at the side entry of the "T" branch, to raise the level of the liquid column and then withdrawn to let the level drop back to its starting location. In the second case, air is injected, at the bottom entry of the "T" branch, to maintain a steady mixture of liquid water and air under the standard room temperature and pressure conditions. Again, liquid water is first injected to raise the level of the mixture, and then withdrawn to let the level drop back to its starting location. The injection and withdrawal of liquid water in both cases at 1.0 m^3/s moves the level across one computational volume in every second.

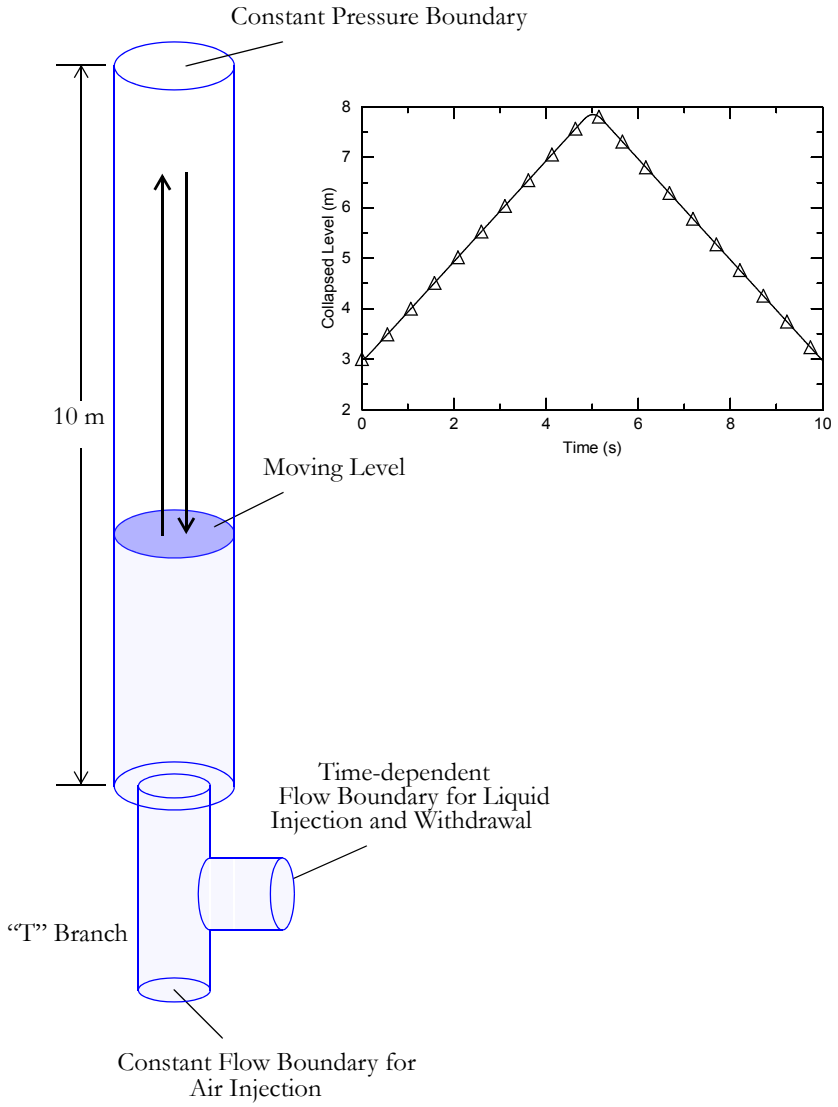

Figure. 7-7. Schematic of the fill and drain test

Conditions are subcooled and isothermal to remove any complications that may result from failures of interfacial heat transfer packages to account properly for the level. Gravity and interfacial drag between air bubbles and liquid water are the only forces that act on the fluid. The wall friction is suppressed in the test so that pressure below the level is due to the hydrostatic gravity head only. Moreover, the isothermal and subcooled conditions at the standard room temperature and pressure conditions force all interfacial mass transfer terms to zero. Hence the solution depends only on the terms of the six-equation model that describe the exchange of fluid by convection across the boundaries of computational volumes and the momentum flux due to convection, interfacial drag, and gravity. The TRACE simulations of the fill and drain test are discussed below.

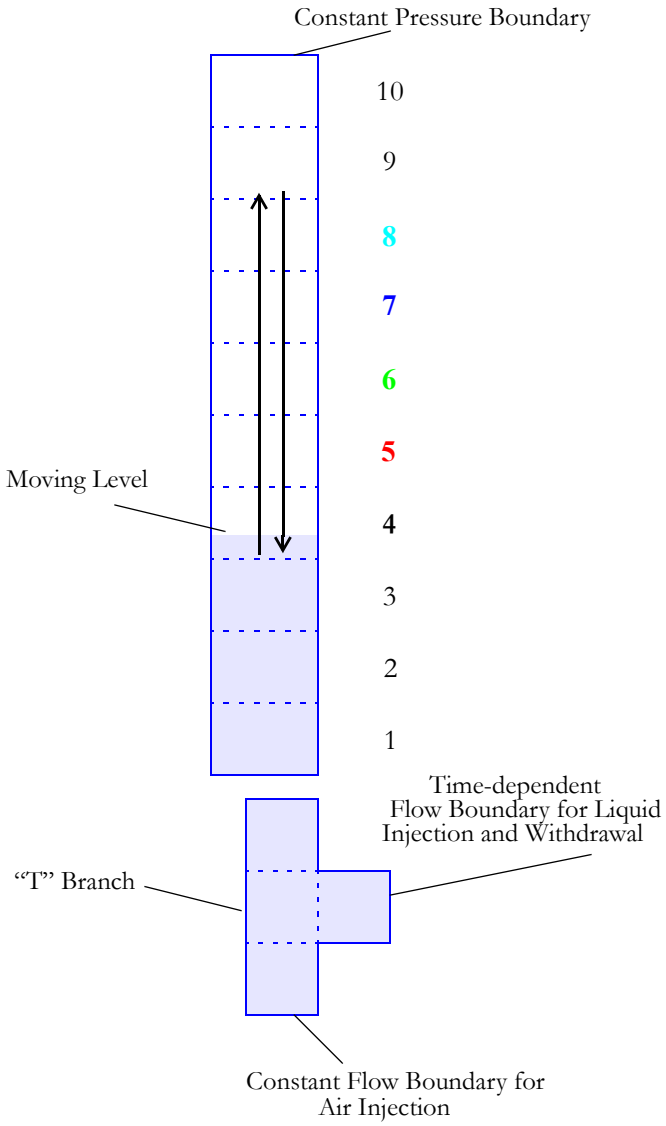

Figure. 7-8. Schematic of the fill and drain test simulated using one-dimensional equations

Shown in Figure 7-8 is the computational model that represents the test pipe, made of ten equal computational volumes. Henceforth, the computational volumes will also be referred to as "cells."

This test problem was simulated using the SETS method of TRACE with the standard upstream donor method. As shown in Figure 7-8, the collapsed water level, which is given by

$$H_{\mathrm{C}}(t) = \sum_{i=1}^{N} [1 - \alpha_i(t)] \Delta x_i \,, \tag{7-93}$$

(where N is the total number of computational cells) is rising and falling back to its starting location at a steady rate. The rising front is expected to fill the computational volumes at a steady rate starting from the bottom of the pipe and move to the next volume above once a volume is full of liquid water. The SETS solution of TRACE with the standard upstream donor method fails to predict this expected behavior of cell void fractions as the water level rises. A plot of void fractions in Figure 7-9 shows that the liquid front moves to the next volume above, before the volume is fully liquid water, trapping a gas bubble behind. This distorted picture of the rising liquid front repeats itself as the water is drained from the test pipe and the water level drops back to its starting location. The liquid front is smeared over several volumes as the descending liquid front leaves significant amount of liquid left behind in its tail. Due to smearing of the liquid front, the "predicted" cell pressures (shown in Figure 7-10) below the moving liquid front do not exhibit the expected behavior as well, i.e. a steady change proportional to the height of the rising and falling water level. Instead, the cell pressures below the water level increase and decrease sporadically indicating sudden acceleration and deceleration of the fluid, a behavior which is absolutely numerical in nature. Figure 7-11 and Figure 7-12 show that the SETS method with the standard donor method continues to suffer severely from similar difficulties when the fluid below the moving liquid front is a mixture of air and liquid water.

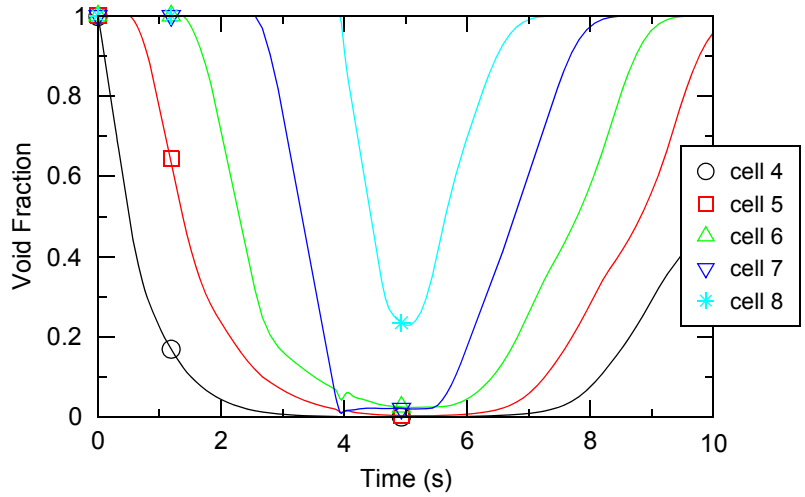

Figure. 7-9. Void fractions of the single-phase fill and drain test (simulated with the standard method of solution)

The two-phase rising and falling level test also shows none of the troubles that were reported in the previous section. For example, the troubling cell void fractions from 0 to 5 seconds seen in Figure 7-11 are no longer present in Figure 7-15. Previously, the cell void fractions approached to zero which was well below the expected value of void fraction for the bubbly mixture of liquid and air simulated in this experiment. The cell pressures reported previously for the same test in Figure 7-12 suffered from spike changes and oscillations as the water level crossed the cell boundaries. The cell pressures shown in Figure 7-16 are clean from these spike changes and oscillations. It should be noted that the sudden drop in cell pressures as the bubbly mixture of

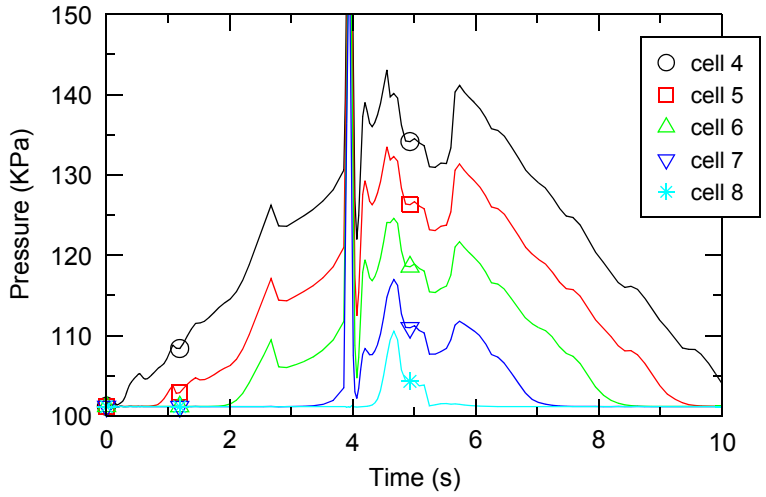

Figure. 7-10. Pressures of the single-phase fill and drain test (simulated with the standard method of solution)

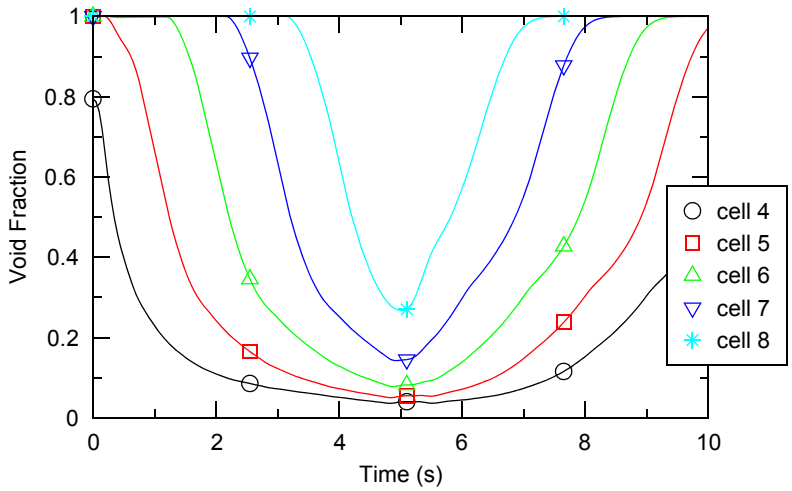

Figure. 7-11. Void fractions of the two-phase fill and drain test (simulated with the standard method of solution)

liquid and gas reverses direction is due to the fluid acceleration in the opposite direction of gravity.

Oscillating Manometer

The U-tube manometer in this test consists of gas and liquid with the liquid forming equal collapsed water levels in each arm. Initially, the liquid slug has a uniform velocity and no acceleration. The top of manometer arms are open to the standard room temperature and pressure

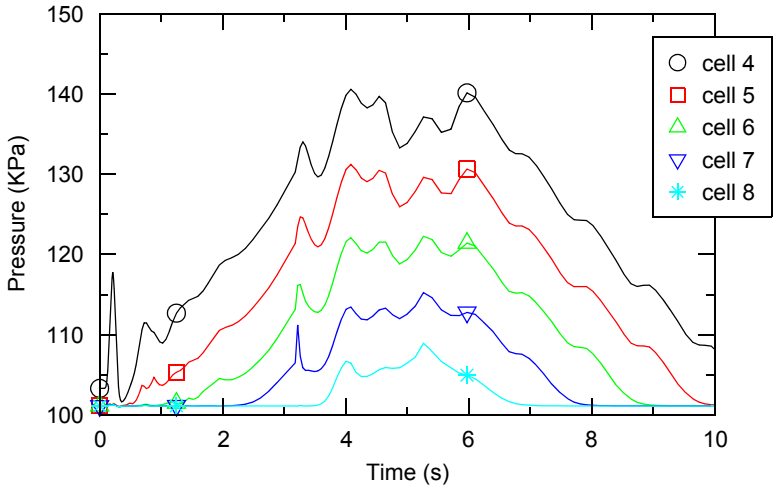

Figure. 7-12. Pressures of the two-phase fill and drain test (simulated with the standard method of solution)

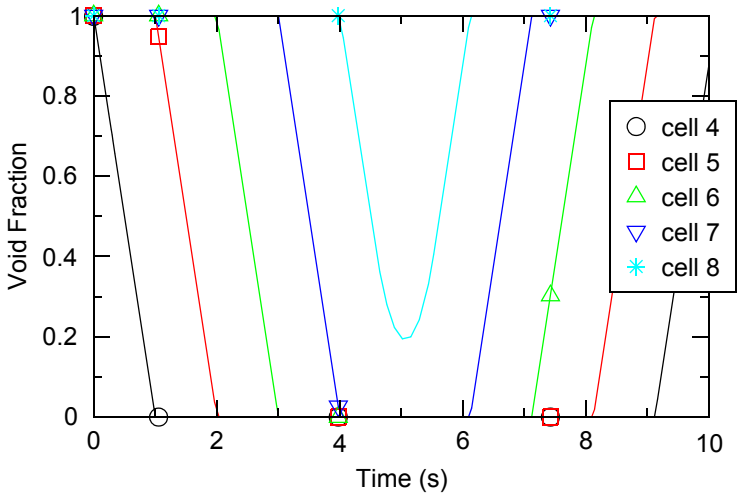

Figure. 7-13. Void fractions of the single-phase fill and drain test (simulated with the level tracking method)

conditions — it should be noted that the original benchmark problem connects the manometer arms at the top, forming a closed system. The schematic of the oscillating manometer test is given in Figure 7-17. Ransom (Ref. 7-23) specifies the problem —

> "The initial conditions for the problem are: isothermal throughout at 50 ^{o}C temperature, pressure at the interfaces between the vapor and liquid equal to 1.01×10^{5} Pa, and corresponding hydrostatic pressures at all other points in the system, ... The initial position of the liquid-vapor interface is 5.0 m from the bottom of each manometer leg and all fluid initially has a velocity of 2.1 m/s. This initial velocity will cause the

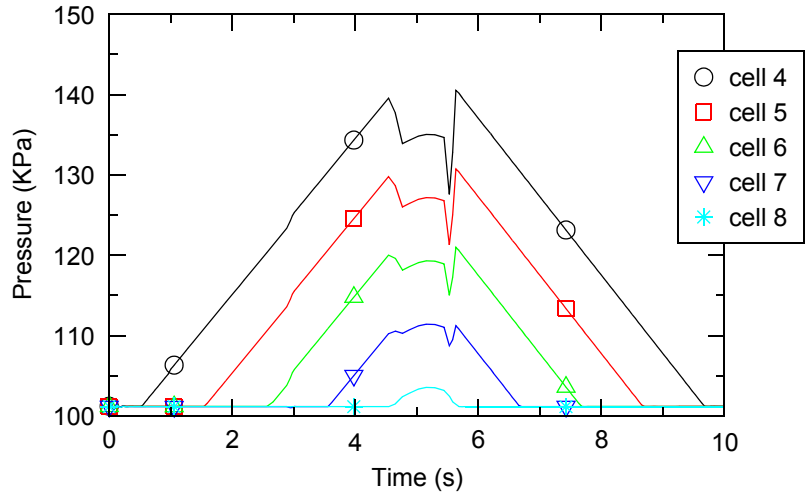

Figure. 7-14. Pressures of the single-phase fill and drain test (simulated with the level tracking method)

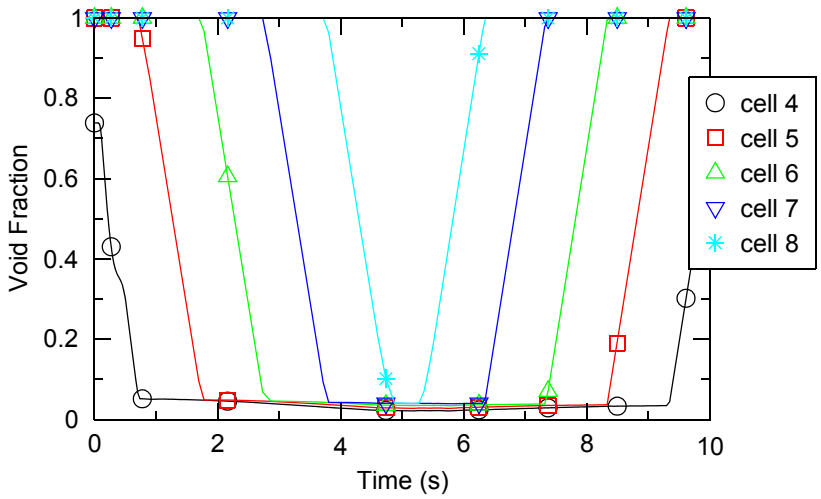

Figure. 7-15. Void fractions of the two-phase fill and drain test (simulated with the level tracking method)

interface to oscillate approximately 1.5 m in height from the initial location ... The system is adiabatic so that the thermal boundary condition is zero flux at the wall."

He further explains the objective of the problem as modeling the period of oscillation, which is analytically known; and evaluating the capability of the numerical discretization scheme to retain the liquid-gas interface.

An analytic solution for the water levels and the pressures at any location inside the two manometer arms can be obtained by applying a mechanical energy balance to the oscillating

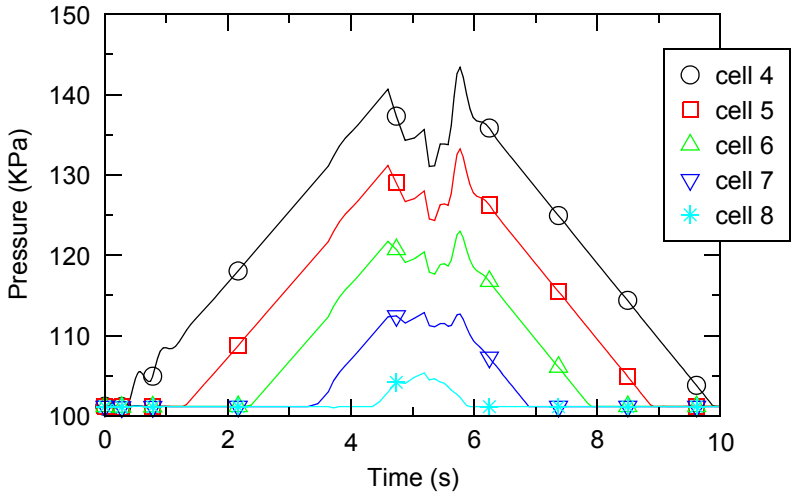

Figure. 7-16. Pressures of the two-phase fill and drain test (simulated with the level tracking method)

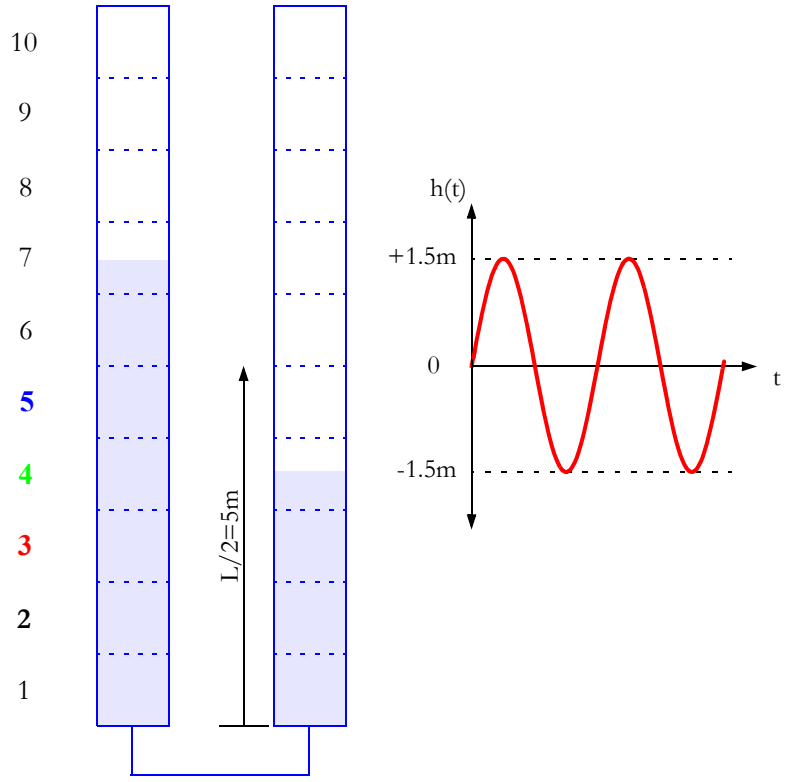

Figure. 7-17. Schematic of the oscillating manometer test

water slug. In the absence of any losses, the mechanical energy balance dictates that the gain of total potential energy is always equal to the loss of total kinetic energy and vice versa.

$$\frac{dK}{dt} + \frac{d\Phi}{dt} = 0 \tag{7-94}$$

Defining the length of the oscillating slug L, and the cross sectional area of the manometer arm S, the distance between the water level at any time to its initial position with $H(t)$, and the velocity of the oscillating slug with $V(t)$, the change of kinetic energy and potential energy with respect to time can be expressed as follows:

$$\frac{d}{dt}\left(\frac{1}{2}\rho V^2(t) SL\right) + \frac{d}{dt}\left(\int_0^{H(t)} \rho g S z dz + \int_{-H(t)}^{0} \rho g S z dz\right) = 0 \tag{7-95}$$

$$L V(t)\frac{d}{dt}V(t) + 2gH(t)\frac{d}{dt}H(t) = 0 \tag{7-96}$$

$$\frac{d^2}{dt}H(t) + \left(\frac{2g}{L}\right)H(t) = 0\,. \tag{7-97}$$

Equation (7-97) can be solved for the location of the manometer water level as function of time, i.e. $H(t)$, with the initial conditions that specify the initial position of the oscillating slug and its velocity:

$$H(t) = 0 \;\;,\;\; \left.\frac{dH}{dt}\right|_{t=0} = V_0 \tag{7-98}$$

The solution of Eq. (7-97) yields the distance between the surface of the oscillating water levels and their starting location inside the left and right manometer arms:

$$H_L(t) = \frac{V_0 T}{2\pi}\sin\left(\frac{2\pi t}{T}\right) \text{ and } H_R(t) = -H_L(t) \tag{7-99}$$

where the period of the oscillating manometer is found to be

$$T = 2\pi\sqrt{\frac{L}{2g}}\,. \tag{7-100}$$

Once the location of the oscillating manometer water level is known as a function of time, pressures at any point along the manometer arm can be determined from a simple force balance between the point of interest and the surface of the oscillating water level. The force balance should include the terms due to fluid acceleration and gravity:

$$\frac{\partial}{\partial t}V(x\,,\,t) = -\frac{1}{\rho}\frac{P_s - P(x\,,\,t)}{\xi(x\,,\,t)} - g\,. \tag{7-101}$$

In the above equation, the length of the water slug between the surface of the oscillating water level and the point of interest is defined as

$$\xi(x\,,\,t) = \begin{cases} \dfrac{L}{2} + H(t) - x & ; \quad x < \dfrac{L}{2} + H(t) \\ 0 & ; \quad x > \dfrac{L}{2} + H(t) \end{cases} \tag{7-102}$$

In Eq. (7-102), variable x is the distance from the point of interest to the bottom of the manometer arm. The solution of Eq. (7-101) for the locations below the oscillating water level then be becomes:

$$P(x\,,\,t) = P_S + \left[\frac{L}{2} + H(t) - x\right]\left[1 - \frac{2H(t)}{L}\right]\rho g \text{ for } x < \frac{L}{2} + H(t) \tag{7-103}$$

Equation (7-103) can be used to compute the cell pressures and then be compared to the TRACE solution. Figure 7-18 shows the resulting pressures from applying Eq. (7-103) to the oscillating manometer test. Another variable which provides insight to the manometer test is the difference between the pressures at the same elevation of the two manometer arms. This variable, given in Eq. (7-104), simply defines the net force acting on the segment of the manometer fluid between the two locations at the same elevation of the opposing arms.

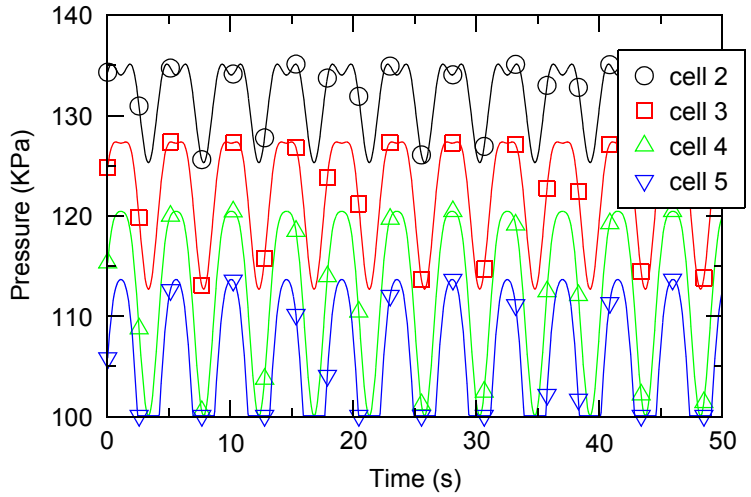

Figure. 7-18. Manometer pressures predicted by a closed form solution

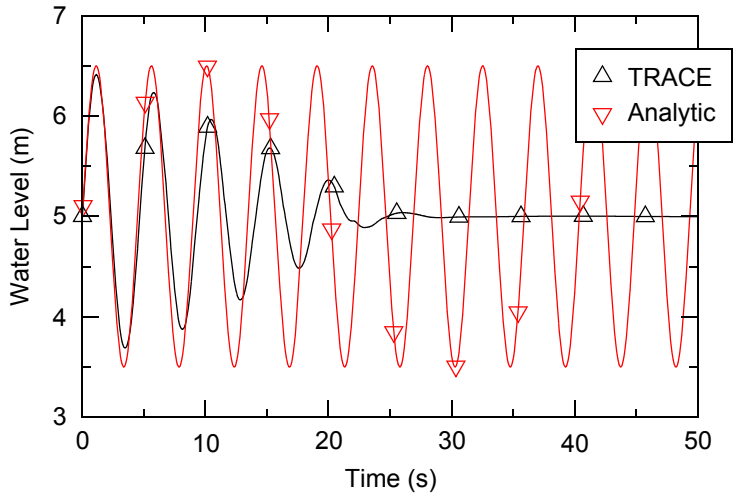

Figure. 7-19. Water level of the oscillating manometer (simulated with the standard method of solution)

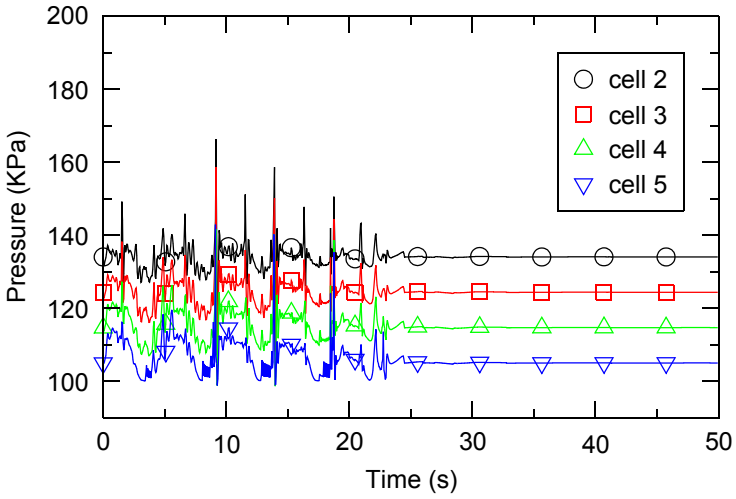

Figure. 7-20. Pressures along the oscillating manometer arm (simulated with the standard method of solution)

$$P_L(x\,,\,t) - P_R(x\,,\,t) = \frac{4x}{L}H(t) \tag{7-104}$$

For a manometer with 10 m long oscillating water slug and 2.1 m/s initial velocity, Eq. (7-99) gives an oscillation amplitude of 1.5 m measured from its starting location. Based on Eq. (7-100), the period of these oscillations should be 4.48 seconds.

This test problem was simulated using the Semi-Implicit method of TRACE. The results show that the standard solution method fails to simulate the manometer oscillations. Figure 7-19

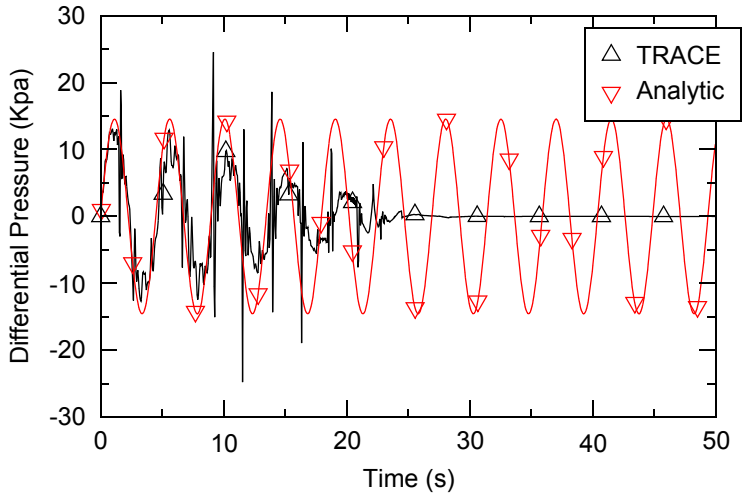

Figure. 7-21. The net force on the fluid segment below 2.5 m elevation of the manometer arms (simulated with the standard method of solution)

compares the collapsed water level predicted by TRACE to the oscillating water level predicted by Eq. (7-99). A comparison of the pressures along the manometer arm predicted by TRACE and Eq. (7-103) (see Figure 7-20) reveals that the standard solution method of TRACE dissipates the kinetic energy of the oscillating fluid very quickly. This conclusion is more obvious when the net force acting on a given segment of the oscillating fluid described by Eq. (7-104) is considered. Figure 7-21 compares the net force acting on a segment of oscillating fluid contained between 2.5 m elevation in one manometer arm to 2.5 m elevation in the opposing arm. This comparison concurs that the solution with the upwind donor method quickly dissipates the kinetic energy of the oscillating fluid. It is therefore concluded that the standard solution method of TRACE, i.e. Semi-Implicit method, fails to simulate the oscillating manometer test.

The oscillating manometer test simulated with level tracking. The solution method with the level tracking failed to simulate this test prior to the additional considerations made for the liquid-gas interface crossing the cell boundaries.

The leading cause of this failure to simulate the oscillating manometer was the pressure spikes caused by the interface crossing cell boundaries. Figure 7-23 shows none of these pressure spikes. Thus, the water level of the manometer arm oscillates without any sign of decay as expected in Figure 7-22. Further, the simulated cell pressures below the oscillating water level in Figure 7-18 compare almost perfectly with the pressures predicted analytically in Figure 7-18. These results for the oscillating manometer test are as close as a dicrete solution can be to the analytical solution for the oscillating manometer, which is a point that demonstrates the success of the approach outlined in this section to propagate interfaces across cell boundaries.

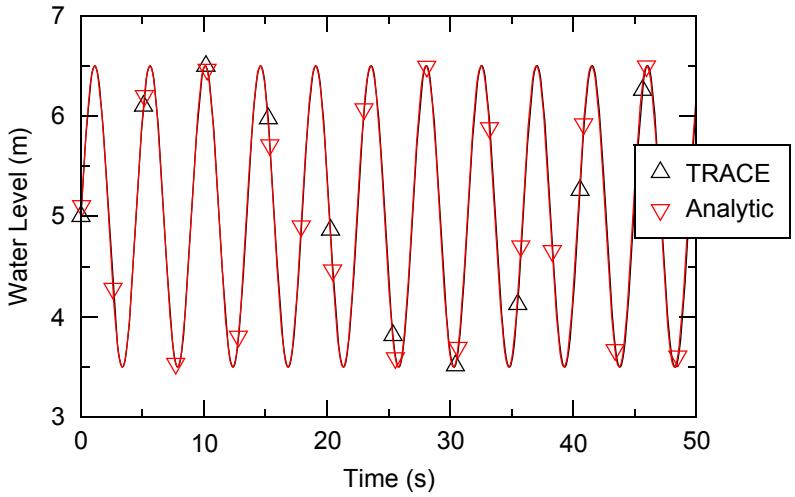

Figure. 7-22. Water level of the oscillating manometer (simulated with the level tracking method)

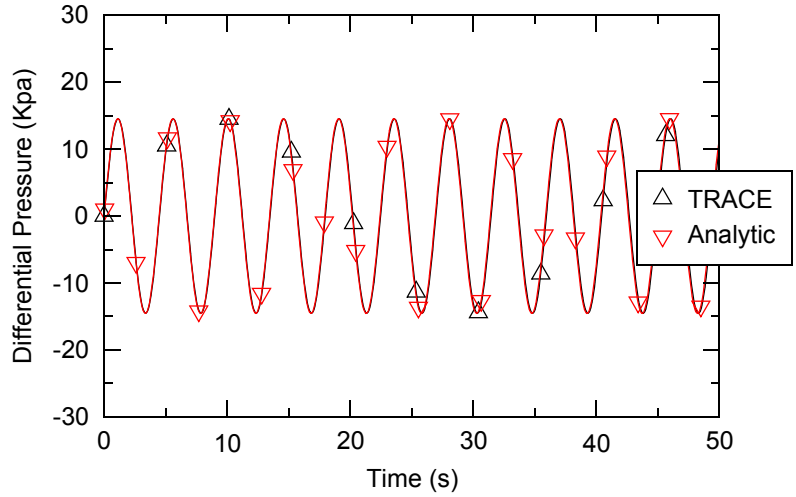

Figure. 7-23. The net force on the fluid segment below 2.5 m elevation of the manometer arms (simulated with the level tracking method)

Expulsion of Superheated Steam by Subcooled Water

The purpose of this test problem is to study the complications in the solution to the six-equation model resulting from failures of the interfacial heat transfer model to account properly for the water levels. The problem, which will be referred to as the "condensation test" from hereon, consists of a vertical pipe, 3 m in height and 1 m in diameter, initially filled with superheated steam at constant temperature and pressure of 163 ^{o}C and 0.4 MPa respectively. The vertical pipe is connected to a very large reservoir of steam. The computational model divides the vertical pipe

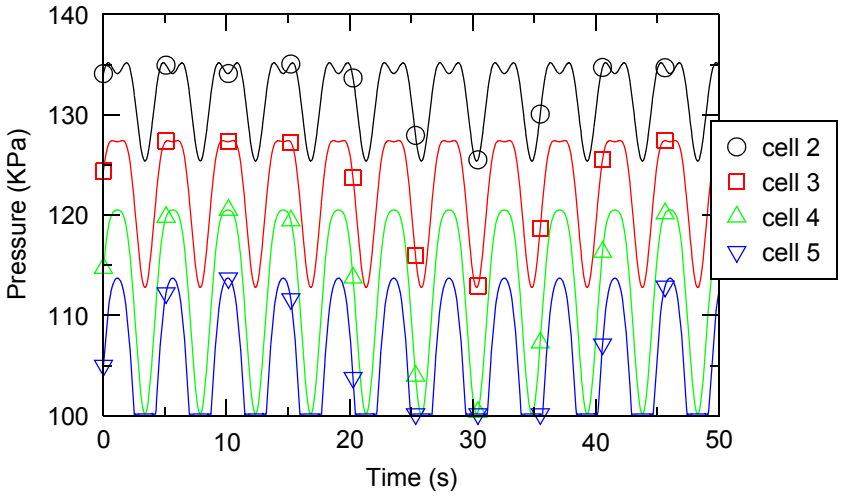

Figure. 7-24. Pressures along the oscillating manometer arm (simulated with the level tracking method)

into ten equal computational volumes. A schematic diagram of the test problem is shown in Figure 7-25. Also shown in Figure 7-25 is the three-dimensional version of the same test that divides the vertical pipe into 80 equal computational volumes. During the test, liquid water subcooled at 50 ^{o}C is injected with 0.5 m/s velocity at the bottom inlet of the pipe until it fills the pipe completely. The recommended maximum timestep size for the simulation of this test is 0.05 seconds.

This test problem was designed to measure the ability of a solution method to cope with the difficulties which arise from inaccurate modelling of the computational volumes as they are filled by the rising liquid front. Predicting the interfacial heat transfer rate in these volumes, and thereof, the condensation of superheated steam in contact with the very subcooled water is very critical to the successful simulation of this test. There is also an added complexity as a saturated layer of liquid builds up in the tail of the rising front that should continuously decrease the condensation rate. A solution method without proper care for these details is expected to suffer severely as a cell becomes “packed” with liquid water when the method fails to turn off the condensation behind the rising liquid front.

The standard solution method of TRACE displays the expected difficulties due to water packing and inaccurate modeling of the condensation at the rising liquid front. Figure 7-26 shows the pressures at each computation volume along the pipe as the subcooled water is injected. The presence of the water packing phenomenon is apparent in this figure. The magnitude of the resulting compression waves from the “numerical” water hammer reaches to 2.5 MPa rendering the TRACE solution unusable. Before drawing a conclusion on the performance of TRACE, the water packing option, an optional method that overcomes the fluid packing problem by dampening the pressure field, must be engaged in the simulation of the condensation test. Figure 7-27 shows the pressures along the test pipe recomputed by TRACE with the water packing option.

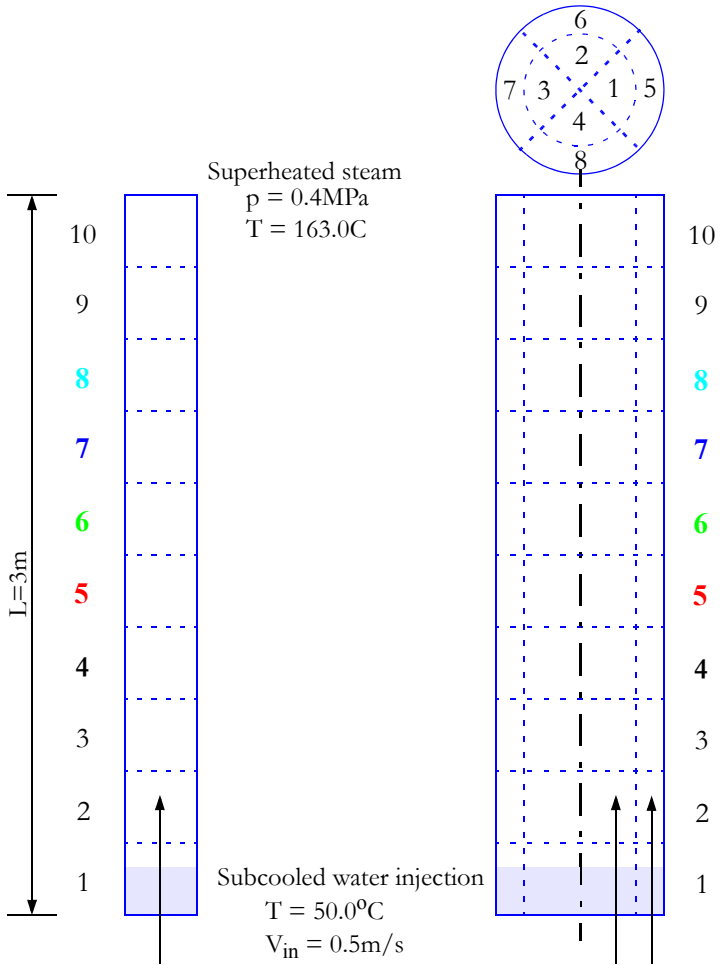

Figure. 7-25. Schematic of the 1D and 3D condensation tests

Although the amplitude of pressure spikes are several times smaller, their mere presence is sufficient to prove that the standard method of solution even with the help from a special method is still unable to handle properly the steam condensation at the rising liquid front.

Another variable of equal interest is the liquid temperature along the pipe which is expected to indicate the build up of a saturated liquid layer behind the rising front. Figure 7-28 shows that the liquid temperatures follow rather closely the sub-cooled temperature with occasional jumps to the saturation temperature in the vicinity of the rising front. As sub-cooled water is injected at the bottom, superheated steam is withdrawn into the pipe at the top replenishing the steam being condensed at such extreme rates. Normally, the direction of steam flow should be an outcome of a balance between the volume rate at which liquid displaces steam and the volume rate at which steam is being condensed at the front. However, the compression waves induced by the fluid packing dominates the TRACE solution causing high bursts of steam flowing out of the test pipe as seen in Figure 7-29.

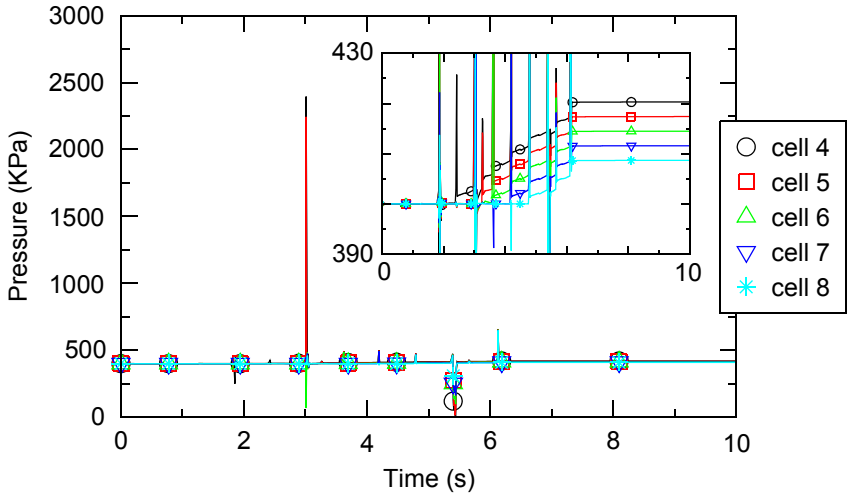

Figure. 7-26. Pressures along the condensation test pipe (simulated with the standard method of solution)

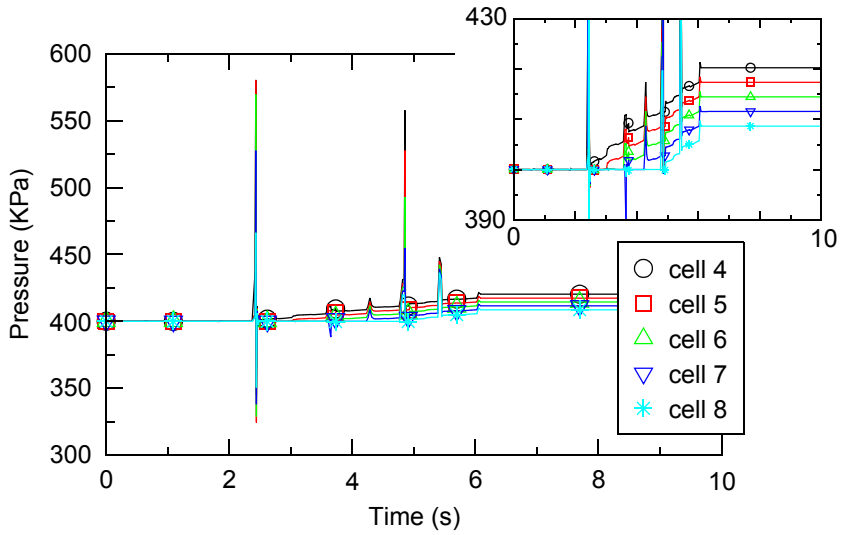

Figure. 7-27. Pressures along the condensation test pipe (simulated with the standard option for water packing treatment)

It should also be noted here that the water packing option of TRACE, at least, achieves a limited success by reducing the severity of the failures mentioned above. This limited success is evident in Figure 7-30 that compares the timestep number as function of the simulation time for the two cases: 1) without the water packing option, 2) with the water packing option.

In conclusion, TRACE fails to predict the constant rate of condensation along the test pipe. As the rising front passes through a cell, the condensation reaches extremely high rates due to apparent problems with the interfacial heat transfer between liquid and gas fields. The root cause of this

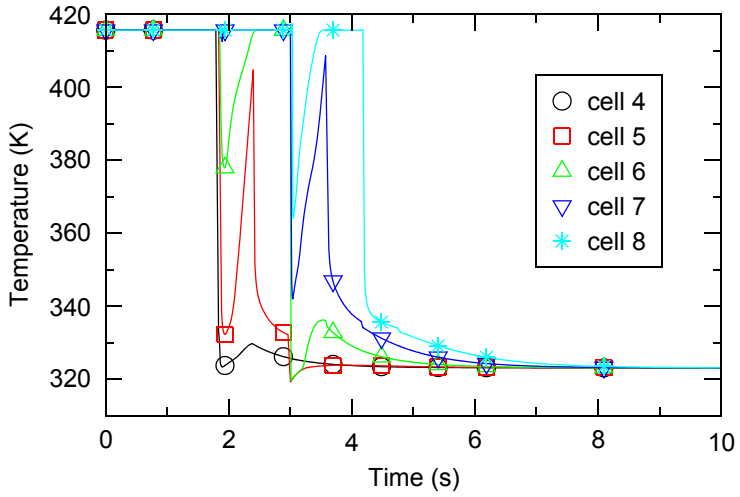

Figure. 7-28. Liquid temperatures along the condensation test pipe (simulated with the standard method of solution)

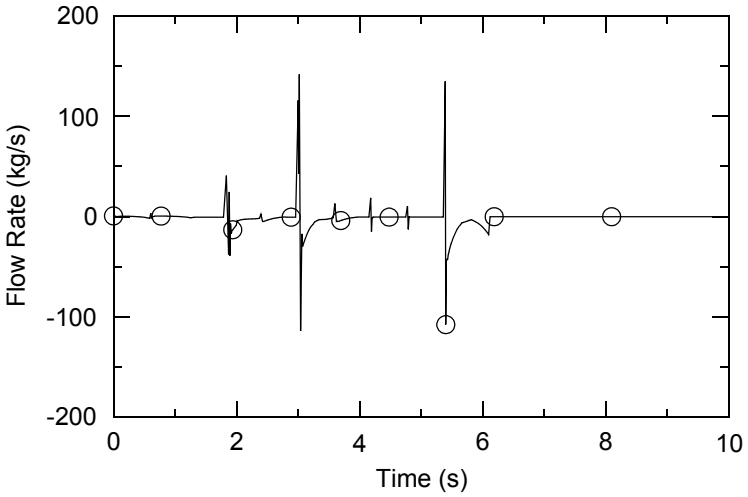

Figure. 7-29. Steam flow at the top of the condensation test pipe (simulated with the standard method of solution)

failure should be sought in the interfacial heat transfer model and its inability to properly describe cells that consist of phases separated by a moving phase front.

The results from the repeated condensation test, after the corrections in additional considerations made for the liquid-gas interface crossing the cell boundaries and Eqs. (7-91) and (7-92) are incorporated into the interfacial heat transfer model, demonstrate significant improvements to the simulation. First, the cell pressures along the test pipe show none of the spikes and other problems that had been recorded previously in Figure 7-26 and Figure 7-27. Previously, this test was simulated without and with the water packing model of TRACE to illustrate the difficulty of

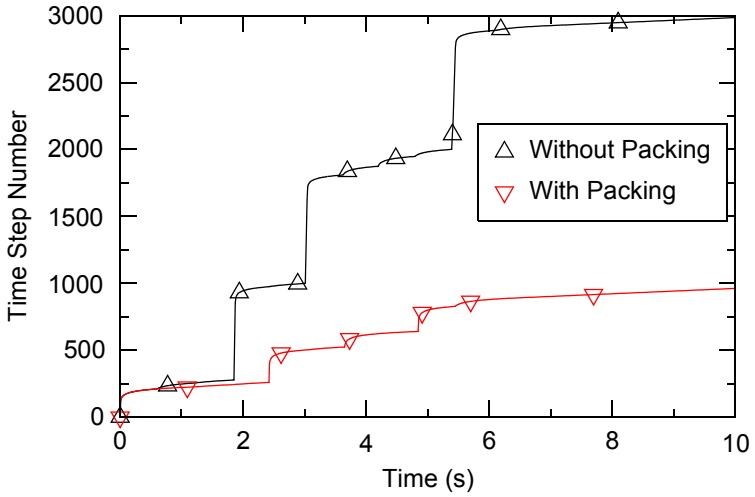

Figure. 7-30. Comparison of total time step numbers of condenstation test simulations (with and without the option for water packing treatment)

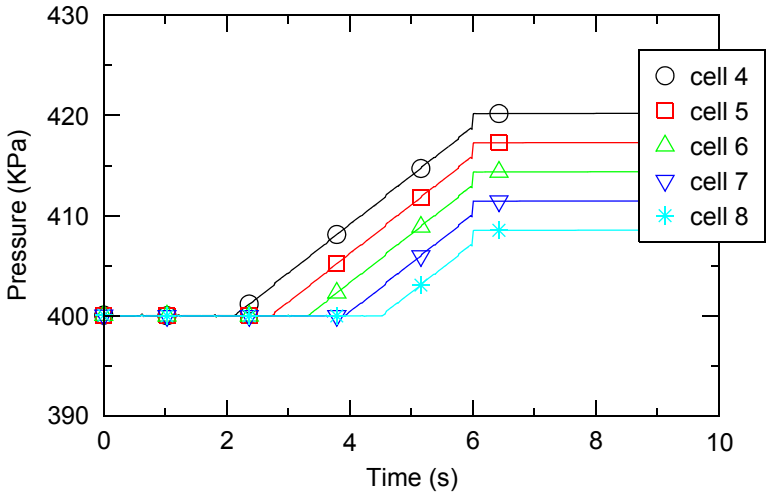

Figure. 7-31. Pressures along the condensation test pipe (simulated with the level tracking method)

simulating this test. A comparison of the required number of time steps as a function of the simulation time from the two simulations in Figure 7-30 had revealed a limited success with the water packing. When the water packing model of TRACE was engaged, the total number of time steps was reduced from 3000 to just below 1000. The adjustments made to the IHT model reduces the total number of time steps to 500. Figure 7-32 compares the number of time steps required to simulate the condenstation test with the standard solution, with the solution aided by the water packing model, and with the solution improved by the level tracking method. It is clear from Figure 7-32 that no additional time steps are needed as the moving crosses the cell boundaries when the level tracking method is engaged. The timestep number as function of simulation time

from the water packing exercise is compared to the repeated simulation following the changes to IHT in Figure 7-32 where the total number of timesteps is reduced to 585. The figure also shows that the solution spends no extra timestep as the moving water level fills up the cells with liquid water. This improvement is expected since the water packing model is a remedy for troubles after a cell is already "packed" while the level tracking method predicts the "packing" before it happens and adjusts the initial conditions of a time step to avoid the "packing."

As discussed previously, the superheated steam is withdrawn into the test pipe at the top to replenish the steam being condensed at it meets the subcooled water at the interface. Previously, large rates of steam flow were recorded in Figure 7-29 because of erroneous condensation taking place inside the test pipe. Figure 7-33 shows that the steam flow rate is much smaller and orderly when the solution is improved by the level tracking method. However, an irregular change in condensation is observed as the water level traverses the "inlet" and "exit" computational volumes of the test pipe. This inaccurate behavior is due to an inconsistent treatment of the end cells of one-dimensional flow segments defined within TRACE, and not due to the level tracking method.

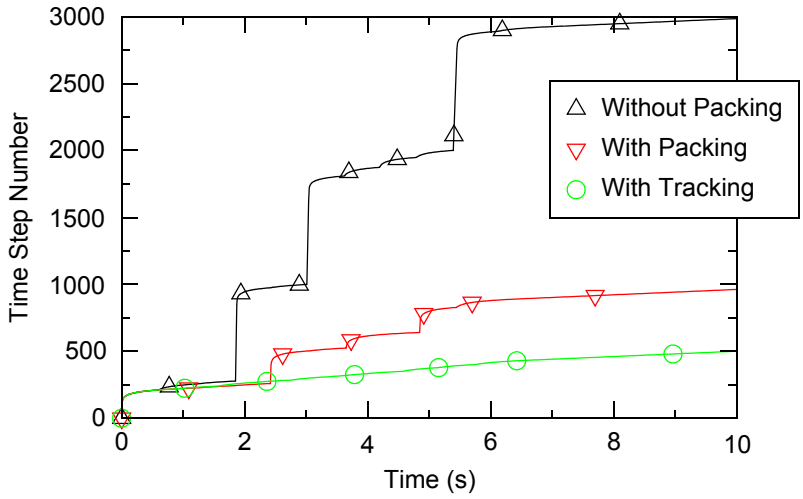

Figure. 7-32. Comparison of total time step numbers of the condenstation test simulations

One of difficulties stated for this exercise was the added complexity due to the build-up of a saturated layer of liquid at the tail of the moving water level. As this layer builds up, it should continuously decrease the rate at which the steam condenses at the surface. While there is no assurance yet for the accuracy of TRACE's ability to predict the condensation at the interface, a slight and gradual decrease in the condensation is observed as the water level traverses the "interior" cells of the test pipe. This observation is also enforced by the liquid temperatures shown in is seen in the simulation was due to an error in IHT coefficients for limiting void fractions, the liquid temperatures in Figure 7-34 that shows the build up of a warmer liquid layer. While a comparison of the liquid temperatures in Figure 7-34 to the temperatures previously recorded in Figure 7-28 leaves no doubt about the improvements to TRACE realized by the level tracking

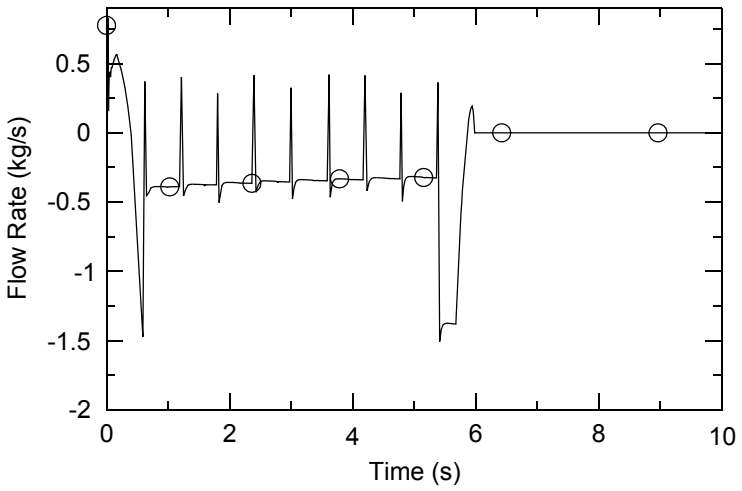

Figure. 7-33. Steam flow at the top of the condensation test pipe (simulated with the level tracking method)

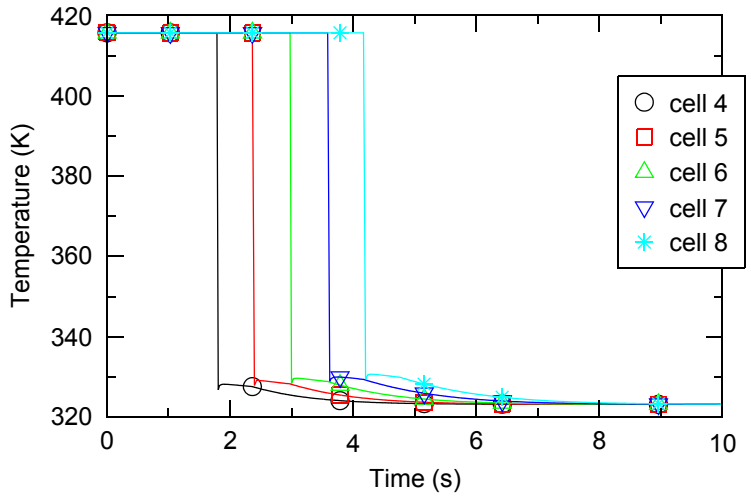

Figure. 7-34. Liquid temperatures along the condensation test pipe (simulated with the level tracking method)

method, it is extremely important to assess TRACE's ability to predict the interfacial heat transfer rate at the surface of liquid-gas interfaces by simulating an experiment with available data. The desired capability for TRACE is to predict the "correct" rate of condensation and the build-up of warmer liquid layer only due to the IHT at the surface of the water level.

Summary of the Simulations

All of the test problems discussed in this chapter are designed to measure the performance of the semi-implicit method of solution to the six-equation model in the presence of moving water levels. However, it should also be emphasized that these problems are designed to reveal the difficulties of a method and magnify them as much as possible, if there is any, so that these difficulties can be identified and studied further.

The results of the numerical experiments presented in this chapter can be summarized as follows:

1) All of the tests reveal that the solution method in TRACE fails to predict accurately the acceleration of liquid and gas fields in vertical paths when both fields are separated by a stratified liquid-gas interface. This failure is evident from the figures that show the transient behavior of fluid pressure in all tests.

2) The solution methods like the semi-implicit method, which are equipped with the standard upstream donor method in general, are unable to retain the liquid-gas interface. The figures that show the void fraction along the test pipes suggest that numerical diffusion of fluid mass is very high in the presence of stratified liquid-gas interface. Unlike the diffusion due to the discrete nature of the solution, the root cause of this failure is hidden behind the inability of the upstream donor method to recognize that a computational volume consists of two sub-volumes separated by a liquid-gas interface.

3) The mixture of steam and water poses added complexities due to the inability of the interfacial heat transfer model to distinguish the two sub-volumes, which are topologically different, separated by the liquid-gas interface. As the interfacial heat transfer model determines the heat transfer coefficients based on volume average void fraction, the interfacial heat transfer between the two fields is over or under predicted for the computational volume that consists of the liquid-gas interface.

4) The current measures built into the solution method, e.g. the water packing option, have limited success in mitigating the consequences of numerical water hammer when the sudden condensation is initiated by moving liquid-gas interfaces.

Offtake Model

The TRACE TEE-component offtake model is designed specifically to handle the case of fluid flow through a small break that is made in a larger pipe containing horizontal stratified flow (Ref. 7-12). One example of a transient that is particularly well-suited for use with the offtake model is a LOCA, in which a small break occurs in one of the large-diameter horizontal pipes of the reactor inlet or outlet legs. During this transient, horizontal stratified flow may occur and the flow quality discharged at the break will depend on whether the break is above or below the liquid level. To accurately follow the progression of the transient, it is essential that the offtake flow be predicted correctly.

The TRACE TEE-component offtake model predicts the offtake flow quality that exits the break based on conditions in the main pipe in a manner similar to that developed for use in the RELAP5/MOD2 code (Ref. 7-13). When the entrance plane to the break is submerged, the offtake flow consists mostly of liquid with possibly an entrained gas component. When the entrance plane is above the liquid level, the offtake flow is mostly gas with possibly an entrained liquid component.

The model is implemented as an option that the user may activate via input. To use the model for its intended purpose, the following three assumptions on the geometry of the problem are enforced in the code:

1) The side tube of the TEE is required to be either top, bottom, or centrally located off the main tube.
2) The angle from the low-numbered side of the main tube to the side tube must be 90°.
3) The main-tube-junction cell must be horizontal.

If these three conditions are not met by the input deck TEE geometry, the problem terminates in the initialization stage with a fatal error concerning inappropriate offtake geometry.

Several studies have been performed to investigate the discharge characteristics of a small break located on a horizontal pipe containing stratified flow. In these studies, the offtake was either top, bottom, or centrally oriented from the main tube as shown in Figure 7-35. The following discussion describes each of these three offtake geometries and the flow correlations developed for Reference 7-13. The TRACE computational sequence for the offtake model and a more detailed description of the original experimental work may be found in **Appendix D** and References 7-14 to 7-17.

In each of the three offtake configurations of Figure 7-35, a critical height at which gas or liquid entrainment begins, h_b, may be calculated using major-phase conditions at the entrance plane, such that:

$$h_b = \frac{C_1 W_k^{0.4}}{(g\rho_k \Delta\rho)^{0.2}} \tag{7-105}$$

where C_1 = a constant determined from data, W_k = major-phase mass-flow rate, g = gravitational constant, ρ_k = major-phase density, and $\Delta\rho = \rho_l - \rho_g$ = phasic density difference. For an upward offtake or for a side-oriented offtake with a liquid level *below* the offtake center, the major phase comprises the gas component. For a downward offtake or for a side-oriented offtake with a liquid level *above* the offtake center, the liquid component constitutes the major phase. The values of the constant C_1 recommended for use by Reference 7-12 are summarized in Table 7-1. This formulation for h_b can be derived theoretically for each of the three offtake geometries by considering the force exerted on the liquid particles by the

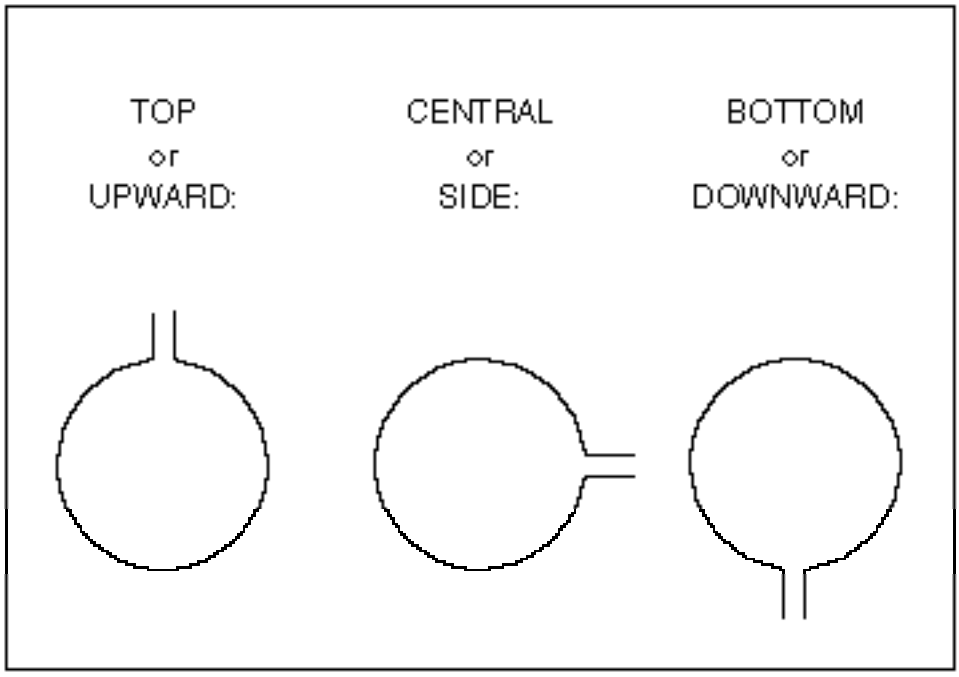

Figure. 7-35. Possible offtake configurations

Table 7-1. Critical Height Correlation Constant

Offtake Geometry	Correlation Constant, C_1
Upward	1.67
Downward	1.50
Side (gas entrain.)	0.75
Side (liquid entrain.)	0.69

accelerating gas flow for liquid entrainment in upward or side-oriented offtakes and by considering surface instability effects for gas entrainment in downward offtakes (Refs. 7-13, 7-16 and 7-17). An actual characteristic height, h, measured as the distance from the offtake entrance plane to the liquid level, may be determined for each of the three offtake geometries as shown in Figure 7-36.

The nondimensional height ratio, R, then may be represented as

$$R = \frac{h}{h_b} \tag{7-106}$$

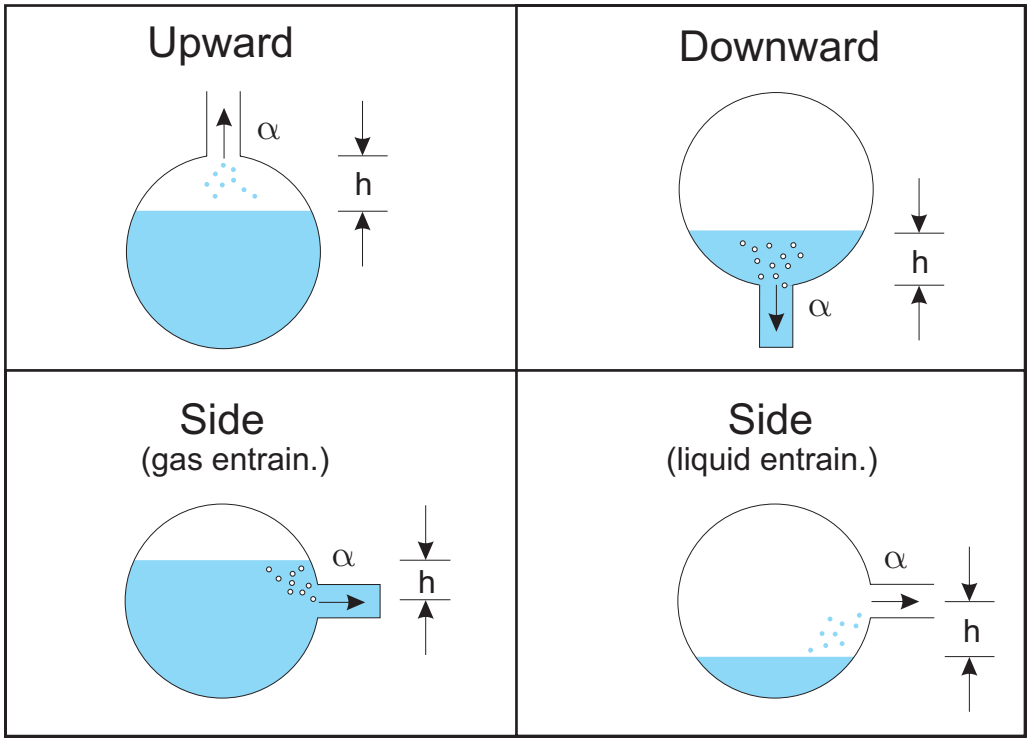

Fig. 7-36. Determination of actual characteristic height, *h*.

where h = actual characteristic height and h_b = critical height [as defined by Eq. (7-105)].

Reference 7-13 recommends that the offtake flow quality x, which has been correlated as a function of the nondimensional height ratio, R, be calculated for each of the three offtake geometries as follows.

For an upward offtake,

$$x = R^{3.25(1-R)^2} \tag{7-107}$$

where R = nondimensional height ratio [as defined by Eq. (7-106)].

For a side-oriented offtake,

$$x = x_0^{(1+C_2R)}\left[1 - 0.5R(1+R)x_0^{(1-R)}\right]^{0.5} \tag{7-108}$$

$$x_0 = \frac{1.15}{1+\sqrt{\frac{\rho_l}{\rho_g}}} \tag{7-109}$$

R = nondimensional height ratio [as defined by Eq. (7-106)], ρ_l = liquid-phase density at the entrance plane, ρ_g = gas-phase density at the entrance plane, and C_2 = 1.09 for gas entrainment or 1.00 for liquid entrainment.

For a downward offtake,

$$x = x_0^{2.5R}[1 - 0.5R(1 + R)x_0^{(1-R)}]^{0.5} \tag{7-110}$$

where x_o is given by Eq. (7-109), R = nondimensional height ratio [as defined by Eq. (7-106)], ρ_l = liquid-phase density at the entrance plane, and ρ_g = gas-phase density at the entrance plane.

From the prediction of the offtake quality and knowledge of the phasic velocities and densities at the break, TRACE finally determines the offtake void fraction.

In conclusion, summarizing, the TRACE TEE-component offtake model predicts the flow discharged from a small break that is located in a large pipe containing horizontal stratified flow. The current model is able to accommodate three different offtake geometries: upward offtake, side-oriented offtake, and downward offtake. TRACE calculates an offtake void fraction from flow correlations for the particular offtake geometry being modeled. As explained in more detail in **Appendix D**, a first prediction of the offtake void fraction is then sent through one interpolation based on the liquid level, one weighting based on the degree of horizontal stratification and one limit based on the maximum allowable entrainment volume to arrive at the final offtake void fraction.

Form Loss Models

There are four contributions to the pressure gradient for steady-state single phase pipe flow: wall drag, gravity head, recoverable flow-area change loss/gain, and irrecoverable loss. The purpose of this section is to document how TRACE deals with the recoverable and irrecoverable contributions to the overall pressure gradient.

The recoverable flow area change loss/gain comes from the change in the momentum flux term in the TRACE momentum equations. Consider the single-phase steady-state momentum equation with gravity and wall shear neglected:

$$\frac{1}{\rho} \cdot \frac{\partial P}{\partial x} + V\frac{\partial V}{\partial x} = 0 . \tag{7-111}$$

For a pipe noded as in Figure 7-37, integration of Eq. (7-111) with the assumptions of steady state and of constant density from point j to point $j+1$ yields a Bernoulli-type equation for the pressure change from point j to point $j+1$ as follows:

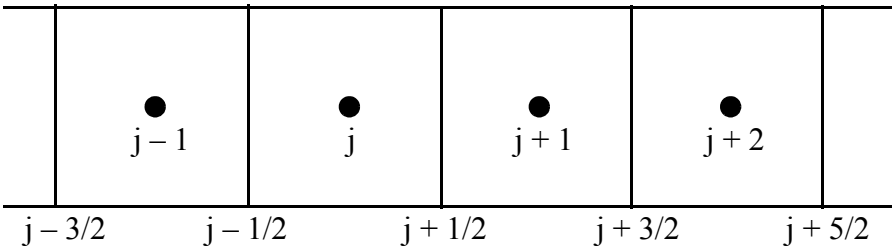

Figure. 7-37. 1D TRACE noding.

$$P_{j+1} - P_j = \rho\left(\frac{V_j^2}{2} - \frac{V_{j+1}^2}{2}\right) \tag{7-112}$$

In terms of the pressure drop from cell center j to cell center $j+1$, Eq. (7-112) becomes

$$\Delta P_{j \to j+1} = -(P_{j+1} - P_j) = \rho\left(\frac{V_{j+1}^2}{2} - \frac{V_j^2}{2}\right). \tag{7-113}$$

Assuming constant volumetric flow from j to $j+1$, then Eq. (7-113) can be written as:

$$\Delta P_{j \to j+1} = \rho\frac{V_j^2}{2}\left[\left(\frac{A_j}{A_{j+1}}\right)^2 - 1\right] \tag{7-114}$$

From Eq. (7-114), it should be obvious that a sudden contraction (see Figure 7-38), where $A_j < A_{j+1}$, will result in a positive pressure drop, while a sudden expansion (see Figure 7-39), where $A_{j+1} < A_j$, will result in a negative pressure drop. It should also be obvious that the pressure loss for a sudden contraction followed by a sudden expansion with the same area ratio will result in complete recovery of the sudden contraction pressure loss. As a result, the pressure difference due to the change in momentum flux is typically referred to as the recoverable flow area change pressure loss/gain.

Note – The TRACE one-dimensional staggered difference scheme involves pressures at cell centers and velocities at cell edges. In addition, the backward differencing for the change in momentum flux has been found to be stable and robust, but does not yield a Bernoulli-like solution for single phase incompressible flow. Therefore, an area ratio model — described in **Chapter 1** — was developed to ensure that the stable and robust differencing in TRACE also accurately conserves momentum flux.

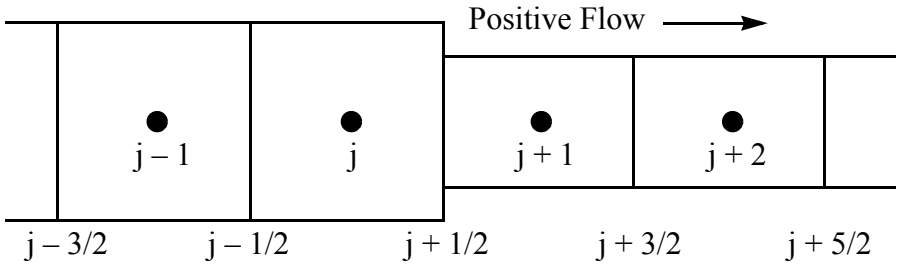

Figure. 7-38. TRACE noding for abrupt contraction if $V_{j+1/2} > 0$ and for abrupt expansion if $V_{j+1/2} < 0$.

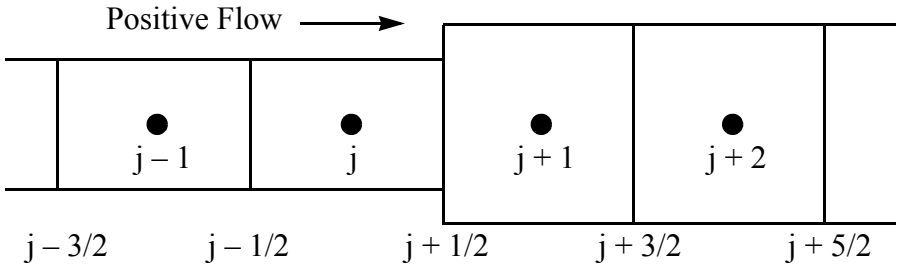

Figure. 7-39. TRACE noding for abrupt expansion if $V_{j+1/2} > 0$ and for abrupt contraction if $V_{j+1/2} < 0$.

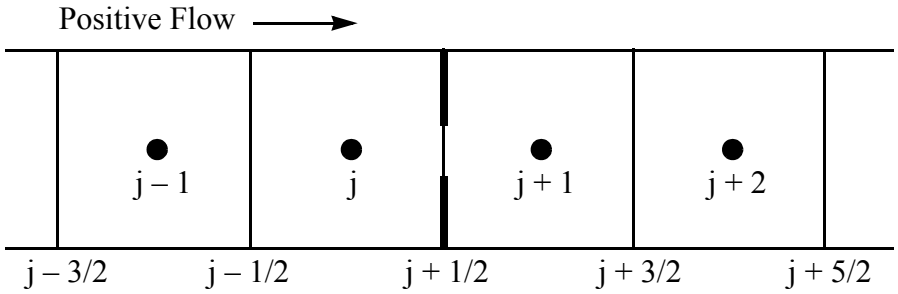

Figure. 7-40. TRACE noding for sharp-edged, thin-plate orifice.

Irrecoverable pressure losses occur at area changes, pipe bends, flow through orifice, flow through tee or manifold, etc. These irrecoverable pressure losses are associated with irrecoverable energy loss from the system typically associated with the creation of turbulence and the deviation of the flow from smooth straight stream lines. The modeling equation in TRACE for this irrecoverable pressure loss is based on a form loss factor of the form

$$\Delta P_{irreversible} \sim \rho K \frac{V^2}{2} \tag{7-115}$$

So let's put this together with what we know already about the reversible losses. Consider the following three situations. If no area change occurs between points j and $j+1$, the velocity of the flow does not change, and Eq. (7-113) predicts

$$\Delta P_{j \to j+1} = 0 \tag{7-116}$$

as expected. If a smooth area change occurs between sections j and $j+1$, then the irreversible losses may be small, and Eq. (7-113) yields an approximation to the pressure drop from point j to $j+1$. If the area change between cells j and $j+1$ is abrupt, however, the irreversible losses cannot be ignored, and it is standard practice to add a form-loss factor like that shown in Eq. (7-115) to Eq. (7-113) to account for the additional irrecoverable pressure loss caused by the area change in question. This yields a general equation for the pressure drop between sections j and $j+1$ when an abrupt area change is present, such that

$$\Delta P_{j \to j+1} = -(P_{j+1} - P_j) = \rho \left(\frac{V_{j+1}^2}{2} - \frac{V_j^2}{2} \right) + \rho K \frac{V_{j+1/2}^2}{2} \tag{7-117}$$

where $V_{j+1/2}$ is the velocity at the cross section where the area change occurs. Once the loss coefficient K for the specific area change in question has been determined, either theoretically or experimentally, the pressure drop at the abrupt area change can be calculated using Eq. (7-117) above.

The big question, of course, is "where do the K-factors come from?" TRACE provides the ability to account for irrecoverable losses via user input by supplying a form loss factor at any 1D or 3D cell edge. Situations that might require the need to specify a non-zero K-factor include flow through abrupt expansions or contractions, flow across a thin-plate orifice, flow around a bend, flow streams that merge or split, flow across obstructions, etc (really, any complex flow topology that leads to separation of the flow from the wall). Normally, it is incumbent upon the user to consult a body of knowledge like Reference 7-18 or 7-19 to determine the appropriate K-factor for the situation at hand.

For the case of abrupt area expansions and contractions in 1D and 3D flow channels, TRACE is able to determine, on its own, the appropriate K-factor, provided you have engaged the proper modeling flag (see the description of the NFF flag in the TRACE User's Guide). In such instances, TRACE will calculate a form-loss coefficient based on the user-input cell-edge flow area, the volume-averaged mesh-cell flow area ($A_j = vol_j/\Delta x_j$), and the direction of the fluid velocity. TRACE then adds this additional form-loss term to the momentum equation to account for the irrecoverable losses caused by the abrupt area change. These models are described in subsections below.

Note – In order to support old TRAC-P input models, TRACE retains the capability for the user to provide additive FRIC values rather than form loss factors to simulate irrecoverable losses. The relationship between form loss factors and FRIC input values is given by $K = (FRIC \cdot L)/D$, where L is the cell-center to cell-center distance and D is the user-supplied hydraulic diameter for the cell edge for which the FRIC value has been input. In general, you should use K-factors, since formulas and data for form loss factors are available, while FRIC values require additional computations for input preparation. In addition, any changes in noding around a user-input FRIC requires that the user re-calculate the input for FRIC

The flow loss of a thin-plate orifice that is modeled at a mesh-cell interface is associated with an abrupt flow-area change. This flow loss is also discussed below, but it is not added by TRACE automatically as an additional loss because . Such losses that are modeled at interfaces need to be defined by the user through additive form-loss-coefficient input data.

In a related way, the existence of a thin-plate orifice creates an abrupt flow-area change and also results in irrecoverable pressure losses. While methods do exist to determine the appropriate loss coefficient analytically, in practice, we have found this impossible to implement as an automatic option because there is no unique criteria for detecting such a flow topology. It is possible to create input models that have cell-edge flow areas that are less than both of the bounding mesh-cell flow areas, even though in reality there is no thin-plate orifice. Therefore, if a thin-plate orifice exists, you must supply your own user-defined K-factors to account for the irreversible losses; there is no internal calculation for such a loss that can be selected via the input. A recommendation for user determination of an appropriate loss coefficient is given in a subsection below.

Before proceeding, it is worth noting that there is no input option to select automatic internal calculation of losses from abrupt expansions or contractions at the three interfaces of the TEE joining cell. Also, the flow-area ratios logic for reversible losses (as documented in **Chapter 1**) is not activated at the three interfaces of the TEE joining cell. As such, you must account for any additional losses that result from flow merging, splitting, or abrupt area changes with appropriate use of the form-loss input array data that specifies K-factors at 1D mesh-cell interfaces. Reference 7-20[1] is a source of such data. The current TEE-component momentum-source-term logic is

1. You are cautioned to note that the correlations for TEE losses in this document include velocities based on experiments that have equal flow areas in all three TEE flow channels.

discussed in **Chapter 1**. We note here that while this model exhibits numerical stability, it does not give perfect predictions of losses at TEE internal junctions. Usually, the current model will underpredict TEE losses, although in some situations the losses will be overpredicted.

Abrupt Expansion

To determine the loss coefficient for an abrupt expansion, consider the expansion of Figure 7-41. If the pipes run full and the flow is assumed steady, two simplifying assumptions may be made that allow the pressure change across the expansion to be calculated. First, assume that the pressure and velocity at section *j* are uniform across the cross section. This assumption is valid for the high Reynolds-number flow found in most practical applications. Second, assume that the pressure and velocity at section $j+1$ are also uniform. This assumption is valid if section $j+1$ is sufficiently downstream of the expansion where the mixing caused by the turbulence has had a chance to even out the velocity profile again. A control-volume analysis using steady-flow equations may now be made on the fluid contained between sections j and $j+1$.

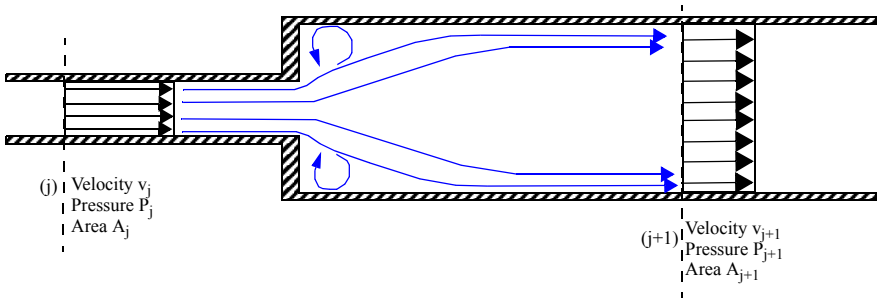

Figure. 7-41. Abrupt expansion.

Application of the momentum equation for steady, incompressible flow neglecting wall friction to the fluid between sections *j* and *j* + 1 yields the following force balance:

$$(P_j - P_{j+1})A_{j+1} = \rho Q(V_{j+1} - V_j) = \rho A_{j+1} V_{j+1}(V_{j+1} - V_j) \tag{7-118}$$

where Q is the volumetric flow rate and $V_j > V_{j+1}$ because of the change in the cross section at $j+1/2$. Therefore,

$$P_j - P_{j+1} = \rho V_{j+1}(V_{j+1} - V_j) \tag{7-119}$$

Application of the Bernoulli equation for an incompressible fluid yields

$$\frac{P_j}{\rho g} + \frac{V_j^2}{2g} - H_L = \frac{P_{j+1}}{\rho g} + \frac{V_{j+1}^2}{2g} \tag{7-120}$$

where H_L is the total head loss across the expansion. Solving Eq. (7-120) for this head loss gives

$$H_L = \frac{P_j - P_{j+1}}{\rho g} + \frac{V_j^2 - V_{j+1}^2}{2g} \tag{7-121}$$

Substitution for the term $P_j - P_{j+1}$ using Eq. (7-119) yields

$$H_L = \frac{(V_j - V_{j+1})^2}{2g} \tag{7-122}$$

From continuity, $A_j V_j = A_{j+1} V_{j+1}$ so that we may rewrite Eq. (7-122) as

$$H_L = \frac{V_j^2}{2g}\left(1 - \frac{A_j}{A_{j+1}}\right)^2 \tag{7-123}$$

Comparison of this result with Eq. (7-115) shows that the loss coefficient K for an abrupt expansion at the $j+1/2$ interface is

$$K = \left(1 - \frac{A_j}{A_{j+1}}\right)^2 . \tag{7-124}$$

Eq. (7-124) is also known as the Borda-Carnot loss coefficient.

Now that the theoretical loss coefficient K has been determined, the pressure change between points j and $j+1$ may be calculated using Eq. (7-117). Substitution of the result for K into Eq. (7-117) yields

$$\Delta P_{j \to j+1} = -(P_{j+1} - P_j) = \rho V_{j+1}(V_{j+1} - V_j) \tag{7-125}$$

which is exactly the result expressed in Eq. (7-119).

Abrupt Contraction

Consider the abrupt contraction of Figure 7-42. Although an abrupt contraction is geometrically the reverse of an abrupt expansion, it is not possible to solve exactly for the loss coefficient for an

abrupt contraction using a control-volume analysis on the fluid between sections j and $j+1$ as was done for the abrupt expansion of Figure 7-41. This is because the pressure at section j just upstream of the contraction varies in an unknown way as a result of the curvature of the streamlines and the acceleration of the fluid. Thus, application of the steady-flow momentum equation to the fluid at section j is not valid. Without the relationship between pressure and velocity provided by the momentum equation [as in Eq. (7-118) for the case of the abrupt expansion], it is not possible to solve explicitly for the total head loss across the contraction. Loss coefficients have been determined experimentally for circular coaxial pipes and fairly high Reynolds numbers, and Massey (Ref. 7-21) recommends the use of Table 7-2 when determining values for *K*.

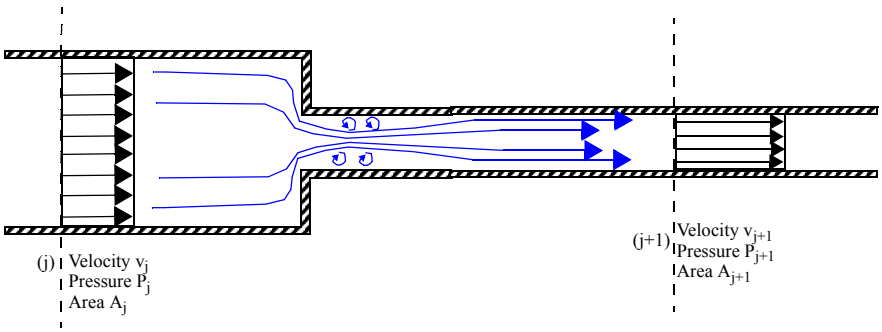

Figure. 7-42. Abrupt contraction.

Table 7-2. Abrupt Contraction Standard Loss-Coefficient Data

	A_{j+1}/A_j					
	0.0	0.04	0.16	0.36	0.64	1.0
K	0.5	0.45	0.38	0.28	0.14	0.0

Once K has been determined using Table 7-2, the pressure drop across the abrupt contraction may be calculated as follows. The flow at section j has a velocity V_j, while the flow upon reaching section $j+1$ has a velocity V_{j+1} that is higher than V_j because of the abrupt cross-section change. Using Eq. (7-117) to calculate the change in pressure from points j to $j+1$ caused by the abrupt area change yields

$$\Delta P_{j \to j+1} = -(P_{j+1} - P_j) = \rho\left(\frac{V_{j+1}^2}{2} - \frac{V_j^2}{2}\right) + \rho K \frac{V_{j+1}^2}{2} \tag{7-126}$$

where K is taken from Table 7-2

Thin-Plate Orifice

As in the case of the abrupt contraction, it is not possible to determine theoretically the loss coefficient across a thin-plate orifice, so experimental data must be used. For a sharp-edged, thin-plate orifice in a straight conduit, as shown in Figure 7-43, Idel'Chik (Ref. 7-18) suggests that the following expression be used for the loss coefficient K in the presence of high Reynolds number flow ($\geq 10^5$):

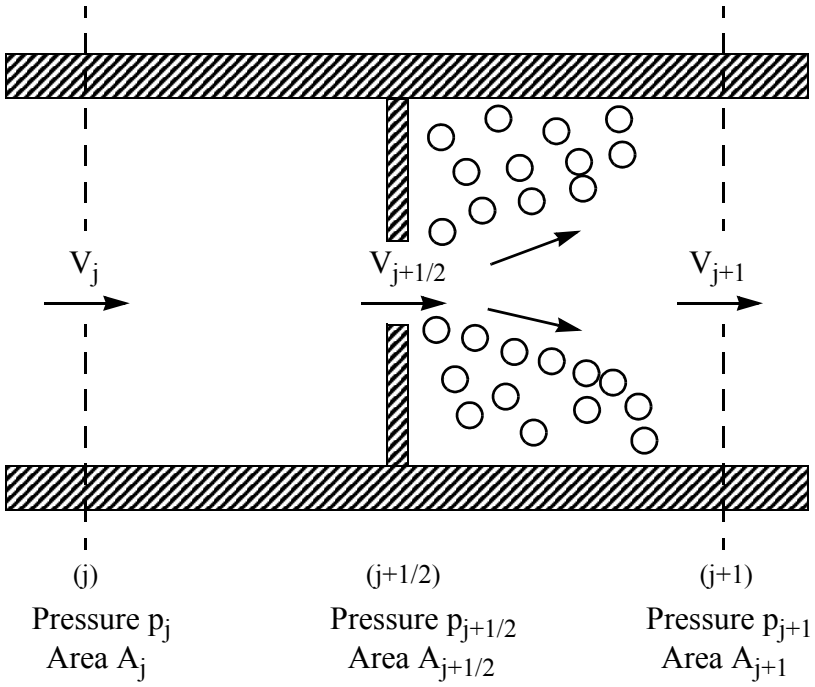

Figure. 7-43. Sharp-edged, thin-plate orifice.

$$K = \left(1 + 0.707\sqrt{1 - \frac{A_{j+1/2}}{A_j}} - \frac{A_{j+1/2}}{A_j}\right)^2 \tag{7-127}$$

This curve fit also agrees well with the data plotted in White (Ref. 7-22) for the irrecoverable head loss across a thin-plate orifice.

Once the loss coefficient K for a sharp-edged, thin-plate orifice has been determined using Eq. (7-127), the pressure drop across the orifice may be calculated as follows. The flow at section j has a velocity V_j, while the flow upon reaching section $j+1/2$ has a velocity $V_{j+1/2}$, which

is higher than V_j because of the abrupt cross-section change. Using Eq. (7-117) to calculate the change in pressure from points j to $j+1/2$ caused by the abrupt area change yields

$$\Delta P_{j\to j+1/2} = -(P_{j+1/2} - P_j) = \rho\left(\frac{V_{j+1/2}^2}{2} - \frac{V_j^2}{2}\right) + \rho K\frac{V_{j+1/2}^2}{2} \tag{7-128}$$

where K is calculated using Eq. (7-127). Another abrupt area change occurs between points $j+1/2$ and $j+1$. The flow at point $j+1/2$ has a velocity $V_{j+1/2}$, while the flow at point $j+1$ has a velocity V_{j+1}, which is less than $V_{j+1/2}$ because of the expansion in cross section. Because the irreversible losses caused by the presence of the orifice have already been accounted for in the pressure drop between j and $j+1/2$ and should not be accounted for twice, the pressure change between $j+1/2$ and $j+1$ is simply

$$\Delta P_{j+1/2\to j+1} = -(P_{j+1} - P_{j+1/2}) = \rho\left(\frac{V_{j+1}^2}{2} - \frac{V_{j+1/2}^2}{2}\right) \tag{7-129}$$

Adding Eq. (7-128) and Eq. (7-129) (noticing that $V_j = V_{j+1}$) shows that the total pressure drop from points j to $j+1$ for the orifice of Figure 7-43 is

$$\Delta P_{j\to j+1} = -(P_{j+1} - P_j) = \rho K\frac{V_{j+1/2}^2}{2} \tag{7-130}$$

where K should be calculated according to Eq. (7-127) and specified manually by the user during input as the additive form-loss coefficient.

Models as Coded

Again consider the momentum equation for single-phase flow, neglecting the gravity-head and wall-shear terms,

$$\frac{1}{\rho}\cdot\frac{\partial P}{\partial x} + \frac{1}{2}\frac{\partial V^2}{\partial x} = 0 \tag{7-131}$$

TRACE differences the momentum-convection term form in Eq. (7-131) (for the pipe noded as in Figure 7-37) as

$$\frac{1}{\rho}(p_{j+1} - p_j) + 0.5(V_{j+1}^2 - V_j^2) = 0 \tag{7-132}$$

Written in terms of a pressure drop between points j and $j+1$,

$$\Delta p_{j \to (j+1)} = -(p_{j+1} - p_j) = 0.5\rho(V_{j+1}^2 - V_j^2). \tag{7-133}$$

This finite-difference result is identical to the integral result of Eq. (7-113).

As before, if no area change occurs between points j and $j+1$, the velocity of the flow does not change, and Eq. (7-133) predicts

$$\Delta p_{j \to j+1} = 0 \tag{7-134}$$

as expected. If an abrupt area change between sections j and $j+1$ does occur, however, then a form-loss factor is again added to the pressure-drop equation to account for irreversible losses. This yields the general equation for a pressure drop between point j and $j+1$ when an abrupt area change is present, such that,

$$\Delta p_{j \to j+1} = -(p_{j+1} - p_j) = 0.5\rho(V_{j+1}^2 - V_j^2) + 0.5K_{TRACE}\rho V_s^2 \tag{7-135}$$

where V_s is the cell-edge velocity at the location of the area change.

In TRACE, pressures are cell-centered quantities whereas velocities are cell-edge quantities. Therefore, approximating the cell-centered velocities in Eq. (7-135) by donoring the interface velocities and assuming continuity of volumetric flow gives for a positive-direction flow velocity,

$$\Delta p_{j+1} = -(p_{j+1} - p_j) = 0.5\rho\left[\frac{A_{j+\frac{1}{2}}}{A_{j+1}} + \frac{A_{j+\frac{1}{2}}}{A_j}\right] V_{j+\frac{1}{2}}\left[\frac{A_{j+\frac{1}{2}}}{A_{j+1}} V_{j+\frac{1}{2}} - \frac{A_{j-\frac{1}{2}}}{A_j} V_{j-\frac{1}{2}}\right] \tag{7-136}$$

Because the pressure-drop equation in TRACE is identical in form to Eq. (7-117), the loss coefficient K_{TRACE} calculated by TRACE is exactly that developed in the previous pages for the cases of abrupt expansion and contraction. Namely, for an abrupt expansion noded as in Figure 7-39, TRACE calculates the loss coefficient as

$$K_{TRACE} = \left(1 - \frac{A_j}{A_{j+1}}\right)^2 \left(\frac{A_{j+1/2}}{A_j}\right)^2 \tag{7-137}$$

The factor $(1-A_j/A_{j+1})^2$ is the *K*-factor to be applied to the minimum flow-area-velocity squared, V_j^2, as presented in Eq. (7-124). The other factor $(A_{j+1/2}/A_j)^2$ converts that *K*-factor to K_{TRACE}, which is applied to the mesh-cell interface-velocity squared, $V_{j+1/2}^2$. This conversion is based on assuming continuity of volumetric flow; i.e., $A_j V_j = A_{j+1/2}\, V_{j+1/2}$. Similarly, the loss coefficient for an abrupt contraction noded as in Figure 7-38 is calculated by TRACE as a curve fit to the data of Table 7-2, such that

$$K_{TRACE} = \left\{0.5 - 0.7\left(\frac{A_{j+1}}{A_j}\right) + 0.2\left(\frac{A_{j+1}}{A_j}\right)^2\right\}\left(\frac{A_{j+1/2}}{A_{j+1}}\right)^2 \tag{7-138}$$

The bracketed factor is the K-factor to be applied to the minimum flow-area-velocity V_{j+1}^2 Multiplying by the following factor $(A_{j+1/2}/A_{j+1})^2$ defines K_{TRACE} to be applied to the mesh-cell interface-velocity squared, $V_{j+1/2}^2$.

TRACE is programmed also to add abrupt flow-area change losses to the 3D VESSEL component. Because NFF is not a VESSEL-component input parameter, the negative values for the liquid additive friction-loss coefficients CFZL-T, CFZL-Z, and CFZL-R are used as a user-defined input flag that turns on the 3D abrupt area change model. TRACE evaluates the same abrupt flow-area change loss and adds it to the absolute value of the input-specified additive friction-loss coefficient. This is done for both liquid and vapor and forward and reverse flow. The volume-averaged flow area in the radial direction for cylindrical geometry is divided by $R_{meanj} = \frac{R_{inj} + R_{outj}}{2}$ [that is, $\Delta\theta_j \cdot R_{meani} \cdot \Delta r_i \cdot \Delta z_k = vol_{ijk}$] to remove the smooth flow-area change effect from cylindrical geometry.

References

7-1 M. S. Sahota and J. F. Lime, "TRAC-PF1 Choked Flow Model", Los Alamos National Laboratory Report LA-UR-82-1666, also CONF-830103-8, Submitted to Second International Topical Meeting on Nuclear Reactor Thermal-Hydraulics, (Santa Barbara, California, January 1983).

7-2 J. W. Burnell, “Flow of Boiling Water through Nozzles, Orifices, and Pipes,” Engineering, pp. 572-576, (1947).

7-3 “RELAP5/MOD1 Code Manual, Volume 1: System Models and Numerical Methods,” Idaho National Engineering Laboratory report EGG-2070 Draft, Rev. 1, also NUREG/CR-1826 (March 1981).

7-4 M. D. Alamgir and J. H. Lienhard, “Correlation of Pressure Undershoot During Hot Water Depressurization,” Transactions of ASME, Journal of Heat Transfer, 103, pp. 52-73, (1981).

7-5 O. C. Jones, Jr., “Flashing Inception in Flowing Liquids,” Brookhaven National Laboratory report BNL-NUREG-51221, also NUREG/CR-1515, (1980).

7-6 N. Abuaf, O. C. Jones, Jr., and B. J. C. Wu, "Critical Flashing Flow in Nozzles with Subcooled Inlet Conditions", BNL-NUREG-27512, Brookhaven National Laboratory, 1980.

7-7 V. H. Ransom and J. A. Trapp, “The RELAP5 Choked Flow Model and Application to a Large Scale Flow Test,” in *ANS/ASME/NRC International Topical Meeting on Nuclear Reactor Thermal-Hydraulics* (Saratoga Springs, New York, 1980), pp. 799–819.

7-8 F. M. White, *Fluid Mechanics* (McGraw-Hill, Inc., New York, 1979), p 515.

7-9 G. B. Wallis, *One Dimensional Two Phase Flow* (McGraw-Hill Book Company, New York, 1969).

7-10 S. S. Kutateladze, *Izv. Akad. Nauk SSSR, Otd. Tekhn. Nauk*, Vol. 8, p. 529 (1951).

7-11 S. G. Bankoff, R. S. Tankin, M. C. Yuen, and C. L. Hsieh, “Countercurrent Flow of Air/Water and Steam/Water through a Horizontal Perforated Plate,” *International Journal of Heat and Mass Transfer*, **24**:8, pp. 1381–1395 (1981).

7-12 L. A. Crotzer, “TRAC-PF1/MOD2 TEE Component Offtake Model: A Completion Report,” Los Alamos National Laboratory report LA-UR-91-4052 (November 1991).

7-13 K. H. Ardron and W. M. Bryce, “Assessment of Horizontal Stratification Entrainment Model in RELAP5/MOD2,” United Kingdom Atomic Energy Authority, AEE Winfrith draft report AEEW-R 2345 (April 1988).

7-14 C. Smoglie, “Two Phase Flow Through Small Break Branches in a Horizontal Pipe with Stratified Flow,” Kernforschungszentrum Karlsruhe report KfK 3861 (December 1984).

7-15 V. E. Schrock, S. T. Revankar, R. Mannheimer, and C. H. Wang, “Small Break Critical Discharge—The Roles of Vapor and Liquid Entrainment in a Stratified Two-Phase Region Upstream of the Break,” Lawrence Berkeley Laboratory report LBL-22024 (NUREG/CR-4761) (December 1986).

7-16 T. Maciaszek and A. Menponteil, “Experimental Study on Phase Separation in a Tee Junction for Steam-Water Stratified Inlet Flow,” European Two-Phase Flow Group Meeting, Munich, Germany, June 10-13, 1986.

7-17 J. L. Anderson and R. L. Benedetti, “Critical Flow Through Small Pipe Breaks,” Electric Power Research Institute report EPRI NP-4532 (May 1986).

7-18 I. E. Idel’Chik, *Handbook of Hydraulic Resistance, Coefficients of Local Resistance and of Friction,* National Technical Information Service Report NTIS AEC-TR-6630, p. 139, (1960).

7-19 “Flow of Fluids through Valves, Fittings, and Pipes,” Metric Edition-SI Units of the Crane Manual, Technical Paper No. 410M, Crane Co., New York (1977).

7-20 R. C. Blevins, *Applied Fluid Dynamics Handbook* (Krieger Publishing Co., Malabar, Florida, 1992).

7-21 B. S. Massey, *Mechanics of Fluids* (D. Van Nostrand Co., New York, 1968), pp. 217-219.

7-22 F. M. White, *Fluid Mechanics* (McGraw-Hill Book Co., New York, 1979), p. 384.

7-23 Ransom, V., “Numerical Benchmark Test No. 2.2: Oscillating Manometer,” *Multiphase Science and Technology*, **6**, Hemisphere Publishing, New York (1992), 591-609.

7-24 B. Aktas, "Level Tracking in Thermal-Hydraulic Simulations of Nuclear Reactors", Ph.D. Thesis, The Pennsylvania State University, State College, PA (2003)

8

Fuel Rod Models

TRACE includes an extensive library of temperature dependent material properties that enables it to model a wide variety of structural materials commonly used in reactor systems and test facilities. Of particular interest in reactor safety however, are the material properties and additional models that are specific to nuclear fuel rods. This section describes the properties and models used by TRACE to represent nuclear fuel and cladding materials. Included are sections to describe models and correlations for UO_2 and mixed oxide fuel thermal expansion, thermal conductivity, specific heat, density, and spectral emissivity for use in the heat-transfer calculations.

Correlations for Zircaloy cladding, Zircaloy dioxide, and fuel-cladding gap gases are also described. Because at high temperatures Zircaloy-based cladding can undergo an exothermic chemical reaction with steam, models for cladding oxidation and metal-water reaction are discussed in this section as well.

The TRACE materials library uses numerical indexes for each specific material. The material indexes in the TRACE library that apply to fuel and cladding are:

1 – mixed-oxide fuel;
2 – Zircaloy;
3 – fuel-clad gap gases; and
11 – Zircaloy dioxide.

Since there is no appreciable difference in material properties between conventional Zircaloy cladding and newer materials such as Zirlo and M5, TRACE uses the same material properties for all cladding types. While all properties include an emissivity for doing a radiative-heat-transfer calculation, the calculation is only done in connection with the gap-conductivity calculation. The film-boiling heat-transfer model also includes a radiative-heat-transfer calculation, but the emissivity is specified in connection with that model.

Nomenclature

The following nomenclature is used in this section:

c_p = specific heat capacity at constant pressure (J/kg-K)

h_{gap} = total gas gap heat transfer coefficient

h_{gas} = gap-gas conductance

$h_{contact}$ = fuel-cladding interfacial contact resistance

$h_{radiation}$ = fuel-to-cladding thermal radiation heat transfer coefficient

k = Boltzmann's constant (J/K) or thermal conductivity (W/m-K)

k_{gap} = gap-mixture thermal conductivity

$\Delta L / L_0$ = linear strain caused by thermal expansion

M = molecular weight

p = pressure (Pa)

p_{gap} = gap-gas pressure

T = temperature (K)

T_C = temperature (°C)

T_F = temperature (°F)

T_{REF} = reference temperature (K) for gas gap calculation

T_{cl} = fuel centerline temperature

T_{surf} = fuel surface temperature

T_f = fuel temperature

T_c = cladding temperature

T_{co} = cladding outside temperature

T_{cl} = cladding inside temperature

T_{gap} = average gap gas temperature

x = mole fraction

f_{TD} = fraction of theoretical fuel density

f_{PuO_2} = weight fraction of PuO_2 in the fuel

f_{UO_2} = weight fraction of UO_2 in the fuel

r = reacting surface radius (m)

m'_{Zr} = mass per unit length of zirconium consumed in metal-water reaction

q'''_{mw} = heat source added to conduction equation from metal-water reaction

Δr_{gap} = fuel-cladding radial gas gap distance

R_o = cladding outer surface radius (m)

R_f, R_f* = radius of the outer fuel surface

R_c, R_I = radius to the inner cladding surface

$u(r)$ = radial displacement of a fuel region

Greek

α = linear thermal-expansion coefficient

δ_r = characteristic dimension for a closed gap

δ_o = initial, undeformed radial thickness of cracked fuel

δ_{cf} = cracked fuel deformed thickness

δ_{gap} = radial gap width after thermal expansion of fuel and cladding

δ_{ZrO_2} = thickness of zirconium oxide layer

ε = emissivity

ε_f = fuel emissivity

ε_w = cladding surface emissivity

η_1, η_2, η_3 = parameters in metal-water reaction model

λ = characteristic fuel RMS roughness

ν = Poisson's ration

ρ = density (kg/m^3)

ρ_{ZrO_2} = density of zirconium oxide (kg/m^3)

σ_{SB} = Stefan-Boltzmann constant (W/m^2/K^4)

τ = kinetic parameter representing total oxygen consumed (kg/m^2)

Subscripts

c = cladding

cl = centerline

f = fuel

cf=cracked fuel

gap = gas gap

i = i-th constituent gas

j = j-th constituent gas

new = value after thermal expansion

r = radial direction

$steam$ = steam

$surf$ = surface

z = axial direction

Superscripts

n = time step

$n+1$ = time-step increment

Nuclear Fuel Mixed-Oxide Properties

TRACE calculates the properties for mixed-oxide (UO_2 and PuO_2) nuclear fuels. The values determined by TRACE are dependent on three input variables: the fraction of theoretical density, the fraction of plutonium dioxide in the fuel, and the fuel burnup. Property changes upon melting are not included in this code version.

Fuel Density

The model for fuel density in TRACE accounts for dimensional changes in the fuel pellets due to temperature. Dimensional changes affect the pellet to cladding gap size, which in turn affects the gap heat transfer and stored energy of the fuel in a safety analysis. The model is valid for UO_2, PuO_2, and their mixed oxides. Fuel density is calculated with a correction factor to account for thermal expansion, which is assumed to be axisymmetric, as

$$\rho = \frac{f_{TD}[(1-f_{PuO_2})\rho_{UO_2} + f_{PuO_2}\rho_{PuO_2}]}{\left(1+3\frac{\Delta L}{L_0}\right)} \tag{8-1}$$

where

ρ = density (kg/m^3)

f_{TD} = fraction of theoretical fuel density,

f_{PuO_2} = weight fraction of PuO_2 in the fuel,

ρ_{UO_2} = 10970 kg/m^3

ρ_{PuO_2} = 11460 kg/m^3

$\frac{\Delta L}{L_0}$ = strain caused by thermal expansion (equal to 0 at 300 K, unitless).

The equations for linear expansion of UO_2 and PuO_2 have the same form. The value calculated for the linear thermal expansion is based on the following expression from MATPRO (Ref. 8-1).

$$\frac{\Delta L}{L_0} = K_1 T - K_2 + K_3 e^{-E_D/kT} \tag{8-2}$$

where T is temperature (K) and k is the Boltzmann's constant ($= 1.38\times10^{-23}$ J/K). The constants K_1, K_2, K_3 and E_D are listed in Table 8-1.

Table 8-1. Fuel Linear Expansion Coefficients

Constants	UO_2	PuO_2 and Mixed Oxides	Units
K_1	1.0×10^{-5}	9.0×10^{-6}	K^{-1}
K_2	3.0×10^{-3}	2.7×10^{-3}	–
K_3	4.0×10^{-4}	7.0×10^{-2}	–
E_D	6.9×10^{-20}	7.0×10^{-20}	J

For mixed UO_2 and PuO_2, the thermal expansion is found by combining the contribution from each constituent in proportion to its weight fraction.

Specific Heat

The expression for fuel specific heat is also obtained from MATPRO (Ref. 8-2), (Ref. 8-3). The following mixed-oxide fuel-specific heat correlations are calculated as:

$$c_P = 15.496\left\{\frac{b_1 b_4^2 \exp(b_4/T)}{T^2[\exp(b_4/T)-1]^2} + 2b_2 T + \frac{b_3 b_5}{b_6 T^2}\exp(-b_5/b_6 T)\right\} \quad (8\text{-}3)$$

where c_P = specific heat capacity (J/kg-K). The constants b_1 through b_6, are listed in Table 8-2.

Table 8-2. Fuel Specific Heat Coefficients

Constants	Uranium Dioxide	Mixed Oxides
b_1	19.145	19.53
b_2	7.8473×10^{-4}	9.25×10^{-4}
b_3	5.6437×10^{6}	6.02×10^{6}
b_4	535.285	539.0
b_5	37694.6	40100.0
b_6	1.987	1.987

Fuel Thermal Conductivity

The thermal conductivity of UO_2 and mixed oxides is a fit to data. The fuel thermal conductivity correlations are taken from the MATPRO (Ref. 8-2). Separate correlations are employed for temperatures $0 < T_C \leq T_L$ deg C, and $T_L < T_C < 2840$ deg C. The break between the low and high temperature regions depends on the oxide. Both expressions include correction factors to account for porosity and density.

For $T_C < T_L$

$$k = c\left[\frac{c_1}{c_2 + T_C} + c_3 \exp(c_4 T_C)\right] \quad (8\text{-}4)$$

and for $T_C > T_L$,

$$k = c\,[c_5 + c_3 \exp(c_4 T_C)] \quad (8\text{-}5)$$

where, T_C is in degrees Celsius and c is the porosity correction factor.

For PuO_2 and mixed oxides the correction factor for porosity is given by:

$$c = 100.0\left[\frac{f_{TD}}{1-\beta(1-f_{TD})}\left(\frac{1+0.04\beta}{0.96}\right)\right] \tag{8-6}$$

and for UO_2 it is given by:

$$c = 100.0\left[\frac{1-\beta(1-f_{TD})}{1-0.05\beta}\right] \tag{8-7}$$

In these expressions, f_{TD} is the fraction of theoretical fuel density and

$$\beta = c_6 + c_7 T_C \tag{8-8}$$

The constants c_1 through c_7, and the transition temperature T_L are listed in Table 8-3.

Table 8-3. Fuel Thermal Conductivity Equation Coefficients

Constants	Uranium Dioxide	Mixed Oxides
c_1	40.4	33.0
c_2	464.0	375.0
c_3	1.216×10^{-4}	1.54×10^{-4}
c_4	1.867×10^{-3}	1.71×10^{-3}
c_5	0.0191	0.0171
c_6	2.58	1.43
c_7	-5.8×10^{-4}	0.0
T_L (°C)	1650.0	1550.0

Fuel Spectral Emissivity

The spectral emissivity of the fuel is used in calculation of the fuel to cladding heat conductance, which is described in a later section. Above approximately 1000 K the emissivity of reactor fuel decreases with temperature, and then becomes constant above about 2050 K. The correlations used in TRACE were obtained from MATPRO (Ref. 8-2). In these correlations, the spectral emissivity of both uranium dioxide and mixed oxide fuel is modeled as a linear function of temperature between 1000 and 2050 K. Outside this range, the emissivity is assumed to be independent of temperature. Eq. (8-9) lists the temperature range and spectral emissivity and Figure 8-1 compares the calculated emissivity with data by Claudson (Ref. 8-8) and Ehlert and Margrave (Ref. 8-9)..

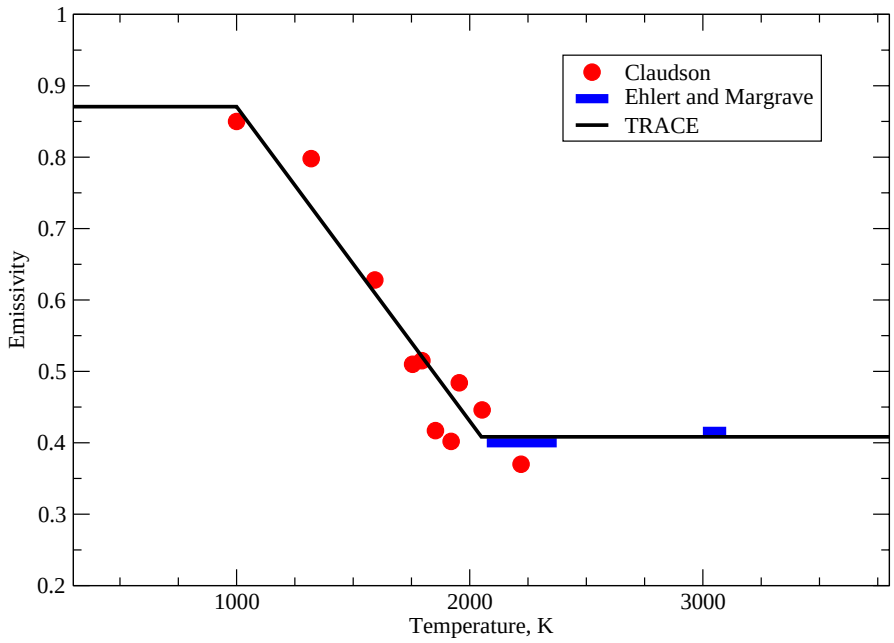

Figure. 8-1. Spectral Emissivity of Reactor Fuel

$$\varepsilon = \begin{cases} 0.8707 & ; \quad T \leq 1000 \text{ K} \\ 1.311 - 4.404 \times 10^{-4} T & ; \quad 1000 < T \leq 2050 \text{ K} \\ 0.4083 & ; \quad T > 2050 \text{ K} \end{cases} \tag{8-9}$$

Fuel Rod Gap Gas Properties

The gap between the fuel pellets and the cladding can be filled with gas mixtures containing helium, argon, xenon, krypton, hydrogen and nitrogen. TRACE models the thermal conductivity of these individual gases and their mixtures. This term is important on calculating the heat transfer between the pellet and the cladding. The thermal conductivity of the gap gas mixture is calculated using correlations obtained from MATPRO. Having said that, gap-gas properties are calculated only when the dynamic fuel-cladding-gap heat transfer coefficient (HTC) option is used (NFCI = 1).

The thermal conductivity is calculated as:

$$k_{\text{gap}} = \sum_{i=1}^{n} \left(\frac{k_i x_i}{x_i + \sum_{\substack{j=1 \\ j \neq 1}}^{n} \Psi_{ij} x_j} \right) \tag{8-10}$$

where, k_{gap} is gap mixture thermal conductivity (W/m-K), and

$$\Psi_{ij} = \phi_{ij} \left(1 + 2.41 \frac{(M_i - M_j)(M_i - 0.142 M_j)}{M_j (M_i + M_j)^2} \right) \tag{8-11}$$

and,

$$\phi_{ij} = \frac{\left[1 + \left(\frac{k_i}{k_j} \right)^{1/2} \left(\frac{M_i}{M_j} \right)^{1/4} \right]^2}{2^{3/2} \left(1 + \frac{M_i}{M_j} \right)^{1/2}} \tag{8-12}$$

In Eq. (8-11) and Eq. (8-12), k_i represents the constituent gas thermal conductivity (W/m-K), M_i is the constituent gas molecular weight, and x_i is constituent gas mole fraction. In TRACE, $2^{3/2}$ is approximated as 2.8284.

Except for water vapor, the thermal conductivity of the constituent gases are calculated using an expression with the general form based on the work of Gandhi and Saxena (Ref. 8-4):

$$k_i = a T^b \tag{8-13}$$

where T is the temperature of the gas mixture (K) and the subscript *i* is an index that denotes the particular gas of interest. The coefficients used in Eq. (8-13) for each gas are listed in Table 8-4.

Table 8-4. Gas Thermal Conductivity Coefficients

Gas	M	a	b
Helium	4.003	3.366×10^{-3}	0.668
Argon	39.944	3.421×10^{-4}	0.701
Xenon	83.80	4.0288×10^{-5}	0.872

Table 8-4. Gas Thermal Conductivity Coefficients

Krypton	131.30	4.726×10^{-5}	0.923
Hydrogen	2.016	1.6355×10^{-3}	0.823
Air/Nitrogen	28.8	2.091×10^{-4}	0.846

For water vapor, thermal conductivity is a function of both pressure and temperature, and the following correlation is used:

$$k_{steam} = (a_1 + a_2 T + a_3 T^2)\frac{p}{T} + \frac{a_4}{(T-273)^{4.2}}\left(\frac{p}{T}\right)^2 + a_5 + a_6 T + a_7 T^2 + a_8 T^3 \qquad (8\text{-}14)$$

where T is the temperature (K) and p is the gas pressure (Pa). The coefficients a_1 through a_8 are listed in Table 8-5. The molecular weight for water is 18.016.

Table 8-5. Water Vapor Thermal Conductivity Coefficients

Constants	Values
a_1	-2.8516 x 10^{-8}
a_2	9.424 x 10^{-10}
a_3	-6.004 x 10^{-14}
a_4	1.009
a_5	8.4083 x 10^{-3}
a_6	1.19998 x 10^{-5}
a_7	6.706 x 10^{-8}
a_8	4.51 x 10^{-11}

The thermal conductivity of a gas mixture is important not only when there is an open gap, but also when the gap is closed and the contact resistance must be determined. When the gap dimension shrinks to the order of the gas mean-free path, a correction factor is applied to the light-gas thermal conductivities to account for the change in energy exchange between the gas and the surface. The correction factor for hydrogen and helium is given in Reference 8-1 as:

$$k = \frac{k_i}{1 + f k_i} \tag{8-15}$$

where,

$$f = \frac{0.2103\sqrt{T_{gap}}}{p_{gap}\lambda} \ . \tag{8-16}$$

In Eq. (8-16), T_{gap} is the average gap gas temperature (K), p_{gap} is the gap-gas pressure, and λ is the characteristic fuel RMS roughness. Consistent with MATPRO, in TRACE the roughness is assumed equal to 4.389×10^{-6} m for commercial nuclear fuel. This correction is only made for hydrogen and helium. No correction is applied to the other component gases.

Zircaloy Cladding Properties

TRACE calculates the properties for Zircaloy and oxidized Zircaloy cladding. TRACE assumes the properties for all common Zircaloy based alloys; Zircaloy-2, Zircaloy-4, Zirlo, M5, E110, etc. to be identical. The only difference in properties between Zircaloy and oxidized Zircaloy is in the thermal conductivity. The equations used are based on the correlations in MATPRO (Ref. 8-1) and/or FRAPTRAN (Ref. 8-11).

Cladding Density

Zircaloy cladding exhibits an asymmetric thermal-expansion behavior. Thermal expansion is calculated in the radial and axial directions, and these effects are included in the density calculation as follows:

$$\rho = \frac{6551.4}{1 + \left[2\left(\frac{\Delta L}{L}\right)_r + \left(\frac{\Delta L}{L}\right)_z\right]} \tag{8-17}$$

where, for $T \leq 1073.15$ K

$$\left(\frac{\Delta L}{L}\right)_r = -2.373\times10^{-4} + 6.721\times10^{-6}\, T_C \tag{8-18}$$

and,

$$\left(\frac{\Delta L}{L}\right)_z = -2.506\times10^{-6} + 4.441\times10^{-6}\,T_C \tag{8-19}$$

For $1073.15 < T \leq 1273.15$,

$$\left(\frac{\Delta L}{L}\right)_r = 5.1395\times10^{-3} - 1.12\times10^{-5}(T - 1073.15) \tag{8-20}$$

and,

$$\left(\frac{\Delta L}{L}\right)_z = 3.5277\times10^{-3} - 1.06385\times10^{-5}(4.441\times10^{-6})\,T_C \tag{8-21}$$

and, for $T > 1273.15$ K:

$$\left(\frac{\Delta L}{L}\right)_r = -6.8\times10^{-3} + 9.7\times10^{-6}\,T_C \tag{8-22}$$

and

$$\left(\frac{\Delta L}{L}\right)_z = -8.3\times10^{-3} + 9.7\times10^{-6}\,T_C \tag{8-23}$$

In Equations (8-18) through (8-23), T = temperature (K) and T_C = temperature (^{o}C).

Cladding Specific Heat

The specific heat for all Zircaloy based alloys is obtained by linear interpolation of values listed in Table 8-6. This is the same table of values used by FRAPTRAN (Ref. 8-11), and represents a fit to several sets of experimental data. Below 1090 K the table values are based on data obtained by Brooks and Stansbury (Ref. 8-12). The standard error for data in this low temperature range is reported to be 1.1 J/kg-K for $300 < T < 800$ K and 2.8 J/kg-K for temperatures between 800 and 1090 K. Because Zircaloy undergoes a phase change (alpha to beta) from 1090 to 1248 K, there is a resultant sharp spike in the specific-heat values during the transition, as shown in Figure 8-2. The specific heat values in this transition region are based on data by Deem and Eldridge

(Ref. 8-13), with a standard error of 10.7 J/kg-K. For temperatures greater than 1248 K, a constant value of c_p = 356 J/kg-K is assigned.

Table 8-6. Zircaloy Specific Heat vs. Temperature for the α Phase and the Transition to the β Phase

T (K)	c_p (J/kg-K)
300	281
400	302
640	381
1090	375
1093	502
1113	590
1133	615
1153	719
1173	816
1193	770
1213	619
1233	469
1248	356

Cladding Thermal Conductivity

The thermal conductivity of Zircaloy is based on a fit to experimental data that included both Zr-2 and Zr-4. It is assumed that this conductivity is applicable to all Zircaloy based cladding. The correlation for Zircaloy thermal conductivity and its database is discussed in Reference (Ref. 8-11). For Zircaloy, the thermal conductivity is given by:

$$k_{Zr} = 7.51 + (2.09\times10^{-2})\,T - (1.45\times10^{-5})\,T^2 + (7.67\times10^{-9})\,T^3 \qquad (8\text{-}24)$$

The standard deviation of this correlation is reported to be 1.01 W/m-K. This correlation should be used for temperatures below 1800 K.

For zirconium dioxide, the following expression is used for thermal conductivity:

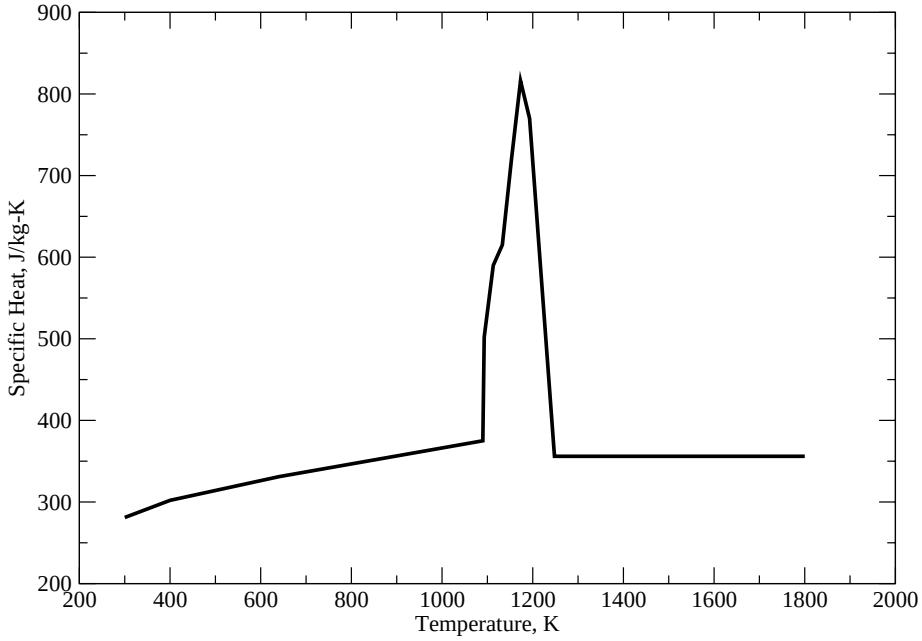

Figure. 8-2. Specific Heat for Zircaloy Based Cladding Materials.

$$k_{ZrO_2} = 1.96 - (2.41\times10^{-4})\,T + (6.43\times10^{-7})\,T^2 - (1.95\times10^{-10})\,T^3 \tag{8-25}$$

The temperature in both Equations (8-24) and (8-25) is in degrees Kelvin.

Cladding Spectral Emissivity

The emissivity of Zircaloy cladding depends on both temperature and thickness of the oxide layer on the surface of the cladding. For oxide layers less than 3.88×10^{-6} m, the emissivity can be estimated by (Ref. 8-11),

$$\varepsilon = 0.325 + (0.1246\times10^{6})\delta_{ZrO_2} \tag{8-26}$$

where δ_{ZrO_2} is the thickness of the zirconium oxide layer in meters.

For fresh fuel with low burnup, the oxide thickness is small and the emissivity is nominally 0.4. However, the emissivity increases with oxide thickness so that for layers exceeding 3.88×10^{-6} m

in thickness the emissivity exceeds 0.8. TRACE does not model the variation of emissivity with oxide thickness, but simply assigns a constant value of $\varepsilon = 0.75$. **Figure 8-3** shows several sets of experimental data for zirconium oxide and the value used by TRACE.

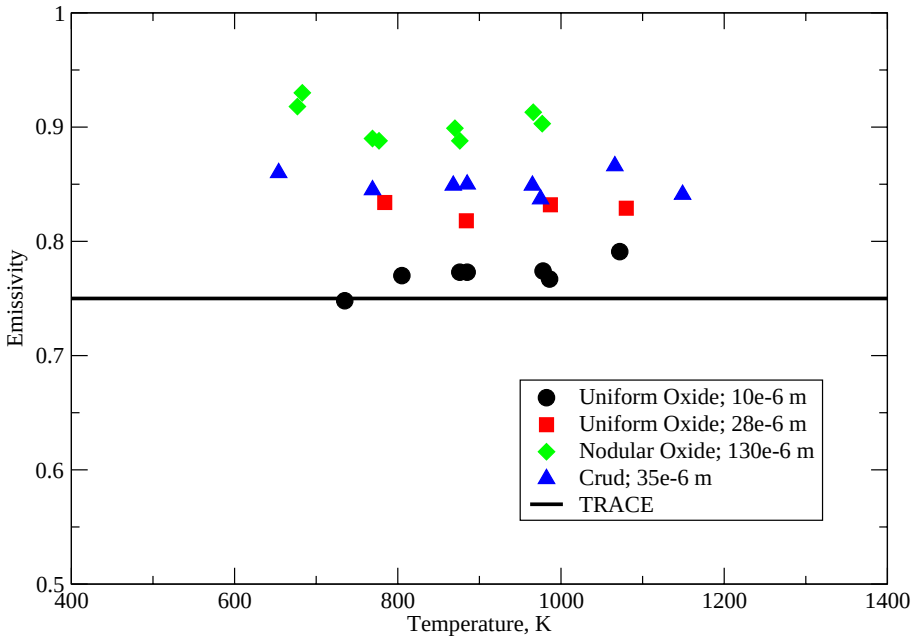

Figure. 8-3. Emissivity of zirconium oxide.

Fuel-Cladding Gap Conductance

The fuel-cladding gap conductance is a function of three components: the gap-gas conductance, fuel-cladding interfacial contact resistance, and fuel to cladding thermal radiation. In TRACE, a total gap heat transfer coefficient h_{gap} is defined as the sum of the heat transfer coefficients for each of these three components:

$$h_{gap} = h_{gas} + h_{contact} + h_{radiation} \tag{8-27}$$

where,

$$h_{gas} = \frac{k_{gas}}{(\Delta r_{gap} + \delta_r)} \tag{8-28}$$

$$h_{radiation} = \frac{\sigma_{SB} F (T_f^4 - T_c^4)}{(T_f - T_c)} \tag{8-29}$$

The view factor between the fuel and cladding assumes thermal radiation between two gray, diffuse, infinitely long concentric cylinders, and:

$$F = \frac{1}{\frac{1}{\varepsilon_f} + \frac{R_f}{R_c}\left(\frac{1}{\varepsilon_w} - 1\right)} \tag{8-30}$$

In Equations (8-28) through (8-30), k_{gas} is the gap-gas thermal conductivity, and T_f and T_c are the temperatures at the fuel outer surface and cladding inner surface at radii R_f and R_c, respectively. The fuel and cladding surface emissivities are ε_f and ε_w, respectively, and σ_{SB} is the Stefan-Boltzmann constant (= 5.67×10^{-8} W/m^2/K^4). The characteristic dimension δ_r for a closed gap is 4.4×10^{-6} m, which accounts for the mean surface roughness of the fuel and the cladding plus the temperature jump distances. The contact conductance, $h_{contact}$ is assumed to be zero.

Fuel - Cladding Gap Dimension

The fuel-cladding radial gas gap, Δr_{gap}, is found by using the uncoupled, quasi-static approximation (Ref. 8-7). In this approximation, the mechanical coupling term in the energy equation and the inertial term in the mechanical force balance are omitted. By neglecting these terms, we assume that the fuel-cladding strains minimally affect the temperature distribution and that displacements are instantaneous. Figure 8-4 shows the fuel-cladding gap system modeled in three regions: solid fuel, cracked fuel, and cladding. Please note that in the figure and in the following discussion on thermal expansion, the radii R_f and R_c are called R_f* and R_I, respectively.

Gap changes are found by calculating the radial displacement of each region caused by thermal expansion. The calculations for the deformation of a hollow or solid circular cylindrical body of outer radius b, inner radius a where $a = 0$ for a solid cylinder), and height h are given in Reference 8-7 for the case where the ratio h/b is large compared to unity. Other assumptions are

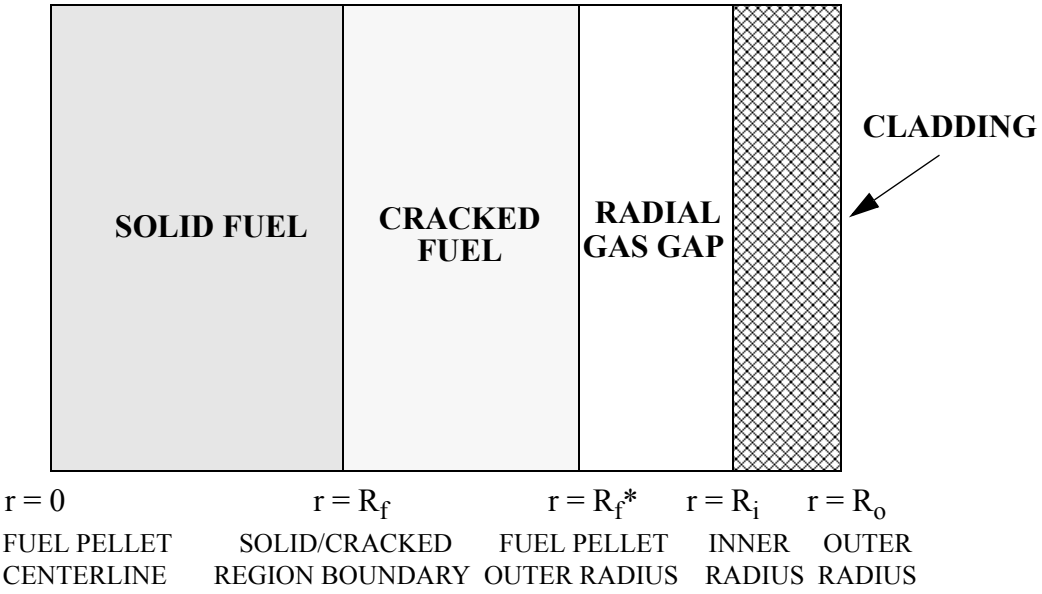

Figure. 8-4. Fuel rod geometry.

made that the cylindrical surfaces are free of forces, axial displacement is allowed, and the temperature distribution is a function of the radial distance only. Because the uncoupled, quasi-static approximation is used, the temperature distributions are assumed to be known from the energy balance. The radial displacement $u(r)$ is given by:

$$u(r) = \frac{\alpha}{r(1-\nu)}\left[(1+\nu)\int_a^r \Delta T r dr + \frac{(1-3\nu)r^2 + a^2(1+\nu)}{b^2 - a^2}\int_a^b \Delta T r dr\right] \tag{8-31}$$

where ν is Poisson's ratio, α is the linear thermal-expansion coefficient, and $\Delta T = (T - T_{REF})$. For purposes of this calculation, T_{REF} is set to 298.0 K. Eq. (8-31) is used to calculate the radial displacement of the cladding inner radius and the solid-fuel radius, $r = R_I$, and $r = R_f$, respectively. When radial symmetry is assumed (so that ν = 0), this expression becomes

$$u(R_I) = \frac{2\alpha R_I}{R_o^2 - R_I^2}\int_{R_I}^{R_o} \Delta T_c r dr \tag{8-32}$$

and,

$$u(R_f) = \frac{2\alpha_f}{R_f} \int_0^{R_f} \Delta T_f \, r \, dr \tag{8-33}$$

The cladding inner radius and the solid-fuel radius after thermal expansion are

$$R_{I,new} = R_I + u(R_I) \tag{8-34}$$

and,

$$R_{f,new} = R_f + u(R_f) \tag{8-35}$$

The cracked-fuel thickness is calculated using,

$$\delta_{cf} = \delta_o \left[1 + \left(\frac{\alpha_f}{R_f^* - R_f} \right) \int_{R_f}^{R_f^*} \Delta T_f \, dr \right] \tag{8-36}$$

where $\delta_o = R_f^* - R_f$ is the initial, un-deformed radial thickness of the cracked fuel.

A parabolic radial temperature distribution is assumed across the fuel pellet,

$$T_f(r) = T_{cl} + (T_{surf} - T_{cl}) \left(\frac{r^2}{R_f^{*2}} \right) \tag{8-37}$$

where T_{cl} is the fuel centerline temperature and T_{surf} is the fuel surface temperature. A linear temperature profile is assumed across the cladding,

$$T_c = T_{cI} + (T_{co} - T_{cI}) \left(\frac{r - R_I}{R_o - R_I} \right) \tag{8-38}$$

where T_{co} and T_{cI} are the cladding outside and inside temperatures, respectively. The radial gap width after thermal expansion is,

$$\delta_{gap} = R_{I,new} - (R_{f,new} + \delta_{cf}) \tag{8-39}$$

or,

$$\delta_{gap} = (R_I - R_f) + \frac{2\alpha_c R_I}{R_o^2 - R_I^2}\int_{R_I}^{R_o} \Delta T_c r dr - \frac{2\alpha_f}{R_f}\int_0^{R_f} (\Delta T_f) r dr - \delta_o\left[1 + \frac{\alpha_f}{R_f^* - R_f}\int_{R_f}^{R_f^*} (\Delta T_f) dr\right] \quad (8\text{-}40)$$

Metal - Water Reaction

When Zircaloy reaches a sufficiently high temperature in a steam environment, an exothermic reaction may occur that influences the peak cladding temperatures. This exothermic reaction, called the zirconium-steam reaction, is given by

$$Zr + 2H_2O \rightarrow ZrO_2 + 2H_2 + heat$$

With a sufficient steam supply, the following reaction-rate equation (Ref. 8-10) is assumed valid:

$$\tau\frac{d\tau}{dt} = \eta_1 e^{-\eta_2/T} \quad (8\text{-}41)$$

where τ represents the total oxygen consumed (kg/m^2), η_1 = 16.8 kg^2/m^{4}s, and η_2 = 20070 K.

The kinetic parameter τ is converted to an effective zirconium-oxide layer thickness according to

$$1.5(R_o - r) = \frac{\tau}{0.26\rho_{ZrO_2}} \quad (8\text{-}42)$$

where r = reacting surface radius (m), R_o = cladding outer radius (m), and ρ_{ZrO_2} = density of zirconium oxide (kg/m^3).

Eq. (8-42) is based on a reacted-material volume expansion of 50% in the radial direction. This assumption leads to $\rho_{ZrO_2} = 0.9\rho_{Zr}$, Eq. (8-42) allows Eq. (8-27) to be rewritten as

$$\tau\frac{d\tau}{dt} = -\eta_3(R_o - r)\frac{dr}{dt} \quad (8\text{-}43)$$

where

$$\eta_3 = (0.351\rho_{Zr})^2 \quad (8\text{-}44)$$

The method outlined in (Ref. 8-10) is used to calculate the zirconium-oxide penetration depth and associated heat source. The mass per unit length of zirconium m'_{Zr} consumed by the reaction in one time step is

$$(m'_{Zr}) = \pi \rho_{Zr} [(r^n)^2 - (r^{n+1})^2] \tag{8-45}$$

Eq. (8-41) is used to calculate r^{n+1}, yielding

$$r^{n+1} = R_o - \left[(R_o - r^n)^2 + 2\left(\frac{\eta_1}{\eta_3}\right)(\Delta t) e^{-\eta_2/T} \right]^{\frac{1}{2}} \tag{8-46}$$

If a single-region cladding is assumed, the heat source q'''_{mw} added to the conduction equation is

$$q'''_{mw} = \frac{(6.45\times10^6) m'_{Zr}}{[(\Delta t)(R_o^2 - R_I^2)\pi]} \tag{8-47}$$

where R_I, is the inner cladding radius and 6.45×10^6 J/kg corresponds to the energy released per kilogram of oxidized zirconium.

The metal-water reaction is calculated only at locations that correspond to hydrodynamic-cell boundaries. The effect of the metal-water reaction is included in the intermediate nodes (fine mesh) by linear interpolation of the effect along the length of the cell. The error produced by this method of accounting for the metal-water reaction is small except in a hydrodyrnamic cell where quenching is occurring. At the bottom of such a cell the rod temperature is low, and the metal-water reaction has no effect. At the top of the cell the metal-water reaction is calculated correctly. When TRACE interpolates in the cell the effect of the metal-water reaction is underestimated. If the rod temperatures exceed the threshold temperature for metal-water reaction of 1273 K (1832 °F), the user should watch for this situation; if the peak cladding-temperature location is in the same hydrodynamic cell as the quench front, the metal heat release may be under predicted.

References

8-1 B-1. D. L. Hagerman, G. A. Reymann, and R. E. Mason, "MATPRO-Version 11 (Revision 1): A Handbook of Material Properties for Use in the Analysis of Light Water Reactor Fuel Rod Behavior," EG&G Idaho, Inc. report TREE-280, Rev. 1 (NUREG/CR-0479) (February 1980).

8-2 B-2. Philip E. MacDonald and Loren B. Thompson, compilers and editors, "MATPRO Version 09: A Handbook of Materials Properties for Use in the Analysis of Light Water Reactor Fuel Rod Behavior," EG&G Idaho, Inc. report (TREE-NUREG-1005) (December 1976).

8-3 B-3. Donald L. Hagerman, Gregory A. Reymann, and Richard E. Mason, "MATPRO Version 11 (Revision 2): A Handbook of Material Properties for Use in the Analysis of Light Water Reactor Fuel Rod Behavior," EG&G Idaho, Inc. report TREE-1280, Rev. 2 (NUREG/CR-0479) (August 1981).

8-4 Gandhi, J. M., and Saxena, S. C., "Correlated Thermal Conductivity Data of Rare Gases and Their Binary Mixtures and Ordinary Pressures," Journal of Chemical and Engineering Data, 13, 3, 1968.

8-5 L-1. L. S. Tong and J. Weisman, *Thermal Analysis of Pressurized Water Reactors,* 2nd ed. (American Nuclear Society, La Grange Park, Illinois, 1979).

8-6 L-2. R E. MacDonald and J. Weisman, "Effect of Pellet Cracking on Light Water Reactor Fuel Temperatures," *Nuclear Technology* 31, 357-366 (1976).

8-7 L-3. B. A. Boley and J. H. Weiner, *Theory of Thermal Stresses* (John Wiley and Sons, Inc., New York, 1960).

8-8 T. T. Claudson, *Emissivity Data for Uranium Dioxides,* HW-55414, November 5, 1958.

8-9 T. C. Ehlert and J. L. Margrave, "Melting Point and Spectral Emissivity of Uranium Dioxide," *Journal of the American Ceramic Society, 41,* 1958, p. 330.

8-10 L-4. J. V. Cathcart, "Quarterly Progress Report on the Zirconium Metal-Water Oxidation Kinetics Program," Oak Ridge National Laboratory report ORNL/ NUREG/TM-41 (August 1976).

8-11 Siefken, L. J., et al. "SCDAP/RELAP/MOD3.3 Code Manual; MATPRO - A Library of Material Properties for Light-Water-Reactor Accident Analysis, " NUREG/CR-6150, Vol. 4, Rev. 2, 2001.

8-12 C. R. Brooks and **E. E.** Stansbury, "The Specific Heat of Zircaloy-2 from 50 to 700 °C'" *Journal of Nuclear Materials, 18,* 1966, p. 223.

8-13 4.3-2 H. W. Deem and E. A. Eldridge, *Specific Heats and Heats of Transformation of Zircaloy-2 and Low Nickel Zircaloy-2,* USAEC BMl-1803, May 31, 1967.

9

Reactor-Core Power Models

The primary energy source for a nuclear-reactor power plant is the reactor core. The initial and transient nuclear-reactor power is specified via the POWER component, while for PWR applications the geometry of the core (i.e., fuel rod radius, height, noding, number of fuel rods, etc.) is specified via the HTSTR component and for BWR applications the geometry of the core (i.e., number BWR fuel assemblies, partial length fuel rods, water rods, etc.) is specified via the CHAN component. For PWR applications, all of the reactor power input is contained within the POWER component, while for BWR applications the CHAN component includes relative fuel rod pin power distributions, rod-to-rod, and CHAN-to-CHAN peaking factor. Complete input specifications for the core power model and examples of its use are provided in the TRACE User's Manual. The reactor power can be specified as a constant or a table or calculated from a point kinetics model or from a 3D transient neutronics simulated. The total reactor power in general has two components (i.e. fission power and decay heat power). The TRACE decay heat models in the POWER component are based on the 1979 and 1994 ANS decay heat standards (Refs. 9-4 and 9-5).

The reactor power can be determined by a full 3D transient neutronics calculation, when TRACE is coupled to the Purdue Advanced Reactor Core Simulator (PARCS) code (Ref. 9-7). When TRACE is coupled with PARCS, the TRACE input must include a POWER component to provide for the allocation of reactor-power distribution arrays in TRACE, which PARCS will fill with the appropriate power densities. The POWER component via the input specification will identify the HTSTR components or CHAN components for which PARCS will provide power densities. The PARCS capability and the coupling of TRACE with PARCS is covered in References 9-7 and 9-8.

TRACE allows the user to model the power generation in the reactor core in several ways: constant power, power specified from a table, point-reactor kinetics with reactivity feedback, or full 3D transient neutronics calculation when TRACE is coupled to PARCS. The point kinetics cases can be run with the reactor core at a constant with a user-specified trip power until a user-specified trip occurs. The core model defines the local, volumetric heat-generation rate q''' in the heat-conduction equation [Eq. (3-1)]. The geometry of the heat structure is defined in the HTSTR or CHAN component input (see the TRACE User's Manual). The radial and axial power distributions and total power is defined via the POWER component input, except for BWR applications where the CHAN component includes fuel pin radial power distribution, rod-to-rod power distribution, and CHAN-to-CHAN power distributions.

There are several user-specified tables involved in the complete description of the reactor-core power model. In this section, we will not belabor the description of these tables and how the code obtains necessary values from them. In particular, we will not describe signal variables, control blocks, and rate-factor tables other than briefly to define them here. Signal variables are predefined parameters, such as time, pressure, coolant levels, etc., that the code calculates and that the user can select as independent variables for tables, trips, and control blocks. Control blocks are predefined mathematical functions and logic switches, which the user can string together to model plant systems, such as control systems, or to calculate quantities not normally available from the code (and which in turn may be used to control component behavior), such as pressure drops across multiple components, liquid mass in one or more cells, etc. With the signal variables and the control blocks, the user can define the necessary independent variables for the tables. The rate-factor table is a means to vary the rate of change of the independent variable of a component-action table. That is, the rate-factor table provides a multiplier to the independent variable of a table that alters its magnitude before the code performs the table lookup. For more information, on TRACE's control procedure and component-action tables, see the TRACE User's Manual.

Nomenclature

The following nomenclature applies to this chapter. On various occasions, mnemonics are used that are equivalent to the TRACE's input variables instead of the symbols. These mnemonics are also listed in the nomenclature.

A_{ij} = horizontal cross-sectional area of fuel-rod node i for heat structure j.

a_1 , a_2 = functions of time defined in Eq. (9-44)

a_l , b_l = linear interpolation parameters for power history defined in Eq. (9-22)

BCR = control-rod-cluster-pin solute concentration (kg · m^{-3})

BCR0, *BCR1* = polynomial coefficients for *BCR* defined in Eq. (9-26)

B_m = core-averaged solute concentration (kg · m^{-3})

BPP = equivalent burnable-poison-pin solute concentration (kg · m^{-3})

BPP0, *BPP1* = polynomial coefficients for *BPP* defined in Eq. (9-25)

B_r = ratio of solute mass to liquid-coolant mass (ppm)

$C_{\alpha i}$ = reactivity feedback coefficient for changes in the void fraction for fluid cell i.

C_{bi} = reactivity feedback coefficient for changes in the boron concentration for fluid cell i (1/ppm).

C_i = power of delayed-neutron precursor concentration in group i (W)

C_{tfi} = reactivity feedback coefficient for changes in the fuel temperature for fuel node i (1/K).

C_{tmi} = reactivity feedback coefficient for changes in the moderator temperature for fluid cell i (1/K).

CPOWR = relative power density of an average rod

CPOWRN = normalized relative power density of an average rod

D, D^* = functions of a_1 and a_2 (Eq. (9-53), Eq. (9-54), Eq. (9-65), and Eq. (9-66))

ED_j = MeV of decay energy per fission per second for decay-heat group j (MeV · fission^{-1} · s^{-1})

E_j = effective energy fraction of decay-heat group j

FISPHI = fissions per initial fissile atom.

H_j = energy of decay-heat precursor concentration group j (W · s)

HTNUM = User input array of HS or CHAN component numbers powered by a given POWER component.

I = number of delayed-neutron groups or total number of radial nodes in a fuel rod

I_{im} = recursive exponential function obtained when integrating delayed-neutron precursor concentration equation over a time step.

I_{jm}^H = recursive exponential function obtained when integrating decay-heat precursor concentration equation over a time step.

J = number of decay-heat groups or total number of average calculational rods in the core

K = number of input-specified coarse-mesh nodes

k = neutron multiplication constant

k_{ex} = excess reactivity expressed in terms of the neutron multiplication constant ($k-1$)

L = number of points in the power history table.

ℓ = prompt-neutron lifetime (s).

LAMDA = delayed neutron time constant(s).

m_i = fuel or coolant mass if x is T_f or T_c in Eq. (9-24); 1 if x is α, B_m or B_r in Eq. (9-24)

m = arbitrary index

N = number of fuel rods

$NCHANS_j$ = number of BWR fuel assemblies associated with HS j.

$NDGX$ = number of delayed neutron groups.

$NDHX$ = number of decay heat groups.

$NHIST$ = number of points in the power history table.

NR = ratio of number of actual fuel rods to number of core average fuel rods for a given heat structure.

$NRDX_j$ = number of actual fuel rods associated with HS j.

$NRSX$ = number of radial rings in a given VESSEL component.

$NTSX$ = number of theta sectors in a given VESSEL component.

$NZPWTB$ = number of axial power shapes

P = thermal power from fission (W)

P_i = power in mesh cell i

P_1, P_2, P^*_1, P^*_2 = polynomial coefficients for P

P_{eff} = effective thermal power

$POWEXP$ = neutron flux distribution parameter

P_{tot} = average core power

Q_k = MeV per fission for a given isotope k

$q(t)$ = function of time defined in Eq. (9-44)

q''' = power density

q'''_{supl} = supplemental rod power-density distribution

q''_{wl} = wall to liquid heat flux (W/m^2).

q''_{wv} = wall to vapor heat flux (W/m^2).

R = neutronic reactivity, including both programmed reactivity and feedback reactivity

r = radial

$RADPW$ = CHAN-to-CHAN power distribution factor

R_1 = polynomial coefficient for R

$RDPWR$ = relative radial-power density

$RDPWRN$ = normalized relative radial-power density

RDX_j = number of fuel rods associated with HS j.

$RPKF$ = power-peaking factors for supplemental or hot rods

$RPWTB$ = user input reactor power table.

S = thermal power from an external source of neutrons (W)

S_f = scale factor to normalize the relative-power distributions

T_c = core-averaged coolant temperature

T_f = core-averaged fuel temperature

T_1 = liquid phase temperature

t = time (s)

V_i = volume for heat structure cell i (m^3).

Vol_j = volume for heat structure j (m^3).

Vol_{avg} = average HS volume (m^3).

x = dummy variable

$ZPOWR$ = normalized and interpolated relative power density

$ZPWTB$ = user input relative axial-power density in a given rod

$ZPWTBN$ = normalized relative axial-power density in a given rod.

WF = weighting factor.

Greek

α = core-averaged gas volume fraction

β = total fraction of delayed neutrons

β_i = fraction of delayed neutrons in group i

Δk = change in reactor multiplication factor

Δt = time-step size

Δz = elevation distance

Λ = effective prompt-neutron lifetime (s)

λ_i = decay constant for delayed-neutron precursors in group i (s^{-1})

λ_j^H = decay constant for decay-heat group j

ρ = density

τ = dummy integration variable

θ = azimuthal

ε = error in estimating P

ε_1 , ε_2 = error bounds in estimating P

Subscripts

avg = average

eff = effective.

$fdbk$ = feedback

i = delayed-neutron group or cell number or dummy index for fuel-rod node

ic = CHAN component index.

j = decay-heat group or dummy index for cell identification

k = dummy isotope index or dummy index for core level

l = power history index

$prog$ = programmed.

tot = total

$supl$ = supplemental or hot rod.

Superscripts

c = control block/signal variable

cor = corrected

est = estimated

$n-1$ = old-time values

n = current-time values

$n+1$ = new-time values

s = scram curve

Partitioning of the Core Power into the Heat-Conduction Mesh

The user must supply as a part of the input for the POWER components several arrays that enable the code to partition the heat generation into the finite-difference mesh cells that describe the fuel rods (or fuel-rod simulators). These arrays include *RDPWR*, the relative radial-power density at the radial node positions in the rod, Figure 9-1; *CPOWR*, the relative power density in each (*r*, *θ*) mesh cell in the horizontal plane, Figure 9-2(A); *ZPWTB*, the relative axial-power density in a given rod, Figure 9-3; and RPKF, the fuel-rod power-peaking factors (relative to the average fuel rod in the horizontal mesh cell) for the additional rods, Figure 9-2(B). Since the additional rod or

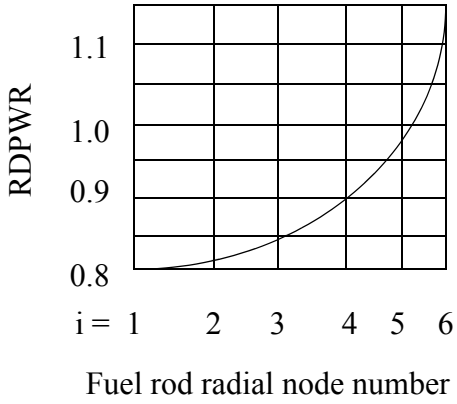

Figure. 9-1. Relative radial-power density at radial node positions in the fuel rod.

supplemental rod peaking is relative to the average fuel rod in the horizontal mesh cell where the supplemental rod is located, then the relative power density for the supplement rods goes as CPOWR * RPKF (see Figure 9-2(C)). The code assumes that all calculational rods powered by a given POWER component that the *CPOWR* and *RPKF* arrays do not vary in the axial direction. Note that the scenario depicted in Figure 9-2 is for PWR geometry.

For BWR geometry with the CHAN component, the CPOWR array is input for each BWR fuel assembly and is the relative rod-to-rod power distribution for that CHAN component. For PWR geometry CPOWR is the relative rod-to-rod power distribution for the full core. In addition, the RPKF array is not available for CHAN components.

For the example given in Figure 9-2, the ordering of the HTSTR components in the horizontal plane for the CPOWR array is dependent upon the order in which the HTSTR component numbers are input in the HTNUM array in the POWER component input. For example, if the HTNUM array input for the example, given in Figure 9-2 is HTNUM(1:8) = 101, 102, 103, 104, 105, 106, 107, 108, that implies that for cell j = 1, the HTSTR component number = 101 is located in that horizontal plane cell, for cell j = 2, the HTSTR component number = 102 is located in that horizontal plane cell, etc. (See Figure 9-2(D)). Where the HTSTR component is located within the VESSEL component is determined via the HTSTR component input. For BWR applications the HTNUM input for the POWER component is for the CHAN component numbers. For BWR applications HTNUM(1:3) = 101, 102, 103 would imply the geometry given in Figure 9-4. Again which VESSEL cell contains which CHAN component is determined via the CHAN component input.

There are a number of input options available for specifying the axial-power shape as discussed in the input description for the POWER component. The code also permits the user to specify the axial-power shape as a function of an independent variable. This independent variable can be either a signal-variable parameter or a control-block output signal. The purpose of this general definition of the axial-power shape is to permit the code user to vary the axial-power shape during

(A) CPOWR - Relative power density in each core mesh cell for hydro/coupled fuel rod elements.

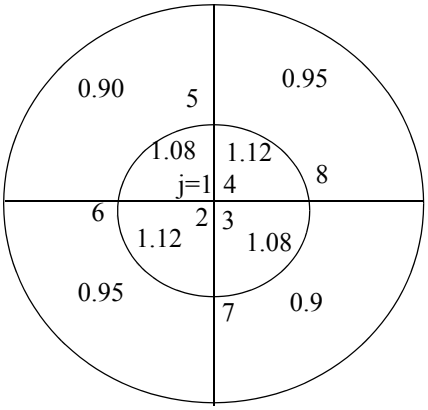

(B) RPKF - Power peaking for supplemental non-hydro/coupled fuel rod elements.

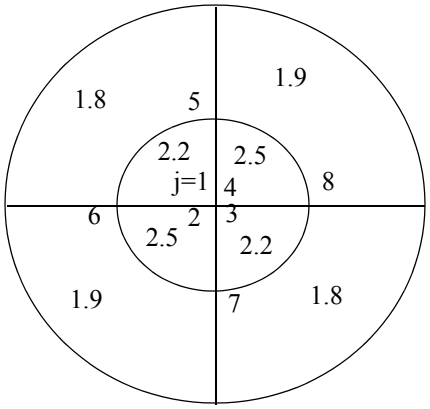

(C) CPOWR * RPKF - Relative power density for supplemental non-hydro/coupled fuel rod elements.

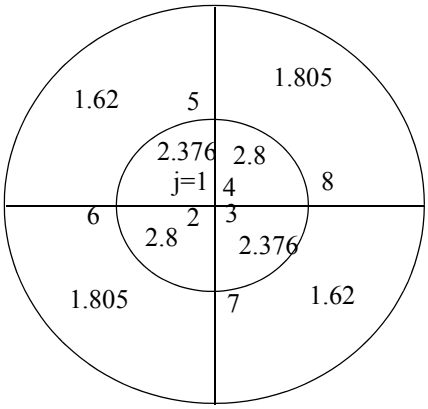

(D) Heat Structure Locations

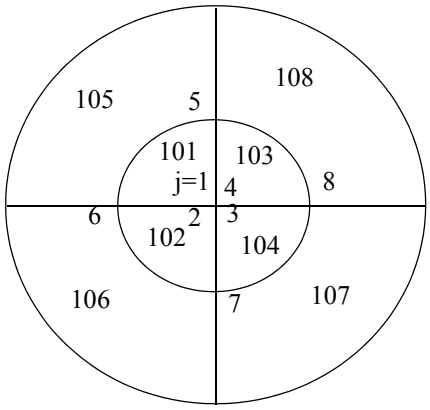

Figure. 9-2. Relative power density in each (r, θ) mesh cell in the horizontal plane, for VESSEL with NRSX = 2 (i.e two radial rings) and NTSX = 4 (i.e. four theta sectors).

the calculation if desired. An example of this variation is to vary the axial-power shape to account for the changes in power distribution resulting from control-rod insertion, as shown in Figure 9-5.

The TRACE input-processing subroutine normalizes each individual axial-power shape by the following formula:

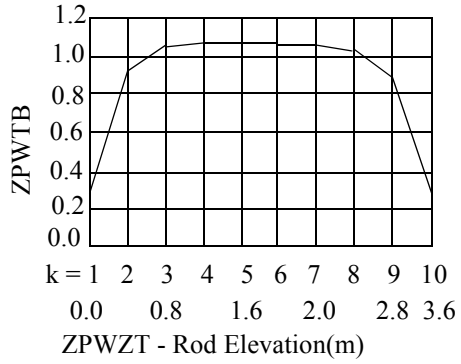

Figure. 9-3. Relative axial-power density in a fuel rod.

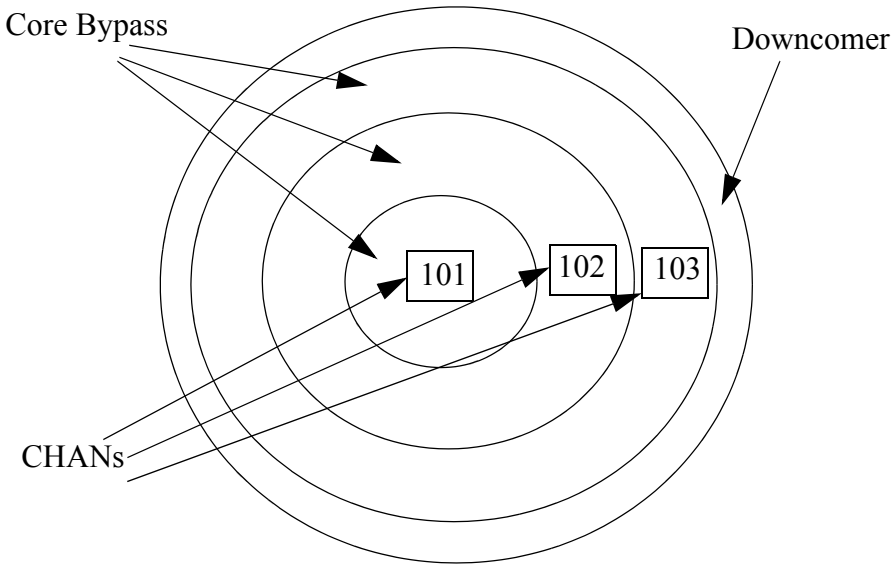

Figure. 9-4. CHANs in VESSEL with NRSX = 4(i.e. four radial rings).

$$ZPWTBN_k = ZPWTB_k \frac{\sum_{i=1}^{K} \Delta z_i}{\sum_{i=1}^{K} ZPWTB_i(\Delta z_i)}, \quad (9\text{-}1)$$

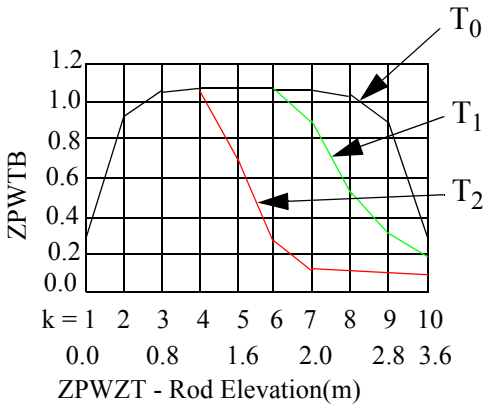

Figure. 9-5. Example of multiple entries of axial-power shape to model control-rod insertion as a function of time.

where *ZPWTB* is the input power shape and *ZPWTBN* is the resulting normalized power shape. The summations are over the axial height of the core and Δz_i is the elevation distance over which the i^{th} shape element applies. *ZPOWR*, the relative power density, is determined by interpolation from the *ZPWTBN* array.

Note the RDPWR array is also normalized based on the cross-sectional area of each radial heat structure node.

$$RDPWRN_{ij} = RDPWR_{ij} \frac{\sum_{i=1}^{I} A_{ij}}{\sum_{i=1}^{I} RDPWR_{ij} A_{ij}} , \tag{9-2}$$

where $RDPWR_{ij}$ is the user input radial pin power distribution array for radial node i for heat structure j, A_{ij} is the cross-sectional area associated with heat structure j and radial node i, and $RDPWRN_{ij}$ is the normalized radial pin power distribution.

The CPOWR array is normalized based on the number of fuel rods associated with each fuel rod group for which CPOWR is input. For PWR applications the number of fuel rods associated with a given CPOWR(j) is the HTSTR component input for NRDX(j). For BWR applications the number of fuel rods associated with a given CPOWR(j) is the CHAN component input for NCHANS times RDX(j), where CPOWR, NCHANS, and RDX are input as part of the CHAN component.

$$CPOWRN_j = CPOWR_j \frac{\sum_{j=1}^{J} N_j}{\sum_{j=1}^{J} CPOWR_j N_j} , \quad (9\text{-}3)$$

where $CPOWR_j$ is the user input for the rod to rod power distribution for heat structure j, N_j is the number of actual fuel rods simulated by heat structure j (i.e. NRDX(j) for PWR applications and NCHANS(j)*RDX(j) for BWR applications). The normalization given by Eq. (9-3) assumes all fuel rod heat structures are the same size (i.e. diameter and length). For applications where the heat structure geometry varies for a given POWER component, the normalization of the CPOWR user input is:

$$CPOWRN_j = CPOWR_j NR_j \frac{\sum_{j=1}^{J} N_j}{\sum_{j=1}^{J} CPOWR_j N_j NR_j} , \quad (9\text{-}4)$$

where, NR_j is the ratio of the number of actual fuel rods to the number of core average fuel rods simulated by heat structure j.

$$NR_j = N_j \frac{\sum_{j=1}^{J} Vol_j}{Vol_j \sum_{j=1}^{J} N_j} , \quad (9\text{-}5)$$

where Vol_j is the volume associated with heat structure j and the core average fuel rod volume is

$$\mathrm{Vol}_{avg} = \frac{\sum_{j=1}^{J} Vol_j}{\sum_{j=1}^{J} N_j} \quad (9\text{-}6)$$

and the number of core average fuel rods for heat structure j is $Vol_j/(Vol_{avg})$.

When the advanced BWR option is used for the CHAN component, then the fuel rods within a given CHAN component may include both full length and partial length fuel rods. The normalization logic for the CHAN component with and without partial length fuel rods is the same as the PWR normalization logic, expect the sums are over only those heat structures associated with a given CHAN component. The intent of this approach is that the axial power profile for the partial length fuel rods, will be the same as the axial power profile for the full length fuel rods, only applied over a smaller fuel rod length. The normalization for CHAN component CPOWR user input is:

$$CPOWRN_j = CPOWR_j \left(\frac{\sum_{j=1}^{J(ic)} N_j}{\sum_{j=1}^{J(ic)} CPOWR_j N_j} \right) , \tag{9-7}$$

where j is for all of the heat structures associated with CHAN component ic. Therefore, CPOWR is normalized relative to the each CHAN component.

The power density q''' in fuel-rod radial node *i* in heat structure *j* in core level *k* is (See Figure 9-6):

$$q'''_{ijk} = S_f P_{tot} RDPWRN_{ij}\ CPOWRN_j\ ZPOWR_{kj} , \tag{9-8}$$

where P_{tot} is the average core power over the time step, $RDPWR_{ij}$ is the relative power density in fuel node *i* for the j^{th} powered heat structure, $CPOWR_j$ is the relative power of the average rod in cell *j*, $ZPOWR_{kj}$ is the relative power density at core elevation *k* for the j^{th} powered heat structure, and S_f is the scale factor that normalizes the three input relative-power distributions to a core volume-averaged value of unity. P_{tot} is given by Eq. (9-9).

$$P_{tot} = \frac{P^n + P^{n+1}}{2} , \tag{9-9}$$

where *P* is the total core power, and the superscripts *n* and *n* + 1 indicate the beginning and end of time step, respectively. The following expression defines the scale factor S_f:

$$S_f = 1 / \left[\sum_{i=1}^{I} \sum_{j=1}^{J} \sum_{k=1}^{K} (A_{ij} \cdot RDPWRN_{ij} \cdot N_j \cdot CPOWRN_j \cdot ZPOWR_{kj} \cdot \Delta z_{kj}) \right], \quad (9\text{-}10)$$

where A_{ij} is the horizontal cross-sectional area for fuel-rod radial node *i* for the j^{th} powered heat structure, and N_j is the number of actual fuel rods in cell *j* for which the average fuel-rod condition is to be evaluated. For PWR applications (i.e., POWER component powering HTSTR components), N_j is equal to user input for $NRDX_j$. For BWR applications (i.e., POWER components powering CHAN components), N_j is equal to RDX_j time *NCHANS*. The summations in Eq. (9-10) are over all nodes in all rods: *I* is the number of radial nodes in a rod (i.e., NODES in the HTSTR input), *J* is the number of average fuel rod HTSTRs in the core (i.e., NUMPWRS in the POWER input), and *K* is the number of input-specified coarse-mesh axial levels (i.e., NZHTSTR in the HTSTR input). In general, the heat structures powered by a given POWER component may not have the same noding and geometry (i.e., fuel rod radial noding may vary or axial noding may vary or etc.). For BWR applications, Eq. (9-10) includes an additional CHAN-to-CHAN peaking factor which is determined from the CHAN component RADPW input. The scale factor for BWR applications is

$$S_f = \frac{1}{\sum_{j=1}^{J} \sum_{i=1}^{I(j)} \sum_{k=1}^{K(j)} (A_{ij} \cdot RDPWRN_{ij} \cdot N_j \cdot RADPW_{jk} \cdot CPOWRN_j \cdot ZPOWR_{kj} \cdot \Delta z_{kj})} \quad (9\text{-}11)$$

Since BWR fuel assemblies may include full length and partial length fuel rods, then in Eq. (9-11), the number of axial levels is a function of the heat structure index j. In addition, the radial fuel rod noding may vary from one heat structure to the next and therefore I is also a function of the heat structure index j. For BWR applications, Eq. (9-8) becomes:

$$q'''_{ijk} = S_f P_{tot} RDPWRN_{ij} \; CPOWRN_j \; ZPOWR_{kj} RADPW_{jk} \quad (9\text{-}12)$$

A consistently defined scale factor ensures that total power is conserved.

$$P_{tot} = \sum_{j=1}^{J} \sum_{i=1}^{I(j)} \sum_{k=1}^{K(j)} q'''_{ijk} \cdot N_j \cdot A_{ij} \cdot \Delta z_k \quad (9\text{-}13)$$

For the supplemental rod *l* in cell *j*, the power density distribution q'''_{supl} is

$$q'''_{supl} = RPFK_j \cdot q'''_{ijk} \ , \tag{9-14}$$

where $RPKF_j$ is the specified peaking factor of the supplemental rod relative to the average rod associated with the supplemental rod. Supplemental or hot rods are defined only for those HTSTR components where NHOT > 0. The *RPKF* array is input with the POWER component input, for the POWER component providing power to the average rod associated with the supplemental rod. Each supplemental rod or hot rod is associated with an average rod heat structure. The supplemental rod sees the same fluid conditions as the average rod, but is at typically a higher power level (i.e. $RPFK_j > 1.0$), then the average rod heat structure. However, the supplement rod does not transfer any energy to the surrounding fluid. The intent of the supplemental rod is to determine the PCT for a given hot fuel rod within a given region in the VESSEL component, while the average rod represents all of the actual fuel rods within that region of the VESSEL component. Currently, there is no hot rod or supplemental rod capability available for the CHAN component. For the heat structure noding given in Figure 9-6, power density at each radial node i, heat structure j, and axial level k is determined by the previous equations. The power density along with the transient conduction solution and the convective heat transfer coefficient models determines the surface heat fluxes from the wall to the liquid phase and from the wall to vapor phase. For average rod heat structures, these surface heat fluxes also appear in the fluid energy equations for the liquid and vapor phases for the fluid surrounding the fuel rod. For the supplemental rod, these heat fluxes are calculated, but do not appear in any fluid energy equations.

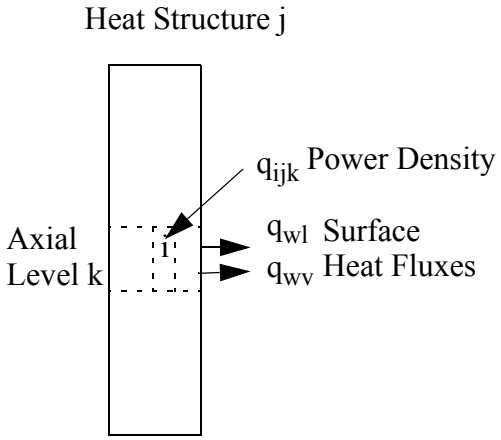

Figure. 9-6. Relative radial-power density at radial node positions in the fuel rod.

The input defines all of the necessary parameters in Eq. (9-1) through Eq. (9-14) for partitioning P_{tot} throughout the 2D heat-conduction mesh for each calculational rod in the core. For the most part, the variable names used above correspond to those used in the input description; the exception is A_{ij}, which is calculated from input radial-node radii RADRD.

Because the axial-power shape is normalized in the input-processing subroutines, the factor does not need to be shown explicitly in the expression for S_f. Also, S_f contains the grouping $A_{ij} \cdot \Delta z_{kj}$, which is the volume of the (i, j, k) mesh cell in the rod; this volume times $NRDX_j$ provides the total volume of actual rods in mesh cell (i, j, k) with the same power density. Therefore, S_f not only normalizes to the total power throughout the core but also converts the power into a volumetric heat-generation rate for the calculational rod.

Power Evaluation and Reactor Kinetics

The code determines the core power in subroutine RKIN by either of two methods. In the first method, the user specifies power to be a constant or to be defined by an RPWTB power table supplied through input. The table is a function of a system signal-variable parameter or a control-block output-signal parameter. Values between entries in the table are determined by linear interpolation. Power determination can be trip-controlled by evaluating the power table when the controlling trip is ON and by holding the power constant when the trip is OFF. In the second method, the user determines power from the solution of the point-reactor-kinetics equations. These equations specify the time behavior of the core power level with neutronic reactivity (R) [the sum of programmed reactivity (R_{prog}) and feedback reactivity (R_{fdbk})] as the driving parameter. The user inputs programmed reactivity (defining reactivity effects not accounted for by feedback reactivity, such as fuel reactivity and control-rod movement) with the same forms that define power in the first method (as a constant or by a RPWTB table). Feedback reactivity based on changes in the core-averaged fuel temperature, coolant temperature, gas volume fraction, and boron concentration is calculated by TRACE.

Point-Reactor Kinetics

The point-reactor-kinetics equations (Refs. 9-1 and 9-2) are a coupled set of $(I + 1)$ first-order differential equations defining the total fission power P and the delayed-neutron precursor concentrations C_i as a function of time. These equations are given by

$$\frac{dP}{dt} = \frac{R - \beta}{\Lambda} P + \sum_{i=1}^{I} \lambda_i C_i + \frac{S}{\Lambda(1 - R)} \tag{9-15}$$

and

$$\frac{dC_i}{dt} = -\lambda_i C_i + \frac{\beta_i P}{\Lambda} \quad \text{for} \quad i = 1, 2, \ldots, I, \tag{9-16}$$

where

P = thermal power (W) that results from fission occurring at time t;
t = time (s);

R = neutronic reactivity, $R = R_{prog} + R_{fdbk} = (k-1)/k$

k = effective neutron multiplication constant = 1 + Δk_{prog} + Δk_{fdbk};
R_{prog} = programmed reactivity = $\Delta k_{prog}/k$;
R_{fdbk} = feedback reactivity = $\Delta k_{fdbk}/k$;

β = total fraction of delayed neutrons = $\sum_{i=1}^{I} \beta_i$;

β_i = fraction of delayed neutrons in group i;
Λ = effective prompt-neutron lifetime (s);
λ_i = decay constant for the delayed-neutron precursors in group i (s^{-1});
C_i = power of the delayed-neutron precursor concentration in group i (W);
I = number of delayed-neutron groups; and
S = thermal power (W) from an external source of neutrons in the reactor cores that are producing fission.

The Kaganove method (Ref. 9-3) outlined in the ***Solution of the Point-Reactor Kinetics*** is used to solve these equations.

The code applies the thermal-power solution to the decay-heat equations

$$\frac{dH_j}{dt} = -\lambda_j^H H_j + E_j P \text{ for } j = 1, 2, \ldots, J, \tag{9-17}$$

where

P = solution of Eq. (9-15) and Eq. (9-16),
H_j = energy of the decay-heat precursor concentration in group j (W · s),
λ_j^H = decay constant for decay-heat group j,
E_j = effective energy fraction of decay-heat group j, and
J = number of decay-heat groups.

After solving each j^{th} equation represented by Eq. (9-17) for the decay-heat group concentration H_j, the code calculates the total thermal power generated in the reactor-core fuel at time t. The total power comprises nuclear fission, fission-product decay, and external sources as shown by

$$P_{eff} = P + \sum_{j=1}^{J} \lambda_j^H H_j + S. \tag{9-18}$$

Eq. (9-18) is consistent with the coding in TRACE version 5.0. However, Eq. (9-18) is in error and should not include the source term S, since the contribution to reactor power associated with the external neutron source has already been included into Eq. (9-15). This will be corrected in future versions of TRACE. It is typical, for an external source of neutrons to be used bring a cold clean reactor up to power. Therefore, the external source term, S, would be used for a simulation from cold startup. The external source term is only used as part of the point-kinetics model and is not used when the reactor power is determined from a table or a constant.

The code requires the number of delayed-neutron groups, I; the delayed-neutron parameters, λ_i and β_i; the number of decay-heat groups, J; the decay-heat parameters, λ_j^H and E_j; and either the total fission-power history $P(t)$ for $-t \le 0$ or the initial delayed-neutron precursor concentrations $C_i(0)$ and decay-heat concentrations, $H_j(0)$.

Default Data for the Delayed-Neutron Groups

If $I \le 0$ is input (input parameter NDGX), TRACE internally sets I to 6 and defines λ_i and β_i with the values in Table 9-1.

Table 9-1. Delayed-Neutron Constants

Group *i*	Decay Constant λ_i (s^{-1})	Neutron Fraction β_i
1	3.87	0.000169
2	1.40	0.000832
3	0.311	0.00264
4	0.115	0.00122
5	0.0317	0.00138
6	0.0127	0.000247

If $I \le 0$ and no total fission-power history is input, the code assumes that an initial steady-state condition exists to initialize $C_i(0)$ internally. The code sets the time derivative in Eq. (9-16) to zero and calculates the initial values of the C_i from the following:

$$C_i(0) = \frac{\beta_i}{\lambda_i \Lambda} P(0) \text{ for } i = 1, 2, \ldots, I, \tag{9-19}$$

where $P(0)$ is the initial power specified through input. This is equivalent to assuming an infinite reactor operating period at the initial power (i.e. P(0)).

If NDGX is input > 0, then the user must supply the delayed-neutron decay constants (LAMDA) and neutron fractions (BETA). IF NDGX > 0 and NHIST = 0, then the initial values for the delayed neutron concentrations (CDGN) must be supplied.

Default Data for the Decay-Heat Groups

If $J \leq 0$ is input (i.e., J is user input for NDHX), TRACE internally sets J to the appropriate number of decay heat groups and defines λ_j^H and ED_j obtained from the 1979 or 1994 ANS decay-heat standard (Refs. 9-4 and 9-5) (i.e., J may be 23, 25, 69, or 71 for the 1979 ANS decay-heat standard and J may be 92 or 94 for the 1994 ANS decay heat standard). If one of the input options for the 1979 standard is used (i.e., NDHX = 69, 71, -23, or -25), the fraction of fission power due to each of the three isotopes, U^{235}, Pu^{239}, and U^{238}, must be input. If one of the input options for the 1994 standard is used (i.e., NDHX = -92 or -94), the fissionable fraction of Pu^{241} must also be input. In addition, in order to convert the decay energy per fission (in MeV) to a fraction of the total fission energy, the energy per fission (in MeV) for each of the three or four isotopes must be input. ED_j is converted to E_j using the following equation:

$$E_j = \frac{ED_j}{\lambda_j^H Q_k} \tag{9-20}$$

where Q_k is the MeV/fission for isotope k and ED_j is the decay energy per fission per second (in MeV/s) for decay-heat group j and λ_j^H is the decay constant for decay-heat group j.

If $J \leq 0$ and no total fission-power history is input, the code assumes that an initial steady-state condition exists to initialize $H_j(0)$ internally. The code sets the time derivative in Eq. (9-17) to zero and calculates the initial values of the H_j from the following:

$$H_j(0) = \frac{E_j}{\lambda_j^H} P(0) \tag{9-21}$$

for $j = 1, 2, \ldots, J$, where $P(0)$ is the initial steady-state power specified through input. This is equivalent to assuming an infinite reactor operating period at the initial power (i.e. P(0)).

Input requirements in the users manual describe corrections to account for fission product neutron absorption (i.e., FISPHI and reactor operating time in power history table) and heavy element

decay (i.e., NDHX = -25, 71, or 94). The user is encouraged to consult References 9-4 and 9-5 for more detailed discussions.

Fission Power History

If the total fission-power history $P(-t)$ is input, TRACE evaluates $C_i(0)$ and $H_j(0)$ from Eq. (9-16) and Eq. (9-17). The $P(-t)$ consists of tabular data pairs (t_l, P_l) for $l = 1, 2, \ldots, L$, where $-t_l + 1 < -t < -t_l$. The code assumes that the total fission power varies linearly between data pairs in the power-history table; that is,

$$P(t) = a_l + b_l t \text{ over the time interval } -t_{l+1} \le t \le -t_l \ . \tag{9-22}$$

Substituting Eq. (8-12) into Eq. (9-16) and integrating the resulting equation analytically from $t = -t_L$ [where $C_i(-t_L) = 0$ is assumed] to $t = 0$ gives

$$C_i(0) = \frac{\beta_i}{\lambda_i \Lambda} \sum_{l=1}^{L-1} \left\{ \left(a_l - \frac{b_l}{\lambda_i} \right) (1 - e^{-\lambda_i (t_{l+1} - t_l)}) + b_l (t_{l+1} e^{-\lambda_i (t_{l+1} - t_l)} - t_l) \right\} e^{-\lambda_i t_l} \tag{9-23}$$

One obtains a similar expression for $H_j(0)$ by doing the same for Eq. (9-17). The expression for $H_j(0)$ is Eq. (9-23) with replacement of C_i by H_j, λ_i by λ_j^H, β_i by E_j, and Λ by 1. TRACE evaluates these two expressions for $C_i(0)$ and $H_j(0)$ when a fission-power-history table is input.

Reactivity Feedback

There are three reactivity-feedback models available in TRACE. The TRAC-P reactivity-feedback model (Ref. 9-9), the TRAC-B reactivity-feedback model (Ref. 9-10), and the RELAP5 reactivity feedback model (Ref. 9-11) are all available in TRACE. The TRAC-P model is available when the input for TRACE is in its native input format, The TRAC-B reactivity-feedback model is used when the input is in the TRAC-B free format, and the RELAP5 reactivity feedback model is available when the RELAP5 input model is used to generate a TRACE TPR file via SNAP.

The TRAC-P reactivity-feedback model is based on the assumption that only changes in the core-averaged fuel temperature (T_f), coolant temperature (T_c), gas volume fraction (α), and solute mass (B_m, solute concentration in the coolant volume, or B_r, ratio of solute mass to liquid-coolant mass multiplied by 1×10^6) affect the neutron-multiplication reactivity of the reactor core. The code

determines core-averaged values by applying a weighting factor defined as the fuel or coolant density times volume times power to the temperatures and solute ratio and a weighting factor defined as the volume times power to the gas volume fraction and solute concentration. These factors approximate the product of the local adjoint flux, neutron flux, and volume. The (power)^2 is the neutron flux times the (fission cross section)^2. The neutron flux times the (fission cross section)^2 is approximating the adjoint flux. The adjoint flux is commonly called the importance function as applied in perturbation theory. The (fission cross section)^2 makes the neutron flux perform like the adjoint flux. This weighting-factor product, i.e., adjoint flux times neutron flux times volume, is from perturbation theory where it is used to spatially weight the change in reaction-rate cross sections to estimate their reactivity change, which is consistent with one group diffusion theory, but not with multi-group or transport theory. TRACE approximates this weighting-factor product by the product of the affecting-material mass (density times volume) and the fission-power density distribution raised to a user-specified power *POWEXP*.

The averaging process over the reactor core for the general reactivity-feedback parameter x happens according to the following relationship:

$$\bar{x} = \begin{cases} \dfrac{\sum_i x_i \rho_i V_i P_i^{POWEXP}}{\sum_i \rho_i V_i P_i^{POWEXP}} & \text{if } x \text{ is } T_f,\ T_c, \text{ or } B_r \\ \\ \dfrac{\sum_i x_i V_i P_i^{POWEXP}}{\sum_i V_i P_i^{POWEXP}} & \text{if } x \text{ is } \alpha \text{ or } B_m \end{cases}, \tag{9-24}$$

where P_i is the power, ρ_i is the density of the fuel or coolant and V_i is the volume of mesh cell i and the summations are over all cells in the reactor core.

For *POWEXP* = 1.0, the fission reaction-rate cross-section distribution approximates the adjoint-flux distribution. For *POWEXP* = 2.0, when the fission reaction-rate cross section is spatially constant, the neutron flux approximates the adjoint flux (Galerkin approximation). The appropriate value to use for *POWEXP* will depend on the fuel-loading distribution in the reactor core. Keep in mind, however, that two levels of approximation are being made. First, it is assumed that the affecting-material density times volume times the fission-power density distribution raised to the *POWEXP* power is a good approximation for the perturbation-theory product of the adjoint flux, neutron flux, and volume. Second, it is assumed that the theoretical basis for the use of that weighting factor for reaction-rate cross sections can be applied to the reactivity-feedback parameters that TRACE averages over the reactor core. The TRACE User's Manual suggests that *POWEXP* be set to 2.0 for the case where the core enrichment is radially

constant. A *POWEXP*=1 value may be more appropriate for the case where the radial-power distribution is constant across the reactor core. The user has the option of replacing any of the three spatial shapes (fuel-rod radial, core horizontal plane, and core axial) in the fission-power density distribution with a different shape to weight the spatial averaging of reactivity-feedback parameters over the reactor core. These spatial-shape replacements are specified through input. The axial-power distribution can be input as a function of some user-defined independent variable. For example, if that independent variable is the programmed reactivity of the control rods, the effect of the control rods on the axial-power shape can be accounted for when the control rods are inserted or withdrawn. An example of this is given in Volume 2 of the TRACE Users Manual.

The user defines a reactivity coefficient for each of the reactivity-feedback independent-variable parameters, $x = T_f$, T_c, α, and B_m or B_r, by choosing one of the reactivity-coefficient forms in Table 9-2. Each reactivity coefficient is defined through input by a table of reactivity-coefficient values that are dependent on all four reactivity-feedback parameters. Each parameter has one or more values specified in defining the table. Defining one value for a parameter corresponds to the reactivity coefficient having no dependence on that reactivity-feedback parameter. Defining two or more values for a parameter gives the reactivity-coefficient dependence on one or more of the reactivity-feedback parameters. Linear interpolation is used to evaluate the reactivity coefficient for values of each parameter between its table values. Multidimensional linear-surface interpolation is performed when the reactivity coefficient is dependent on two or more of the reactivity-feedback parameters. An example of defining input data for the reactivity feedback model is given in Volume 2 of the TRACE User's Manual.

Solute in the derivative and solute dependence of a reactivity coefficient is defined in terms of the solute concentration in the coolant channel, B_m, in units of kg/m^3, a macroscopic density, or the solute mass to liquid-coolant mass ratio, B_r, in units of parts solute per million parts liquid coolant (ppm). The solute reactivity coefficient is based on the change in the amount of solute without changing T_c and α when the coefficient is defined as a derivative of B_r. The reactivity-coefficient derivative of B_m is affected by changes in T_c and α. Consequently, having the reactivity coefficient as a derivative of B_r is better if data are available. The solute dependence of a reactivity coefficient is important when the reactivity coefficient is sensitive to a shift in the neutron-energy spectrum. Through the proportionality to the amount of neutron capture in solute, the B_m- or B_r-dependence characterizes this shift. Cross-section/neutronics codes are needed to determine this dependence separate from TRACE.

Table 9-2. Reactivity-Coefficient Forms

Form Number	Reactivity-Coefficient Form
0	$\frac{\partial k}{\partial x}$
1	$\frac{1}{k}\frac{\partial k}{\partial x} \cong \frac{\partial R}{\partial x}$

Table 9-2. Reactivity-Coefficient Forms

2	$x\frac{\partial k}{\partial x}$
3	$\frac{x}{k}\frac{\partial k}{\partial x} \cong x\frac{\partial R}{\partial x}$

All forms of solute in the reactor core are included in the evaluation of B_m or B_r for solute dependence of the reactivity coefficients. Examples include dissolved boric acid in the liquid coolant, boric acid plated on core structure, borosilicate glass in burnable-poison pins, and boron oxide in control-rod-cluster pins. The first two forms are based on boric-acid convection into the reactor core throughout the modeled system and on plate-out of boric acid in the reactor core as a result of coolant dryout. For the latter two forms, the TRACE user defines the burnable-poison-pin and control-rod-cluster-pin forms through input with what would be their equivalent solute concentrations in the coolant channel. *BPP* or *BCR* define the equivalent concentration in the coolant. A first-order-polynomial function of the core-averaged coolant temperature T_c, the coefficients of which are input parameters, describes the equivalent burnable-poison-pin solute concentration as

$$BPP = BPP0 + BPP1 \cdot T_c \tag{9-25}$$

Whereas the physical amount of solute in the burnable-poison pins is constant during the transient, its effective concentration for neutron capture increases with coolant temperature because of reduced spatial self-shielding of solute to neutrons in those pins. The amount of control-rod-cluster-pin solute in the reactor core depends on the amount of control-rod insertion into the core. Its effective concentration is input as a first-order-polynomial function of programmed reactivity R_{prog} as follows:

$$BCR = BCR0 + BCR1 \cdot R_{prog} \tag{9-26}$$

Both *BPP* and *BCR* in the previous two equations have units of macroscopic solute density ($kg \cdot m^{-3}$) in the coolant-channel volume. Programmed reactivity is assumed to be proportional to the amount of effective solute-mass change caused by control-rod movement in the core. Initially, when the reactor core is at steady-state conditions, $BCR = BCR0$.

Only the dissolved boric acid and that plated on solid structures in the reactor core are included in the evaluation of B_m or B_r for the solute reactivity-coefficient derivative parameter because the amount of solute in burnable-poison pins is constant during the transient that is being evaluated. Control-rod movement changes the amount of solute, but the reactivity change associated with this movement is accounted for in the user-defined programmed reactivity R_{prog}. There is no reactivity feedback from control-rod movement because it is already accounted for in R_{prog}.

After all four reactivity coefficients are evaluated by linear interpolation in their four dimensionally dependent tables, and the feedback reactivity is evaluated in terms of its change in the neutron multiplication constant over the last time step, $\Delta t^{n-1} = t^n - t^{n-1}$,

$$k^n R^n_{fdbk} = \sum_{j=1}^{4} (\Delta k_{fdbk})_j \tag{9-27}$$

where

$$(\Delta k_{fdbk})_j = \frac{1}{2}\left[\left(\frac{\partial k}{\partial x_j}\right)^n + \left(\frac{\partial k}{\partial x_j}\right)^{n-1}\right] \times [x_j^n - x_j^{n-1}] \ ,$$

and x_1 is T_f, x_2 is T_c, x_3 is α, and x_4 is B_m or B_r.

The superscripts n and $n-1$ indicate that the parameter is evaluated at the beginning of the current time step and at the beginning of the previous time step, respectively. There are four reactivity-coefficient-defining forms in Table 9-2. Forms 1, 2, and 3 as input are converted to form 0 by TRACE for use in Eq. (9-27). TRACE obtains the value of $(\partial k/\partial x_j)^n$ in Eq. (9-27) by multiplying the reactivity coefficients defined by reactivity-coefficient forms 1, 2, and 3 (Table 9-2) by k^{n-1}, $1/x_j^n$, and k^{n-1}/x_j^n, respectively. Using k^{n-1} rather than k^n (which is not yet known) to convert reactivity-coefficient forms 1 and 3 to $(\partial k/\partial x_j)^n$ is an approximation. The values of $(\partial k/\partial x_j)^n$ and x_j at time t^n (the start of the present time step) are evaluated as described above; their values at time t^{n-1} are those saved from their evaluation at the start of the previous time step.

The change in x_i over the last time step (with the other x_i parameters held constant in defining the reactivity coefficient) is defined in the last factor of Eq. (9-27). The term B_m or B_r includes only dissolved boric acid in the liquid coolant and boric acid plated on the core structure. There is no change in the B_r-equivalent solute concentration in burnable-poison pins when T_f, T_c, and α are not considered to vary.

To determine reactivity feedback during the current time step $\Delta t^n = t^{n+1} - t^n$, TRACE would need to know the end-of-time-step values of T_f, T_c, α, B_m, or B_r. To evaluate that reactor-core state requires knowing the current core state and the total energy-generation rate, $P_{eff}(t)$, over

the time step Δt^n. The neutronic reactivity $R(t)$ defined by the reactivity-feedback contribution, $R_{fdbk}(t)$ must be known to determine the value of $P_{eff}(t)$ from the solution of the point-reactor-kinetics equations. Thus, the evaluation of reactivity feedback during the current time step requires first knowing the time-step solution.

The TRACE code handles this difficulty of needing to know the reactivity feedback in order to evaluate it in time step Δt^n by assuming the Δk feedback-reactivity rate is zero. The Δk programmed-reactivity rate is assumed to be the same as in the previous time step, Δt^{n-1},

$$(\Delta k_{prog}^{\text{est}})^{n+1} = \Delta t^n \left\{ \frac{\Delta k_{prog}^n}{\Delta t^{n-1}} \right\} . \tag{9-28}$$

We estimate $(k_{prog})^n$ because the input-defined independent variable needed to evaluate its tabular definition at t^{n+1} is a function of the reactor-core state that is known at time t^n. We have tested a similar approximation for $(\Delta k_{prog}^{\text{est}})^n$ in TRAC, but near steady state it caused the sign of $(\Delta k_{fdbk}^{\text{est}})^n$ to change each time step. It is better to assume that $(\Delta k_{fdbk}^{\text{est}})^n$ is zero than to estimate its value based on its value in the previous time step. Feedback effects for each time step are more tightly coupled to $(\Delta k_{fdbk}^{\text{est}})^n$ than to $(\Delta k_{prog}^{\text{est}})^n$, which causes the former estimate to be numerically unstable in some situations. Thus, estimates for the neutron-multiplication constant and neutronic reactivity for the reactor state at the end of the present time step are

$$(k^{\text{est}})^{n+1} = k^n + (\Delta k_{prog}^{\text{est}})^{n+1} \tag{9-29}$$

and

$$(R^{\text{est}})^{n+1} = \frac{[(k^{\text{est}})^{n+1} - 1]}{(k^{\text{est}})^{n+1}} \tag{9-30}$$

After each Δt^{n+1} time-step solution, TRACE compares the actual programmed reactivity with its estimated value. The code corrects any discrepancy by applying

$$(\Delta k^{\text{cor}})^n = [(\Delta k_{prog})^n - (\Delta k_{prog}^{\text{est}})^n] \cdot \min\left(\frac{\Delta t^{n-1}}{\Delta t^n}, 2 \right) \tag{9-31}$$

during the next time step, Δt^n. To prevent a time-step reactivity correction from becoming very large by applying it over a time step $\Delta t^n \ll \Delta t^{n-1}$, TRACE constrains $(\Delta k^{\text{cor}})^n$ in Eq. (9-31) to

be no more than twice the Δt^{n-1} time-step value. Including this correction in Δk from the previous time step in the neutron-multiplication constant end-of-time-step estimate at Δt^{n+1} gives Eq. (9-29) in the modified form,

$$(k^{\text{est}})^{n+1} = k^n + (\Delta k_{prog}^{\text{est}})^{n+1} + (\Delta k^{\text{cor}})^n \ , \tag{9-32}$$

where

$$k^n = k^{n-1} + (\Delta k_{prog})^n + (\Delta k_{fdbk})^n \ .$$

In this procedure, we assume that $(\Delta k^{\text{cor}})^n$ and $(\Delta k_{fdbk})^{n-1}$ are small enough not to require an iterative evaluation of the present time-step solution and that $(\Delta k^{\text{cor}})^n$ is large enough to be included in the next time-step solution rather than be neglected. The code applies a similar estimate and correction procedure to the end-of-time-step power for the case in which the total reactor-core power is specified directly by a table.

The TRAC-B reactivity feedback model (Ref. 9-10) is based on the assumption that for BWR applications accurate reactivity feedback cannot be obtained based on the change in core average parameters (i.e., core average void fraction, core average moderator temperature, core average fuel temperature, and core average boron concentration). A more accurate approximation is to sum the reactivity change for each node (i.e., fluid node for void fraction, moderator temperature and boron concentration and fuel rod node for fuel temperature reactivity-feedback). The total change in reactivity is given by Eq. (9-33).

$$\begin{aligned} R^n = & \sum_{i=1}^{NFluid} C_{\alpha i} \times (\alpha_i^n - \alpha_i^{n-1}) \times WF_{ci} + \\ & \sum_{i=1}^{NFluid} C_{tmi} \times (T_{li}^n - T_{li}^{n-1}) \times WF_{ci} \times (1 - \alpha_i^n) + \\ & \sum_{i=1}^{NFluid} C_{bi} \times (B_i^n - B_i^{n-1}) \times WF_{ci} + \\ & \sum_{i=1}^{NFuel} C_{tfi} \times \left((T_{fi}^n)^{1/2} - (T_{fi}^{n-1})^{1/2} \right) \times WF_{fi} \end{aligned} \tag{9-33}$$

where,

NFluid = Total number of fluid cells in the core, include fluid cells inside the BWR fuel assemblies, water rods, and core bypass.

NFuel = Total number of fuel nodes in the core, include all average rod groups associated with each CHAN component in the model.

$C_{\alpha i}$ = Reactivity feedback coefficient for changes in the void fraction for fluid cell i.

C_{tmi} = Reactivity feedback coefficient for changes in the moderator temperature for fluid cell i.

C_{bi} = Reactivity feedback coefficient for changes in the boron concentration for fluid cell i.

C_{tfi} = Reactivity feedback coefficient for changes in the fuel temperature for fuel node i.

WF_{ci} = Weighting factor for fluid cell i.

WF_{fi} = Weighting factor for fuel node i.

α_i^n = Void fraction in fluid cell i at time step n.

T_{li}^n = Liquid temperature in fluid cell i at time step n.

B_i^n = Boron concentration in fluid cell i at time step n.

T_{fi}^n = Fuel temperature in fuel node i at time step n.

The reactivity feedback coefficients are based on the following fits:

$$C_\alpha = C_{\alpha 1} + C_{\alpha 2} \cdot \alpha + C_{\alpha 3} \cdot \alpha^2 \tag{9-34}$$

$$C_{tm} = C_{tm1} + C_{tm2} \cdot T_l + C_{tm3} \cdot T_l^2 \tag{9-35}$$

$$C_{tf} = C_{tf1} + C_{tf2} \cdot \alpha + C_{tf3} \cdot \alpha^2 \tag{9-36}$$

$$C_b = C_{b1} + C_{b2} \cdot B + C_{b3} \cdot B^2 \tag{9-37}$$

The RELAP5 model (Ref. 9-11) available in TRACE for RELAP5 input converted to a TRACE TPR file via SNAP includes two models (i.e., a separable feedback model and a tabular feedback model). The separable feedback model assumes that the reactivity feedback due to changes in moderator density, moderator temperature, fuel temperature, and boron concentration can be separated and are not dependent upon changes in the other reactivity feedback parameters. This

assumption is typically valid for reactor core close to critical and with relatively small boron concentrations. The tabular feedback model assumes that there are interactions between the different reactivity feedback effects, which cannot be neglected. For example during an ATWS, the reactivity feedback due to moderator density may be a function of the boron concentration, moderator temperature, and/or fuel temperature.

The reactivity feedback for the separable feedback model can be written as:

$$R^n = \sum_{i=1}^{nScram} R^n{}_{si} + \sum_{i=1}^{nControl} R^n{}_{ci} + R_\rho(\rho_m^n) + R_f(T_F^n) + R_B(B^n) + R_m(T_m^n) \quad (9\text{-}38)$$

where,

nScram = Number of general table scram curves.

nControl = Number of signal variables/control blocks used to specify programmed or reactivity feedback.

$R^n{}_{si}$ = Reactivity associated general table scram curves at time step n.

$R^n{}_{ci}$ = Reactivity associated signal variable/control blocks.

$R_\rho(\rho_m)$ = Moderator density reactivity feedback table as a function of core average moderator density.

$R_F(T_F)$ = Fuel temperature reactivity feedback table as a function of fuel temperature.

$R_m(T_M)$ = Moderater temperature reactivity feedback table as a function of moderator temperature.

$R_B(B)$ = Boron solute reactivity feedback table as a function of boron concentration.

The reactivity feedback model for the tabular feedback is given as:

$$R^n = R_T(T_F^n, \rho_m^n, T_m^n, B^n) \quad (9\text{-}39)$$

where $R_T(T_F^n, \rho_m^n, T_m^n, B_c^n)$ is the total reactivity table for a given fuel temperature, moderator density, moderator temperature, and boron concentration.

For the separable and tabular reactivity feedback models, the moderator density may be replaced with void fraction, depending upon the RELAP5 options selected in the original RELAP5 input model. The RELAP5 options for reactivity feedback have not been fully tested and should be used with caution. Note that currently the RELAP5 options for reactivity feedback are only available if the RELAP5 input was converted to a TRACE TPR file via SNAP. The capability to

access these models via TRACE ASCII input will be provided in future versions of TRACE as determined by user needs.

Solution of the Point-Reactor Kinetics

The code solves the point-reactor-kinetics equations Eq. (9-15) through Eq. (9-17) by the Kaganove method (Ref. 9-3). Its derivation approximates the time dependence of *P* and $k_{ex} = k - 1 = R/(1-R)$ over each integration time step by second-order polynomials and assumes $\Lambda(t) = \ell/(1 + k_{ex}(t))$ where ℓ is a constant. For TRACE, it is more appropriate to approximate the time dependence of *P* by a second-order polynomial, *R* by a first-order polynomial, and Λ by a constant because TRACE linearly extrapolates its estimate of $R(t)$ over the fluid-dynamics time step to be evaluated and because the weak time dependence of Λ generally is unknown. These modified assumptions, when applied to the point-reactor-kinetics equations, simplify the form that these equations take when analytically integrated over the neutronics integration time step Δ*t*. The derivation of those analytically integrated equations is given below. TRACE then evaluates them for $\Delta t^n/\Delta t$ integration time steps during the Δt^n fluid-dynamics time step.

In TRACE, the neutronics solution is solved before the hydraulic and heat-conduction solutions. Otherwise, the linear extrapolation estimates in the previous sub-section would not have to be done if the hydraulic and heat-conduction solutions were solved first. The heat-conduction solution would be more implicit if it were done after the neutronics solution. Another order would be to do the hydraulics solution first, the neutronics solution next, and then the heat-conduction solution.

We assume

$$P(t) = P(0) + P_1 t + P_2 t^2 \tag{9-40}$$

$$R(t) = R(0) + R_1 t \tag{9-41}$$

where $P(0)$, $R(0)$, and $R_1 = [(R^{\text{est}})^n - R(0)]/\Delta t^n$ are all known values, and that Λ, λ_i, β_i, λ_j^H, and E_j are constant over the interval $0 \le t \le \Delta t$,

Solving Eq. (9-16) for $C_i(t)$ in terms of a functional of the fission power $P(t)$ gives

$$C_i(t) = C_i(0)\,e^{-\lambda_i t} + \frac{\beta_i}{\Lambda}\int_0^t e^{-\lambda_i(t-\tau)} P(\tau)\,d\tau \tag{9-42}$$

Substituting Eq. (9-42) into Eq. (8-6) and integrating the resulting equation term-by-term gives

$$P(t) = P(0) + \int_0^t \frac{R(\tau)P(\tau)}{\Lambda}\,d\tau - \sum_{i=1}^{I}\frac{\beta_i}{\Lambda}\int_0^t e^{-\lambda_i(t-\tau)} P(\tau)\,d\tau + \tag{9-43}$$

$$\sum_{i=1}^{I} C_i(0)[1 - e^{-\lambda_i t}] + \frac{S}{\Lambda R_1}\ln\left[\frac{1 - R(0)}{1 - R(0) - R_1 t}\right]$$

Note that Eq. (9-43) assumes R_1 is not equal to zero. If R_1 is zero, then the last term in Eq. (9-43) is $\frac{St}{\Lambda(1-R(0))}$. Substituting Eq. (9-33) for $P(\tau)$ and Eq. (9-41) for $R(\tau)$ in Eq. (9-43), evaluating the integrals, and rearranging the resulting equation in terms of the P_1 and P_2 unknowns gives

$$a_1(t)P_1 + a_2(t)P_2 = q(t) \tag{9-44}$$

where

$$a_1(t) = t\Lambda - t^2\left[\frac{1}{2}R(0) + \frac{1}{3}R_1 t\right] + \sum_{i=1}^{I}\beta_i t^2 I_{i1}(t) \tag{9-45}$$

$$a_2(t) = t^2\Lambda - t^3\left[\frac{1}{3}R(0) + \frac{1}{4}R_1 t\right] + \sum_{i=1}^{I}\beta_i t^3 I_{i2}(t) \tag{9-46}$$

$$q(t) = \frac{S}{R_1}\ln\left[\frac{1-R(0)}{1-R(0)-R_1 t}\right] + t\left[R(0)+\frac{1}{2}R_1 t\right]P(0) + \sum_{i=1}^{I}[\Lambda\lambda_i C_i(0) - \beta_i P(0)]tI_{i0}(t) \quad (9\text{-}47)$$

or if R_1 is zero

$$q(t) = \frac{St}{1-R(0)} + tR(0)P(0) + \sum_{i=1}^{I}[\Lambda\lambda_i C_i(0) - \beta_i P(0)]tI_{i0}(t) \quad (9\text{-}48)$$

and

$$I_{im}(t) = \frac{\int_0^t e^{-\lambda(t-\tau)}\tau^m d\tau}{t^{m+1}} \quad \text{for } m = 0,\ 1,\ 2 \quad (9\text{-}49)$$

Note the coding in TRACE is currently in error in that the source term in Eq. (9-47) appears as:

$$q(t) = S\left[1-R(0)t-\frac{1}{2}R_1 t^2\right] + t\left[R(0)+\frac{1}{2}R_1 t\right]P(0) + \sum_{i=1}^{I}[\Lambda\lambda_i C_i(0) - \beta_i P(0)]tI_{i0}(t) \quad (9\text{-}50)$$

This will be corrected in a future version of TRACE.

The P_1 and P_2 polynomial coefficients are evaluated by requiring Eq. (9-44) to be satisfied for $t = \Delta t$ (at the end of the integration time step) and $t = \Delta t/2$ (at the midpoint of the integration time step). Solving the two equations

$$a_1(\Delta t)P_1 + a_2(\Delta t)P_2 = q(\Delta t) \tag{9-51}$$

and

$$a_1\left(\frac{\Delta t}{2}\right)P_1 + a_2\left(\frac{\Delta t}{2}\right)P_2 = q\left(\frac{\Delta t}{2}\right) \tag{9-52}$$

for P_1 and P_2 gives

$$P_1 = \frac{\left[q(\Delta t)\,a_2\left(\frac{\Delta t}{2}\right) - q\left(\frac{\Delta t}{2}\right)a_2(\Delta t)\right]}{D} \tag{9-53}$$

and

$$P_2 = \frac{\left[a_1(\Delta t)\,q\left(\frac{\Delta t}{2}\right) - a_1\left(\frac{\Delta t}{2}\right)q(\Delta t)\right]}{D} \tag{9-54}$$

where

$$D = a_1(\Delta t)\,a_2\left(\frac{\Delta t}{2}\right) - a_1\left(\frac{\Delta t}{2}\right)a_2(\Delta t)\ .$$

The total fission power at the end of the integration time step $t = \Delta t$ from Eq. (9-40) is

$$P(\Delta t) = P(0) + P_1\Delta t + P_2\Delta t^2\ . \tag{9-55}$$

If we know $P(t)$ for $0 \le t \le \Delta t$ we can evaluate $C_i(\Delta t)$ by substituting Eq. (9-40) into Eq. (9-42) and using

$$\Delta t I_{i0}(\Delta t) = \frac{1 - e^{-\lambda_i \Delta t}}{\lambda_i} \tag{9-56}$$

$$\Delta t^{m+1} I_{im}(\Delta t) = \frac{\Delta t^m - m\Delta t^m I_{im-1}(\Delta t)}{\lambda_i} \quad \text{for } m = 1,\ 2 \tag{9-57}$$

by analytically integrating its definition in Eq. (9-44) as follows:

$$C_i(\Delta t) = C_i(0)[1 - \lambda_i \Delta t I_{i0}(\Delta t)] + \frac{\beta_i}{\Lambda}\left[P(0)\Delta t I_{i0}(\Delta t) + P_1 \Delta t^2 I_{i1}(\Delta t) + P_2 \Delta t^3 I_{i2}(\Delta t) \right] \tag{9-58}$$

for $i = 1, 2, \ldots, I$.

The code evaluates the decay-heat equations in the same way to give

$$H_j(\Delta t) = H_j(0)[1 - \lambda_j^H \Delta t I_{j0}^H(\Delta t)] + E_j\left[P(0)\Delta t I_{j0}^H(\Delta t) + P_1 \Delta t^2 I_{j1}^H(\Delta t) + P_2 \Delta t^3 I_{j2}^H(\Delta t) \right] \tag{9-59}$$

for $j = 1, 2, \ldots, J$, and where

$$\Delta t^{m+1} I_{jm}^H(\Delta t) = \int_0^{\Delta t} e^{-\lambda_j^H(\Delta t - \tau)} \tau^m d\tau \ . \tag{9-60}$$

The code evaluates $\Delta t^{m+1} I_{im}(\Delta t)$ with the following recursion relation:

$$\Delta t^{m+1} I_{jm}^H(\Delta t) = \frac{\Delta t^m - m\Delta t^m I_{jm-1}^H(\Delta t)}{\lambda_j^H} \quad \text{for } m = 1, 2 \tag{9-61}$$

once

$$\Delta t I_{i0}^H(\Delta t) = \frac{1 - e^{-\lambda_j^H \Delta t}}{\lambda_j^H}$$

is first evaluated. For $\lambda_i \Delta t < 1$, Eq. (9-61) results in the loss of several least-significant digits of accuracy with each application of the recursion formula. Thus, for $\lambda_i \Delta t < 1$, TRACE first evaluates $\Delta t^3 I_{i2}(\Delta t)$ using the Maclaurin expansion,

$$\Delta t^{m+1} I_{im}(\Delta t) = \Delta t^{m+1} m! \left[\frac{1}{(m+1)!} - \frac{\lambda_i \Delta t}{(m+2)!} + \frac{(\lambda_i \Delta t)^2}{(m+3)!} - \ \ldots \right] \tag{9-62}$$

for $m = 2$, and then evaluates the reciprocal of the Eq. (9-59),

$$\Delta t^m I_{im-1}(\Delta t) = \frac{\Delta t^m - \lambda \Delta t^{m+1} I_{im}(\Delta t)}{m} \quad \text{for } m = 2,\ 1 \tag{9-63}$$

A maximum of the first 13 terms in the series expansion for Eq. (9-62) is included if $\lambda_i \Delta t < 1$. The sum is terminated if the absolute value of the next term in the series divided by the sum of all previous terms is less than 10^{-14}. For $\lambda_i \Delta t \geq 1$, the analytical solution given by Eq. (9-61) is used.

The accuracy of the second-order polynomial approximation for $P(t)$ can be increased by decreasing the integration time-step size Δt. We would like Δt to be as large as possible, however, while we maintain a desired level of accuracy in approximating $P(t)$. To achieve this, the following procedure for automatically adjusting the reactor-kinetics time step in TRACE is used. In the same manner that Eq. (9-51) and Eq. (9-52) were defined, Eq. (9-43) also could be required to be satisfied at $t = \Delta t/4$ by

$$a_1\left(\frac{\Delta t}{4}\right) P_1 + a_2\left(\frac{\Delta t}{4}\right) P_2 = q\left(\frac{\Delta t}{4}\right) . \tag{9-64}$$

The above equation together with Eq. (9-52), which is evaluated at $t = \Delta t/2$, are solved over the time range $0 \leq t \leq \Delta t/2$ for $P_1 = P_1^*$ and $P_2 = P_2^*$ to give

$$P_1^* = \frac{q\left(\frac{\Delta t}{2}\right) a_2\left(\frac{\Delta t}{4}\right) - q\left(\frac{\Delta t}{4}\right) a_2\left(\frac{\Delta t}{2}\right)}{D^*} \tag{9-65}$$

and

$$P_2^* = \frac{q\left(\frac{\Delta t}{4}\right) a_1\left(\frac{\Delta t}{2}\right) - q\left(\frac{\Delta t}{2}\right) a_1\left(\frac{\Delta t}{4}\right)}{D^*} \tag{9-66}$$

where

$$D^* = a_1\left(\frac{\Delta t}{2}\right) a_2\left(\frac{\Delta t}{4}\right) - a_2\left(\frac{\Delta t}{2}\right) a_1\left(\frac{\Delta t}{4}\right)$$

This solution over half the integration time step provides a more accurate value for $P(t)$ at $t = \Delta t/2$,

$$P^*\left(\frac{\Delta t}{2}\right) = P(0) + P_1^*\left(\frac{\Delta t}{2}\right) + P_2^*\left(\frac{\Delta t}{2}\right)^2 \tag{9-67}$$

than the solution over the full integration time step at $t = \Delta t/2$,

$$P\left(\frac{\Delta t}{2}\right) = P(0) + P_1\left(\frac{\Delta t}{2}\right) + P_2\left(\frac{\Delta t}{2}\right)^2 \tag{9-68}$$

The code uses the difference between these two values as a measure of the error in the solution over the full integration time step Δt

$$\epsilon(\Delta t) = \left| \frac{P\left(\frac{\Delta t}{2}\right) - P^*\left(\frac{\Delta t}{2}\right)}{P^*\left(\frac{\Delta t}{2}\right)} \right| \tag{9-69}$$

It is desirable to increase Δt if the above ε is too small and to decrease Δt if ε is too large. Toward this end, the code defines two error bounds, ε_1 and ε_2, to provide the desired convergence such that,

1) if $\varepsilon_1 < \varepsilon(\Delta t) < \varepsilon_2$, the code maintains the present value of reactor-kinetics time step Δt;

2) if $\varepsilon_1 < \varepsilon_2 \leq \varepsilon(\Delta t)$, the code halves the value of Δt because the error in $P(\Delta t)$ is too large; and

3) if $\varepsilon(\Delta t) \leq \varepsilon_1 < \varepsilon_2$, the code doubles the value of Δt because the error in $P(\Delta t)$ is too small.

When Δt is halved, the integration time step is reevaluated. When the third criterion is satisfied, the number of remaining integration time steps to be evaluated over the fluid-dynamics time step must be an even number for the integration time step to be doubled (and the number of remaining integration time steps to be halved). TRACE is programmed to use $\varepsilon_1 = 10^{-6}$ and $\varepsilon_2 = 10^{-4}$. A numerical study showed these values to yield a maximum fractional error less than 10^{-4} and an

average fractional error less than 10^{-5} in the fission power solution. The point-reactor-kinetics solution required < 1% of TRACE execution time.

Conclusions Regarding the Reactor-Core Power Model

The core-power model in TRACE, with all the options and features, has proved to be sufficiently general for describing core assemblies in most reactor-safety-related experiments, particularly ones that are integral in nature, and in reactor plants, provided that the power shape only changes in time in the axial direction. For this to be true, the axial-power shape must be specified as a function of some user-defined independent variable for the axial-power-shape table. The option to specify core power directly with a tabular prescription is generally sufficient for modeling most transients of interest where the power-level behavior is known.

The point-reactor kinetics with reactivity feedback model has demonstrated (for many cases of the TRACE developmental assessment problem set) the ability to describe the transient power response of a reactor core. For example, in the case of anticipated transients without scram, the core-power behavior would not be known because of reactivity-feedback effects, and in this case, reactor kinetics is a necessary capability. In analyzing experiments from the LOFT facility (for example, the L6-1 test simulating a loss-of-steam-load transient) and transients from power plants (for example, the Zion PWR standard test problem), reactor kinetics has demonstrated a good predictive capability. For performing best-estimate analyses of large-break LOCAs, reactor kinetics has demonstrated the ability to predict the shutdown of core power by core voiding before the control-rod scram is effective.

For a specific reactor transient where multi-dimensional transient neutronics is important, TRACE coupled with PARCS can be used for this simulation (i.e. BWR stability transients). However, for a number of accident scenarios, point-kinetics or specified is power is sufficient.

The decay heat models available in TRACE can be used to accurately simulate the decay heat power levels associated with a nuclear reactor and determine the amount of decay heat for a given reactor power history. The user has the option to use a few group decay heat model with a minimum of user input, which will give approximate results or as many as 92 decay heat groups consistent with the 1994 decay heat standard. The decay power levels can be based on a specified reactor operating history or infinite operation at the initial power level and is calculated consistent with the decay heat model selected by the user.

The deficiencies of the core-power model are principally related to the fact that reactor kinetics is based on a point-reactor assumption, and the power distribution is defined by a superposition of fuel-rod-radial, core-axial, and (r, θ)-plane shapes. Axial-shape changes in the power distribution with a known dependence can be simulated, but fuel-rod-radial and core (r, θ)-plane power-shape changes and power distributions that are not definable by superimposed fuel-rod-radial, core-axial, and (r, θ)-plane shapes cannot be modeled. Reactivity feedback is also based on the point-

reactor assumption with little theoretical justification for the procedure used to core average the reactivity-feedback parameters. Asymmetric and localized reactivity-feedback effects and control-rod movements in the reactor core cannot be modeled accurately. However, within these modeling limitations, the core-power model is accurate and efficient in determining the time-dependent behavior of the reactor-core power. To further assess the point-kinetics model requires having good core neutronics data (power shape, reactivity coefficients, etc.) and use of neutronics codes to generate the point-kinetics input data.

For transients in which 3D neutronics effects are important (i.e., BWR instabilities), TRACE can be coupled to the PARCS. When TRACE is coupled to PARCS a POWER component is still required in the TRACE model to ensure that necessary power density arrays have been allocated so that the PARCS transient 3D power can be loaded into the appropriate array element locations in TRACE.

References

9-1 Reactor Physics Constants," Argonne National Laboratory report ANL-5800, 2nd ed. (July 1963).

9-2 A. Rodkowsky, Ed., "Naval Reactors Physics Handbook, Vol. 1: Selected Basic Techniques," Library of Congress Number 65-60008 (1964).

9-3 J. J. Kaganove, "Numerical Solution of the One-Group Space-Independent Reactor Kinetics Equations for Neutron Density Given the Excess Reactivity," Argonne National Laboratory report ANL-6132 (1960).

9-4 American National Standard for Decay Heat Power in Light Water Reactors," American Nuclear Society publication ANSI/ANS-5.1 (1979).

9-5 American National Standard for Decay Heat Power in Light Water Reactors," American Nuclear Society publication ANSI/ANS-5.1 (1994).

9-6 TRACE Users Manual.

9-7 Joe, H.C., Barber, D., Jiang, G., and Downar, T. J., "PARCS, A Multi-Dimensional Two-Group Reactor Kinetics Code Based on the Nonlinear Analytic Nodal Method," PU/NE-98-26, Sept. 1998.

9-8 Volume 2: User Manual for the PARCS Kinetic Core Simulator Module.

9-9 J. W. Spore, et.al., "TRAC-M/FORTRAN 90 Version 3.0 Theory Manual," NUREG/CR-6724, July, 2001.

9-10 M. M. Giles, et. al., "TRAC-BF1/MOD1: An Advanced Best Estimate Computer Program for Boiling Water Reactor Accident Analysis, Volume I: Model Description," May 1992, INEL.

9-11 RELAP5/MOD3.3 Code Manual Volume I: Code Structure, System Models, and Solution Methods," NSAD, December, 2001, ISL, Rockville, Maryland, Idaho Falls, ID

10

Special Component Models

Some one-dimensional components in TRACE perform special functions that require modification of the solution of the 1D fluid equations. These modifications are more than simply altering the normal closure relations that have been discussed in previous chapters; these components either alter the normal finite differencing of the fluid equations, introduce source terms to the equations, or use complex logic to alter the closure relations to accomplish a specific modeling requirement. The PUMP component produces a momentum source term in the form of an additional ΔP on the right-hand side of the momentum equation to model the pressure rise across the pump impeller. The PRIZER component models a PWR pressurizer. The steam/water separator/dryer component (SEPD) permits the user to model the swirl separators and chevron dryers in a BWR reactor. The JETP component models the jet pumps found in BWR systems by use of the TEE component momentum source in the TEE joining cell and jet pump specific singular loss coefficients.

Nomenclature

A^* = area ratio of outlet to inlet flow area for the jet pump

A_n = swirl vane flow area in separator

A_i = standpipe flow area in separator

C_c = contraction constant for the jet pump

C_e = expansion constant for the jet pump

C_f = friction coefficient

C_K = total loss coefficient in the discharge passage of the separator

C_{NOZ} = contraction loss coefficient

$CDIM$ = critical dryer inlet moisture

CO = carry-over ratio

CU = carry-under ratio

c_p = specific heat at constant pressure

D_D = hydraulic diameter in the discharge passage of the separator

$DELDIM$ = range of inlet moisture over which the dryer capacity goes from one to zero for a fixed vapor inlet velocity

DIM = dryer inlet moisture

$EFFLD$ = effective L/D coefficient at the separator pick-off ring

F_a = axial component of frictional force on swirling water later

F_f = resultant frictional force

F_t = tangential component of frictional force on swirling water layer

g = gravitational acceleration

$GDRY$ = SEPD capacity factor

h = normalized pump head

$h_{1\phi}$ = normalized pump head from the single-phase performance curve

$h_{2\phi}$ = normalized pump head from the two-phase fully degraded performance curve

H = pump head

H_R = rated pump head

$H_{1\phi}$ = single-phase pump head

$H_{2\phi}$ = two-phase fully-degraded pump head

H_{sk} = axial distance between the separator hub and the bottom of the discharge passage

H_D = length of separator barrel

H_{12} = height of the liquid pool surrounding the separator relative to the bottom of the discharge passage

I = pump moment of inertia

jcell = cell index on the primary side of a TEE component, where the secondary side is connected to the primary side.

K_c = contraction irreversible loss factor for the jet pump

K_e = expansion irreversible loss factor for the jet pump

LMT = total liquid mass in the PRIZER

$\dot{m}$ = mass flow rate

M = ratio of liquid mass flow rate in the drive nozzle of the jet pump to liquid mass flow rate in the suction of the jet pump

$M(\alpha)$ = pump head degradation multiplier

N = ratio of specific energy increase in the suctio flow to the specific energy decrease in the drive nozzle flow

$N(\alpha)$ = pump torque degradation multiplier

P_1 = TRACE calculated pressure in cell 1 of the PRIZER

ΔP_{max} = user-supplied pressure offset at which heater/sprays achieve maximum effectiveness

P_o = pressure in the vapor core of the separator

P_{set} = user-supplied pressure setpoint for the PRIZER

P_w = pressure at the separator wall

q = normalized pump volumetric flow

q_{fric} = heat generated by pump due to friction

Q = pump volumetric flow

Q_f = energy added/removed from liquid in an individual PRIZER cell

Q_{heat} = user-supplied maximum effective power of the PRIZER heater/sprays

Q_{in} = energy added/removed from the PRIZER

Q_R = rated pump volumetric flow

r = radius

r_f = inner radius of the water layer in the separator

r_w = radius of the separator barrel

r_r = radius of the separator pick-off ring

RE_L = liquid Reynolds number

S = slip ratio

S_{mom} = pump momentum source term

t = time

T = pump hydraulic torque acting on the impeller

T_f = pump friction torque acting on the rotating parts of the motor

T_{hy} = hydraulic torque

T_R = rated pump torque

V = velocity

V_a = axial velocity

V_{af} = axial velocity in the water layer

V_{ag} = axial velocity in the vapor core

V_{an} = axial velocity at the swirl vane

V_D = velocity in the discharge passage

V_t = tangential velocity

V_{tn} = tangential velocity at the swirl vane

V_{tw} = tangential velocity on the wall

V_w = resultant swirling velocity on the wall

$VDRY1$ = vapor velocity below which any amount of moisture is assumed to be separated from the vapor stream

$VDRY2$ = vapor velocity above which no amount of moisture, however small, can be separated from the vapor stream

Vol = volume

Vol_{liq} = total liquid volume in the pressurizer

W = mass flow rate

W_i = total flow rate

W_D = total discharge flow

Δx = cell length

x or X = quality

X_i = inlet flow quality

X_L = collapsed liquid level

α = void fraction or angle of the jet pump diffuser

β = normalized pump hydraulic torque

$\beta_{1\phi}$ = normalized pump hydraulic torque from single phase torque curves

$\beta_{2\phi}$ = normalized pump hydraulic torque from two phase fully-degraded torque curves

ρ = density

$\overline{\rho}$ = mean density

ω = normalized pump speed

Ω = pump speed (impeller angular velocity)

Ω_R = rated pump speed

θ = angle between swirl vanes and the horizontal plane

Subscripts

CO = denotes a liquid carry-over quantity

CU = denotes a vapor carry-under quantity

DIS = applies to the discharge arm of the SEPD

$donor$ = denotes a donor-cell (upstream) quantity

d = denotes the drive nozzle of a jet pump

ds = denotes the discharge of a jet pump

EX = applies to the exit of the SEPD

f or l = denotes a liquid quantity

g = denotes a gas phase quantity

hy = denotes a hydraulic quantity

IN = applies to the inlet of the SEPD

j = denotes a quantity that applies to the cell center

$j+1/2$ = denotes a quantity that applies to a cell edge (center of a momentum cell)

$j+1$ = denotes a quantity that applies to the downstream cell

k = index of cell in PRIZER that contains the collapsed liquid level

m = denotes a mixture quantity

s = denotes the suction line of a jet pump

Superscripts

n = denotes an old-time level quantity

$n+1$ = denotes a current or new-time level quantity

PUMP Component

The PUMP component describes the interaction of the system fluid with a centrifugal pump. It calculates the pressure differential across the pump impeller and the pump impeller's angular velocity as a function of the fluid flow rate and fluid properties. The model can simulate any centrifugal pump and allows for the inclusion of two-phase effects.

The following considerations were made in creating the PUMP component:

1) compatibility with adjacent components should be maximized,
2) choking at the pump-impeller interface should be predicted automatically by the pump-curve data, and
3) the calculated pressure rise across the pump-impeller interface should agree with that measured at steady-state conditions.

The first two criteria preclude the use of a lumped-parameter model. Instead, the PUMP component has been implemented as a variant of the PIPE component, but with pump-curve correlations that define an extra momentum source at the pump-impeller interface. At its heart, the PUMP component is really nothing more than a means of specifying a cell edge that should act like the impeller in a pump, imparting momentum to the fluid around it.

Pump Governing Equations

While the User Guide presents several possible PUMP component representations, Figure 10-1 illustrates a generic way of conceptualizing the pump model. It shows two mesh cells, labeled j and $j+1$, that straddle the pump impeller interface (labeled with index $j+1/2$). Superimposed over that is the momentum cell over which the motion equations for the interface are solved (denoted by the dashed box). When modeled in the traditional manner[1], (i.e. the PUMP has two or more cells), cells j and $j+1$ correspond to cells 1 and 2, respectively. However, because a PUMP component can be modeled as a single face with zero cells, cells j and $j+1$ may actually belong to other 1D components.

The PUMP-component model is identical to the 1D PIPE-component model except that the motion equations for the interface between cells j and $j+1$ are approximated by

1. In the legacy model inherited from TRAC-P, PUMP components must have two or more computational cells, with the pump-impeller interface hardwired to exist at the second face. The ability to model a PUMP as a single cell face with zero cells was added later, as part of the NRC's code consolidation project (to recapture some of RELAP5's capabilities). It is not possible to define a PUMP component with just one mesh cell.

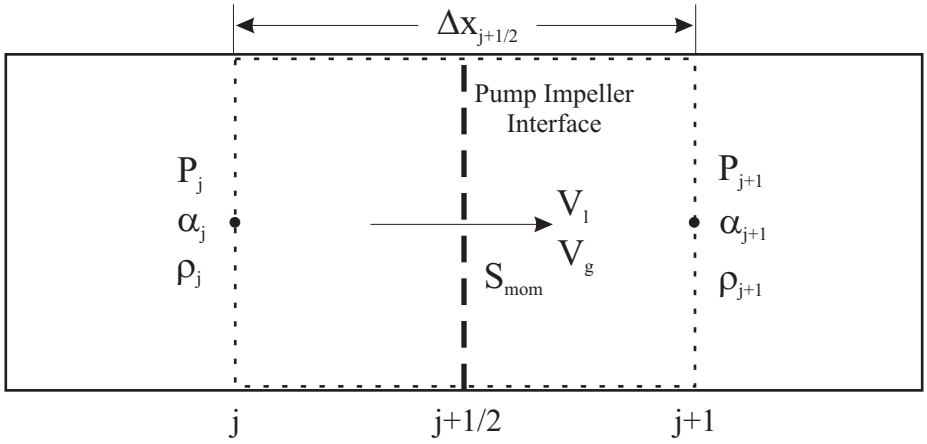

Figure. 10-1. Generic PUMP model conceptualization.

$$\frac{V_g^{n+1} - V_g^n}{\Delta t} = \frac{[P_j^{n+1} - P_{j+1}^{n+1} + S_{mom}^{n+1}]}{(\overline{\rho}_m)_{j+1/2}^n \cdot \Delta x_{j+1/2}} - g \cdot \cos\theta \tag{10-1}$$

and

$$V_l^{n+1} = V_g^{n+1} \ , \tag{10-2}$$

where $\Delta x_{j+1/2}$ is the length of the momentum cell, $(\overline{\rho}_m)_{j+1/2}$ is the mean mixture density of the momentum cell, and S_{mom} is the first-order approximated pressure rise momentum source across the pump-impeller interface evaluated from the pump-curve correlations. It is given by the following expression:

$$S_{mom}^{n+1} = \left\{ \Delta P^n + \left(\frac{\partial \Delta P}{\partial V} \right)^n \cdot (V_g^{n+1} - V_g^n) \right\} \tag{10-3}$$

The pressure rise, ΔP^n, and its derivative with respect to the coolant velocity, $\left(\frac{\partial \Delta P}{\partial V} \right)^n$, for the pump-impeller interface is evaluated only once at the beginning of each timestep. This momentum source is applied in the coolant motion equation at the pump-impeller interface. The mean mixture density is calculated from the following relationship:

$$(\overline{\rho}_m)_{j+1/2}^{n} = \alpha_{donor}(\overline{\rho}_g)_{j+1/2}^{n} + (1-\alpha_{donor})(\overline{\rho}_l)_{j+1/2}^{n} \tag{10-4}$$

where α_{donor} is a donor-cell evaluated void fraction. Given that the phasic densities are known at the cell-center, the mean phasic densities at the cell edge are calculated using a cell-length weighting procedure, as given by:

$$(\overline{\rho}_g)_{j+1/2}^{n} = \frac{\Delta x_j (\rho_g)_j^n + \Delta x_{j+1} (\rho_g)_{j+1}^n}{\Delta x_j + \Delta x_{j+1}} \tag{10-5}$$

$$(\overline{\rho}_l)_{j+1/2}^{n} = \frac{\Delta x_j (\rho_l)_j^n + \Delta x_{j+1} (\rho_l)_{j+1}^n}{\Delta x_j + \Delta x_{j+1}} \tag{10-6}$$

where Δx_j and Δx_{j+1} represent the cell lengths of the j and $j+1$ cells, respectively. In all of the above equations, the n and $n+1$ superscripts indicate that quantities should be evaluated at the old-time and new-time levels, respectively.

Friction and form losses do not enter explicitly into Eq. (10-1) because we assume that the friction effects are normally included in the homologous curves defining the pump head. Therefore, wall drag and additive friction losses are not modeled between the centers of cells j and $j+1$.

During a steady state, the pressure rise across the pump can be determined by recognizing that the velocity difference terms in Eq. (10-1) become zero, giving rise to the following equation:

$$\Delta P = P_{j+1} - P_j + (\overline{\rho}_m)_{j+1/2} \cdot \Delta x_{j+1/2} \cdot g \cdot \cos\theta \ , \tag{10-7}$$

The time level superscripts have been eliminated as they are irrelevant for a steady state.

Pump Head Modeling

The pump modeling in TRACE is based on the standard homologous-curves approach. These curves represent the performance of the pump in a normalized format, giving the normalized pump head as a function of the normalized volumetric flow and normalized pump speed. Homologous curves (one curve segment represents a family of curves) are used for this description because of their simplicity. These curves describe, in a compact manner, all operating states of the pump obtained by combining positive or negative pump-impeller angular velocities with positive or negative fluid volumetric flows. While TRACE maintains several sets of built-in curves for some well-used pump types, you are also offered the option of supplying your own.

The following definitions are used in the subsequent development:

H = the pump head, $(\Delta P)/\rho_m$ (Pa-m^3/kg, m^2/s^2, or N-m/kg),

Q = the impeller-interface volumetric flow rate, $A_{j+1/2} \cdot V_{j+1/2}$ (m^3/s), and

Ω = the pump-impeller angular velocity (rad/s),

where ΔP is the pressure rise across the pump-impeller interface and ρ_m is the impeller-interface upstream coolant-mixture density. To allow one set of curves to be used for a variety of pumps, the following normalized quantities are used:

$$h = H/H_R \tag{10-8}$$

$$q = Q/Q_R \tag{10-9}$$

$$\omega = \Omega/\Omega_R \tag{10-10}$$

where H_R is the rated head, Q_R is the rated volumetric flow, and Ω_R is the rated pump-impeller rotational speed for the pump[1]. The pump similarity relations (Ref. 10-2) show that

$$h/\omega^2 = f(q/\omega) \tag{10-11}$$

For small ω, this correlation is not satisfactory, so the following combination of variables is used,

$$h/q^2 = f(\omega/q)\,. \tag{10-12}$$

Eq. (10-11) is used in the range $0 \le |q/\omega| \le 1$ and results in two separate curves, one for $\omega > 0$ and one for $\omega < 0$. Eq. (10-12) is used in the range $0 \le |\omega/q| \le 1$ and yields two separate curves, one for $q > 0$ and one for $q < 0$. The four resulting curve segments, as well as the curve selection criteria used in TRACE, are shown in Table 10-1.

1. The rated quantities are provided through input

Table 10-1. Definitions of the four curve segments that describe the homologous pump-head curves[a]

Curve Segment	$\left\|\frac{q}{\omega}\right\|$	ω	q	Correlation
1	≤ 1	> 0	N/A	$\frac{h}{\omega^2} = f\left(\frac{q}{\omega}\right)$
4	≤ 1	< 0	N/A	
2	> 1	N/A	> 0	$\frac{h}{q^2} = f\left(\frac{\omega}{q}\right)$
3	> 1	N/A	< 0	

a. For the special case of both $\omega = 0.0$ and $q = 0.0$, the code sets $h = 0.0$

To account for two-phase coolant effects on pump performance, the pump curves are divided into two separate regimes. Data indicate that two-phase coolant pump performance in the void fraction range of 0.2 to 0.8 is degraded significantly in comparison with its performance at void fractions outside this range. One set of curves describes the pump performance for single-phase coolant (at a 0.0 or 1.0 void fraction), and another set describes the two-phase, fully degraded performance at void fractions between 0.0 and 1.0.

The pump head at any void fraction is calculated from the relationship,

$$H = H_{1\phi} - M(\alpha) \cdot [H_{1\phi} - H_{2\phi}] \ , \tag{10-13}$$

where

H = the total pump head,

$H_{1\phi} = h_{1\phi} H_R$ = the single-phase pump head ($h_{1\phi}$ is the non-dimensional head from the single-phase homologous head curves),

$H_{2\phi} = h_{2\phi} H_R$ = the two-phase fully degraded pump head ($h_{2\phi}$ is the non-dimensional head from the fully degraded homologous head curves),

$M(\alpha)$ = the head degradation multiplier, and

α = the upstream void fraction.

The head degradation multiplier is a function of void fraction and serves as a means of ramping between the single-phase and two-phase fully-degraded pump head contributions. TRACE obtains this multiplier either from the built-in curve sets, or a user-supplied table of values. A value of zero implies that there is no two-phase degradation and a value of one implies the flow through the pump is fully-degraded. As such, when supplying the table of values yourself, take care to ensure the values are nonzero only in the void fraction range where the pump head is either partially or fully degraded.

At this point, no knowledge of the coolant mixture density is required to calculate H from the homologous head curves. However, the upstream coolant mixture density is used to convert the total pump head H to the pressure rise across the pump impeller, by the definition of Eq. (10-1).

Pump Torque Modeling

The development of homologous torque curves parallels the previous development for homologous head curves. The dimensionless hydraulic torque is defined by:

$$\beta = T_{hy} / T_R , \tag{10-14}$$

where T_{hy} is the hydraulic torque and T_R is the rated torque. The convention used is that a positive T_{hy} works to retard positive pump angular velocity. The dimensionless torque β is correlated as either β/ω or β/q, just as the dimensionless head h was correlated. Thus we have the following relationships:

$$\beta/\omega^2 = f(q/\omega) \tag{10-15}$$

and

$$\beta/q^2 = f(\omega/q) \tag{10-16}$$

As with the head curves, these correlations yield eight additional corresponding curve segments — four corresponding to the performance of the pump under single phase conditions and four corresponding to performance for two-phase fully degraded conditions. The homologous torque-curve segments are correlated in the same manner as the head-curve segments shown in Table 10-1 (simply replace h with β). For the special case of $\omega = q = 0.0$, TRACE sets $\beta_{1\phi} = \beta_{2\phi} = 0.0$.

The single-phase torque $T_{1\phi}$ is dependent upon the fluid density and is calculated from

$$T_{1\phi} = \beta_{1\phi} \cdot T_R \cdot (\rho_m / \rho_R), \tag{10-17}$$

where $\beta_{1\phi}$ is the dimensionless hydraulic torque from the single-phase homologous torque curves, ρ_m is the pump upstream mixture density, and ρ_R is the rated density. The density ratio is needed to correct for the density difference between the pumped fluid and the rated condition. Similarly, two-phase fully degraded torque $T_{2\phi}$ is obtained from

$$T_{2\phi} = \beta_{2\phi} \cdot T_R \cdot (\rho_m / \rho_R), \tag{10-18}$$

where $\beta_{2\phi}$ is the dimensionless hydraulic torque from the two-phase fully degraded homologous torque curves. For two-phase conditions, the pump-impeller torque is calculated from

$$T = T_{1\phi} - N(\alpha) \cdot [T_{1\phi} - T_{2\phi}], \tag{10-19}$$

where T is the total pump-impeller torque and $N(\alpha)$ is the torque degradation multiplier (it works like the head degradation multiplier, as discussed above).

Pump Speed

The PUMP component treats the pump-impeller angular velocity Ω as a constant value that is input each timestep (and may vary) when the motor is energized. After the drive motor is tripped, the time rate of change of the pump-impeller angular velocity Ω is proportional to the sum of the moments acting on it and is calculated from

$$I\frac{\partial \Omega}{\partial t} = -\sum_i T_i = -(T_{hy} + T_f), \tag{10-20}$$

where I is the combined impeller, shaft, and motor-assembly moment of inertia, T_{hy} is the hydraulic torque on the pump-impeller, and T_f is the torque caused by friction and by the bearing and windage.

$$T_f = \begin{cases} C_0 + C_1\frac{\Omega}{\Omega_R} + C_2\frac{\Omega|\Omega|}{\Omega_R^2} + C_3\frac{\Omega^3}{\Omega_R^3} & ; \quad \Omega \geq 0 \\ -C_0 + C_1\frac{\Omega}{\Omega_R} + C_2\frac{\Omega|\Omega|}{\Omega_R^2} + C_3\frac{\Omega^3}{\Omega_R^3} & ; \quad \Omega < 0 \end{cases}, \tag{10-21}$$

where C_0, C_1, C_2, and C_3 are user-supplied constants. If the pump-impeller angular velocity (pump speed) drops below a user-defined threshhold, then a second set of constants are used to determine T_f.

$$T_f = \begin{cases} C'_0 + C'_1\frac{\Omega}{\Omega_R} + C'_2\frac{\Omega|\Omega|}{\Omega_R^2} + C'_3\frac{\Omega^3}{\Omega_R^3} & ; \quad \Omega \geq 0 \\ -C'_0 + C'_1\frac{\Omega}{\Omega_R} + C'_2\frac{\Omega|\Omega|}{\Omega_R^2} + C'_3\frac{\Omega^3}{\Omega_R^3} & ; \quad \Omega < 0 \end{cases}, \tag{10-22}$$

where C'_0, C'_1, C'_2, and C'_3 are user-supplied constants. The constants C_0, C_1, C_2, C_3, C'_0, C'_1, C'_2, and C'_3 should be determined from experimental data. Note that as the pump speed approaches zero, the C_0 and C'_0 contributions do not disappear, ensuring there is always some resistance available to prevent the pump from coasting indefinitely.

The hydraulic torque T is evaluated using the homologous torque curves and Eq. (10-19); it is a function of the volumetric flow, the upstream void fraction, the upstream coolant-mixture density, and the pump-impeller angular velocity. For timestep $n+1$, Eq. (10-20) is evaluated explicitly as

$$\Omega^{n+1} = \Omega^n - \frac{\Delta t}{I}\left[T(Q, \alpha, \rho, \Omega) + C_0 + C_1\frac{\Omega^n}{\Omega_R} + C_2\frac{\Omega^n|\Omega^n|}{\Omega_R^2} + C_3\frac{(\Omega^n)^3}{\Omega_R^3} \right]. \tag{10-23}$$

Pump Friction Heating

The pump model is able to account for energy deposited to the fluid though irreversible friction losses in the pump impellers by adding source terms to the liquid and vapor energy equations. The heat is added to the downstream cell, so for normal pump operation, that corresponds to cell $j+1$, and for reverse pump operation, that corresponds to cell j. The heat generated is determined, very simply, by the following relationship

$$q_{fric} = T\Omega - gH\dot{m} \tag{10-24}$$

where $\dot{m}$ is the mass flow rate through the pump. As you can see, the thermal energy generated is the amount of energy added by the motor minus the head times the flow rate obtained. The thermal energy is partitioned by the liquid and vapor absorption capacity fraction. Thus the amount of energy going to the liquid is

$$q_{l,fric} = \frac{q_{fric}(1-\alpha)\rho_l c_{pl}}{(1-\alpha)\rho_l c_{pl} + \alpha\rho_v c_{pv}} \tag{10-25}$$

and the amount going to vapor is

$$q_{v,fric} = \frac{q_{fric}\alpha\rho_v c_{pv}}{(1-\alpha)\rho_l c_{pl} + \alpha\rho_v c_{pv}} \tag{10-26}$$

where α is the void fraction, c_{pl} is the specific heat of the liquid phase, c_{pv} is the specific heat of the vapor phase, and ρ_l and ρ_v are the phasic densities.

Warning – There is currently a bug in the PUMP friction model that will prevent any energy contributions from being applied to the downstream cell when the PUMP is defined as a single face (a so-called SJC PUMP). The energy contributions are properly handled when the PUMP adheres to a more traditional representation (NCELLS > 1).

PRIZER Component

The PRIZER component is designed to simulate a PWR pressurizer. Figure 10-2 illustrates a typical nodalization for such a compoent. As shown, TRACE assumes that the PRIZER consists of a vertical stack of cells, with cell 1 at the top and cell N at the bottom.

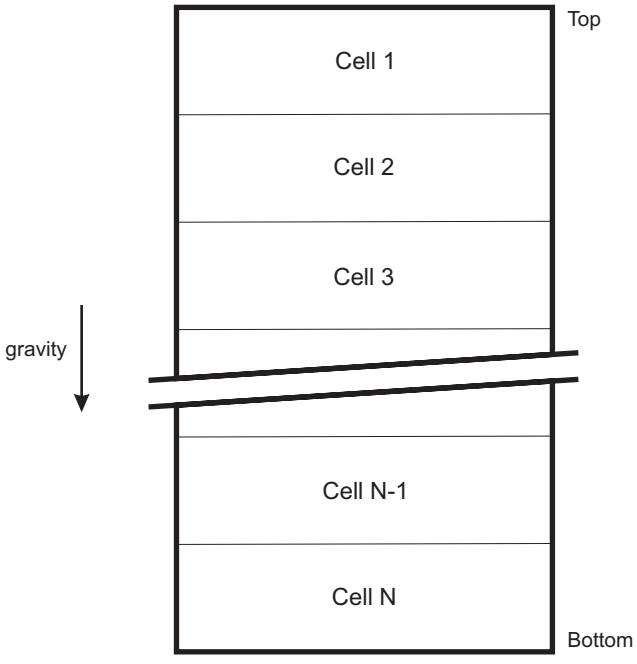

Figure. 10-2. Typical PRIZER nodalization

Collapsed Liquid Level

The procedure for determining the collapsed liquid level in the PRIZER can be described by the following set of steps:

1) First, the total liquid volume is summed over all mesh cells of the PRIZER component, as follows

$$Vol_{liq} = \sum_{j=1}^{N} (1 - \alpha_j) \cdot Vol_j \tag{10-27}$$

where α_j is the gas volume fraction in volume Vol_j of each cell denoted by the index j.

2) then, the volume Vol_j of each cell, starting at the bottom cell N and working upward, is sequentially subtracted from Vol_{liq} until the remainder of that subtraction operation is less than or equal to the volume of the next cell. We'll denote the index of that next cell by the letter k.

3) Knowing the value of k, the collapsed liquid level may be expressed by the following relationship if $N \neq k$:

$$X_L = \sum_{j=N+1}^{k+1} \Delta x_j + \Delta x_k \cdot \frac{\left(Vol_{liq} - \sum_{j=N+1}^{k+1} Vol_j \right)}{Vol_k} \tag{10-28}$$

where Δx_j is the length of a cell. If $N = k$, then Eq. (10-28) can be simplified into the following expression

$$X_L = \Delta x_k \cdot \frac{Vol_{liq}}{Vol_k} \tag{10-29}$$

Note that X_L may not represent the true vertical height of the collapsed liquid as it fails to take into account area changes that might exist in cell k. If the area in cell k is uniform, then X_L will represent the vertical height of the collapsed column of liquid.

Heater/Sprays

The PRIZER component models the effect of pressurizer heaters and sprays by manipulating the energy deposited into or extracted from the liquid in the PRIZER. The idea behind the heater/ sprayer model is that as the pressure in the first (top-most) cell of the PRIZER deviates from a user-defined setpoint, some amount of energy is added to or removed from the PRIZER (to condense the steam or boil the liquid) to return the pressure to the desired setpoint. The rate at which energy is added or removed varies linearly between zero and a user-defined maximum effective power of the heaters/sprays. The linear function with which the energy addition is varied is nothing more than a ratio between the deviation of the pressure in the first cell from the user-defined setpoint and a user-defined pressure difference which results in maximum heater or sprayer effectiveness. Expressing this relationship in equation form, the energy added or removed from the PRIZER, denoted by Q_{in} is given by

$$Q_{in} = \begin{cases} Q_{heat} & ; \quad \text{if} \quad \left(\frac{P_{set} - P_1}{\Delta P_{max}}\right) \geq 1 \\ Q_{heat}\left(\frac{P_{set} - P_1}{\Delta P_{max}}\right) & ; \quad \text{if} \quad -1 < \left(\frac{P_{set} - P_1}{\Delta P_{max}}\right) < 1 \\ -Q_{heat} & ; \quad \text{if} \quad \left(\frac{P_{set} - P_1}{\Delta P_{max}}\right) \leq 1 \end{cases} \tag{10-30}$$

where Q_{heat} is the user-defined maximum effective power of the heaters and the sprays, P_{set} is the user-input pressure to which the system is controlled, ΔP_{max} is the user-input pressure offset at which the heaters or sprays achieve their maximum effectiveness, and P_1 is the calculated pressure in the first (top) cell of the PRIZER. We must note that Eq. (10-30) only applies if the collapsed level, X_L, as calculated from Eq. (10-28), is greater than a user-supplied value, denoted by Z_{HTR}. When $X_L \leq Z_{HTR}$, then the energy contribution becomes

$$Q_{in} = 0 \tag{10-31}$$

The heater/sprayer power, Q_{in}, is distributed over all the cells containing liquid such that the power deposited to (extracted from) each cell j can be expressed according to the following expressions:

$$Q_{in} = \sum_{j=1}^{N} Q_{fj} \tag{10-32}$$

$$Q_{fj} = Q_{in}\left(\frac{\rho_{lj}(1-\alpha_j)\,Vol_j}{LMT}\right) \tag{10-33}$$

where LMT is the total liquid mass in the PRIZER, as defined by

$$LMT = \sum_{j=1}^{N} \rho_{lj}(1-\alpha_j)\,Vol_j \tag{10-34}$$

For each cell j, ρ_l is the microscopic liquid density, α is the void fraction, Vol is the cell volume, and Q_f is the power deposited in/extracted from the liquid phase. It is worth noting that if there is no liquid in the PRIZER, LMT will be zero, causing TRACE to not perform the calculation to distribute the heat load among the individual cells. In this instance, all Q_f values are zero.

The sign of Q_{in}, and hence of Q_f, indicates whether heat is added or subtracted from the liquid. If the calculated pressure P_1 is above the control pressure P_{set}, the sprays are assumed to be on and heat is removed from the liquid phase. In this instance, the model is not mechanistic for four reasons: (1) the reduction in pressure relies on condensation of vapor on the surface of the liquid pool as opposed to the spray itself, (2) removing energy from the liquid results in artificially subcooling the entire liquid pool, (3) there is a net energy extraction from the PRIZER that does not actually occur, and (4) the mass flows associated with the sprays do not occur in the PRIZER.

However, the case when $P_1 < P_{set}$ requires that the heaters be on. This case is reasonably mechanistic in that the heat is added to the liquid, as will occur in a real pressurizer. However, the distribution of the energy is not necessarily correct nor does the 1D modeling with a single liquid velocity permit calculating the convective currents within the liquid pool set up by the heat addition.

SEPD Component

The steam separators and dryers in a nuclear plant ensure that the steam exiting from the "nuclear island" is dry and meets the requirements of the turbine plant. In TRACE, the SEPD component is

usually employed to model these steam separators and moisture dryers, which are located on top of the nuclear core inside the reactor vessel of boiling water reactors, or on top of the steam generator pipes in the secondary side of pressurized water reactors. A sketch of a SEPD component inside of a BWR VESSEL component is given in Figure 10-3. Note that in general a SEPD component is a special case of a TRACE TEE component.

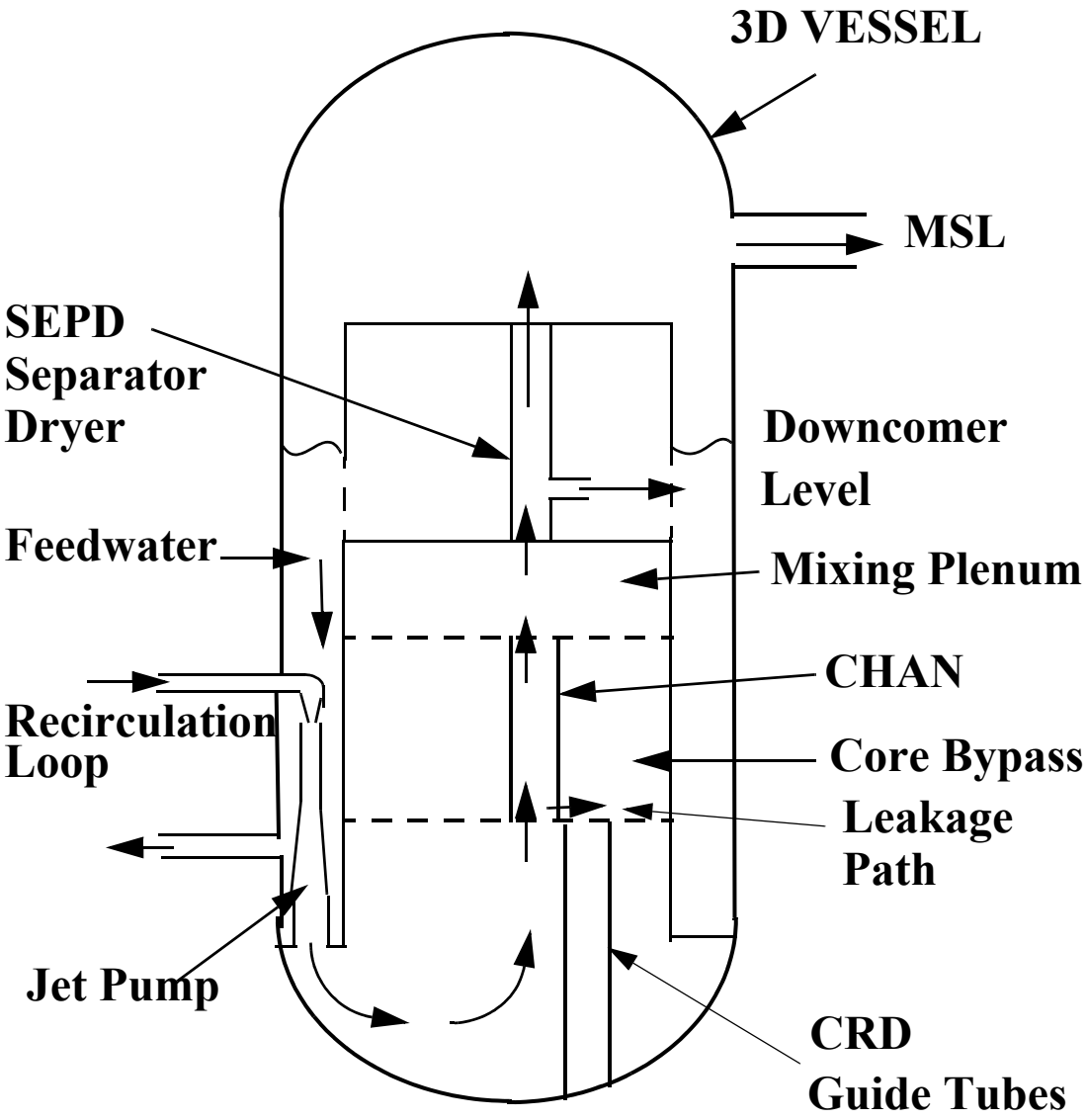

Figure. 10-3. TRACE BWR Reactor Vessel Model

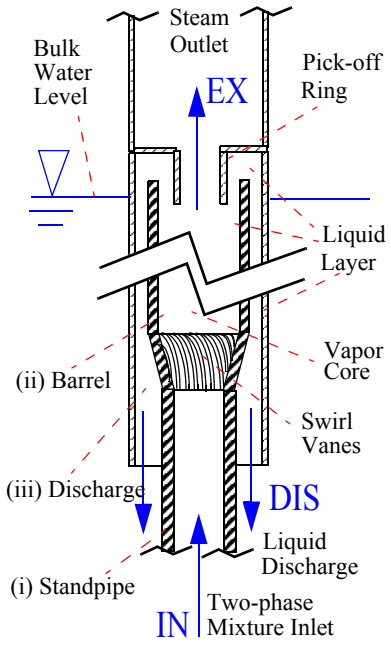

Figure. 10-4. Schematic of a steam separator (first stage)

A steam separator component is based on the principle of centrifugal separation, where the liquid/gas phase separation occurs as a mixture of water and steam flows upward in a vortex motion within vertical separator tubes. A single steam separator (**Figure 10-4**) typically consists of *(i)* a standpipe that directs the inlet two-phase flow into *(ii)* the separator barrel, which has at its inlet a flow spinner with curved vanes that give the steam-water mixture an axial rotation in the upward direction; the centrifugal acceleration acting on the rotating mixture inside the separator cylinder forces the liquid to migrate to the exterior of the vortex (because the liquid phase is much heavier than the gas phase), with formation of a continuous liquid film on the barrel wall; the flow of such a liquid layer is then diverted into the *(iii)* discharge passage, by means of a pick-off ring or a perforated region (or a combination thereof, depending on the particular separator design). The outcome of the steam separator is therefore a flow of steam out from the top exit and a flow of liquid water from the discharge to the bulk water surrounding the separator barrel. This described process refers to a single separation stage. Some steam separator designs work on a multi-stage separation process, where two or three separator stages may be used in series.

The steam dryer component uses chevron vanes to remove the moisture from the separator's outlet steam flow. The chevron vanes provide a curved flow path that must be followed by the liquid droplets carried by the continuous steam flow if they are to flow through the dryer. Nevertheless, because their inertia is higher than the carrying gas phase, the liquid droplets tend to assume straight trajectories and hit the wall of the vanes, feeding a liquid film that eventually streams out of the dryer's region into the recirculating water, thus de-moisturizing the steam flow.

In TRACE, suitable models for the simulation of the separator's and dryer's function are coded into the SEPD component. The underlying theoretical scheme behind the SEPD component is presented in this section.

Definitions

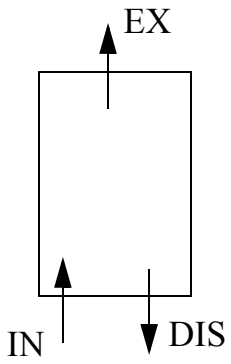

Figure. 10-5. The separator as a "black box"

Let us make reference to Figure 10-5 and represent the separator component as a confined control volume ("black box") with three flow junctions: a single inlet and two outlets. Suppose that we observe and measure a two-phase, liquid-gas mixture entering the separator; let $\dot{m}_{l,IN}$ be the inlet mass flow rate of liquid and $\dot{m}_{g,IN}$ the inlet mass flow rate of gas. Suppose further that we observe and measure a bulk gas flow, containing a small amount of liquid, flowing out of the first outlet (the separator *exit*); let $\dot{m}_{l,EX}$ be the liquid and $\dot{m}_{g,EX}$ the gas mass flow rates at such exit. Suppose, finally, that we observe and measure a bulk flow of liquid, with a very small weight fraction of gas, exiting from the second outlet (the separator *discharge*); let $\dot{m}_{l,DIS}$ be the liquid and $\dot{m}_{g,DIS}$ the gas mass flow rates at such discharge. The presence of liquid traces in the exit bulk gas flow and the presence of gas traces in the discharge bulk liquid flow are indications of an imperfect phase separation process, whereas *perfect* (or *ideal*) separation would result in pure gas flow at the exit and pure liquid flow at the discharge. Some parameters for characterizing the performance of a liquid/gas separation process are defined as follows.

The *separator inlet quality* is defined as the ratio:

$$x_{IN} = \frac{\dot{m}_{g,IN}}{\dot{m}_{g,IN} + \dot{m}_{l,IN}} \tag{10-35}$$

The *liquid carry-over quality* is defined as the ratio:

$$x_{CO} = \frac{\dot{m}_{l,EX}}{\dot{m}_{l,EX} + \dot{m}_{g,EX}} \tag{10-36}$$

The *vapor carry-under quality* is defined as the ratio:

$$x_{CU} = \frac{\dot{m}_{g,DIS}}{\dot{m}_{g,DIS} + \dot{m}_{l,DIS}} \tag{10-37}$$

An ideal (perfect) separator would perform with $x_{CO} = 0$ and $x_{CU} = 0$. In reality, imperfect separation always occurs and the performance characteristics of a separator component are often represented by expressing x_{CO} and x_{CU} as functions of x_{IN}.

Conceptual Structure of the SEPD Component

In TRACE, the SEPD component is in effect a modified TEE for which a special solution is obtained at the joining cell (J-cell). The TRACE separator model can be ideally described as working on two levels.

At the first conceptual level, the separator model is a "black-box" consisting of a control cell with three flow junctions for the separator inlet (two-phase mixture), exit (wet steam) and discharge (bulk liquid with traces of gas) flows. At this "black-box" level, the TRACE separator/dryer model triggers a special solution of the field equations to result, when possible, with the prescribed separator performance, given in terms of x_{CO} and x_{CU}, at exit and discharge junctions.

The separator performance parameters x_{CO} and x_{CU} are determined at the second conceptual level of the model. At this specialized level, several options are available to the user for describing the phase separation process occurring "inside the black-box." These options range from the simplest approach, that is the user-definition of constant x_{CO} and x_{CU} (including the particular case of ideal separation, where $x_{CO} = 0$ and $x_{CU} = 0$), to a more elaborated option consisting in the user-definition of variable x_{CO} and x_{CU}, to the mechanistic separator option, in which the separator performance is calculated by the code as a function of the local flow conditions, according to an analytical model developed in past years by General Electric Co. Available at this second level is also the dryers option, whose net result is a further modification of the SEPD x_{CO}, based on a calculated dryer's efficiency.

Assumptions

The TRACE separator model is based on the following assumptions, which are enforced in the code:

1) Homogeneous flow at the exit and discharge flow junctions.
2) No phase change inside the SEPD component.
3) During regular SEPD operation, the void fraction of the jcell follows the void fraction of the cell J-1 (i.e., the void fraction history of the fluid in the separator barrel follows the void fraction history of the fluid in the standpipes).
4) Vertical configuration of the jcell.

Assumptions 1) and 2) are introduced during the derivation of the analytical model, as described in the next section. During normal separator operation, the exit flow is expected to be in the mist

regime (bulk gas carrying small liquid droplets) and the discharge flow is in the dispersed bubbles regime; for both situations, the assumption of homogeneous flow seems reasonable since the high interfacial forces that are characteristic of finely dispersed flow regimes tend to equalize the phasic velocities. The assumption of no phase change is not expected to significantly deviate from the real flow behavior for two reasons; (1) because the separation process is rather quick and can be approximated as adiabatic, and (2) because the incoming two-phase flow from the upper plenum mixing region can be assumed to be in thermal equilibrium.

Assumption 3) is introduced when the level tracking logic is applied to the SEPD component, as described later. It allows for simulation of transient flow scenarios within the separator. Essentially, this assumption enforces the rule that the void fraction of the SEPD jcell (modeling the separator barrel) follows closely the void fraction history of the incoming flow from cell J-1 (standpipes), going to single-phase gas or liquid when the incoming flow also becomes single phase. This assumption removes the possibility of non-physical results from the code when, for any reason, the incoming standpipe flow becomes single phase.

Assumption 4) is also introduced when the level tracking logic is applied to the SEPD component and it is consistent with the usual configuration of steam separators in LWR plants.

Fundamental Analytical Model

At the "black-box" separator level, given the inlet flow conditions (phasic mass flow rates) and the desired separator performance parameters (x_{CO} and x_{CU}), the goal is to determine the flow variables at the exit and discharge junctions of the SEPD jcell.

Let us consider the relation between void fraction α and flow quality x at a given flow station (Ref. 10-7):

$$\alpha = \frac{1}{1 + \frac{1-x}{x} \cdot S \cdot \frac{\rho_V}{\rho_L}} = \frac{x}{x + (1-x) \cdot S \cdot \frac{\rho_V}{\rho_L}} = \frac{\dot{m}_V}{\dot{m}_V + \dot{m}_L \cdot S \cdot \frac{\rho_V}{\rho_L}}, \tag{10-38}$$

where the slip ratio, S, is defined as the ratio between gas velocity over liquid velocity; ρ is the density and $\dot{m}$ is the mass flow rate of the gas or liquid phase, as indicated by the subscript g or l, respectively. Writing Eq. (10-38) for the exit and discharge flow sections of a separator, assuming homogeneous flow (S=1), yields:

$$\alpha_{EX} = \frac{\dot{m}_{g,EX}}{\dot{m}_{g,EX} + \dot{m}_{l,EX} \cdot \frac{\rho_V}{\rho_L}} \tag{10-39}$$

and

$$\alpha_{DIS} = \frac{\dot{m}_{g,DIS}}{\dot{m}_{g,DIS} + \dot{m}_{l,DIS} \cdot \frac{\rho_V}{\rho_L}} \tag{10-40}$$

In Eq. (10-39) and (10-40), the phasic mass flow rates are the unknown variables that the separator model must resolve. For this purpose, let us assume that no phase change occurs within the separator component and steady-state operation, so that the phasic mass flow rates are conserved within the separator:

$$\dot{m}_{l,IN} = \dot{m}_{l,EX} + \dot{m}_{l,DIS} \tag{10-41}$$

$$\dot{m}_{g,IN} = \dot{m}_{g,EX} + \dot{m}_{g,DIS} \tag{10-42}$$

By the definitions Eq. and of carry-over and carry-under qualities:

$$\dot{m}_{l,EX} = (\dot{m}_{l,EX} + \dot{m}_{g,EX}) \cdot x_{CO} \tag{10-43}$$

$$\dot{m}_{g,DIS} = (\dot{m}_{l,DIS} + \dot{m}_{g,DIS}) \cdot x_{CU} \tag{10-44}$$

Equations (10-41), (10-42), (10-43) and (10-44) form a system of four algebraic, linear equations with the four unknowns $\dot{m}_{l,EX}$, $\dot{m}_{g,EX}$, $\dot{m}_{l,DIS}$ and $\dot{m}_{g,DIS}$. If the four equations are independent, then a solution to the system exists and is unique. A way to obtain the solution to Eq. (10-41) through (10-44) is the following:

Using Equations (10-43) and (10-44), let us define the total exit and discharge mass flow rates $\dot{m}_{EX}$ and $\dot{m}_{DIS}$, for which:

$$\dot{m}_{l,EX} = \dot{m}_{EX} \cdot x_{CO} \tag{10-45}$$

$$\dot{m}_{g,DIS} = \dot{m}_{DIS} \cdot x_{CU} \tag{10-46}$$

Similarly, it can be found that:

$$\dot{m}_{g,EX} = \dot{m}_{EX} - \dot{m}_{l,EX} = \dot{m}_{EX} \cdot (1 - x_{CO}) \tag{10-47}$$

$$\dot{m}_{l,DIS} = \dot{m}_{DIS} - \dot{m}_{g,DIS} = \dot{m}_{DIS} \cdot (1 - x_{CU}) \tag{10-48}$$

Entering the results of Equations (10-45), (10-46), (10-47) and (10-48) into (10-41) and (10-42), yields:

$$\dot{m}_{l,IN} = X_{CO} \cdot \dot{m}_{EX} + (1 - X_{CU}) \cdot \dot{m}_{DIS} \tag{10-49}$$

$$\dot{m}_{g,IN} = (1 - X_{CO}) \cdot \dot{m}_{EX} + X_{CU} \cdot \dot{m}_{DIS} \tag{10-50}$$

Equations (10-49) and (10-50) form a system of two linear algebraic equations, equivalent to Equations (10-41) through (10-44), in the unknowns $\dot{m}_{EX}$ and $\dot{m}_{DIS}$. It can be written in a more compact matrix form:

$$\begin{bmatrix} X_{CO} & (1 - X_{CU}) \\ (1 - X_{CO}) & X_{CU} \end{bmatrix} \begin{bmatrix} \dot{m}_{EX} \\ \dot{m}_{DIS} \end{bmatrix} = \begin{bmatrix} \dot{m}_{l,IN} \\ \dot{m}_{g,IN} \end{bmatrix} \tag{10-51}$$

$$\underline{\underline{A}} \qquad \underline{x} \quad = \quad \underline{b}$$

If det(a) is non-zero, then the original Equations (10-41), (10-42), (10-43) and (10-44) are independent and the unique solution of the system can be found by solving Eq. (10-51)(10-51). The algebraic system represented in Eq. (10-51) can be obtained, one among many ways, by employing the following "shortcut" to invert a 2x2 square matrix (Ref. 10-11), in the following way.

Let us define the matrix $\tilde{A}$, obtained from A by inverting and switching the sign of the main diagonal terms:

$$\tilde{A} = \begin{bmatrix} -X_{CU} & (1 - X_{CU}) \\ (1 - X_{CO}) & -X_{CO} \end{bmatrix} \tag{10-52}$$

The solution to Equation (10-51) is given by:

$$\begin{bmatrix} \dot{m}_{EX} \\ \dot{m}_{DIS} \end{bmatrix} = \frac{1}{rdet(\tilde{A})} \begin{bmatrix} -X_{CU} & (1 - X_{CU}) \\ (1 - X_{CO}) & -X_{CO} \end{bmatrix} \begin{bmatrix} \dot{m}_{l,IN} \\ \dot{m}_{g,IN} \end{bmatrix} \tag{10-53}$$

where the reverse determinant is defined as:

$$rdet(\tilde{A}) = (1 - X_{CO}) \cdot (1 - X_{CU}) - X_{CU} \cdot X_{CO}$$

Explicitly, the solution to Equation (10-53) is written as:

$$\dot{m}_{EX} = \frac{1}{rdet(\tilde{A})}\left[(1 - X_{CU}) \cdot \dot{m}_{g,IN} - X_{CU} \cdot \dot{m}_{l,IN}\right] \tag{10-54}$$

and

$$\dot{m}_{DIS} = \frac{1}{rdet(\tilde{A})}\left[(1 - X_{CO}) \cdot \dot{m}_{l,IN} - X_{CO} \cdot \dot{m}_{g,IN}\right] \tag{10-55}$$

Finally, the individual phasic mass flow rates at the exit and discharge sections can be obtained by entering the solution to Equations (10-54) and (10-55) into the definitions from Equations (10-45), (10-46), (10-47) and (10-48). With that information available, and knowing the phasic densities, the void fractions at the exit and discharge sections are also known by using Equations (10-39) and (10-40).

The knowledge of the void fractions α_{EX} and α_{DIS} is a key point in the TRACE separator model. In fact, once the values of the junction void fractions and phasic flow rates are determined from the prescribed x_{CO} and x_{CU} and inlet flow rates, then the TRACE separator model transfers the information into a modified solution scheme for the SEPD component. This modified solution scheme relies on the computational framework that is available in TRACE for water level tracking **[See Chapter 6 Section Level Tracking of this manual]**.

In a nutshell, the TRACE level tracking logic can be described by making reference to the schematic shown Figure 10-6.

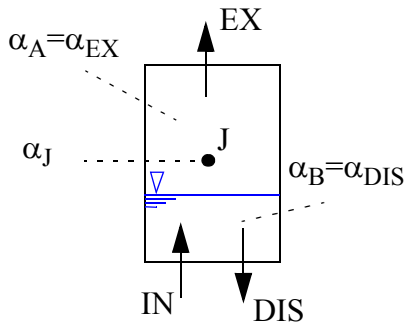

Figure. 10-6. Level Tracking Framework applied on top of the Separator "black box"

For a computational cell where the presence of a water level is detected, additional variables are introduced, among which are the void fractions α_A and α_B of the regions above and below the liquid/gas interface (and convected through the two open edges of the cell). Then, within the level tracking framework, the field equations are modified in order to make opportune use of those variables for the evaluation of the convected macroscopic quantities and the flux terms. From this description, it should become clear how the separator model makes use of the Level Tracking framework. Figure 10-6 shows the level tracking structure that is applied on top of the separator black-box. If the SEPD jcell (i.e., primary cell index where the secondary side connects to the primary side) is viewed as a computational cell with a water level, and if the interface is located above the discharge edge and below the exit edge, then the correspondence between the level tracking variables α_A and α_B and the separator model variables x_{CO} and x_{CU} can be intuitively recognized and is analytically identified by Equations (10-39) and (10-40), which have been previously derived formally.

The application of the level tracking logic to the SEPD jcell presents two complications in that (i) the jcell has three flow junctions to the neighboring cells, whereas a regular 1D level tracking cell has only two junctions, and that (ii) no information is given about the average void fraction of the SEPD jcell and its value would remain undetermined for this black-box type of separator.

The first difference is overcome when the discharge velocity at the jcell side junction, which is assumed common to both phases, is imposed to the solution rather than addressed by the level tracking logic. The magnitude of the homogeneous discharge velocity is obtained from the considerations discussed earlier (assuming balanced inlet and outlet flow rates) and depends on the prescribed separator performance:

$$V_{H,DIS} = \frac{\dot{m}_{V,DIS}}{\alpha_{DIS} \cdot (FA \cdot \rho_V)} = \frac{\dot{m}_{L,DIS}}{(1-\alpha_{DIS}) \cdot FA \cdot \rho_L} \tag{10-56}$$

where FA is the flow area of the discharge section and the phasic mass flow rates are given by Equations (10-46), (10-48) and (10-55) as functions of the separator performance parameters and inlet flow rates.

To address the second complication regarding the determination of the jcell average void fraction, the magnitude of the discharge velocity is adjusted within the separator model logic (with a simple proportional control scheme) in order to impose an additional restrictive condition that the difference between the void fraction in the jcell and the void fraction in the adjacent cell from the inlet side (cell j-1) be minimized. That is, the discharge velocity is used to regulate the void fraction of the jcell, in such way that the jcell void fraction follows as close as possible a target value, which is chosen to be the void fraction of the cell preceding the jcell (in the direction of the two-phase flow entering the SEPD jcell in regular operation).

Two facts should be noted in conclusion. First, the assumption of balanced inlet and outlet mass flows is used to calculate the void fractions and an initial value for the discharge velocity; that assumption is then "dropped" when the discharge velocity is changed and adjusted to control the jcell void fraction. Thus, the TRACE separator model effectively allows for non-equilibrium inlet and outlet flows, with transient mass accumulation or removal from the SEPD jcell. In fact, logic is implemented in the code to bypass the separator model (and the SEPD component becomes a regular TEE) during a calculation when the local flow conditions become inconsistent with the regular function of flow separation, such as for situations of single phase flow or reversed flows (when the jcell void fraction becomes 1 or 0 or the velocities change sign). This feature of the model is explained in detail in the TRACE User's Guide. Finally, it should be noted that the level tracking framework is applied "on top of the black box," in order to reproduce and enforce in the code a phase separation process, given some performance parameters as input. Therefore, the application of the level tracking is not an attempt to model the underlying physics of the two-phase flow separation occurring "inside the black box." This latter task of describing the separator performance is left to the user, with the option of using a more mechanistic model.

Mechanistic Separator Modeling

In the early 1980's, a model for the centrifugal separator was developed by the General Electric Company as part of the joint US NRC - EPRI - General Electric Company sponsored BWR Refill-Reflood Program (Ref. 10-3). This model is optionally available to the TRACE user as a means to simulate the physical processes occurring inside the separator "black box", with the features and limitations reported in the TRACE User's Guide.

The primary measures of separator performance are the carryover mass quality of entrained liquid in the steam leaving the separator, the carryunder mass quality of steam in the liquid leaving the discharge passage of the separator, and the separator pressure drop. Thus, the mechanistic model was developed to calculate the carryover, carryunder and separator pressure drop. The modeled separators are made up of either two or three stages connected in series. The mechanistic separator model determines the separating performance of a single stage, feeding the output of one stage to the input of the next stage.

With reference to Figure 10-7, the following description of the mechanistic separator model is adapted from References 10-1 and 10-3.

Assumptions and Model Equations

In this model, the following assumptions are made for the axial location near the pick-off ring.

1) There is one uniform axial velocity in each of the flow regions, i.e.,

$$0 \le r \le r_f \quad : \quad V_a = V_{ag}, \text{ uniform in vapor core} \tag{10-57}$$

$$r_f \le r \le r_w \quad : \quad V_a = V_{af}, \text{ uniform in water layer} \tag{10-58}$$

where r_f is the inner radius of the water layer.

2) The tangential velocity in each region is proportional to C which is related to the vortex strength, and is a function of r as follows:

$$V_t = \begin{cases} \dfrac{rC}{r_f^{3/2}} & ; \quad 0 \le r \le r_f \\ \dfrac{C}{\sqrt{r}} & ; \quad r_f \le r \le r_w \end{cases} \tag{10-59}$$

3) The void profiles are assumed as follows:

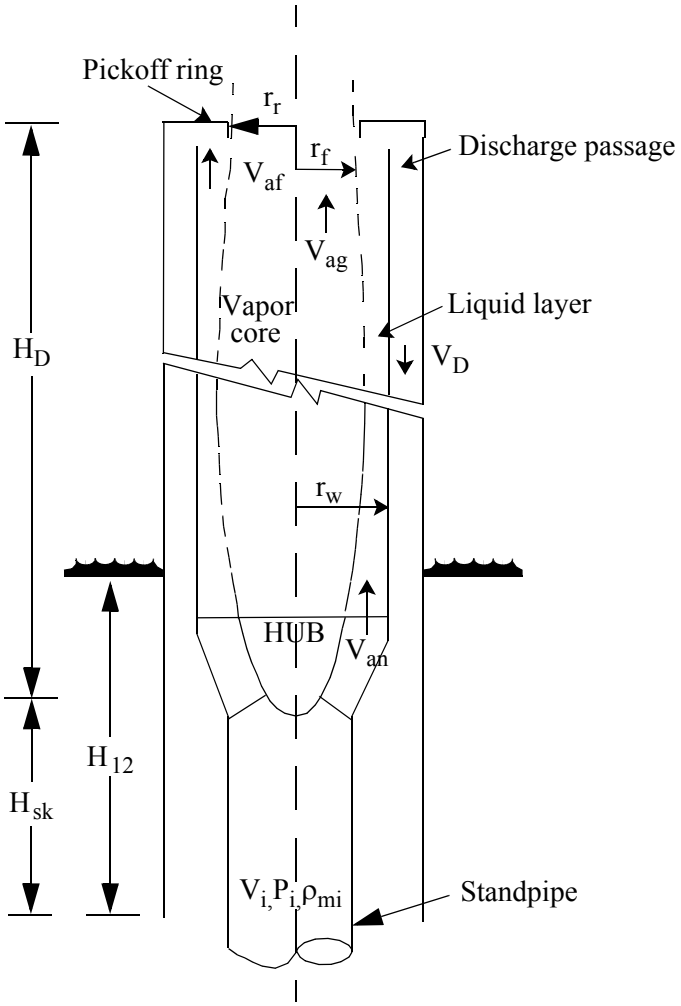

Figure. 10-7. Schematic of first stage of mechanistic separator.

$$\alpha = \begin{cases} 1 - b\dfrac{r}{r_w} & ; \quad 0 \le r \le r_f \\ a\left(\dfrac{r_w}{r} - 1\right) & ; \quad r_f \le r \le r_w \end{cases} \tag{10-60}$$

and

$$a = \begin{cases} AA\left(\frac{\sqrt{gr_w^2}}{C}\right)^{0.5} X_i^2 & ; \quad X_i < 0.15 \\ AA\left(\frac{\sqrt{gr_w^2}}{C}\right)^{0.5} (0.09335) X_i^{0.75} & ; \quad X_i > 0.15 \end{cases} \tag{10-61}$$

$$b = BB\left(\frac{\sqrt{gr_w^2}}{C}\right)^{0.5} (1 - X_i)^3 \tag{10-62}$$

where X_i is the inlet flow quality, and AA and BB are parameters to be fitted with data.

4) The pressure in the vapor core (P_o) is assumed to be uniform radially and axially, and the pressure at the separator wall (P_w) is related to P_o by centrifugal force across the water layer.

For the first stage of the separator, a total of six unknowns are introduced in this model. These are V_{ag}, V_{af}, C, r_f, P_o, and P_w. The required equations are formulated from conservation of water mass, vapor mass, axial momentum, and angular momentum entering and leaving the separating barrel, from centrifugal pressure drop across the water layer and from pressure drop in the discharge passage. The above unknowns can now be solved from given conditions of pressure, P_i, total flow rate, W_i, and flow quality at the swirl vane inlet, X_i.

The mass and momentum conservation equations for flows entering and leaving the separating barrel are:

Water mass.

$$(1 - X_i) W_i = 2\pi \int (1 - \alpha) \rho_f V_a r dr = \tag{10-63}$$

$$2\pi V_{ag} \rho_f \left(\frac{1}{3} \frac{r_f b}{r_w}\right) r_f^2 + 2\rho_f \pi V_{af} \left\{ \left(\frac{1 + a}{2}\right) [(r_w^2 - r_f^2) - a(r_w - r_f)] \right\}$$

Vapor Mass.

$$X_i W_i = 2\pi \int_0^{r_w} \alpha \rho_g V_g r dr = \tag{10-64}$$

$$2\pi \rho_g V_{ag} \left(\frac{1}{2} - \frac{1}{3} b \frac{r_f}{r_w} \right) r_f^2 + 2\pi \rho_g V_{af} a \frac{1}{2} (r_w - r_f)^2 \quad .$$

Angular Momentum.

$$\int_{r_h}^{r_w} V_{tn} r (2\pi r \rho_{mi} V_{an}) dr = \int_0^{r_w} V_t r (2\pi r \rho V_a) dr + F_t r_w \tag{10-65}$$

Axial Momentum.

$$\pi r_h^2 P_o = 2\pi \int_0^{r_w} (\rho_{mi} V_{an}^2 + P_n) r dr = 2\pi \int_0^{r_w} (\rho V_a^2 + P) r dr + F_a \tag{10-66}$$

Assuming that the flow through the swirl vane passages is homogeneous and that the swirl vane passages act as a nozzle, the pressure and velocity entering the separating barrel are related to the conditions in the standpipe as follows.

$$W_i = \rho_{mi} V_i A_i = \rho_{mi} V_{an} A_n \tag{10-67}$$

$$P_i + \frac{1}{2} \rho_{mi} V_i^2 = P_n + \frac{1}{2} \rho_{mi} (V_{an}^2 + V_{tn}^2)(1 + C_{NOZ}) \tag{10-68}$$

$$\frac{V_{an}}{V_{tn}} = \tan\theta \tag{10-69}$$

where θ is the angle between the swirl vanes and the horizontal plane, ρ_{mi} is the inlet mixture density, and C_{NOZ} is the contraction loss coefficient defined as:

$$C_{NOZ} = 0.5 \left(1 - \frac{A_n}{A_i} \right) \tag{10-70}$$

where A_n is the swirl vane flow area and A_i is the standpipe flow area.

F_a and F_t in Eq. (10-65) and Eq. (10-66) are the axial and tangential components of the frictional force on the swirling water layer,

$$F_a = F_f\left(\frac{V_{af}}{V_w}\right) \tag{10-71}$$

$$F_t = F_f\left(\frac{V_{tw}}{V_w}\right) \tag{10-72}$$

where V_{tw} is the tangential velocity on the wall,

$$V_{tw} = \frac{C}{\sqrt{r_w}} \tag{10-73}$$

and V_w is the resultant swirling velocity on the wall,

$$V_w = \sqrt{V_{tw}^2 + V_{af}^2} \tag{10-74}$$

F_f is the resultant frictional force,

$$F_f = \frac{1}{2}\rho_f C_F V_w^2 (2\pi r_w) H_D \tag{10-75}$$

Assuming that the liquid film is thin with respect to the radius of curvature of the separator barrel, the flow can be considered to be film flow over a flat plate. For turbulent flow over a flat plate,

$$C_F = \frac{0.455}{(\log Re_L)^{2.58}} \tag{10-76}$$

where Re_L is defined as

$$Re_L = \frac{\rho V_w}{\mu}\frac{H_D V_w}{V_{af}} \tag{10-77}$$

The radial pressure drop across the water layer due to centrifugal force is

$$\int_{P_0}^{P_w} dP = \int_{r_f}^{r_w} \rho \frac{V_t^2}{r}\, dr \tag{10-78}$$

or

$$P_o = P_w - [\rho_f + a(\rho_f - \rho_g)]\, C^2\left(\frac{1}{r_f} - \frac{1}{r_w}\right) + a(\rho_f - \rho_g)\, C^2\left(\frac{r_w}{r_f}\frac{1}{r_r} - \frac{1}{r_w}\right) \tag{10-79}$$

The pressure drop in the discharge passage is

$$\frac{\int_{r_r}^{r_w}\left(\frac{1}{2}\rho V_a^2 + P\right) dA}{\int_{r_r}^{r_w} dA} = \frac{1}{2}\rho_{M,D} V_D^2\left[1 + 2\, C_F\left(\frac{H_D}{D_D} + EFFLD\right) + C_K\right] + [P_o + \rho_f g H_{12} - \rho_D g(H_D + H_{sk})] \tag{10-80}$$

where $\rho_{M,D}$ and V_D are the mixture density and velocity in the discharge passage, H_D and D_D are the length of the separator barrel and hydraulic diameter of the discharge passage, EFFLD is the effective L/D coefficient at the pick-off ring, C_K is the total loss coefficient in the discharge passage, H_{12} is the height of the liquid pool surrounding the separator relative to the bottom of the discharge passage, and H_{sk} is the axial distance between the separator hub and the bottom of the discharge passage.

For the discharge passage,

$$C_F = \frac{0.079}{Re^{0.25}} \tag{10-81}$$

The steam and water flows discharged through the discharge passage are calculated as follows:

$$W_{g,cu} = 2\pi \int_{r_r}^{r_w} \alpha \rho_g V_a r\, dr \tag{10-82}$$

$$W_{f,cu} = \int_{r_r}^{r_w} (1 - \alpha) \rho_f V_a r\, dr \tag{10-83}$$

For a water layer thicker than the gap between the pick-off ring and the separator barrel, i.e., $r_f < r_r$, the steam and water flows through the discharge passage are

$$W_{g,cu} = \pi \rho_g V_{af} a (r_w - r_w)^2 \tag{10-84}$$

$$W_{f,cu} = \pi \rho_f V_{af} [(r_w^2 - r_r^2) - a(r_w - r_r)^2] \tag{10-85}$$

For a water layer thinner than the gap between the pick-off ring and the separator barrel wall, i.e., $r_r < r_f$, the liquid and vapor flow rates in the discharge passage are

$$W_{g,cu} = X_i W_i - 2\pi \rho_g V_{ag} \left(\frac{1}{2} - \frac{1}{3} b \frac{r_r}{r_w}\right) r_r^2 \tag{10-86}$$

$$W_{f,cu} = (1 - X_i) W_i - 2\pi \rho_f V_{ag} r_r^2 \left(\frac{1}{2}\right) b \frac{r_r}{r_w} \tag{10-87}$$

The steam and water flows leaving the present stage and entering the next stage are

$$W_{g,co} = (\text{steam flow})_{in} - W_{g,cu} \tag{10-88}$$

$$W_{f,co} = (\text{water flow})_{in} - W_{f,cu} \tag{10-89}$$

The total discharge flow is

$$W_D = W_{g,cu} + W_{f,cu} \tag{10-90}$$

Assuming homogeneous flow in the discharge passage, the mean void fraction is

$$\alpha_{cu} = \frac{W_{g,cu}}{W_{g,cu} + W_{f,cu} \dfrac{\rho_g}{\rho_f}}, \tag{10-91}$$

the mixture density in the discharge passage is

$$\rho_{M,D} = \alpha_{cu} \rho_g + (1 - \alpha_{cu}) \rho_f \tag{10-92}$$

and the velocity in the discharge passage is

$$V_D = \frac{W_D}{\rho_{M,D} A_D} \quad . \tag{10-93}$$

In summary, for given swirl vane inlet conditions, P_i, X_i, and W_i, the unknowns V_{ag}, V_{af}, C, r_f, P_o, and P_w are calculated by solving Equations Eq. (10-63) to Eq. (10-80) simultaneously.

Similar equations can be written for the second- and third-stages. Since it is assumed that P_o is uniform axially, i.e., the vapor core pressure drop in the axial direction is small, the axial momentum equation can be neglected in the solution for the upper stages. For these stages, the unknowns are reduced to V_{ag}, V_{af}, C, r_f, and P_w, and the equations are the conservation of water mass, vapor mass, angular momentum, the pressure drop across the water layer, and the pressure drop in the discharge passage.

The right hand sides of Equations Eq. (10-63), Eq. (10-64), and Eq. (10-65) represent the water flow, vapor flow, and angular momentum entering the separator barrel. For the second- and third-stages, these terms are modified as follows:

$$\begin{aligned}
(\text{Water flow})_{in} &= (W_{f,co})_{\text{previous stage}} \\
(\text{Steam flow})_{in} &= (W_{g,co})_{previous\ stage} \\
(\text{Angular momentum})_{in} &= \left[\int_0^{r_r} V_t r (2\pi\rho V_a) r\, dr\right]_{\text{previous stage}} .
\end{aligned} \tag{10-94}$$

Carryover and Carryunder Qualities

The total vapor flow that is carried under consists of two parts; i.e., the steam flow through the first discharge passage which discharges its fluid below the liquid level and the steam entrained by the water discharged from higher stages. The exits of the discharge passages of the higher stages are located above the liquid level. It is assumed that the entrainment is proportional to the square of the total water flow discharged from the higher stages, i.e.,

$$\left(W_{g,cu}\right)_{total} = \left(W_{g,cu}\right)_1 + CC\left[\sum_{i=2}^{N}\left(W_{f,cu}\right)_i^2\right] \tag{10-95}$$

where N=2 for a two-stage separator, N=3 for a three-stage separator and CC is a constant to be fitted with data.

The total water that is carried over consists of two parts, the water flow through the last stage and the water flow entrained by the steam discharged from the higher stages through their discharge passages. Similarly, the second part is assumed to be proportional to the square of the total steam flow discharged from the higher stages, i.e.,

$$\left(W_{f,co}\right)_{total} = \left(W_{f,co}\right)_{N} + DD\left[\sum_{i=2}^{N}\left(W_{g,cu}\right)_{i}^{2}\right] \tag{10-96}$$

where DD is a constant to be fitted with data.

The carryunder and carryover are defined as

$$CU = \frac{\left(W_{g,cu}\right)_{total}}{\text{Total downward water flow}}$$
$$CO = \frac{\left(W_{f,co}\right)_{total}}{\text{Total upward steam flow}} \quad . \tag{10-97}$$

The parameters AA, BB, CC, and DD were tuned to fit the available test data (Refs. 10-4, 10-5, and 10-6) for two- and three-stage separators. Table 10-2 summarizes the values for these parameters.

Table 10-2. Summary of fitted parameters in the mechanistic separator model.

	2-Stage Separator		3-Stage Separator		
Parameter	**1st Stage**	**2nd Stage**	**1st Stage**	**2nd Stage**	**3rd Stage**
AA	110.	20.	110.	20.	20.
BB	0.5	0.25	0.5	0.25	0.55
CC	0.0004	---	0.0004	---	---
DD	0.009	---	0.11	---	---

Dryer Modeling

This description is taken from Reference 10-1.

The steam dryer uses chevron vanes to remove the moisture which is discharged from the steam separators. The vanes provide a curved path which the liquid droplets must follow if they are to flow through the dryer. If the interfacial force is too low, it cannot drag the liquid droplets along the curved path due to their inertial and they hit the vanes, are de-entrained, and the resultant liquid film flows down the vanes under the force of gravity into collecting trays and then back to the liquid pool surrounding the separators. If the vapor velocity is high, it exerts a larger

interfacial force on the droplets and more of the entrained liquid gets through the dryer vanes. Thus the dryer efficiency depends on the steam velocity and the moisture content of the steam flow entering the dryer. For a given steam inlet velocity, there is a critical dryer inlet moisture. Good moisture separation is achieved if the inlet moisture is lower than the critical value. If the inlet moisture is above the critical value, the dryer separating capacity is exceeded and the moisture can pass through the dryer.

The dryer capacity is simulated by a capacity factor GDRY which is defined in the following way. For a given steam velocity V at the inlet to the dryer, the critical dryer inlet moisture CDIM is calculated as:

$$CDIM = \begin{cases} 1 & ; \quad V \leq VDRY1 \\ 1 - \dfrac{V - VDRY1}{VDRY2 - VDRY1} & ; \quad VDRY1 < V < VDRY2 \\ 0 & ; \quad V \geq VDRY2 \end{cases} \tag{10-98}$$

where CDIM is the critical inlet moisture, VDRY1 is the vapor velocity below which any amount of moisture is assumed to be separated from the vapor stream, and VDRY2 is the vapor velocity above which no amount of moisture, however small, can be separated from the vapor stream.

The dryer inlet moisture (DIM) is computed assuming homogeneous flow as

$$DIM = 1 - \frac{\alpha_g}{\alpha_g + (1 - \alpha_g)\dfrac{\rho_f}{\rho_g}} \tag{10-99}$$

where α_g, ρ_f, and ρ_g are the vapor void fraction, liquid density, and the vapor density in the dryer.

The capacity factor GDRY is defined as

$$GDRY = \begin{cases} 1 & ; \quad DIM \leq CDIM \\ 1 + \dfrac{CDIM - DIM}{DELDIM} & ; \quad CDIM < DIM < (CDIM + DELDIM) \\ 0 & ; \quad DIM \geq (CDIM + DELDIM) \end{cases} \tag{10-100}$$

where DELDIM is the range of inlet moisture over which the dryer capacity goes from one to zero for a fixed vapor inlet velocity. These relations are shown schematically in Figure 10-8.

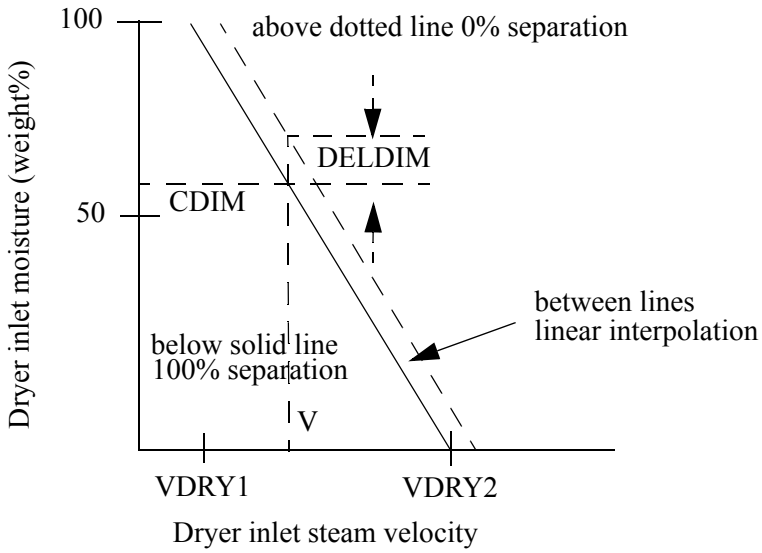

Figure. 10-8. Dryer capacity.

The capacity factor GDRY is used to modify the void fraction in the dryer outlet junction such that if the dryer capacity is one, the "donored" void fraction is one; if the dryer capacity is zero, the regular donor void fraction is used, and if the dryer capacity is between zero and one, the void fraction is interpolated between the values for the capacities of zero and one.

JETP Component

Jet pumps are used inside the reactor pressure vessels of some Boiling Water Reactors (BWRs) as part of the reactor recirculation system. In particular, BWR/3 through BWR/6 designs have been equipped with jet pumps (Ref. 10-8). A typical BWR uses 20 jet pumps, divided into two groups of ten jet pumps, with each group associated with a recirculation loop outside of the pressure vessel. Jet pumps are located inside the RPV in the downcomer annulus between the core shroud and the RPV wall (See Figure 10-3) and provide the flow through the core of a BWR.

The drive flow is from one of two recirculation lines which exit the RPV through a penetration in the lower downcomer and is pumped to a higher pressure using a variable speed recirculation pump (BWR/3s, BWR/4s, and some BWR/5s) or a two speed pump and flow control valve combination (some BWR5s and BWR6s), and then distributed through a manifold into a number of risers (i.e. each riser supplies jet pump drive flow to two jet pumps). Each riser penetrates the vessel low in the downcomer annulus and continues to rise until capped with a rams head flow divider which directs the flow from the riser into two jet pump nozzles.

The high velocity and relatively high momentum flow through the drive line nozzle entrains fluid from the downcomer into the suction of the jet pump. The two flows (i.e. drive and suction) merge together in the jet pump throat or mixing section. The diffuser section below the mixing section recovers some of the velocity head as static head and discharges the merged flow into the lower plenum. The suction flow can be as large as twice the magnitude of the drive flow. The major components within a jet pump are given in Figure 10-9.

The JETP component is a special case of a TEE component. The TRACE JETP component assumes that the users have defined the geometric input for the major components for a jet pump (i.e. drive line, drive nozzle, throat or mixing section, diffuser, and tail pipe). Based on the user specified geometry, the JETP component calculates irreversible loss factors for the smooth area changes associated with the nozzle and diffuser. The user input for flow loss factors is replaced with flow loss factors based on Idel'Chik (Ref. 10-9) for smooth area expansions and contractions for all of the cell edges internal to the JETP component (i.e. not component boundary cell edges). Component boundary cell edges are at the suction inlet, the discharge outlet, and the inlet to drive line. Only the user input for these three component boundary cell edges will not be overwritten by the JETP component internal irreversible loss factor logic.

For an expansion through a smooth area change, the irreversible loss factor based on Idel'Chik is:

$$K_e = C_e(\tan\alpha)^{1.5}(1 - A^*)^2 \tag{10-101}$$

where,

K_e = Expansion irreversible loss factor.
C_e = Expansion constant.
α = Angle of the diffuser.
A^* = Area ratio of outlet to inlet flow area.

For contraction through a diffuser/nozzle the irreversible loss factor is:

$$K_c = C_c\sin\alpha(1 - A^*) \tag{10-102}$$

where,

K_c = Contraction irreversible loss factor.
C_c = Contraction constant.

Based on comparison with the data given in Reference 10-10, expansion and contraction constants were found to be C_e = 5.5 and C_c = 0.38, respectively. The angle of the diffuser is given by the following formula:

$$\alpha = \text{atan}\left[\frac{HD(j+1) - HD(j)}{2\,DX(j)}\right] \tag{10-103}$$

See Figure 10-10 for the geometric basis for this formula. In the above irreversible loss factor formulas, the area ratio is the small area divided by the large area (i.e. $A^* \leq 1$).

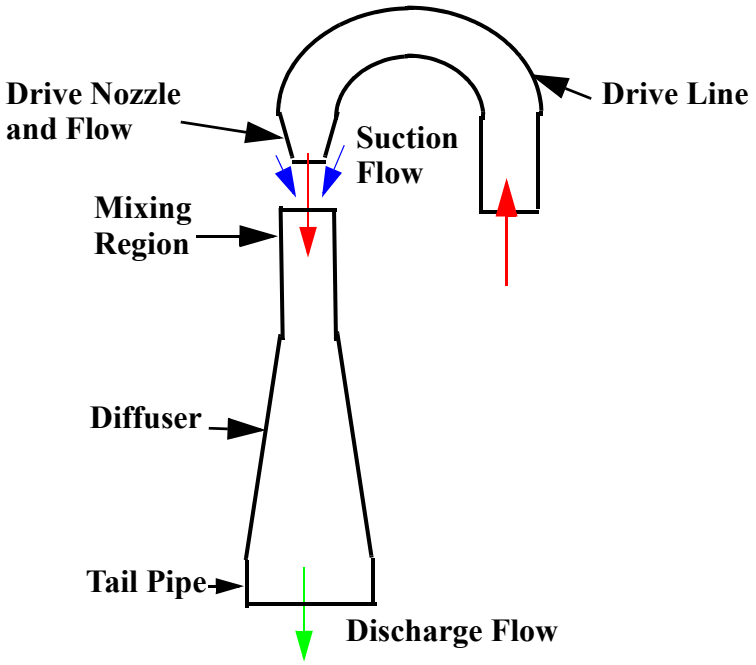

Figure. 10-9. Jet Pump Components.

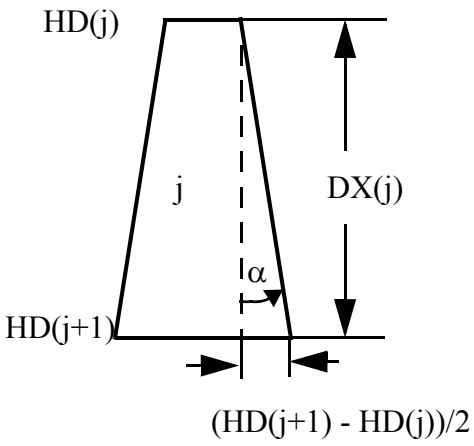

Figure. 10-10. Diffuser Angle for a Smooth Area Change.

Table 10-3. Mixing, Nozzle, and Suction Irreversible Losses

Regime	Mixing Losses $\frac{\Delta P}{\rho(V_d)^2}$	Nozzle Losses $\frac{\Delta P}{\rho(V_d)^2}$	Suction $\frac{\Delta P}{\rho(V_s)^2}$
1	0	0	0
2	$-0.3 \cdot M^2$	$[M \cdot (0.08 \cdot M - 0.06)]$	0
3	$-(0.1 - 0.0333 \cdot M)$	$Min[2.5 , M \cdot (0.08 \cdot M - 0.06)]$	0
4	0	$Max[0 , 0.48 - M \cdot (0.33 - 0.055 \cdot M)]$	0
5	0	$[0.48 - M \cdot (0.33 - 1.74 \cdot M)]$	$\left(\left(\frac{A_s}{A_{ds}}\right)^2 - 1\right)$
6	0	2.55	$\left(\left(\frac{A_s}{A_{ds}}\right)^2 - 1\right)$

The mixing and nozzle losses are due to the incomplete mixing of the high velocity drive nozzle with the low velocity suction flow. The mixing and nozzle loss model for the JETP component depends upon the flow configuration or flow regime. There are six possible steady-state flow regimes for a jet pump, in terms of the direction of the flow at the nozzle, suction, and discharge of the jet pump or normal and off-normal operation of a jet pump. Three flow configurations for positive drive nozzle flow and three flow regime configurations for negative drive nozzle flow are given in Figure 10-11. The M ratio in Figure 10-11 is defined as:

$$M = \frac{W_d}{W_s} \tag{10-104}$$

where,

W_d = Liquid mass flow rate in the drive nozzle of the jet pump.
W_s = Liquid mass flow rate in the suction of the jet pump.
W_{ds} = Liquid mass flow rate in the discharge of the jet pump.

The mixing loss and nozzle loss formulas for the flow dependent irreversible losses are given in Table 10-3 and are based on comparison to data (Ref. 10-10). For the jcell of the JETP component, where the drive flow and suction mixes, there are three momentum cells (i.e. one for each cell edge - drive nozzle, suction, and discharge). The jcell of a TEE component, is the cell where the secondary side connects to the primary side. The mixing loss factor given in Table 10-3 is applied to the discharge cell edge for the jcell control volume given in Figure 10-12. The

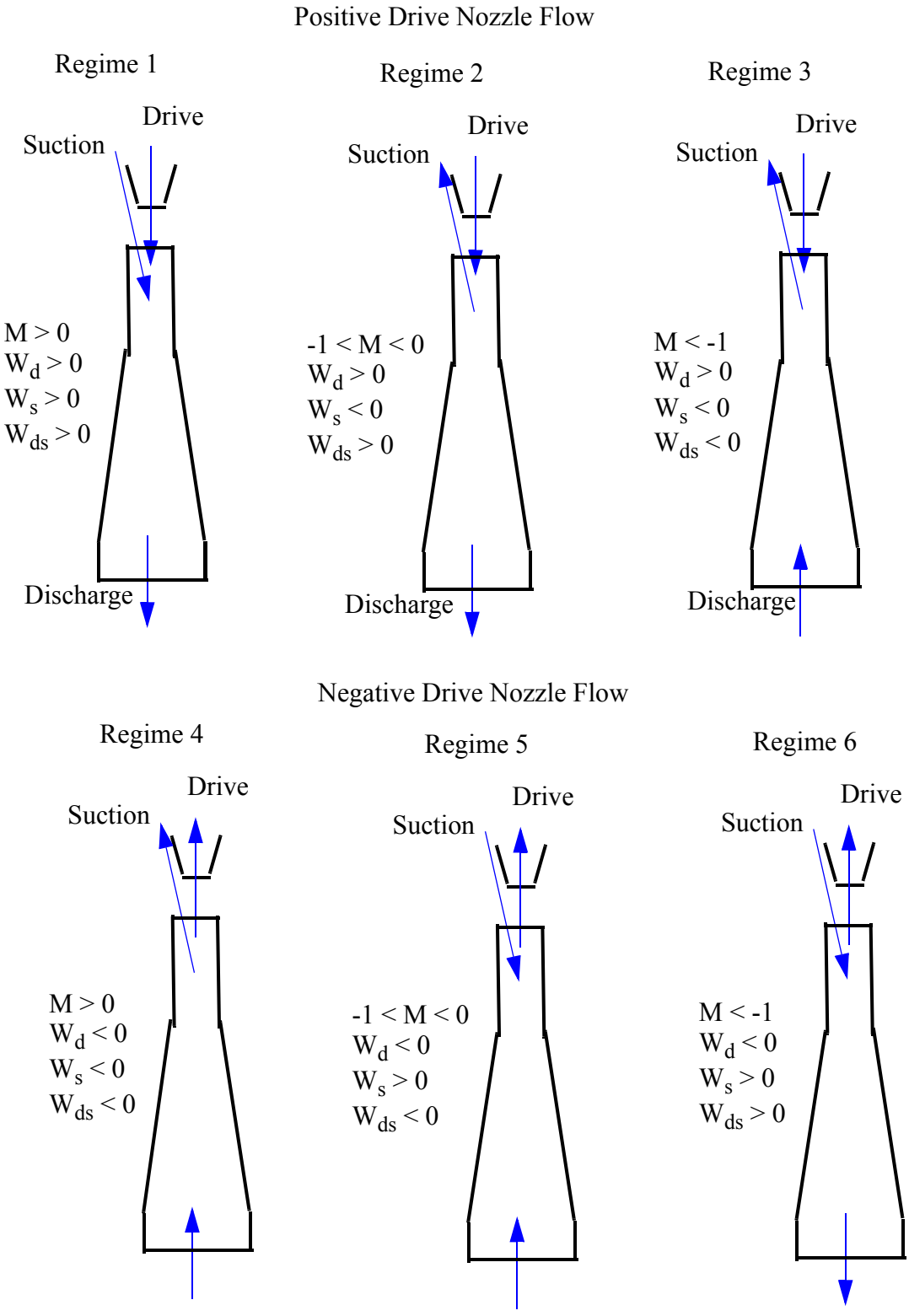

Figure. 10-11. Jet Pump Flow Regimes or Configurations

nozzle loss factor given in Table 10-3 is applied to the drive nozzle cell edge for the jcell control volume given in Figure 10-12. The suction loss factor is applied to the suction cell edge given in Figure 10-12. The loss factors given in Table 10-3 may be positive or negative and have been determined based on experimental data to be the correction required for the 1D TRACE momentum solution to be consistent with the multi-dimensional flow within a jet pump.

TRACE results for the INEL 1/6th scale jet pump for the M-N curve is given in Figure 10-13 and is consistent with experimental data for that test facility. The M-ratio in Figure 10-13 is given by Eq. (10-104) and the N-Ratio in Figure 10-13 is given by Eq. (10-105). The N-ratio is the ratio of the specific energy increase of the suction flow divided by the specific energy decrease of the drive nozzle flow.

$$N = \frac{P_{ds} - P_s}{P_d - P_{ds} + \frac{\rho V_d^2}{2}} \tag{10-105}$$

where,

P_{ds} is the pressure in the discharge of the jet pump.
P_d is the pressure in the drive line of the jet pump.
P_s is the pressure in the suction of the jet pump.
V_d is the velocity in the drive nozzle.
ρ is the density in the drive nozzle.

In Figure 10-13 there is one curve for positive flow in the drive nozzle and one curve for negative flow in the drive nozzle. The six flow regimes identified in Figure 10-11 are covered by the two curves in Figure 10-13, except for Regime 3 (i.e. positive drive flow with M < -1). There is a discontinuity in the mixing loss between regimes 2 and 3 at M = -1, which will be addressed in a future version of the TRACE computer code.

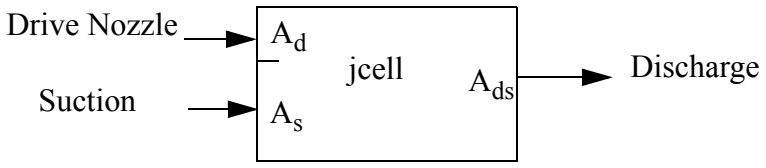

Figure. 10-12. JCELL or Mixing Cell Control Volume

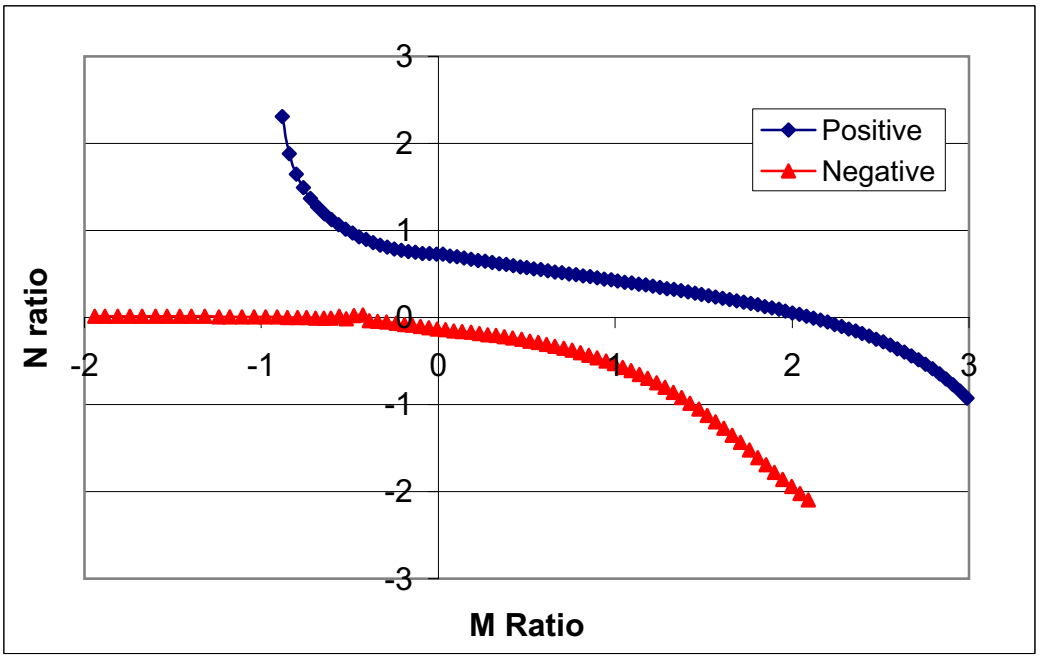

Figure. 10-13. M-N Curve for INEL 1/6th Scale Jet Pump

References

10-1 K. E. Carlson, R. A. Riemke, S. Z. Rouhani, R. W. Shumway, and W. L. Weaver, "RELAP5/MOD3 Code Manual — Volume 1: Code Structure, System Models, and Solution Methods," Idaho National Engineering Laboratory report NUREG/CR-5535, EGG-2596 (Draft), June 1990.

10-2 V. L. Streeter and E. B. Wylie, *Hydraulic Transients,* (McGraw-Hill Book Company, New York, New York, 1967) pp. 151–160.

10-3 Y. K. Cheung, V. Parameswaran, and J. C. Shaug, "BWR Refill-Reflood Program, Task 4.7-Model Development, TRAC-BWR Component Models," NUREG/CR-2574, EPRI NP-2376, GEAP-22052, April 1983.

10-4 R. H. Moen, et al., "Advances in Boiling Water Reactor Steam Separator Systems," *ASME-60-WA/NE-5,* November 1969.

10-5 E. L. Burley, "Performance of Internal Steam Separator System in Boiling Water Reactors," *ASME-69-WA/NE-24,* November 1969.

10-6 S. Wolf and R. H. Moen, "Advances in Steam-Water Separators for Boiling Water Reactors," *ASME-73-WA/PWR-4,* November 1973.

10-7 N. Todreas and M. S. Kazimi, "Nuclear Systems I - Thermal Hydraulic Fundamentals", Taylor&Francis Publ., second printing 1993.

10-8 R.T. Lahey, Jr, and F. J. Moody, "The Thermal-Hydraulics of a Boiling Water Reactor," ANS, 1977.

10-9 Idel'Chik, "Handbook of Hydraulic Resistance Coefficient of Local Resistance and Friction," AEC-TR-6630(1966).

10-10 Wilson, G.E., "INEL One-Sixth Scale Jet Pump Data Analysis," EGG-CAAD-5357 (February 1981).

10-11 Weisstein, Eric W. "Matrix Inverse." From MathWorld — A Wolfram Web Resource, http://mathworld.wolfram.com/MatrixInverse.html

11

Fluid Properties

TRACE can model several different working fluids as well as multiple non-condensable gas species. The fluids available in TRACE are H_20 (Refs. 11-1, 11-5, and 11-9), D_20, Na, PbBi, and the following noncondensable gases, or predefined mixtures of these gases: air, argon, helium, hydrogen, krypton, nitrogen, xenon, and non-ideal helium. With regards to the properties for water, TRACE offers two schemes by which those properties can be obtained — either from polynomial fits to steam-table data (the default method), or from interpolation of the steam table data that conforms to the IAPWS-95 standard. Water properties presented in later sections of this chapter refer to the original TRACE water properties which are based on polynomial fits to steam-table data for water. Information about the IAPWS-95 water properties can be found in the original source (Ref. 11-9). Tables 11-1 through 11-11, which list the values of the constants used to obtain property values, are provided throughout this chapter.

Nomenclature

c_p = constant-pressure specific heat ($J \cdot kg^{-1} \cdot K^{-1}$)

c_v = constant-volume specific heat ($J \cdot kg^{-1} \cdot K^{-1}$)

e = internal energy

ELP = change in energy required to move along the isotherm at T_1 between two different pressure values

h = enthalpy

h_{lv} = latent heat of vaporization

h_{lvs} = enthalpy of evaporation

k = thermal conductivity

M = numerical constant

p = pressure (Pa)

PSL = saturation pressure corresponding to T_l

R = gas constant ($J \cdot kg^{-1} \cdot K^{-1}$)

T = temperature (K)

v = specific volume

γ = ratio of specific heats

μ = viscosity

ρ = density

σ = surface tension

Subscripts

a = noncondensable gas

$approx$ = approximate

$critical$ = critical

g = gas

$ideal$ = ideal gas behavior

l = liquid

m = steam-gas mixture

sat, s = saturation

v = steam

Thermodynamic Properties

The input variables to the TRACE equation-of-state (EOS) package are the total pressure; the partial pressure of the noncondensable gas, if any is present; and the liquid- and gas-phase temperatures, where the gas phase is either steam, a noncondensable gas, or a steam-gas mixture. The output variables include the saturation temperature corresponding to the total pressure and its derivative with respect to the total pressure; the saturation temperature corresponding to the partial pressure of steam and its derivative with respect to the steam partial pressure; the internal energies and densities of the liquid and gas phases, and their partial derivatives with respect to pressure (at constant temperature) and with respect to temperature (at constant pressure); and, finally, the saturated liquid and saturated steam enthalpies and their derivatives with respect to pressure.

The TRACE EOS package supplies thermodynamic properties valid for temperatures and pressures within the following ranges:

$$273.15\ K\ \leq\ T_l\ \leq\ 713.94025779311\ K\ , \tag{11-1}$$

$$273.15\ K\ \leq\ T_g\ \leq\ 3000.0\ K\ , \tag{11-2}$$

and

$$1.0\ Pa\ \leq\ p\ \leq\ 45.0\times 10^6\ Pa \tag{11-3}$$

If the EOS package is provided with data outside this range, it adjusts the data to the corresponding limit and issues a warning message.

Equations for the various properties used in TRACE are given below. Tables 11-1 through 11-6 list the values of the constants.

Saturation Properties

Relationship Between Saturation Temperature and Pressure

Four temperature and pressure regions are used to evaluate the saturation pressure, saturation temperature, and derivative of saturation temperature with respect to saturation pressure.

610.8 Pa $\leq p_s <$ 90.56466 $\times 10^3$ Pa and 273.15 K $\leq T_s <$ 370.4251 K

A linear function of temperature accurately represents the enthalpy of evaporation h_{lvs} such that

$$h_{lvs} = 3180619.59 - 2470.2120\ T_s \tag{11-4}$$

for all $T_s\ \leq\ 425.01\,\mathrm{K}$ (corresponding to all $p_s\ \leq\ 0.5\times 10^6\,\mathrm{Pa}$). The Clausius-Clapeyron equation, which assumes that steam is an ideal gas and neglects liquid volume compared to steam volume, can be written as

$$\frac{d\,p_s}{d\,T_s} = \frac{h_{lvs}\,p_s}{R_v\,T_s^2}\ , \tag{11-5}$$

where R_v is the gas constant for steam (Table 11-1). Substituting for h_{lvs} and integrating using the boundary condition $p_s = 24821.0\ \mathrm{Pa}$ at $T_s = 338.0\,\mathrm{K}$, gives

$$p_s = 24821.0\ (T_s/338.0)^{-5.3512}\exp(20.387(T_s - 338.0)/T_s) \tag{11-6}$$

TRACE calculations also require determination of T_s from a given p_s, which can only be calculated by trial and error from the above equation. A simplified logic for calculating T_s is used that guarantees solution in two iterations with an error of only a fraction of a percent. First, an approximate value of T_s is calculated from

$$T_{s,approx} = \frac{-2263.0}{0.434 \ln(p_s/100000.0) - 6.064}, \tag{11-7}$$

which gives $T_{s,approx}$ within a few degrees of the actual value. Integration of the Clausius-Clapeyron equation, assuming constant h_{lvs} between $T_{s,approx}$ and T_s, calculates the first iteration value of T_s to be

$$T_s = \frac{T_{s,approx}}{1 - \frac{R_v T_{s,approx}}{h_{lvs,approx}} \ln\left(\frac{p_s}{p_{s,approx}}\right)} \tag{11-8}$$

The resulting T_s value is then input into this equation again as the new $T_{s,approx}$ value. Both $h_{lvs,approx}$ and $p_{s,approx}$ are calculated corresponding to $T_{s,approx}$ using the equations given above.

Table 11-1. Ideal Gas Constants

R_v	=	461.4975 [J/(kg·K)]	R_a	=	287.0516 [J/(kg·K)] for air 4124.2988 [J/(kg·K)] for hydrogen 2077.2345 [J/(kg·K)] for helium
g_{ideal}	=	1.3			
$c_{pv,ideal}$	=	$\frac{\gamma_{ideal} R_v}{\gamma_{ideal} - 1}$	c_{pa}	=	1004.832 [J/(kg·K)] for air 14533.2 [J/(kg·K)] for hydrogen 5193.086 [J/(kg·K)] for helium
$c_{vv,ideal}$	=	$\frac{R_v}{\gamma_{ideal} - 1}$	c_{va}	=	$c_{pa} - R_a$

Inverting the Clausius-Clapeyron equation allows the derivative of the saturation temperature with respect to the saturation pressure to be evaluated, such that

$$\frac{dT_s}{dp_s} = \frac{R_v T_s^2}{h_{lvs} p_s} \tag{11-9}$$

For values of p_s such that $1.0\,\text{Pa} \le p_s < 610.8\,\text{Pa}$, TRACE will reset the value of p_s to 610.8 Pa, and proceed with the calculation of T_s and dT_s/dp_s.

90.56466 × 10³ Pa ≤ p_s < 13.969971285053 × 10⁶ Pa and 370.4251 ≤ T_s < 609.62462615967 K

Reference 11-2 recommends using the following relationships between saturation temperature and pressure within this range:

$$p_s = 1.0 \times 10^5 \left(\frac{T_s - 255.2}{117.8} \right)^{\frac{1}{0.223}} \tag{11-10}$$

$$T_s = 117.8(1.0 \times 10^{-5} p_s)^{0.223} + 255.2\ , \tag{11-11}$$

and

$$\frac{dT_s}{dp_s} = \frac{0.223\,(T_s - 255.2)}{p_s} \tag{11-12}$$

13.969971285053 × 10⁶ Pa ≤ p_s < 22.12 × 10⁶ Pa and 609.62462615967 K ≤ T_s <647.3 K

The relationships given below are based on an equation-of-state of the form

$$\ln(p_r) = a + \frac{b}{T_r} + \frac{c}{T_r^2} \tag{11-13}$$

In the above relation,

$$p_r = \frac{p_s}{p_{critical}} \tag{11-14}$$

and

$$T_r = \frac{T_s}{T_{critical}}\ , \tag{11-15}$$

where p_s and T_s are the saturation pressure and temperature and $p_{critical}$ and $T_{critical}$ are the critical pressure and temperature (Ref. 11-3). These relationships were formulated to provide a good fit to the data and to provide a smooth transition between the preceding and the following temperature and pressure ranges:

$$p_s = 7.2166948490268 \times 10^{11} \exp\left(\frac{-8529.6481905883 + \frac{1166669.3278328}{T_s}}{T_s}\right) , \qquad (11\text{-}16)$$

$$T_s = \frac{4264.8240952941 + \sqrt{-13666986.708428 + 1166669.3278328(\ln(p_s))}}{27.304833093884 - \ln(p_s)} , \qquad (11\text{-}17)$$

and

$$\frac{dT_s}{dp_s} = \frac{-T_s^2}{p_s\left(-8529.6481905883 + \frac{2333338.6556656}{T_s}\right)} . \qquad (11\text{-}18)$$

22.12 × 10^6 Pa ≤ p_s ≤ 45.0 × 10^6 Pa and 647.3 K ≤ T_s ≤ 713.94025779311 K

The relationships given below are based on an equation-of-state of the form

$$\frac{d}{d\left[\ln\left(\frac{1}{T_r}\right)\right]}[\ln(p_r)] = M , \qquad (11\text{-}19)$$

where p_r and T_r are defined as in the previous pressure and temperature range and M is a constant (Ref. 11-3):

$$p_s = 22.12 \times 10^6 \exp\left(7.6084087 - \frac{4924.9229}{T_s}\right) , \qquad (11\text{-}20)$$

$$T_s = \frac{4924.9229}{24.520401 - \ln(p_s)} , \qquad (11\text{-}21)$$

and

$$\frac{dT_s}{dp_s} = \frac{2.0304886238506 \times 10^{-4} T_s^2}{p_s} . \qquad (11\text{-}22)$$

Saturated Steam Internal Energy

Two main pressure regions exist when calculating the internal energy of steam at saturation, e_{vs}, and the derivative of e_{vs} with respect to the partial pressure of steam, p_v. In this section, T_{sv} denotes the saturation temperature corresponding to p_v.

1.0 Pa < p_v < 0.5 × 10^6 Pa

$$e_{vs} = h_{vs} - \frac{p_v}{\rho_{vs}} = h_{vs} - R_v T_{sv} \tag{11-23}$$

and

$$\frac{de_{vs}}{dp_v} = \frac{dh_{vs}}{dp_v} - R_v \frac{dT_{sv}}{dp_v} \tag{11-24}$$

where h_{vs} and $\frac{dh_{vs}}{dp_v}$ are calculated as described in ***Saturated Steam Enthalpy*** for the same pressure range, $1.0 \text{ Pa} \le p_v \le 0.5 \times 10^6 \text{ Pa}$.

0.5 × 10^6 Pa< p_v ≤45.0 × 10^6 Pa

A sequence of polynomials in the partial pressure of steam, p_v, is used to calculate e_{vs} and de_{vs}/dp_v as

$$e_{vs} = AVE(i) + BVE(i)\, p_v + CVE(i)\, p_v^2 + DVE(i)\, p_v^3 \tag{11-25}$$

and

$$\frac{de_{vs}}{dp_v} = BVE(i) + 2\, CVE(i)\, p_v + 3\, DVE(i)\, p_v^2 \ , \tag{11-26}$$

where

$i = 1$ for $0.5 \times 10^6 < p_v \le 2.0 \times 10^6$ Pa ,
$i = 2$ for $2.0 \times 10^6 < p_v < 5.0 \times 10^6$ Pa ,
$i = 3$ for $5.0 \times 10^6 \le p_v < 10.0 \times 10^6$ Pa ,
$i = 4$ for $10.0 \times 10^6 \le p_v < 15.0 \times 10^6$ Pa ,
$i = 5$ for $15.0 \times 10^6 \le p_v < 20.0 \times 10^6$ Pa ,

$i = 6$ for $20.0 \times 10^6 \le p_v \le 22.0 \times 10^6$ Pa ,
$i = 7$ for $22.0 \times 10^6 < p_v < 25.0 \times 10^6$ Pa ,
$i = 8$ for $25.0 \times 10^6 \le p_v < 30.0 \times 10^6$ Pa ,
$i = 9$ for $30.0 \times 10^6 \le p_v < 35.0 \times 10^6$ Pa ,
$i = 10$ for $35.0 \times 10^6 \le p_v < 40.0 \times 10^6$ Pa , and
$i = 11$ for $40.0 \times 10^6 \le p_v \le 45.0 \times 10^6$ Pa .

Table 11-2 lists the constants *AVE(i)*, *BVE(i)*, *CVE(i)*, and *DVE(i)* for the given pressure ranges.

Function de_{vs}/dp_v is discontinuous near the critical point at junction point $p_v = 22.0 \times 10^6$ Pa. At this point the left-side value of the function is 4.37931×10^{-3} while the right-side value is 0.0, giving a fractional change across the junction point of 1.00.

Table 11-2. Saturated Steam Internal Energy Constants

i	*AVE*(*i*)	*BVE*(*i*)	*CVE*(*i*)	*DVE*(*i*)
1	2.4949771766385E+06	2.0855856331827E–01	– 1.3553894579716E–07	2.8522684989198E–14
2	2.5600870370371E+06	3.1086111111026E–02	–6.8988888888580E–09	4.3203703703379E–16
3	2.5915500000006E+06	8.7749999997567E–03	–1.7499999999663E–09	4.2999999998503E–17
4	2.6606000000024E+06	–1.3545000000581E–02	6.4250000004682E–10	–4.2100000001248E–17
5	3.8201600000097E+06	–2.3019900000170E–01	1.4068900000098E–08	–3.1786000000187E–16
6	–1.2103411633350E+08	1.8018803375785E+01	–8.7442426507726E–07	1.4091076856088E–14
7	2.2000000000000E+06	0.0	0.0	0.0
8	2.2000000000000E+06	0.0	0.0	0.0
9	2.2000000000000E+06	0.0	0.0	0.0
10	2.2000000000000E+06	0.0	0.0	0.0
11	2.2000000000000E+06	0.0	0.0	0.0

Saturated Liquid Internal Energy

A sequence of polynomials in the saturated liquid temperature, $\underline{T}_{\text{sat}}$, is used to calculate the internal energy of saturated liquid, e_{ls}, and its derivatives with respect to T_{sat}. We use

$$e_{ls} = ALE(i) + BLE(i)\,T_{sat} + CLE(i)\,T_{sat}^2 + DLE(i)\,T_{sat}^3 \text{ and} \tag{11-27}$$

$$\frac{d\,e_{ls}}{d\,T_{sat}} = BLE(i) + 2\,CLE(i)\,T_{sat} + 3\,DLE(i)\,T_{sat}^2 \ , \tag{11-28}$$

where

$i = 1$ for $273.15 \le \underline{T}_{sat} < 423.15$ K ,
$i = 2$ for $423.15 \le \underline{T}_{sat} < 473.15$ K ,
$i = 3$ for $473.15 \le \underline{T}_{sat} < 523.15$ K ,
$i = 4$ for $523.15 \le \underline{T}_{sat} < 573.15$ K ,
$i = 5$ for $573.15 \le \underline{T}_{sat} < 623.15$ K ,
$i = 6$ for $623.15 \le \underline{T}_{sat} \le 645.15$ K ,
$i = 7$ for $645.15 < \underline{T}_{sat} < 673.15$ K , and
$i = 8$ for $673.15 \le \underline{T}_{sat} \le 713.94025779311$ K .

Table 11-3 lists the constants *ALE(i)*, *BLE(i), CLE(i)*, and *DLE(i)* for the given temperature ranges.

Table 11-3. Saturated Liquid Internal Energy Constants

i	*ALE*(*i*)	*BLE*(*i*)	*CLE*(*i*)	*DLE*(*i*)
1	–1.1436668993222E+06	4.1868000000000E+03	0.	0.
2	8.0957542810383E+06	–5.7008855264640E+04	1.3443632119671E+02	–9.7879669155946E–02
3	–1.9373932457007E+06	9.7492797103351E+03	–1.3299615999876E+01	1.0879999999922E–02
4	–5.3245827703670E+06	2.9179372045334E+04	–5.0452192000967E+01	3.4560000000583E–02
5	–6.3583523639930E+07	3.2873715263424E+05	–5.6371182000208E+02	3.2760000000116E–01
6	–6.6239163195929E+09	3.1605562257270E+07	–5.0263730855532E+04	2.6650075114186E+01
7	–5.4759091078157E+09	2.4635618770681E+07	–3.6931079506707E+04	1.8454719393083E+01
8	–7.1536399439453E+07	3.0560801674842E+05	–4.2424553999630E+02	1.9719999999823E–01

Saturated Steam Enthalpy

Two main pressure regions exist when the enthalpy of steam at saturation is calculated. T_{sv} in this section denotes the saturation temperature corresponding to the partial pressure of steam, p_v.

1.0 Pa $\le p_v \le$ 0.5 $\times 10^6$ Pa

Within this pressure region, the enthalpy of saturated steam at temperature T_{sv} is approximated as the sum of the enthalpy of saturated liquid water at the reference temperature of 273.15 K, plus the enthalpy necessary to raise the saturated liquid water temperature from 273.15 K to T_{sv}, plus the latent heat of vaporization needed to convert saturated liquid water at T_{sv} to saturated steam at T_{sv}. If we define the enthalpy of saturated water at 273.16 K to be exactly zero, this gives

$$h_{vs} = 4186.8(273.15 - 273.16) + 4186.8(T_{sv} - 273.15) + h_{lvs} , \quad (11\text{-}29)$$

where h_{lvs} is evaluated at T_{sv} as described earlier in ***Relationship Between Saturation Temperature and Pressure***. The derivative with respect to the partial pressure of the vapor, p_v, becomes

$$\frac{dh_{vs}}{dp_v} = 4186.8\frac{dT_{sv}}{dp_v} + \frac{dh_{lvs}}{dp_v} = (4186.8 - 2470.2120)\frac{dT_{sv}}{dp_v} \tag{11-30}$$

0.5 × 10⁶ Pa < p_v ≤ 45.0 × 10⁶ Pa

$$h_{vs} = e_{vs}\gamma_s \tag{11-31}$$

and

$$\frac{dh_{vs}}{dp_v} = \gamma_s\frac{de_{vs}}{dp_v} + e_{vs}\frac{d\gamma_s}{dp_v}\ , \tag{11-32}$$

where

$$\gamma_s = AVG(i) + BVG(i)p_v + CVG(i)p_v^2 + DVG(i)p_v^3\ , \tag{11-33}$$

$$\frac{d\gamma_s}{dp_v} = BVG(i) + 2\ CVG(i)\ p_v + 3\ DVG(i)\ p_v^2\ , \tag{11-34}$$

and

i = 1 for 0.5 × 10⁶ < p_v ≤ 2.0 × 10⁶ Pa ,
i = 2 for 2.0 × 10⁶ < p_v < 5.0 × 10⁶ Pa ,
i = 3 for 5.0 × 10⁶ ≤ p_v < 10.0 × 10⁶ Pa ,
i = 4 for 10.0 × 10⁶ ≤ p_v < 15.0 × 10⁶ Pa ,
i = 5 for 15.0 × 10⁶ ≤ p_v < 20.0 × 10⁶ Pa ,
i = 6 for 20.0 × 10⁶ ≤ p_v ≤ 22.0 × 10⁶ Pa ,
i = 7 for 22.0 × 10⁶ < p_v < 25.0 × 10⁶ Pa ,
i = 8 for 25.0 × 10⁶ ≤ p_v < 30.0 × 10⁶ Pa ,
i = 9 for 30.0 × 10⁶ ≤ p_v < 35.0 × 10⁶ Pa ,
i = 10 for 35.0 × 10⁶ ≤ p_v < 40.0 × 10⁶ Pa , and
i = 11 for 40.0 × 10⁶ ≤ p_v ≤ 45.0 × 10⁶ Pa .

Table 11-4 lists the constants *AVG(i)*, *BVG(i)*, *CVG(i)*, and *DVG(i)* for the given pressure ranges.

Functions $h_{vs}/\mathrm{d}p_v$ and $\mathrm{d}\gamma_s/\mathrm{d}p_v$ are both discontinuous near the critical point at junction point $p_v = 22.0 \times 10^6$ Pa. At this point, the left-side value of $h_{vs}/\mathrm{d}p_v$ is 4.6073×10^{-3} and the right-side value -5.1790×10^{-6} for a fractional change here of 1.0011. The left-side value of $d\gamma_s/dp_v$ is 6.6694×10^{-12} and the right-side value is -2.3541×10^{-2} giving a fractional change at this junction point of 1.3530.

Table 11-4. Saturated Steam Enthalpy Constants

i	*AVG*(*i*)	*BVG*(*i*)	*CVG*(*i*)	*DVG*(*i*)
1	1.0666845123419E+00	2.8310838172462E–08	–2.1151097428905E–14	4.7404001285964E–21
2	1.0735412407407E+00	2.6518055555551E–09	–6.3461111111128E–16	3.9824074074117E–23
3	1.0777730000000E+00	–2.4300000008021E–11	–7.1979999998378E–17	4.8799999990422E–25
4	1.0851130000007E+00	–1.9307000001824E–09	8.9100000014826E–17	–3.8960000003946E–24
5	1.1639800000015E+00	–1.6338350000254E–08	9.5856000001448E–16	–2.1194000000274E–23
6	3.8898867259868E+00	–3.8595945559811E–07	1.7476370114910E–14	–2.6377008249858E–22
7	2.7168710524682E+00	–2.2832718294604E–07	1.0417331983836E–14	–1.5842822199773E–22
8	3.9749829999964E+00	–3.0657099999960E–07	1.0637899999985E–14	–1.2257999999981E–22
9	1.2946929999997E+00	–2.4834999999979E–08	7.8979999999944E–16	–8.0799999999948E–24
10	1.0590519999963E+00	–2.4615999996941E–09	8.8399999991573E–17	–8.0799999992269E–25
11	1.1430199999838E+00	–7.7095999988588E–09	1.9335999997331E–16	–1.4639999997924E–24

Saturated Liquid Enthalpy

From the definition of enthalpy,

$$h_{ls} = e_{ls} + \frac{p}{\rho_{ls}} \tag{11-35}$$

and

$$\frac{d\,h_{ls}}{d\,p} = \frac{d\,e_{ls}}{d\,T_{sat}}\frac{d\,T_{sat}}{d\,p} + \frac{1}{\rho_{ls}} - \frac{p}{\rho_{ls}^2}\left[\left(\frac{\partial\rho_{ls}}{\partial p}\right)_{T_{sat}} + \left(\frac{\partial\rho_{ls}}{\partial\,T_{sat}}\right)_p \frac{d\,T_{sat}}{d\,p}\right], \tag{11-36}$$

where e_{ls} and its derivative are evaluated as shown in ***Saturated Liquid Internal Energy***, and where ρ_{ls} and its derivatives are evaluated using the equations in ***Density*** with T_l equal to T_{sat}.

Heat Capacity of Saturated Steam at Constant Pressure

Although the heat capacity of saturated steam is not used directly in the solution of the two-phase flow equations, subsequent steam property calculations that appear below do require its definition. In this section, T_{sv} denotes the saturation temperature corresponding to the partial pressure of steam, p_v. The heat capacity of saturated steam is

$$c_{pvs} = ACP(i) + BCP(i)\,T_{sv} + CCP(i)\,T_{sv}^2 + DCP(i)\,T_{sv}^3 \tag{11-37}$$

and

$$\frac{d\,c_{pvs}}{d\,p_v} = [BCP(i) + 2\,CCP(i)\,T_{sv} + 3\,DCP(i)\,T_{sv}^2]\frac{d\,T_{sv}}{d\,p_v}\ , \tag{11-38}$$

where

i = 1 for 273.15 ≤ T_{sv} < 323.15 K ,
i = 2 for 323.15 ≤ T_{sv} < 373.15 K ,
i = 3 for 373.15 ≤ T_{sv} < 423.15 K ,
i = 4 for 423.15 ≤ T_{sv} < 473.15 K ,
i = 5 for 473.15 ≤ T_{sv} < 523.15 K ,
i = 6for 523.15 ≤ T_{sv} < 573.15 K ,
i = 7 for 573.15 ≤ T_{sv} < 623.15 K ,
i = 8 for 623.15 ≤ T_{sv} < 647.3 K ,
i = 9 for 647.3 < T_{sv} < 673.15 K , and
i = 10 for 673.15 ≤ T_{sv} < 713.94025779311 K .

Table 11-5 lists the constants *ACP(i), BCP(i), CCP(i), and DCP*(*i*) for the given temperature ranges.

Table 11-5. Saturated Steam heat Capacity Constants

i	*ACP*(*i*)	*BCP*(*i*)	*CCP*(*i*)	*DCP*(*i*)
1	–7.9678485852270E+02	2.8187658437259E+01	–1.0180624999920E–01	1.2499999999912E–04
2	–9.7082632232795E+02	2.8324981030402E+01	–9.7656200001157E–02	1.1600000000110E–04
3	–1.6649701690752E+03	3.3159363169596E+01	–1.0861179999898E–01	1.2399999999915E–04
4	–6.1420486441088E+03	6.3630987079837E+01	–1.7762319999965E–01	1.7599999999975E–04
5	–8.2289951961933E+04	5.3773958896061E+02	–1.1612491999609E+00	8.5599999997375E–04
6	–6.5842104212475E+05	3.7934294783212E+03	–7.2924928000022E+00	4.7040000000014E–03
7	3.4561620732510E+05	–2.2129380791446E+02	–2.4524285999925E+00	3.1479999999958E–03
8	1.9798369474597E+06	–1.4782551342826E+04	3.1656481897637E+01	–2.0843356864237E–02

Table 11-5. Saturated Steam heat Capacity Constants

i	*ACP*(*i*)	*BCP*(*i*)	*CCP*(*i*)	*DCP*(*i*)
9	–9.6249385211359E+07	4.3633668884423E+05	–6.5887615106930E+02	3.3146147264269E–01
10	–1.1074934463333E+07	4.8073794630970E+04	–6.9212173247881E+0l	3.3091693999800E–02

Liquid Properties

Internal Energy

Given a liquid at some temperature, T_l, and some pressure, *p*, the liquid internal energy associated with that state is calculated by beginning with the internal energy of the saturated liquid state described by T_l and PSL, where PSL is the saturation pressure corresponding to T_l, and adding an additional term that represents the change in internal energy from the state (T_l, PSL) to the state (T_l, *p)* That is,

$$e_l(T_l,\ p) = e_{ls}(T_l,\ PSL) + ELP\ . \tag{11-39}$$

The additional term, ELP, which represents the change in energy required to move along the isotherm at T_l between two different pressure values, namely PSL and *p*, is represented as

$$ELP = (p - PSL)\left(\frac{\partial e_l}{\partial p}\right)_{T_l}, \tag{11-40}$$

where

$$\left(\frac{\partial e_l}{\partial p}\right) = -8.329595 \times 10^{-4}\left[1 - e^{1.450382 \times 10^{-6} PSL}\right] - 2.245825 \times 10^{-17} PSL^2 \tag{11-41}$$

Therefore, the partial derivative with respect to T_l of the internal energy is calculated as

$$\left(\frac{\partial e_l}{\partial T_l}\right)_p = \frac{d e_{ls}}{d T_{sat}} + ERT \tag{11-42}$$

where

$$ERT = \left[\frac{\partial}{\partial T_l}(ELP)\right]_p$$

$$= \left\{-8.329595\times10^{-4}[-1 + e^{-1.450382\times10^{-6}PSL} \times [1 + 1.450382\times10^{-6}(p - PSL)]]\right.$$

$$\left. - 2.245825\times10^{-17}(2p \cdot PSL - 3PSL^2)\right\}\frac{d}{dT_l}(PSL)$$

and de_{ls}/dT_{sat} is calculated as in ***Saturated Liquid Internal Energy***

Density

Initial Calculation

Given the pressure *p* and temperature T_l of liquid water, Tait's equation-of-state in the form

$$\frac{v(0\ ,\ T_l) - v(p\ ,\ T_l)}{v(0\ ,\ T_l)} = \frac{1}{n}\ln\left[1 + \frac{p}{B(T_l)}\right] \tag{11-43}$$

is used to determine the liquid density and its partial derivatives, where v is the specific volume of the liquid. The constant n is quoted in work by Richardson, Arens, and Haverson (Ref. 11-4) to be 7.146. The terms $v(0\ ,\ T_l)$ and $B(T_l)$ are third-order polynomials of liquid temperature fitted to steam-table data, such that

$$v(0\ ,\ T_l) = AVO(i) + BVO(i)\ T_l + CVO(i)\ T_l^2 + DVO(i)\ T_l^3 \tag{11-44}$$

and

$$B(T_l) = AFN(i) + BFN(i)\ T_l + CFN(i)\ T_l^2 + DFN(i)\ T_l^3\ , \tag{11-45}$$

where

i = 1 for 273.15 ≤ T_l < 373.15 K ,
i = 2 for 373.15 ≤ T_l < 473.15 K ,
i = 3 for 473.15 ≤ T_l < 573.15 K ,
i = 4 for 573.15 ≤ T_l < 603.15 K ,
i = 5 for 603.15 ≤ T_l < 613.15 K ,
i = 6 for 613.15 ≤ T_l < 623.15 K ,
i = 7 for 623.15 ≤ T_l < 633.15 K ,

$i = 8$ for $633.15 \le T_l < 643.15$ K ,
$i = 9$ for $643.15 \le T_l < 653.15$ K ,
$i = 10$ for $653.15 \le T_l < 663.15$ K ,
$i = 11$ for $663.15 \le T_l < 673.15$ K , and
$i = 12$ for $673.15 \le T_l \le 713.94025779311$ K .

Table 11-6 lists the constants *AVO*(*i*), *BVO*(*i*), *CVO*(*i*), *DVO*(*i*), *AFN*(*i*), *BFN*(*i*), *CFN*(*i*), and *DFN*(*i*) for the given temperature ranges.

Table 11-6. Liquid Density Constants

i	*AVO*(*i*)	*BVO*(*i*)	*CVO*(*i*)	*DVO*(*i*)
1	1.7057666777468E–03	–6.0320895569365E–06	1.5944423965594E–08	–1.2149418561177E–11
2	5.2145931517155E–04	3.5189228252915E–06	–9.7304881862624E–09	1.0856688130631E–11
3	–1.4931865836934E–02	9.7931556400429E–05	–2.0172817692512E–07	1.4080475270259E–10
4	–4.9334201381918E–01	2.5928571576499E–03	–4.5387107397840E–06	2.6537936475365E–09
5	–3.4558955902321E+00	1.7351793841884E–02	–2.9047483637289E–05	1.6220227777320E–08
6	–1. 1952528427292E+01	5.8904962031842E–02	–9.6786687447220E–05	5.3029284583415E–08
7	–3.7446629978341E+01	1.8173474403006E–01	–2.9404991620713E–04	1.5863005350824E–07
8	–3.9713284923576E+02	1.8801824705202E+00	–2.9673900150051E–03	1.5612171739106E–06
9	–2.3142714272157E+03	1.0710216457395E+01	–1.6521763202064E–02	8.4955209566212E–06
10	2.0481569977849E+03	–9.3452783115489E+00	1.4212077056589E–02	–7.2037202704367E–06
11	–7.3864713248117E+01	3.3144939132191E–01	–4.9608715522591E–04	2.4771793009809E–07
12	–2.1891320674084E+01	9.6758467414310E–02	–1.4289074953436E–04	7.0567217785700E–08

i	***AFN*(*i*)**	***BFN*(*i*)**	***CFN*(*i*)**	***DFN*(*i*)**
1	–4.2486354144244E+09	3.7516769853867E+07	–1.0064945851796E+05	8.7507285129715E+01
2	–2.7936308563236E+08	5.5663179995300E+06	–1.4921749894688E+04	1.0834095198280E+01
3	–1.1761210016041E+08	4.3832221802974E+06	–1.2088373365747E+04	8.6034520917150E+00
4	–4.5415129389018E+09	2.7368608704680E+07	–5.1 894794477625E+04	3.1581281016141E+01
5	–4.0104325667716E+10	2.0292575433752E+08	–3.4075971373732E+05	1.9000660267975E+02
6	–6.0173879922257E+10	2.9984925450490E+08	–4.9675963282729E+05	2.7368658401451E+02
7	2.0678826351719E+10	–8.9503807129603E+07	1.2822787819385E+05	–6.0722291833340E+01
8	8.3793557728900E+10	–3.8997180562867E+08	6.0502628698976E+05	–3.1291965911464E+02
9	9.2402374347985E+10	–4.2674923965292E+08	6.5695613829284E+05	–3.3711122197289E+02
10	–2.7547713637194E+10	1.2580004134443E+08	–1.9147491048695E+05	9.7136148925404E+01
11	6.8608195287374E+08	–3.0636028439513E+06	4.5613625244005E+03	–2.2642074876391E+00
12	4.3458430609231E+07	–1.8379937116289E+05	2.5971646178490E+02	–1.2244044950391E–01

This allows the density, ρ_l to be calculated as

$$\rho_l = \frac{1}{v(0\ ,\ T_l)\left\{1.0 - \frac{1}{7.146}\ \ln\left[1.0 + \frac{p}{B(T_l)}\right]\right\}} \tag{11-46}$$

Therefore,

$$\left(\frac{\partial \rho_l}{\partial p}\right)_{T_l} = \frac{\rho_l^2\ v(0\ ,\ T_l)}{7.146\ [p + B(T_l)]} \tag{11-47}$$

and

$$\left(\frac{\partial \rho_l}{\partial T_l}\right)_p = -\rho_l\left(\frac{v'(0\ ,\ T_l)}{v(0\ ,\ T_l)}\right) - B'(T_l)\left(\frac{p}{B(T_l)}\right)\left(\frac{\partial \rho_l}{\partial p}\right)_{T_l} \tag{11-48}$$

where

$$v'(0\ ,\ T_l) = BVO(i) + 2\ CVO(i)\ T_l + 3\ DVO(i)\ T_l^2 \tag{11-49}$$

and

$$B'(T_l) = BFN(i) + 2\ CFN(i)\ T_l + 3\ DFN(i)\ T_l^2 \tag{11-50}$$

The polynomial constants for $v'(0\ ,\ T_l)$ and $B'(T_l)$ are the same as for $v(0\ ,\ T_l)$ and $B(T_l)$ and are given in Table 11-6

Residual Void Correction[1]

After evaluation in the above section, ρ_l and its derivatives are corrected to reflect a residual void fraction. In the following, the values calculated above are denoted by a tilde (˜).

$p \geq 4.0 \times 10^5$ Pa

$$\left(\frac{\partial \rho_l}{\partial T_l}\right)_p = \left(1 - \frac{1000}{p}\right)\left(\frac{\partial \tilde{\rho}_l}{\partial T_l}\right)_p , \tag{11-51}$$

1. This artificial compressibility of liquid is presently turned off in the code. It can be turned on by setting the flag NOAC to 0 in subroutine RHOLIQ if it is needed.

$$\left(\frac{\partial \rho_l}{\partial p}\right)_{T_l} = \left(1 - \frac{1000}{p}\right)\left(\frac{\partial \tilde{\rho}_l}{\partial p}\right)_{T_l} + \frac{1000\tilde{\rho}_l}{p^2} \tag{11-52}$$

and

$$\rho_\ell = \left(1 - \frac{1000}{p}\right)\tilde{\rho}_\ell \ . \tag{11-53}$$

p < 4.0 ×10^5 Pa

$$\left(\frac{\partial \rho_l}{\partial T_l}\right)_p = (0.995 + 6.25\times10^{-9}p)\left(\frac{\partial \tilde{\rho}_l}{\partial T_l}\right)_p \ , \tag{11-54}$$

$$\left(\frac{\partial \rho_l}{\partial p}\right)_{T_l} = (0.995 + 6.25\times10^{-9}p)\left(\frac{\partial \tilde{\rho}_l}{\partial p}\right)_{T_l} + 6.25\times10^{-9}\tilde{\rho}_l \ , \tag{11-55}$$

and

$$\rho_l = (0.995 + 6.25\times10^{-9}p)\,\tilde{\rho}_l \tag{11-56}$$

Steam Properties

Superheated Vapor

$(T_g - T_{sv}) > 0$, where T_{sv} is the saturation temperature corresponding to the partial pressure of the vapor, p_v, throughout this section. The constant-pressure specific heat of steam at temperature T_g is approximated as

$$c_{pv} = \left(\frac{\partial h_v}{\partial T_v}\right)_{p_v} = \frac{c_{pv,\,ideal}}{2}\left[1 + \frac{T_g}{\sqrt{T_g^2 - \beta}}\right] \tag{11-57}$$

where

$$\beta = T_{sv}^2 \left[1 - \frac{1}{\left(\frac{2\, c_{pvs}}{c_{pv,\,ideal}} - 1 \right)^2} \right] \tag{11-58}$$

The term c_{pvs} is calculated as defined in ***Heat Capacity of Saturated Steam at Constant Pressure***, and $c_{pv,\,ideal}$ is defined by ideal gas behavior, such that

$$c_{pv,\,ideal} = \frac{R_v \gamma_{ideal}}{\gamma_{ideal} - 1} \ , \tag{11-59}$$

where R_v is the gas constant for steam (Table 11-1) and γ_{ideal} is the ratio of ideal specific heats for steam (Table 11-1).

Integrating the equation for c_{pv} along a constant p_v line gives

$$h_v = h_{vs} + \frac{c_{pv,\,ideal}}{2} \left[(T_g - T_{sv}) \ + \ (T_g^2 - \beta)^{1/2} \ - \ \frac{T_{sv}}{\left(\frac{2\, c_{pvs}}{c_{pv,\,ideal}} - 1 \right)} \right] \tag{11-60}$$

The internal energy of vapor is therefore calculated as

$$e_v = e_{vs} + \frac{c_{pv,\,ideal}}{2} \left[(T_g - T_{sv}) \ + \ (T_g^2 - \beta)^{1/2} \ - \ \frac{T_{sv}}{\left(\frac{2\, c_{pvs}}{c_{pv,\,ideal}} - 1 \right)} \right] - \ p_v \left(\frac{1}{\rho_v} + \frac{1}{\rho_{vs}} \right) \tag{11-61}$$

The definitions of enthalpy and internal energy allow the density of the water vapor to be written, such that

$$\rho_v = \frac{p_v}{h_v - e_v} = \frac{p_v}{[h_{vs} + c_{pv,ideal}(T_g - T_{sv})] - [e_{vs} + c_{vv,ideal}(T_g - T_{sv})]} = \frac{p_v}{(h_{vs} - e_{vs}) + (\gamma_{ideal} - 1)(e_v - e_{vs})} \tag{11-62}$$

where $c_{vv,ideal}$ is defined in Table 11-1

Internal Energy

Substitution of ρ_v and ρ_{vs}, as defined by the preceding equation, into the equation for the internal energy of the vapor gives the following equations.

For $p_v \leq 1.9\times10^7$ Pa

$$e_v = e_{vs} + \frac{c_{vv,ideal}}{2}\left[(T_g - T_{sv}) + (T_g^2 - \beta)^{1/2} - \frac{T_{sv}}{\left(\frac{2c_{pvs}}{c_{pv,ideal}} - 1\right)}\right] \tag{11-63}$$

where again $c_{vv,ideal}$ is the constant-volume specific heat for steam, as defined by ideal gas behavior (Table 11-1). Therefore,

$$\left(\frac{\partial e_v}{\partial T_g}\right)_{p_v} = \frac{c_{vv,ideal}}{\left(1 - \frac{\beta}{\kappa^2}\right)} \tag{11-64}$$

and

$$\left(\frac{\partial e_v}{\partial p_v}\right)_{T_g} = -\frac{1}{2}\left(\frac{\partial e_v}{\partial T_g}\right)_{p_v}\left[\left(1 - \frac{\beta}{\kappa^2}\right)\kappa_p' + \frac{1}{\kappa}\frac{d\beta}{dp_v}\right], \tag{11-65}$$

where

$$\kappa = \frac{2}{c_{vv,\,ideal}}(e_v - e_{vs}) + T_{sv}\left[1 + \frac{1}{\dfrac{2c_{pvs}}{c_{pv,ideal}} - 1}\right], \tag{11-66}$$

and

$$\kappa_p{}' = \left(\frac{\partial \kappa}{\partial p_v}\right)_{T_g} = -\frac{2}{c_{vv,\,ideal}}\frac{de_{vs}}{dp_v} + \left[1 + \frac{1}{\left(\dfrac{2c_{pvs}}{c_{pv,\,ideal}} - 1\right)}\right]\frac{dT_{sv}}{dp_v} \tag{11-67}$$

$$-\frac{2}{c_{pv,\,ideal}}\left[\frac{T_{sv}}{\left(\dfrac{2c_{pvs}}{c_{pv,\,ideal}} - 1\right)^2}\right]\frac{dc_{pvs}}{dp_v}$$

and

$$\frac{d\beta}{dp_v} = \frac{2}{T_{sv}}\left\{\beta\frac{dT_{sv}}{dp_v} + \frac{2}{c_{pv,\,ideal}}\left[\frac{T_{sv}}{\left(\dfrac{2c_{pvs}}{c_{pv,\,ideal}} - 1\right)}\right]\frac{dc_{pvs}}{dp_v}\right\} \tag{11-68}$$

For $p_v \geq 2.0\times10^7$ Pa,

$$e_v = e_{vs} + \frac{c_{pv,\,\text{ideal}}}{2\gamma_s}\left[\frac{(T_g - T_{sv}) + (T_g^2 - \beta)^{1/2} - T_{sv}}{\left(\dfrac{2c_{pvs}}{c_{pv,\,\text{ideal}}} - 1\right)}\right], \tag{11-69}$$

$$\left(\frac{\partial e_v}{\partial T_g}\right)_{p_v} = \frac{c_{pv,\,\text{ideal}}}{2\gamma_s}\left(1 + \frac{T_g}{(T_g^2 - \beta)^{1/2}}\right), \tag{11-70}$$

and

$$\left(\frac{\partial e_v}{\partial p_v}\right)_{T_g} = \frac{de_{vs}}{dp_v} - \frac{e_v - e_{vs}}{\gamma_s}\frac{d\gamma_s}{dp_v} + \frac{c_{pv,\,ideal}}{2\gamma_s}\cdot\left[\left(-\frac{dT_{sv}}{dp_v}\right) - \frac{1}{2}\left(\frac{d\beta}{dp_v}\right)\left(\frac{1}{\sqrt{T_g^2-\beta}}\right)\right.$$
$$\left. - \frac{dT_{sv}}{dp_v}\cdot\left(\frac{1}{\left(\frac{2c_{pvs}}{c_{pv,\,\mathrm{ideal}}}-1\right)}\right) + \frac{2}{c_{pv,\,ideal}}\left[\frac{T_{sv}}{\left(\frac{2c_{pvs}}{c_{pv,\,\mathrm{ideal}}}-1\right)^2}\right]\frac{dc_{pvs}}{dp_v}\right] \tag{11-71}$$

where

$$\frac{\partial\beta}{\partial p_v} = \frac{2}{T_{sv}}\left\{\beta\frac{dT_{sv}}{dp_v} + \frac{2}{c_{pv,\,ideal}}\left[\frac{T_{sv}}{\left(\frac{2c_{pvs}}{c_{pv,\,\mathrm{ideal}}}-1\right)}\right]^3\frac{dc_{pvs}}{dp_v}\right\} \tag{11-72}$$

For $1.9\times10^7\ \mathrm{Pa} < p_v < 2.0\times10^7\ \mathrm{Pa}$ the values of e_v and its derivatives are calculated by interpolating between the values of the two curve fits.

Density

If $p_v \le 1.9\times10^7\ \mathrm{Pa}$ the vapor density is calculated as

$$\rho_v = \frac{\rho_v}{(\gamma_s-1)e_{vs} + (\gamma_{ideal}-1)(e_v - e_{vs})} \tag{11-73}$$

Therefore,

$$\left(\frac{\partial p_v}{\partial T_g}\right)_{p_v} = -\left(\frac{\partial e_v}{\partial T_g}\right)_{p_v}\left[\frac{(\gamma_{ideal}-1)\rho_v}{(\gamma_s-1)e_{vs} + (\gamma_{ideal}-1)(e_v - e_{vs})}\right], \tag{11-74}$$

and

$$\left(\frac{\partial\rho_v}{\partial p_v}\right)_{T_g} = \left\{(1-\rho_v)\left[e_{vs}\frac{d\gamma_s}{dp_v} + (\gamma_s-\gamma_{ideal})\frac{de_{vs}}{dp_v}\right]\cdot\right.$$
$$\left.\left[\frac{1}{(\gamma_s-1)e_{vs} + (\gamma_{ideal}-1)(e_v - e_{vs})}\right]\right\} + \left(\frac{\partial\rho_v}{\partial e_v}\right)_{p_v}\left(\frac{\partial e_v}{\partial p_v}\right)_{T_g} \tag{11-75}$$

where

$$\left(\frac{\partial \rho_v}{\partial e_v}\right)_{p_v} = \frac{(\gamma_{ideal}-1)\rho_v}{(\gamma_s-1)e_{vs}+(\gamma_{ideal}-1)(e_v-e_{vs})} \ . \tag{11-76}$$

If $p_v \geq 2.0\times10^7$ Pa, the vapor density is calculated as

$$\rho_v = \frac{p_v}{(\gamma_s-1)e_v} \tag{11-77}$$

Therefore,

$$\left(\frac{\partial p_v}{\partial T_g}\right)_{p_v} = \left(\frac{\partial \rho_v}{\partial e_v}\right)_{p_v}\left(\frac{\partial e_v}{\partial T_g}\right)_{p_v} \tag{11-78}$$

and

$$\left(\frac{\partial \rho_v}{\partial p_v}\right)_{T_g} = \left(1-\rho_v e_v \frac{d\gamma_s}{dp_v}\right)\frac{1}{(\gamma_s-1)e_v} + \left(\frac{\partial \rho_v}{\partial e_v}\right)_{p_v}\left(\frac{\partial e_v}{\partial p_v}\right)_{T_g} \tag{11-79}$$

where

$$\left(\frac{\partial \rho_v}{\partial e_v}\right)_{p_v} = -\frac{\rho_v}{e_v} \ . \tag{11-80}$$

If 1.9×10^7 Pa $< p_v < 2.0\times10^7$ Pa, the vapor density and its derivatives are calculated by linearly interpolating between the values of the two curve fits.

Minimum and maximum limits are placed on the calculated values of the density, and its partial derivatives. In low-pressure regions where the above equations may predict a negative density, the density and its derivatives are recalculated based on ideal gas behavior. If ρ_v is less than zero, the vapor density and its derivatives are superseded by

$$\rho_v = \frac{p_v}{R_v T_g} \ , \tag{11-81}$$

$$\left(\frac{\partial \rho_v}{\partial T_v}\right)_{p_v} = -\frac{\rho_v}{T_g} \ , \tag{11-82}$$

and

$$\left(\frac{\partial \rho_v}{\partial p_v}\right)_{T_g} = -\frac{\rho_v}{p_g} \ . \tag{11-83}$$

Near the critical point, it is necessary to impose the following limit on the density ratio when the pressure is less than the critical pressure.

$$\frac{\rho_v}{\rho_l} \leq 0.999 \tag{11-84}$$

to avoid singularities when calculating certain parameters. If the calculated value of ρ_v exceeds $0.999\rho_l$ the vapor density and its derivatives are superseded by

$$\rho_v = 0.999\rho_l \ , \tag{11-85}$$

$$\left(\frac{\partial \rho_v}{\partial T_g}\right)_{p_v} = 0.999\left(\frac{\partial \rho_l}{\partial T_l}\right)_p \ , \tag{11-86}$$

and

$$\left(\frac{\partial \rho_v}{\partial p_v}\right)_{T_g} = 0.999\left(\frac{\partial \rho_l}{\partial p}\right)_{T_l} \tag{11-87}$$

For conditions above the critical pressure, ρ_v is retained.

Enthalpy

The EOS package calculates the enthalpy of the superheated vapor using the definition of enthalpy, such that

$$h_v = e_v + \frac{p_v}{\rho_v} \tag{11-88}$$

where e_v and ρ_v are calculated from Eqs. (11-63) (or (11-69)) and (11-73) (or (11-77), or (11-81)), respectively.

Subcooled Vapor

$(T_g - T_{sv}) \leq 0$ where T_{sv} refers to the saturation temperature corresponding to the partial pressure of the vapor, p_v throughout this section.

Internal Energy

$$e_v = e_{vs} + (T_g - T_{sv}) \frac{c_{pvs}}{\gamma_{ideal}} , \tag{11-89}$$

$$\left(\frac{\partial e_v}{\partial T_g}\right)_{p_v} = \frac{c_{pvs}}{\gamma_{ideal}} , \tag{11-90}$$

and

$$\left(\frac{\partial e_v}{\partial p_v}\right)_{T_g} = \frac{d e_{vs}}{d p_v} + \left(\frac{e_v - e_{vs}}{c_{pvs}}\right)\frac{d c_{pvs}}{d p_v} - \frac{\partial e_v}{\partial T_g}\frac{d T_{sv}}{d p_v} \tag{11-91}$$

Density

The method used to determine the subcooled vapor density, and its derivatives for all pressure ranges is identical to the one outlined in the case of superheated vapor for $p_v \leq 1.9\times10^7$ Pa, as given by Eq. (11-73).

Enthalpy

TRACE calculates the enthalpy of the subcooled vapor using the definition of enthalpy, such that

$$h_v = e_v + \frac{p_v}{\rho_v} , \tag{11-92}$$

where e_v and ρ_v are calculated from Eqs. (11-89) and (11-73). respectively.

Noncondensable Gas (Air, Hydrogen, or Helium) Properties

In general, TRACE treats the noncondensable field as an ideal gas. You have the option of choosing any of the following gases: air, argon, hydrogen, or helium[1], krypton, nitrogen, or

xenon. TRACE allows you to model either a single species of noncondensable gas or some combination thereof.

TRACE calculates the thermodynamic properties for the non-condensible gas field with the following correlations:

Internal Energy

The internal energy and its derivatives are given by (see Reference 11-14, pp. 21-22, Eqs. 1.29-1.32, for air and hydrogen and Reference 11-15, p. 247, for helium)

$$e_a = c_{va} T_g \ , \tag{11-93}$$

$$\left(\frac{\partial e_a}{\partial T_g} \right)_{p_a} = c_{va} \ , \tag{11-94}$$

and

$$\left(\frac{\partial e_a}{\partial p_a} \right)_{T_g} = 0.0 \ . \tag{11-95}$$

The constant-volume specific heat, c_{va}, is calculated from

$$c_{va} = c_{pa} - R_a \ , \tag{11-96}$$

where c_{pa} is the specific heat at constant pressure for noncondensable gases (determined as described below in the section ***Constant-Pressure Specific Heat***) and R_a is the gas constant for the noncondensable gas, as determined from

$$R_a = \frac{R}{M_a} , \tag{11-97}$$

1. More accurate properties also are available for helium. These optional properties for helium are not discussed here; see Reference 11-18 for complete details. Currently, these properties are only available for light water models (H_2O).

where R is the universal gas constant and M_a is the mass of one mole (molecular weight with units of kg) of the noncondensible gas. Since R and M_a are both constants for a give noncondensible gas, the values of R_a used by TRACE are provided in Table 11-1.

Density

We use the ideal-gas law for the air, hydrogen, and helium density correlations. Because the ideal-gas law accurately predicts gas behavior for low pressure and high temperature, and TRACE usually deals with this range of pressures and temperatures, we consider the ideal-gas correlation to provide an adequate approximation for the gas densities. The density is calculated according to the following set of relationships (Ref. 11-16):

$$\rho_a = \frac{p_a}{R_a T_g} , \tag{11-98}$$

$$\left(\frac{\partial \rho_a}{\partial p_a}\right)_{T_g} = \frac{1}{R_a T_g} , \tag{11-99}$$

and

$$\left(\frac{\partial \rho_a}{\partial T_g}\right)_{p_a} = -R_a \rho_a \left(\frac{\partial \rho_a}{\partial p_a}\right)_{T_g} \tag{11-100}$$

where ρ_a is the microscopic density, P_a is the noncondensible partial pressure, T_g is the temperature of the gas, and R_a is the noncondensible gas constant, as defined in the previous section.

Enthalpy

TRACE calculates the enthalpy of the noncondensable gas, such that

$$h_a = e_a + \frac{p_a}{\rho_a} , \tag{11-101}$$

where e_a and ρ_a are calculated from Eqs. (11-93) and (11-98) respectively.

Steam-Gas Mixture Properties

Internal Energy

The EOS package calculates the steam-noncondensible gas mixture internal energy, such that

$$e_m = \frac{e_v \rho_v + e_a \rho_a}{\rho_v + \rho_a} \ , \tag{11-102}$$

where e_v is calculated according to Eq. (11-61) or Eq. (11-89), depending upon whether the vapor is superheated or subcooled, e_a is calculated according to Eq. (11-93), ρ_v is the water vapor density as calculated in Eq. (11-73) or Eq. (11-77), and ρ_a is the noncondensable-gas density as calculated in Eq. (11-98).

Density

The EOS package calculates the steam-noncondensible gas mixture density, such that

$$\rho_m = \rho_v + \rho_a \ , \tag{11-103}$$

where ρ_v is the water vapor density as calculated in Eq. (11-73) or Eq. (11-77) and ρ_a is the noncondensable-gas density as calculated in Eq. (11-98).

Enthalpy

The EOS package calculates the steam-noncondensible gas mixture enthalpy, such that

$$h_m = \frac{h_v \rho_v + h_a \rho_a}{\rho_v + \rho_v} = e_m + \frac{p}{\rho_m} \ , \tag{11-104}$$

where e_m is calculated according to Eq. (11-102), ρ_m is calculated according to Eq. (11-103), and p is the total pressure.

Transport Properties

The EOS package is used to obtain transport properties for liquid- and vapor-phase water, noncondensable gases, and steam-gas mixtures. The input variables in this case are the saturation temperature corresponding to the total pressure; the internal energies, densities, and temperatures

of the liquid and gas phases where the gas is either steam, a noncondensable gas, or a steam-gas mixture; the total pressure; and the partial pressure of the noncondensable gas, if any is present. The output transport variables include the latent heat of vaporization, the constant-pressure specific heats, viscosities, and thermal conductivities of the liquid and gas phases, and the surface tension of the liquid.

The polynomial equation fits for the transport properties used in TRACE are described in the remainder of this section. Values of the constants are given in Tables 11-7 through 11-11

Latent Heat of Vaporization

TRACE calculates the latent heat of vaporization as

$$h_{lv} = h_{vs} - h_{ls} \ , \tag{11-105}$$

where h_{vs} and h_{ls} are calculated according to Eqs. (11-29) (or (11-31)) and (11-35) respectively.

Constant-Pressure Specific Heat

The EOS package calculates the constant-pressure specific heats for the liquid and the steam, gas, or steam-gas mixture, respectively. Constants used in this section are given in Table 11-7

Table 11-7. Constant-Pressure Specific Heat Constants

B_{0l}	= 2.394907×10^{-4}	B_{1l}	= $-5.196250 \times 10^{-13}$
C_{0l}	= 1.193203×10^{-11}	C_{1l}	= 2.412704×10^{-18}
D_{0l}	= $-3.944067 \times 10^{-17}$	D_{1l}	= $-1.680771 \times 10^{-24}$

C_{1v}	=	1.68835968×10^{3}
C_{2v}	=	0.6029856
C_{3v}	=	$4.820979623 \times 10^{2}$
C_{4v}	=	2.95317905×10^{7}
C_{5v}	=	1.8
C_{6v}	=	4.60×10^{2}

Liquid

TRACE calculates the liquid constant-pressure specific heat, such that

$$c_{pl} = \{ h_l [h_l (D_{0l} + D_{1l} p) + (C_{0l} + C_{1l} p)] + B_{0l} + B_{1l} p \}^{-1} \tag{11-106}$$

The maximum permitted value for c_{pl} is 4.0×10^4 and if the above calculation of c_{pl} yields a value greater than this, it is reset to be 4.0×10^4

Steam

TRACE calculates the steam constant-pressure specific heat, such that

$$c_{pv} = C_{1v} + C_{2v} T_g + \frac{C_{3v} p}{(C_{5v} T_g - C_{6v})^{24}} + \frac{C_{4v} p^3}{(C_{5v} T_g - C_{6v})^9} . \tag{11-107}$$

Noncondensable Gas

Although the specific heat at constant pressure c_p is temperature-dependent, TRACE assumes the constant-pressure specific heat of the noncondensable gas to be constant, such that

c_{pa} = 1004.832 [J/(kg·K)] for air, (11-108)

c_{pa} = 14533.2 [J/(kg·K)] for hydrogen, (11-109)

and

c_{pa} = 5193.086 [J/(kg·K)] for helium. (11-110)

This assumption introduces errors that are deemed to be inconsequential to most transients of interest in PWRs.

Steam-Gas Mixtures

TRACE uses an averaging technique to calculate the specific heat of a steam-air, steam-hydrogen, or steam-helium mixture, such that

$$c_{pg} = \frac{(p - p_a) c_{pv} + p_a c_{pa}}{p} , \tag{11-111}$$

where c_{pv} and c_{pa} are calculated as in Eqs. (11-107) through (11-110).

Please note that because these values of specific heats are used only for calculating heat-transfer coefficients, these fits were chosen for simplicity and smoothness and are not necessarily consistent with those derivable from the thermodynamic routines.

Fluid Viscosity

The code is able to calculate the fluid viscosities for the liquid and the steam, for the gas, or for the steam-gas mixture. Constants used in this section are given in Tables 11-8, 11-9, and 11-11

Liquid

The evaluation of liquid viscosity is divided into three different enthalpy ranges. Table 11-8 gives the constants used in this section.

$h_l \le 0.276 \times 10^6$ J/kg

$$\mu_l = [A_{0l} + A_{1l}x + A_{2x}x^2 + A_{3x}x^3 + A_{4x}x^4] - [B_{0l} + B_{1l}\eta + B_{2l}\eta^2 + B_{3l}\eta^3](p - p_i) \quad (11\text{-}112)$$

where

$$x = (h_l - c_{0n})h_0 \quad (11\text{-}113)$$

and

$$\eta = (h_l - e_{c0n})\, e_{h0} \quad (11\text{-}114)$$

Table 11-8. Liquid Viscosity Constants

$A_{0\ell}$	=	$1.298102340 \times 10^{-3}$	$B_{0\ell}$	=	-6.5959×10^{-12}
$A_{1\ell}$	=	$-9.264032108 \times 10^{-4}$	$B_{1\ell}$	=	6.763×10^{-12}
$A_{2\ell}$	=	$3.81047061 \times 10^{-4}$	$B_{2\ell}$	=	-2.88825×10^{-12}
$A_{3\ell}$	=	$-8.219444458 \times 10^{-5}$	$B_{3\ell}$	=	4.4525×10^{-13}
$A_{4\ell}$	=	$7.022437984 \times 10^{-6}$			

Table 11-8. Liquid Viscosity Constants (Continued)

$D_{0\ell}$	=	$3.026032306 \times 10^{-4}$	$E_{0\ell}$	=	$1.4526052612 \times 10^{-3}$
$D_{1\ell}$	=	$-1.836606896 \times 10^{-4}$	$E_{1\ell}$	=	$-6.9880084985 \times 10^{-9}$
$D_{2\ell}$	=	$7.567075775 \times 10^{-5}$	$E_{2\ell}$	=	$1.5210230334 \times 10^{-14}$
$D_{3\ell}$	=	$-1.647878879 \times 10^{-5}$	$E_{3\ell}$	=	$-1.2303194946 \times 10^{-20}$
$D_{4\ell}$	=	$1.416457633 \times 10^{-6}$			

$F_{0\ell}$	=	$-3.8063507533 \times 10^{-11}$	h_0	=	$8.581289699 \times 10^{-6}$
$F_{1\ell}$	=	$3.9285207677 \times 10^{-16}$	c_{0n}	=	4.265884×10^{4}
$F_{2\ell}$	=	$-1.2585799292 \times 10^{-21}$	p_i	=	$6.894575293 \times 10^{5}$
$F_{3\ell}$	=	$1.2860180788 \times 10^{-27}$			

h_{00}	=	$3.892077365 \times 10^{-6}$	e_{h0}	=	$6.484503981 \times 10^{-6}$
e_{c0n}	=	5.53588×10^{4}	c_n	=	4.014676×10^{5}

0.276 × 10⁶ J/kg < h_l ≤ 0.394 × 10⁶ J/kg

$$\mu_l = [E_{0l} + E_{1l}h_l + E_{2l}h_l^2 + E_{3l}h_l^3] + [F_{0l} + F_{1l}h_l + F_{2l}h_l^2 + F_{3l}h_l^3](p - p_i) \ . \quad (11\text{-}115)$$

h_l > 0.394 × 10⁶ J/kg

$$\mu_l = D_{0l} + D_{1l}z + D_{2l}z^2 + D_{3l}z^3 + D_{4l}z^4 \ , \quad (11\text{-}116)$$

where

$$z = (h_l - c_n)h_{00} \quad (11\text{-}117)$$

Steam

Three gas temperature ranges are used when evaluating the steam viscosity. Constants used in this section are given in Table 11-9

$T_g \le 573.15$ K

$$\mu_v = [B_{1v}(T_g - 237.15) + C_{1v}] - \rho_v[D_{1v} - E_{1v}(T_g - 273.15)] \ . \quad (11\text{-}118)$$

If $\mu_v < 1\times10^{-7}$, it is set to that value.

573.15 K < T_g < 648.15 K

$$\begin{aligned}\mu_v = {} & B_{1v}(T_g - 237.15) + C_{1v} + \rho_v[F_{0v} - F_{1v}(T_g - 273.15) \\ & + F_{2v}(T_g - 237.15)^2 + F_{3v}(T_g - 237.15)^3] \\ & + \rho_v[G_{0v} + G_{1v}(T_g - 237.15) + G_{2v}(T_g - 237.15)^2 \\ & + G_{3v}(T_g - 237.15)^3](A_{0v} + A_{1v}\rho_v + A_{2v}\rho_v^2)\end{aligned} \quad (11\text{-}119)$$

$T_g \ge 648.15$ K

$$\mu_v = B_{1v}(T_g - 237.15) + C_{1v} + \rho_v(A_{0v} + A_{1v}\rho_v + A_{2v}\rho_v^2) \ . \quad (11\text{-}120)$$

Table 11-9. Noncondensable-Gas Viscosity Constants

H_{a0}	=	1.707623×10^{-5}	H_{b0}	=	1.735×10^{-5}
H_{a1}	=	5.927×10^{-8}	H_{b1}	=	4.193×10^{-8}
H_{a2}	=	-8.14×10^{-11}	H_{b2}	=	-1.09×10^{-11}
H_{c0}	=	4.175×10^{-6}	H_{d1}	=	5.9642×10^{-6}
H_{c1}	=	1.588×10^{-8}	H_{d2}	=	5.2047×10^{-8}
H_{c2}	=	7.6705×10^{-13}	H_{d3}	=	-1.5345×10^{-11}

Noncondensable Gas

The equations used for calculating the viscosity of noncondensible gases were obtained by fitting a quadratic polynomial to data with a least-squares method. The constants to these polynomials are given in Table 11-10. The viscosity is not a strong functions of pressure (Ref. 11-16), so the correlations used for this quantity does not include a pressure dependence.

Table 11-10. Noncondensable-Gas Viscosity Constants

$H_{a1} = 1.707623 \times 10^{-5}$ N·s·m^{-2}

$H_{a2} = 5.927 \times 10^{-8}$ N·s·(m^2·K)$^{-1}$

$H_{a3} = -8.14 \times 10^{-11}$ N·s·(m^{-2}·K^{-2})

$H_{b1} = 1.735 \times 10^{-5}$ N·s·m^{-2}

$H_{b2} = 4.193 \times 10^{-8}$ N·s·(m^2·K)$^{-1}$

$H_{b3} = -1.09 \times 10^{-11}$ N·s·(m^{-2}·K^{-2})

$H_{c1} = 4.175 \times 10^{-6}$ N·s·m^{-2}

$H_{c2} = 1.588 \times 10^{-8}$ N·s·(m^2·K)$^{-1}$

$H_{c3} = 7.6705 \times 10^{-13}$ N·s·(m^{-2}·K^{-2})

$H_{d1} = 5.9642 \times 10^{-6}$ N·s·m^{-2}

$H_{d2} = 5.2047 \times 10^{-8}$ N·s·(m^2·K)$^{-1}$

$H_{d3} = -1.5345 \times 10^{-11}$ N·s·(m^{-2}·K^{-2})

Air

If the noncondensable gas is air, two ranges of the gas temperature, T_g, are used to determine the gas viscosity.

$$\mu_a = \begin{cases} H_{a1} + H_{a2}(T_g - 273.15) + H_{a3}(T_g - 273.15)^2 & ; \quad T_g \le 502.15 \text{ K} \\ H_{b1} + H_{b2}(T_g - 273.15) + H_{b3}(T_g - 273.15)^2 & ; \quad T_g > 502.15 \text{ K} \end{cases}, \qquad (11\text{-}121)$$

where the polynomial constants H_{an} and H_{bn} (for n=1 to 4) are given in Table 11-10.

The range of data over which the viscosity correlations for air was developed was 273.15 K ≤ T ≤ 1073.15 K (Ref. 11-15). TRACE uses this correlation, however, for

273.15 K ≤ T_g ≤ 3000 K and 1.0 Pa ≤ P ≤ 45.0 MPa. The reference cited has no data for air viscosities with temperatures greater than 1073.15 K. However, Holman (Ref. 11-16) has viscosity of air to 2773.15 K. Validation of the correlations against the Holman data within the context of TRAC-P and documented in its Theory Manual, show that as the temperature increases from 1100 K to 2500 K, the percent error with respect to Holman grows approximately linearly, from less than 1% to 25% (underprediction). This is not generally considered to be a problem as TRACE will probably never have to calculate viscosity with such high temperatures, anyway.

Hydrogen

If the noncondensable gas is hydrogen, the gas viscosity is calculated as

$$\mu_a = H_{c1} + H_{c2} T_g + H_{c3} T_g^2, \tag{11-122}$$

where the polynomial constants H_{cn} (for n=1 to 3) are given in Table 11-10.

As with the air correlations, the range of data over which the viscosity correlations for hydrogen was developed was 273.15 K ≤ T ≤ 1073.15 K (Ref. 11-15). TRACE uses this correlation, however, for 273.15 K ≤ T_g ≤ 3000 K and 1.0 Pa ≤ P ≤ 45.0 MPa. The reference cited has no data for hydrogen viscosities with temperatures greater than 1073.15 K. However, Holman (Ref. 11-16) has viscosity of hydrogen to 1173.15 K.

Helium

If the noncondensable gas is helium, the gas viscosity is calculated as

$$\mu_a = H_{d1} + H_{d2} T_g + H_{d3} T_g^2 \tag{11-123}$$

where the polynomial constants H_{dn} (for n=1 to 3) are given in Table 11-10.

The range of data over which the helium viscosity correlation was developed is 255 K ≤ T_g ≤ 1090.15 K (Ref. 11-17). TRACE uses this correlation for 273.15 K ≤ T_g ≤ 3000 K and 1.0 Pa ≤ P ≤ 45.0 MPa. The error associated with the viscosity of helium over the range 273.15 K ≤ T_g ≤ 1090.15 K is no greater than 5.6%. The reference cited has no data for helium viscosities at temperatures greater than 1090.15 K.

Steam-Gas Mixture

An averaging technique is used when calculating the viscosity of a steam-noncondensible gas mixture, such that

$$\mu_g = \frac{(p - p_a)\mu_v + p_a \mu_a}{p}, \tag{11-124}$$

where μ_v and μ_a are calculated according to Eqs. (11-118) through (11-123).

Fluid Thermal Conductivity

TRACE calculates the fluid thermal conductivities for the liquid and the steam, gas, or steam-gas mixture, respectively. Constants used in this section are given in Table 11-11

Table 11-11. Thermal Conductivity Constants

h_0	=	5.815×10^5
A_{l0}	=	0.573738622
A_{l1}	=	0.2536103551
A_{l2}	=	–0.145468269
A_{l3}	=	–0.01387472485
C	=	2.1482×10^5
A_{v0}	=	1.76×10^{-2}
A_{v1}	=	3.87×10^{-5}
A_{v2}	=	1.04×10^{-7}
A_{v3}	=	-4.51×10^{-11}
B_{v0}	=	1.0351×10^{-4}
B_{v2}	=	0.4198×10^{-6}
B_{v3}	=	-2.771×10^{-11}

Liquid

TRACE calculates the liquid-water thermal conductivity, such that

$$k_l = A_{l0} + A_{l1} x_k + A_{l2} x_k^2 + A_{l3} x_k^3 \ , \tag{11-125}$$

where

$$x_k = \frac{h_l}{h_0} \ . \tag{11-126}$$

If $k_l < 0.09$, it is set to that value.

Steam

The code uses two gas temperature ranges to calculate the steam thermal conductivity.

273.15 K ≤ T_g ≤ 273.25 K.

$$k_v = x_1 + \rho_v \left[x_2 + \frac{C\rho_v}{(0.1)^{4.2}} \right] , \tag{11-127}$$

where

$$x_1 = A_{v0} + A_{v1}(0.1) + A_{v2}(0.1)^2 + A_{v3}(0.1)^3 \tag{11-128}$$

and

$$x_2 = B_{v0} + B_{v1}(0.1) + B_{v2}(0.1)^2 \ . \tag{11-129}$$

273.25 K < T_g ≤ 713.94025779311 K.

$$k_v = x_1 + \rho_v \left[x_2 + \frac{C\rho_v}{(T_g - 273.15)^{4.2}} \right] , \tag{11-130}$$

where

$$x_1 = A_{v0} + A_{v1}(T_g - 273.15) + A_{v2}(T_g - 273.15)^2 + A_{v3}(T_g - 273.15)^3 \tag{11-131}$$

and

$$x_2 = B_{v0} + B_{v1}(T_g - 273.15) + B_{v2}(T_g - 273.15)^2 \ . \tag{11-132}$$

If $k_v < 1.0\times10^{-4}$, it is set equal to that value.

Noncondensable Gas

Given that thermal conductivity is a strong function of temperature and a weak function of pressure TRACE assumes the thermal conductivity of the noncondensable gas to be an exponential function of temperature only, such that

$$k_a = 2.091\times10^{-4}\, T_g^{0.846} \quad [\mathrm{W/m\cdot K}] \text{ for air} \tag{11-133}$$

$$k_a = 1.6355\times10^{-3}\, T_g^{0.8213} \quad [\mathrm{W/m\cdot K}] \text{ for hydrogen} \tag{11-134}$$

and

$$k_a = 3.366\times10^{-3}\, T_g^{0.668} \quad [\mathrm{W/m\cdot K}] \text{ for helium} \tag{11-135}$$

This assumption should introduce inconsequential errors to most transients of interest in PWRs.

Steam-Gas Mixtures

TRACE uses an averaging technique to calculate the thermal conductivity of a steam-air, steam-hydrogen, or steam-helium mixture, such that

$$k_g = \frac{(p - p_a)k_v + p_a k_a}{p}\ , \tag{11-136}$$

where k_v and k_a are calculated as in Eqs. (11-127), (11-130) and (11-133) through (11-135).

Surface Tension

TRACE uses two ranges of the saturation temperature corresponding to the total pressure to determine the surface tension of liquid water.

273.15 K ≤ T_{sat} ≤ 582.435 K.

Within this range, the surface tension of liquid water is calculated using the following ASME Steam Tables Recommended Interpolation Equation (Ref. 11-5):

$$\sigma = 0.2358\left(1 - 0.625\left(\frac{647.15 - T_{sat}}{647.15}\right)\right)\left(\frac{647.15 - T_{sat}}{647.15}\right)^{1.256}\ . \tag{11-137}$$

The ASME Steam Tables state that this equation is valid for temperatures between the triple point (273.16 K) and the critical point, which the reference assumes to be 647.15 K. It is necessary in TRACE, however, to place a lower limit on the calculated value of the surface tension to avoid singularities when evaluating such things as the Chen nucleate-boiling relation. For this reason, the surface tension is set equal to a constant value for the remaining TRACE temperature range, 582.435 K to 713.94025779311 K.

582.435 K < T_{sat} ≤ 713.94025779311 K

A constant value of surface tension is calculated in this range to keep the surface tension from becoming too low. Constraining the temperature difference ratio to be no less than 0.1 gives

$$\sigma = 0.2358[1 - 0.625(0.1)]\ (0.1)^{1.256} \quad . \tag{11-138}$$

Liquid Solute Properties

TRACE has an extra mass-continuity equation for tracking a liquid solute (orthoboric acid or a user-defined solute) through all hydro components [see Eqs. (1-46) and (1-114) through (1-116)]. If the liquid solute is orthoboric acid, its concentration in the reactor-core region can be used to determine its neutronic reactivity-feedback effect on the point-reactor kinetics solution for the reactor-core power. The liquid solute has no other effect on the liquid-field processes and properties. The equations solved in TRACE require a correlation for the maximum solubility of the solute material in liquid water.

Because there is no hydraulic feedback effect from the liquid solute on the fluid dynamic solution, the solute mass provides the capability to investigate numerical-diffusion effects and the movement and subsequent distribution of injected coolant.

Model Description

The solubility model for the solute is based on a simple linear correlation between the solute concentration and the liquid temperature. This model is appropriate for dilute solutions of orthoboric acid. The solubility model was developed based on information from Reference 11-19.

TRACE simulates orthoboric acid with its liquid solute model because of boron's useful design characteristics. Boron has a thermal-neutron-capture cross section of 755 barns that can be used to introduce negative neutronic reactivity to control the reactor-core power. Its reference concentration molality of 0.32 allows appropriate amounts to be dissolved in the liquid-water coolant. Orthoboric acid is also physically and chemically very stable over its range of application (Ref. 11-20). The default solute in TRACE is orthoboric acid, which can be used in the reactivity-feedback calculation. If you wish to use a solute other than orthoboric acid, you can do so by defining new solubility specifications through input (see the ISOLCN namelist variable).

TRACE calculates the solute concentration for both 1D and 3D components. The evaluation procedure has two steps. The first step calculates the solute density and the second step calculates the amount of plated-out solute as well as the final solute concentration in each of the component's mesh cells for the time step.

TRACE calculates the solute density with Eq. (1-46). This equation calculates the solute density directly, with no regard for the solubility of orthoboric acid or for the possible occurrence of plating out. At this point, TRACE assumes infinite solubility of the material already in solution. In doing this calculation for any given mesh cell, the code considers each interface with an adjoining mesh cell. The amount of solute mass entering through a mesh-cell interface is defined by

$$m_{solute} = V_l \cdot \rho_l \cdot m \cdot \Delta t \cdot (1 - \alpha) \cdot A \tag{11-139}$$

where ρ_l is the donor-cell liquid density, m is the ratio of donor-cell solute mass to liquid mass, and A is the flow area between the mesh cells. The convected solute mass is evaluated implicitly by its stabilizer mass equation.

The second set of calculations computes the amount of plated-out solute and obtains the final liquid-solute-concentration ratio. If the cell has voided completely during the time step, all solute in the cell must have either convected out or plated out, and the liquid solute concentration is zero. If the cell has not voided completely (that is, if the cell still contains some liquid coolant), TRACE determines the maximum solubility of orthoboric acid as a function of temperature. This solubility value is known at 303 K and 373 K (Ref. 11-19). For temperatures between these two values, TRACE determines the solubility by linear interpolation. For temperatures less than 303 K, TRACE uses the value at 303 K; for temperatures greater than 373 K, the code uses the value at 373 K. The maximum possible solute density is the water density times the maximum solubility. If the new solute density exceeds this maximum, TRACE assumes the excess has plated out, and the solute density becomes the maximum value. If the new solute density is less than the maximum, the code assumes that plated-out solute, if it exists in the cell, reenters solution at an infinite rate to the extent that either all the plated-out solute dissolves or the solution becomes saturated. TRACE uses Eqs. (1-115) and (1-116) to calculate the final solute density and the amount plated out. TRACE then finds the new concentration ratio by dividing the new solute density by the coolant density. Plated-out solute remains in the cell until it redissolves.

If a solute other than orthoboric acid is defined, you must input new maximum and minimum temperatures, as well as solubility values for both temperatures. TRACE calculates the maximum solubility using linear interpolation.

The boron concentration in orthoboric acid is one of four parameters that affect the neutronic reactivity of the reactor core. TRACE calculates their core-region averaged values in subroutine RFDBK. (For a more complete description of reactivity feedback, see **Chapter 9**). When calculating reactivity feedback from boron, TRACE takes into account all forms of boron in the reactor core,

1) dissolved orthoboric acid in the liquid coolant,
2) orthoboric acid plated on core structure,
3) borosilicate glass in burnable-poison pins, and
4) boron oxide in control-rod-cluster pins.

The solubility model for orthoboric acid affects items 1 and 2.

TRACE makes the following assumptions when implementing the solute-tracking feature of the code:

1) The presence of solute in the coolant does not affect any of the liquid properties of the coolant, nor does it affect interfacial or wall heat transfer in any way (this assumption makes the solute concentration a good marker with which the fluid from a particular source can be followed).
2) While the code does allow for plated-out solute, it does not take into account the effects of such solute buildup except through neutronic reactivity feedback when the solute is orthoboric acid. Plated-out solute on structure surfaces could affect wall heat transfer and surface friction (Ref. 11-20).
3) Plating out occurs instantaneously if the concentration exceeds the maximum solubility, such as when liquid coolant boils or flashes. Similarly, the plated-out material dissolves at an infinite rate. No allowance is made for a supersaturated orthoboric solution.
4) The code assumes that the solubility is a function of temperature and is not pressure dependent.
5) The maximum-solubility temperature dependence is assumed to be linear and defined over a limited temperature range.

Reference 11-19 indicates that the maximum solubility of orthoboric acid at 303 K is 6.35 g/100 cm^3 of water, and at 373 K, it is 27.6 g/100 cm^3 of water. We interpreted this to mean respective maximum solute concentrations of 0.0635 and 0.276 kg solute/kg water at 303 K and 373 K; this interpretation is consistent with the data in Reference 11-21.

We are now aware of data that would permit the construction of a solubility curve in TRACE that is valid over a much wider range of temperatures, although there is still a question of how to treat solubility in the metastable range above 442 K. We believe that such a model should be incorporated. For now, the user can input a linearly-dependent maximum-solubility curve fit to data over the temperature range of interest if the default maximum-solubility curve is inappropriate. We do not believe that it is important to incorporate rates into the dissolution/plating processes because most transients in PWRs will not approach the solubility limits.

Verification

The thermodynamic and transport property fits used in TRACE have been compared with steam-table data over a wide range of parameters. The agreement is satisfactory in the saturation region and in the superheated steam region for $p < p_{critical}$ and $T_g < 823.0$ K. For example, the saturation temperature corresponding to a given pressure is always calculated within a maximum

error of ± 1 K. However, in most situations, the error is significantly smaller. The agreement also is good in the subcooled-water region for $T_l < T_{critical}$.

Further verification was performed by comparing the TRACE polynomial fits with the WATER package (Ref. 11-1) over a wider range of nonequilibrium [99 K of both superheat and subcooling (liquid superheat or vapor subcooling exceeding 99 K are highly unlikely in reactor applications)] for pressures up to 20 MPa. The comparisons showed good agreement for both the thermodynamic and transport properties throughout the saturation and nonequilibrium regions, except for very extreme cases. However, at high degrees of subcooling or superheat, some minor inconsistencies were noticed. Because there are no data in these extreme cases, it is impossible to compare TRACE and the WATER package adequately.

In addition, the output of the variables p_v, e_v, e_ℓ, and ρ_v was checked against values generated from the Sesame database. Sesame is a database, developed by members of the Theoretical Division at LANL, that includes various equation-of-state data (Ref. 11-6). For all of the results below, we used the EOSPAC program (Ref. 11-7) to read the Sesame data. Sesame material 7152 (water) was used in these data comparisons. This particular data fit for water was originally developed by the National Bureau of Standards [NBS, now known as the National Institute for Standards and Technology (NIST)]. A 64-term fit was used by the NBS to closely model equation-of-state data (Ref. 11-8). Sesame data for material 7152 can be assumed to be accurate to within 1% for materials on the saturation line and within 5% for metastable regions off the saturation line. Because the NBS data were based on a fit to experimental data for equilibrium states, no attempt has been made to compare the data with our values for the metastable states corresponding to subcooled steam or superheated liquid.

The ρ_v values from the TRACE EOS package agreed very well with Sesame data. On the saturation line at pressures below the critical pressure ($p_{crit} = 2.2232 \times 10^7$ Pa,) the agreement is excellent. Here the fractional error is less than 1%. Above p_{crit} (see Figure 11-1), the TRACE ρ_v values also agree with the Sesame data (dashed lines in graphs), often to better than 1% accuracy. However, there is a slight departure between the two curves in the pressure range $p_{crit} < p_v < 2.8 \times 10^7$ Pa. Here the fractional error is about 5%. For superheating, the plots near the saturation line also appear good. For superheats of 8 K and less, the TRACE ρ_v plot follows the Sesame data fairly well. Larger than 10 K superheat yields fractional errors larger than 10% (Figure 11-2).

For the e_v plot on the saturation line, Sesame and TRACE seem to agree well up to p_{crit} (Figure 11-3). However, one significant departure is noted in the pressure range $1.0 \times 10^5 < p_v < 2.0 \times 10^6$ Pa. Here, although the fractional error is only 0.5%, the slope of the TRACE plot goes slightly negative in the pressure range $1.3 \times 10^6 < p_v < 2.0 \times 10^6$ Pa, while

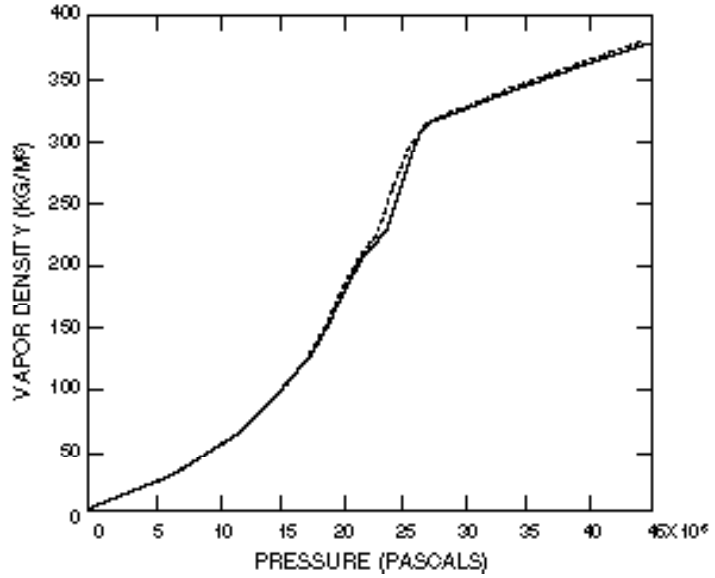

Figure. 11-1. Vapor density vs. pressure along the saturation line. Solid: TRACE; Dashed: Sesame.

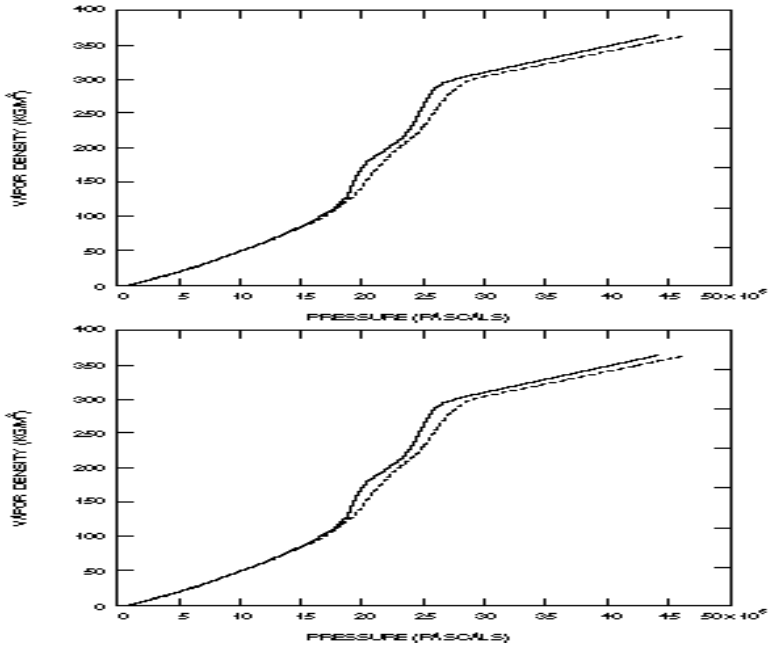

Figure. 11-2. Vapor density vs. pressure at a superheat of 8 K. Solid: TRACE; Dashed: Sesame.

the Sesame slope remains positive. It should be noted that the TRACE e_v slope is only slightly negative, and then only for a short pressure range. At pressures above p_{crit} along the saturation line (Figure 11-3), the difference between the TRACE curve and the Sesame data becomes more

significant. At approximately $p_v = 2.75 \times 10^7$ Pa, the fractional error between the two curves is almost 4%. The fractional error decreases as pressure increases until, at $p_v = 4.5 \times 10^7$ Pa, the fractional error between the two curves is about 1.5%. For superheating, the Sesame data follow the TRACE e_v plot well up to p_{crit}, and departures between the Sesame and TRACE curves are more significant above p_{crit} (Figure 11-4). Superheated conditions yield small departures of the TRACE e_v curve from the Sesame data above p_{crit}. Superheats as great at 100 K have fractional errors less than 6% across the pressure range $2.5 \times 10^7 < p_v < 3.0 \times 10^7$ Pa. Here also, the fractional error is only about 3% at $p_v = 4.5 \times 10^7$ Pa.

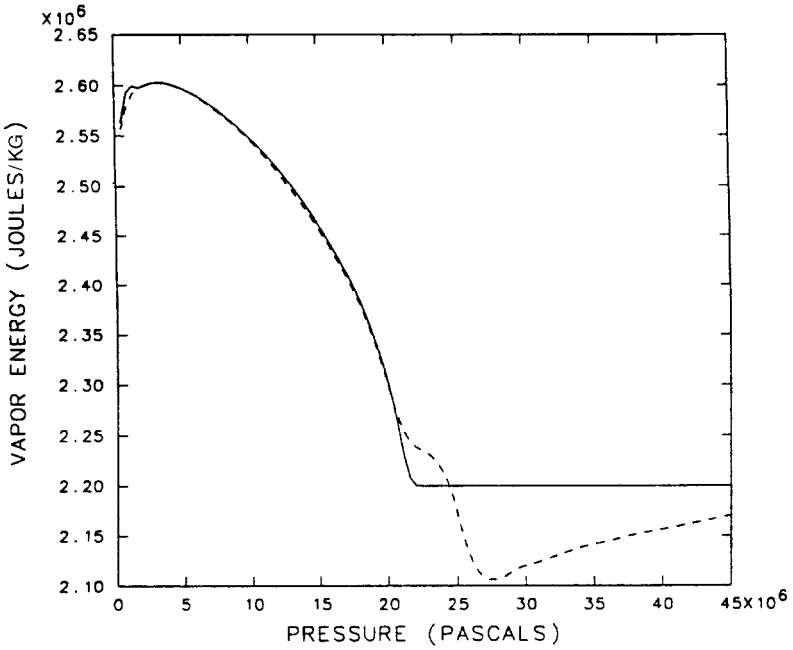

Figure. 11-3. Vapor energy vs. pressure along the saturation line. Solid: TRACE; Dashed: Sesame.

The ρ_l plot of TRACE seems to agree well with the Sesame liquid density data on the saturation line over the full range of pressures ($1.0 < p_v < 4.5 \times 10^7$ Pa) (Figure 11-5). However, significant "scalloping" in the Sesame plot is evident. This is due to errors in the EOSPAC interpolation between different data sets to generate a pressure-vs.-liquid density plot. For greater than 100 K subcooling values, the TRACE plots show general agreement with the Sesame subroutine. Here also, however, there is scalloping present. Because of the presence of this scalloping, it is difficult to establish whether there are any departures between the TRACE ρ_l curve and true data points.

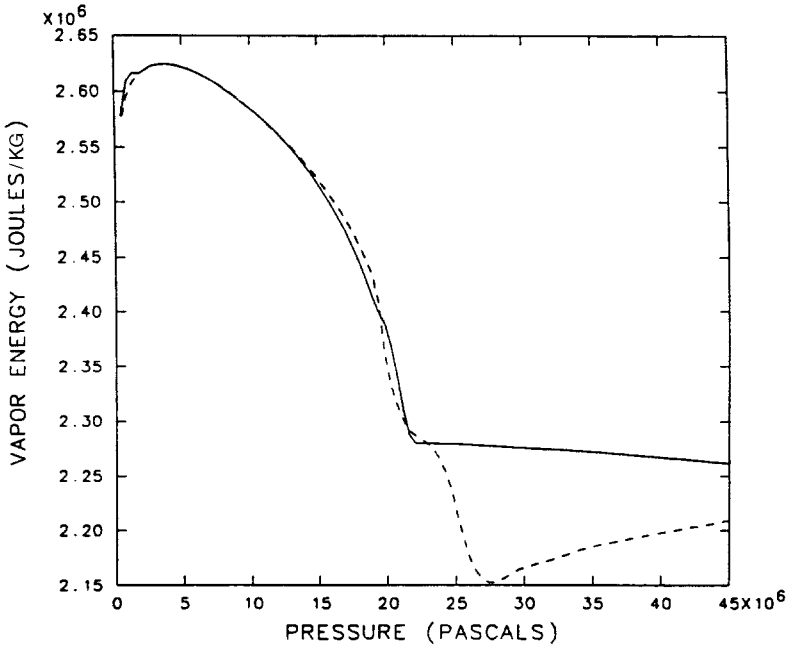

Figure. 11-4. Vapor energy vs. pressure at a superheat of 8 K. Solid: TRACE; Dashed: Sesame.

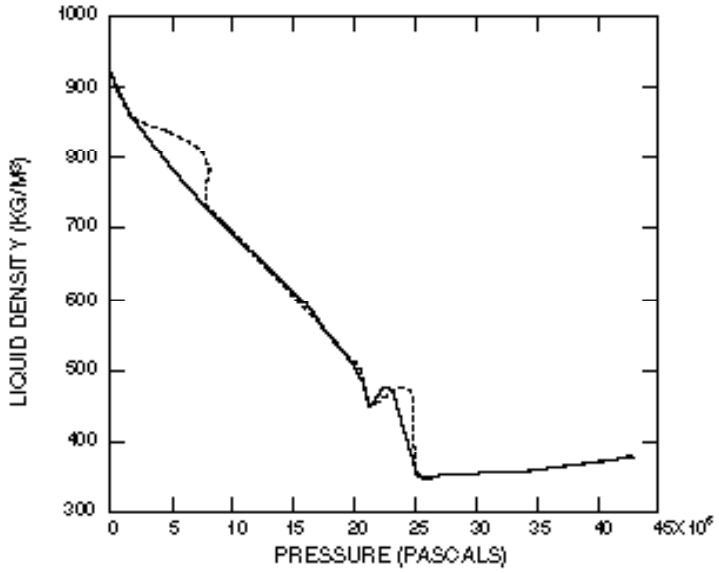

Figure. 11-5. Liquid density vs. pressure along the saturation line. Solid: TRACE; Dashed: Sesame.

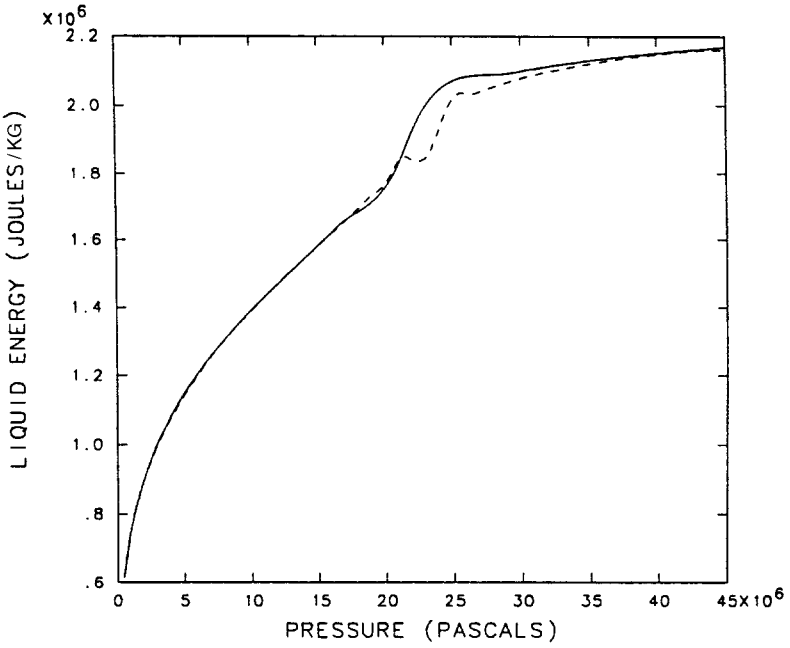

Figure. 11-6. Liquid energy vs. pressure along the saturation line. Solid: TRACE; Dashed: Sesame.

The TRACE plot of e_l on the saturation line agrees very well with the Sesame data for liquid internal energy, at pressures below p_{crit}. In this range, accuracy appears to be far better than 1%. At pressures above p_{crit}, a departure between the two curves is noted (Figure 11-6). In the pressure range $2.1 \times 10^7 < p_v < 3.0 \times 10^7$ Pa, fractional errors as great as 8% between the curves for the e_l data are observed. These departures, however, occur when the curves of the Sesame and TRACE e_ℓ plots are rising steeply. For this reason, the size of the fractional errors is not as significant. Also, because the TRACE output variable ρ_l must be input into the Sesame routine to generate the Sesame data for liquid energy and because of the aforementioned difficulty in determining the accuracy of the TRACE ρ_l data, it follows that the validity of departures in the e_l plots is also questionable. TRACE plots of subcooled liquid also follow Sesame e_l data closely (Figure 11-7). For subcooling as great as 100 K for pressures below p_{crit}, the TRACE and the Sesame plots are quite close, with fractional errors in e_l between the two curves of less than 1%. The Sesame and TRACE curves, however, begin to depart in the region $p_{crit} < p_v < 3.3 \times 10^7$ Pa. Here the fractional errors in e_l between the two curves reach as high as 8%, although the errors are not as significant, as they again occur where both the Sesame and the TRACE curves

are rising steeply. At pressures above 3.3×10^7 Pa, the curves begin to depart again, although here reaching only a 3% fractional error.

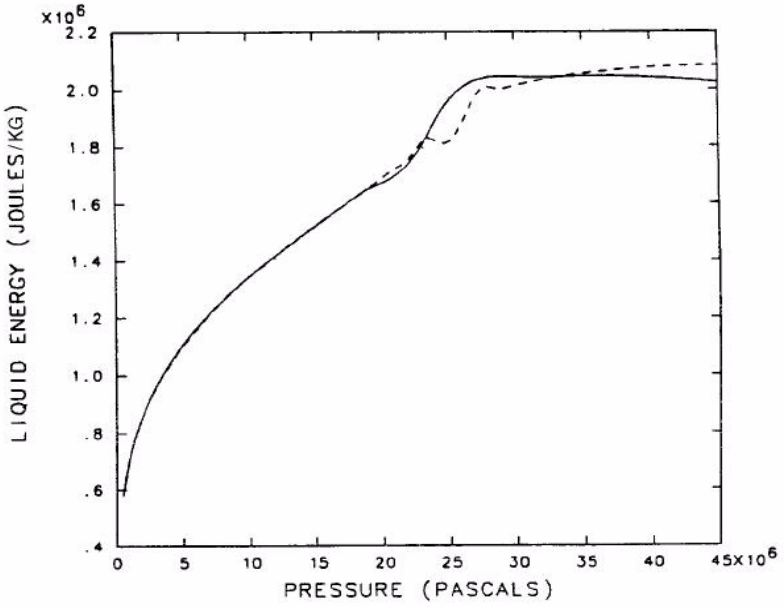

Figure. 11-7. Liquid energy vs. pressure for 8 K subcooling. Solid: TRACE; Dashed: Sesame.

In conclusion, for most TRACE applications, the thermodynamic and transport property routines provide realistic values up to the critical point.

Verification of Boron Solubility Model

TRACE will use the above model to calculate the solubility and concentration of orthoboric acid for temperatures from 273.15 K, the triple-point temperature, to 647.3 K, the critical-point temperature of water. Figure 11-8 shows a comparison of the TRACE approximation for solubility with the data from Reference 11-21; the data in Reference 11-20 are similar. The linear approximation for the solubility of boric acid compares well with the data in the temperature range bounded by the two temperatures. On the low end of the temperature scale where we approximate the solubility at 273 K by the solubility at 303, there is a 134% error. Reference 11-21 indicates that the solubility is 1 kg/kg water at 444 K, where there is a –72% error associated with the TRACE approximation. The solubility curve based on Reference 11-21 becomes very steep as the temperature approaches 444 K.

If the solubility limits are exceeded, we believe that the typical result would be the creation of a supersaturated solution and/or a suspended precipitate that would not be plated out on the structure surface.

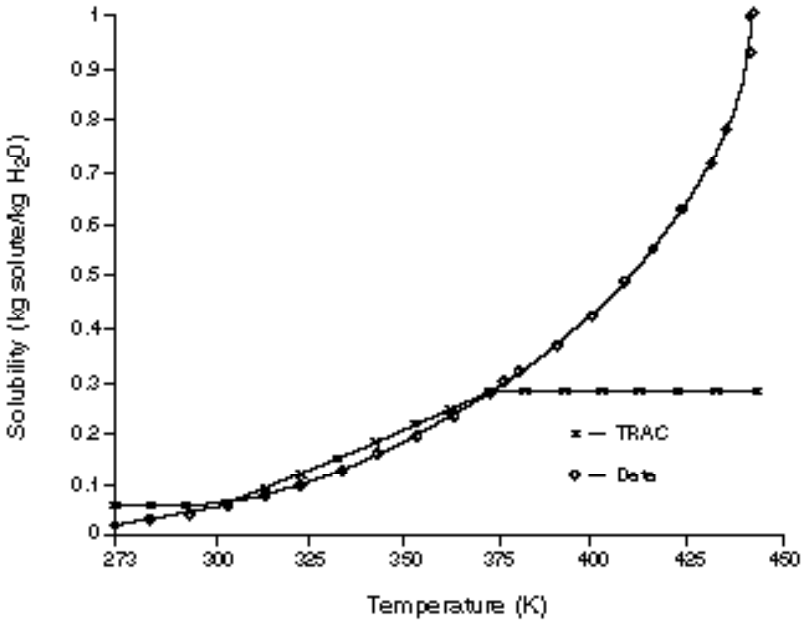

Figure. 11-8. Orthoboric-acid solubility vs. liquid temperature.

References

11-1 W. A. Coffman and L. L. Lynn, "WATER: A Large Range Thermodynamic and Transport Water Property FORTRAN-IV Computer Program," Bettis Atomic Power Laboratory report WAPD-TM-568 (December 1966).

11-2 W. C. Rivard and M. D. Torrey, "Numerical Calculation of Flashing from Long Pipes Using a Two-Field Model," Los Alamos Scientific Laboratory report LA-6104-MS (November 1975).

11-3 J. J. Martin and Y. Hou, "Development of an Equation of State for Gases," *AIChE Jour.* **1**(2), 142–151 (1955).

11-4 J. M. Richardson, A. B. Arons, and R. R. Halverson, "Hydrodynamic Properties of Sea Water at the Front of a Shock Wave," *The Journal of Chemical Physics* **15**(11), 785–794 (1947).

11-5 *ASME Steam Tables: Thermodynamic and Transport Properties of Steam,* 5th ed. (The American Society of Mechanical Engineers, New York, 1983).

11-6 K. S. Holian, "T-4 Handbook of Material Data Bases Volume 1C: Equations of State," Los Alamos National Laboratory, report LA-10160-MS (November 1984).

11-7 C. Cranfill, "EOSPAC: A Subroutine Package for Accessing the Los Alamos Sesame EOS Data Library," Los Alamos National Laboratory report LA-9728-M (August 1983).

11-8 L. Haar, J. Gallagher, and G. Kell, "A Thermodynamic Surface for Water: The Formulation and Computer Program," National Bureau of Standards report NBSIR 81-2253 (May 1981).

11-9 K. Watanabe, R.B. Dooley, IAPWS Release on the IAPWS Formulation 1995 for the Thermodynamic Properties of Ordinary Water Substance for General and Scientific Use, Fredericia, Denmark, Sept. 1996.

11-10 J. W. Spore, Pratap Sadasivan, D. R. Liles,"Accelerator Transmutation of Waste Updates for TRAC-M", LA-UR-01-3660, June 2001.

11-11 Jay W. Spore, D.R. Liles, "Improvements to the Accelerator Transmutation of Waste Updates for TRAC-M", LA-UR-01-6219, September 2001.

11-12 The Thermal Hydraulics Group, RELAP5/MOD3 CODE MANUAL, VOLUME I: CODE STRUCTURE, SYSTEM MODELS,AND SOLUTION METHODS, NUREG/CR-5535-Vol. I, June 1999.

11-13 The Thermal Hydraulics Group, RELAP5/MOD3 CODE MANUAL, VOLUME IV: MODELS AND CORRELATIONS, NUREG/CR-5535 Volume IV, June 1999.

11-14 Frank M. White, *Fluid Mechanics* (McGraw-Hill Book Co., Inc., New York, 1979).

11-15 Kuzman Raznjevic, *Handbook of Thermodynamic Tables and Charts* (McGraw-Hill Book Co., Inc., New York, 1976).

11-16 J. P. Holman, *Heat Transfer* (McGraw-Hill Book Co., Inc., New York, 1981).

11-17 J. M. Sicilian and R. P. Harper, *Heavy-Water Properties for the Transient Reactor Analysis Code*, Flow Science, Inc. report FSI-85-Q6-1 (1985).

11-18 E. A. Haytcher and J. C. Lin, "Modification to Helium Properties in the TRAC-PF1/MOD2 Code," Los Alamos National Laboratory report LA-N7-1 (December 1992).

11-19 *CRC Handbook of Chemistry and Physics*, 62nd ed., p. B-84, (The CRC Press, Inc., Boca Raton, Florida, 1981).

11-20 Paul Cohen, *Water Coolant Technology of Power Reactors*, pp. 218-221, (Gordon and Breach Science Publishers, New York, 1969).

11-21 Leopold Gmelin, *Gmelins Handbuch der Anorganischen Chemie,* Supplement to Volume 1, System Number 13 (Boron), pp. 149-156, (Verlag Chemie, Gmbh., Weinheim/Bergstrasse, 1954).

12

Structural Material Properties

An extensive library of temperature-dependent material properties is incorporated in the TRACE code. The entire library is accessible by the HTSTR (heat-structure) component while the remaining components have access to structural material-property sets only. There are 12 sets of material properties that make up the library. Each set supplies values for thermal conductivity, specific heat, density, and spectral emissivity for use in the heat-transfer calculations.

The material indexes in the library are

1 – mixed-oxide fuel;
2 – Zircaloy;
3 – fuel-clad gap gases;
4 – boron-nitride insulation;
5 – Constantan/Nichrome heater coil;
6 – stainless steel, type 304;
7 – stainless steel, type 316;
8 – stainless steel, type 347;
9 – carbon steel, type A508;
10 – Inconel, type 718;
11 – Zircaloy dioxide; and
12 – Inconel, type 600.

The first three sets and set 11 contain properties for materials that are part of nuclear fuel rods. Properties for these materials, including models for thermal expansion that are important as rods deform, are discussed in **Chapter 8**. Sets 4 and 5 are used in modeling electrically heated fuel rod simulators, which are used in many separate and integral test facilities. Sets 6 through 10 and set 12 are for structural materials, including stainless steels, carbon steel, and Inconels. Properties for sets 4 through 10 and 12 are discussed in this section. In addition, since other material properties may be necessary to model a test facility or plant, TRACE includes an option that enables you to define and supply properties for materials not included in the above list.

Nomenclature

The following nomenclature is used in this section:

c_p = specific heat capacity at constant pressure (J · kg^{-1} · K^{-1})

k = thermal conductivity (W/m/K)

p = pressure (Pa)

T = temperature (K)

T_C = temperature (°C)

T_F = temperature (°F)

ε = emissivity

ρ = density (kg/m^3)

Electrical Fuel-Rod Insulator (BN) Properties

The code calculates values for boron nitride insulators that are used in electrically heated nuclear fuel-rod simulators. Magnesium oxide insulators are assumed to have roughly equivalent values.

Density

A constant value of 2002.0 kg/m^3 from Reference 12-1 is used.

Specific Heat

A four-term polynomial is used to calculate the specific heat. The independent variable is temperature in degrees Fahrenheit, and the constants, which are modifications of those reported in an EPRI report (Ref. 12-2), are listed in the equation below:

$$c_p = 760.59 + 1.7955\,T_F - 8.6704\times10^{-4}\,T_F^{\,2} + 1.5896\times10^{-7}\,T_F^{\,3} \qquad (12\text{-}1)$$

Thermal Conductivity

The boron-nitride thermal-conductivity calculation, based on a conversion to SI units of a curve fit reported in Reference 12-3, is

$$k = 25.27 - 1.365 \times 10^{-3}\,T_F\ . \qquad (12\text{-}2)$$

Spectral Emissivity

A constant value of unity is used for the boron nitride spectral emissivity.

Electrical Fuel-Rod Heater-Coil (Constantan) Properties

The code calculates property values for Constantan heater coils as used in electrically heated nuclear fuel-rod simulators. We assume that Nichrome coils, used in some installations in place of Constantan, have similar properties. The correlations used are from Reference 12-3.

Density

A constant value of 8393.4 kg/m^3 is used.

Specific Heat

The specific heat is

$$c_p = 110\, T_F^{0.2075} \tag{12-3}$$

Thermal Conductivity

The thermal conductivity is given by

$$k = 29.18 + 2.683 \times 10^{-3}(T_F - 100)\ . \tag{12-4}$$

Spectral Emissivity

A constant value of unity is used.

Structural Material Properties

The code supplies property values for six types of structural materials normally used in LWRs: stainless steel, type 304; stainless steel, type 316; stainless steel, type 347; carbon steel, type

A508; and Inconel, types 718 and 600. These properties were obtained from Reference 12-3 through Reference 12-6. A tabulation of the correlations used is given in Tables 12-1 through 12-6.

Table 12-1. Stainless Steel, Type 304, Properties

Property	Independent Variable	Polynomial Constants	Reference Number
ρ	T	$a_0 = 7984.0$	12-4
		$a_1 = -2.651 \times 10^{-}$	
		$a_2 = -1.158 \times 10^{-4}$	
c_p	T_F	$a_0 = 426.17$	12-4
		$a_1 = 0.43816$	
		$a_2 = -6.3759 \times 10^{-4}$	
		$a_3 = 4.4803 \times 10^{-7}$	
		$a_4 = -1.0729 \times 10^{-10}$	
k	T	$a_0 = 8.116$	12-4
		$a_1 = 1.618 \times 10^{-2}$	
ε	—	$a_0 = 0.84$	12-4

ρ = density ($kg \cdot m^{-3}$)
c_p = specific heat ($J \cdot kg^{-1} \cdot K^{-1}$)
k = thermal conductivity ($W \cdot m^{-1} \cdot K^{-1}$)
T = temperature (K)
T_F = temperature (°F)
$y = a_0 + a_1x + a_2x^2 + \ldots + a_mx^m$

Table 12-2. Stainless Steel, Type 316, Properties

Property	Independent Variable	Polynomial Constants	Reference Number
ρ	T	$a_0 = 8084.0$	12-5
		$a_1 = -4.209 \times 10^{-1}$	
		$a_2 = -3.894 \times 10^{-5}$	

Table 12-2. Stainless Steel, Type 316, Properties

Property	Independent Variable	Polynomial Constants	Reference Number
c_p	T_F	$a_0 = 426.17$	12-5
		$a_1 = 0.43816$	
		$a_2 = -6.3759 \times 10^{-4}$	
		$a_3 = 4.4803 \times 10^{-7}$	
		$a_4 = -1.7029 \times 10^{-10}$	
k	T	$a_0 = 9.248$	12-5
		$a_1 = 1.571 \times 10^{-2}$	
ε	—	$a_0 = 0.84$	12-5

ρ = density ($kg \cdot m^{-3}$)
c_p = specific heat ($J \cdot kg^{-1} \cdot K^{-1}$)
k = thermal conductivity ($W \cdot m^{-1} \cdot K^{-1}$)
T = temperature (K)
T_F = temperature (°F)
$y = a_0 + a_1x + a_2x^2 + \ldots + a_mx^m$

Table 12-3. Stainless Steel, Type 347, Properties

Property	Independent Variable	Polynomial Constants	Reference Number
ρ	T	$a_0 = 7913.0$	12-3
c_p	$(T_F - 240)$	$a_0 = 502.416$	12-3
		$a_1 = 0.0984$	
k	T_F	$a_0 = 14.1926$	12-3
		$a_1 = 7.269 \times 10^{-3}$	
ε	—	$a_0 = 0.84$	12-3

Table 12-3. Stainless Steel, Type 347, Properties

Property	Independent Variable	Polynomial Constants	Reference Number
ρ = density (kg · m^{-3}) c_p = specific heat (J · kg^{-1} · K^{-1}) k = thermal conductivity (W · m^{-1} · K^{-1}) T = temperature (K) T_F = temperature (°F) $y = a_0 + a_1x + a_2x^2 + \ldots + a_mx^m$			

Table 12-4. Inconel, Type 718, Properties

Property	Independent Variable	Polynomial Constants	Reference Number
ρ	T_f	$a_0 = 8233.4$ $a_1 = -1.8351 \times 10^{-1}$ $a_2 = -9.8415 \times 10^{-6}$ $a_3 = -6.5343 \times 10^{-9}$	12-4
c_p	T_F	$a_0 = 418.18$ $a_1 = 0.1204$	12-4
k	T_F	$a_0 = 10.8046$ $a_1 = 8.8293 \times 10^{-3}$	12-4
ε	—	$a_0 = 0.84$	12-4
ρ = density (kg · m^{-3}) c_p = specific heat (J · kg^{-1} · K^{-1}) k = thermal conductivity (W · m^{-1} · K^{-1}) T = temperature (K) T_F = temperature (°F) $y = a_0 + a_1x + a_2x^2 + \ldots + a_mx^m$			

Table 12-5. Carbon Steel, Type A508, Properties

Property	Independent Variable	Polynomial Constants	Reference Number
ρ	T_F	$a_0 = 7859.82$ $a_1 = -2.6428 \times 10^{-2}$ $a_2 = -4.5471 \times 10^{-4}$ $a_3 = 3.3111 \times 10^{-7}$	12-4
c_p	T_F	$a_0 = 66.155$ $a_1 = 0.4582$ $a_2 = -6.5532 \times 10^{-4}$ $a_3 = 5.3706 \times 10^{-7}$	12-4
k	T	For $T < 283$ K, $k = 48.16 \frac{W}{m \cdot K}$ For 283 K ≤ T ≤ 1144 K, $a_0 = 55.29$ $a_1 = -5.6134 \times 10^{-2}$ $a_2 = 1.7064 \times 10^{-4}$ $a_3 = -2.466 \times 10^{-7}$ $a_4 = 1.056 \times 10^{-10}$ For 1144 K < T < 4000 K, interpolation between 1144 K, $k = 26.04 \frac{W}{m \cdot K}$ 4000 K, $k = 29.72 \frac{W}{m \cdot K}$	12-6

Table 12-5. Carbon Steel, Type A508, Properties

Property	Independent Variable	Polynomial Constants	Reference Number
		For T > 4000K, $k = 29.72 \frac{W}{m \cdot K}$	
ε	—	$a_0 = 0.84$	12-4
ρ = density (kg · m^{-3}) c_p = specific heat (J · kg^{-1} · K^{-1}) k = thermal conductivity (W · m^{-1} · K^{-1}) T = temperature (K) T_F = temperature (°F) $y = a_0 + a_1x + a_2x^2 + \ldots + a_mx^m$			

Table 12-6. Inconel, Type 600[a], Properties

Property	Independent Variable	Polynomial Constants	Reference Number
ρ	T_F	$a_0 = 5.261008 \times 10^{2}$	12-4
		$a_1 = -1.345453 \times 10^{-2}$	
		$a_2 = -1.194357 \times 10^{-7}$	
c_p	T_F	$a_0 = 0.1014$	12-4
		$a_1 = 4.378952 \times 10^{-5}$	
		$a_2 = -2.046138 \times 10^{-8}$	
		$a_3 = 3.418111 \times 10^{-11}$	
		$a_4 = -2.060318 \times 10^{-13}$	
		$a_5 = 3.682836 \times 10^{-16}$	
		$a_6 = -2.458648 \times 10^{-19}$	
		$a_7 = 5.597571 \times 10^{-23}$	
k	T_F	$a_0 = 8.011332$	12-4
		$a_1 = 4.643719 \times 10^{-3}$	

Table 12-6. Inconel, Type 600[a], Properties

Property	Independent Variable	Polynomial Constants	Reference Number
		$a_2 = 1.872857 \times 10^{-6}$	
		$a_3 = -3.914512 \times 10^{-9}$	
		$a_4 = 3.475513 \times 10^{-12}$	
		$a_5 = -9.936\,696 \times 10^{-16}$	
ε	—	$a_0 = 0.84$	12-4

ρ = density ($kg \cdot m^{-3}$)
c_p = specific heat ($J \cdot kg^{-1} \cdot K^{-1}$)
k = thermal conductivity ($W \cdot m^{-1} \cdot K^{-1}$)
T = temperature (K)
T_F = temperature (°F)
$y = a_0 + a_1x + a_2x^2 + \ldots + a_mx^m$

a. Inconel type 600 coefficients are in British units; ρ is multiplied by 16.01846 $(kg \cdot m^{-3})/(lb_m \cdot ft^{-3})$, c_p by 4.1868×10^3 $(J \cdot kg^{-1} \cdot K)/(Btu \cdot lb_m^{-1} \cdot °F^{-1})$, and k by 1.729577 $(W \cdot m^{-1} \cdot K^{-1})/(Btu \cdot h^{-1} \cdot ft^{-1} \cdot °F^{-1})$. The conversion factor for the thermal conductivity k assumes the thermochemical BTU instead of the international BTU.

References

12-1 Y. S. Touloukian, editor, Thermophysical Properties of High Temperature Solid Materials (MacMillan Co., New York, 1967).

12-2 "A Prediction of the SEMISCALE Blowdown Heat Transfer Test S-02-8 (NRC Standard Problem Five)," Electric Power Research Institute report EPRI/NP-212 (October 1976).

12-3 W. L. Kirchner, "Reflood Heat Transfer in a Light Water Reactor," US Nuclear Regulatory Commission report (NUREG-0106) Vols. I and II (August 1976).

12-4 J. C. Spanner, editor, "Nuclear Systems Materials Handbook—Vol. 1 Design Data," Hanford Engineering Development Laboratory report TID-26666 (1976).

12-5 "Properties for LMFBR Safety Analysis," Argonne National Laboratory report ANL-CEN-RSD-76-1 (1976).

12-6 *ASME Boiler and Pressure Vessel Code, Section II, Part D - Properties*, American Society of Mechanical Engineers, 2001

A

Quasi-Steady Assumption and Averaging Operators

The coupled-equation set that combines the single-phase, multidimensional, fluid field equations for mass, momentum, and energy with the equation for heat diffusion within a bounding wall is called the conjugate problem. The transient two-phase flow problem becomes even more difficult because an additional set of field equations for the second fluid phase must be solved simultaneously together with the necessary closure relations to couple the two fluid phases. The TRACE code, as well as most other similar codes, invokes a quasi-steady approach to the heat-transfer coupling between the wall and the fluid as well as the closure relations for interfacial heat transfer and drag and wall-to-fluid drag. This quasi-steady approach assumes detailed knowledge of the local fluid parameters and ignores time dependencies such that the time rate of change in the closure relationships becomes infinite and the time constants are zero. The quasi-steady approach has the advantages of being reasonably simple and generally applicable to a wide range of problems and of not requiring previous knowledge of the given transient.

In this appendix, the quasi-steady approach and the averaging operators used in TRACE are discussed.

Nomenclature

A = area

A_{wg} = fraction of wall contacted by gas

A_{wl} = fraction of wall contacted by liquid

f_l = area fraction contacted by liquid

q = local phasic heat flux

q_{total} = total heat flux

q' = area-averaged effective phasic heat flux

q'' = area-averaged phasic heat flux

S = dimensionless number defined by Eq. (A-20)

t = time

X = generic for independent variable

Y = generic for dependent variable

Greek

Δt or δt = time-step size

θ = ratio of transient and phenomenological time constants

τ = transient time constraint

τ_c = phenomenological time constant

ψ = weighting factor between old- and new-time values

Subscripts

g = gas

i = independent-variable indices

l = liquid

max = maximum

min = minimum

qs = quasi-steady

ss = steady state

tr = transient

$used$ = old-time weighted new-time value

w = wall

wg = wall-to-gas

wl = wall to-liquid

Superscripts

n = new-time value

$n-1$ = old-time value

Introduction

An alternative to the quasi-steady approach does exist on a case-by-case basis. If the necessary initial and boundary conditions are known, the solution of the conjugate problem requires a priori knowledge of the wall-to-fluid convective heat transfer. Studies such as those of Sucec (Refs. A-7 and A-8) have used this latter approach to obtain both analytical and numerical solutions for many single-phase transients. The results, when compared to those using the quasi-steady approach, have led to an understanding of the conditions under which the quasi-steady approach produces valid results.

For the heat-transfer coupling between the wall and the fluid, the quasi-steady approach works well provided that the fluid responds more rapidly than the wall. For example, the fluid boundary layer responds so quickly that the surface temperature of a thick, high-conductivity wall does not have time to change. When the wall changes faster than the fluid, however, one must use transient closure relations to solve the problem accurately.

Despite the difficulties and limitations of the quasi-steady solution approach to the conjugate problem for two-phase flow, this approach is the only method available to simulate transient conditions in large, complex, two-phase systems such as a nuclear power plant. Often, in order to obtain an answer to a difficult problem, engineers apply codes like TRACE even when the quasi-steady assumption is not valid. The literature does contain many papers in which the closure relationships have been modified to obtain agreement with what is, in fact, transient data. Although this process can provide valuable insight, the resulting relationships may be misleading and may produce inaccurate results when applied either to other transient experiments or to truly quasi-steady transients. Unfortunately, within the English literature, there are very few systematic studies of the problems inherent to the quasi-steady assumptions. The initial study by Nelson (Ref. A-9) and the more recent work of Pasamehmetoglu and Nelson (Ref. A-10) do address the problem. As Kuznetsov (Ref. A-11) presented in his overview, the Soviets at least may have defined more clearly the existence of these limitations.

Chapter 1 indicated the importance of the quasi-steady assumption and the averaging operators (volume and temporal) on the closure relationships. While these considerations are of equal importance to all the closure relationships, it is not possible to discuss each set individually. This section will investigate those considerations relative to the wall-to-fluid heat-transfer process. Extension to the other relationships follows similar logic.

The wall-to-fluid heat transfer appears in the two-phase-fluid equation set within the total-energy equation as $q_{wl} + q_{wg}$ and the combined-gas-energy equation as q_{wg}. These terms, q_{wl} and q_{wg}, represent the rate of sensible energy per unit volume being transferred into the phasic components of the fluid [see **Chapter 1**, Eqs. (1-28) and (1-29)]. Mass transfer resulting from the superheating of a liquid and its subsequent evaporation, for example, must take place through the phasic-change equation represented by Eqs. (1-25) through (1-27) in **Chapter 1**. The total wall-to-fluid heat flux, $q'_{wl} + q'_{wg}$ is also required in order to provide the boundary condition necessary for the solution of all structures exposed to the fluid.

Perhaps the easiest way to envision these phasic terms arising is to realize that, within the volume-averaged equations, the total surface area over which one integrates can be decomposed into two parts [see term number 5 of Reference A-12, Eq. (2-125), p. 70]. One part has liquid contacting it while the other has gas contacting it, so that

$$A_w = A_{wl} + A_{wg} \ . \tag{A-5}$$

Thus,

$$\int_{A_w} q dA \ = \int_{A_{wt}} q dA + \int_{A_{wg}} q dA \ . \tag{A-6}$$

By defining the following terms,

$$\int_{A_{wl}} q dA \ \equiv q''_{wl} \ A_{wl} \ , \tag{A-7}$$

$$\int_{A_{wg}} q dA \ \equiv q''_{wg} \ A_{wg} \ , \tag{A-8}$$

and

$$\int_{A_w} q dA \ \equiv q_{total} A_w , \tag{A-9}$$

Eq. (A-6) becomes

$$q_{total} = q'_{wg} \ + q'_{wl} \ = q''_{wl} \ f_l + q''_{wg} \ (1 - f_l) \ , \tag{A-10}$$

where

$$f_l = \frac{A_{wl}}{A_w} \ .$$

Integration of Eqs. (A-6) through (A-10) with respect to time is an obvious step not shown here and produces “volume-time” averaged quantities required by the two-phase conservation equations [see **Chapter 1**, Eqs. (1-11) through (1-16)]. The time interval δt over which the

integration is performed must meet those requirements described by Bergles et al. (Ref. A-12). The right-hand sides of Eqs. (A-7) through (A-9) and Eq. (A-10) are assumed to reflect the temporal averaging without any further notation change.

The influence of the spatial-averaging operator is realized principally through its influence in data reduction and is therefore inherent within the closure relationships. The code makes no checks to investigate the influence of the spatial averaging; we discuss this in greater detail below in the section ***Spatial-Averaging Operator***.

A temporal effect is present in both the quasi-steady assumption and the temporal-averaging operator. To further differentiate between the problems that may arise from these two sources, we will first assume that the transient under consideration is slow enough that the quasi-steady assumption is valid. The question becomes what is the relationship among the time-step size desired by the code, $\Delta t,$ the time constant of the physical phenomena, τ_c (the minimum time of integration for the temporal averager), and the time constant of the transient, τ (some fraction of this time will be the maximum time of integration for the temporal averager). This relationship is the point raised by Bergles, et al. (Ref. A-12), which was noted earlier. Nelson (Ref. A-9) further refined the question concerning the minimum time of integration, denoted as δt_{min}, by pointing out that δt_{min} must include a sufficient number of events of the governing phenomena, reflected by τ_c, to make the integral "independent" of time. Therefore, the question becomes what should happen when $\Delta t < \delta t_{min} or \Delta t > \tau$.

Generally, the second part of the above question, $\Delta t > \tau$ is not important in TRACE because calculations are controlled frequently by the rate of change of the quantities. In the future, however, as time-step sizes continue to increase as a result of improved numerics, this portion of the question may become more important. For TRACE, the first part of the question is important and is a condition that frequently arises in the code. Again, Nelson (Ref. A-9) has pointed out that in addressing this question, we must decide which of two questions we wish to answer. If we wish to model the instantaneous response inside the time interval represented by δt_{min}, a transient closure model is required even for "steady-state" conditions. In general, this representation is beyond the state of the art. Thus, only the average response during these "small" time steps, $\Delta t < \delta t_{min}$, can be defined and the quasi-steady closure relationship should be constant over the time interval corresponding to δt_{min}. Early in the TRACE development, we observed the effect of δt_{min} and developed crude averagers to minimize the observed problems. (It is not clear that early code developers had interpreted these problems as arising from this cause.) Only recently have calculations again identified these temporal-averaging problems as significant; the new observations center on noding and time-step sensitivities in the calculated results. The sections ***Averagers and Limiters Arising from Temporal-Averager Considerations*** and ***Variations in the***

Application of Temporal Averagers and Limiters will discuss the models currently in TRACE to address this problem of $\Delta t < \delta t_{min}$.

In the preceding discussion, we assumed the quasi-steady assumption was valid. The question remains as to when the assumption breaks down. As pointed out by Nelson (Ref. A-9), one way of perceiving this breakdown arises from temporal-averaging considerations. The observed characteristic is that when Δt is decreased to the δt_{min}, the resulting quantity will still show a sensitivity to Δt. Once this happens, the transient is a true transient. The section ***Validity of the Quasi-Steady Assumption*** will discuss more recent techniques for determining when the quasi-steady assumption is valid. Because the code at this time only implements the quasi-steady assumption, we offer no alternative procedures for dealing with a true transient.

Averagers and Limiters Arising from Temporal-Averager Considerations

A potential problem that one sees in transient analysis using the quasi-steady approach is that the closure relations are free to respond instantaneously (within a single time step) to any changes occurring within the flow field. Thus, unless some type of averager and/or limiter is used, flow regimes may change instantly. While the averagers/limiters used in TRACE vary among closure packages, they are typically represented by the following relations. Averagers from one time step to the next generally appear as

$$Y^n_{used} = \psi\, Y^{n-1} + (1-\psi)\, Y^n \,, \tag{A-11}$$

where Y represents some closure quantity, ψ is a fraction between zero and one, and the superscripts $n-1$ and n indicate old- and new-time values of Y, respectively. The Y^n_{used} is the closure-relationship value used in the current time step and becomes Y^{n-1} for the next time step. Thus, as ψ approaches one, Y_{used} would change very slowly, and for ψ equal to zero, Y_{used} would change instantly. Typical limiters are given as

$$Y_{min} < Y^n < Y_{max} \,,$$

where Y_{min} and Y_{max} are reasonable bounds for Y and depend on the phenomenon addressed by the closure relationship.

A third approach is to use an averager equation that is based on the time step size and the time constant for the phenomena of interest. For example, Eq. (A-12) is an averager formula that is

relatively simple to evaluate and has consistent limits as the time step size decrease to small values or increases to large values.

$$Y^n_{used} = \frac{\tau Y^{n-1} + \Delta t Y^n}{\tau + \Delta t} \tag{A-12}$$

In the limit as the time step size approaches zero, Y^n_{used} approaches Y^{n-1} and as the time step size becomes large relative to the time constant for the phenomena of interest, Y^n_{used} approaches Y^n. When the time step size is the same order of magnitude as the time constant for the phenomena of interest, then Y^n_{used} is an average of old and new predicted parameter. The time averager formula given by Eq. (A-12) eliminates some of the time step sensitivities that appear when Eq. (A-11) is used.

An alternative method to these averagers and/or limiters is the use of additional transport equations within the code to convect such quantities as interfacial area or drop/bubble diameter. While these transport equations do "stabilize" the potential "instantaneous-response" problem, however, they do not directly address the problem that still exists—that the closure relationships are quasi-steady at best.

Variations in the Application of Temporal Averagers and Limiters

The problem with the above averager [given by Eq. (A-11)] is that it produces a time-averaging scheme which is time-step-size dependent. For example, if we were to run a transient calculation with a fixed time-step size of 100 ms and then repeat the calculation with a time-step size of 10 ms, we would obtain a change in the answer because of this type averager. Fortunately, this sensitivity has been found to be limited to those flow regimes where either large interfacial heat-transfer or interfacial area changes may take place. Eq. (A-13) represents an averager/limiter that minimizes the time-step size sensitivity and is based upon the concept that below δt_{min}, the closure property should remain constant. Eq. (A-12) is a time averaging formula that also reduces this sensitivity of the results to time step size.

Another potential problem with Eq. (A-11) can occur when Δt is very small. For example, assume that due to a rapid transient, the time-step size, Δt, is reduced by the time-step controller to 10^{-6} s. This might occur as the code limits Δt as a result of the allowable changes in the void fraction, pressure, temperature, etc. This Δt is typically much smaller than any δt that an experimentalist might use in time averaging his data. This example is another case where the code should hold this closure quantity constant. But, due to the time averaging such as, Eq. (A-11) this quantity would be allowed to change over short time spans (remember 10 time steps would still be

only 10^{-5} s) and could further aggravate the problem. In effect, the numerics of the code are being forced to track unreal physical phenomena within the time interval δt_{min} and the time-step controls may continue to prevent the time-step size from increasing.

Consequently, during transient calculations, we chose to use relaxation-type relations as limiters during transient calculations for interfacial shear and interfacial heat transfer. These relaxation relationships can be cast into the following general format:

$$Y^{n-1} C_1^{-C_2 \Delta t} \leq Y^n_{\text{used}} \leq Y^{n-1} C_1^{C_2 \Delta t} \ . \tag{A-13}$$

While this kind of approach reduces the time-step dependency of a transient solution, it does not eliminate it completely. Furthermore, C_1 and C_2 are currently based upon engineering judgment. As our understanding of transient problems and phenomenological time constants continues to evolve, the relaxation relationships will possibly receive further improvements.

For wall heat transfer, the averager given by Eq. (A-12) is used with a time constant of 0.1 seconds. This time constant was chosen based on engineering judgement for the time constant associated with a heat transfer regime change. As the time step size becomes small compared to τ, the used value approaches the old time value consistent with the quasi-steady approximation. As the time step size becomes large compared to τ, the used value approaches the new time value, which is the desired behavior for large time step sizes. Eq. (A-12) requires less cpu time to evaluate and significantly reduces the time step sensitivities that would be introduced by Eq. (A-11). It should be noted that for steady-state calculations, where the final steady-state solution is of importance and not the transient approach to steady-state, Eq. (A-11) is used, with $\psi = 0.1$.

Spatial-Averaging Operator

Spatial averaging enters our consideration through the definitions in Eqs. (A-7) through (A-9). Nelson (Ref. A-14) discusses the requirements and influence of those spatial-averaging operations upon the wall-to-fluid heat transfer. An area average often enters the data-reduction procedure when steady-state experiments are analyzed. For upflow in a tube or rod bundle, thermocouples at different axial levels often define the midpoint of the area. Flowing experiments in a tube or rod bundle with a progressing quench front may contain either an area average or a line average (around the circumference of the tube/rod). Line-average data may be reported/ obtained, provided the experimenter sampled the data at a sufficient rate to determine dT_w/dt accurately, that can be transformed to dT_w/dz, based on a constant quench front velocity assumption applied between thermocouples. Therefore, the reduced area-averaged data frequently include the effect of the area-averaging arising from the thermocouple spacing. If analyzed in sufficient detail, the reduced line-averaged data may provide either heat flux as a function of

distance from the quench front or heat flux with the accompanying dT_w/dz. It can be noted that the area-averaged data contain the same information but it is present on an average basis, i.e., it has been averaged over some axial length. When a quench front is present on either a thin tube or rod bundle, area-averaging frequently presents a problem because it will typically average over a length greater than the length of the quench front.

When the local-conditions hypothesis is used to develop correlations from the reduced data, the averaging operators also pose a potential problem if precautions are not taken. This problem is analogous to the δt_{min} problem discussed above but arises from spatial considerations. The problem is described best by considering the example of quenching. Near the quench front, steep gradients of the wall temperature are encountered frequently. If a closure relation is developed using a history effect such as z_{CHF}, the correct amount of energy may be obtained based upon code renodalization (as described above). This assumes that the correlation is being applied to a situation similar to the data upon which it was based, i.e., dT_w/dz must have the same type of distribution. If a closure relation is developed using the local-conditions hypothesis with the wall temperature alone, additional precautions must be taken to ensure that the correct amount of energy is taken out when renodalization of the conduction solution to include axial-conduction effects occurs. These precautions must check that if the renodalization is becoming smaller than some minimum length (which must be determined from the data and its dT_w/dz), then the total heat flux over this Δz_{min} is preserved. Without this check, codes using a fine-mesh renodalization scheme will continue to increase the steepness of the quench front until axial conduction limits the process.

Validity of the Quasi-Steady Assumption

This section contains information on how the quasi-steady assumption should enter into the consideration of whether the use of quasi-steady closure relations is valid. The information is principally of recent origin and was unavailable to earlier code developers. It is included within this document, however, to provide a basis for understanding some problems that exist within the current code and the need for future work.

A generic and systematic discussion of the quasi-steady versus transient heat-transfer problems was provided by Nelson (Refs. A-9 and A-13). This discussion is based upon the total rate of change of the dependent variable when the independent variable(s) is (are) under transient. For example, let us assume a simple steady-state constitutive relationship in the form

$$Y_{ss} = F(X_i) \ , \qquad \text{(A-14)}$$

where i is the index denoting the different independent variables. If the independent variable, X_i, changes with time, then the time, t, must enter into the closure relationship as another independent variable as follows:

$$Y_{tr} = F(t\,,\, X_i)\ . \tag{A-15}$$

As a result, the total rate of change of the dependent variable, Y_{tr}, becomes

$$\frac{dY_{tr}}{dt} = \frac{\partial Y_{tr}}{\partial t} + \sum_{i=1}^{N} \frac{\partial Y_{tr}}{\partial X_i}\frac{dX_i}{dt}\ , \tag{A-16}$$

where N is the total number of time-dependent independent variables. In Eq. (A-16), if

$$\left|\frac{\partial Y_{tr}}{dt}\right| \ll \left|\frac{\partial Y_{tr}}{\partial X_i}\frac{dX_i}{dt}\right|\ ,$$

and

$$\left|\frac{\partial Y_{tr}}{\partial t}\right| \ll \left|\sum_{i=1}^{N}\left|\frac{\partial Y_{tr}}{\partial X_i}\ \frac{dX_i}{dt}\right.\right.\ ,$$

then the problem becomes quasi-steady for both separate-effects and combined-effects transients. Consequently, a steady-state closure relationship may be used to quantify the transient-dependent parameter, Y_{tr}, such that

$$Y_{tr} \cong Y_{qs} = F\{X_i(t)\}\,. \tag{A-17}$$

Further discussion of Eqs. (A-15), (A-16), and (A-17) may be found in the studies of Nelson and Pasamehmetoglu (Refs. A-9 and A-10). This discussion includes consideration of the time constant of the physical phenomena and the influence of the averaging operator (Ref. A-9). Equation (A-16) has its merits in the original discussion of the quasi-steady versus transient problems, and provides a sound mathematical basis for differentiating them. The practical use, however, of Eq. (A-16) is difficult. The different terms on the right-hand side of Eq. (A-16) cannot be readily quantified. Because the decision on whether a problem is quasi-steady is based upon the relative magnitude of these terms, Eq. (A-16) does not directly lead to a firm criterion.

A more practical equivalent to Eq. (A-16) may be developed (see Reference A-10) by considering Eq. (A-16) relative to a simple generic transient model. The physical model with a single independent variable ($N = 1$) consists of a signal source that emits signals with a time-dependent property, a filter or amplifier that processes this signal in a prescribed form, and a receiver that receives the altered signals delayed by τ_c. In this simple example, τ_c may be regarded as the time required for a signal to travel from the source to the receiver. In a more general case, τ_c represents the time constant of the phenomena and may vary in time. The τ_c may be a function of the characteristic properties of the signal or the signal processor or both. This model may symbolize a more concrete example, such as the transient heat-transfer problem, in which the signal emitted may represent a time-dependent wall temperature, the processor may represent the convective heat-transfer phenomena, and the received signal may represent the fluid temperature.

From this simple model, the signal received at time t is equal to the delayed signal emitted at time $t - \tau_c$ and processed through the filter. Thus if we assume Y_{ss} to be the filter (we will determine the requirement for this assumption to be valid),

$$Y_{tr}(t\,,\,X) = Y_{ss}[X(t-\tau_c)] \quad . \tag{A-18}$$

Using the Taylor series expansion for small τ_c, the right-hand side of Eq. (A-18) can be rewritten to yield

$$Y_{tr}(t\,,\,X) = Y_{ss}(X) - \tau_c \frac{dY_{ss}}{dX}\frac{dX}{dt} \quad , \tag{A-19}$$

where higher-order terms are neglected. Defining a parameter *S* to be

$$S = \frac{X}{Y_{ss}}\frac{dY_{ss}}{dX} \quad , \tag{A-20}$$

Eq. (A-19) may be written as

$$Y_{tr}(t\,,\,X) = Y_{ss}[X(t)]\left[1 - S\frac{\tau_c}{X}\frac{dX}{dt}\right] \quad . \tag{A-21}$$

Equation (A-21) suggests that, for the quasi-steady approach to be valid as assumed by Eq. (A-18) the following condition must be satisfied:

$$\left|\frac{dX}{dt}\,\frac{\tau_c}{X}\right| \ll \left|\frac{1}{S}\right| \quad , \tag{A-22}$$

where S can be calculated by using the definition given by Eq. (A-20) once the steady-state closure relationship Y_{ss} is known. When the inequality in Eq. (A-22) is satisfied, the problem is quasi-steady and

$$Y_{qs}(t, X) \cong Y_{ss}[X(t)]. \tag{A-23}$$

Otherwise, the problem is a true transient. In this case, Eq. (A-23) is no longer valid, and a transient closure relationship is required.

It is important to note that Eq. (A-21) is merely an approximation for a transient closure relationship obtained by simply translating the steady-state closure relationship along the time axis by an amount τ_c. It is derived for the purpose of obtaining a criterion for limiting the quasi-steady approach. In reality, τ_c is not constant but is a function of time and of the magnitudes and time rates of changes of the dependent and independent variables. This functionality is why each transient yields a unique closure relationship. If τ_c can be appropriately correlated as a function of these variables, however, Eq. (A-21) may be used as a generic form for transient closure relationships. Equation (A-21) is a practical alternative to Eq. (A-16) because it can be used more easily to identify and quantify the time constants of the different phenomena.

Another commonly used qualitative criterion for the quasi-steady approach is in terms of the time-constants ratio. If the time constant of the transient is much greater than the time constant of the representative phenomenon, then the problem is quasi-steady. Notice that, when applied to an exponential transient in the form,

$$X = X_0 \exp(\pm t/\tau), \tag{A-24}$$

Eq. (A-22) reduces to

$$\left|\frac{1}{\theta}\right| \ll \left|\frac{1}{S}\right|, \tag{A-25}$$

where $\theta = \tau/\tau_c$. This example readily illustrates the concepts of time-constants ratio mentioned above, although Eq. (A-22) is not restricted to exponential transients. For an exponential decay, then, we can classify the transient problem as follows:

$$\theta \gg |S| \quad \text{(quasi-steady)}$$

$$\theta \ll |S| \quad \text{(truly transient)}$$

$$\theta \sim |S| \quad \text{(transition).}$$

Figure A-1 shows a tentative map for the quasi-steady criterion from Reference A-10. Note that the boundaries between the different transients are tentatively assigned, assuming that << or >> means at least an order of magnitude difference. Especially, the difference between the transition and truly transient problems is not very clear but the problem is, at some point, within the transition region when the quasi-steady approach becomes invalid.

The dimensionless group on the left-hand side of Eq. (A-22) was previously discussed by Pasamehmetoglu and Gunnerson (Refs. A-15 and A-16) in the context of transient critical heat flux (CHF). The final transient CHF correlation explicitly includes the time-constants ratio in Eq. (12) of Reference A-17. From the overview of Kuznetsov (Ref. A-11), the Soviets appear to use a similar dimensionless group in conjunction with *unsteady problems*.[1] However, to the best of our knowledge, the English literature does not contain anything regarding the origin or the quantitative application of this dimensionless group.

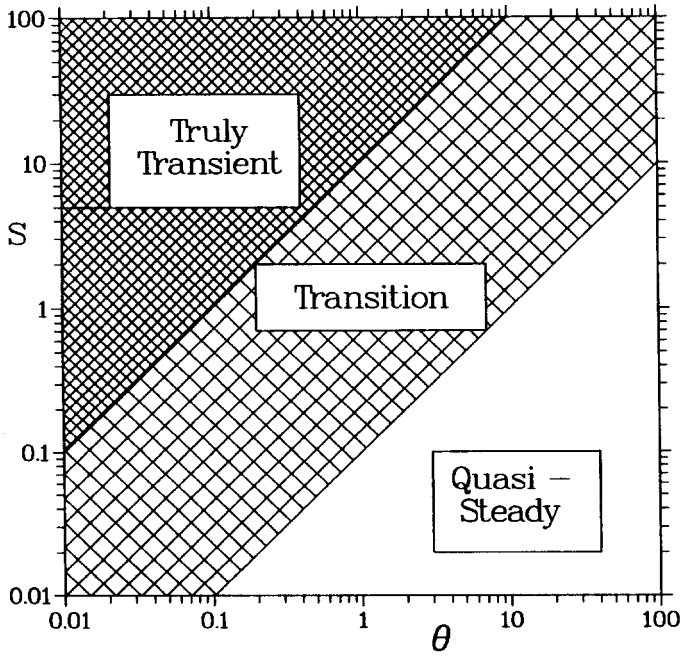

Figure. A-1. Tentative map for transient problems.

1. In Soviet literature, the term *unsteady problem* is equivalent to what we refer to as a truly transient problem.

Concluding Remarks

This appendix has discussed the influence of the quasi-steady assumption and the temporal-averaging operator upon the closure relations. It has been pointed out in this appendix that most of the code's current time averagers are time-step-size insensitive. Work needs to continue in this area on either development of improved averagers or use of additional transport equations within the code to minimize the use of averagers and limiters. No estimate of how much inaccuracy is introduced into the code due to current averagers is available, but it is a function that will increase as the speed of the transient increases. Problems related to spatial averaging of quantities during data reduction and model development have also been discussed.

References

A-7 J. Sucec, "Unsteady Heat Transfer Between a Fluid, With a Time Varying Temperature, and a Plate: An Exact Solution," *International Journal of Heat Mass Transfer* 18, 25–36 (1975).

A-8 J. Sucec, "Analytical Solution for Unsteady Heat Transfer in a Pipe," presented at the ASME Winter Annual Meeting (Anaheim, California, December 7-12, 1986) ASME paper 86-WA/HT-75.

A-9 R. A. Nelson, "Mechanisms of Quenching Surfaces," in *Handbook of Heat and Mass Transfer*, N. P. Cheremisinoff, Ed., Vol. 1: Heat Transfer Operations (Gulf Publishing Company, Houston, Texas, 1986), pp. 1103–1153.

A-10 K. O. Pasamehmetoglu and R. A. Nelson, "Investigation of The Quasi-Steady Approach Used In Transient Two-Phase Flow Analysis," ANS Proceedings of 1988 National Heat Transfer Conf. (Houston, Texas), HTC-Vol. 3, pp. 279-290.

A-11 Y. Kuznetsov, "Overview of Mathematical Models for Nuclear Reactor Safety Heat Transfer Codes and Experiments," in *Heat Transfer in Nuclear Reactor Safety*, S. G. Bankoff and N. H. Afgan, Eds. (Hemisphere Publishing Corporation, New York, 1982), pp. 111–132.

A-12 A. E. Bergles, J. S. Collier, J. M. Delhaye, G. F. Hewitt, and F. Mayinger, *Two-Phase Flow and Heat Transfer in the Power and Process Industries* (Hemisphere Publishing Corp., New York; McGraw-Hill Book Co., New York, 1981), pp. 70-71.

A-13 R. A. Nelson, "Forced Convective Post-CHF Heat Transfer and Quenching," *Trans. ASME, Journal of Heat Transfer* 104, 48-54 (1982).

A-14 R. A. Nelson, "Mechanisms of Quenching Surfaces," in *Handbook of Heat and Mass Transfer*, "Vol. 1: Heat Transfer Operations," N. P. Cheremisinoff, editor (Gulf Publishing Company, Houston, Texas 1986), pp. 1129-1132

A-15 K. O. Pasamehmetoglu, "Transient Critical Heat Flux," Ph. D. Dissertation, University of Central Florida (August 1986) (also EIES report number 86-87-1).

A-16 K. O. Pasamehmetoglu and F. S. Gunnerson, "Theoretical Considerations of Transient Critical Heat Flux," *Proceedings of the 3rd International Topical Meeting on Reactor-Thermal Hydraulics* (Newport, Rhode Island, October 15–18, 1985), Vol. 2, paper 18-F.

A-17 K. O. Pasamehmetoglu, R. A. Nelson, and F. S. Gunnerson, "A Theoretical Prediction of Critical Heat Flux in Saturated Pool Boiling During Power Transients," in *Nonequilibrium Transport Phenomena* (ASME, New York, 1987), HTD-Vol. 77, pp. 57–64.

B

Finite Volume Equations

This chapter provides more details on the derivation of the finite volume equations presented in **Chapter 1**. The focus here is on the spatial discretization of the finite volume momentum equations, with no further discussion of time level selection for the terms in the finite volume equation. There are three primary sections following the listing of nomenclature. The first is an expansion of the section in **Chapter 1** titled ***Basic Finite-Volume Approximations to the Flow Equations*** with a focus on the details of the derivation of the momentum equation. Some of the previous material is repeated, but more details are provided for the steps in the derivation. The next section in this chapter looks at special cases for side junction flow, providing underlying theory by which some simplifying assumptions in TRACE can be judged. The final section presents the results of some simple loop flow problems demonstrating the behavior of TRACE flow simulations when pipe bends and side connections are present.

Nomenclature

The nomenclature used in this section is the same as that introduced in **Chapter 1**, but the description is repeated here for the convenience of the reader. In our nomenclature, the term "gas" implies a general mixture of water vapor and the noncondensable gas. The subscript g will denote a property or parameter applying to the gas mixture; the subscript v indicates a quantity applying specifically to water vapor (referred to as simply "vapor"); and the subscript a (for "air") signifies a quantity associated with mixture of one or more noncondensable gases. The term "liquid" implies pure liquid water, and the subscript l denotes a quantity applying specifically to liquid water. For convenience, we define the following terms that will be used in the subsequent equations and list them alphabetically, with the Greek symbols and subscripts to follow. The following notation applies to the discussion of numerical methods. A caret ($\hat{}$) above a variable denotes an explicit predictor value. A tilde ($\tilde{}$) above a variable denotes an intermediate result, and a line ($\bar{}$) above denotes an average operation. Details of the specific average are provided in discussion of the equations in which it occurs. A horizontal arrow (or half-arrow) above a variable denotes a vector quantity (in the physical sense such that it has both a magnitude and direction).

A = flow area between mesh cells

A_i = interfacial area per unit volume between the liquid and gas phases

c = speed of sound

C = shear coefficient

E_i = rate of energy transfer per unit volume across phase interfaces

e = internal energy

f = force per unit volume

$\vec{g}$ or $\vec{g}$ = gravity vector

g = magnitude of the gravity vector

h = heat-transfer coefficient (HTC)

h_{sg} = gas saturation enthalpy

$h_{wg} = (1 - f_l) h'_{wg}$, the effective wall HTC to gas

$h_{wl} = f_l \, h'_{wl}$, the effective wall HTC to liquid

h_l' = liquid enthalpy of the bulk liquid if the liquid is vaporizing or the liquid saturation enthalpy if vapor is condensing

h_v' = vapor enthalpy of the bulk vapor if the vapor is condensing or the vapor saturation enthalpy if liquid is vaporizing

K = form-loss coefficient or wall friction coefficient

m = solute concentration in the liquid (mass of solute per unit mass of liquid)

M_i = rate of momentum transfer per unit volume across phase interfaces

P = fluid pressure or total pressure

q = heat-transfer rate per unit volume

q_d = power deposited directly to the gas or liquid (without heat-conduction process)

q_{gl} = liquid-to-gas sensible heat transfer

q' = heat flux

r = radius

R = ideal gas constant (including effects of molecular weight)

R = Reynolds/viscous stress tensor

S = factor applied to the 1D component so that its positive flow direction becomes the positive flow direction of the vessel

S_c = plated-out solute density (mass of plated solute divided by cell volume)

SC = product of an orifice factor

S_m = source term in the solute-mass differential equation

t = time

T = temperature

T = stress tensor

T_{sv} = saturation temperature corresponding to the vapor partial pressure

$\vec{V}$ or $\vec{V}$ = velocity vector

V = magnitude of the velocity

vol = hydrodynamic-cell volume

w = weighting factor

x = distance

X = mass fraction of an additional noncondensable gas species

Y = dummy variable

z = axial coordinate

Greek

α = gas volume fraction

β = momentum-convection temporal expansion flags

γ = weighting factor

Γ = interfacial mass-transfer rate (positive from liquid to gas)

Γ^+ = maximum of Γ and 0

Γ^- = minimum of Γ and 0

ρ = density

ΔP = pressure difference

Δr = radial ring increment for 3D components

Δt = time-step size

ΔV = velocity change

Δx = cell length for 1D components

Δz = axial level increment for 3D components

$\Delta\theta$ = azimuthal segment increment for 3D components

δP = linear Taylor series expansion term for pressure

δT = linear Taylor series expansion term for temperature

$\delta \alpha$ = linear Taylor series expansion term for void fraction

θ = inclination angle from vertical or the azimuthal coordinate

ϕ = angle between the main and side tubes in a TEE component

Subscripts

$1\mathrm{D}$ = one dimensional

$3\mathrm{D}$ = three dimensional

$donor$ = donor cell

T = the first cell in the side leg of the TEE or the interface between the j^{th} cell of the primary and the first cell in the side leg

a = noncondensable gas

d = 1) generic index for r, θ, or z or i, j, or k ; 2) denotes direct heating when used with energy source (q)

g = gas mixture

i = interfacial

j = cell-center index

$j+1$ = downstream cell-center index

$j+1/2$ = downstream cell-edge index

$j-1$ = upstream cell-center index

$j-1/2$ = upstream cell-edge index

k = index on additional noncondensable gas species

l = liquid

max = maximum

min = minimum

r = radial

sat = saturation

v = water vapor

w = wall

z = axial

θ = azimuthal

Superscripts

n = current-time quantity

$n+1$ = new-time quantity

$'$ = last estimate

In the discussion of the finite-difference equations, all quantities except for the velocities are centered in the hydrodynamic cell (cell-centered), and the velocities are cell-edge quantities.

Approximation of the Momentum Equations

The field equations introduced in **Chapter 1** have gone through a volume averaging process to generate the wall terms in the energy and momentum equations, and fit well with a finite volume solution approach. This section focuses on generation of a discrete approximation to a momentum equation, because the process is significantly more complex than derivation of finite volume mass and energy equations. Momentum equations and the primary associated velocities are evaluated at the surfaces separating the volumes used for conservation of mass and energy. Figure B-2 illustrates the edge (labeled j+1/2) between two adjacent mass/energy conservation volumes (j and j+1). The figure illustrates the fact that a given computational volume can have a non-uniform cross-sectional area, and that discontinuous changes in flow area can be modeled at the junction between mass volumes. The center of a mass conservation volume is taken to be halfway between the bounding flow surfaces along the center of the flow channel. In Figure B-2 dotted lines through these center points represent surfaces that will bound a volume to be used in the derivation of the finite volume form of the momentum equation. Since the fundamental evaluation of velocities is not at these dotted surfaces through point j and j+1, a special averaging procedure is needed to obtain velocities at these surfaces for use in momentum transport terms. This needs to be consistent with the upwind procedure discussed for the mass conservation equation. However, because rapid area changes are permitted from volume to volume, the upwind approach is applied to the product of flow area and velocity. For the flow direction chosen in Figure B-2 we get $V_{j+1} = A_{j+1/2}V_{j+1/2}/A_{j+1}$ and $V_j = A_{j-1/2}V_{j-1/2}/A_j$. .

Figure B-3 focuses on the momentum volume consisting of the right half of mass volume j and left half of mass volume j+1. To cut the length of subscript notation, the surfaces at locations j and j+1 in Figure B-2 are now designated by subscripts 1 and 2 respectively and assigned areas A_1 and A_2. The central surface between the two mass volumes (edge j+1/2) is given a subscript c, and to cover side junctions in the derivation, side flow through an area A_3 is permitted. Users need to know that more than one such side junction may exist. Because of the upstream approximations used for spatial averages, only those side junctions upstream from the center of the momentum cell can contribute to momentum fluxes. In the final implementation of the finite volume

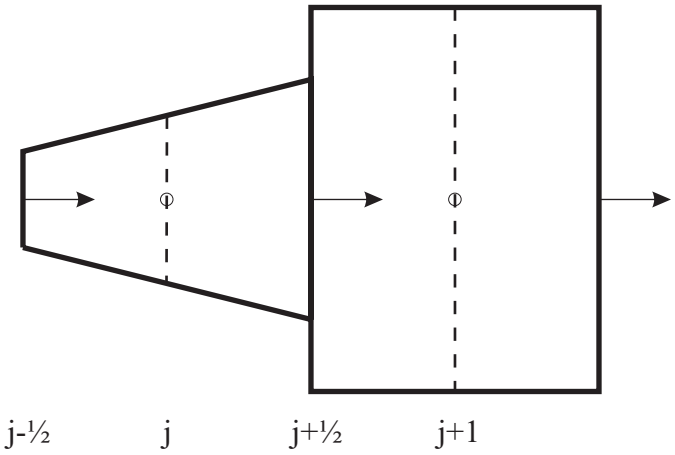

Figure. B-2. Two mass/energy conservation volumes

momentum equation, this upstream requirement can result in a shift in association of a side junction from one momentum volume to its immediate neighbor as flow velocities switch sign.

Basic approximations used in generation of the final discrete equations are modified slightly. Thermodynamic state variables such as density, pressure, and volume fraction are still constant over mass conservation volumes, so within the momentum volume, density (for example) has one uniform value upstream of the central flow area (A_c), and a second uniform value downstream of the central area. However, it is the product of velocity and channel flow area (volumetric flow) that is treated as constant on either side of the central flow area, using the upwind formulation outlined above to obtain actual values.

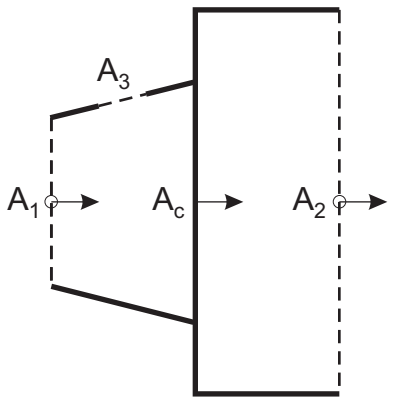

Figure. B-3. Volume for momentum equation integration

As a simple example of generation of a discrete momentum equation, integrate the gas momentum equation over the momentum volume associated with flow surface A_c located between two mass/energy conservation volumes (designated $Vol_{j+1/2}$ in equations below).

(B-26)

$$\int_V \frac{\partial}{\partial t}\left(\alpha\rho_g\vec{V}_g\right)dV + \int_S \alpha\rho_g\vec{V}_g\vec{V}_g\cdot d\vec{S} + \int_V \alpha\nabla P\,dV = \int_V \left(\Gamma\vec{V}_i + \vec{f}_i + \vec{f}_w + \alpha\rho\vec{g}\right)dV$$

or

(B-27)

$$\int_V \frac{\partial}{\partial t}\left(\alpha\rho_g\vec{V}_g\right)dV + \sum_{k=1,3}\overline{\left(\alpha\rho_g\vec{V}_g\vec{V}_g\right)}_k\cdot\vec{A}_k + \int_V \alpha\nabla P\,dV = \int_V \left(\Gamma\vec{V}_i + \vec{f}_i + \vec{f}_w + \alpha\rho\vec{g}\right)dV$$

Next integrate the mass conservation equations over the portions of the volume to the right and left of A_c. Area vectors for areas 1 through 3 are chosen to have a positive sense out of the momentum volume. The area vector associated with an area splitting the momentum volume in the middle (A_c) has a sign convention that is positive towards end area 2.

(B-28)

$$\int_{V_r} \frac{\partial}{\partial t}\left(\alpha\rho_g\right)dV - \overline{\left(\alpha\rho_g\vec{V}_g\right)}_c\cdot\vec{A}_c + \overline{\left(\alpha\rho_g\vec{V}_g\right)}_2\cdot\vec{A}_2 = \int_{V_r}\Gamma dV$$

and

(B-29)

$$\int_{V_\ell} \frac{\partial}{\partial t}\left(\alpha\rho_g\right)dV + \overline{\left(\alpha\rho_g\vec{V}_g\right)}_1\cdot\vec{A}_1 + \overline{\left(\alpha\rho_g\vec{V}_g\right)}_c\cdot\vec{A}_c + \overline{\left(\alpha\rho_g\vec{V}_g\right)}_3\cdot\vec{A}_3 = \int_{V_\ell}\Gamma dV$$

Changing notation to use of the volume and area averages seen in the derivation of the finite volume mass equation, the integrated momentum equation can be written as:

(B-30)

$$\frac{\partial}{\partial t}\overline{\left(\alpha\rho_g\vec{V}_g\right)}Vol_{j+1/2} + \sum_{k=1,3}\overline{\left(\alpha\rho_g\vec{V}_g\vec{V}_g\right)}_k\cdot\vec{A}_k + \overline{\alpha\nabla P}Vol_{j+1/2} = \left(\overline{\Gamma\vec{V}}_i + \overline{\vec{f}}_i + \overline{\vec{f}_w} + \overline{\alpha\rho\vec{g}}\right)Vol_{j+1/2}$$

In a consistent notation the mass equations for the left (subscript *l*) and right (subscript *r*) halves of the momentum volume are:

(B-31)

$$\frac{\partial}{\partial t}\left(\overline{\alpha\rho_g}\right)+\left(\overline{\alpha\rho_g\vec{V}_g}\right)_1\cdot\vec{A}_1+\left(\overline{\alpha\rho_g\vec{V}_g}\right)_c\cdot\vec{A}_c+\left(\overline{\alpha\rho_g\vec{V}_g}\right)_3\cdot\vec{A}_3=\overline{\Gamma}_l Vol_l$$

and

(B-32)

$$\frac{\partial}{\partial t}\left(\overline{\alpha\rho_g}\right)Vol_r-\left(\overline{\alpha\rho_g\vec{V}_g}\right)_c\cdot\vec{A}_c+\left(\overline{\alpha\rho_g\vec{V}_g}\right)_2\cdot\vec{A}_2=\overline{\Gamma}_r Vol_r$$

Next rearrange these mass equations to get end fluxes along the primary direction of flow.

(B-33)

$$\left(\overline{\alpha\rho_g\vec{V}_g}\right)_1\cdot\vec{A}_1=\overline{\Gamma}_l Vol_\ell-\frac{\partial}{\partial t}\left(\overline{\alpha\rho_g}\right)_\ell Vol_\ell-\left(\overline{\alpha\rho_g\vec{V}_g}\right)_c\cdot\vec{A}_c-\left(\overline{\alpha\rho_g\vec{V}_g}\right)_3\cdot\vec{A}_3$$

and

(B-34)

$$\left(\overline{\alpha\rho_g\vec{V}_g}\right)_2\cdot\vec{A}_2=\overline{\Gamma}_r Vol_r-\frac{\partial}{\partial t}\left(\overline{\alpha\rho_g}\right)_r Vol_r+\left(\overline{\alpha\rho_g\vec{V}_g}\right)_c\cdot\vec{A}_c$$

Now we use the assumption that the area and volume averages of the products are equal to the product of the individually averaged terms. Generally, the argument supporting this assumption is that turbulence produces fairly flat velocity profiles across a pipe. However, even in single phase flow, the validity of this argument is adversely affected for volumes in which the cross-sectional flow area is changing rapidly, or for area averages in the midst of such a change in wall dimensions. Two-phase flow can also cause problems with this assumption, particularly when a single liquid field is used to model a mix of liquid film on a wall and droplets carried by the gas flow.

All velocities have already been time averaged, and turbulence effects have been included in wall and interfacial force terms, so no further loss of turbulence effects is implied by this assumption about time and volume averaging. To simplify notation beyond this point we will drop the bar over flow variables.

(B-35)

$$\frac{\partial}{\partial t}\left(\alpha\rho_g\vec{V}_g\right)Vol_{j+1/2}+\sum_{k=1,3}\left(\alpha\rho_g\vec{V}_g\vec{V}_g\right)_k\cdot\vec{A}_k+\alpha\nabla PVol_{j+1/2}=\left(\Gamma\vec{V}_i+\vec{f}_i+\vec{f}_w+\alpha\rho\vec{g}\right)Vol_{j+1/2}$$

Next multiply Eq. (B-33) by $V_{g,1}$ and Eq. (B-34) by $V_{g,2}$.

(B-36)

$$\left(\alpha\rho_g\vec{V}_g\vec{V}_g\right)_1\cdot\vec{A}_1=\Gamma_\ell\,\vec{V}_{g,1}Vol_\ell-\vec{V}_{g,1}\frac{\partial}{\partial t}\left(\alpha\rho_g\right)_\ell Vol_\ell-\vec{V}_{g,1}\left(\alpha\rho_g\vec{V}_g\right)_c\cdot\vec{A}_c-\vec{V}_{g,1}\left(\alpha\rho_g\vec{V}_g\right)_3\cdot\vec{A}_3$$

(B-37)

$$\left(\alpha\rho_g\vec{V}_g\vec{V}_g\right)_2\cdot\vec{A}_2=\Gamma_r\,\vec{V}_{g,2}Vol_r-\vec{V}_{g,2}\frac{\partial}{\partial t}\left(\alpha\rho_g\right)_r Vol_r+\vec{V}_{g,2}\left(\alpha\rho_g\vec{V}_g\right)_c\cdot\vec{A}_c$$

Substituting Eq. (B-36) and Eq. (B-37) into the momentum flux terms associated with Eq. (B-35) gives:

(B-38)

$$\sum_{k=1,3}\left(\alpha\rho_g\vec{V}_g\vec{V}_g\right)_k\cdot\vec{A}_k=\vec{V}_{g,2}\left(\alpha\rho_g\vec{V}_g\right)_c\cdot\vec{A}_c-\vec{V}_{g,1}\left(\alpha\rho_g\vec{V}_g\right)_c\cdot\vec{A}_c+\left(\vec{V}_{g,3}-\vec{V}_{g,1}\right)\left(\alpha\rho_g\vec{V}_g\right)_3\cdot\vec{A}_3$$
$$+\Gamma_r\,\vec{V}_{g,2}Vol_r+\Gamma_\ell\,\vec{V}_{g,1}Vol_\ell-\vec{V}_{g,2}\frac{\partial}{\partial t}\left(\alpha\rho_g\right)_r Vol_r-\vec{V}_{g,1}\frac{\partial}{\partial t}\left(\alpha\rho_g\right)Vol_\ell$$

or

(B-39)

$$\sum_{k=1,3}\left(\alpha\rho_g\vec{V}_g\vec{V}_g\right)_k\cdot\vec{A}_k=\left(\alpha\rho_g\vec{V}_g\right)_c\cdot\vec{A}_c\left(\vec{V}_{g,2}-\vec{V}_{g,1}\right)+\left(\vec{V}_{g,3}-\vec{V}_{g,1}\right)\left(\alpha\rho_g\vec{V}_g\right)_3\cdot\vec{A}_3$$
$$+\Gamma_r\,\vec{V}_{g,2}Vol_r+\Gamma_\ell\,\vec{V}_{g,1}Vol_\ell-\vec{V}_{g,2}\frac{\partial}{\partial t}\left(\alpha\rho_g\right)_r Vol_r-\vec{V}_{g,1}\frac{\partial}{\partial t}\left(\alpha\rho_g\right)_\ell Vol_\ell$$

It's worth noting that if Eq. (B-35) and Eq. (B-36) are extended to multiple (m-2) side junctions then a more general form of Eq. (B-39) is:

(B-40)

$$\sum_{k=1,m}\left(\alpha\rho_g\vec{V}_g\vec{V}_g\right)_k\cdot\vec{A}_k=\left(\alpha\rho_g\vec{V}_g\right)_c\cdot\vec{A}_c\left(\vec{V}_{g,2}-\vec{V}_{g,1}\right)+\sum_{k=3,m}\left(\vec{V}_{g,k}-\vec{V}_{g,1}\right)\left(\alpha\rho_g\vec{V}_g\right)_k\cdot\vec{A}_k$$
$$+\Gamma_r\,\vec{V}_{g,2}Vol_r+\Gamma_\ell\,\vec{V}_{g,1}Vol_\ell-\vec{V}_{g,2}\frac{\partial}{\partial t}\left(\alpha\rho_g\right)_r Vol_r-\vec{V}_{g,1}\frac{\partial}{\partial t}\left(\alpha\rho_g\right)_\ell Vol_\ell$$

To further clean up the equation we start by looking at the time derivative of the momentum per unit volume. The volume average of this quantity can be broken into contributions from the left and right sides of the momentum volume.

$$\frac{\partial}{\partial t}(\alpha\rho_g\vec{V}_g)\,Vol_{j+1/2} = \int_V \frac{\partial}{\partial t}(\alpha\rho_g\vec{V}_g)\,dV = \int_V \vec{V}_g \frac{\partial}{\partial t}(\alpha\rho_g)\,dV + \int_V \alpha\rho_g \frac{\partial \vec{V}_g}{\partial t}\,dV \tag{B-41}$$

$$= \int_{V_{rrr}} \vec{V}_g \frac{\partial}{\partial t}(\alpha\rho_g)\,dV + \int_{V_l} \vec{V}_g \frac{\partial}{\partial t}(\alpha\rho_g)\,dV + \int_V \alpha\rho_g \frac{\partial \vec{V}_g}{\partial t}\,dV$$

$$\approx \vec{V}_{g,1} \frac{\partial}{\partial t}(\alpha\rho_g)_l\, Vol_l + \vec{V}_{g,2} \frac{\partial}{\partial t}(\alpha\rho_g)_r\, Vol_r + \alpha\rho_g \frac{\partial \vec{V}_g}{\partial t}\, Vol_{j+1/2}$$

Although an approximation has been made in Eq. (B-41), it is consistent with the first order method used in TRACE. When Eq. (B-39) is substituted into Eq. (B-35) the time derivative terms in Eq. (B-35) combine with the time derivative in Eq. (B-39) to give:

(B-42)

$$\frac{\partial}{\partial t}\left(\alpha\rho_g\vec{V}_g\right)Vol_{j+1/2} - \vec{V}_{g,2}\frac{\partial}{\partial t}\left(\alpha\rho_g\right)_r Vol_r - \vec{V}_{g,1}\frac{\partial}{\partial t}\left(\alpha\rho_g\right)_\ell Vol_\ell = \alpha\rho_g \frac{\partial \vec{V}_g}{\partial t} Vol_{j+1/2}$$

A similar split of the volume integration can be done for phase change terms.

$$\Gamma \vec{V}_g\, Vol_{j+1/2} = \int_{V_r} \Gamma \vec{V}_g\, dV + \int_{V_l} \Gamma \vec{V}_g\, dV \tag{B-43}$$

$$\approx \Gamma_l \vec{V}_{g,1}\, Vol_l + \Gamma_r \vec{V}_{g,2}\, Vol_r$$

The combination of phase change terms resulting from substitution of Eq. (B-39) into Eq. (B-35) is:

(B-44)

$$\Gamma\vec{V}_i Vol_{j+1/2} - \Gamma_r \vec{V}_{g,2} Vol_r - \Gamma_\ell \vec{V}_{g,1} Vol_\ell = \Gamma\left(\vec{V}_i - \vec{V}_g\right) Vol_{j+1/2}$$

The final result of these time derivative and phase change substitutions into Eq. (B-35) is a simpler form of the finite volume momentum equation.

(B-45)

$$\alpha\rho_g \frac{\partial \vec{V}_g}{\partial t} Vol_{j+1/2} + \left(\alpha\rho_g\vec{V}_g\right)_c \cdot \vec{A}_c\left(\vec{V}_{g,2} - \vec{V}_{g,1}\right) + \left(\vec{V}_{g,3} - \vec{V}_{g,1}\right)\left(\alpha\rho_g\vec{V}_g\right)_3 \cdot \vec{A}_3 + \alpha\nabla P Vol_{j+1/2} =$$
$$\left[\Gamma\left(\vec{V}_i - \vec{V}_g\right) + \vec{f}_i + \vec{f}_w + \alpha\rho_g\vec{g}\right] Vol_{j+1/2}$$

or in the multiple side junction form:

(B-46)

$$\alpha\rho_g \frac{\partial \vec{V}_g}{\partial t} Vol_{j+1/2} + \left(\alpha\rho_g \vec{V}_g\right)_c \cdot \vec{A}_c \left(\vec{V}_{g,2} - \vec{V}_{g,1}\right) + \sum_{k=3,m} \left(\vec{V}_{g,k} - \vec{V}_{g,1}\right)\left(\alpha\rho_g \vec{V}_g\right)_k \cdot \vec{A}_k$$
$$\left[\Gamma\left(\vec{V}_i - \vec{V}_g\right) + \vec{f}_i + \vec{f}_w + \alpha\rho_g \vec{g}\right] Vol_{j+1/2}$$

At this point, to obtain results useful for a computer solution, we need to employ the previously mentioned assumptions about the spatial dependence of state variables within the volumes of interest. Here void fraction, densities, and pressure are taken as constant within the left portion of the momentum volume and a separate set of constant values over the right portion of the momentum volume. Consistent with previous comments on the method by which V_1 and V_2 are obtained from $V_{j-1/2}$ and $V_{j+1/2}$, the basis functions for velocities are modified to deal with the cross-sectional area changes. Rather than taking the velocity to be constant, the product of area averaged velocity and area is taken as constant.

Expressions for volume averages need to be reexamined under the first order assumptions to provide useful forms for these terms. One additional quantity useful in this context is the distance "Δs" along the centerline of the flow channel between bounding areas A_1 and A_2. Within TRACE the areas associated with the centers of mass volumes (e.g. A_1 and A_2) are taken to be the volume of the mass conservation cell divided by the distance between its two edge faces. As a result Δs can be related to volumes and areas defined in this problem.

$$\Delta s = \frac{Vol_l}{A_1} + \frac{Vol_r}{A_2} = \Delta s_l + \Delta s_r \tag{B-47}$$

Also note that the product of velocity and area is taken as a constant within the momentum volume. As a result the following relation can be applied in a channel cross-section average at any point along the length of the momentum volume.

$$\int_A \vec{V}_g \, dA = \vec{V}_{g,c} \, A_c \tag{B-48}$$

Given the restriction that discontinuous area changes only take place at the center of the momentum volume, it is possible to express the area averaged velocities within the left and right regions of the momentum volume as:

$$\vec{V}_{g,l} = \vec{V}_{g,c} \frac{A_c}{A_1}, \text{ and} \tag{B-49}$$

$$\vec{V}_{g,r} = \vec{V}_{g,c}\frac{A_c}{A_2}. \tag{B-50}$$

Three of the averages in Eq. (B-45) are:

$$\alpha\rho_g\frac{\partial\vec{V}_g}{\partial t}Vol_{j+1/2} = \int_V \alpha\rho_g\frac{\partial\vec{V}_g}{\partial t}dV = \int_{\Delta S}\int_A \alpha\rho_g\frac{\partial\vec{V}_g}{\partial t}dA\,ds = \int_{\Delta S}\alpha\rho_g\left(\frac{\partial}{\partial t}\int_A \vec{V}_g dA\right)ds = \tag{B-51}$$

$$[(\alpha\rho_g\Delta s)_l + (\alpha\rho_g\Delta s)_r]\frac{\partial\vec{V}_{g,c}}{\partial t}A_c = \overline{\alpha\rho_g}\frac{\partial\vec{V}_{g,c}}{\partial t}A_c\Delta s$$

(B-52)

$$\Gamma\left(\vec{V}_i - \vec{V}_g\right)Vol_{j+1/2} = \int_V \Gamma\left(\vec{V}_i - \vec{V}_g\right)dV = \int_{\Delta s}\int_A \Gamma\left(\vec{V}_i - \vec{V}_g\right)dA\,ds = \int_{\Delta s}\Gamma\int_A\left(\vec{V}_i - \vec{V}_g\right)dA\,ds$$
$$= \left[(\Gamma\Delta s)_\ell + (\Gamma\Delta s)_r\right]\left(\vec{V}_i - \vec{V}_g\right)_c A_c = \overline{\Gamma}\left(\vec{V}_i - \vec{V}_g\right)_c A_c\Delta s$$

and

(B-53)

$$\alpha\rho_g\vec{g}Vol_{j+1/2} = \int_V \alpha\rho_g\vec{g}dV = \left(\alpha\rho_g\right)_\ell Vol_\ell\vec{g}_\ell + \left(\alpha\rho_g\right)_r Vol_r\vec{g}_r = \overline{\alpha\rho_g\vec{g}}\;\; Vol_{j+1/2}$$

Evaluation of the total contribution of pressure forces is greatly simplified by the first order assumption that state variables are constant over sub-regions of the integration volume. For this particular case with pressure and void constant to the left and right of A_c, we divide the integral of the pressure force term into integration over three sub-volumes. One is centered on A_c with an infinitesimal thickness 2δ perpendicular to A_c. The other two sub-volumes cover the remainder of the momentum volume to the left and right of A_c. The integral over these two large volumes will be zero because the pressure gradient is zero throughout both. However, the integral over the central volume is non-zero due to the discontinuity in pressure. The result is obtained through use of Heavyside step functions to represent the functional forms of pressure and void fraction. In terms of the dimension orthogonal to A_c:

$$\alpha(x) = \alpha_l + (\alpha_r - \alpha_l)H(x) \tag{B-54}$$
$$P(x) = P_l + (P_r - P_l)H(x)$$

hence,

$$\int_V \alpha \nabla P dV = \vec{A}_c \int_{-\delta}^{\delta} [\alpha_l + (\alpha_r - \alpha_l) H(x)](P_r - P_l) \frac{\partial H(x)}{\partial x} dx \tag{B-55}$$

$$\vec{A}_c \left(\left[\alpha_l H(x) + (\alpha_r - \alpha_l) \frac{H^2(x)}{2} \right] (P_r - P_l) \right) \Bigg|_{-\delta}^{\delta} = \vec{A}_c \frac{(\alpha_l + \alpha_r)}{2} (P_r - P_l)$$

For those accustomed to the derivation of loss coefficients for an abrupt expansion, this approximation will look wrong. In the classic abrupt expansion case, the pressure P_l is assumed to also be appropriate in the right sub-volume over the wall area aligned with the center surface of the momentum volume. Unfortunately, the finite volume calculation must be able to deal with a wide variety of channel shapes. Rather than doing subgrid calculations to obtain better values of surface pressure distributions, we have elected to account for the discrepancy by using loss coefficients. The approach taken in Eq. (B-55) produces the lowest irrecoverable pressure loss of all possible assumptions about wall pressure distribution. Some simple examples of the consequences of this assumption, will be presented in the final section of this chapter. It is up to the user to provide loss coefficients in the model's input specification that result in the correct irrecoverable pressure loss.

The force terms for interfacial and wall shear have proportionality to velocity, so the volume multiplying those terms ($Vol_{j+1/2}$) can be converted to the product $A_c \Delta s$. Substituting all of the approximations to the volume integrals into the last form of the momentum equation and dividing everything by $\alpha\rho_g A_c \Delta s$ gives:

(B-56)

$$\frac{\partial \vec{V}_g}{\partial t} + \frac{\left(\alpha\rho_g \vec{V}_g\right)_c}{\overline{\alpha\rho_g} A_c dx} \cdot \vec{A}_c \left(\vec{V}_{g,2} - \vec{V}_{g,1}\right) + \frac{\left(\vec{V}_{g,3} - \vec{V}_{g,1}\right)}{\overline{\alpha\rho_g} A_c dx} \left(\alpha\rho_g \vec{V}_g\right)_3 \cdot \vec{A}_3 + \frac{\overline{\alpha}\left(p_r - p_\ell\right)}{\overline{\alpha\rho_g} dx} \hat{i} =$$
$$\frac{1}{\overline{\alpha\rho_g}} \left[\Gamma\left(\vec{V}_{i,c} - \vec{V}_{g,c}\right) + \vec{f}_{i,c} + \vec{f}_{w,c} + \overline{\alpha\rho_g} \vec{g} \frac{Vol_{j+1/2}}{A_c dx} \right]$$

The actual momentum equations in TRACE were derived from a finite difference approach, and ratios with the product of volume fraction and density in numerator and denominator are set to one.

(B-57)

$$\frac{\partial \vec{V}_g}{\partial t} + \frac{\left(\vec{V}_g\right)_c}{A_c \Delta s} \cdot \vec{A}_c \left(\vec{V}_{g,2} - \vec{V}_{g,1}\right) + \frac{\vec{V}_{g,3} - \vec{V}_{g,1}}{\overline{\alpha\rho_g} A_c \Delta s} \left(\alpha\rho_g \vec{V}_g\right)_3 \cdot \vec{A}_3 + \frac{\overline{\alpha}\left(p_r - p_\ell\right)}{\overline{\alpha\rho_g} \Delta s} \hat{i} =$$
$$\frac{1}{\overline{\alpha\rho_g}} \left[\Gamma\left(\vec{V}_{i,c} - \vec{V}_{g,c}\right) + \vec{f}_{i,c} + \vec{f}_{w,c} \right] + \vec{g}$$

To this point the time and volume averaged momentum equation is still 3-D. Three steps are necessary to make it useful for a 1-D model. First the equation is applied in a coordinate system in which one dimension follows the flow channel. From the standpoint of this coordinate system, there are no bends in the piping. The piping's centerline can be treated as the axis of the primary dimension. Second, take the dot product of Eq. (B-57) with a unit vector along the primary dimension to isolate the component of the velocity along the piping. Finally introduce a term to account for irrecoverable losses of momentum masked by the volume averaging, hidden here in $f_{w,g}$. This accounts for wall pressure distributions and effects of recirculation zones not resolved due the scale of volume averaging.

(B-58)

$$\frac{\partial V_g}{\partial t}+\frac{\left(V_g\right)_c}{\Delta s}\left(V_{g,2}-V_{g,1}\right)-\frac{\left|V_{g,3}\right|\cos\phi-V_{g,1}}{\overline{\alpha\rho_g}A_c\Delta s}\left(\alpha\rho_g\left|V_g\right|\right)_3 A_3+\frac{\overline{\alpha}\left(p_r-p_\ell\right)}{\overline{\alpha\rho_g}\Delta s}=$$
$$\frac{1}{\overline{\alpha\rho_g}}\left[\Gamma\left(V_{i,c}-V_{g,c}\right)+f_{i,c}+f_{w,c}\right]-g\cos\theta$$

In the above equation ϕ is the angle between the unit vector along the pipe centerline and velocity vector for flow entering from the side leg, and θ is the angle between the unit vector along the centerline in a positive direction and a vector pointing vertically upward (against gravity). Note that this specific form of the equations is only valid when flow is entering the main flow path from the side leg. What appears to be a change in sign for the side junction momentum source term, simply reflects the fact that the vector associated with area A_3 and the velocity vector for inflow from the side leg are in opposite directions, so that the dot product between them is negative one.

Within TRACE the side leg velocity $V_{g,3}$ has a sign convention that is positive when the flow is out of the momentum volume. The angle ϕ used in Eq. (B-58) can be restated simply in terms of the mesh geometry as the angle between a line out the centerline of the side leg and a line directed in the negative sense along the centerline of the primary flow path. Applying these definitions of sign convention and angle, Eq. (B-58) can be written in a general form to cover both inflow and outflow at the side junction.

(B-59)

$$\frac{\partial V_g}{\partial t}+\frac{\left(V_g\right)_c}{\Delta s}\left(V_{g,2}-V_{g,1}\right)-\frac{V_{g,3}\cos\phi+V_{g,1}}{\overline{\alpha\rho_g}A_c\Delta s}\left(\alpha\rho_g V_g\right)_3 A_3+\frac{\overline{\alpha}\left(p_r-p_\ell\right)}{\overline{\alpha\rho_g}\Delta s}=$$
$$\frac{1}{\overline{\alpha\rho_g}}\left[\Gamma\left(V_{i,c}-V_{g,c}\right)+f_{i,c}+f_{w,c}\right]-g\cos\theta$$

Eq. (B-58) is a clearer form for understanding contributions from side junction inflow but Eq. (B-59) reflects the term as implemented in TRACE for the case of inflow. The next section will discuss what is actually done for outflow through a side leg.

During the evolution of the TRACE momentum equation implementation several deviations have occurred from the formal definition of terms in this derivation.

- "The mean volume fraction of gas used in the pressure gradient term is currently a cell length weighted rather than simple average.
- "The value of $\alpha\rho_g$ in the denominator of the flux term for side connection momentum is currently donor cell averaged rather than cell length weighted.
- "When a side junction is not present, V_1 and V_2 are obtained from area scaling of upwind edge velocities, and in the momentum flux term $V_{g,c}$ is a simple area weighted average of V_1 and V_2, chosen this way to give Bernoulli equation results in the limit of steady state and constant density.
- When a side junction is present, TRACE guidelines instruct users to use a straight run of pipe, so that all areas in the above discussion are the same. If a user ignores these guidelines and associated runtime warning messages, TRACE constructs the momentum transfer term as if all areas were equal to A_c. It also uses the local value of $V_{g,c}$ rather than the average mentioned in the bullet above.

Special Cases for Side Junction Flow

TRACE does not model all cases of momentum exchange involving side junctions. The terms currently in the code were driven by considerations of flow patterns in reactor safety problems, and should not be expected to perform well in all possible flow path topologies. Results presented in the previous section reflect the importance of correct momentum transfer within a jet pump model or in situations where ECCS liquid is being injected into a steam flow through a reactor coolant pipe. A rigorous formulation for momentum transfer terms has not been developed for the case were flow is out through the side connection. When this happens in normal reactor scenarios, the split in mass flows between the main and side legs of the connection is driven by pressure rather than momentum terms. Under these circumstances, TRACE or any thermal hydraulics code using 1-D modeling can produce a reasonable prediction of the split in mass flow between the main and side flow paths. However, such codes can not capture details of the pressure drops, and if the flow split is momentum driven they should be expected to miss the distribution of mass flow between the flow paths. Details of flow splitting can only be captured from first principles with a full CFD simulation. With the lumped approach available in TRACE, the only option for improved results is through the use of loss coefficients tuned to relevant experimental results. This section begins the examination of the impact of TRACE approximations on flow models. Specific examples are presented in the final section of this chapter.

Flow Out a Side Junction

For the case of flow splitting illustrated in Figure B-4, Eq. (B-59) can still be applied, remembering that $V_{g,3}$ now has a positive value. Also note the angle ϕ used in Eq. (B-59) has a specific definition related to the tee geometry, rather than the angle between velocity vectors.

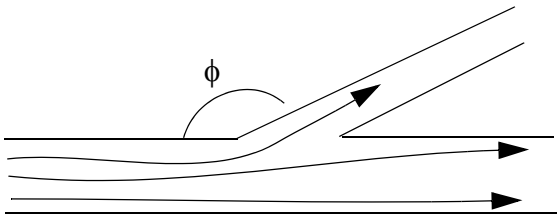

Figure. B-4. Primary Flow Splitting at a tee junction.

The impact of the momentum source term resulting from flow out the side leg can be seen more clearly by moving it to the right hand side of the momentum equation for the main leg.

(B-60)

$$\frac{\partial V_g}{\partial t}+\frac{(V_g)_c}{\Delta s}\left(V_{g,2}-V_{g,1}\right)+\frac{\overline{\alpha}\left(p_r-p_\ell\right)}{\overline{\alpha\rho_g}\Delta s}=\frac{V_{g,3}\cos\phi+V_{g,1}}{\overline{\alpha\rho_g}A_c\Delta s}\left(\alpha\rho_g V_g\right)_3 A_3$$
$$+\frac{1}{\overline{\alpha\rho_g}}\left[\Gamma\left(V_{i,c}-V_{g,c}\right)+f_{i,c}+f_{w,c}\right]-g\cos\theta$$

For the simple case of flow out a right angle tee side leg, the source term on the right side of Eq. (B-60) is positive, resulting in an additional increase in pressure for main leg flow across the junction region. This driving term resulted in non-physical flows when first tested in TRAC-PF1, and so was dropped. It has not been restored in TRACE. In addition, the previous comments about use of the local value of $V_{g,c}$ in the momentum transfer term, and fixing the area for scaling to A_c hold for this case. Returning to the notation introduced in Figure B-2, the momentum equation just down stream of the side junction becomes:

(B-61)

$$\frac{\partial V_{g,j+1/2}}{\partial t}+\frac{V_{g,j+1/2}}{\Delta s}\left(V_{g,j+1/2}-V_{g,j-1/2}\right)+\frac{\overline{\alpha}\left(p_r-p_\ell\right)}{\overline{\alpha\rho_g}\Delta s}=$$
$$+\frac{1}{\overline{\alpha\rho_g}}\left[\Gamma\left(V_{i,c}-V_{g,c}\right)+f_{i,c}+f_{w,c}\right]-g\cos\theta$$

In the limit of steady, constant density flow the above equation can be compared to the Bernoulli equation relating pressure to velocity along streamlines in the main flow path of Figure B-4 that do not exit the side junction. The result is that Eq. (B-61) introduces a loss coefficient consistent with abrupt expansion of these streamlines across the region of the side junction. Irrecoverable pressure losses for the main flow path in this flow pattern will be higher in TRACE simulations than in the actual flows.

Normally, at the first edge in the side leg, constant area is enforced and hence Eq. (B-61) is applied. In this case $V_{g,\,j-1/2}$ is the velocity at the main leg face just upstream of the side junction, multiplied by the complement of ϕ, or zero if ϕ is less than or equal to 90 degrees. If the component is a jet pump, variable areas are permitted at the side leg junction. This special case is possible, because ϕ is zero degrees in a jet pump. One subtle consequence of the momentum equation applied at the first junction to a side leg, is that the momentum volume associated with this cell edge overlaps a momentum volume in the main flow path. This results in a non-physical, but usually relatively small, increase in the fluid inertia for the system.

Side Junction Inflow, Splitting in the Main Leg

The initial momentum derivation implied side junction flow joining a main leg flow in a single direction. However, situations may exist in which the side junction is the only source of fluid, and the flow splits upon entering the main flow path, exiting in both directions. In principle Eq. (B-58) can be applied to this situation. However, closer inspection of the details reveals a problem that became very apparent in some flow tests with TRAC-PF1, where the magnitude of main leg velocities to either side of the side junction could become unphysically large. The reason can be quickly seen by rearranging Eq. (B-58) to place the source term associated with side leg flow on the right of the equation.

(B-62)

$$\frac{\partial V_{g,c}}{\partial t}+\frac{\left(V_g\right)_c}{\Delta s}\left(V_{g,2}-V_{g,1}\right)+\frac{\overline{\alpha}\left(p_r-p_\ell\right)}{\overline{\alpha\rho_g}\Delta s}=\frac{\left|V_{g,3}\right|\cos\phi-V_{g,1}}{\overline{\alpha\rho_g}A_c\Delta s}\left(\alpha\rho_g\left|V_g\right|\right)_3 A_3$$
$$\frac{1}{\overline{\alpha\rho_g}}\left[\Gamma\left(V_{i,c}-V_{g,c}\right)+f_{i,c}+f_{w,c}\right]-g\cos\theta$$

For the upwind method used in TRACE $V_{g,1}$ is obtained from area scaling of $V_{g,\,j-1/2}$ (see Figure B-2). Since this velocity is negative, the net effect is a positive source to the acceleration of $V_{g,c}$. The greater the magnitude of $V_{g,\,j-1/2}$, the greater the positive acceleration on $V_{g,c}$ ($V_{g,\,j+1/2}$). When the momentum equation is adapted to the flow at face j-1/2, a related pattern is seen. The larger the velocity at face j+1/2, the more negative acceleration is created by the side junction source term for face j-1/2. This can create an unphysical feedback, leading to very large flow speeds in the main flow path. The problem was resolved in TRAC-PF1 by noting the basis function for velocity in the junction volume is flawed, and that a better approximation to $V_{g,1}$ in this instance is simply zero. As a result for this particular flow pattern Eq. (B-62) becomes:

(B-63)

$$\frac{\partial V_{g,c}}{\partial t}+\frac{\left(V_g\right)_c}{\Delta s}\left(V_{g,2}-V_{g,1}\right)+\frac{\overline{\alpha}\left(p_r-p_\ell\right)}{\overline{\alpha\rho}_g\Delta s}=\frac{\left|V_{g,3}\right|\cos\phi}{\overline{\alpha\rho}_g A_c\Delta s}\left(\alpha\rho_g\left|V_g\right|\right)_3 A_3$$
$$\frac{1}{\overline{\alpha\rho}_g}\left[\Gamma\left(V_{i,c}-V_{g,c}\right)+f_{i,c}+f_{w,c}\right]-g\cos\theta$$

C

Critical Flow Model: Computational Details

This Appendix describes in detail the calculational sequence of the critical flow model.

Nomenclature

The nomenclature that applies to this section follows:

a_{HE} = homogeneous equilibrium sound speed

C = virtual mass coefficient

D = diameter

g = gravitational acceleration

P = pressure

P_c = pressure at the choking plane

P_{up} = pressure upstream of the choking plane

R = gas constant

s = entropy

t = time

T_o = stagnation temperature

V = velocity

V_{cg} = critical velocity for single-phase vapor

V_{cl} = subcooled-liquid choking velocity

V_{up} = velocity upstream of the choking plane

x = distance

Greek

α = gas volume fraction

γ = specific heat ratio

$\Delta\rho$ = difference between the phasic densities

ΔT = temperature difference

Δt = time step

λ_i = characteristic roots

ρ = density

σ = surface tension

Subscripts

a = noncondensable gas

c = cell-centered value

g = combined-gas mixture

k = phase index (liquid or gas)

l = liquid

m = total mixture

up = conditions upstream of the choking plane

v = vapor

e = edge-based value (may be accompanied by a + or - superscript to indicate which side of cell center the edge is on)

Superscripts

n = current-time quantity

$n+1$ = new-time quantity

p = predicted quantity

Determining the Sound Speed

The evaluation of Eqs. (7-3) and (7-4) in the subcooled-liquid choking model and the solution of Eq. (7-39) in the two-phase, two-component choking model require that conditions at the cell-edge where the choking criterion is applied be known. Subroutine CHOKE calls subroutine SOUND to calculate a homogeneous equilibrium sound speed and to estimate the corresponding cell-edge conditions, given the conditions at cell center. Three basic calculational sequences exist in subroutine SOUND:

1) If the cell contains pure noncondensable gas, the homogeneous equilibrium sound speed and corresponding cell-edge conditions are computed by assuming an isentropic expansion of an ideal gas.

2) If the cell length-to-hydraulic-diameter ratio, L/D, is greater than or equal to 1.5, or if some noncondensable gas is present in the vapor phase of a two-phase flow at cell center (regardless of the value of L/D), then the conditions at cell center are required to come to equilibrium by means of an isenthalpic process before stagnation conditions are calculated. Once the stagnation conditions have been determined, a homogeneous equilibrium sound speed and the corresponding cell-edge conditions are calculated by first assuming thermal equilibrium and no slip at the cell edge and an isentropic expansion from stagnation to cell edge. We then iterate for the cell-edge pressure, which results in the maximum or critical mass flux at the cell edge (a classical technique used in generating the HEM tables).

3) If the cell length-to-hydraulic-diameter ratio, L/D, is less than 1.5, or if only the superheated vapor phase or the subcooled-liquid phase exists at the cell center, then the stagnation conditions are calculated from the actual cell-center properties, rather than from the effective equilibrium properties as in (2). Once stagnation conditions have been determined, a homogeneous equilibrium sound speed and the corresponding cell-edge conditions are determined either by assuming an isentropic expansion of an ideal gas (for the case of superheated vapor phase at the cell edge) or by iterating for the cell-edge pressure, which gives the maximum mass flux as in (2) above.

The details of each procedure follow.

Isentropic Expansion of Ideal Gas

When the cell-center conditions represent a pure noncondensable-gas field, the sound speed and cell-edge conditions are calculated using ideal-gas theory. First, a cell-edge temperature and a cell-edge pressure are computed, such that

$$T_e = \frac{2\,T_g}{\gamma_a + 1}\left(1 + \frac{V_{gc}^2}{2\,c_{pa}\,T_g}\right) \tag{C-1}$$

and

$$p_e = p\left[\frac{2}{\gamma_a + 1}\left(1 + \frac{V_{gc}^2}{2 c_{pa} T_g}\right)\right]^{\gamma_a/(\gamma_a - 1)} , \tag{C-2}$$

where T_g is the cell-center gas temperature, γ_a is the specific heat ratio for the noncondensable gas (as calculated by the TRACE Equation-of-State (EOS) package), V_{gc} is the cell-center gas velocity [as given in **Chapter 7**, Eq. (7-43)], c_{pa} is the constant-pressure specific heat for the noncondensable gas (as defined in the TRACE EOS package), and p is the cell-center total pressure.

Next, a cell-edge noncondensable-gas density is calculated according to

$$\rho_{ae} = \frac{p_e}{R_a T_e} , \tag{C-3}$$

where R_a is the noncondensable-gas constant (as defined in the TRACE EOS package), and p_e and T_e are the cell-edge pressure and temperature calculated in Eq. (C-1) and Eq. (C-2) above.

Knowing the cell-edge temperature, the gas sound speed can be expressed by

$$a_{HE} = \sqrt{\gamma_a R_a T_e} , \tag{C-4}$$

where γ_a is the specific heat ratio for the noncondensable gas, R_a is the noncondensable-gas constant, and T_e is the cell-edge temperature calculated in Eq. (C-1) above.

This concludes the calculation of the gas sound speed and cell-edge conditions for the case of pure noncondensable gas at cell center. At this point, the logic returns to subroutine CHOKE.

L/D ≤ 1.5 or Noncondensable Gas Present in Two-Phase Flow at Cell Center

Subroutine SOUND calculates the stagnation conditions using the effective equilibrium void fraction, rather than the actual void fraction, if the cell center is not in equilibrium. The calculational sequence to arrive at the cell-edge conditions and the homogeneous equilibrium sound speed is as follows.

Initially, the TRACE EOS package is called with the actual cell-center total pressure, p; the partial pressure of any noncondensable gas that may be present, p_a; and the steam/gas-mixture and liquid temperatures, T_g and T_l. With these variables, TRACE calculates the actual mixture density, actual quality, and liquid, steam, noncondensable-gas, steam/gas-mixture, and steam/liquid mixture enthalpies:

$$\rho_m = \alpha_{actual}\rho_g + (1-\alpha)\rho_l \ , \tag{C-5}$$

$$x_{actual} = \alpha_{actual}\left(\frac{\rho_g}{\rho_m}\right) \ , \tag{C-6}$$

$$h_l = e_l + \frac{p}{\rho_l} \ , \tag{C-7}$$

$$h_v = e_v + \frac{p - p_a}{\rho_g - \rho_a} \ , \tag{C-8}$$

$$h_a = e_a + \frac{p_a}{\rho_a + 1.0 \times 10^{-20}} \ , \tag{C-9}$$

$$h_g = e_g + \frac{p}{\rho_g} \ , \tag{C-10}$$

and

$$h_m = x_{actual}h_v + (1 - x_{actual})h_l \ , \tag{C-11}$$

where α_{actual} is the actual cell-center void fraction, x_{actual} is the actual cell-center quality, and all fluid properties are actual cell-center values.

If the cell-center conditions do not represent an equilibrium state, an effective equilibrium void fraction at the cell center is determined assuming an isenthalpic process from the actual cell-center state. A call to the EOS package with the saturation temperature corresponding to the cell-center partial pressure of steam allows cell-center liquid, steam, noncondensable-gas, and steam/gas-mixture saturated enthalpies to be determined. From this, the equilibrium quality at cell center and equilibrium void fraction at cell center may be calculated, such that

$$x_{equil} = \frac{h_m - h_{l,equil}}{h_{v,equil} - h_{l,equil} + \frac{\rho_{a,equil}}{\rho_{g,equil}}(h_{a,equil} - h_a - h_{v,equil} + h_v)} \tag{C-12}$$

and

$$\alpha_{equil} = \frac{x_{equil}\,\rho_{l,equil}}{\rho_{g,equil} + x_{equil}\left(\rho_{l,equil} - \rho_{g,equil}\right)} \ , \tag{C-13}$$

where h_m is the cell-center steam/liquid-water-mixture actual enthalpy from Eq. (C-11); $h_{l,equil}$, $h_{v,equil}$, and $h_{a,equil}$ are the cell-center liquid, steam, and noncondensable-gas equilibrium enthalpies for the saturation temperature corresponding to the cell-center partial pressure of steam; h_v and h_a are the cell-center steam and noncondensable-gas actual enthalpies [Eqs. (C-8) and (C-9)]; and $\rho_{l,equil}$, $\rho_{a,equil}$, and $\rho_{g,equil}$ are the cell-center liquid, noncondensable-gas, and steam/gas-mixture equilibrium densities for the saturation temperature corresponding to the cell-center partial pressure of steam.

Such quantities as constant-pressure specific heats, constant-volume specific heats, and specific-heat ratios are now defined for the fluid. If the fluid at cell center is a single-phase saturated vapor, the steam specific-heat ratio is defined as

$$\gamma_v = 1.3 \ . \tag{C-14}$$

However, if the fluid at cell center is two-phase or subcooled, the steam ratio of specific heats is defined as

$$\gamma_v = 1.035 + 0.1\alpha_{equil}\left(\frac{\rho_{g,equil} - \rho_{a,equil}}{\alpha_{equil}\,\rho_{g,equil} + (1-\alpha_{equil})\rho_{l,equil}}\right) , \tag{C-15}$$

where α_{equil} is the cell-center equilibrium void fraction and $\rho_{g,equil}$, $\rho_{a,equil}$, and $\rho_{l,equil}$ are cell-center steam/gas-mixture, noncondensable-gas, and liquid equilibrium densities at the saturation temperature corresponding to the cell-center partial pressure of steam.

The steam and steam/gas-mixture specific heats are then defined, such that

$$c_{pv} = \frac{\gamma_v R_v}{\gamma_v - 1} \ , \tag{C-16}$$

$$c_{vv} = c_{pv} - R_v \ , \tag{C-17}$$

$$c_{pg} = c_{pa}\left(\frac{\rho_{a\,,\,equil}}{\rho_{g\,,\,equil}}\right) + c_{pv}\left(1 - \frac{\rho_{a\,,\,equil}}{\rho_{g\,,\,equil}}\right) \ , \tag{C-18}$$

and

$$c_{vg} = c_{va}\left(\frac{\rho_{a\,,\,equil}}{\rho_{g\,,\,equil}}\right) + c_{vv}\left(1 - \frac{\rho_{a\,,\,equil}}{\rho_{a\,,\,equil}}\right) \ , \tag{C-19}$$

where γ_g is the steam specific-heat ratio [as defined by Eqs. (C-14) or (C-15)], R_v is the steam gas constant (defined by subroutine SETEOS), and $\rho_{a\,,\,equil}$ and $\rho_{g\,,\,equil}$ are the cell-center noncondensable-gas and steam/gas-mixture equilibrium densities at the saturation temperature corresponding to the cell-center partial pressure of steam.

The steam/gas-mixture ratio of specific heats becomes

$$\gamma_g = \frac{c_{pg}}{c_{vg}} \ . \tag{C-20}$$

Cell-center liquid, steam, noncondensable-gas, steam/gas-mixture, and steam/liquid-water-mixture equilibrium entropies for the saturation temperature corresponding to the cell-center partial pressure of steam are calculated, such that

$$s_{l\,,\,equil} = c_{vl} \ln\left(\frac{T_{sv}}{273.15}\right) \ , \tag{C-21}$$

$$s_{v\,,\,equil} = c_{vl} \ln\left(\frac{T_{sv}}{273.15}\right) + \frac{h_{fg\,,\,equil}}{T_{sv}} \ , \tag{C-22}$$

$$s_{a,equil} = c_{pa}\ln\left(\frac{T_{sv}}{273.15}\right) - R_a\ln\left(\frac{Max(p_a, 1\times10^{-5})}{1.0\times10^5}\right) , \tag{C-23}$$

$$s_{g,equil} = s_{a,equil}\left(\frac{\rho_{a,equil}}{\rho_{g,equil}}\right) + s_{v,equil}\left(1-\frac{\rho_{a,equil}}{\rho_{g,equil}}\right) , \tag{C-24}$$

and

$$s_{m,equil} = x_{equil}\,s_{v,equil} + (1-x_{equil})s_{l,equil} , \tag{C-25}$$

where T_{sv} is the saturation temperature corresponding to the cell-center partial pressure of steam, c_{vl} is the liquid constant-volume specific heat (defined in subroutine SETEOS), $h_{fg,\text{equil}}$ is the latent heat of vaporization at T_{sv}, c_{pa} is the noncondensable-gas constant-pressure specific heat (defined by subroutine SETEOS), R_a is the noncondensable-gas constant (defined in subroutine SETEOS), p_a is the cell-center partial pressure of the noncondensable gas, $\rho_{a,\text{equil}}$ and $\rho_{g,\text{equil}}$ are the cell-center noncondensable-gas and steam/gas-mixture equilibrium densities at the saturation temperature corresponding to the cell-center partial pressure of steam, and x_{equil} is the cell-center effective equilibrium quality as computed in Eq. (C-12).

Finally, stagnation conditions are computed according to the following:

$$h_o = x_{equil}\left(h_{g,equil} + \frac{1}{2}V_{gc}^2\right) + (1-x_{equil})\left(h_{l,equil} + \frac{1}{2}V_{lc}^2\right) , \tag{C-26}$$

$$p_o = x_{equil}p\left(1+\frac{1}{2}\frac{V_{gc}^2}{c_{pg}T_{sv}}\right)^{\frac{\gamma_g}{\gamma_g-1}} + (1-x_{equil})\left(p+\frac{1}{2}\rho_l V_{lc}^2\right) , \tag{C-27}$$

and

$$s_o = x_{equil}s_{g,equil} + (1-x_{equil})s_{l,equil} , \tag{C-28}$$

where x_{equil} is the cell-center effective equilibrium quality as computed in Eq. (C-12), $h_{\text{l,equil}}$ and $h_{g,\text{equil}}$ are the cell-center liquid and steam/gas-mixture equilibrium enthalpies evaluated at the saturation temperature corresponding to the cell-center partial pressure of steam, V_{lc} and V_{gc} are the cell-center liquid and steam/gas-mixture velocities [as computed in Eqs. (7-43) and (7-44)], p is the cell-center total pressure, γ_g is the ratio of specific heats [as defined in Eq. (C-20)], c_{pg} is the

steam/ gas-mixture specific heat at constant pressure [as defined in Eq. (C-18)], T_{sv} is the saturation temperature corresponding to the cell-center partial pressure of steam, ρ_l is the cell-center liquid actual density, and $s_{l,equil}$ and $s_{g,equil}$ are the cell-center liquid and steam/gas-mixture equilibrium entropies evaluated at the saturation temperature corresponding to the cell-center partial pressure of steam [as in Eqs. (C-21) and (C-24)].

Iterations can now be performed to determine the maximum mass flux and the corresponding cell-edge conditions.

An initial cell-edge pressure equal to that predicted by ideal-gas expansion theory is guessed by using the relationship

$$p_e = p_o\left(\frac{2}{\gamma_g + 1}\right)^{\gamma_g/(\gamma-1)} , \tag{C-29}$$

where p_o is the stagnation pressure [as in Eq. (C-27)] and γ_g is the steam/gas-mixture specific-heat ratio [as in Eq. (C-20)].

Subroutine THERMO is then called to determine the saturation properties at the cell edge corresponding to the cell-edge pressure, p_e.

Saturated cell-edge values for liquid, steam, and steam/gas-mixture enthalpies and for liquid, steam, and noncondensable-gas entropies are computed, such that

$$h_{lc} = e_{lc} + \frac{p_e}{\rho_{lc}} , \tag{C-30}$$

$$h_{ve} = e_{ve} + \frac{p_e - p_{ae}}{\rho_{ge} - \rho_{ae}} , \tag{C-31}$$

$$h_{ge} = e_{ge} + \frac{p_e}{\rho_{ge}} , \tag{C-32}$$

$$s_{lc} = c_{vl}\ln\left(\frac{T_e}{273.15}\right) , \tag{C-33}$$

$$s_{ve} = s_{lc} + \frac{h_{ve} - h_{le}}{T_e} , \tag{C-34}$$

and

$$s_{ae} = c_{pa}\ln\left(\frac{T_e}{273.15}\right) - R_a\ln\left(\frac{Min\left\{p_{ae}, 1.0\times10^{-5}\right\}}{1.0\times10^{5}}\right), \tag{C-35}$$

where e_{le}, e_{ve}, and e_{ge} are the cell-edge liquid, steam, and steam/gas-mixture saturated internal energies for the pressure p_e; p_e is the cell-edge pressure; p_{ae} is the cell-edge partial pressure of the noncondensable gas given by $p_{ae} = p_a(p_e)/p$; ρ_{le}, ρ_{ae}, and ρ_{ge} are the cell-edge liquid, noncondensable-gas, and steam/gas-mixture saturated densities for the pressure p_e; c_{vl} is the liquid constant-volume specific heat (as defined in subroutine SETEOS); T_e is the cell-edge temperature equal to the saturation temperature at p_e; c_{pa} is the noncondensable-gas constant-pressure specific heat (as defined in subroutine SETEOS); and R_a is the noncondensable-gas constant (as defined in subroutine SETEOS).

Then, assuming a constant entropy expansion from the stagnation condition, a cell-edge quality may be calculated from

$$x_e = \frac{s_{m,\,equil} - s_{lc}}{s_{ve} - s_{lc} + \left(\frac{\rho_{ae}}{\rho_{ge}}\right)\left(s_{ae} - s_{a,\,equil} - s_{ve} - s_{v,\,equil}\right)}, \tag{C-36}$$

where $s_{m,\text{equil}}$, $s_{v,\text{equil}}$, and $s_{a,\text{equil}}$ are the cell-center steam/liquid-water-mixture, steam, and noncondensable-gas equilibrium entropies for the saturation temperature corresponding to the cell-center partial pressure of steam [as in Eqs. (C-25), (C-22), and (C-23)]; s_{le}, s_{ve}, and s_{ae} are the cell-edge liquid, steam, and noncondensable-gas saturated entropies for the pressure p_e [as computed above in Eqs. (C-33), (C-34), and (C-35)]; and ρ_{ae} and ρ_{ge} are the cell-edge noncondensable-gas and steam/gas-mixture saturated densities for the pressure p_e.

Once the cell-edge quality has been determined, a cell-edge total mixture enthalpy and cell-edge total mixture density are calculated as follows:

$$h_{me} = x_e h_{ge} + (1 - x_e)h_{le} \tag{C-37}$$

and

$$\rho_{me} = \frac{\rho_{lc}\rho_{ge}}{x_e(\rho_{lc} - \rho_{ge}) + \rho_{ge}}, \tag{C-38}$$

where x_e is the cell-edge quality [as in Eq. (C-36)]; h_{le} and h_{ge} are the cell-edge liquid and steam/gas-mixture saturated enthalpies for the pressure p_e [as in Eqs. (C-30) and (C-32)]; and ρ_{le} and ρ_{ge} are the cell-edge liquid and steam/gas-mixture saturated densities for the pressure p_e.

The mass flux, then, for a cell-edge pressure of p_e becomes

$$G = \rho_{me}\sqrt{2(h_o - h_{me})} \ , \tag{C-39}$$

where ρ_{me} is the cell-edge total mixture density [as in Eq. (C-38)], h_o is the stagnation enthalpy [as in Eq. (C-26)], and h_{me} is the cell-edge total mixture enthalpy [as in Eq. (C-37)].

The pressure is varied slightly and the iteration is repeated until the pressure that gives the maximum or critical mass flux as predicted by Eq. (C-39) is determined. Once the cell-edge pressure corresponding to the critical flux has been found, the saturated cell-edge conditions become known, and a homogeneous equilibrium sound speed, a_{HE}, is computed as follows:

$$a_{HE} = \frac{G_{max}}{\rho_{me}} \ . \tag{C-40}$$

This concludes the calculation of the homogeneous equilibrium sound speed and the corresponding cell-edge conditions for the case of nonsuperheated vapor phase at cell center when L/D ≥ 1.5 or when noncondensable gas is present in two-phase cell-center flow. At this point, the logic returns to subroutine CHOKE.

L/D < 1.5 or Only Superheated Vapor Phase, or Only Subcooled-Liquid Phase Present at Cell Center

In this case, instead of allowing the cell-center conditions to come to equilibrium along an isenthalpic process (if the cell center is not originally in equilibrium), the stagnation conditions are derived from the cell-center actual properties. The method of arriving at these stagnation conditions follows that of the $\mathrm{L/D} \geq 1.5$ case, except that actual properties are used instead of equilibrium properties. Then, as in the case for L/D ≥ 1.5, SOUND determines a homogeneous equilibrium sound speed and the corresponding cell-edge conditions by again assuming thermal equilibrium, no slip at the cell edge, and a constant entropy expansion between stagnation and cell edge, and by again iterating for the cell-edge pressure that gives the maximum mass flux at the cell edge if two-phase flow is predicted at the cell edge. Otherwise, the homogeneous equilibrium sound speed and corresponding cell-edge conditions are found by assuming an isentropic expansion of the superheated vapor phase existing at cell center according to ideal-gas behavior. The following gives the exact coding in detail.

As before, subroutine THERMO is called with the actual cell-center total pressure, p; the partial pressure of any noncondensable gas that may be present, p_a; and the steam/gas-mixture and liquid-phase temperatures, T_g and T_l. With these variables, THERMO calculates such properties as actual mixture density, actual quality, and liquid, steam, noncondensable-gas, steam/gas-mixture, and steam/liquid-water-mixture enthalpies, such that,

$$\rho_m = \alpha_{actual}\rho_g + (1 - \alpha_{actual})\rho_l \ , \tag{C-41}$$

$$x_{actual} = \alpha_{actual}\left(\frac{\rho_g}{\rho_m}\right) \ , \tag{C-42}$$

$$h_l = e_l + \frac{p}{\rho_l} \ , \tag{C-43}$$

$$h_v = e_v + \frac{p - p_a}{\rho_g - \rho_a} \ , \tag{C-44}$$

$$h_a = e_a + \frac{p_a}{\rho_a + 1.0 \times 10^{-20}} \ , \tag{C-45}$$

$$h_g = e_g + \frac{p}{\rho_g} \ , \tag{C-46}$$

and

$$h_m = x_{actual}h_v + (1 - x_{actual})h_l \ , \tag{C-47}$$

where α_{actual} is the actual cell-center void fraction, x_{actual} is the actual cell-center quality, and all fluid properties are actual cell-center values.

Such quantities as constant-pressure specific heats, constant-volume specific heats, and specific-heat ratios are now defined for the fluid. If the fluid at cell center is a superheated vapor, the steam specific-heat ratio is defined as

$$\gamma_v = 1.3 \ . \tag{C-48}$$

However, if the fluid at cell center is two-phase or subcooled, the steam ratio of specific heats is defined as

$$\gamma_v = 1.035 + 0.1\alpha_{actual}\left(\frac{\rho_g - \rho_a}{\rho_m}\right) \ , \tag{C-49}$$

where α_{actual} is the cell-center actual void fraction and ρ_g, ρ_a, and ρ_m are cell-center steam/gas-mixture, noncondensable-gas, and total mixture actual densities.

Next the steam and steam/gas-mixture specific heats are defined, such that

$$c_{pv} = \frac{\gamma_v R_v}{\gamma_v - 1} \ , \tag{C-50}$$

$$c_{vv} = c_{pv} - R \ , \tag{C-51}$$

$$c_{pg} = c_{pa}\left(\frac{\rho_a}{\rho_g}\right) + c_{pv}\left(1 - \frac{\rho_a}{\rho_g}\right) \ , \tag{C-52}$$

and

$$c_{vg} = c_{va}\left(\frac{\rho_a}{\rho_g}\right) + c_{vv}\left(1 - \frac{\rho_a}{\rho_g}\right) \ , \tag{C-53}$$

where γ_v is the steam specific-heat ratio [as defined by Eqs. (C-48) or (C-49)], R_v is the steam gas constant (defined by subroutine SETEOS), and ρ_a and ρ_g are the cell-center noncondensable-gas and steam/gas-mixture actual densities.

The steam/gas-mixture ratio of specific heats becomes

$$\gamma_g = \frac{c_{pg}}{c_{vg}} \ . \tag{C-54}$$

Cell-center liquid, steam, noncondensable-gas, steam/gas-mixture, and steam/liquid-water-mixture actual entropies are calculated, such that

$$s_l = c_{vl}\ln\left(\frac{T_l}{273.15}\right) \ , \tag{C-55}$$

$$s_v = c_{vl}\ln\left(\frac{T_{sv}}{273.15}\right) + \frac{h_{fg,\,equil}}{T_{sv}} + c_{pv}\ln\left(\frac{T_g}{T_{sv}}\right) \ , \tag{C-56}$$

$$s_a = c_{pa}\ln\left(\frac{T_g}{273.15}\right) - R_a\ln\left(\frac{max\{p_a\,,\,1.0\times10^{-5}\}}{1.0\times10^{5}}\right) \ , \tag{C-57}$$

$$s_g = s_a\left(\frac{\rho_a}{\rho_g}\right) + s_v\left(1 - \frac{\rho_a}{\rho_g}\right) \ , \tag{C-58}$$

and

$$s_m = x_{actual} s_v + (1 - x_{actual}) s_l \ , \tag{C-59}$$

where T_l is the cell-center liquid temperature, T_{sv} is the saturation temperature corresponding to the cell-center partial pressure of steam, c_{v1} is the liquid constant-volume specific heat (defined in subroutine SETEOS), $h_{fg,\text{equil}}$ is the latent heat of vaporization at T_{sv}, c_{pv} and c_{pa} are the steam and noncondensable-gas constant-pressure specific heats [defined by Eq. (C-50) and subroutine SETEOS, respectively], T_g is the cell-center steam/gas-mixture temperature, R_a is the noncondensable-gas constant (defined in subroutine SETEOS), p_a is the cell-center partial pressure of the noncondensable gas, ρ_a and ρ_g are the cell-center noncondensable-gas and steam/gas-mixture actual densities, and x_{actual} is the cell-center actual quality as computed in Eq. (C-42).

Finally, stagnation conditions are computed according to the following:

$$h_o = x_{actual}\left(h_g + \frac{1}{2} V_{gc}^2\right) + (1 - x_{actual})\left(h_l + \frac{1}{2} V_{lc}^2\right) \ , \tag{C-60}$$

$$p_o = x_{actual} p\left(1 + \frac{1}{2}\frac{V_{gc}^2}{c_{pg} T_g}\right)^{\frac{\gamma_g}{\gamma_g - 1}} + (1 - x_{actual})\left(p + \frac{1}{2}\rho_l V_{lc}^2\right) \ , \tag{C-61}$$

and

$$s_o = x_{actual} s_g + (1 - x_{actual}) s_l \ , \tag{C-62}$$

where x_{actual} is the cell-center actual quality as computed in Eq. (C-42), h_l and h_g are the cell-center liquid and steam/gas-mixture actual enthalpies, V_{gc} and V_{lc} are the cell-center steam/gas-mixture and liquid velocities [as computed in Eqs. (7-43) and (7-44)], p is the cell-center total pressure, γ_g is the ratio of specific heats [as defined in Eq. (C-54)], c_{pg} is the steam/gas-mixture specific heat at constant pressure [as defined in Eq. (C-52)], T_g is the cell-center steam/gas-mixture temperature, ρ_{l} is the cell-center liquid actual density, and s_{l} and s_g are the cell-center liquid and steam/gas-mixture actual entropies [as in Eqs. (C-55) and (C-58)]. At this point, the logic splits to handle either superheated vapor phase at cell center or nonsuperheated vapor phase at cell center based on a check of the cell-center steam/gas-mixture temperature and the cell-center actual quality [Eq. (C-42)].

Superheated Vapor Phase at Cell Center

If the cell-center steam/gas-mixture temperature, T_g, is greater than the saturation temperature corresponding to the cell-center partial pressure of steam or if the cell-center actual quality [Eq. (C-42)] is equal to 1, then TRACE determines the cell-center fluid to be a superheated vapor phase, and the homogeneous equilibrium sound speed and corresponding cell-edge conditions are computed as follows.

A cell-edge pressure, p_e, is calculated from the stagnation pressure, p_o, using the ideal-gas expansion theory, such that

$$p_e = p_o\left(\frac{2}{\gamma_g + 1}\right)^{\gamma_g/(\gamma_g - 1)} , \tag{C-63}$$

where γ_g is the steam/gas-mixture specific-heat ratio [as in Eq. (C-54)]. A downstream cell-edge temperature, T_e, is estimated from the cell-center steam/gas-mixture temperature, T_g, again using the ideal-gas expansion theory,

$$T_e = T_g\left(\frac{2}{\gamma_g + 1}\right) , \tag{C-64}$$

where T_g is assumed to be close to the stagnation temperature.

When T_e is greater than the saturation temperature at p_e, the fluid flow at cell-edge is predicted to be superheated by the ideal-gas relations, and the following logic occurs. Subroutine THERMO is called to determine the cell-edge properties for the superheated steam/gas mixture at pressure p_e and temperature T_e. The continuity equation, in conjunction with the ideal-gas relations, then yields a cell-edge steam/gas-mixture choking velocity,

$$V_{ge} = \frac{p_o}{\rho_{ge}\sqrt{T_g}}\sqrt{\frac{\gamma_g}{R_g}\left(\frac{2}{\gamma_g + 1}\right)^{(\gamma_g + 1)/(\gamma_g - 1)}} , \tag{C-65}$$

where p_o is the stagnation pressure [as in Eq. (C-61)]; ρ_{ge} is the cell-edge steam/gas-mixture density; T_g is the cell-center steam/gas-mixture temperature, which is assumed to be approximately equal to the stagnation temperature; and γ_g is the steam/gas-mixture specific-heat ratio [as in Eq. (C-54)]. R_g is the steam/gas-mixture gas constant and is defined by

$$R_g = R_a\left(\frac{\rho_a}{\rho_g}\right) + R_v\left(1 - \frac{\rho_a}{\rho_g}\right) , \tag{C-66}$$

where R_v and R_a are the steam and noncondensable-gas constants (defined by subroutine SETEOS), ρ_a and ρ_g are the cell-center noncondensable-gas and steam/gas-mixture actual densities.

If, in addition, the enthalpy at cell edge is greater than the stagnation enthalpy, the first law of thermodynamics also is used to calculate a cell-edge steam/gas-mixture choking velocity,

$$V_{ge} = \sqrt{2(h_o - h_{ge})} , \tag{C-67}$$

where h_o is the stagnation enthalpy [as in Eq. (C-59)] and h_{ge} is the steam/gas-mixture cell-edge enthalpy calculated from the cell-edge properties as

$$h_{ge} = e_{ge} + \frac{p_e}{\rho_{ge}} \ . \tag{C-68}$$

When both Eqs. (C-65) and (C-67) are used to compute a velocity, the actual steam/gas-mixture choking velocity is chosen to be the larger of the two calculated values. This concludes the calculation of the homogeneous equilibrium sound speed and the corresponding cell-edge conditions for the case of a superheated vapor phase at cell edge. At this point, the logic returns to subroutine CHOKE.

When T_e is less than or equal to the saturation temperature at p_e, one additional check is made to determine whether the fluid at cell edge is a superheated vapor phase. A steam/gas-mixture sound speed at cell edge is calculated from

$$V_{ge} = \sqrt{2\left[h_o - \left(e_{ge} + \frac{p_e}{\rho_{ge}}\right)\right]} \ , \tag{C-69}$$

where h_o is the stagnation enthalpy [as in Eq. (C-60)], p_e is the cell-edge pressure [as in Eq. (C-63)], and e_{ge} and ρ_{ge} are the cell-edge steam/gas-mixture internal energy and density as determined in the call to THERMO for the pressure p_e and the temperature T_e.

In addition, a sound speed for an ideal gas at the same temperature is calculated from

$$a_{HE} = \sqrt{\gamma_g R_g T_e} \ , \tag{C-70}$$

where γ_g is the steam/gas-mixture specific-heat ratio [Eq. (C-54)], R_g is the steam/gas-mixture gas constant [Eq. (C-66)], and T_e is the cell-edge temperature [Eq. (C-64)].

If the steam/gas-mixture velocity at the cell edge computed in Eq. (C-69) is greater than (or equal to) the ideal-gas sound speed of Eq. (C-70), then a superheated vapor phase is assumed to occur at the cell edge, and the choking velocity is calculated by maximizing the mass flux through pressure iterations in the following way.

Initially, the code chooses the cell-edge pressure and temperature to be equal to those values predicted by ideal-gas theory as in Eqs. (C-63) and (C-64). After calling THERMO to determine the cell-edge steam/gas-mixture properties corresponding to p_e and T_e, a steam/gas-mixture sound speed at cell edge is calculated using Eq. (C-69). A mass flux may then be computed from

$$G = V_{ge}\rho_{ge} \ , \tag{C-71}$$

where ρ_{ge} is the steam/gas-mixture cell-edge density and V_{ge} is the steam/gas-mixture cell-edge sound speed [Eq. (C-69)].

The cell-edge pressure guess is varied slightly, and the calculation of cell-edge mass flux is repeated until the pressure that gives the maximum mass flux is located. Once the maximum mass flux and the cell-edge properties for that particular cell-edge pressure have been found, a homogeneous equilibrium sound-speed velocity is calculated according to

$$a_{HE} = \frac{G_{max}}{\rho_{ge}} \ . \tag{C-72}$$

This concludes the calculation of the homogeneous equilibrium sound speed and the corresponding cell-edge conditions for the case of a slightly superheated vapor phase at cell edge. At this point, the logic returns to subroutine CHOKE.

If neither T_e is greater than the saturation temperature corresponding to the partial pressure of steam at cell edge, nor is the steam/gas-mixture sound speed greater than the ideal-gas sound speed [Eqs. (C-69) and (C-70)], then two-phase saturated fluid is assumed to be present at the cell edge. In this case, the pressure iteration necessary to determine the maximum mass flux and corresponding cell-edge conditions is exactly that described in the L/D ≥ 1.5 section. This method assumes that no delay in condensation occurs as the steam/gas mixture expands to the saturation temperature corresponding to the cell-edge partial pressure of steam. The equations are repeated here for completeness.

An initial cell-edge pressure equal to that predicted by ideal-gas expansion theory is guessed as

$$p_e = p_o\left(\frac{2}{\gamma_g + 1}\right)^{\gamma_g/(\gamma_g - 1)} \ , \tag{C-73}$$

where p_o is the stagnation pressure [as in Eq. (C-61)] and γ_g is the steam/gas-mixture specific-heat ratio [as in Eq. (C-54)].

Subroutine THERMO is then called to determine the saturation properties at the cell edge corresponding to the cell-edge pressure, p_e.

Saturated cell-edge values for liquid, steam, and steam/gas-mixture enthalpies and for liquid, steam, and noncondensable-gas entropies are computed, such that

$$h_{le} = e_{le} + \frac{p_e}{\rho_{lc}} \tag{C-74}$$

$$h_{ve} = e_{ve} + \frac{p_e - p_{ae}}{\rho_{ge} - \rho_{ae}} \ , \tag{C-75}$$

$$h_{ge} = e_{ge} + \frac{p_e}{\rho_{ge}} \ , \tag{C-76}$$

$$s_{lc} = c_{vl} \ln\left(\frac{T_e}{273.15}\right) \ , \tag{C-77}$$

$$s_{ve} = s_{le} + \frac{h_{ve} - h_{le}}{T_e} \ , \tag{C-78}$$

and

$$s_{ae} = c_{pa} \ln\left(\frac{T_e}{273.15}\right) - R_a \ln\left(\frac{min\{p_{ae}, 1.0 \times 10^{-5}\}}{1.0 \times 10^{5}}\right) \ , \tag{C-79}$$

where e_{le}, e_{ve}, and e_{ge} are the cell-edge liquid, steam, and steam/gas-mixture saturated internal energies for the pressure p_e; p_e is the cell-edge pressure; p_{ae} is the cell-edge partial pressure of the noncondensable gas given by $p_{ae} = p_a(p_e/p)$; ρ_{le}, ρ_{ae}, and ρ_{ge} are the cell-edge liquid, noncondensable-gas, and steam/gas-mixture saturated densities for the pressure p_e; c_{vl} is the liquid constant-volume specific heat (as defined in subroutine SETEOS); T_e is the cell-edge temperature equal to the saturation temperature at p_e; c_{pa} is the noncondensable-gas constant-pressure specific heat (as defined in subroutine SETEOS); and R_a is the noncondensable-gas constant (as defined in subroutine SETEOS).

Then, assuming a constant entropy expansion from the stagnation condition, a cell-edge quality may be calculated from

$$x_e = \frac{s_m - s_{le}}{s_{ve} - s_{le} + \left(\frac{\rho_{ae}}{\rho_{ge}}\right)(s_{ae} - s_a - s_{ve} - s_v)} \ , \tag{C-80}$$

where s_m, s_v, and s_a are the cell-center steam/liquid-water-mixture, steam, and noncondensable-gas actual entropies for the saturation temperature corresponding to the cell-center partial pressure of steam [as in Eqs. (C-59), (C-56), and (C-57)]; s_{le}, s_{ve}, and s_{ae} are the cell-edge liquid, steam, and noncondensable-gas saturated entropies for the pressure p_e [as computed above in Eqs. (C-77), (C-78), and (C-79)]; and ρ_{ae} and ρ_{ge} are the cell-edge noncondensable-gas and steam/gas-mixture saturated densities for the pressure p_e.

Once the cell-edge quality has been determined, a cell-edge total mixture enthalpy and cell-edge total mixture density are calculated as

$$h_{me} = x_e h_{ge} + (1 - x_e) h_{le} \tag{C-81}$$

and

$$\rho_{me} = \frac{\rho_{le}\rho_{ge}}{x_e(\rho_{le} - \rho_{ge}) + \rho_{ge}} \ , \tag{C-82}$$

where x_e is the cell-edge quality [as in Eq. (C-80)]; h_{le} and h_{ge} are the cell-edge liquid and steam/gas-mixture saturated enthalpies for the pressure p_e [as in Eqs. (C-74) and (C-76)]; and ρ_{le} and ρ_{ge} are the cell-edge liquid and steam/gas-mixture saturated densities for the pressure p_e.

The mass flux, then, for a cell-edge pressure of p_e, becomes

$$G = \rho_{me}\sqrt{2(h_o - h_{me})} \tag{C-83}$$

where ρ_{me} is the cell-edge total mixture density [as in Eq. (C-82)], h_o is the stagnation enthalpy [as in Eq. (C-60)], and h_{me} is the cell-edge total mixture enthalpy [as in Eq. (C-81)].

The pressure is varied slightly and the iteration is repeated until the pressure that gives the maximum or critical mass flux as predicted by Eq. (C-83) is determined. Once the cell-edge pressure corresponding to the critical flux has been found, the saturated cell-edge conditions become known, and a homogeneous equilibrium sound speed, a_{HE}, is computed as follows:

$$a_{HE} = \frac{G_{max}}{\rho_{me}} \ . \tag{C-84}$$

This concludes the calculation of the homogeneous equilibrium sound speed and the corresponding cell-edge conditions for the case of a nonsuperheated vapor phase at the cell edge when a superheated vapor phase existed at cell center. At this point, the logic returns to subroutine CHOKE.

Nonsuperheated Vapor Phase at Cell Center

If the cell-center steam/gas-mixture temperature, T_g, is less than or equal to the saturation temperature corresponding to the cell-center partial pressure of steam, or if the cell-center actual quality [Eq. (C-42)] is less than 1, the cell-center fluid is determined to be a nonsuperheated vapor phase, and the homogeneous equilibrium sound speed and corresponding cell-edge conditions are computed using the same iterative process outlined in ***L/D £ 1.5 or Noncondensable Gas Present in Two-Phase Flow at Cell Center***, once the stagnation properties have been identified. The equations are repeated here for completeness.

An initial cell-edge pressure equal to that predicted by ideal-gas expansion theory is guessed as

$$p_e = p_o\left(\frac{2}{\gamma_g + 1}\right)^{\gamma_g/(\gamma_g - 1)} \ , \tag{C-85}$$

where p_o is the stagnation pressure [as in Eq. (C-61)] and γ_g is the steam/gas-mixture specific-heat ratio [as in Eq. (C-54)].

Subroutine THERMO is then called to determine the saturation properties at the cell edge corresponding to the cell-edge pressure, p_e.

Saturated cell-edge values for liquid, steam, and steam/gas-mixture enthalpies and for liquid, steam, and noncondensable-gas entropies are computed, such that

$$h_{le} = e_{le} + \frac{p_e}{\rho_{le}} \ , \tag{C-86}$$

$$h_{ve} = e_{ve} + \frac{p_e - p_{ae}}{\rho_{ge} - \rho_{ae}} \ , \tag{C-87}$$

$$h_{ge} = e_{ge} + \frac{p_e}{\rho_{ge}} \ , \tag{C-88}$$

$$s_{le} = c_{vl} \ln\left(\frac{T_e}{273.15}\right) \ , \tag{C-89}$$

$$s_{ve} = s_{le} + \frac{h_{ve} - h_{lc}}{T_e} \ , \tag{C-90}$$

and

$$s_{ae} = c_{pa} \ln\left(\frac{T_e}{273.15}\right) - R_a \ln\left(\frac{min\{p_{ae}, 1.0 \times 10^{-5}\}}{1.0 \times 10^5}\right) \ , \tag{C-91}$$

where e_{le}, e_{ve}, and e_{ge} are the cell-edge liquid, steam, and steam/gas-mixture saturated internal energies for the pressure p_e; p_e is the cell-edge pressure; p_{ae} is the cell-edge partial pressure of the noncondensable gas given by $p_{ae} = p_a(p_e/p)$; ρ_{le}, ρ_{ae}, and ρ_{ge} are the cell-edge liquid, noncondensable-gas, and steam/gas-mixture saturated densities for the pressure p_e; c_{vl} is the liquid constant-volume specific heat (as defined in subroutine SETEOS); T_e is the cell-edge temperature equal to the saturation temperature at p_e; c_{pa} is the noncondensable-gas constant-pressure specific heat (as defined in subroutine SETEOS); and R_a is the noncondensable-gas constant (as defined in subroutine SETEOS).

Then, assuming a constant entropy expansion from the stagnation condition, the code calculates a cell-edge quality from

$$x_e = \frac{s_m - s_{lc}}{s_{ve} - s_{lc} + \left(\frac{\rho_{ae}}{\rho_{ge}}\right)(s_{ae} - s_a - s_{ve} - s_v)} \quad , \tag{C-92}$$

where s_m, s_v, and s_a are the cell-center steam/liquid-water-mixture, steam, and noncondensable-gas actual entropies for the saturation temperature corresponding to the cell-center partial pressure of steam [as in Eqs. (C-59), (C-56), and (C-57)]; s_{le}, s_{ve}, and s_{ae} are the cell-edge liquid, steam, and noncondensable-gas saturated entropies for the pressure p_e [as computed above in Eqs. (C-89), (C-90), and (C-91)]; and ρ_{ae} and ρ_{ge} are the cell-edge noncondensable-gas and steam/gas-mixture saturated densities for the pressure p_e.

Once the cell-edge quality has been determined, a cell-edge total mixture enthalpy and cell-edge total mixture density are calculated as

$$h_{me} = x_e h_{ge} + (1 - x_e) h_{le} \tag{C-93}$$

and

$$\rho_{me} = \frac{\rho_{le}\rho_{ge}}{x_e(\rho_{le} - \rho_{ge}) + \rho_{ge}} \quad , \tag{C-94}$$

where x_e is the cell-edge quality [as in Eq. (C-92)]; h_{le} and h_{ge} are the cell-edge liquid and steam/gas-mixture saturated enthalpies for the pressure p_e [as in Eqs. (C-86) and (C-88)]; and ρ_{le} and ρ_{ge} are the cell-edge liquid and steam/gas-mixture saturated densities for the pressure p_e.

The mass flux, then, for a cell-edge pressure of p_e becomes

$$G = \rho_{me}\sqrt{2(h_o - h_{me})} \quad , \tag{C-95}$$

where ρ_{me} is the cell-edge total mixture density [as in Eq. (C-94)], h_o is the stagnation enthalpy [as in Eq. (C-60)], and h_{me} is the cell-edge total mixture enthalpy [as in Eq. (C-93)].

The pressure is varied slightly and the iteration is repeated until the pressure that gives the maximum or critical mass flux as predicted by Eq. (C-95) is determined. Once the cell-edge pressure corresponding to the critical flux has been found, the saturated cell-edge conditions become known and a homogeneous equilibrium sound speed, a_{HE}, is computed as follows:

$$a_{HE} = \frac{G_{max}}{\rho_{me}} \quad . \tag{C-96}$$

This concludes the calculation of the homogeneous equilibrium sound speed and the corresponding cell-edge conditions for the case of a nonsuperheated vapor at cell center when L/

D < 1.5 or the case of only subcooled liquid at cell center. At this point, the logic returns to subroutine CHOKE.

Model as Coded

Initial Calculations

Upon entry to subroutine CHOKE, several preliminary calculations are performed to prepare for either a subcooled-liquid choking calculation; a two-phase, two-component choking calculation; or a single-phase vapor choking calculation.

The two choked-flow multipliers are set to the user-input values as specified in the INOPTS NAMELIST data or are defaulted to 1.0 if no user-input values are specified.

The cell length-to-hydraulic-diameter ratio, L/D, is checked to determine how subroutine SOUND will calculate the stagnation properties given the cell-center conditions.

For $L/D \leq 1.5$, complete thermal equilibrium is assumed to exist at the cell edge. If the cell-center conditions are not initially in thermal equilibrium, thermal equilibrium conditions are calculated at the cell center assuming a constant-enthalpy process. Once thermal equilibrium has been established at cell center, the equilibrium void fraction is used to determine which choking model to use (subcooled-liquid; two-phase, two-component; or single-phase vapor). Stagnation properties computed in subroutine SOUND to determine the homogeneous equilibrium sound speed and the corresponding cell-edge conditions are calculated using the cell-center thermal equilibrium conditions, rather than any nonequilibrium cell-center conditions that may exist.

For $0.0000011111 \leq L/D < 1.5$, the actual cell-center void fraction is used to determine which choking model is used (either subcooled-liquid; two-phase, two-component; or single-phase vapor). Complete thermal equilibrium is still assumed to exist at the cell edge, but the stagnation conditions computed in subroutine SOUND to calculate the homogeneous equilibrium sound speed and the corresponding cell-edge conditions are calculated using the actual cell-center conditions (which may be either equilibrium or nonequilibrium conditions).

For $L/D < 0.0000011111$, complete nonequilibrium is assumed to exist at the choking plane (cell edge).

In TRACE, the low value of 0.0000011111 for the L/D check means that nonequilibrium equations are not evaluated. In addition, when a noncondensable gas is present in the vapor component, the logic described above for the case when $L/D \geq 1.5$ is followed throughout the choking calculation, regardless of the actual value of L/D.

Next the mixture density, mixture velocity, and slip ratio are calculated from the momentum-solution velocities according to the following:

$$\rho_{mc} = \alpha_c \rho_{gc} + (1.0 - \alpha_c)\rho_{lc} \ , \tag{C-97}$$

$$V_m = \frac{\alpha_c \rho_{gc} V_g + (1.0 - \alpha_c)\rho_{lc} V_l}{\rho_{m_c}} \ , \tag{C-98}$$

and

$$S = \frac{V_g}{V_l} \ , \tag{C-99}$$

where α_c is the cell-center void fraction, ρ_{ge} and ρ_{le} are the cell-center phasic densities, and V_g and V_l are the momentum-solution phasic velocities. If a negative slip is calculated, the slip is reset to 1.0, and the calculational sequence proceeds. This should never occur, but in the event that countercurrent flow is sent to CHOKE, a slip of 1.0 will allow CHOKE to run without failing (choked flow will not occur in this case anyway).

Determination of Choking Velocities Using the Appropriate Model

At this point, subroutine CHOKE branches to the appropriate choked-flow model based on the void fraction (either actual or equilibrium as determined by the L/D check described above).

If $\alpha \leq 1.0\times10^{-8}$, a subcooled-liquid choking calculation is done.

If $1.0\times10^{-8} < \alpha < 1.0\times10^{-5}$, an interpolation between the subcooled-liquid and the two-phase, two-component choking calculation is performed to determine the choking velocities.

If $1.0\times10^{-5} \leq \alpha \leq 0.999$, a two-phase, two-component choking calculation is done.

And if $\alpha > 0.999$, a single-phase vapor choking calculation is performed.

Subcooled Liquid

If $\alpha \leq 1.0\times10^{-8}$, a subcooled-liquid calculation is done to determine the choking velocities.

First, subroutine SOUND is called to determine the maximum mass flux and the corresponding cell-edge conditions, as described in ***Determining the Sound Speed***. From this maximum mass flux, the value of the homogeneous equilibrium sound speed to be used in conjunction with the donor-cell conditions to give the correct mass flow is then calculated, such that

$$a_{HE} = \frac{G_{max}}{\rho_{mc}} \ , \tag{C-100}$$

where G_{max} is the critical mass flux returned by SOUND and ρ_{mc} is the (donor-cell) cell-center mixture density calculated in Eq. (C-97).

Next, a nucleation pressure, which may be lower than the saturation pressure corresponding to the local (donor-cell) liquid temperature, is calculated for the cell edge using the Jones nucleation delay model [Eq. (7-4)]. With the critical temperature, T_c, equal to 647.3 K and Boltzmann's constant, k, equal to 1.380622×10^{-23} J·K^{-1} Eq. (7-4) becomes

$$p_{nuc} = p_{sat}$$

$$-max\left\{ 0.0 \ , 5.691364 \times 10^{-30} \frac{\sigma^{1.5} T_l^{13.76} \left[1 + 13.25 \left(-\frac{1}{1.01325 \times 10^{11}} \frac{Dp}{Dt} \right)^{0.8} \right]^{0.5}}{1 - \frac{\rho_{ge}}{\rho_{le}}} \right.$$

$$\left. -0.069984 \left(\frac{A_e}{A_c} \right)^2 \rho_l V_l^2 \right\} \ , \tag{C-101}$$

where p_{sat} is the saturation pressure corresponding to T_l, the donor-cell liquid temperature; σ is the surface tension; ρ_{le} and ρ_{ge} are cell-edge densities; A_e and A_c are cell-edge and cell-center flow areas; and V_l is the momentum-solution liquid velocity. The term Dp/Dt is the substantial derivative of pressure and is given by

$$\frac{Dp}{Dt} = max\left\{ 1.0 \times 10^{-10} \ , -\frac{2 \left| V_l \right| (p_e - p_c)}{\Delta x} \right\} \ , \tag{C-102}$$

where V_l is again the momentum-solution liquid velocity, p_e is the cell-edge (choke-plane or throat) pressure returned by subroutine SOUND, p_c is the cell-center pressure, and Δx is the cell length.

The code then evaluates Bernoulli's equation to give the following cell-edge velocity:

$$V_{lc\,,\,Bernoulli} = \left[V_{lc}^2 + \frac{2\,Max\left\{ 0.0 \ , (p_c - p_{nuc}) \right\}}{\rho_{le}} \right]^{\frac{1}{2}} \tag{C-103}$$

where V_{lc} is the cell-center liquid velocity calculated from Eq. (7-44) as described in **Chapter 7**, ρ_{le} is the cell-edge liquid density as evaluated in subroutine SOUND, p_c is the cell-center pressure, and p_{nuc} is the cell-edge nucleation pressure [Eq. (C-101)].

The liquid choking velocity is taken as the maximum of the Bernoulli-predicted velocity and the homogeneous equilibrium sound speed as determined in SOUND. That is,

$$V_{le} = Max\left\{ a_{HE}\,,\, V_{le\,,\,Bernoulli} \right\}. \tag{C-104}$$

If a sound-speed multiplier was specified through the user-input INOPTS NAMELIST data, this is applied to the liquid choking velocity to give a final predicted value of

$$V_{le}^{p} = CHMLT1 \cdot Max\left\{ a_{HE}\,,\, V_{le\,,\,Bernoulli} \right\}. \tag{C-105}$$

If the liquid velocity as determined in the momentum solution is less than this maximum choking velocity, the flow is flagged as being unchoked and the calculation is ended. If, however, the liquid velocity determined in the momentum solution is greater than or equal to this maximum choking velocity, then the liquid velocity is reset to be equal to the choking velocity. In addition, a predicted steam/gas-mixture velocity is calculated according to

$$V_{ge}^{p} = V_{le}^{p} S\,, \tag{C-106}$$

where S is the slip ratio [as determined in Eq. (C-99)]. If the predicted steam/gas-mixture choking velocity, V_{ge}^{p}, has changed directions from the momentum-solution steam/gas-mixture velocity, V_g, the steam/gas-mixture choking velocity is reset to zero.

Two-Phase, Two-Component Fluid

If $1.0\times10^{-5} \le \alpha \le 0.999$ a two-phase, two-component choking calculation is done to determine the predicted choking velocities.

Equation (7-39) is extremely difficult to solve analytically. Thus, TRACE obtains the characteristic roots of Eq. (7-39) numerically. This method advantageously maintains generality and facilitates computations under different assumptions.

The solution of Eq. (7-39) requires that p_a, p_v, α, ρ_a, ρ_v, ρ_l, s_a, s_v, and s_l and their derivatives be specified at the cell edge, where the choking criterion is applied. However, these quantities are known only at the cell center. Direct use of the cell-center quantities yields erroneous results caused by the presence of steep gradients near the choking plane. Therefore, an estimate of the

thermodynamic state at the cell edge is necessary. To obtain this estimate, subroutine SOUND is called. In addition to determining the thermodynamic state at the cell edge, SOUND also calculates the homogeneous equilibrium sound speed which is used as a first estimate for the largest characteristic root. (When the non-homogeneous effects are not dominant, the desired root is close to the homogeneous equilibrium sound speed.) The procedure used by SOUND to arrive at the cell-edge thermodynamic state and the homogeneous equilibrium sound speed is described in full detail in ***Determining the Sound Speed*** above.

Because equilibrium is assumed to occur at the cell edge, subroutine THERMO is called to determine saturation properties at the cell edge corresponding to the cell-edge pressure, p_e, estimated in the call to SOUND. The cell-edge void fraction may then be calculated, such that

$$\alpha_e = \frac{\rho_{le} - \rho_{me}}{\rho_{le} - \rho_{ge}} \ , \tag{C-107}$$

where ρ_{me} is the cell-edge mixture density calculated by subroutine SOUND, and ρ_{le} and ρ_{ge} are the saturated liquid and steam/gas-mixture densities for a cell-edge pressure of p_e.

In addition, entropies and the quantities ρ_{le}^*, ρ_{ge}^*, s_{le}^*, s_{ge}^* necessary for evaluating the elements of matrix $\underline{\underline{B}}$ (as shown in Figure 7-25) are defined at the cell-edge, such that

$$s_{le} = c_{vl} \ln\left(\frac{T_e}{273.15}\right) \ , \tag{C-108}$$

$$s_{ve} = c_{vl} \ln\left(\frac{T_e}{273.15}\right) + \left(\frac{1}{\rho_{ve}} - \frac{1}{\rho_{le}}\right)\frac{dT}{dp_v} \ , \tag{C-109}$$

$$s_{ae} = c_{pa} \ln\left(\frac{T_e}{273.15}\right) - R_a \ln\left(\frac{max\{p_{ae}, 1.0 \times 10^{-5}\}}{1.0 \times 10^5}\right) \ , \tag{C-110}$$

$$s_{ge} = s_{ae}\left(\frac{\rho_{ae}}{\rho_{ge}}\right) + s_{ve}\left(1 - \frac{\rho_{ae}}{\rho_{ge}}\right) \ , \tag{C-111}$$

and

$$\rho_{le}^* \left(\frac{\partial \rho_{le}}{\partial p}\right)_T + \left(\frac{\partial \rho_{le}}{\partial T}\right)_p \frac{dT}{dp_v} \ , \tag{C-112}$$

$$\rho_{ve}^* = \left(\frac{\partial \rho_{ve}}{\partial p_v}\right)_T + \left(\frac{\partial \rho_{ve}}{\partial T}\right)_{p_v} \frac{dT}{dp_v} \ , \tag{C-113}$$

$$s^*_{ve} = \frac{1}{T_e}\left[\left(\frac{\partial e_{ve}}{\partial p_v}\right)_T + \left(\frac{\partial e_{ve}}{\partial T}\right)_{p_v}\frac{dT}{dp_v}\right] - \frac{p_{ve}}{\rho^2_{ve}T_e}\left[\left(\frac{\partial e_{ve}}{\partial p_v}\right)_T + \left(\frac{\partial e_{ve}}{\partial T}\right)_{p_v}\frac{dT}{dp_v}C\right], \tag{C-114}$$

and

$$s^*_{le} = \frac{1}{T_e}\left[\left(\frac{\partial e_{le}}{\partial p}\right)_T + \left(\frac{\partial e_{le}}{\partial T}\right)_{p}\frac{dT}{dp_v}\right] - \frac{p_e}{\rho^2_{le}T}\left[\left(\frac{\partial \rho_{le}}{\partial p}\right)_T + \left(\frac{\partial \rho_{le}}{\partial T}\right)_{p}\frac{dT}{dp_v}\right], \tag{C-115}$$

where T_e is the cell-edge saturation temperature corresponding to the cell-edge partial pressure of steam, p_{ve}; c_{vl} is the liquid constant-volume specific heat (defined in subroutine SETEOS); ρ_{ae}, ρ_{ve}, ρ_{ge}, and ρ_{le} are the cell-edge saturation densities corresponding to the cell-edge pressure, p_e; c_{pa} and R_a are the noncondensable-gas constant-pressure specific heat and the gas constant (both defined in subroutine SETEOS); and p_{ae} is the cell-edge partial pressure of the noncondensable gas as estimated by SOUND.

Next, CHOKE tries to determine the mass flux such that none of the characteristic roots of the governing system of partial differential equations given by Eqs. (7-5) through (7-9) has a positive real part and that the maximum root is zero.

The solution of Eq. (7-39) for a set of λ that includes $\lambda_1 = 0$ requires that

$$\det|\underline{\underline{B}}| = 0 . \tag{C-116}$$

Therefore, CHOKE first tries to solve Eq. (C-116).

To set up the elements of matrix $\underline{\underline{B}}$, CHOKE calculates first-guess approximations of the steam/gas-mixture and liquid cell-edge velocities from the homogeneous equilibrium sound speed, a_{HE}, and the cell-center momentum-solution slip value [computed in Eq. (C-99)], such that

$$V_{ge} = \frac{a_{HE}S\rho_{me}}{\alpha_e\rho_{ge}S + (1-\alpha_e)\rho_{le}} \tag{C-117}$$

and

$$V_{le} = \frac{V_{ge}}{(S + 1.0\times10^{-20})} , \tag{C-118}$$

where a_{HE} is the homogeneous equilibrium sound speed by returned subroutine SOUND, S is the slip ratio calculated from the momentum-solution steam/gas-mixture and liquid velocities [as in Eq. (C-99)], α_e is the cell-edge void fraction [computed in Eq. (C-107)], ρ_{me} is the cell-edge total mixture density returned by subroutine SOUND, and ρ_{le} and ρ_{ge} are the saturated cell-edge liquid and steam/gas-mixture densities for the cell-edge pressure p_e.

The virtual mass coefficient in the two phasic momentum equations [Eqs. (7-6) and (7-7)] is assumed to be fixed at a value of 10. Values for the virtual mass coefficient such as 5, 10, and 20 were found to give good mass-flow predictions when compared to data. The value of 10 was arbitrarily chosen because small variations in the virtual mass coefficient in this range (5 to 20) did not significantly affect the calculation.

The determinant of matrix $\underline{\underline{B}}$ may now be evaluated. An iterative procedure is used to vary the mixture velocity around a_{HE} until the rate of change of V_{ge} is less than (or equal to) $0.001a_{\mathrm{HE}}$ per iteration step while satisfying the requirement that the determinant be zero.

Once converged values of V_{ge} and V_{le} have been found using the iteration above, CHOKE sets up the elements in matrix $\underline{\underline{A}}$ and solves for the eigenvalues and eigenvectors of $\underline{\underline{A}}^{-1}\,\underline{\underline{B}}$. This is equivalent to solving Eq. (7-39) if the signs of the eigenvalues are reversed. CHOKE also checks that the absolute value of the root with the largest real part is indeed real and less than (or equal to) $0.01a_{\mathrm{HE}}$.

The predicted values of the choking velocities to be used in conjunction with the donor-cell conditions to give the correct mass-flow rate are now calculated, such that

$$V_{me}^{p} = \frac{\alpha_e \rho_{ge} V_{ge} + (1-\alpha_e)\rho_{le} V_{le}}{\rho_{mc}} \ , \tag{C-119}$$

$$V_{le}^{p} = CHMLT2 \cdot \frac{V_{me}^{p} \rho_{mc}}{\rho_{gc}\alpha_c S + \rho_{lc}(1-\alpha_c)} \ , \tag{C-120}$$

and

$$V_{ge}^{p} = S V_{le}^{p} \ , \tag{C-121}$$

where α_e is the cell-edge void fraction calculated in Eq. (C-107); ρ_{ge} and ρ_{le} are the cell-edge saturation densities corresponding to the cell-edge pressure, p_e; ρ_{gc}, ρ_{lc}, and ρ_{mc} are the cell-center steam/gas-mixture, liquid, and total mixture densities; S is the slip ratio calculated from the momentum-solution steam/gas-mixture and liquid velocities as in Eq. (C-99); and CHMLT2 is a user-input choked-flow multiplier.

If the mixture velocity as determined in the momentum solution is less than this predicted mixture velocity, the flow is flagged as being unchoked and the calculation is ended. If, however, the mixture velocity determined in the momentum solution is greater than (or equal to) the predicted mixture choking velocity, then the steam/gas-mixture, liquid, and total mixture velocities are reset to the predicted choking values.

Interpolation Region Between Subcooled and Two-Phase Models

If $1.0\times10^{-8} < \alpha < 1.0\times10^{-5}$, an interpolation between the subcooled-liquid and the two-phase, two-component choking calculation is performed to determine the predicted choking velocities.

Initially, liquid and steam/gas-mixture choking velocities are calculated using the two-phase, two-component model. In addition, liquid and steam/gas-mixture choking velocities are calculated using the subcooled-liquid choking model. These velocities are combined to produce the predicted liquid and steam/gas-mixture choking velocities using a linear interpolation in alpha, such that,

$$V_{le}^{p} = V_{l,sc} + \left(\frac{\alpha_c - \alpha_{min}}{\alpha_{max} - \alpha_{min}}\right)\left(V_{l,tp} - V_{l,sc}\right) \tag{C-122}$$

and

$$V_{ge}^{p} = V_{g,sc} + \left(\frac{\alpha_c - \alpha_{min}}{\alpha_{max} - \alpha_{min}}\right)\left(V_{g,tp} - V_{g,sc}\right) , \tag{C-123}$$

where $V_{l,sc}$ and $V_{g,sc}$ are the liquid and steam/gas-mixture choking velocities calculated using the subcooled-liquid model; $V_{l,tp}$ and $V_{g,tp}$ are the liquid and steam/gas-mixture choking velocities calculated using the two-phase, two-component choking model; α_c is the cell-center void fraction (either actual or equilibrium, depending on the value of L/D); and α_{min} and α_{max} are the limits on the void fraction for the interpolation region, currently set to 1.0×10^{-8} and 1.0×10^{-5}, respectively.

Single-Phase Vapor

If $\alpha > 0.999$, a single-phase vapor model is used to determine the choking velocities. Subroutine SOUND is first called to determine cell-edge conditions and the maximum mass flux as described in ***Determining the Sound Speed*** above. From this maximum mass flux, the value of the homogeneous equilibrium sound speed to be used in conjunction with donor-cell conditions to give correct mass flow is then calculated, such that

$$a_{HE} = \frac{G_{max}}{\rho_{mc}} , \tag{C-124}$$

where G_{max} is the critical mass flux returned by SOUND and ρ_{me} is the (donor-cell) cell-center mixture density calculated in Eq. (C-97). If a sound-speed multiplier was specified through the user-input INOPTS NAMELIST data, this is applied to the steam/gas-mixture sound speed to give a predicted steam/gas-mixture choking velocity of

$$V_{ge}^{p} = CHMLT2 \cdot a_{HE} \ . \tag{C-125}$$

If the momentum-solution steam/gas-mixture velocity, V_g, is less than this predicted steam/gas-mixture choking velocity, the flow is flagged as being unchoked and the calculation is ended. If, however, the steam/gas-mixture velocity as determined in the momentum solution is greater than or equal to the predicted choking velocity, then the steam/gas-mixture velocity is reset to be equal to the predicted steam/gas-mixture choking velocity. In addition, a predicted liquid velocity is calculated according to

$$V_{le}^{p} = \frac{V_{ge}^{p}}{(S + 1.0 \times 10^{-20})} \ , \tag{C-126}$$

where *S* is the slip ratio as determined in Eq. (C-99). If the predicted liquid choking velocity at the cell edge, V_{le}^{p}, has changed directions from the momentum-solution liquid velocity, V_l, it is reset to zero.

New-Time Choking Velocities

Finally, new-time phasic choking velocities are computed by time-averaging the old-time velocities with the predicted choking velocities just calculated, such that

$$V_{l}^{n+1} = 0.1\, V_{le}^{p} + 0.9\, V_{l}^{n} \tag{C-127}$$

and

$$V_{g}^{n+1} = 0.1\, V_{ge}^{p} + 0.9\, V_{g}^{n} \ , \tag{C-128}$$

where V_{le}^{p}, and V_{ge}^{p} are the predicted liquid and steam/gas-mixture choking velocities just calculated, and V_{l}^{n} and V_{g}^{n} are the old-time liquid and steam/gas-mixture velocities (either momentum solution or choking). This old-time, new-time method of weighting limits the change in the choking velocity for either phase to only 10% of the actual calculated change and ensures that the choking model lags slightly behind any pressure transients so that the effects of unnatural pressure changes caused by fluid inertia are limited.

This concludes the first pass through the choking model calculation. A second pass is necessary to evaluate the velocity derivatives. This is described in the next section.

Second-Pass for Velocity Derivatives

To calculate the derivatives of the liquid and steam/gas-mixture choking velocities with respect to pressure, a second pass through subroutine CHOKE is made with the pressure at cell center equal to 0.99 of the actual cell-center value. A second set of predicted liquid and steam/gas-mixture choking velocities is calculated for this 99% pressure value, using either a subcooled-liquid, a two-phase two-component fluid, or a superheated vapor calculation, exactly as was done in the first pass through subroutine CHOKE. These second-pass predicted choking velocities are then time-averaged to determine new-time choking velocities for the 99% pressure value in a manner similar to that used in the first pass, such that

$$V_{l,2nd}^{n+1} = 0.1\, V_{le,2nd}^{p} + 0.9\, V_{l}^{n} \tag{C-129}$$

and

$$V_{g,2nd}^{n+1} = 0.1\, V_{ge,2nd}^{p} + 0.9\, V_{g}^{n}\ , \tag{C-130}$$

where $V_{l,2nd}^{p}$ and $V_{g,2nd}^{p}$ are the second-pass predicted liquid and steam/gas-mixture choking velocities, and V_{l}^{n} and V_{g}^{n} are the old-time liquid and steam/gas-mixture velocities (either momentum-solution or choked).

Once the actual and second-pass new-time liquid and steam/gas-mixture choking velocities have been determined, the derivatives with respect to pressure are calculated as follows:

$$\frac{dV_l}{dp} \approx \frac{\Delta V_l}{\Delta p} = \frac{\left(V_l^{n+1} - V_{l,2nd}^{n+1}\right)}{(p - 0.99p)} \tag{C-131}$$

$$= 100.0\,\frac{\left(V_l^{n+1} - V_{l,2nd}^{n+1}\right)}{p}$$

and

$$\frac{dV_g}{dp} \approx 100.0\frac{\left(V_g^{n+1} - V_{g,2nd}^{n+1}\right)}{p}\ , \tag{C-132}$$

where V_{l}^{n+1} and V_{g}^{n+1} are the actual new-time choking velocities, and $V_{l,2nd}^{n+1}$ and $V_{g,2nd}^{n+1}$ are the second-pass, new-time choking velocities for a cell-center pressure of 0.99*p*.

With the determination of the new-time choking velocities and their derivatives with respect to pressure, the choking calculation performed in subroutines CHOKE and SOUND is now complete. At this point, the logic returns to the calling subroutine.

D

Tee Offtake Model: Computational Details

This Appendix describes in detail the calculational sequence of the TEE-component offtake model.

Nomenclature

The nomenclature that applies to this section follows:

A_j = flow area at the offtake (sidetube) entrance plane

C_1, C_2 = correlation constants in offtake model

D = diameter

f = interpolation weighting factor

g = gravitational acceleration constant

h_1 = the main-tube-junction cell liquid depth

h_b = critical entrainment height

h_c = the critical main-tube-junction cell liquid depth at which the liquid level just reaches the offtake entrance plane

h_{up}, h_{dn}, h_{sd} = characteristic heights for the upward, downward, and side-oriented offtake cases, respectively

R = nondimensional height ratio for offtake model

S = old-time slip ratio

V = velocity

W = mass flow rate in offtake model

WF_{HF} = horizontally stratified flow weighting factor, corresponds to Fortran variable WFHF in TRACE

x = offtake entrance-plane flow quality

Greek

α = gas volume fraction

ρ = density

Subscripts

1 = applies to the main-tube junction cell in the TEE

g = applies to the gas phase

l = applies to the liquid phase

m = total mixture

ot = applies to the offtake entrance plane

Superscripts

n = current-time quantity

$n+1$ = new-time quantity

Offtake Model Computational Sequence

Based on the offtake geometry and the liquid level conditions in the junction cell of the main tube, TRACE calculates the void fraction that exits out the main tube break. Upon entry into the subroutine that handles the offtake model calculation, several preliminary calculations take place. First, the offtake void fraction is initialized to be the same as the void fraction of the main-tube-junction cell. In addition, the average flow diameter of the offtake is calculated such that

$$D_{ot} = \sqrt{\frac{4.0 A_j}{\pi}} \ , \tag{D-1}$$

where A_j is the offtake flow area at the entrance plane.

Next, several tests are performed to determine whether to continue the calculation. TRACE is designed to handle only the case of two-phase, co-current flow out of the main tube break. If these conditions are not met, the offtake calculation is not attempted. This is also true if horizontal stratified flow does not exist in the main-tube-junction cell (as indicated by the Fortran variable

WFHF) or if the average diameter of the offtake is greater than or equal to the main-tube-junction cell average diameter.

However, if co-current, horizontal stratified flow out of the main-tube-junction cell does exist, TRACE continues with its preliminary calculations. The liquid level in the main-tube-junction cell is calculated from the void fraction and average diameter. In addition, an old-time slip ratio at the offtake entrance plane is calculated as the ratio of old-time gas and liquid velocities such that

$$S = \frac{V_g^n}{V_l^n} , \tag{D-2}$$

where V_g^n is the old-time, entrance-plane gas velocity and V_l^n is the old-time, entrance-plane liquid velocity. This slip is limited to a minimum value of 1.0×10^{-7}.

Once these preliminary calculations are complete, the logic splits to handle each of the three possible geometries: upward offtake, side-oriented offtake, or downward offtake. For each of the three possible offtake geometries, the offtake model solution procedure follows the same logic. Once a first prediction of the offtake void fraction is determined, three adjustments are performed to obtain the final offtake void-fraction prediction. The first adjustment is an interpolation based on liquid level to ensure that the predicted offtake void fraction tends toward certain limits as the liquid level approaches certain limits. For example, as the liquid level approaches the top of the main-tube-junction cell, the offtake void fraction for an upward offtake is expected to approach the value of the main-tube-junction cell void fraction. The second adjustment is a simple weighting using the horizontal weighting factor to ensure that the offtake void fraction tends toward the main-tube-junction cell void fraction as the flow moves away from a stratified-flow regime. The final adjustment is a limit to ensure that the volume of liquid or gas being entrained does not exceed the volume of the entrained component that exists in the main-tube-junction cell. Each of these adjustments is performed once the first prediction of the offtake void fraction is obtained, regardless of the offtake geometry. The specific algebraic equations used for these calculations are detailed in the appropriate subsection below.

Upward Offtake

For the case of the upward offtake, the major-flow component is the gas phase. The actual characteristic height for the upward offtake is approximated as

$$h_{up} = D_1 - h_1 , \tag{D-3}$$

where D_1 is the main-tube-junction cell average diameter and h_1 is the main-tube-junction cell liquid depth.

The major-phase mass-flow rate at the offtake entrance plane is calculated as

$$W_g = \alpha_{ot}^{n} \rho_g^{n+1} A_j V_g^{n+1} \quad , \tag{D-4}$$

where α_{ot}^{n} is the old-time offtake void fraction, ρ_g^{n+1} is the new-time donor-cell gas density, A_j is the offtake entrance-plane flow area, and V_g^{n+1} is the new-time entrance-plane gas velocity.

The critical entrainment height then may be calculated such that

$$h_b = \frac{C_1 W_g^{0.4}}{\left[g\rho_g^{n+1} (\rho_l^{n+1} - \rho_g^{n+1}) \right]^{0.2}} \quad , \tag{D-5}$$

where C_1 = 1.67 for an upward offtake, W_g is the major-phase (gas) mass-flow rate [as defined by Eq. (D-4)], g is the gravitational constant, ρ_g^{n+1} is the new-time donor-cell gas density, and ρ_{l}^{n+1} is the new-time donor-cell liquid density. This critical entrainment height is limited to a minimum value of 1.0×10^{-6}.

The offtake flow quality at the entrance plane is then

$$x = R^{3.25(1-R)^2} \quad , \tag{D-6}$$

where R is the nondimensional height ratio of h_{up} [as defined by Eq. (D-3)] to h_b [as defined by Eq. (D-5)], which is limited such that $0.0 \leq R \leq 1.0$.

Thus, the first prediction of the new-time offtake-model void fraction at the entrance plane is calculated as

$$\alpha_m^{n+1,1} = \frac{x\rho_l^{n+1}}{x\rho_l^{n+1} + (1-x)\rho_g^{n+1} S} \quad , \tag{D-7}$$

where x is the offtake entrance-plane flow quality [as defined by Eq. (D-6)], ρ_{l}^{n+1} is the new-time donor-cell liquid density, ρ_g^{n+1} is the new-time donor-cell gas density, and S is the old-time slip ratio [as defined by Eq. (D-2)]. At this point, three adjustments are performed to obtain the final offtake void-fraction prediction.

First, if the liquid level in the main-tube-junction cell is above the offtake entrance plane, the offtake void fraction predicted by Eq. (D-7) is modified to ensure that it approaches the value of the void fraction in the main-tube-junction cell as the liquid level reaches the top of the main-tube-junction cell. This interpolation is performed linearly with the main-tube-junction cell liquid depth, h_1, such that

$$\alpha_m^{n+1,2} = f\alpha_m^{n+1,1} + (1-f)\,\alpha_1^{n+1}, \tag{D-8}$$

where

$$f = \frac{h_1 - D_1}{h_c - D_1}, \tag{D-9}$$

h_1 is the main-tube-junction cell liquid depth, D_1 is the main-tube-junction cell average diameter, h_c is the critical main-tube-junction cell liquid depth at which the liquid level just reaches the offtake entrance plane, $\alpha_m^{n+1,1}$ is the first offtake void-fraction prediction [as defined by Eq. (D-7)], and α_1^{n+1} is the new-time main-tube-junction cell void fraction.

Next, this offtake void-fraction result is weighted using the horizontal stratified-flow weighting factor to ensure that the offtake void fraction tends toward the main-tube-junction cell void fraction as the flow, moves away from a stratified-flow regime such that

$$\alpha_m^{n+1,3} = WF_{HF}\,\alpha_m^{n+1,2} + (1 - WF_{HF})\,\alpha_1^{n+1}, \tag{D-10}$$

where WF_{HF} is the horizontal-flow weighting factor, $\alpha_m^{n+1,2}$ is the second offtake void-fraction prediction [as defined by Eq. (D-8)], and α_1^{n+1} is the new-time main-tube-junction cell void fraction.

Finally, the offtake void-fraction prediction is limited to ensure that the volume of liquid entrained does not exceed the volume that exists in the main-tube-junction cell such that

$$\alpha_{ot}^{n+1} = Max\left(\alpha_m^{n+1,3}, \alpha_1^{n+1}\right), \tag{D-11}$$

where $\alpha_m^{n+1,3}$ is the third offtake void-fraction prediction [as defined by Eq. (D-10)] and α_1^{n+1} is the new-time main-tube-junction cell void fraction. At this point, the new-time offtake void fraction, α_{ot}^{n+1}, is returned to the calling routine.

Side-Oriented Offtake

For the case of the side-oriented offtake, the major-flow component may be either the gas phase or the liquid phase. When the liquid level in the main tube is below the offtake center, the gas phase is the major-flow component and liquid entrainment may occur. However, if the liquid level in the main tube is above the offtake center, the liquid phase becomes the major-flow component and gas entrainment may be possible. The following description first details the case of when the gas phase is the major-flow component and liquid entrainment may occur, and then outlines the case when the liquid phase is the major-flow component and gas entrainment may be possible.

Liquid Entrainment Scenario

For the case of the side-oriented offtake with a gas major-flow component (the case of possible liquid entrainment), the actual characteristic height is approximated as

$$h_{sd} = h_1 - 0.5 D_1 \ , \tag{D-12}$$

where h_1 is the main-tube-junction cell liquid depth and D_1 is the main-tube-junction cell average diameter. Notice that for this offtake configuration, h_{sd} is a negative value, which later causes the nondimensional height ratio, R, to also be negative in value.

The major-phase mass-flow rate at the offtake entrance plane is calculated as

$$W_g = \alpha_{ot}^{n} \rho_g^{n+1} A_j V_g^{n+1} \ , \tag{D-13}$$

where α_{ot}^{n} is the old-time offtake void fraction, ρ_g^{n+1} is the new-time donor-cell gas density, A_j is the offtake entrance-plane flow area, and V_g^{n+1} is the new-time entrance-plane gas velocity.

The critical entrainment height then may be calculated such that

$$h_b = \frac{C_1 W_g^{0.4}}{\left[g \rho_g^{n+1} (\rho_l^{n+1} - \rho_g^{n+1}) \right]^{0.2}} \ , \tag{D-14}$$

where $C_1 = 0.69$ for a side-oriented offtake with a gas major-flow component, W_g is the major-phase (gas) mass-flow rate [as defined by Eq. (D-13)], g is the gravitational constant, ρ_g^{n+1} is the new-time donor-cell gas density, and ρ_{l}^{n+1} is the new-time donor-cell liquid density. This critical

entrainment height is limited to be no less than the larger of 1.0×10^{-6} and $0.5D_{ot}$ [see Eq. (D-1)].

The offtake flow quality at the entrance plane is then

$$x = x_o^{(1+C_2R)}[1-0.5R(1+R)x_o^{(1-R)}]^{0.5}, \tag{D-15}$$

where

$$x_o = \frac{1.15}{1+\sqrt{\frac{\rho_l^{n+1}}{\rho_g^{n+1}}}}, \tag{D-16}$$

R is the nondimensional height ratio of h_{sd} [as defined by Eq. (D-12)] to h_b [as defined by Eq. (D-14)], ρ_l^{n+1} is the new-time donor-cell liquid density, ρ_g^{n+1} is the new-time donor-cell gas density, and C_2 = 1.00 for liquid entrainment.

Thus, the first prediction of the new-time offtake-model void fraction at the entrance plane is calculated as

$$\alpha_m^{n+1,1} = \frac{x\rho_l^{n+1}}{x\rho_l^{n+1}+(1-x)\rho_g^{n+1}S}, \tag{D-17}$$

where x is the offtake entrance-plane flow quality [as defined by Eq. (D-15)], ρ_l^{n+1} is the new-time donor-cell liquid density, ρ_g^{n+1} is the new-time donor-cell gas density, and S is the old-time slip ratio [as defined by Eq. (D-2)]. At this point, three adjustments are performed to obtain the final offtake void-fraction prediction.

First, if the liquid level in the main-tube-junction cell is between the bottom and the centerline of the offtake entrance, the offtake void fraction predicted by Eq. (D-17) is modified to ensure that it approaches the value of the void fraction in the main-tube-junction cell as the diameter of the offtake approaches the diameter of the main-tube-junction cell. This interpolation is performed linearly with the main-tube-junction cell liquid depth, h_1 such that

$$\alpha_m^{n+1,2} = f\alpha_m^{n+1,1} + (1-f)\alpha_1^{n+1}, \tag{D-18}$$

where

$$f = \frac{h_c}{h_1} \ , \tag{D-19}$$

and where h_c is the critical main-tube-junction cell liquid depth at which the liquid level just reaches the offtake entrance, h_1 is the main-tube-junction cell liquid depth, $\alpha_m^{n+1,1}$ is the first offtake void-fraction prediction [as defined by Eq. (D-17)], and α_1^{n+1} is the new-time main-tube-junction cell void fraction.

Next, this offtake void-fraction result is weighted using the horizontal stratified-flow weighting factor to ensure that the offtake void fraction tends toward the main-tube-junction cell void fraction as the flow moves away from a stratified-flow regime such that

$$\alpha_m^{n+1,3} = WF_{HF} \cdot \alpha_m^{n+1,2} + (1 - WF_{HF})\, \alpha_1^{n+1} \ , \tag{D-20}$$

where WF_{HF} is the horizontal-flow weighting factor, $\alpha_m^{n+1,2}$ is the second offtake void-fraction prediction [as defined by Eq. (D-18)], and α_1^{n+1} is the new-time main-tube-junction cell void fraction.

Finally, the offtake void-fraction prediction is limited to ensure that the volume of liquid entrained does not exceed the volume that exists in the main-tube-junction cell such that

$$\alpha_{ot}^{n+1} = Max\left(\alpha_m^{n+1,3}, \alpha_1^{n+1}\right) \ , \tag{D-21}$$

where $\alpha_m^{n+1,3}$ is the third offtake void-fraction prediction [as defined by Eq. (D-20)] and α_1^{n+1} is the new-time main-tube-junction cell void fraction. At this point, the new-time offtake void fraction, $\alpha_{\mathrm{ot}}^{n+1}$, is returned to the calling routine.

Gas Entrainment Scenario

For the case of the side-oriented offtake with a liquid major-flow component (the case of possible gas entrainment), the actual characteristic height is approximated as

$$h_{sd} = h_1 - 0.5 D_1 \ , \tag{D-22}$$

where h_1 is the main-tube-junction cell liquid depth and D_1 is the main-tube-junction cell average diameter.

The major-phase mass-flow rate at the offtake entrance plane is calculated as

$$W_l = (1 - \alpha_{ot}^n)\rho_l^{n+1} A_j V_l^{n+1} \ , \tag{D-23}$$

where $\alpha_{\rm ot}^n$ is the old-time offtake void fraction, $\rho_{\rm l}^{n+1}$ is the new-time donor-cell liquid density, A_j is the offtake entrance-plane flow area, and $V_{\rm l}^{n+1}$ is the new-time entrance-plane liquid velocity.

The critical entrainment height then may be calculated such that

$$h_b = \frac{C_1 W_l^{0.4}}{\left[g\rho_l^{n+1}(\rho_l^{n+1} - \rho_g^{n+1})\right]^{0.2}} \ , \tag{D-24}$$

where $C_1 = 0.75$ for a side-oriented offtake with a liquid major-flow component, W_l is the major-phase (liquid) mass-flow rate [as defined by Eq. (D-23)], g is the gravitational constant, $\rho_{\rm l}^{n+1}$ is the new-time donor-cell liquid density, and ρ_g^{n+1} is the new-time donor-cell gas density. This critical entrainment height is limited to be no less than the larger of 1.0×10^{-6} and $0.5D_{ot}$ [see Eq. (D-1)].

The offtake flow quality at the entrance plane is then

$$x = x_o^{(1+C_2R)}\left[1 - 0.5R(1+R)x_o^{(1-R)}\right]^{0.5} \tag{D-25}$$

for the range

$$0.0 \le R \le 0.9 \ ,$$

where

$$x_o = \frac{1.15}{1 + \sqrt{\dfrac{\rho_l^{n+1}}{\rho_g^{n+1}}}} \ , \tag{D-26}$$

R is the nondimensional height ratio of h_{sd} [as defined by Eq. (D-22)] to h_b [as defined by Eq. (D-24)], $\rho_{\rm l}^{n+1}$ is the new-time donor-cell liquid density, ρ_g^{n+1} is the new-time donor-cell gas density, and $C_2 = 1.09$ for gas entrainment.

In Eq. (D-25), as R approaches 1, x approaches 0 very rapidly. To avoid an exponential approach toward zero, the term $R(1+R)$ was replaced with a linear function for the range $0.9 \le R \le 1.0$, resulting in the following formulation for flow quality:

$$x = -10.0\, x_o^{(1+C_2R)} [1 - 0.855\, x_o^{0.1}]^{0.5} (R - 1.0) \tag{D-27}$$

for the range

$$0.9 \le R \le 1.0 \ ,$$

where x_o is defined by Eq. (D-26), $C_2 = 1.09$ for gas entrainment, and R is again the nondimensional height ratio.

Thus, the first prediction of the new-time offtake-model void fraction at the entrance plane is calculated as

$$\alpha_m^{n+1,1} = \frac{x\rho_l^{n+1}}{x\rho_l^{n+1} + (1-x)\rho_g^{n+1} S} \ , \tag{D-28}$$

where x is the offtake entrance-plane flow quality [as defined by Eq. (D-25) or Eq. (D-27)], ρ_l^{n+1} is the new-time donor-cell liquid density, ρ_g^{n+1} is the new-time donor-cell gas density, and *S* is the old-time slip ratio [as defined by Eq. (D-2)]. At this point, three adjustments are performed to obtain the final offtake void-fraction prediction.

First, if the liquid level in the main-tube-junction cell is between the centerline and the top of the offtake entrance, the offtake void fraction predicted by Eq. (D-28) is modified to ensure that it approaches the value the of the void fraction in the main-tube-junction cell as the diameter of the offtake approaches the diameter of the main-tube-junction cell. This interpolation is performed linearly with the main-tube-junction cell liquid depth, h_1 such that

$$\alpha_m^{n+1,2} = f\alpha_m^{n+1,1} + (1-f)\alpha_1^{n+1} \ , \tag{D-29}$$

where

$$f = \frac{D_1 - h_c}{D_1 - h_1} \ , \tag{D-30}$$

D_1 is the main-tube-junction cell average diameter, h_c is the critical main-tube-junction cell liquid depth at which the liquid level just reaches the offtake entrance, h_1 is the main-tube-junction cell liquid depth, $\alpha_m^{n+1,1}$ is the first offtake void-fraction prediction [as defined by Eq. (D-28)], and α_1^{n+1} is the new-time main-tube-junction cell void fraction.

Next, this offtake void-fraction result is weighted using the horizontal stratified-flow weighting factor to ensure that the offtake void fraction tends toward the main-tube-junction cell void fraction as the flow moves away from a stratified-flow regime such that

$$\alpha_m^{n+1,3} = WF_{HF}\,\alpha_m^{n+1,2} + (1 - WF_{HF})\,\alpha_1^{n+1} \ , \tag{D-31}$$

where WF_{HF} is the horizontal-flow weighting factor, $\alpha_m^{n+1,2}$ is the second offtake void-fraction prediction [as defined by Eq. (D-29)], and α_1^{n+1} is the new-time main-tube-junction cell void fraction.

Finally, the offtake void-fraction prediction is limited to ensure that the volume of gas entrained does not exceed the volume that exists in the main-tube-junction cell such that

$$\alpha_{\rm ot}^{n+1} = Min\left(\alpha_m^{n+1,3}, \alpha_1^{n+1}\right) \ , \tag{D-32}$$

where $\alpha_m^{n+1,3}$ is the third offtake void-fraction prediction [as defined by Eq. (D-31)] and α_1^{n+1} is the new-time main-tube-junction cell void fraction. At this point, the new-time offtake void fraction, $\alpha_{\rm ot}^{n+1}$, is returned to the calling routine.

Downward Offtake

For the case of the downward offtake, the major-flow component is the liquid phase. The actual characteristic height for the downward offtake is approximated as

$$h_{dn} = h_1 \ , \tag{D-33}$$

where h_1 is the main-tube-junction cell liquid depth.

The major-phase mass-flow rate at the offtake entrance plane is calculated as

$$W_l = (1 - \alpha_{ot}^n)\rho_l^{n+1} A_j V_l^{n+1} \ , \tag{D-34}$$

where α_{ot}^{n} is the old-time offtake void fraction, ρ_{l}^{n+1} is the new-time donor-cell liquid density, A_j is the offtake entrance-plane flow area, and V_{l}^{n+1} is the new-time entrance-plane liquid velocity.

The critical entrainment height then may be calculated such that

$$h_b = \frac{C_1 W_l^{0.4}}{\left[g\rho_l^{n+1}(\rho_l^{n+1} - \rho_g^{n+1})\right]^{0.2}} , \tag{D-35}$$

where $C_1 = 1.50$ for a downward offtake, W_l is the major-phase (liquid) mass-flow rate [as defined by Eq. (D-34)], g is the gravitational constant, ρ_{l}^{n+1} is the new-time donor-cell liquid density, and ρ_g^{n+1} is the new-time donor-cell gas density. This critical entrainment height is limited to a minimum value of 1.0×10^{-6}.

The offtake flow quality at the entrance plane is then

$$x = x_o^{2.5R}[1 - 0.5R(1+R)x_o^{(1-R)}]^{0.5} \tag{D-36}$$

for the range

$$0.0 \le R < 0.9 ,$$

where

$$x_o = \frac{1.15}{1 + \sqrt{\dfrac{\rho_l^{n+1}}{\rho_g^{n+1}}}} , \tag{D-37}$$

R is the nondimensional height ratio of h_{dn} [as defined by Eq. (D-33)] to h_b [as defined by Eq. (D-35)], ρ_{l}^{n+1} is the new-time donor-cell liquid density, and ρ_g^{n+1} is the new-time donor-cell gas density.

In Eq. (D-36), as R approaches 1, x approaches 0 very rapidly. To avoid an exponential approach toward zero, the term $R(1+R)$ was replaced with a linear function for the range $0.9 \le R \le 1.0$ resulting in the following formulation for flow quality:

$$x = -10.0\, x_o^{2.5R}\left[1 - 0.855\, x_o^{0.1}\right]^{0.5}(R - 1.0) \tag{D-38}$$

for the range

$$0.9 \le R \le 1.0 \ ,$$

where x_o is defined by Eq. (D-35) and R is again the nondimensional height ratio.

Thus, the first prediction of the new-time model void fraction at the entrance plane is calculated as

$$\alpha_m^{n+1,1} = \frac{x\rho_l^{n+1}}{x\rho_l^{n+1} + (1-x)\rho_g^{n+1} S} \ , \tag{D-39}$$

where x is the offtake entrance-plane flow quality [as defined by Eq. (D-36) or Eq. (D-38)], ρ_1^{n+1} is the new-time donor-cell liquid density, ρ_g^{n+1} is the new-time donor-cell gas density, and S is the old-time slip ratio [as defined by Eq. (D-2)]. At this point, three adjustments are performed to obtain the final offtake void-fraction prediction.

First, if the liquid level in the main-tube-junction cell is below the offtake entrance plane, the offtake void fraction predicted by Eq. (D-39) is modified to ensure that it approaches the value of the void fraction in the main-tube-junction cell as the liquid level reaches the bottom of the main-tube-junction cell. This interpolation is performed linearly with the main-tube-junction cell liquid depth, h_1 such that

$$\alpha_m^{n+1,2} = f\alpha_m^{n+1,1} + (1-f)\,\alpha_1^{n+1} \ , \tag{D-40}$$

where

$$f = \frac{h_1}{h_c} \ , \tag{D-41}$$

h_1 is the main-tube-junction cell liquid depth, h_c is the critical main-tube-junction cell liquid depth at which the liquid level reaches the offtake entrance plane, $\alpha_m^{n+1,1}$ is the first offtake void-fraction prediction [as defined by Eq. (D-39)], and α_1^{n+1} is the new-time main-tube-junction cell void fraction.

Next, this offtake void-fraction result is weighted using the horizontal stratified-flow weighting factor to ensure that the offtake void fraction tends toward the main-tube-junction cell void fraction as the flow moves from a stratified-flow regime such that

$$\alpha_m^{n+1,3} = WF_{HF} \cdot \alpha_m^{n+1,2} + (1 - WF_{HF})\, \alpha_1^{n-1} \ , \tag{D-42}$$

where WF_{HF} is the horizontal-flow weighting factor, $\alpha_m^{n+1,2}$ is the second offtake void-fraction prediction [as defined by Eq. (D-40)], and α_1^{n+1} is the new-time main-tube-junction cell void fraction.

Finally, the offtake void-fraction prediction is limited to ensure that the volume of gas entrained does not exceed the volume that exists in the main-tube-junction cell such that

$$a_{ot}^{n+1} = Min\left(\alpha_m^{n+1,3}, \alpha_1^{n+1}\right) \ , \tag{D-43}$$

where $\alpha_m^{n+1,3}$ is the third offtake void-fraction prediction [as defined by Eq. (D-42)] and α_1^{n+1} is the new-time main-tube-junction cell void fraction. At this point, the new-time, offtake void fraction, $\alpha_{\mathrm{ot}}^{n+1}$, is returned to the calling routine.